Reinforced Soil Engineering

Advances in Research and Practice

edited by

Hoe I. Ling
Columbia University
New York, New York, U.S.A.

Dov Leshchinsky
University of Delaware
Newark, Delaware, U.S.A.

Fumio Tatsuoka
University of Tokyo
Tokyo, Japan

MARCEL DEKKER

MARCEL DEKKER, INC. NEW YORK • BASEL

Library of Congress Cataloging-in-Publication Data
A catalog record for this book is available from the Library of Congress.

ISBN: 0-8247-4254-0

This book is printed on acid-free paper.

Headquarters
Marcel Dekker, Inc., 270 Madison Avenue, New York, NY 10016, U.S.A.
tel: 212-696-9000; fax: 212-685-4540

Distribution and Customer Service
Marcel Dekker, Inc., Cimarron Road, Monticello, New York 12701, U.S.A.
tel: 800-228-1160; fax: 845-796-1772

Eastern Hemisphere Distribution
Marcel Dekker AG, Hutgasse 4, Postfach 812, CH-4001 Basel, Switzerland
tel: 41-61-260-6300; fax: 41-61-260-6333

World Wide Web
http://www.dekker.com

The publisher offers discounts on this book when ordered in bulk quantities. For more information, write to Special Sales/Professional Marketing at the headquarters address above.

Current printing (last digit):

10 9 8 7 6 5 4 3 2 1

PRINTED IN THE UNITED STATES OF AMERICA

Civil and Environmental Engineering

A Series of Reference Books and Textbooks

Editor

Michael D. Meyer

Department of Civil and Environmental Engineering
Georgia Institute of Technology
Atlanta, Georgia

1. **Preliminary Design of Bridges for Architects and Engineers**
   Michele Melaragno
2. **Concrete Formwork Systems**
   Awad S. Hanna
3. **Multilayered Aquifer Systems: Fundamentals and Applications**
   Alexander H.-D. Cheng
4. **Matrix Analysis of Structural Dynamics: Applications and Earthquake Engineering**
   Franklin Y. Cheng
5. **Hazardous Gases Underground: Applications to Tunnel Engineering**
   Barry R. Doyle
6. **Cold-Formed Steel Structures to the AISI Specification**
   Gregory J. Hancock, Thomas M. Murray, and Duane S. Ellifritt
7. **Fundamentals of Infrastructure Engineering: Civil Engineering Systems: Second Edition, Revised and Expanded**
   Patrick H. McDonald
8. **Handbook of Pollution Control and Waste Minimization**
   edited by Abbas Ghassemi
9. **Introduction to Approximate Solution Techniques, Numerical Modeling, and Finite Element Methods**
   Victor N. Kaliakin
10. **Geotechnical Engineering: Principles and Practices of Soil Mechanics and Foundation Engineering**
    V. N. S. Murthy
11. **Estimating Building Costs**
    Calin M. Popescu, Kan Phaobunjong, and Nuntapong Ovararin
12. **Chemical Grouting and Soil Stabilization: Third Edition, Revised and Expanded**
    Reuben H. Karol

13. **Multifunctional Cement-Based Materials**
Deborah D. L. Chung
14. **Reinforced Soil Engineering: Advances in Research and Practice**
Hoe I. Ling, Dov Leshchinsky, and Fumio Tatsuoka

Additional Volumes in Production

Project Scheduling Handbook
Jonathan F. Hutchings

Preface

This book consists of 25 chapters focusing on the latest developments in reinforced soil technology. These chapters address geotechnical earthquake issues, as well as applications and case histories from several countries. Several chapters are based on presentations given during the Columbia Workshop (the International Workshop on Seismic Design of Reinforced Soil Structures).

The Columbia Workshop was part of a project called "Seismic Performance and Design of Reinforced Soil Structures with Reference to Lessons Learned from the 1999 Earthquakes of Taiwan and Turkey," which was funded by the Geotechnical Program of the National Science Foundation (PIs: Hoe I. Ling and Dov Leshchinsky; Grant No. CMS-0084449; Program Director: Dr. Richard J. Fragaszy). The workshop was a $1\frac{1}{2}$-day event featuring speakers and panelists from leading institutions in the United States, Canada, Japan, Taiwan, and Turkey. About 40 researchers and engineers attended the workshop.

The study of seismic performance of reinforced soil structures has received much attention since the 1995 Kobe earthquake, and especially since the failures reported during the 1999 Ji-Ji earthquake in Taiwan. In recent years, the National Science Foundation and some state departments of transportation have initiated research projects on this subject. In Japan, works were initiated by various groups of researchers at academic institutions and government agencies. However, there has been rather limited discussion among the researchers working on this subject. Therefore, the need arose to document lessons learned from past experience, to share knowledge about ongoing achievements in this field, and to allow for intensive discussion by identifying problems noted and data gathered.

The Columbia Workshop was held at the Faculty House of Columbia University on October 30 and 31, 2000. It was inaugurated by Professor Rimas Vaiacitis, Chair of the Department of Civil Engineering and Engineering Mechanics, Columbia University. The first day consisted of 14 invited presentations. (Information on the meeting, including abstracts and representative publications of the presenters, is also available at http://www.civil.columbia.edu/~ling/taiwan.) Following invited presentations, three discussion sessions were organized, focusing on design issues, testing and experimental studies, and numerical methods and modeling. These sessions were chaired by Jerry DiMaggio of FHWA, Fumio Tatsuoka of the University of Tokyo, and Andrew Whittle of MIT. The workshop was subsidized by the Federal Highway Administration through the arrangement of Mr. Mike Adams, with matching funds from the Dean's Office of the School of Engineering and Applied Science at Columbia University.

The case histories presented here help to advance the state of the art in this field; the failures documented should not discourage us from using existing technologies or developing new technologies. The knowledge shared in this workshop led to the organizing of two special technical sessions during the International Conference on Geosynthetics in Nice, France, in September 2002.

The contributions of all authors herein are greatly appreciated. We acknowledge the efforts of Professor Vaicaitis, especially during the editing of the book. Hoe Ling is supported by an NSF Career Award (CMS-0092739; Program Director: Dr. Clifford Astill). Last but not least, we express sincere thanks to the editors at Marcel Dekker, Inc., especially Mr. Michael Deters, for his efforts in making this book a reality.

Hoe I. Ling
Dov Leshchinsky
Fumio Tatsuoka

Contents

Contributors

A. W. Cadden Schnabel Engineering Associates, Inc., West Chester, Pennsylvania, U.S.A.

Luiz E. P. Campos Federal University of Bahia, Salvador, Brazil

Soon Hoe Chew Department of Civil Engineering, National University of Singapore, Singapore

Nelson N. S. Chou Genesis Group/Taiwan, Taipei, Taiwan

M. Dechasakulsom Road Research and Development Center, Bangkok, Thailand

J. H. Dixon Tensar International, Blackburn, U.K.

André R. S. Fahel Department of Civil and Environmental Engineering, University of Brasilia, Brasilia, Brazil

Chia-Cheng Fan Genesis Group/Taiwan, Taipei, Taiwan

Li Guangxin Department of Hydraulic Engineering, Tsinghua University, Beijing, China

Erol Guler Bogazici University, Istanbul, Turkey

B. N. Huang Department of Civil Engineering, National Cheng Kung University, Tainan, Taiwan

Ching-Chuan Huang Department of Civil Engineering, National Cheng Kung University, Tainan, Taiwan

S. Ihara Kumagai-gumi Co. Ltd., Tokyo, Japan

Muhannad Ismeik Al-Isra University, Amman, Jordan

G. Y. Jean Department of Civil Engineering, National Cheng Kung University, Tainan, Taiwan

V. N. Kaliakin Department of Civil and Environmental Engineering, University of Delaware, Newark, Delaware, U.S.A.

G. P. Karunaratne Department of Civil Engineering, National University of Singapore, Singapore

Toshinori Kawabata Department of Agriculture and Environmental Engineering, Kobe University, Kobe, Japan

Kenichi Kojima Railway Technical Research Institute, Tokyo, Japan

Junichi Koseki Institute of Industrial Science, University of Tokyo, Tokyo, Japan

Dov Leshchinsky Department of Civil and Environmental Engineering, University of Delaware, Newark, Delaware, U.S.A.

A. L. Leu Department of Civil Engineering, National Cheng Kung University, Tainan, Taiwan

Hoe I. Ling Department of Civil Engineering and Engineering Mechanics, Columbia University, New York, New York, U.S.A.

Sik-Cheung Robert Lo Department of Civil Engineering, University of New South Wales, Sydney, Australia

C. H. Loh National Center for Research on Earthquake Engineering, Taipei, Taiwan

James R. Martin II Department of Civil Engineering, Virginia Tech, Blacksburg, Virginia, U.S.A.

S. F. Masri Department of Civil Engineering, University of Southern California, Los Angeles, California, U.S.A.

Yoshiyuki Mohri National Research Institute of Agriculture Engineering, Tsukuba, Japan

Yulman Munaf Department of Civil Engineering, University of Missouri–Rolla, Rolla, Missouri, U.S.A.

Chiew Chiat Ng Department of Civil Engineering, National University of Singapore, Singapore

Y. Okabe Tokyo Soil Research Co., Tsukuba, Japan

C. Guney Olgun Department of Civil Engineering, Virginia Tech, Blacksburg, Virginia, U.S.A.

Ennio M. Palmeira Department of Civil and Environmental Engineering, University of Brasilia, Brasilia, Brazil

G. S. Paxson Schnabel Engineering Associates, Inc., West Chester, Pennsylvania, U.S.A.

C. M. Reith Schnabel Engineering Associates, Inc., West Chester, Pennsylvania, U.S.A.

G. Sembenelli SC Sembenelli Consulting, Milan, Italy

P. Sembenelli SC Sembenelli Consulting, Milan, Italy

H. Y. Shan Department of Civil Engineering, National Chiao Tung University, Hsinchu, Taiwan

A. W. Smyth Department of Civil Engineering and Engineering Mechanics, Columbia University, New York, New York, U.S.A.

Akihiro Takahashi Tokyo Institute of Technology, Tokyo, Japan

Jiro Takemura Asian Institute of Technology, Bangkok, Thailand

Siew Ann Tan Department of Civil Engineering, National University of Singapore, Singapore

S. Tani National Research Institute of Agricultural Engineering, Tsukuba, Japan

Masaru Tateyama Railway Technical Research Institute, Tokyo, Japan

Fumio Tatsuoka Department of Civil Engineering, University of Tokyo, Tokyo, Japan

W. Voskamp Colbond Geosynthetics, Arnhem, The Netherlands

Kenji Watanabe Railway Technical Research Institute, Tokyo, Japan

J. F. Wu Department of Civil Engineering, National Cheng Kung University, Tainan, Taiwan

Y. Yokota Maeda Kousen Co. Ltd., Fukui, Japan

Dongyi Yue Department of Earth and Environmental Engineering, Columbia University, New York, New York, U.S.A.

Wang Zhao Tsinghua University, Beijing, China

1

Civil and Environmental Applications of Geosynthetics

Hoe I. Ling
Columbia University, New York, New York, U.S.A.

1 INTRODUCTION

Geosynthetics include exclusively manmade polymeric products such as geotextiles, geogrids, geonets, geomembranes, geosynthetic clay liners, and geocomposites. The term "geosynthetic" is used in favor of geotextiles and geofabrics because (1) additional polymeric products are being developed and used with soils and (2) the application is becoming more diversified.

Polypropylene, polyester, polyethylene, polyamide, polyvinyl choride, and polystyrene are the major polymers used to manufacture geosynthetics. It is not the properties of the polymers, but the properties of the final polymeric products that are of interest to civil and environmental engineering applications. Geosynthetics are used as part of the geotechnical, transportation, and environmental facilities. Geosynthetic products perform five main functions: separation, reinforcement, filtration, drainage, and containment (hydraulic barrier). However, in most applications, geosynthetics typically perform more than one major function.

2 TESTING STANDARDS AND DESIGN

2.1 Testing Standards

Some basic standards used for geotextiles are adopted from the textile industries. However, geotechnical engineers realized the deficiencies and started to develop the standards relevant to their applications. The American Society for Testing and Materials (ASTM) is one developer of standardized testing procedures for different geosynthetics. Most testing standards adopted or developed in other countries are outgrowths of ASTM standards. The Geosynthetic Research Institute (GRI) also provides testing standards to serve industrial needs, especially when related ASTM standards have not been developed. GRI standards are usually removed as related ASTM standards become available.

ASTM standards, developed under Committee D35 for Geosynthetics, are listed in the Appendix. These standards were developed under several subcommittees: terminology, mechanical properties, endurance properties, permeability and filtration, geosynthetic clay liners, geosynthetic erosion control, and geomembranes. New standards are constantly being developed. Details of test standards are published in ASTM (2000).

While ASTM standards are *index tests*, many civil engineering designs and applications require the geosynthetic materials to be tested with site-specific soils, with the testing conditions representing those in the field. These kinds of tests are known as *performance tests*.

2.2 Design by Function

Different organizations, agencies, and manufacturers provide design guidelines for geosynthetic applications. These design methods are determined by cost, specification (design by specification), or function (design by function). Public agencies have widely adopted the design-by-specification method. The minimum required value of the geosynthetic properties used in a particular application is specified.

In the design-by-function method, the primary function of the geosynthetic material is identified. The available and required value of the particular property for that function is assessed to give a factor of safety (FS):

$$FS = \frac{\text{allowable property from testing}}{\text{required property for design}}$$

Designs require a factor of safety greater than unity to account for various uncertainties.

3 GEOTEXTILES, GEOGRIDS, AND GEONETS/GEOCOMPOSITES

Geotextiles are the earliest type of multifunctional geosynthetic material. Their functions include reinforcement, separation, filtration, and drainage. When impregnated, they are used as containment. However, some newly developed products perform better than geotextiles in certain functions. For example, geogrids are developed specifically to tensile reinforce soil, while geonets are used to convey large-capacity flow. Although geotextile may also be made impermeable and used as containment by spraying bitumen or other polymers on it, geomembranes should be considered for a watertight containment system. The functions of geotextiles, geogrids, and geonets are described collectively in this section, where one material can be referred to the other.

Geotextile sheets are manufactured from fibers or yarns. Polymers are melted and forced through a spinneret to form fibers and yarns. They are subsequently hardened and stretched. The manufacturing process produces woven or nonwoven geotextiles. In producing woven fabrics, conventional textile-weaving methodologies are used. For the nonwoven fabrics, the filaments are bonded together by thermal, chemical, or mechanical means (i.e., heating, using resin, or needle-punching).

Geogrids are mainly used as tensile reinforcement. Although biaxial geogrids are available, most geogrids are manufactured to function uniaxially. In manufacturing uniaxial geogrids, circular holes are punched on the polymer sheet, which is subsequently drawn to improve the mechanical properties. For biaxial geogrids, square holes are made on the polymer sheet, which is then drawn longitudinally and transversely. For some geogrids, the junctions between the longitudinal and transverse ribs are bonded by heating or knit-stitching. Geogrid manufactured from yarns are typically coated with a polymer, latex, or bitumen. Geogrids have higher stiffness and strength than most geotextiles.

The chapter now describes some major applications of geotextiles and related products.

3.1 Reinforcement of Steep Slopes, Retaining Structures, and Embankments

Geotextiles and geogrids are used to tensile reinforce steep slopes, retaining structures, and embankments constructed over soft foundation (Fig. 1). Sheets of geotextile/geogrid are embedded horizontally in these soil structures. The shear stress developed in the soil mass is transferred to the geotextile sheets as tensile force through friction. The tensile strength of geotextile/geogrid and its frictional resistance with the soil are the primary items required for design.

The tensile strength of geosynthetic is obtained from the wide-width test. The ASTM standard specifies an aspect ratio (width-to-length) of 2 (i.e., 20 cm to 10 cm). Soil confinement may increase the stiffness and strength of nonwoven spun-bonded needle-punched geotextile because of the interactions among the fibers, but it has negligible effect on the heat-bonded nonwoven geotextiles and woven geotextiles. Reduction factors (also known as partial factors of safety) are

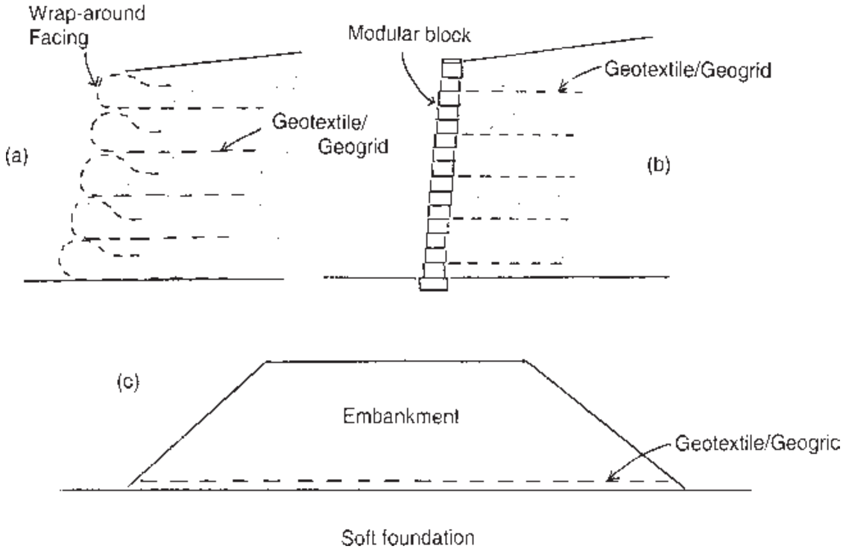

Figure 1 Geosynthetics in soil reinforcement: (a) wraparound wall; (b) modular-block wall; (c) embankment over soft foundation.

applied considering possible strength reduction of geotextiles by installation damage, creep, chemical and biological actions. Geotextiles may degrade by exposure to ultraviolet rays, high temperature, oxidation, and hydrolysis (when the environment is highly alkaline), but the effect is minimized when buried in soils.

The frictional behavior of a geotextile with site-specific soil must be determined by direct shear tests. Although the ASTM standard specifies a direct shear box with dimensions of 30 cm by 30 cm, the box with a plane area of 10 cm by 10 cm would be adequate for geotextiles. Pullout tests have been proposed in the last few decades for determining the anchorage capacity of geosynthetics; such tests are not relevant in determining the design parameters because they are subject to scale and boundary effects.

For embankments and dikes constructed over a soft foundation that lacks bearing capacity and global stability, a layer or more of geotextile is laid at the base of the embankment. Vertical wick drains of geosynthetic composites or sand drains may be used to accelerate consolidation of the soft foundation. Geotextiles have also been used in conjunction with the underwater sand capping of contaminated submarine sediments. In these applications, the seam strength may dominate the design.

Both geotextiles and geogrids are used to reinforce steep slopes and retaining walls. For applications where large tensile stiffness and strength of reinforcement are required, geogrids should be used. A large shear box is required to determine the frictional properties of the geogrid because the aperture size is large relative to the geotextile. Unlike geotextiles, where frictional behavior dominates the interaction with soil, the junction of some geogrids may provide interlocking. As geotextiles are very flexible, they are typically wrapped around the face of the slope or retaining wall and protected by vegetation, gunite, timber face, or concrete panels to prevent degradation by ultraviolet rays and vandalism.

Geogrids are increasingly used with modular blocks to provide an aesthetically pleasant wall appearance. As such, the connection between the blocks and geogrids plays an important role in design. The creep and stress relaxation behavior of geogrids are also studied in conjunction with wall design. In the design of reinforced slopes and walls, a limit equilibrium approach is used. The structure is checked for internal and external stabilities. In the internal stability analysis, a failure wedge is postulated and it is tied back into the stable soil zone. An adequate strength and length of reinforcement are secured. The external stability is evaluated in a manner similar to conventional gravity/-cantilever wall design. In the external stability analysis, possible modes of failure, such as direct sliding, overturning, and bearing capacity, are evaluated. The seismic design of reinforced slopes and retaining walls has also received wide attention in recent years.

3.2 Filter and Drainage Layer

Geotextiles are used to replace granular soil filters in the underdrain, as well as paved and unpaved roads. They are also used as chimney drain in an earth dam and behind retaining walls (Fig. 2). The hydraulic properties are a major consideration in design. The flow rate obtained from the tests is reduced using reduction factors considering soil clogging and blinding, creep reduction of void space, intrusion of adjacent materials into geotextile voids, chemical clogging, and biological clogging.

When functioning as a filter, the geotextile sheet is required to retain the soil while possessing adequate permeability to allow cross-plane flow to occur. The permittivity or permeability and apparent opening size or equivalent opening size of the geotextile are used in design. Permittivity is the coefficient of hydraulic conductivity normalized by the thickness of the geotextile. The filter is also expected to function without clogging throughout the lifetime of the system. The gradient ratio test and long-term flow tests may be used to investigate the clogging potential.

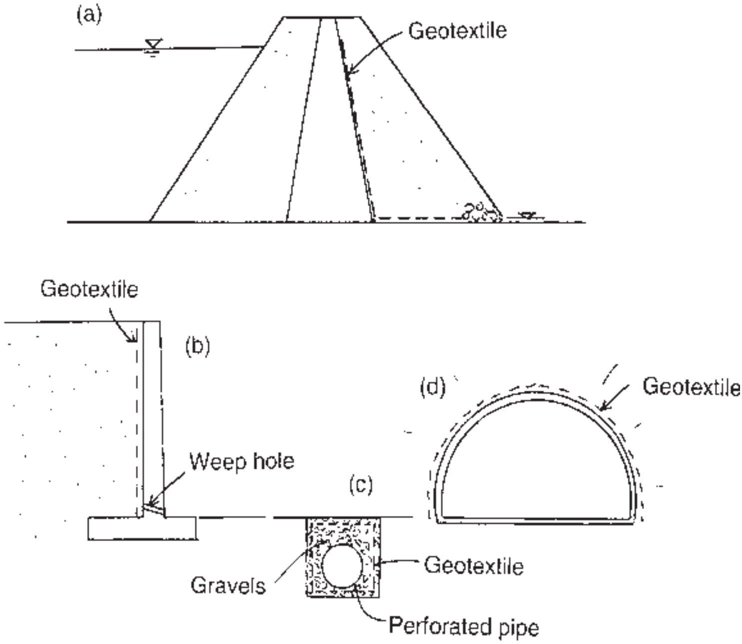

Figure 2 Geotextile as drainage layer or filter: (a) chimney drain in earth dam; (b) drain behind retaining wall; (c) underdrain; (d) drainage layer in tunnel.

If the geotextiles (usually nonwoven needle-punched geotextiles) are used as a drainage layer, the in-plane permeability is considered. Because the thickness decreases with increasing normal stress acting on it, the term "transmissivity" is used, where the coefficient of hydraulic conductivity is normalized by the geotextile thickness.

3.3 Large-Capacity Flow with Geonets/Geocomposites

For drainage applications (such as landfills and surface impoundments), geonets and geocomposites are preferable to geotextiles. These are specifically manufactured to allow for large-capacity flow. Geonets have a parallel set of ribs overlying similar sets at various angles for drainage of fluids. Most geonets are manufactured from polyethylene. They are laminated with geotextiles on one or both surfaces to form drainage geocomposites (Fig. 3). Geonets are mostly manufactured from polyethylene; thus they have high resistance to leachate.

In geonets/geocomposites, the flow is no longer laminar, and thus Darcy's law is invalid. The flow rate is used in lieu of transmissivity or coefficient of

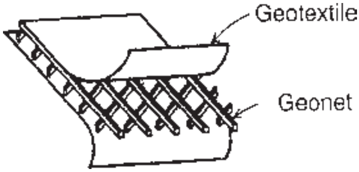

Figure 3 Geocomposite.

hydraulic conductivity to account for the turbulent flow. Because of the large normal stress acting on the plane of geonet/geocomposites, the crushing strength of the core has to be assessed. Geocomposites are sometimes tested with site-specific soils and liquid. A reduction in the flow rate is expected because of the intrusion of the geotextiles into the core. It is also important to ensure that geotextile sheets, if installed along the slope, do not delaminate from the geonets due to shear stress, because geocomposites are installed at a gradient to allow for gravity flow. The drainage systems of a geocomposite are usually constructed for allowance of cleaning by flushing because they are normally subject to biological action.

3.4 Separation and Reinforcement in Roadways

In the unpaved roads and railways, geotextile separates the subgrade and stonebase/ballast (Fig. 4). The California bearing ratio (CBR) of the soil subgrade may be used to determine if an unpaved road should be designed for separation or for separation and reinforcement. The intrusion of stone aggregates into the soil subgrade is prevented by the geotextile in a roadway. In a railway, the fine soil particles are stopped from pumping into the stone aggregates. In addition to tensile strength, other mechanical properties of geotextiles, such as resistance to burst, tear, impact, and puncture, are used for designing geotextiles as a separator. However, existing practice does not emphasize design when geotextiles are used as a separator compared to reinforcement and drainage applications.

For unpaved roadways, the use of geotextile reinforcement results in cost savings because the thickness of stone aggregates may be reduced. In paved roads, the geotextiles may prevent reflective cracking. The geotextile or biaxial geogrids may be placed above the cracked old pavement followed by the asphalt overlays. The life of the overlay is prolonged in the presence of geosynthetic materials, or a reduced thickness of overlay may be used while keeping the lifetime equivalent to the case without using the geotextile. In addition to preventing reflective cracking, the geosynthetic reinforces the asphalt pavement.

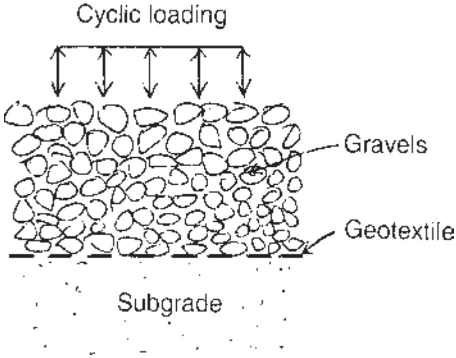

Figure 4 Geotextile as separator in unpaved roadway.

3.5 Coastal and Environmental Protection

Geotextiles are placed under erosion control structures, such as rock ripraps and precast concrete blocks (Fig. 5a). They are also used as silt fences at construction sites so that the soil particles are arrested from the runoff water.

Geotextiles are also used as geocontainers on land or underwater as storage for slurry and for coastal protection. On land, the dredged materials or sands are pumped under pressure into sewn geotextile sheets. The geotextile inflates to form a tube (Fig. 5b). Geotextile tubes are extremely effective in dewatering the high-water-content slurry/sludge by acting as a filter. The geotextile tube may also be used as an alternative to dike and coastal protection. In such applications, the strength and filter characteristics of the geotextile are important design criteria.

Geocontainers are used for the disposal of potentially hazardous dredged materials and offer a more environmental-friendly means of disposing dredged materials offshore. The geotextile sheets are laid at the bottom of dump barges, filled with dredged sediments, and sewn. The containers are then transported to the disposal site and dumped via a split hull barge.

4 GEOMEMBRANES AND GEOSYNTHETIC CLAY LINERS

4.1 Geomembranes

Geomembranes are thin sheets of polymeric material that inhibit the flow of liquid or gas. They are produced as panels and seamed at the site. Polyethylene and polyvinyl chloride are two major polymers used to manufacture

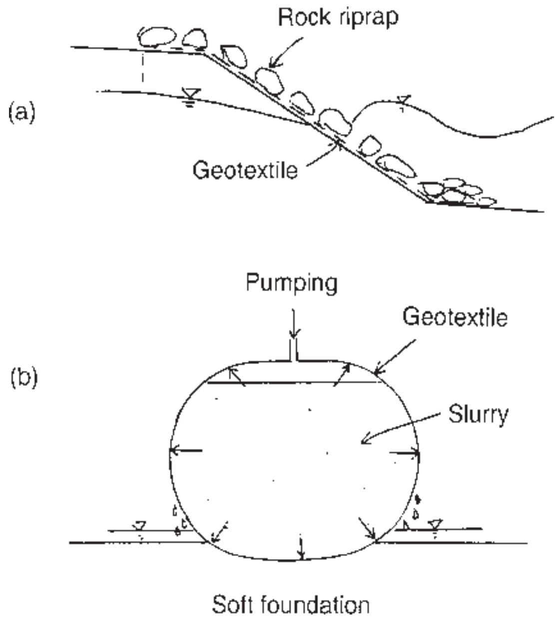

Figure 5 (a) Geotextile used in coastal protection; (b) geotextile tube.

geomembranes. Geomembranes of other polymer types are also available. They are used in liquid impoundments and waste containments as base/side liner and cover. The surface of a geomembrane may be smooth or textured. The texture improves the frictional resistance between the soil and geomembrane when the liners are constructed along the slope.

The permeability of geomembranes is in the range of 1×10^{-12} to 1×10^{-15} m/s. Because of the watertight requirement of a geomembrane, several major properties that affect the performance are discussed:

Geomembranes are practically impermeable. To measure their permeability, water vapor is used as the permeant, and diffusion is considered as the mechanism. This test is called a water-vapor transmission test. In a sealed aluminum cup, the relative humidity across a geomembrane specimen is controlled, and the gain or loss in weight over time is measured. A test typically takes from 3 to 30 days. The organic solvent may result in a very different transmission rate: thus site-specific solvent-vapor transmission tests are suggested.

In addition to the wide-width test, axisymmetric tests are conducted to measure the tensile strength of the geomembrane. Loading is conducted using air pressure, and the displacement at the center of inflated geomembrane specimen is measured. The stress-strain behavior is deduced from the measured results.

The seams of geomembrane rolls and panels are provided in the field. The watertightness of the seam constitutes a successful function of a containment system. Four major seaming methods are available: extrusion welding, thermal fusion/melt bonding, chemical fusion, and adhesive seaming. High-density polyethylene (HDPE) and polyvinyl chloride (PVC) geomembranes are typically welded using extrusion fillet and solvent, respectively. The strength of the seam can be weaker than the geomembrane itself and is determined by the shear tests and peel tests. Several nondestructive testing methods are available to assess the seams in the field, where the vacuum box method is widely used. However, the ultrasonic shadow method seems promising considering its use in difficult locations, such as slopes and corners, where the use of vacuum box method would not be possible.

The shear strength between the geomembrane and soils, and between the geomembrane and other geosynthetic materials used in the liner, is one of the most important design issues, especially when the liner is constructed along the slopes. Liner failures attributed to inadequate interface shear strength were reported. A shear box of dimensions 10 cm by 10 cm would be adequate for conducting direct shear tests between the geomembrane and site-specific soils under simulated field conditions.

Although HDPE is chemically resistant, it may suffer from environmental stress cracking. The notched constant-load tension test appeared to be a more relevant test for determining the potential of stress cracking. In the test, a dumbbell-shaped test specimen is sustained under a constant tensile load and immersed in a surface-wetting agent at an elevated temperature. The transition time for the behavior to change from ductile to brittle is recorded. A transition time of 100 hr or greater is considered acceptable.

4.2 Application of Geosynthetics in a Waste Containment System

Geosynthetics are used in solid waste containment systems to create a watertight environment. Geomembranes are used with clay to form a single or double composite liner along the side and bottom of the landfill to prevent migration of leachate into the underlying groundwater (Fig. 6). They are also used as a cover liner, acting as a barrier against precipitation, after a landfill has been closed. In the watertight environment, other geosynthetics, such as geotextiles, geocomposite, and pipes, are used to facilitate drainage, collection, and removal of leachate generated by waste decomposition and/or precipitation. In the United States, the use of geomembranes in a waste containment system is regulated by federal laws (Subtitle D).

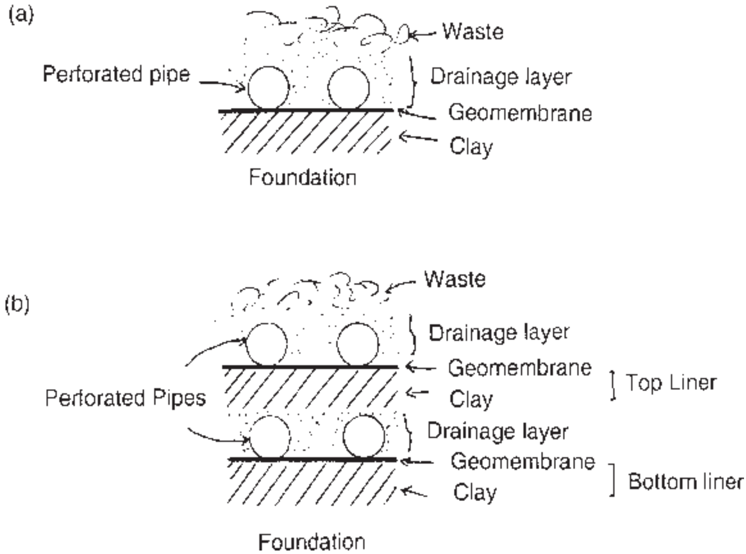

Figure 6 Geosynthetic applications in waste containment: (a) single composite liner; (b) double composite liner.

Because of the impermeability requirement of the geomembrane liner, permeation and leakage due to defects, such as pinholes, seams, cracks, punctures, and tears, are evaluated. Theoretical and empirical equations are available to determine the amount of leakage (which depends on the type of linear), field soil conditions, and leachate head (which is typically kept below 30 cm). It is well known that the use of a double composite liner minimizes the leakage rate.

Waste decomposition generates a significant amount of gas, such as methane and carbon dioxide, in municipal solid waste landfill. Methane is lighter than air; it rises to the top of the waste and is trapped under the cover. The gas may uplift the cover and damage the geomembrane. Thus a proper gas collection and removal system is required. Also, because of the large settlement encountered in the landfill, a provision for differential settlement has to be made in the design of the cover system.

The long-term exposure of the geomembrane to heat induces wrinkles/-waves and leads to evaporation of moisture from the underlying clay liner. Subsequent cooling allows the condensate to drip back to the clay. Along the slope, the desiccation of clay liner occurs at the top, whereas the condensate tends to accumulate at the toe, especially along the path of wrinkles, giving rise to wet clay. The problems may be alleviated through the use of white-surface geomembranes and very flexible polyethylene (VFPE) geomembranes. New geomembrane products are expected to overcome existing problems.

4.3 Geosynthetic Clay Liners as Hydraulic Barriers

Geosynthetic clay liners (GCLs) are proprietary products that are beginning to replace geomembrane and clay liners. They are finding increased use in waste containment systems (mostly landfill liners and covers) and reservoirs. GCLs consist of very low-permeability bentonite or other clay materials supported by geotextiles and/or geomembranes on one side or both. They are bonded together by needling, stitching, or chemical adhesive (Fig. 7).

GCLs offer many advantages over conventional clay liners or geomembrane-clay composite liners. GCLs are factory manufactured; thus the quality is well controlled. Sodium bentonite is usually used in GCLs. The permeability of bentonite is around 10^{-10} to 10^{-12} m/s, which is much lower than native soils available in the field. While clay liners are typically from 30 cm to 1 m thick, GCLs are approximately 5 mm thick. This results in space saving in a containment system. The installation of GCLs is rapid and simple. Unlike geomembranes that require special welding equipment and skills, the seaming of GCLs is provided by an overlapping length of about 15 cm. GCLs offer a self-healing capability under puncture, as the availability of moisture typically leads to swelling of bentonite.

Installation of CGLs is conducted under dry conditions. Hydration may affect the properties of GCLs. It is also affected by the hydration liquid. Bentonite

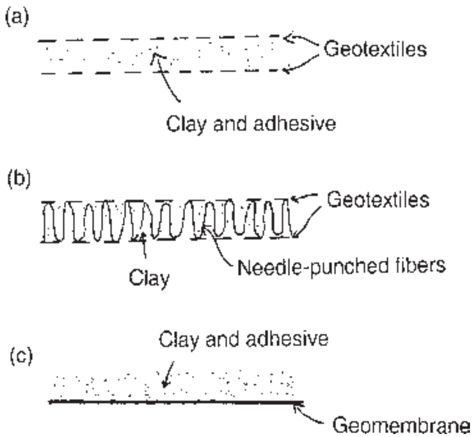

Figure 7 Typical examples of geosynthetic clay liner.

normally swells in the presence of liquid, but if the use with hydrocarbons and nonpolar fluids is expected, prehydration with water is required before the containment is put into service. The permeability of GCLs is also affected by the type of permeant; therefore, the expected leachate should be used in the permeability tests.

The shear strength is an issue of concern, especially when GCLs are used as liners along the slope. The shear strength of GCLs is the largest under dry conditions. It is reduced by hydration and is affected by the hydrating liquid as well. Mechanical bonding by needle punching and stitching renders a higher shear strength of GCLs compared to chemical bonding or adhesive.

5 REMARKS

The information provided in this chapter is merely a brief summary of major items related to geosynthetic applications in civil and environmental engineering [similar in nature to Whittle and Ling (2001)]. Geofoam and plastic pipe are excluded. Interested readers should consult Koerner (1998), which is a publication detailing geosynthetic materials and design applications. Giroud (1993) provided two volumes of publication listing the papers on geosynthetic materials. New geosynthetic products, applications, and design procedures will continue to be developed. Two international journals that are devoted to geosynthetics, *Geosynthetics International* and *Geotextiles and Geomembranes*, as well as the ASCE *Journal of Geotechnical and Geoenvironmental Engineering*, are useful sources of information.

APPENDIX: ASTM TESTING STANDARDS (COMMITTEE D35 ON GEOSYNTHETICS)

Terminology

D4439-00 Standard Terminology for Geosynthetics

Mechanical Properties

D4354-99 Standard Practice for Sampling of Geosynthetics for Testing

D4533-91(1996) Standard Test Method for Trapezoid Tearing Strength of Geotextiles

D4595-86(1994) Standard Test Method for Tensile Properties of Geotextiles by the Wide-Width Strip Method

D4632-91(1996) Standard Test Method for Grab Breaking Load and Elongation of Geotextiles

D4759-88(1996) Standard Practice for Determining the Specification Conformance of Geosynthetics

D4833-00 Standard Test Method for Index Puncture Resistance of Geotextiles, Geomembranes, and Related Products

D4884-96 Standard Test Method for Strength of Sewn or Thermally Bonded Seams of Geotextiles

D5261-92(1996) Standard Test Method for Measuring Mass per Unit Area of Geotextiles

D5321-92(1997) Standard Test Method for Determining the Coefficient of Soil and Geosynthetic or Geosynthetic and Geosynthetic Friction by the Direct Shear Method

D5818-95(2000) Standard Practice for Obtaining Samples of Geosynthetics from a Test Section for Assessment of Installation Damage

D6241-99 Standard Test Method for the Static Puncture Strength of Geotextiles and Geotextile-Related Products Using a 50-mm Probe

D6244-98 Standard Test Method for Vertical Compression of Geocomposite Pavement Panel Drains

D6364-99 Standard Test Method for Determining the Short-Term Compression Behavior of Geosynthetics

D6637-01 Standard Test Method for Determining Tensile Properties of Geogrids by the Single or Multi-Rib Tensile Method

D6638-01 Standard Test Method for Determining Connection Strength Between Geosynthetic Reinforcement and Segmental

Concrete Units (Modular Concrete Blocks)

Endurance Properties

D1987-95 Standard Test Method for Biological Clogging of Geotextile or Soil/Geotextile Filters

D4355-99 Standard Test Method for Deterioration of Geotextiles from Exposure to Ultraviolet Light and Water (Xenon-Arc Type Apparatus)

D4594-96 Standard Test Method for Effects of Temperature on Stability of Geotextiles

D4873-01 Standard Guide for Identification, Storage, and Handling of Geosynthetic Rolls and Samples

D4886-88(1995)el Standard Test Method for Abrasion Resistance of Geotextiles (Sand Paper/Sliding Block Method)

D5262-97 Standard Test Method for Evaluating the Unconfined Tension Creep Behavior of Geosynthetics

D5322-98 Standard Practice for Immersion Procedures for Evaluating the Chemical Resistance of Geosynthetics to Liquids

D5397-99 Standard Test Method for Evaluation of Stress Crack Resistance of Polyolefin Geomembranes Using Notched Constant Tensile Load Test

D5496-98 Standard Practice for In-Field Immersion Testing of Geosynthetics

D5596-94 Standard Test Method for Microscopic Evaluation of the Dispersion of Carbon Black in Polyolefin Geosynthetics

D5721-95 Standard Practice for Air-Oven Aging of Polyolefin Geomembranes

D5747-95a Standard Practice for Tests to Evaluate the Chemical Resistance of Geomembranes to Liquids

D5819-99 Standard Guide for Selecting Test Methods for Experimental Evaluation of Geosynthetic Durability

D5885-97 Standard Test Method for Oxidative Induction Time of Polyolefin Geosynthetics by High-Pressure Differential Scanning Calorimetry

D5970-96 Standard Practice for Deterioration of Geotextiles from Outdoor Exposure

D6213-97 Standard Practice for Tests to Evaluate the Chemical Resistance of Geogrids to Liquids

D6388-99 Standard Practice for Tests to Evaluate the Chemical Resistance of Geonets to Liquids

D6389-99 Standard Practice for Tests to Evaluate the Chemical Resistance of Geotextiles to Liquids

D6392-99 Standard Test Method for Determining the Integrity of Nonreinforced Geomembrane Seams Produced Using Thermo-Fusion Methods

Permeability and Filtration

D4491-99a Standard Test Methods for Water Permeability of Geotextiles by Permittivity

D4716-00 Standard Test Method for Determining the (In-Plane) Flow Rate per Unit Width and Hydraulic Transmissivity of a Geosynthetic Using a Constant Head

D4751-99a Standard Test Method for Determining Apparent Opening Size of a Geotextile

D5101-99 Standard Test Method for Measuring the Soil-Geotextile System Clogging Potential by the Gradient Ratio

D5141-96(1999) Standard Test Method for Determining Filtering Efficiency and Flow Rate of a Geotextile for Silt Fence Application Using Site-Specific Soil

D5199-01 Standard Test Method for Measuring the Nominal Thickness of Geosynthetics

D5493-93 (1998) Standard Test Method for Permittivity of Geotextiles Under Load

D5567-94(1999) Standard Test method for Hydraulic Conductivity Ratio (HCR) Testing of Soil/Geotextile Systems

D6088-97 Standard Practice for Installation of Geocomposite Pavement Drains

D6140-00 Standard Test Method to Determine Asphalt Retention of Paving Fabrics Used in Asphalt Paving for Full-Width Applications

D6523-00 Standard Guide for Evaluation and Selection of Alternative Daily Covers (ADCs) for Sanitary Landfills

D6574-00 Test Method for Determining the (In-Plane) Hydraulic Transmissivity of a Geosynthetic by Radial Flow

Geosynthetic Clay Liners

D6454-99 Standard Test Method for Determining the Short-Term Compression Behavior of Turf Reinforcement Mats (TRMs)

D6524-00 Standard Test Method for Measuring the Resiliency of Turf Reinforcement Mats (TRMs)

D6525-00 Standard Test Method for Measuring Nominal Thickness of Permanent Rolled Erosion Control Products

D6566-00 Standard Test Method for Measuring Mass per Unit Area of Turf Reinforcement Mats

D6567-00 Standard Test Method for Measuring the Light Penetration of a Turf Reinforcement Mat (TRM)

D6575-00 Standard Test Method for Determining Stiffness of Geosynthetics Used as Turf Reinforcement Mats (TRMs)

Geosynthetic Erosion Control

D6454-99 Standard Test Method for Determining the Short-Term Compression Behavior of Turf Reinforcement Mats (TRMs)

D6524-00 Standard Test Method for Measuring the Resiliency of Turf Reinforcement Mats (TRMs)

D6525-00 Standard Test Method for Measuring Nominal Thickness of Permanent Rolled Erosion Control Products

D6566-00 Standard Test Method for Measuring Mass per Unit Area of Turf Reinforcement Mats

D6567-00 Standard Test Method for Measuring the Light Penetration of a Turf Reinforcement Mat (TRM)

D6575-00 Standard Test Method for Determining Stiffness of Geosynthetics Used as Turf Reinforcement Mats (TRMs)

Geomembranes

D4437-99 Standard Practice for Determining the Integrity of Field Seams Used in Joining Flexible Polymeric Sheet Geomembranes

D4545-86(1999) Standard Practice for Determining the Integrity of Factory Seams Used in Joining Manufactured Flexible Sheet Geomembranes

D4885-88(1995) Standard Test Method for Determining Performance Strength of Geomembranes by the Wide Strip Tensile Method

D5323-92(1999) Standard Practice for Determination of 2% Secant Modulus for Polyethylene Geomembranes

D5494-93(1999) Standard Test Method for the Determination of Pyramid Puncture Resistance of Unprotected and Protected Geomembranes

D5514-94 Standard Test Method for Large-Scale Hydrostatic Puncture Testing of Geosynthetics

D5617-99 Standard Test Method for Multi-Axial Tension Test for Geosynthetics

D5641-94c1 Standard Practice for Geomembrane Seam Evaluation by Vacuum Chamber

D5820-95 Standard Practice for Pressurized Air Channel Evaluation of Dual Seamed Geomembranes

D5884-99 Standard Test Method for Determining Tearing Strength of Internally Reinforced Geomembranes

D5886-95 Standard Guide for Selection of Test Methods to Determine Rate of Fluid Permeation Through Geomembranes for Specific Applications

D5994-98 Standard Test Method for Measuring Core Thickness of Textured Geomembrane

D6214-98 Standard Test Method for Determining the Integrity of Field Seams Used in Joining Geomembranes by Chemical Fusion Methods

D6365-99 Standard Practice for the Nondestructive Testing of Geomembrane Seams Using the Spark Test

D6434-99 Standard Guide for the Selection of Test Methods for Flexible Polypropylene (fPP) Geomembranes

D6455-99 Standard Guide for the Selection of Test Methods for Prefabricated Bituminous Geomembranes (PBGM)

D6497-00 Standard Guide for Mechanical Attachment of Geomembrane to Penetrations or Structures

D6636-01 Standard Test Method for Determination of Ply Adhesion Strength of Reinforced Geomembranes

REFERENCES

ASTM, Standards on Geosynthetics, 5th ed. . Philadelphia, PA: ASTM, 2000.

JP Giroud. *Geosynthetics Bibliography*. Vols. 1 & 2. St. Paul, MN: International Fabrics Assoc. International, 1993.

RM Koerner. *Designing with Geosynthetics*, 4th ed. . Upper Saddle River, NJ: Prentice Hall, 1998.

AJ Whittle, Hoe I. Ling. Geosynthetics in construction. In *Material Encyclopedia*. New York: Elsevier, 2001.

2
Performance Properties of Geogrids

W. Voskamp
Colbond Geosynthetics, Arnhem, The Netherlands

1 SYNOPSIS

With BS 8006, FHWA-SA-96-071, and independent certification of product characteristics by the British Board of Agrément, a sound base for the use of reinforcing products, whether flexible or stiff, is now available. A range of geogrid products with varying strength and made in different ways is now available from which users can select the product best suited to their purpose. However, it should be emphasized that in the design specification for a project all relevant design parameters must be listed. The required design strength should clearly be specified for a design life, and the design conditions that influence the various partial factors should also be listed. Alternatively, the factors used in the design for the different polymers must be listed. This allows the contractor to select between various products while the advantages in lower material factors, which are listed in the BS 8006 for products that have a record of extensive tests, are fully used as competitive edge and for the benefit of the user. In an earlier publication, Voskamp (1995) makes a comparison between the partial material factors and some other characteristics of stiff and flexible geogrids. This chapter gives the latest results and comparisons with other standards.

2 INTRODUCTION

The first geogrids appeared on the market in the late 1970s. They were made of HDPE and, after intensive research on product characteristics and design methods, have since been increasingly adopted for civil engineering applications.

The strength of the geogrids varies between 20 and 250 kN/m, and they are used in both road constructions and reinforced slopes.

At that time, the strong PET fabrics that were used commercially for basal embankment reinforcement were, in fact, too strong for slope reinforcement, which typically requires strengths of < 100 kN/m. The only other materials then available were various types of nonwovens and lightweight wovens. Due to the unique structure of the geogrid, and the strength range in which it was available, it was highly suitable for use in slope reinforcement applications and for bearing capacity improvement applications in roads. The success of the product since its introduction proved its usefulness.

As with all products developed for specific applications, other competitive and new products came on the market as the market matured. Today we can choose from a variety of stiff geogrid products and flexible geogrid products.

The history of flexible geogrids differs from that of the stiff types, because polyester fibers had already been used for quite some time in soil reinforcement applications, mainly for basal reinforcement of embankments. The first commercial application of these reinforcing fabrics goes back to 1977, when a highway embankment was built near Muiden in The Netherlands. This reinforcing fabric, type Stabilenka, was used in large projects, especially in Asia, for basal reinforcement applications in land reclamation projects and road constructions. The reason for this start in Asia was that a technical need existed for the use of basal reinforcement, as the soil conditions in those projects were very bad and infrastructural works had to be constructed there. For slope reinforcement applications, the reinforcing mat was simply too strong and therefore too expensive.

It was technically impossible to make a reinforcing fabric with a strength less than 150 kN/m in the traditional fabric form. A leap forward was made in 1985, when an open-fabric mesh, coated with PVC, was developed. Now it was possible to use PET yarns with their superior properties to make a grid-type structure with the required lower strength. Further, the PVC coating provided an excellent protection against mechanical damage, which made the product even more attractive. So, at the end of the 1990s, more geogrids appeared on the market, which increased competition between the products.

Geogrids can be divided into two groups:

1. Stiff geogrids, mostly HDPE with a monolithic mesh structure
2. Flexible geogrids, mostly PET with PVC or acrylic coating with mechanically connected longitudinal and transverse elements

Over the past years many advantages and disadvantages have been claimed for the various products. It is the intention of this paper to make an updated generic comparison between the two groups of products on the basis of specific properties. The purpose is to give the necessary background information to allow engineers to judge for themselves if any special requirement is needed.

3 MAIN DESIGN PARAMETERS

A design of a reinforced soil structure must be made in accordance with the valid design codes and standards in that country.

The main design requirements for the use of geogrids in soil structures result from the geotechnical design. This includes the calculation of different failure modes resulting in requirements for:

Axial tensile design strength of the geogrid
Maximum strain requirements in the geogrid

The practice is to design for the ultimate limit state (strength requirement) and to check for the serviceability state (strain level and deformation). In BS 8006 (1996), different requirements are formulated for the design of reinforced walls, abutments, and reinforced slopes.

Important parameters of the geogrids necessary for these designs are the design strength and strain characteristics during the service life of the structure and the bond coefficient, which in turn depends heavily on the fill and underlying soil (Fig. 1).

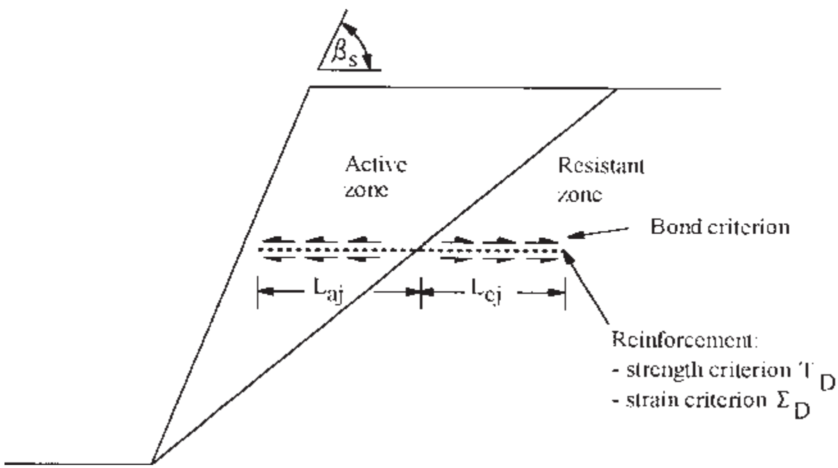

Figure 1 Reinforcing mechanisms in walls and slopes.

4 DESIGN STRENGTH

As outlined by Jewell (1990a), soil reinforcement designs have separate requirements for maximum allowable strength and for stiffness or maximum allowable deformation of the structure. Both criteria must be checked for the entire lifetime of the structure and are based on the creep and stress-rupture behavior of the geogrid (Figs. 2–4). More than 15 years ago, Voskamp (1986) proposed calculating the maximum allowable strength (today defined as design strength) from the general equation

$$P_{\text{all}} = (P_{\text{char}}[t, T])/(f_m \cdot f_e \cdot f_d) \tag{1}$$

where

- P_{all} is the allowable design strength for the design life time, t.
- P_{char} is the characteristic tensile strength for the design lifetime t, and design temperature T.
- f_m is the partial factor for extrapolation and accuracy of test data.
- f_e is the partial factor for environmental aspects.
- f_d is the partial factor for mechanical damage (Fig. 5).

For tensile rupture failure, a similar formulation has been embodied in BS 8006 (1996):

$$T_d = T_c/f_m \tag{2}$$

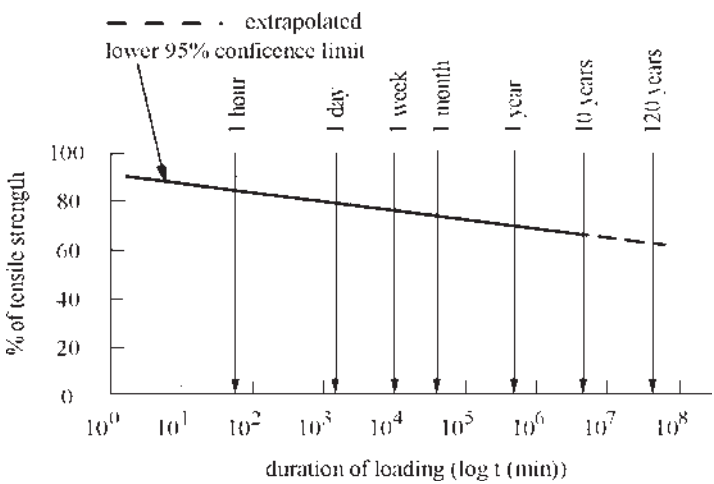

Figure 2 Stress-rupture line, Fortrac. (From BBA, 1997).

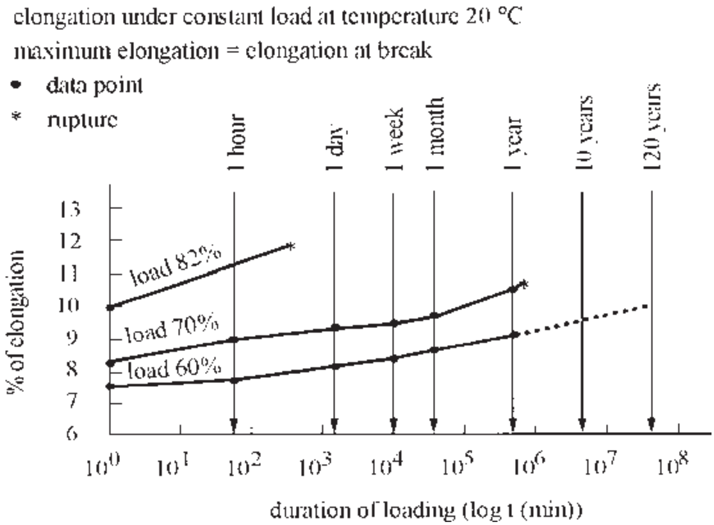

Figure 3 Typical creep graphs, Fortrac.

where

T_d is the design strength.

T_c is the characteristic strength above which the material fails in tension from peak loading during the design life of the structure.

f_m is a material factor $f_m = f_{m1} \cdot f_{m2}$, where $f_{m1} = f_{m11} \cdot f_{m12}$ and $f_{m2} = f_{m21} \cdot f_{m22}$.

The various factors f_{mxx} are described in the BS 8006 and cover factors for manufacture/control values, extrapolation of test data, susceptibility to damage, and environment. The values of the above parameters differ for flexible and stiff grids. Various loads factors f are used in the design to complete the ultimate limit state design. This method complies with the approach followed in Eurocode 7 for geotechnical designs. $P_{\text{char}}\,[t, T]$ or T_c for HDPE grids is derived from a creep deformation limit of 10% during a design life (Jewell and Greenwood, 1988). In the case of polyester (PET) grids, this value is obtained from stress-rupture data produced by tests on yarns running more than 10 years and tests on actual products running for more than 9 years now. All these data are summarized in one stress-rupture graph, which is normalized as a percentage of the short-term ultimate tensile strength, to give the so-called stress-rupture graph, in which a 95% confidence limit indicates the characteristic levels (Voskamp, 1990).

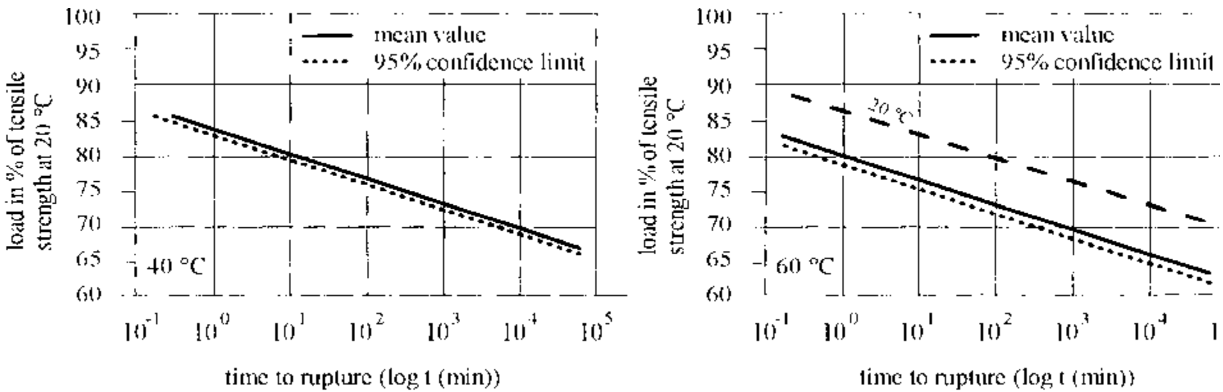

Figure 4 Stress-rupture lines at 40°C and 60°C for Fortrac. (From den Hoedt, 1994.)

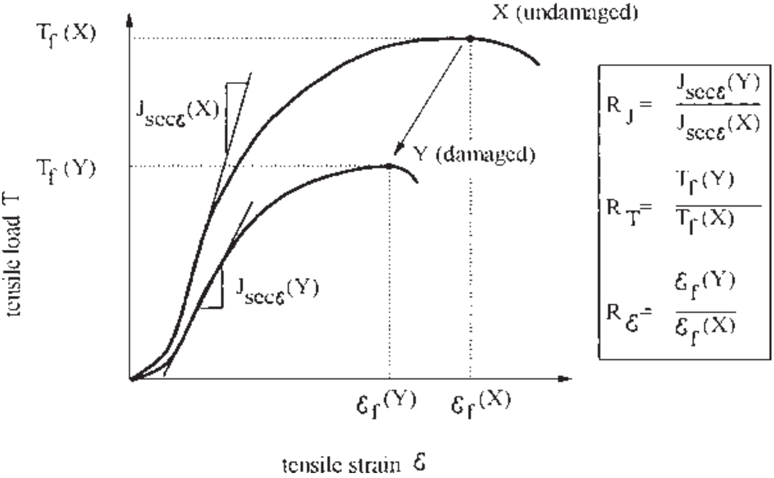

Figure 5 Mechanical damage. (From Allen and Bathurst, 1994.)

The FHWA (1997) uses

$$T_{\text{all}} = T_{\text{ult}}/(RF_{\text{CR}} \cdot RF_{\text{D}} \cdot RF_{\text{ID}} \cdot FS)$$

where

- T_{all} is the long-term tensile strength.
- T_{ult} is the ultimate (or yield) tensile strength based on minimum average roll value (MARV).
- RF_{CR} is the creep reduction factor.
- RF_{b} is the durability reduction factor (typically 1.1–2.0).
- RF_{ID} is the installation damage factor (ranging from 1.05–3.00).
- FS is the overall factor of safety to account for uncertainties in the geometry of the structure, fill properties, reinforcement properties, and external applied loads.

For permanent mechanically stabilized earth walls (>70°), $FS_{\text{min}} = 1.5$. For reinforced soil structures, $FS = 1.0$, as the required factor of safety is accounted for in the stability analysis.

Detailed comparison of the creep data for the yarns and for the product made of these yarns made it possible to combine the data to confine the extrapolation to one decade of time.

Later testing at 40°C and 60°C confirmed the normalized stress-rupture graph by time–temperature superposition.

5 PARTIAL FACTORS

The P_{char} must be reduced because damage to the geogrid as a result of construction activities such as compaction of fill layers occurs. This damage results in a reduction of the strength of the material. Also, environmental conditions during the service life of the structure influence the strength.

The mechanical damage factors are product- and application-related. Most products have been tested under controlled field conditions, and specific factors are quoted by manufacturers. With a view to, for example, BBA certification, independent checks have been made to certify these values. The values are typically in the range of 1.05–1.7 depending on the type of fill and the type of geogrid (BBA, 1997).

Allen and Bathurst (1994) have evaluated 3500 index tests on different geosynthetic reinforcement products. They concluded that damage results in reduction in strength and in reduction in strain. The secant modulus remains the same.

A chemical environment factor must also be applied. All polymer materials are vulnerable to certain specific chemical conditions. It is therefore useful to determine whether these conditions will occur in the design case and what the concentration of chemicals will be. Polyester, for example, is sensitive to an alkaline environment with pH levels higher than 9.5 combined with a temperature above 50°C.

Under normal soil conditions, the phenomena of hydrolysis will not have an impact on the allowable strength (BBA, 1997;Schmidt et al., 1994). Special high-alkaline conditions, continuing for most of the design life of the structure, must be evaluated more closely. The results of three years of recent testing at high temperatures in Germany confirmed these conclusions (Wilmers, 1997). Thermo-oxidation is a process that influences the ductile behavior of polyolefins like HDPE and PP. Also, this item must be evaluated if the lifetime conditions include the existence of chemicals that may lead to dissolution of additives. These plasticizers or other additives in the polymer composition are evaporated or slowly washed away from the polymer. Extensive testing in various laboratories has shown that the reduction in strength and other properties of the geogrids is negligible when the material is used in normal soil conditions. Also the CEN committee TC 189 is developing standard test methods as index tests for chemical attack. HDPE material is sensitive to environmental stress cracking. However, extensive studies by ERA, Small and Greenwood (1993) have not revealed such a sensitivity in the HDPE geogrids tested.

Resistance to fungi and other biological attacks has to be evaluated. As far as we know, all geogrids are capable of withstanding this type of attack without loss of strength.

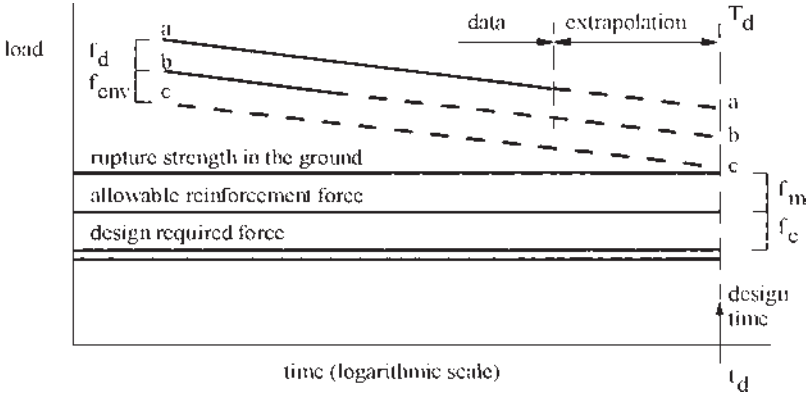

Figure 6 Reinforcement strength against time. (From Jewell and Greenwood, 1988.)

The CEN TC 189 committee has produced harmonized test methods on all relevent tests for geosynthetics. These norms are today the only valid test methods in Europe. The last norms were approved by the member states in 2000. The uniformity in testing procedures and documents that state which parameters engineers must specify with certain uses of the geosynthetic materials is a very big step ahead on the road to full acceptance of these materials by the civil engineering world.

There are also material factors that cover for uncertainties in extrapolation, accuracy of testing, and so on. First introduced by Jewell and Greenwood (1988), they are now modified and incorporated in BS 8006. To overcome this uncertainty, a separate factor f_{m12} is used in BS 8006. Based on the quantity of tests, time of extrapolations, and so forth, this value can vary between 1.0 and 2.5. The lower value should only be selected when allowed by approved certifying bodies after extensive evaluation of the test results.

Figure 6 summarizes the relationship between the rupture strength and allowable reinforcement force, the design strength, which is a function of the design life, t_d, and the design temperature, T_d.

6 STIFFNESS

As stated earlier, the second design requirement is stiffness. Most soil reinforcement structures will deform to a certain extent only. This design requirement can be translated into a maximum strain requirement for the geogrids (BS 8006, 1996). In such a case, the requirement limits the strain during construction as well as the additional strain occurring during the service life of

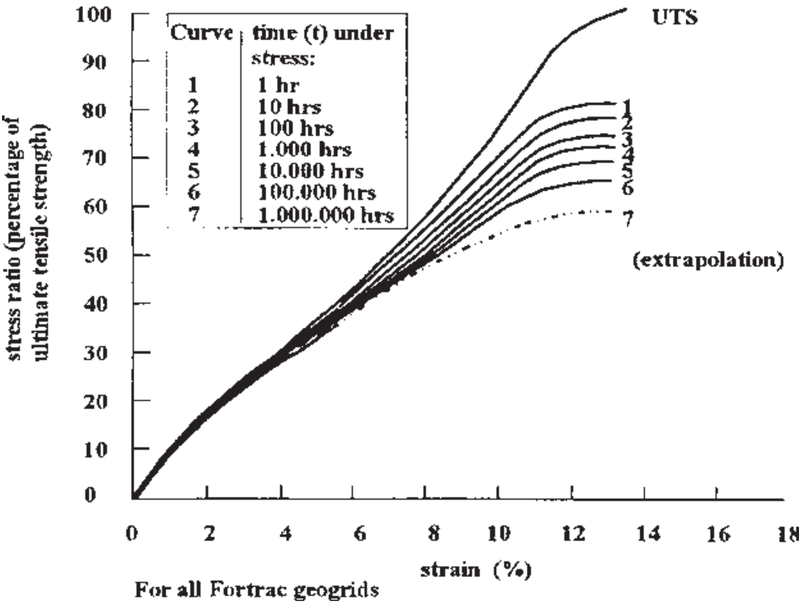

Figure 7 Isochronous curves for PET yarn.

the structure. In some cases, these strain requirements can be more restrictive than the strength requirements. The values for the strain in the products can be obtained from isochronous curves, which are available for most geogrids (Figs. 7–9).

It should be emphasized that stress-rupture and creep-strain data are product-specific. Even with flexible geogrids made of PET, knowing that they are made of PET is not enough. In such a case, details about the type of yarn used should be supplied and verified as the creep can vary for different products made of the same polymer but in a different composition.

7 COMPARISON OF DESIGN METHODS IN THE UNITED STATES AND EUROPE

In the past there were differences between the used design methods in the United States and Europe, mainly in the calculation of the allowable design strength of the geogrid. The new FHWA manual (1997), however, is now more in line with the European practice and specifies the RF_{cr} as creep reduction factor equal to the ratio of the ultimate load to the maximum sustainable load within the design life.

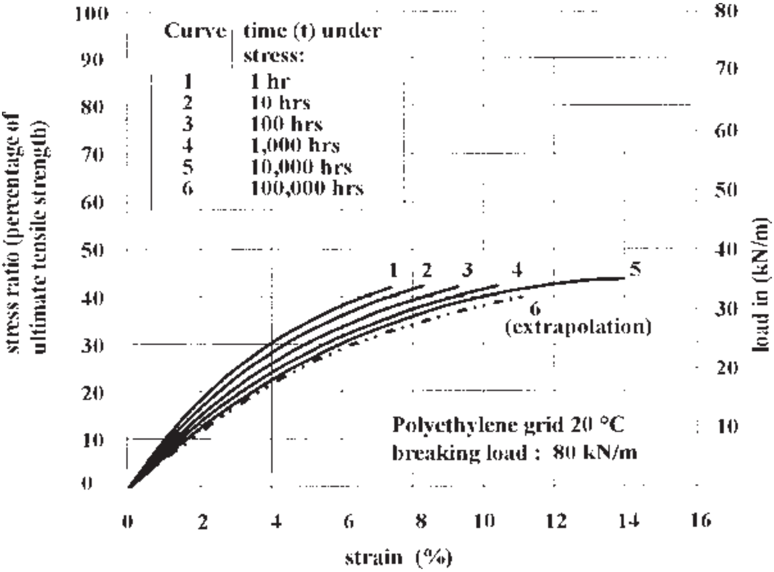

Figure 8 Isochronous curves for polypropylene yarn. (From Jewell and Greenwood, 1988.)

Overlaps in the direction of the primary tensile load force were allowed in the United States, and a special RF_{joint} was used to reduce the design strength of the geogrid to cover the overall reduction in allowable load due to overlaps. The new FHWA manual (1997) no longer mentions this method, although it probably will still be used.

8 SOIL REINFORCEMENT INTERACTION

Failure of a reinforced structure, specifically the reinforcement, can take place in two ways: tensile rupture of the geogrid or pullout of the grid. These potential failure modes are assessed separately.

To determine the pullout resistance of a geogrid, mainly pullout tests are used in which either the coefficient of interaction between the geogrid and soil is determined or the minimum anchor length is calculated (Voskamp, 1992). Oostveen et al. (1994) conducted an extensive study of the pullout behavior of geogrids and executed many tests in a 1000 mm by 2000 mm pullout box, comparing extensible geogrids, both stiff and flexible, with nonextensible, steel grids. This study revealed that the behavior of flexible grids differed completely

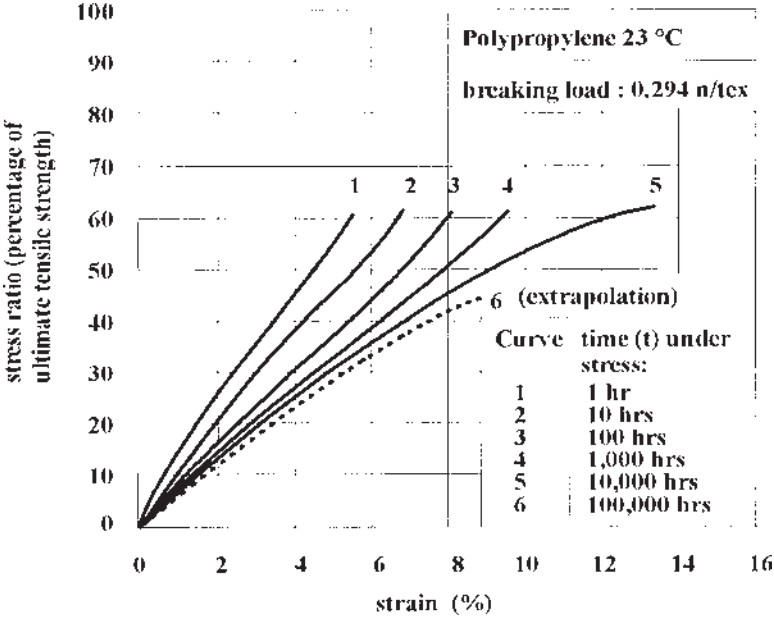

Figure 9 Isochronous curves for polyethylene grid. (From Jewell and Greenwood, 1988.)

from that of steel grids, with regard to the load transfer between the grid and surrounding soil.

Unlike stiff, nondeformable steel mesh, extensible geogrids do not have a constant load transfer by shear. This also means that the coefficient of interaction is not a constant value. The total anchor length required, however, is no more than that calculated with a constant value for the coefficient of interaction. Further research is being conducted. Whichever method is chosen, pullout or maximum anchor length, the load is transferred by the maximum mobilized number of junctions in the anchor zone, e.g., anchor length multiplied by the width.

Not once during the pullout tests that were executed on flexible geogrids, Fortrac, under various test conditions and with various fill materials was a junction failure observed. This proves that the junction strength under confined conditions is always sufficiently high.

If an anchor length of 1 m is assumed, the number of junctions over this length is approximately 1600 if 40 rib junctions occur over 1.00 m. As the load is always transferred over a certain anchor length, the requirement of a high junction strength, sometimes specified as 90%, is not necessary. Such a requirement is clearly biased as it strongly favors monolithic junctions. The only valid requirement in this case is a bond coefficient (C.O.I.) or an anchor length requirement based on performance testing (Voskamp, 1992).

Further, the junction strength has no influence on the strength of the geogrid and should therefore not be related to a safety consideration for the strength of the geogrid as was suggested by Task Force 27 in "Design guidelines for the use of extensible reinforcements," AASHTO-AGC-ARTBA (1989). Later design guidelines, such as that published by the FHWA (1997), no longer specify this.

FHWA (1997) describes that the stress transfer mechanisms in pullout are by friction and/or passive resistance.

The pullout resistance is given by

$$P_r = F^* \cdot \alpha \cdot \sigma'_v \cdot L_e \cdot C$$

where

- F^* is the pullout resistance factor.
- α is the scale effect correction factor, for a nonlinear stress reduction over the embedded length of highly extensible reinforcements ($\alpha = 0.6–1.0$ for geosynthetics).
- σ'_v is the effective vertical stress at the soil reinforcement interface.
- $L_e \cdot C$ is the total surface area per unit width of the reinforcement in the resistive zone behind the failure surface.
- L_e is the embedment length in the resistive zone.
- C is the reinforcement effective unit perimeter ($C = 2$ for strips and grids).

F^* can be obtained from laboratory or field testing. Alternatively, F^* can be estimated:

$$F^* = F_q \cdot \alpha_\beta + \tan \rho$$

where

- F_q is the embedment bearing capacity factor.
- α_β is the bearing factor for passive resistance based on the thickness of the bearing member.
- ρ is the soil reinforcement interactive friction angle.

Default values are given for geosynthetic geogrids:

$\alpha = 0.8$, in case grid opening size/$d_{50} > 1$.
In case F_1 is derived from tests: $\tan \rho$ is not applicable.
In case $\tan \rho$ is derived from tests (in case grid mesh/$d_{50} < 1$): F_q is not applicable, use $\tan \rho$ only).

Long-term pullout tests are advised to determine F^*. As default values are mentioned:

Geosynthetic sheet reinforcement: $F* = 2/3 \cdot \tan \phi$.
Geogrids: $F* = 0.8 \cdot \tan \phi$.
ϕ = peak friction angle of the soil.

For reinforced soil slopes (RSS) as lower bound value $\phi = 28°$ is advised; for mechanically stabilized earth walls (MSE) walls $\phi = 34°$ in case granular backfill is used.

This document contains requirements for geogrid pullout such as

Quick, effective stress pullout tests and through-the-junction creep testing of the geogrid per GRI-GG3a Test Method, or
Quick, effective stress pullout tests of the geogrid with severed transverse ribs, or
Quick, effective stress pullout tests of the entire geogrid structure if the summation of the strengths of the joints occurring in a 300-mm-(12″) long grid sample is equal to or greater than the ultimate strength of the grid element to which they are attached, or
Long-term effective stress pullout tests of the entire geogrid structure.

Research on the long-term effective stress pullout of four flexible grids and one stiff grid, Wilson-Fahmy and Koerner (1995), showed that, "For practical purposes the pullout strength of the geogrids tested is independent of time within the observed 1000 hours test duration."

Whenever a safety factor is required for pullout, it should be related to the anchor length or grid length in the embankment and not to the allowable strength as suggested and used in the United States (AASHTO-AGC-ARTBA,1989; Washington FHWA, 1997).

In the design method developed by Jewell (1990b), the effect of the junction strength or anchor length is taken into account in the calculation of the bond length. Even with very low values, it shows that the effect is minimal. The bond factor has a very limited effect on the anchor length. Together with the findings of recent research work, Oostveen et al. (1994), especially the extra safety in the anchor length due to the fact that the design is for an allowable strength compared to the available rupture forces, it is concluded that a separate factor of safety for junction

Table 1 Availability of Load/Strain/Time Data

Load/strain/time data	Flexible	Stiff
Stress–strain curves	Available	Available
Long-term stress-rupture	Available	Sherby–Dorn plots
Stiffness (strain vs. time)	Available	Sherby–Dorn plots
Junction strength	Minimum strength	Unlimited strength

Table 2 Partial Factors

Partial factors	Flexible	Stiff
Mechanical damage	1.05–1.7	1.1–1.7
Chemical attack	N/A–1.0	N/A–1.0
Hydrolysis	pH < 9, $T < 50°$:1.0	N/A
Thermo-oxidation	N/A	In special cases
Environmental attack	1.0	1.0

strength is not correct and therefore not applicable. BS 8006 does not require such a factor either but uses a partial factor in the calculation of the anchor length instead. FHWA (1997) follows the same design approach.

9 SUMMARY

The availability of data relating to stress-strain curves, long-term stress rupture against time and stiffness, together with the basis for definition of junction strength are summarized in Table 1 for flexible and stiff geogrids. Data determined by direct testing are classified as *available* and data derived from graphical construction are classified as *Sherby–Dorn plots*.

Typical values for partial factors for mechanical damage, chemical attack, hydrolysis, thermo-oxidation, and environmental attack are summarized in Table 2.

10 CONCLUSIONS

With the present BS 8006, FHWA, and independent certification of product characteristics as carried out by BBA, a sound base for the use of geogrids products is now available. The many geogrid products offer a range of products from which specifiers and contractors can select the product best suited to their specific purpose. However, it should be emphasized that the proper design parameters must be accurately specified to enable the selection of the correct geogrid.

The design strength should be clearly specified for a design life while the design conditions that influence the various partial factors should also be listed. In fact, the designer should specify which partial factors he has used in his design. When a product is proposed to be used with different characteristics, it is then possible to analyze the differences between the products with regards to the design strength in a proper way, fully in accordance with the meaning of the standards like BS 8006. Alternatively, the designer must list the applicable material factors to be used with the different polymers, and the supplier has to prove properties of the products for verification by the site engineer.

The manufacturers should supply the appropriate stress-rupture line and certification of the partial factors applicable for the stated design conditions. Alternatively, they should supply independently verified test reports for the site conditions mentioned. Requirements for material or extrapolation factors must be clearly specified.

Further, the stiffness must be specified in the form of a strain requirement either as maximum level after a certain lifetime or as a maximum value during construction together with a maximum value for creep during a certain number of years after construction.

When specifications are compiled in this way, there need not be 199 discussions about applicability and product specific parameters. Instead, a straightforward calculation can be made to prove whether or not a product fulfills the design requirements. Thus, competition between the products will be used to maximize the benefits for designers and contractors alike.

REFERENCES

AASHTO-AGC-ARTBA. *Design guidelines for use of extensible reinforcements for mechanically stabilized earth walls in permanent applications*. Task Force 27 Report, 1989.

TM Allen, R Bathurst. Characterization of geosynthetic load–strain behavior after installation damage. *Geosynth. Int.* 1(2): 181–199, 1994.

BBA CERTIFICATE No. 97/R096, Road and Bridges Agrément Certificate for FORTRAC *Geogrids*. British Board of Agrément, UK, 1997.

BS 8006, *Code of Practice for Strengthened Reinforced Soils and Other Fills*. British Standardization Institute, 1996.

G den Hoedt, W Voskamp, CJM van der Heuvel. *Creep and time-to-rupture of polyester geogrids at elevated temperatures*. Proceedings 5th International Conference on Geotextiles, Geomembranes and Related Products, Singapore. 1994, Vol. 3, pp 1125–1136.

RA Jewell. *Strength and deformation in reinforced soil design*. Proceedings 4th International Conference on Geotextiles, Geomembranes and Related Products, The Hague, 1990a, Vol. 3, pp 913–947.

RA Jewell. *Revised design charts for steep reinforced slopes*. Reinforced Embankments. London: Thomas Telford, pp 1–30, 1990b.

RA Jewell, JH Greenwood. *Long-term strength and safety in steep soil slopes reinforced by polymer materials*. Geotext Geomembr. 7(1&2): 81–118, 1988.

JP Oostveen, KC Maas, CSH Hendikse. *The coefficient of interaction for geogrids in non cohesive soil*. Proceedings 5th International Conference on Geotextiles, Geomembranes and Related Products, Singapore, 1994 Vol. 1, pp 427–432.

HM Schmidt, FWT te Pas, P Risseeuw, W Voskamp. *The hydrolytic stability of PET yarns under medium alkaline conditions*. Proceedings 5th International conference on Geotextiles, Geomembranes and Related Products, Singapore, 1994 Vol. 3, pp 1153–1159.

GD Small, JH Greenwood, A review of the phenomenon of stress rupture in HDPE Geogrids, Geo Report 19, Geotechnical Engineering Office, Civil Engineering Department, Hong Kong, 1993.

W Voskamp. *Maximum allowable load, bond and other specific design parameters for high modulus polyester reinforcing mats*. Proceedings Seminar on Soil Reinforcement. Hong Kong Inst. of Engineers, Hong Kong, 1986.

W Voskamp. *Determination of allowable design strength of polyester reinforcing mats*. Reinforced Embankments. London: Thomas Telford, pp 67–81, 1990.

W Voskamp. *Determination of maximum allowable load and anchor length of polyester Geogrids*. Proceedings of Kyushu '92, Earth Reinforcement Practice Kyushu. Balkema Rotterdam, 1992, pp 173–178.

W Voskamp. *Flexible or stiff geogrids—state-of-the-art*. The Practice of Soil Reinforcing in Europe. London: Thomas Telford, 1995.

W Wilmers. *Hydrolysis of polyester products—state of the art*. Geosynthesis in Foundation Engineering Information Meeting. Munich, Germany, 1997.

RF Wilson-Fahmy, RM Koerner. *Long term pull-out behaviour of polymeric geogrids*. GRI Report, 1995.

3
Unit Cell Testing of Reinforced Soils

Hoe I. Ling
Columbia University, New York, New York, U.S.A.

1 BASIC PRINCIPLE OF SOIL REINFORCEMENT

Henri Vidal, the person who proposed the principle of reinforced earth (Vidal, 1969), described reinforced earth as "a material formed by combining earth and reinforcement." According to his definition, "earth" covers all types of ground found in nature, or produced by physical or chemical means, including both granular soils and earth that exhibits some slight cohesion. He defined "reinforcement" as all linear components that can withstand major tensile stresses.

Since the introduction of the principle of reinforced earth, construction has advanced much faster than research and theoretical development. Ingold (1982) summarized the early development of soil reinforcement. Described below are the most common theories proposed for reinforced soil and some of the major experimental studies. Reinforced cohesionless soil is described first and then reinforced cohesive soil.

1.1 Pseudocohesion Concept

If bonding by friction is assumed at the soil–reinforcement interface, reinforced soil has a greater strength than its unreinforced counterpart, as shown in Fig. 1. Vidal proposed that reinforcement assisted in introducing a pseudocohesion to the sand which initially possesses no true cohesion.

Schlosser and Long (1973) conducted a more detailed study on reinforced sand using a cylindrical soil specimen reinforced with circular discs of aluminum foil using a triaxial apparatus. Different reinforcement spacings were used in their

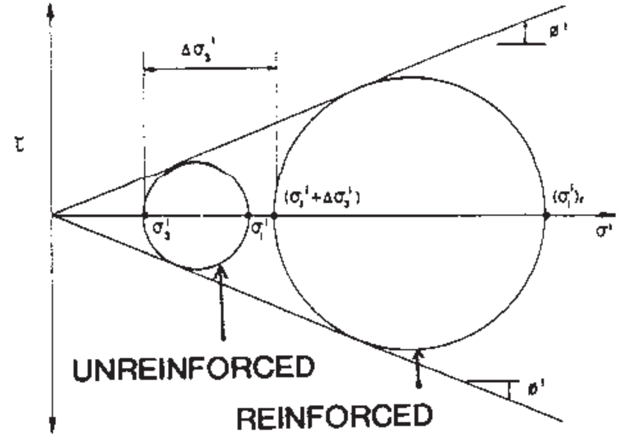

Figure 1 Mohr circle for unreinforced and reinforced soils.

study. The test results showed that the strength of reinforced sand increased with confining pressure, σ'_{3c}. However, beyond a critical value of confining stress, the strength of a reinforced specimen was controlled by the rupture strength of reinforcement, and thus, the slope of the failure line for the reinforced specimen was parallel to that of the unreinforced soil (Fig. 2a). Based on this consideration, they put forward a theory for the mechanism of soil reinforcement.

By giving a term, $\Delta\sigma'_1$, in addition to the strength offered by unreinforced specimen, $K_p\sigma'_3$, the following relationship can be obtained for the strength of reinforced soil specimen:

$$\sigma'_1 = K_p\sigma'_3 + \Delta\sigma'_1 \tag{1}$$

where $K_p = (1 + \sin\phi')/(1 - \sin\phi')$ is the coefficient of passive lateral earth pressure.

By relating the above equation to the Rankine equation for a cohesive-frictional soil, that is,

$$\sigma'_1 = K_p\sigma'_3 + 2\sqrt{K_p}c' \tag{2}$$

the cohesion is obtained as

$$c' = \frac{\Delta\sigma'_1}{2\sqrt{K_p}} \tag{3}$$

With the aid of the force diagram in which the failure plane is inclined at an angle α to the horizontal (Fig. 2b), the following equation is obtained:

$$F + \sigma'_3 A \tan\alpha = \sigma'_1 A \tan(\alpha - \phi') \tag{4}$$

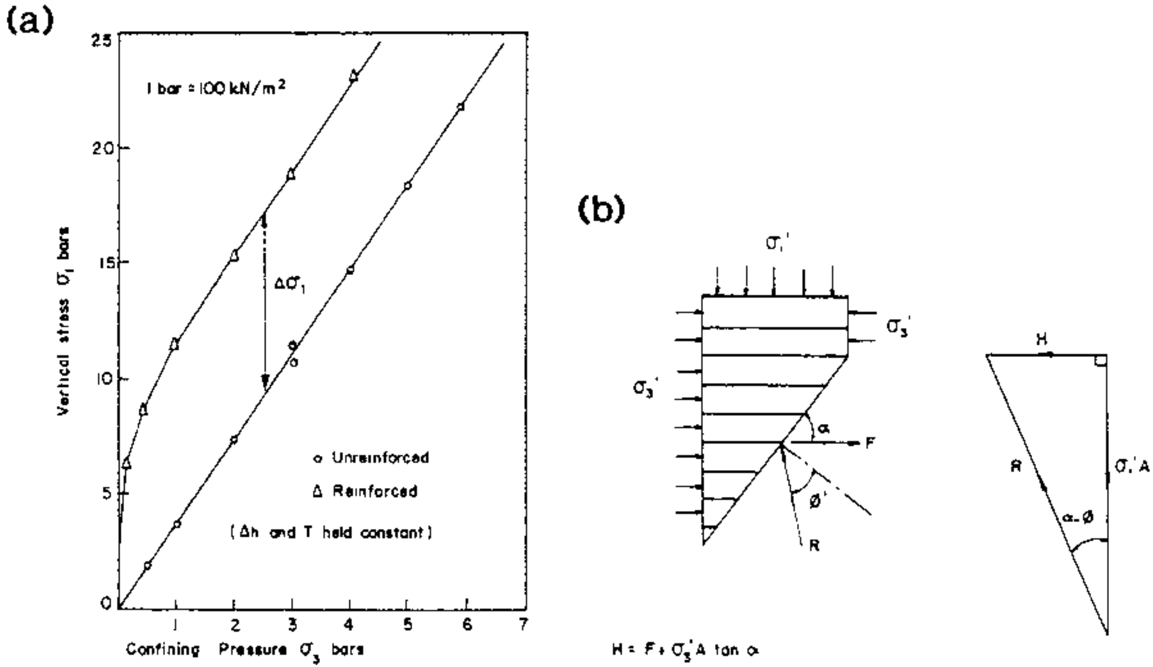

Figure 2 (a) Failure envelopes for unreinforced and reinforced soils; (b) force diagram for reinforced soil. (From Ingold, 1982.)

where F is the tensile force developed in the reinforcement, and A is the cross-sectional area of the specimen. If the spacing h is assumed to be small relative to the specimen height, the following relationship is obtained by equating the horizontal force:

$$F = \frac{A \tan \alpha}{h} T \tag{5}$$

where T is the force in a layer of reinforcement.

The major principal stress is $\sigma_1' = (\sigma_3' + T/h) \tan \alpha \cot(\alpha - \phi')$. Because the maximum value of σ_1' occurs at $\alpha = 45° + \phi'/2$, it is found that

$$\sigma_1' = K_p \sigma_3' + K_p T/h \tag{6}$$

This gives the increment in major principal stress as $\Delta\sigma_1' = K_p T/h$, which is related to the cohesion as

$$c' = \frac{\sqrt{K_p} T}{2h} \tag{7}$$

The experimental results showed reasonable agreement with the theory, which states that the effect of reinforcement is proportional to the tensile rupture strength of reinforcement and inversely proportional to the spacing.

1.2 Confining Pressure Enhancing Concept

Yang (1972) conducted a series of triaxial tests on a cylindrical sand specimen reinforced with discs of fiberglass net or stainless steel. He considered that sandy soil, which is in fact cohesionless, should not be assumed to possess cohesion by inclusion of reinforcement. According to him, the increase in strength due to reinforcement should be regarded as a change in the stress state of soil that resulted in an enhancement of confining stress, $\Delta\sigma_3'$.

The reinforced sand failed at a constant effective stress ratio $\sigma_3' = K_a \sigma_1'$, in which K_a is obtained from the test of unreinforced specimen. Therefore, the strength in a reinforced specimen is

$$\sigma_1' = K_p \sigma_3' + \Delta\sigma_3' \tag{8}$$

Hence, the increase in confining stress can be obtained as the measured value of σ_1' and σ_3' for the reinforced specimen and ϕ' for the corresponding unreinforced specimen. Yang found that $\Delta\sigma_3'$ increased linearly with σ_3' until a critical value is reached, after which it remained constant (Fig. 3). The test results indicated that below this critical confining pressure, the strength of reinforced specimens was controlled by either (1) the slippage at the interface between the reinforcement

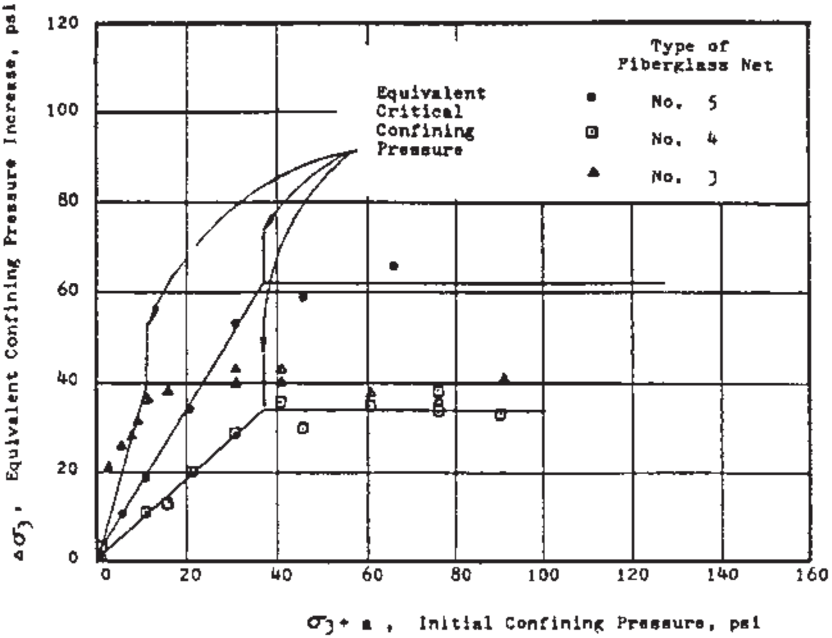

Figure 3 Relationships between initial confining pressure and equivalent confining pressure increase. (From Yang, 1972.)

and sand if the amount of reinforcement is relatively large, or (2) the excessive lateral deformation at the mid-height of specimen.

2 REINFORCED SANDS

The studies described in Sec. 1 were mainly for understanding the fundamental mechanism of soil reinforcement; they chiefly dealt with the effects of spacing and initial confining stress on the strength of the reinforced specimen. With the development of polymeric fabric, the study has tended to focus on geotextiles, both woven and nonwoven, and geogrid. This section gives a brief discussion of experimental work on sand reinforced with geotextile by means of triaxial compression tests (e.g., Broms, 1977; Holtz et al., 1982), plane strain compression tests (e.g., McGown and Andrawes, 1977; Tatsuoka, 1986a), and direct shear tests (e.g., Gray and Ohashi, 1983; Jewell and Wroth, 1987; Shewbridge and Sitar, 1989).

2.1 Triaxial Compression Test

Broms (1977) tested a dry fine sand reinforced with geotextile in a triaxial apparatus to study the effects of spacing, relative density of sand, and confining pressure on the strength of reinforced soil. As can be seen in Fig. 4, the inclusion of geotextile at the specimen mid-height increased the strength. Moreover, the effect of reinforcement, in terms of strength increase, is found to be dependent on the confining stress.

He proposed an equation for calculating the ultimate load in a reinforced soil (Fig. 5a):

$$P = \frac{\pi \sigma'_{ho} K_{av} D^2}{2 \tan^2 \phi'_a} \left(\exp \frac{2 \tan \phi'_a R}{D K_{av}} - \frac{2 \tan \phi'_a R}{D K_{av}} - 1 \right) \tag{9}$$

Where

P: ultimate axial load,
σ'_{ho}: lateral confining pressure at the perimeter of the specimen,
K_{av}: coefficient of lateral earth pressure,
ϕ'_a: frictional angle between the soil and geotextile,
D: geotextile spacing,
R: radius of soil specimen.

In deriving Eq. (9), it is assumed that the stress condition in the soil between the adjacent geotextile discs is constant at the radius r. This is, however, only an approximation of the actual stress condition. An averaged value between the Rankine coefficient for active earth pressure K_a and $K_b = 1/(1 + 2\tan^2 \phi')$ is used for obtaining K_{av}. Equation (9) has since been modified for prediction of ultimate load in reinforced sand under axisymmetric loading through the use of a multiplication factor (Chandrasekaran et al., 1989):

$$P = \frac{\pi \sigma'_{ho} K_{av} R D}{K_a \tan(\alpha \phi'_a)} \left(\exp \frac{\tan(\alpha \phi'_a) R}{D K_{av}} - 1 \right) \tag{10}$$

An equation has also been proposed for determining the tensile force in the reinforcement:

$$T = \frac{\sigma'_{ho} K_{av} D}{K_a} \left(\exp \frac{\tan(\alpha \phi'_a)}{D K_{av}} \frac{R^2 - r^2}{R} - 1 \right) \tag{11}$$

which gives the maximum tensile load in it as

$$T = \frac{\sigma'_{ho} K_{av} D}{K_a} \left(\exp \frac{\tan(\alpha \phi'_a)}{D K_{av}} R - 1 \right) \tag{12}$$

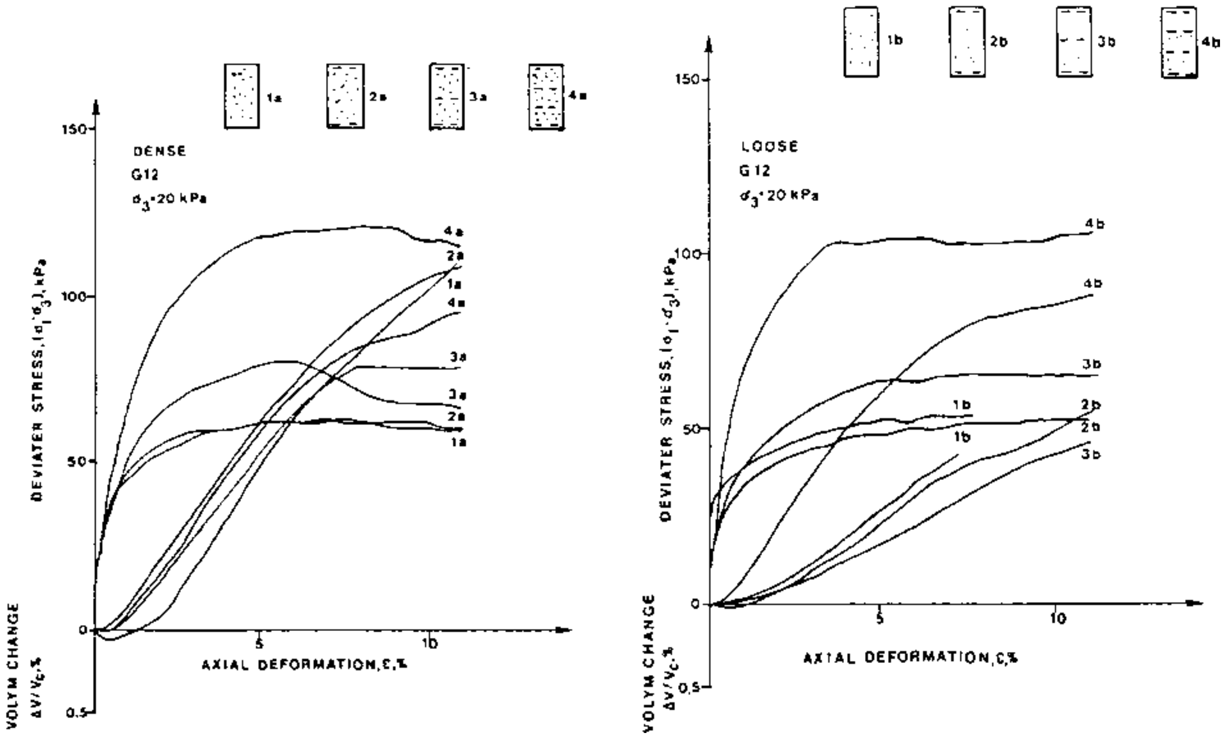

Figure 4 Stress–strain relationships of unreinforced and reinforced sand specimens. (From Broms, 1977).

(a)

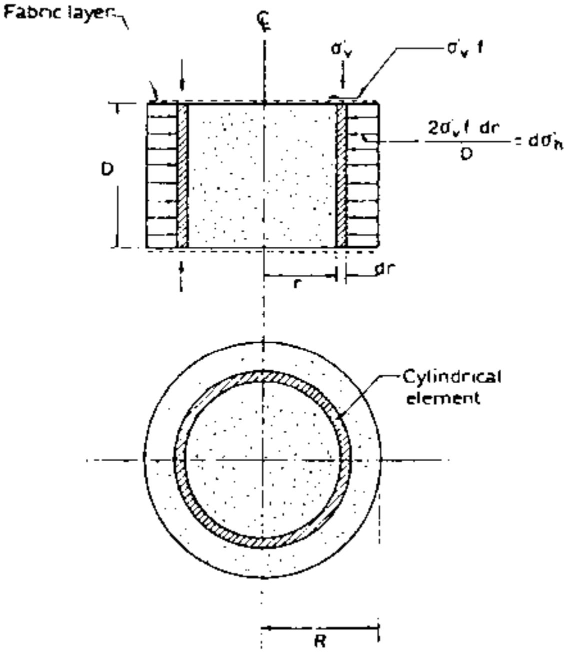

(b)

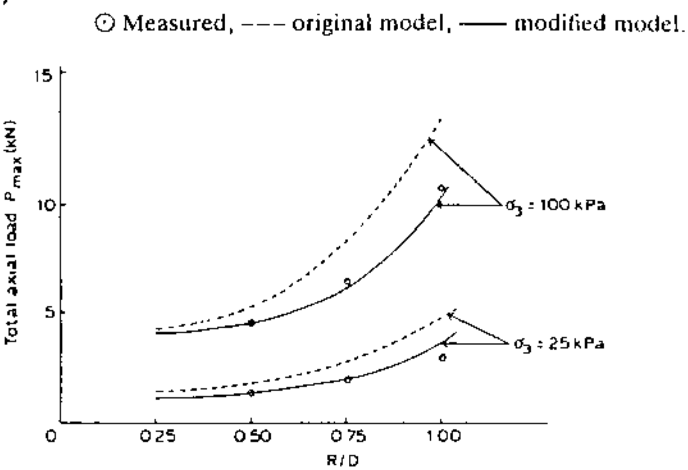

Figure 5 (a) Cylindrical reinforced soil specimen; (b) and (c) comparison between theory and experimental results. (From Chandrasekaran et al., 1989.)

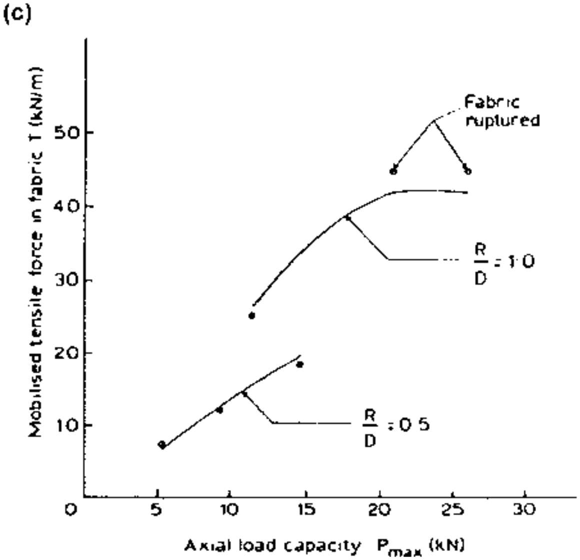

Figure 5 Continued.

Figure 5b compares the measured strength with the modified and original equations. Figure 5c shows the predictive capability of Eq. (12) compared to the tensile load. Note again that this method is based on the crude approximation, and a further development cannot be expected. A more rigorous method of analysis can be performed using the stress characteristics method (Sokolovskii, 1956) as has been performed by Tatsuoka (1986b).

Holtz et al. (1982) performed both short- and long-term tests on sandy soil reinforced with geotextiles. In addition to the strength, they also looked into the deformation modulus of reinforced soil specimen. The strength and deformation modulus were increased due to reinforcement. However, at higher confining pressure, the initial modulus decreased by reinforcing. Holtz et al. (1982) did not explain the reduction in the initial modulus with confining pressure, but the author regards this as a consequence of the isotropic consolidation prior to shearing, as discussed subsequently.

2.2 Plane Strain Compression Test

The above-mentioned studies were based on a cylindrical soil specimen, which does not closely simulate most of the field stress conditions, namely plane strain. McGown and Andrawes (1977) studied reinforced sand using a plane strain apparatus. Leighton Buzzard sand and River Welland sand were used with a heat-bonded nonwoven geotextile. In a dense state, the reinforcement weakened the sand, but it strengthened the sand in loose states. The axial strain to peak strength was increased for reinforced specimens. The effect of angle of inclination of reinforcement on the strength of a reinforced specimen was also studied. The sand was weakened at certain inclination angles, which are close to the zero-extension line. McGown et al. (1978) reported a similar study using the plane strain cell, but focused specifically on "extensible" and "inextensible" materials in which Leighton Buzzard sand was used with a heat-bonded nonwoven geotextile, aluminum foil, and aluminum mesh. The difference in performance of reinforced sand with extensible and inextensible reinforcements was reported.

Tatsuoka (1986a) and Tatsuoka and Yamauchi (1986) performed a study on reinforced sand using different materials as reinforcement in a plane strain apparatus. Moreover, a theoretical study was conducted to investigate the reinforcement effect due to the reinforcement and soil properties, spacing, and initial confining pressure. In the study, the reinforcement material is assumed to be isotropic and linear elastic (Fig. 6a).

Consider a reinforced soil composite that has been consolidated isotropically to a stress state $\sigma_1' = \sigma_2' = \sigma_3'$. It was then sheared to failure at the major principal stress $\sigma_{10}' = K_p \sigma_{30}'$, where $K_p = (1 + \sin\phi')/(1 - \sin\phi')$.

Due to the restraining effect of reinforcement in the composite, the confining pressure in the composite is enhanced to a value

$$\sigma_{3R}' = \sigma_{30}' + \Delta\sigma_3' \tag{13}$$

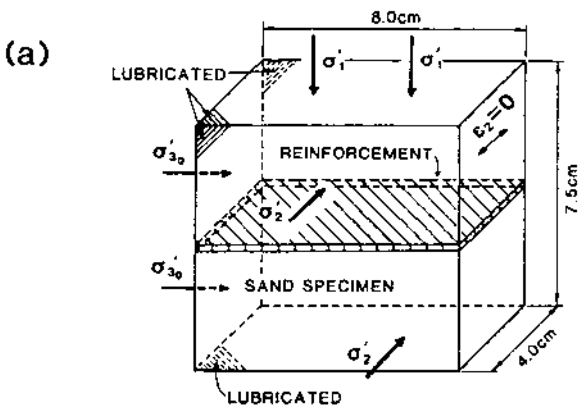

Figure 6 Reinforced sand under plane strain conditions: (a) schematic sketch; (b) stress–strain curves; (c) relationships between R and Et. (From Tatsuoka and Yamauchi, 1986.)

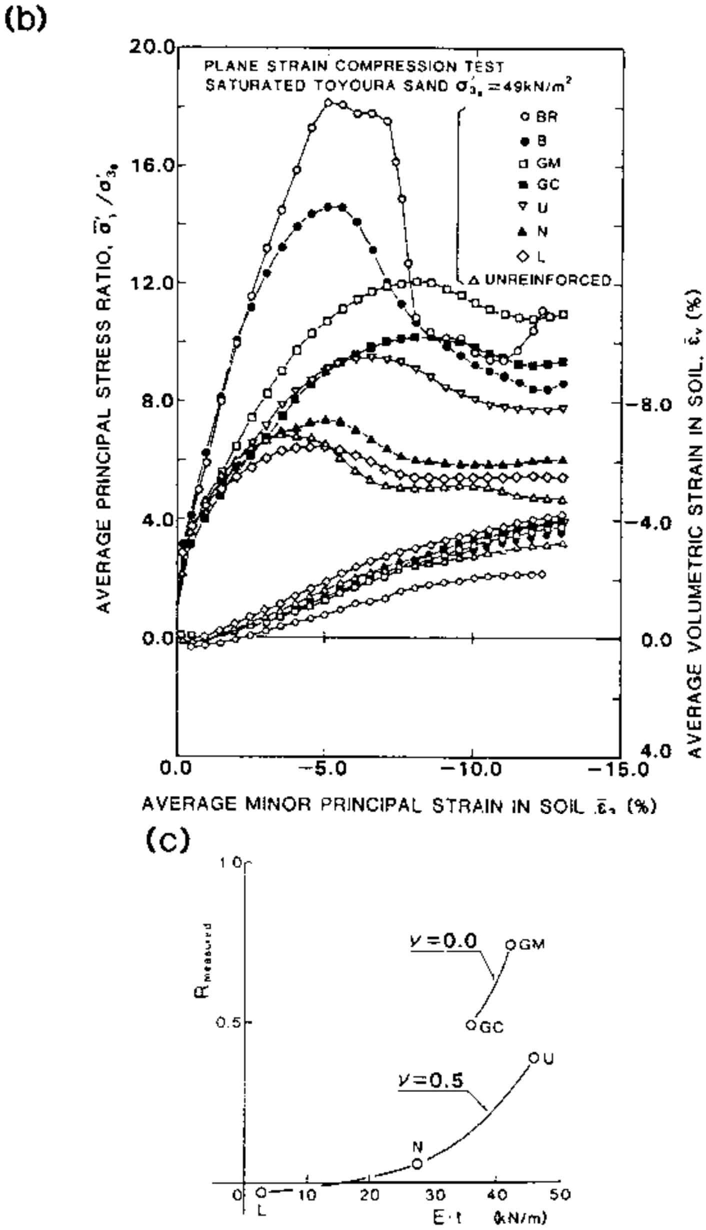

Figure 6 Continued.

That is, the major principal stress in it is $\sigma'_{1R} = K_p \sigma'_{3R}$. Note that these are the averaged values in the composite due to the nonuniform stress distribution in it. The reinforcing ratio is thus defined as

$$R = \frac{\sigma'_{1R}}{\sigma_1} - 1 = \frac{\Delta\sigma'_3}{\sigma'_3} \tag{14}$$

If the lateral strain in the composite, ε_{3R}, and that in the soil, ε_{xR}, are considered rather close, the tensile force per unit width developed in the reinforcement with Young's modulus E and thickness t will be

$$T = \Delta\sigma'_3 \Delta H = (\varepsilon_{xR} - \varepsilon_{3R})Et \tag{15}$$

The reinforcement lateral strain is determined by considering it to be compressed by σ'_{1R} at its plane, subject to a confining pressure σ'_{30}. Consider the composite with reference to Hooke's law at the plane strain condition,

$$\varepsilon_{2R} = \frac{1}{E}[(\bar{\sigma}'_2 - \sigma'_{30}) - v(\sigma'_{1R} - \sigma'_{30})] = 0 \tag{16}$$

On the other hand, for the reinforcement, its lateral strain is

$$\varepsilon_{xR} = \frac{1}{E}[-v(\sigma'_{1R} - \sigma'_{30}) + (\bar{\sigma}'_2 - \sigma'_{30})] = -\frac{v}{E}(\sigma'_{1R} - \sigma'_{30})(1 + v) \tag{17}$$

Substituting Eq. (16) into Eq. (17) gives

$$\varepsilon_{xR} = -\frac{(1 + v)v}{E}(K_p - 1)\sigma'_{30} + K_p\Delta\sigma'_3 \tag{18}$$

By equating Eq. (17) with Eq. (15) for the lateral strain in a reinforcement, the reinforcing ratio is obtained as

$$R = \frac{\Delta\sigma'_3}{\sigma'_{30}} = \frac{-\frac{\varepsilon_{3R}}{\sigma'_{30}} - \frac{(1+v)v}{E}(K_p - 1)}{\frac{\Delta H}{Et} + \frac{(1+v)v}{E}K_p} \tag{19}$$

The equation indicates clearly that a smaller value of v, ΔH, σ'_{30}, and a large value of Et would lead to a greater effect of reinforcing. A greater reinforcing effect will be obtained if a reinforcement has (1) a large value of E with any value of v, (2) a small value of v but a large value of E, (3) a small value of E and also a small value of v. A testing program has been conducted to investigate the validity of Eq. (19) using materials of different values of E and v with the results shown in

Fig. 6b. As shown in Fig. 6c, the trend of relationship between reinforcement ratio (R) and stiffness (Et) was well depicted. A close agreement between the experimental and theoretical values of reinforcement ratio was obtained.

Whittle et al. (1992) conducted an experimental and theoretical study to investigate the mechanism of stress transfer in a reinforced soil mass. The experimental study was conducted using a plane strain cell, which was modified to enable tension force in the reinforcement to be measured directly (Fig. 7a). In the initial stage of test, a steel plate with known elastic properties was used with Ticino sand.

A theoretical study based on the shear lag analysis was also conducted for determining the tensile force developed in reinforcement when the soil undergoes shear deformation. The tensile stress is expressed as

$$\sigma_{xx}^{f} = \frac{K_{2\sigma}}{K_1}\left[1 - \frac{\cosh\sqrt{K_1}(L/2 - x)}{\cosh\sqrt{K_1}(L/2)}\right] \tag{20}$$

where

$$K_{2\sigma} = K_2^1\sigma_1 + K_2^3\sigma_3 \tag{21}$$

and

$$K_1 = \frac{6}{mf}\frac{(1 - v_m)a + 2(G_m/E_f)(1 + v_f)(1 - v_f)}{1 + 0.25v_m - 1.5(G_m/E_f)(1 + v_f)v_f} \tag{22}$$

$$K_2^1 = \frac{6}{mf}\frac{v_m - 2(G_m/E_f)(1 + v_f)v_f}{1 + 0.25v_m - 1.5(G_m/E_f)(1 + v_f)v_f} \tag{23}$$

$$K_2^3 = -\frac{6}{mf}\frac{(1 - v_m)(1 + a)}{1 + 0.25v_m - 1.5(G_m/E_f)(1 + v_f)v_f} \tag{24}$$

Here G_m and E_f are the shear modulus of soil and elastic modulus of reinforcement, respectively. v_m and v_f are the Poisson's ratios of the soil and reinforcement, respectively, and $a = f/m$, with f and m as indicated in Fig. 7b. The maximum load in a very long reinforcement is determined as

$$\sigma^f(L = \infty) = \frac{K_{2\sigma}}{K_1} \tag{25}$$

Figure 7c compares the prediction with the experimental data. The distribution and magnitude of the tensile stress were well predicted.

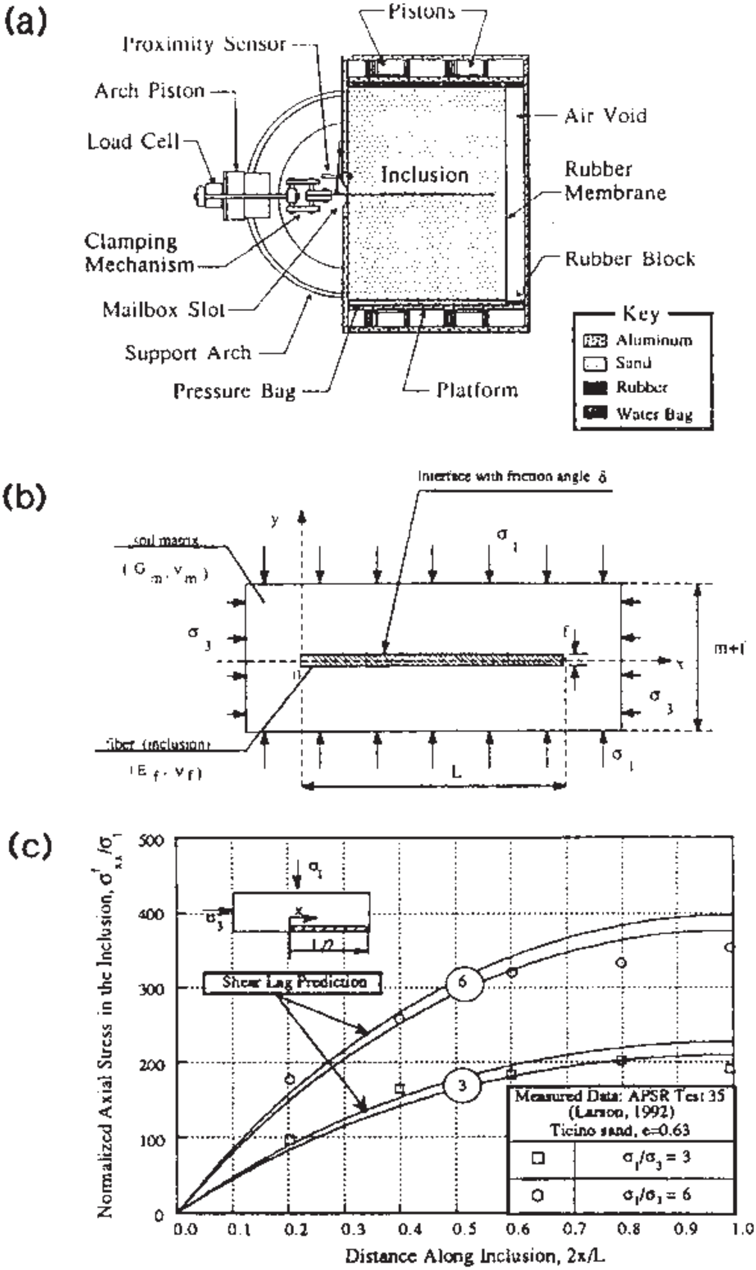

Figure 7 (a) Automated plane strain reinforcement cell; (b) geometry of reinforced soil element; (c) predicted and measured axial stress in reinforcement. (From Whittle et al., 1992.)

2.3 Direct Shear Test

Gray and Ohashi (1983) considered a reinforcement embedded perpendicularly or at an inclination to the shear zone in a direct shear box (Fig. 8). At distortion, tensile force is mobilized in the reinforcement, which can be discomposed into components normal and tangential to the shear plane. The normal component increases the confining stress on the failure plane, thereby mobilizing additional shear resistance in the sand whereas the tangential component directly resists shear. The reinforcement bending stiffness is not considered.

The increase in strength due to reinforcement installed perpendicularly and at an inclination is expressed in Eqs. (26) and (in a more compact form) (27),

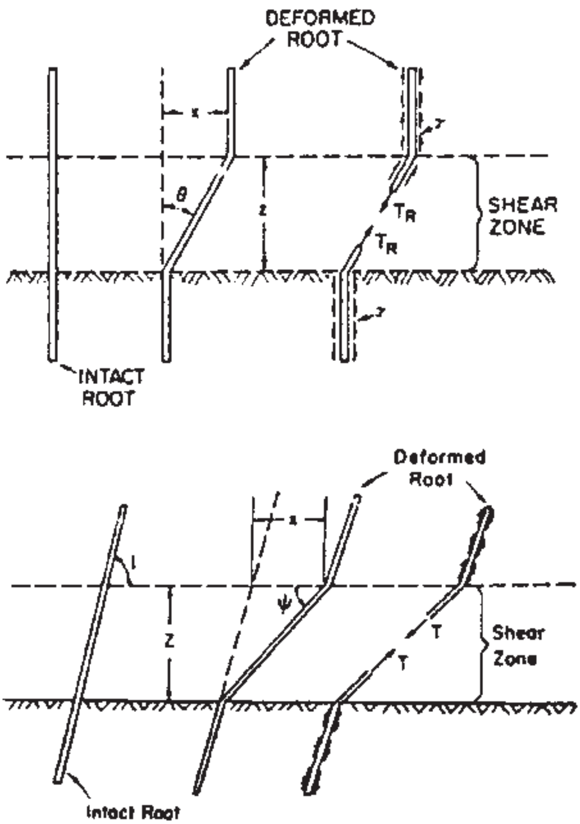

Figure 8 Fiber reinforcement model in direct shear. (From Gray and Ohashi, 1983.)

respectively:

$$\Delta S_R = \frac{A_R}{A}\sigma_R(\sin\theta + \cos\theta\tan\phi') \tag{26}$$

$$\Delta S_R = \frac{A_R}{A}\sigma_R(\cos\psi + \sin\psi\tan\phi') \tag{27}$$

where

$$\psi = \tan^{-1}\frac{1}{k + 1/\tan^{-1} i} \tag{28}$$

ΔS_R: shear strength increase due to reinforcement,
σ_R: tensile stress in reinforcement at shear plane,
A_R/A: reinforcement area to total area in the shear plane,
θ: angle of shear distortion,
i: initial angle of inclination wrt shear plane,
$k(=x/z)$: distortion ratio,
x is the horizontal shear displacement and z is the thickness of the shear zone.

It is necessary to assume the distribution of tensile stress in the reinforcement, either linear or parabolic, in order to estimate the strength increase based on the above equations. Moreover, the thickness of the shear zone should be assumed in using the equations.

Direct shear tests were performed on dry sand reinforced with different types of discrete reinforcement. The effect due to the reinforcement stiffness, diameter, orientation; reinforcement area ratio; friction between sand and reinforcement; and the angle of friction and density of sand were investigated. It was found that the shear strength increase was proportional to the fiber area ratio up to a certain limit and that an inclination of 60° produced the greatest increase in shear strength. While McGown et al., 1978 reported that the increase in strength was more significant for loose sand than dense sand, Gray and Ohashi (1983) reported that the increase was approximately the same for sand in the loose and dense states. These findings were found to be applicable to other types of reinforcement.

There was a critical confining pressure in the failure envelope, similar to that reported by Yang (1972) for a triaxial compression test, below which failure occurred by the pullout of reinforcement. Above this confining pressure, the failure envelopes are parallel to each other due to the rupture strength of reinforcements.

Jewell and Wroth (1987) manufactured a direct shear box for investigating the behavior of both unreinforced and reinforced sand. Leighton Buzzard sand was used. Reinforcement with different stiffness was aligned during shearing as shown in Fig. 9a. Figure 9b shows the effect of reinforcement stiffness on the shear stress–displacement relationship of the composite. At the initial stage of

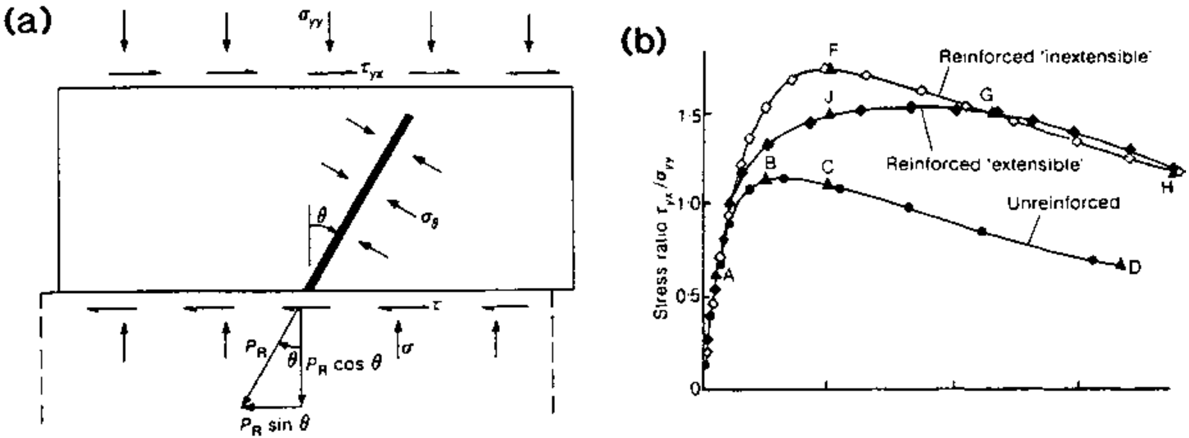

Figure 9 Reinforced sand direct shear test: (a) test configuration; (b) typical test results. (From Jewell and Wroth, 1987.)

shearing, no positive effect of reinforcing was shown, but a difference was noticed for the peak strength between the unreinforced and reinforced specimens. Moreover, extensible and inextensible reinforcements lead to different performance of the reinforced soil.

A consideration similar to that of Gray and Ohashi (1983) regarding the increase in shear strength was put forward. They considered an overall effect of reinforcement in increasing the shearing resistance of soil as expressed by the mobilized angle of friction by an amount

$$\tau_{EXT} = \frac{P_R}{A_s}(\cos\theta \tan\phi' + \sin\theta) \tag{29}$$

By considering strain compatibility between extension in the surrounding soil, mainly governed by plastic strain, and the reinforcement extension, the following relationship was established to relate the increase in the maximum reinforcement force, dP_{RM}, with the shear displacement in sand, dx:

$$\frac{dP_{RM}}{dx} = \frac{K}{L_R \cos\theta}\left[\tan\psi + \frac{\sin(\psi + 2\theta)}{\cos\psi}\right] \tag{30}$$

where

ψ is the angle of dilation,
K is the stiffness of reinforcement,
L_R is the length of reinforcement.

Other notations are indicated in Fig. 9a. A good agreement between theoretical and experimental results was obtained. The angle of friction between the reinforcement and soil was also estimated based on the experimental results, and it was found that the direct shear angle of friction of soil can be the limiting value for the bond.

In view of the importance of the thickness of the shear zone for predicting the strength increase by reinforcement in a direct shear test, as proposed by Gray and Ohashi (1983), Shewbridge and Sitar (1989) conducted a study to examine the mechanism of shear zone development in it. Monterey sand #*O* was used with different types of reinforcement. Based on observation, the geometry of deformed reinforcement was proposed to be as shown in Fig. 10a, and the width of the shear zone was found to be dependent on the reinforcement concentration, stiffness, and bond between sand and reinforcement. It is wider in the reinforced soil than in the unreinforced soil. Similar findings to those of Gray and Ohashi (1983) were obtained regarding reinforcement stiffness, and reinforcement concentration on the strength. Figure 10b shows the relationship between the increase in strength and reinforcement ratio for all the tests. Whereas the relationship was found to be linear by Gray and Ohashi (1983), it is was found to be nonlinear by Shewbridge and Sitar (1989). In Shewbridge and Sitar (1990),

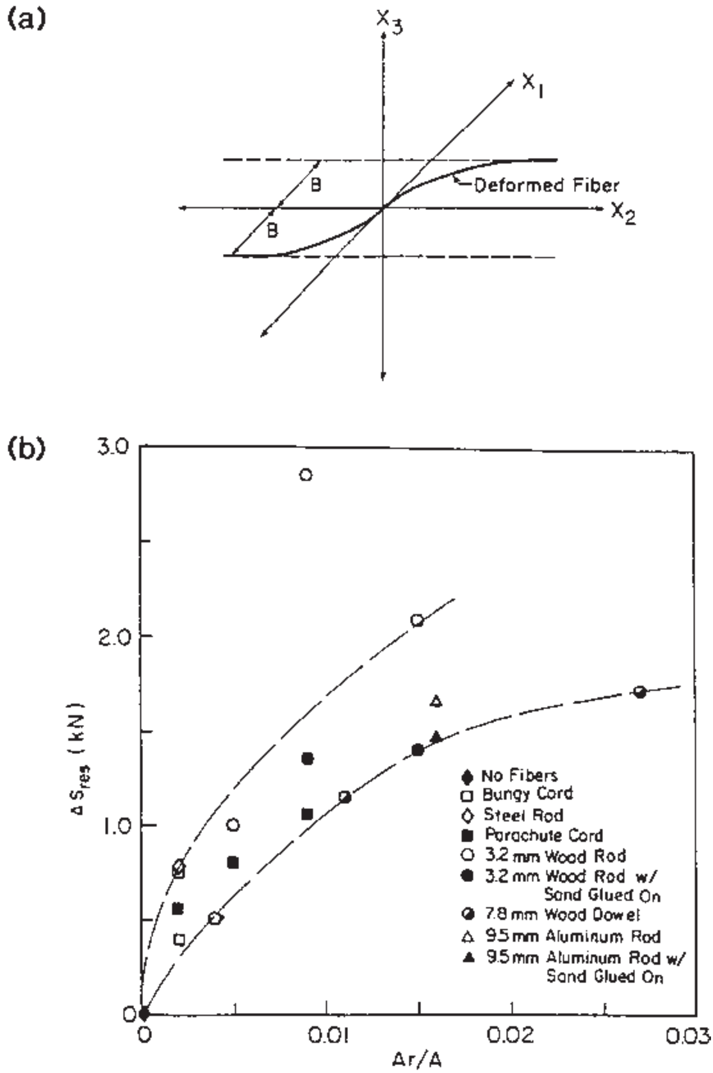

Figure 10 (a) Configuration of deformed reinforcement; (b) relationships between shear strength increase and reinforcement ratio. (From Shewbridge and Sitar, 1989.)

a closed-form solution was derived for determining the tension force in reinforcement when the soil undergoes shear deformation. A more theoretical study was presented in which the effects of different parameters on the width of the shear zone were investigated.

3 REINFORCED CLAY

It is difficult to restrict the type of soil used for reinforced structures to cohesionless soil. As cohesive soil behaves differently when compared to cohesionless soil under otherwise identical conditions, a few research projects had been pioneered using laboratory tests.

3.1 Triaxial Compression Test

Ingold (1979) performed a theoretical study on reinforced soil. His theory is basically similar to that of Broms (1977). It considered the compression of a thick disc of material undergoing compression between frictional platens, which reached an expression for the strength ratio of reinforced soil to unreinforced soil at the following four different conditions:

$$\text{Fully drained: } \exp\frac{\tan\delta}{3Ka\alpha} \tag{31}$$

$$\text{Fully drained at soil reinforcement only: } \exp\frac{\tan\delta}{3\alpha} \tag{32}$$

$$\text{Fully undrained: } 1+\frac{\mu}{4\alpha} \tag{33}$$

$$\text{Internal failure before bond failure: } 1+\frac{1}{4\alpha} \tag{34}$$

where

$\alpha = h/2R$ is the aspect ratio,
δ is the angle of friction between the reinforcement and soil,
μ is a factor that relates bond stress to undrained shear strength of clay.

Experiments were conducted on Kaolin clay reinforced with either porous disc or aluminum foil in unconfined condition. A comparison between the theory and experimental results under drained condition and rapid shear (undrained) is given in Fig. 11. The general trend of relationship between the strength ratio and the aspect ratio was well depicted.

Ingold and Miller (1983) conducted a study on the drained behavior of reinforced clay using triaxial compression tests. Kaolin clay and porous plastic were used. Both unconfined and confined tests were performed. The test results showed an increase in the compressive strength of the reinforced clay, and the ratio of increase became greater in the case of smaller reinforcement spacing.

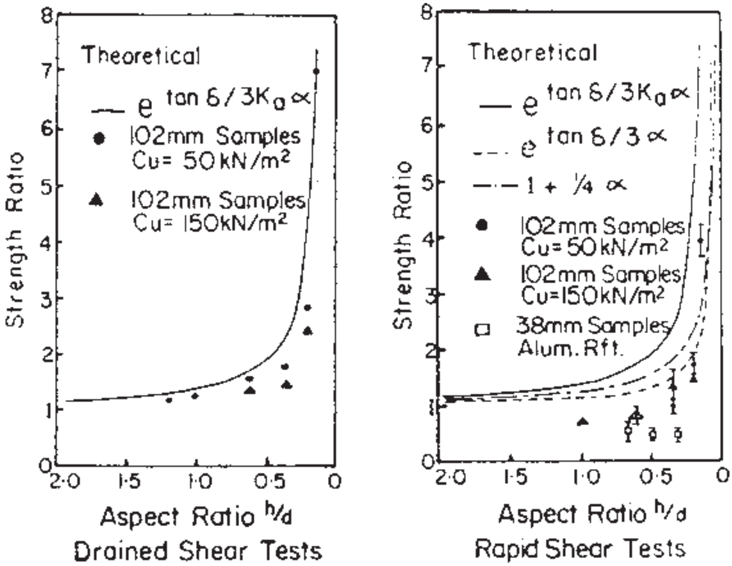

Figure 11 Relationships between strength ratio and aspect ratio. (From Ingold, 1979.)

Ingold and Miller (1982a) also conducted a study on reinforced clay under undrained conditions. Kaolin clay, Boulder clay, and London clay were used. The reinforcements used were porous sintered polythene, needle-punched felt, and heat-bonded geotextiles. A series of triaxial compression tests was performed.

In the unconfined test at a large spacing where the inverse aspect ratio was less than 4, a negative reinforcement effect was found. Ingold and Miller (1982a) believed that it was due to the longer drainage path. They also reasoned that the large pore water pressure generated in the inner part of the specimen caused a premature failure. However, when a larger inverse aspect ratio was used, the strength obtained was close to that at the drained condition. A separate paper by Ingold (1983a) reports results of a similar study.

3.2 Direct Shear Test

Ingold (1981, 1983b) conducted direct shear tests to investigate the adhesion factor between reinforcements of different roughness and the clay in which they were embedded. The undrained shear strength of reinforced soil, c_{uR}, is due to the true undrained strength of soil, c_u, and increment due to reinforcement, Δc_u. Consider the arrangement of reinforcement as in Fig. 12a; the mobilized tensile force in it is determined as

$$T = 2\alpha c_u Lb \tag{35}$$

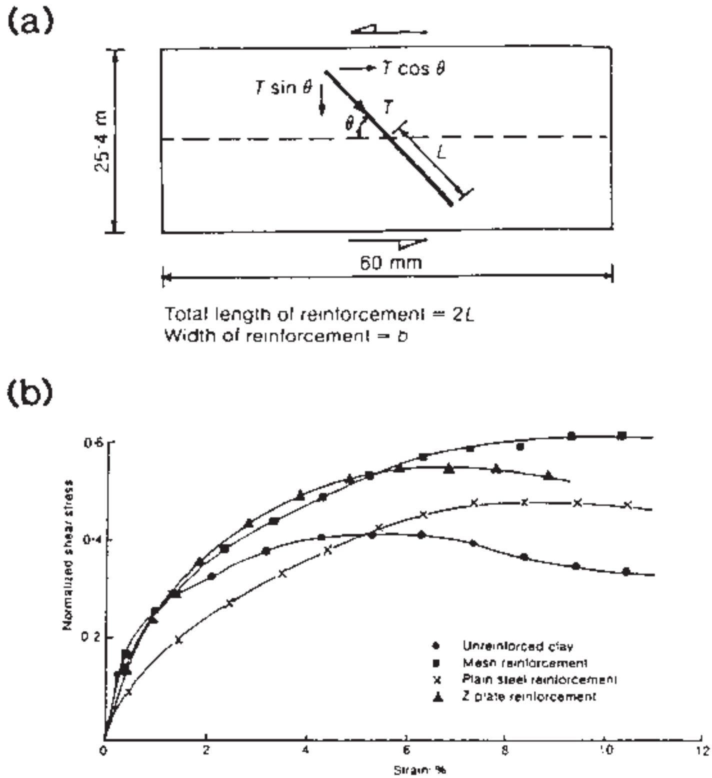

Figure 12 Arrangement of reinforcement in shear box; (b) shear stress–strain relationships. (From Ingold, 1981.)

The vertical and horizontal forces due to N reinforcement would be

$$T_v = 2N\alpha c_u Lb \sin\theta \tag{36}$$

$$T_h = 2N\alpha c_u Lb \cos\theta \tag{37}$$

Assuming that the increment in undrained shear strength by reinforcement, Δc_u, is due to the horizontal force, the adhesion factor is determined as

$$\alpha = \frac{\Delta c_u A}{2Nc_u Lb \cos\theta} \tag{38}$$

where A is the area of the shear box.

Figure 12b shows the results for unreinforced and reinforced clay specimens. There was a relationship between values of Δc_u and α for different materials. The results were applied to the analysis of simulated earth walls.

Ingold and Miller (1982b) extended their study to reinforced clay under undrained conditions and sheared by plane strain compression. Plastic geogrid was used to reinforce London clay, and the test was performed in a plane strain apparatus. It was considered that the reinforcement had imparted an equivalent undrained shear strength to the clay. That is,

$$c_u' = c_u(1 + \alpha B/4S) \tag{39}$$

where α is the adhesion factor. A comparison between this theory and experimental results gave favorable agreement.

Yamauchi (1986) performed triaxial compression tests on unreinforced as well as reinforced Kanto loam (silty clay) specimens. These tests were performed at an effective confining stress of 50 kPa subjected to a back pressure of 200 kPa. Four layers of nonwoven geotextile were used in the reinforced specimen. These test results were reported in Murata et al. (1991) as well.

As shown in Fig. 13a, almost no effect of reinforcement was realized for the undrained test. For the drained test (Fig. 13b), reinforcement effect in terms of strength increase was realized, but the stiffness was much smaller in the reinforced specimen when compared to the unreinforced one. The difference in the ultimate strength between the drained and undrained tests can be explained by two factors—the effect of tensile reinforcing and the effect of excess pore water pressure due to the compressibility of the nonwoven geotextile. Because the effect of the latter was not realized in the drained test, the overall effect was positive. For the undrained tests, the effects due to these two factors may have been balanced.

Fabian (1988) performed triaxial undrained and drained compression tests on a Kaolin clay reinforced with different kinds of geosynthetic. In the undrained tests, unconsolidated and consolidated tests were performed. A lower stiffness was noticed for the reinforced specimen when compared to the unreinforced one, especially the strength ratio was less than or about unity for some of the unconsolidated undrained tests. In the drained tests, a similar finding to Yamauchi's (1986) was obtained. The strength ratio was greater than unity, but the stiffness was much lower in the reinforced specimens when compared to the unreinforced specimens.

It was shown in his study that geosynthetics with drainage capability helps in improving the undrained strength of reinforced clay. He provided a similar reason to Ingold's (1982a) regarding the lower strength in reinforced specimen when compared to the corresponding unreinforced specimen. That is, a higher excess pore water pressure generated in the middle of specimen led to

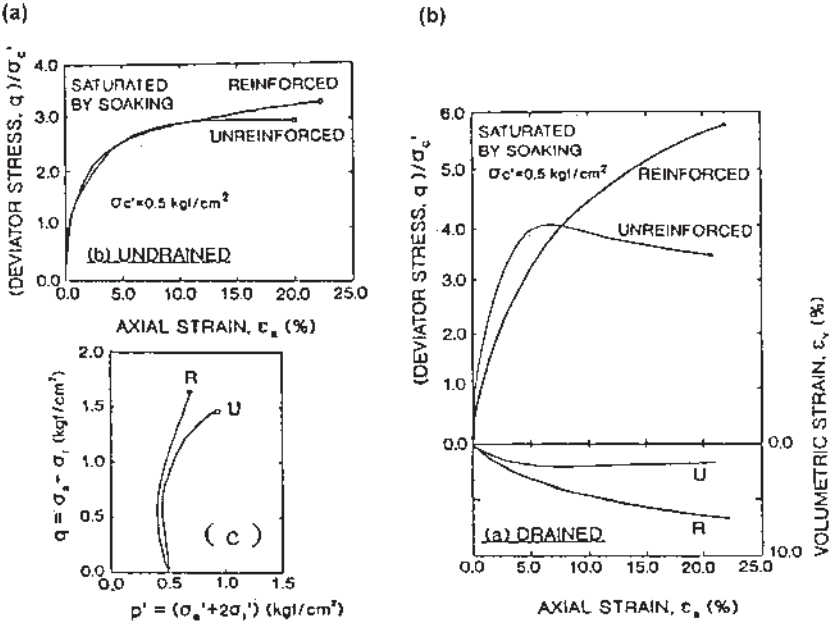

Figure 13 Stress–strain relationships of reinforced clay: (a) undrained and (b) drained tests. (From Murata et al., 1991.)

premature failure. However, when a permeable geotextile is used, this pore pressure is evenly distributed in the specimen and, therefore, the strength is enhanced.

3.3 Anisotropically Consolidated Plane Strain Compression Tests

All above triaxial and plane strain compression tests on a reinforced cell unit were conducted on isotropically consolidated specimen. The isotropic consolidation generated compression along the axial direction of reinforcement and thus inhibits its function as tensile reinforcement until lateral tensile strain is remobilized. This strain path is in contradiction to field conditions.

Ling (1993) and Ling and Tatsuoka (1994) conducted a series of plane strain compression tests on a silty clay that has been consolidated isotropically and anisotropically, under both drained and undrained conditions. The test setup is shown in Fig. 14a, and three different types of reinforcement and initial stress ratios were used. The results for undrained and drained tests are shown in Figures 14b and c, respectively. A smaller initial stress ratio and large reinforcement

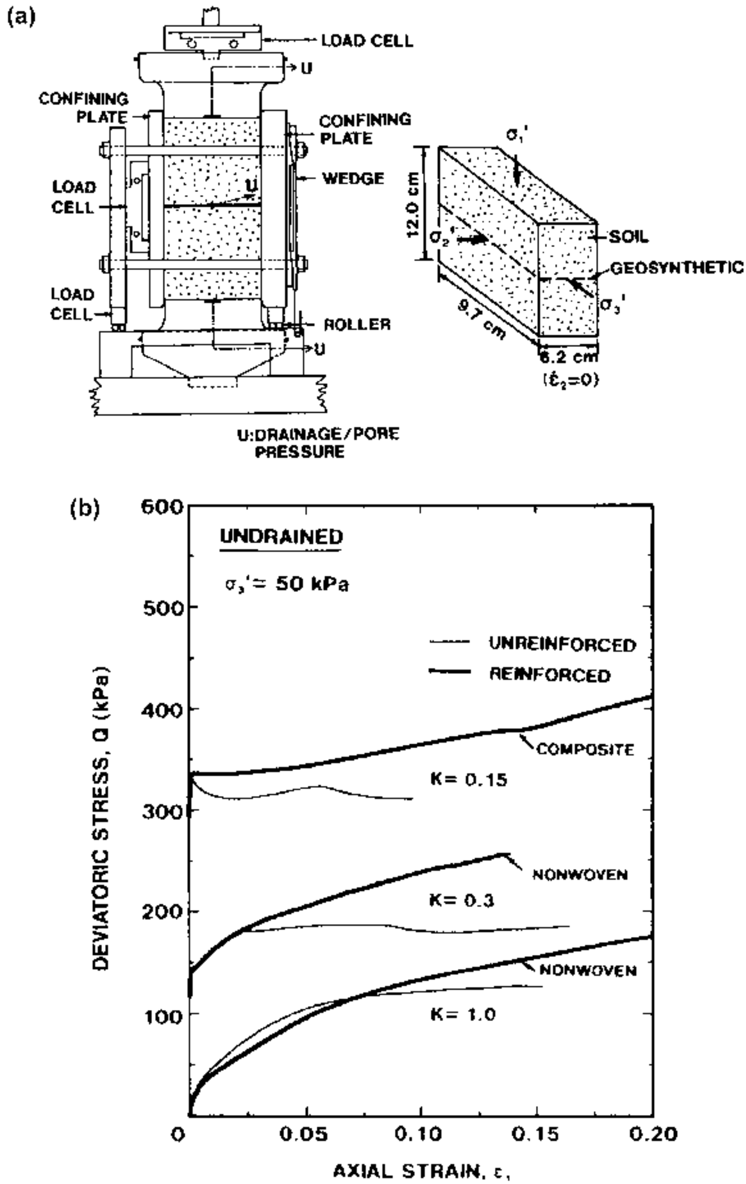

Figure 14 (a) Plane strain compression device; (b) test results under undrained conditions.

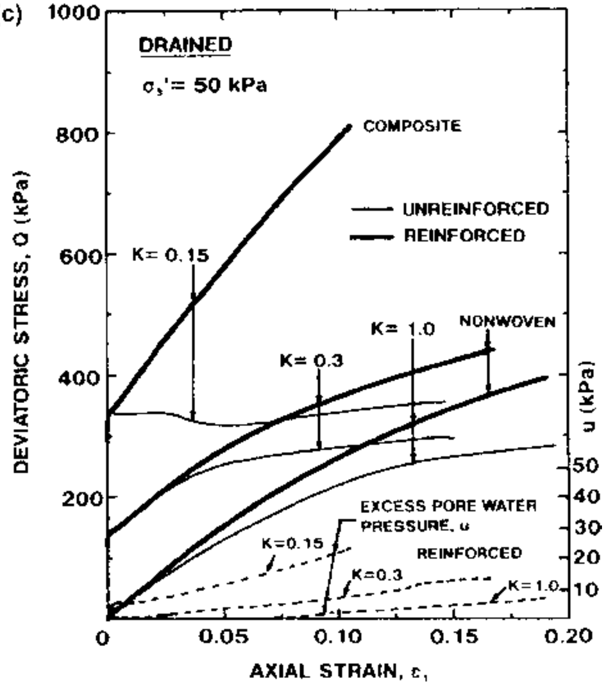

Figure 14 (c) Test results under drained conditions. [(a)–(c) From Ling, 1993; Ling and Tatsuoka, 1994.]

stiffness resulted in large reinforcement effects for drained conditions. Under undrained conditions, very little reinforcement effects were realized.

4 THEORY OF REINFORCEMENT WITH REFERENCE TO STRAIN FIELDS

Instead of a theory based on the stress and strength of the materials, some researchers, such as, McGown et al. (1978), Bassett and Last (1978), and Tatsuoka (1986b), investigated the strain fields in reinforced soil mass. The study was theoretically conducted, with the aid of the Mohr circle of strain increment (Fig. 15).

In the Mohr circle of strain increment, the pole or origin of planes determines the directions of the major and minor principal strain increments $\dot{\varepsilon}_1$

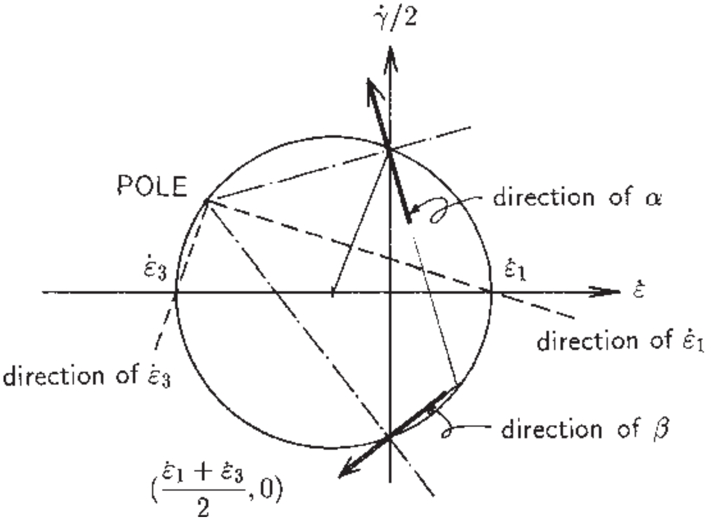

Figure 15 Mohr circle of strain increments.

and $\dot{\varepsilon}_3$, and the α and β planes. The planes are connected to form zero extension trajectories, which give the potential slip surface in a soil mass.

It is found that the reinforcement should be placed in the tensile arc for it to be effective, and the optimum direction should be parallel to the $\dot{\varepsilon}_3$ direction. On the other hand, the reinforcement placed along the zero-extension trajectories would not function; it may weaken the soil mass under certain circumstances. For example, if the frictional bond between the reinforcement and soil is less than that of the soil at the interface, slippage would occur.

With the inclusion of reinforcement, the strain field in the soil mass can be significantly modified. Figure 16a shows the results by Jewell and Wroth (1987), in which the increase in strength was realized when the reinforcement was placed vertically ($\dot{\varepsilon}_3$-direction), whereas no effect was realized when placed horizontally (zero-extension direction). Tatsuoka (1986a) performed model tests on the bearing capacity of footing on unreinforced and reinforced Toyoura sand. Figure 16b shows the strain fields in unreinforced and reinforced foundations at peak value strength. The modification of strain fields after placing the reinforcement along the $\dot{\varepsilon}_3$-direction was noticed.

In applying strain field analysis to the reinforcement of bearing capacity, slope, embankment foundation, and so on, it is necessary that experiments be performed using reduced scale or centrifuge models. A more powerful and versatile method for this purpose would be that based on the finite-element

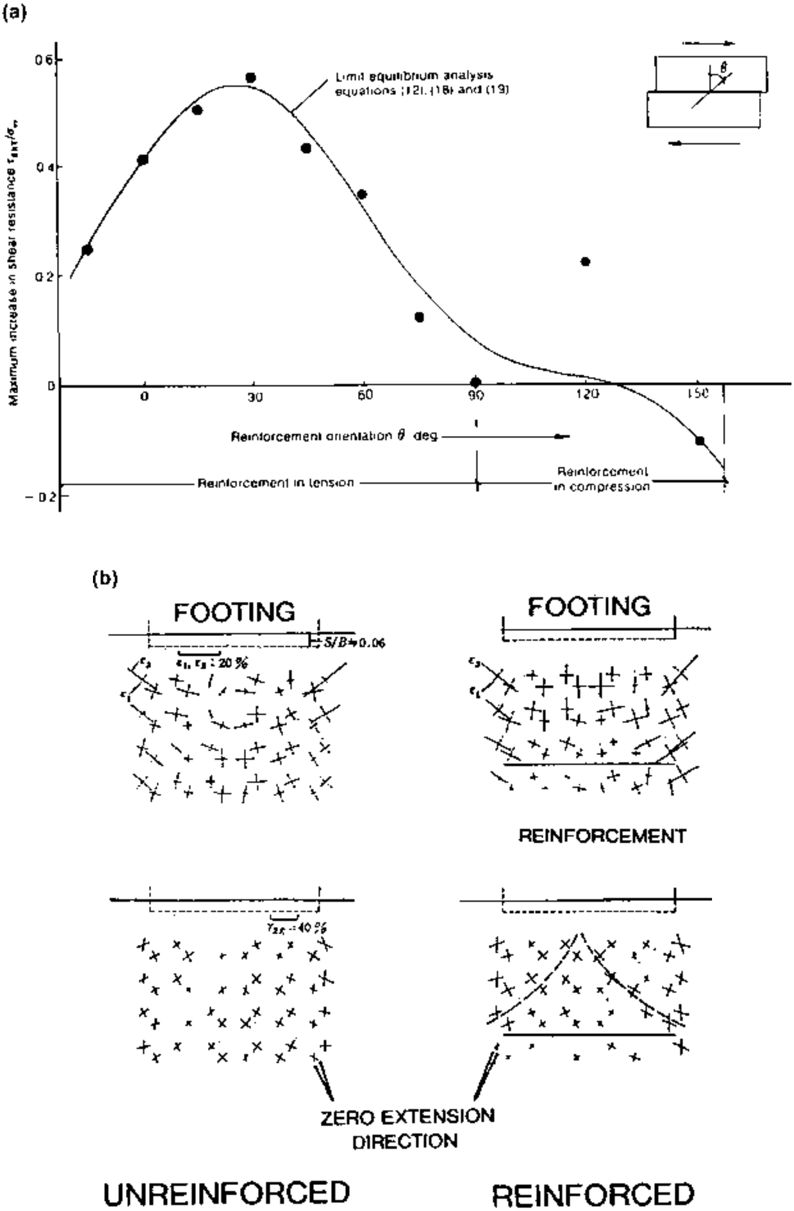

Figure 16 (a) Effects of reinforcement orientation on increase of shear strength in direct shear test. (From Jewell and Wroth, 1987.) (b) Strain fields beneath unreinforced and reinforced foundations. (From Tatsuoka, 1986b.)

procedure. The zone of shear stress concentrations and thus potential failure surface can be depicted from the results of analysis.

5 CONCLUSIONS

The use and limitations of different unit cell devices in studying the reinforcing mechanism of soils are discussed. The strain path of reinforcement is an important issue to be considered, and the drainage conditions if cohesive is used. For boundary-value problems, unit cell testing will not be relevant. In addition to the study of mechanism, the triaxial compression test may also be used to determine the input parameters for constitutive models in finite-element analysis based on the "composite" approach, in which the soil–geosynthetic composite was treated as a locally homogeneous material (e.g., Wu et al., 1992).

REFERENCES

RH Bassett, NC Last. Reinforcing earth below footings and embankments. *Proceedings of Symposium on Earth Reinforcement*. Pittsburgh, 1978, ASCE, pp 202–231.

BB Broms. Triaxial tests with fabric-reinforced soil. *C.R. Coll. Int. Sols Text. Paris*: 129–133, 1977.

B Chandrasekaran, BB Broms, KS Wong. Strength of fabric reinforced sand under axisymmetric loading. *Geotext. Geomembr.* 8: 293–310, 1989.

K Fabian. Clay geotextile interaction in triaxial tests. Chapter 5 in *Clay–Geotextile Interaction Laboratory and Model Tests.* Thesis submitted for the degree of Doctor of Philosophy, University of Queensland, Australia, pp 5-1–5-38, 1988.

DH Gray, H Ohashi. Mechanics of fiber reinforcement in sand. *J. Geotech. Eng. ASCE* 109(3): 335–353, 1983.

RD Holtz, WR Tobin, WW Burke. Creep characteristics and stress–strain behavior of a geotextile-reinforced sand. *Proceedings of Second International Conference on Geotextiles*, Las Vegas, 1982, pp 805–809.

TS Ingold. Reinforced clay—A preliminary study using the triaxial apparatus. *C.R. Coll. Renforcement des Sols. Paris*: 59–64, 1979.

TS Ingold. A laboratory simulation of reinforced clay walls. *Geotechnique* 31(3): 399–412, 1981.

TS Ingold. Mechanics and concept. *Reinforced Earth*, Chapter 2. London: Thomas Telford, 1982, pp 4–32.

TS Ingold. Reinforced clay subject to undrained triaxial loading. *J. Geotech. Eng. ASCE* 109(5): 738–744, 1983a.

TS Ingold. A laboratory investigation of grid reinforcements in clay. *Geotech. Testing J. ASTM* 6(3): 112–119, 1983b.

TS Ingold, KS Miller. The behavior of geotextile reinforced clay subject to undrained loading. *Proceedings of Second International Conference on Geotextiles*, Las Vegas, 1982a, pp 593–597.

TS Ingold, KS Miller. Analytical and laboratory investigations of reinforced clay. *Proceedings of Second International Conference on Geotextiles*, Las Vegas, 1982b, pp 587–592.

TS Ingold, KS Miller. Drained axisymmetric loading of reinforced clay. *J. Geotech. Eng. ASCE* 109(7): 883–898, 1983.

RA Jewell, CP Wroth. Direct shear tests on reinforced sand. *Geotechnique* 37(1): 53–68, 1987.

HI Ling. Performance of geosynthetic-reinforced cohesive soil mass at plane strain compression. Doctoral Thesis, University of Tokyo, Tokyo, Japan, 1993.

HI Ling, F Tatsuoka. Performance of anisotropic geosynthetic-reinforced cohesive soil mass. *J. Geotech. Eng. ASCE* 120(7): 1166–1184, 1994.

A McGown, KZ Andrawes. The influences of non-woven fabric inclusions on the stress strain behavior of a soil mass. *C.R. Coll. Int. Sols. Text. Paris*: 161–166, 1977.

A McGown, KZ Andrawes, MM Al-Hasani. Effect of inclusion properties on the behavior of sand. *Geotechnique* 28(3): 327–346, 1978.

O Murata, M Tateyama, F Tatsuoka. A reinforcing method for earth retaining walls using short reinforcing members and a continuous rigid facing. *Proceedings of Geotechnical Engineering Congress 1991*. Geotechnical Special Publication No. 27. New York: ASCE, 1991, pp 935–946.

F Schlosser, NT Long. Etude du comportement du materiau terre armee. *Annales de l'Inst. Techq. du Batiment et des Trav. Publ.* Suppl. No. 304, Ser. Mater. No. 45, 1973.

SE Shewbridge, N Sitar. Deformation characteristics of reinforced sand in direct shear. *J. Geotech. Eng. ASCE* 115(8): 1134–1147, 1989.

SE Shewbridge, N Sitar. Deformation-based model for reinforced sand. *J. Geotech. Eng. ASCE* 116(7): 1153–1170, 1990.

W Sokolovskii. *Statics of Granular Material*. New York: Pergamon Press, 1956.

F Tatsuoka. Forces acting on reinforced soil mass. *Soil Reinforcement Method*. Geotechnical Library 29, Chapter 2, in Japanese Geotechnical Society. Tokyo, Japan, 1986a, pp 53–71.

F Tatsuoka. Relationship between properties of tensile reinforcement, spacing, and reinforcement effect. *Soil Reinforcement Method*. Geotechnical Library 29, Chapter 3, in Japanese Geotechnical Society. Tokyo, Japan, 1986b.

F Tatsuoka, H Yamauchi. A reinforcing method for steep clay slopes using a nonwoven geotextile. *Geotext. Geomembr.* 4: 241–268, 1986.

H Vidal. The principle of reinforced earth. *Highway Res. Record No. 282*: 1–16, 1969.

AJ Whittle, JT Germaine, DG Larson, M Abrament. Measurement and interpretation of reinforcement stresses in the APSR cell. *Proceedings of International Symposium on Earth reinforcement Practice*, Fukuoka, 1992, pp 179–184.

JTH Wu, BD Siel, NNS Chou, HB Helwany. The effectiveness of geosynthetic reinforced embankments constructed over weak foundations. *Geotext. Geomembr.* 11(2): 133–150, 1992.

H Yamauchi. Investigation of reinforcing effect by laboratory model tests *A Reinforcing Method for Steep Clay Slopes Using a Non-woven Geotextile* Doctoral Thesis, Chapter 4. University of Tokyo, Tokyo, Japan.

Z Yang. Strength and deformation characteristics of reinforced sand Ph.D. Thesis, University of California, Los Angeles.

4

Modeling the Time-Dependent Behavior of Geosynthetically Reinforced Soil Structures with Cohesive Backfill

V. N. Kaliakin
University of Delaware, Newark, Delaware, U.S.A.

M. Dechasakulsom
Road Research and Development Center, Bangkok, Thailand

1 INTRODUCTION

The popularity of soil structures reinforced with mechanical inclusions has brought to light the important issues of service life and durability. Unlike other civil structures, the load-bearing elements of reinforced soil structures are difficult to inspect, and essentially impossible to maintain. In addition, they are buried in soil, a complex environment with physical and chemical characteristics that may vary greatly from site to site.

When geosynthetics such as geotextiles and geogrids are used as the reinforcement, long-term performance becomes an even more important issue. This is because geosynthetics are generally manufactured from polymer materials that exhibit a load, load rate, and temperature-dependent elastic-viscoplastic behavior.

For geosynthetically reinforced soil structures with a long design life (e.g., 70–120 years), long-term performance is obviously of importance. In the design of such structures, stability and serviceability considerations require that the reinforcement (1) not attain its ultimate state of collapse; i.e., tensile rupture (a strength criterion), and (2) not develop excessive strain over its design life (a strain criterion). For example, in the case of polyester geogrids, long-term design strength is usually governed by tensile rupture; for polyethylene, the long-term design strength may be governed by either strain or rupture (Ingold et al., 1994).

Recently, a limited number of geosynthetically reinforced soil structures with cohesive backfill have performed favorably. In particular, the results of experimental and full-scale tests demonstrated that both the short-term and long-term strength of cohesive soil might be increased by grid reinforcement (Jewell and Jones, 1981). Bergado et al. (1993) reported that appropriately compacted cohesive soils could generate pullout capacities comparable to those associated with granular soils. This indicates that such structures have the potential of being used in lieu of granular backfill, with the possibility of significant savings in construction costs.

The rational analysis of geosynthetically reinforced soil structures with cohesive soil requires a time-dependent representation of not only the reinforcement, but also of the backfill. The latter, which is typically not an issue for granular soils, tends to complicate the analysis. As an aid to analysts, this paper presents a critical review of the state of the art in time-dependent modeling and analysis of geosynthetically reinforced soil structures with cohesive backfill. It is tacitly assumed that the analysis will be carried out numerically using the finite-element method.

The numerical aspects of time-dependent finite-element analyses are well understood. Details pertaining to such aspects are, however, beyond the scope of this paper. The interested reader is directed to references on the subject, such as Zienkiewicz and Taylor (2000).

2 GENERAL PROBLEM FORMULATION

The use of cohesive soils, possibly with low permeability, as backfill has the potential of complicating the problem formulation. In particular, if the backfill is largely saturated, the issues of excess pore pressure and flow of pore fluid become significant. Consequently, the problem must be cast in the framework of a coupled deformation-flow ("Biot") formulation. In such a mixed formulation, the primary dependent variables are typically displacements and pore pressures.

If excess pore pressures are not a concern, an irreducible formulation with displacements as primary dependent variables is sufficient. Provided that nearly incompressible material idealizations are avoided, a rather wide range of irreducible elements can be used in the analysis. These are briefly discussed in the next section.

3 SPATIAL DISCRETIZATION OF SOIL

Mixed formulations complicate finite-element analyses in that the particular elements used to discretize the problem must be chosen judiciously—not all elements will yield meaningful results (Hughes, 1987). To date, very few coupled deformation-flow analyses of geosynthetically reinforced soil structures have been performed.

Irreducible finite-element analyses of reinforced soil structures have employed various continuum elements to discretize the backfill soil. Constant strain triangles (Banerjee, 1975), four-node quadrilaterals (Herrmann and Al-Yassin, 1978; Al-Yassin and Herrmann, 1979; Seed and Duncan, 1986; Ling et al., 2000), nonconforming five-node quadrilaterals (Romstad et al., 1976; Shen et al., 1976; Chang and Forsyth, 1977; Al-Hussaini and Johnson, 1978; Ebeling et al., 1992), and six-node quadrilaterals (Naylor, 1978; Naylor and Richards, 1978) have all been used in such analyses.

For the most part, the above analyses were confined to "working stress" (nonfailure) conditions. If the analysis is to be continued to failure, the choice of element type and their spatial distribution is more critical. Past work (Nagtegaal et al., 1974; Sloan and Randolph, 1982) indicates that constant, linear, quadratic, and cubic strain triangles are capable of accurately simulating failure conditions, particularly for soft soils under undrained conditions. Eight-node quadrilateral elements employing reduced integration do not appear to give as accurate results (Sloan, 1984).

In developing finite-element models of reinforced soil structures, one important aspect that is sometimes overlooked is the extent of the boundaries of the solution domain. If a specific structure has fixed boundaries due to the manner in which it was constructed (e.g., if it is built in the laboratory in a frame and resting on a rigid floor), then the boundaries of the solution domain are directly known. However, if a field structure is analyzed, the boundaries of the domain are not explicitly known. There are two approaches for modeling domain boundaries for the latter case.

In the first approach, the exterior boundary of the solution domain is fixed at a large but finite distance. Using standard finite elements, the domain is then discretized only up to this exterior boundary. The extent of this boundary is fixed by performing mesh sensitivity studies in which the boundary is progressively extended outward until further increases in the boundary have no appreciable effect on the solution. This approach has the potential disadvantage of possibly introducing new error sources. In particular, in quasi-static analyses, the stiffness of an infinite domain differs from that for a finite domain; in dynamic analyses, infinite domains do not include boundaries that reflect waves, whereas finite domains do.

A second, and more elegant, way of analyzing such problems is to look at the domains in their entirety. More precisely, the portion of the domain in which the response is of interest is discretized using standard finite elements. Along the boundary, the domain is represented by so-called 'infinite' elements, which were first proposed by Bettess (1977). During the last 20 years, a number of authors have refined this element type (Bettess, 1980; Curnier, 1983; Zienkiewicz et al., 1983; Marques and Owen, 1984; El-Esnawy et al., 1995), so that today analysts can make use of this procedure for static and dynamic analyses in a straightforward manner. One big advantage of this method is that it merely implies an addition to the element library of the finite-element code being used and yet allows for an accurate representation of semi-infinite half-spaces. The application of "infinite" elements to the modeling and analysis of geotechnical problems was recently studied by Fuchs (1999) and Dechasakulsom (2000), who critically assessed the advantages and drawbacks of such an approach.

4 CHARACTERIZATION OF COHESIVE BACKFILL

In mathematically modeling the cohesive soil retained by the geosynthetically reinforced soil structure, it is important to account for its time dependence. This is best realized by characterizing the soil as an elasto-viscoplastic continuum. From a practical point of view, the analysis is complicated by the need to account for material nonlinearities.

Many constitutive models have been proposed that can provide a time-dependent material characterization. The two general types of models are elastic-viscoplastic (Adachi and Oka, 1982; Nova, 1982; Sekiguchi, 1984; Borja and Kavazanjian, 1985; Oka, 1985) and coupled elastoplastic–viscoplastic (Kaliakin and Dafalias, 1990) based formulations. Further details pertaining to such models are beyond the scope of this paper. The interested reader is directed to the above references and to the state-of-the-art review of Adachi et al. (Adachi et al., 1996).

While there is no question that modeling cohesive soils in a time-dependent manner is a correct and rational approach, it is timely to note that a rather large number of past analyses of geosynthetically reinforced soil structures involving such soils has instead employed time-independent models. These have typically been variants of the quasi-linear elastic ("hyperbolic") idealization of Duncan and Chang (1970). While such models are quite easy to implement, recent numerical studies (Dechasakulsom, 2000) have shown their use to be quite inaccurate at best.

5 CHARACTERIZATION OF FOUNDATION SOIL

One advantage of reinforced soil structures over conventional ones is a tolerance to deformations and stresses induced by yielding in the foundation. This allows such structures to be constructed on less than ideal sites, with various types of foundations. Depending on its stiffness, the foundation may have a significant effect on the performance of the reinforced structure. When the foundation is soft, the reinforcement will be affected by settlement of the underlying soil. If, on the other hand, the foundation is quite stiff, its deformation will be negligible and will not appreciably affect the behavior of the structure.

From the point of view of numerical analyses, a soft foundation has the added potential of producing finite strains and rotations in the soil and reinforcement. As a result, the analysis is complicated by the need to account for not only material nonlinearities, but geometric ones as well. The associated computational effort typically increases rather sharply.

6 SPATIAL DISCRETIZATION OF GEOSYNTHETIC REINFORCEMENT

Since their inception, soil reinforcement techniques have employed many different types of reinforcement. For the case of soil walls and embankments, metal strips, geotextiles, and geogrids represent the primary types of reinforcement. Such materials are quite thin and possess volume fractions that, compared to the soil mass, are quite low. As a result, the bending stiffness of the reinforcement is negligible; it is only the axial stiffness that contributes to the behavior of a reinforced soil structure. In general, geosynthetics are ductile materials; their strain at failure exceeds 10%.

Typically the reinforcement is modeled using one-dimensional bar (axial), bending (axial-flexural), or large deformation "membrane" elements in which transverse loading induces axial deformations. Nonlinearity of the stress–strain behavior and yield can also be accounted for by making the element equations functions of the stress or strain level.

In the case of mixed formulations, the reinforcement may also be used for drainage. As such, the elements used to discretize the reinforcement must complement displacements with pore pressure unknowns. The element formulation can be semicoupled or uncoupled. In the former, the deformation of the element affects the flow properties by reducing the area available for flow. In the latter, the flow is independent of the element deformation.

7 CHARACTERIZATION OF GEOSYNTHETIC REINFORCEMENT

Over the years, a large amount of experimental work has been done to study the time-dependent behavior of geosynthetic reinforcement (Kaliakin and Dechasakulsom, 2001a). The majority of these studies focused on creep response, with relaxation experiments perceived as overly complex. Numerous mathematical models of the geosynthetics, possessing varying levels of sophistication, have been developed in conjunction with many of the aforementioned experimental studies. With minor exceptions, for purposes of mathematically representing typical geosynthetic reinforcement, the models have assumed uniaxial stress and strain states. This is in keeping with the observation (den Hoedt et al., 1994) that geosynthetics commonly used for reinforcement exhibit negligible lateral contraction.

Some models proposed to simulate creep and relaxation response of geosynthetics are reviewed next. The discussion is limited to response under isothermal conditions, as very few models have been proposed that account for both thermal and mechanical response. A more thorough overview of time-dependent models for geosynthetic reinforcement is available in Kaliakin and Dechasakulsom (2001b).

7.1 Models Proposed to Simulate Creep Response

The most basic models developed to simulate creep response of geosynthetics are simple, empirical, mathematical equations. For example, the following expressions have been proposed:

$$\varepsilon = \varepsilon_o + A \log t \tag{1}$$

$$\varepsilon = \varepsilon^o + \varepsilon^+ t^n \tag{2}$$

$$\varepsilon = \varepsilon_1 t^n \tag{3}$$

$$\varepsilon(t) = m \log_{10} t + \varepsilon(t_o) \tag{4}$$

In Eq. (1), ε represents the total strain, ε_o and A are functions of stress, temperature, and nature of the material, and t denotes time. Using this expression, Finnigan (1977) and Van Leeuween (1977) have reported success in modeling short-term creep behavior.

In Eq. (2), which was developed by Findley (1987) for polyvinyl chloride (PVC) and polyethylene (PE), ε represents the strain, t is the time, and ε^o, ε^+, and n are constants. From other work (Findley et al. 1976), it has been shown that

n is typically a constant independent of stress and temperature, whereas ε^{o} and ε^{+} are stress- and temperature-dependent. In addition, Lai and Findley (1973) found n generally to be less than 1.

Based on the results of confined creep tests, Matichard et al. (1990) and Blivet et al. (1992) proposed Eq. (3), where ε_1 represents the strain at the end of the loading phase. Blivet et al. (1992) noted that for woven polypropylene, tested with or without confinement, the value of n is about 0.10. For woven polyester, the value of n is about 0.01 and is again independent of the presence of confining soil. For nonwoven geotextiles, the values of n are similar to those for woven geotextiles. For polypropylene n is about 0.12; for polyester it is about 0.015. These values are in agreement with ones determined by Matichard et al. (1990).

Viezee et al. (1990) found that measured creep could be predicted by Eq. (4), where $\varepsilon(t_o)$ denotes the intercept at one hour (in percent), m is the creep gradient (in percent per decade), and t denotes time. This expression was also used by Miki et al. (1990) to represent the primary and secondary phases of creep of spun-bonded, nonwoven fabrics.

Next in complexity after mathematical equations are rheological models consisting of combinations of springs and dashpots. For example, Paute and Segouin (1977) used a three-element rheological model consisting of a spring and a Kelvin model in series to model the very short-term (8-hour) creep behavior of geotextiles.

Shrestha and Bell (1982) modeled the time-dependent behavior of geotextiles both by a four-parameter Berger model and by the three-parameter creep formula proposed by Singh and Mitchell (1968) for the simulation of triaxial creep of soils. In the rheological model the viscous element was represented by two constants whose values were determined from the rate process theory (Eyring et al., 1941). The basic difference between the rate process theory-based approach and the three-parameter model is that in the former the creep rate is assumed to be continuously decreasing during the transient phase until a minimum value is reached. During the secondary phase of creep, it remains constant at this minimum value until the beginning of the tertiary phase. During the latter phase, the strain rate increases very rapidly until failure. Conversely, in the three-parameter creep formula, the strain rate is considered to be continuously decreasing. Using these two approaches, Shrestha and Bell (1982) found that the creep response predicted by the four-parameter rheological model was more consistent with experimental results. For nonwoven geotextiles, the time to reach failure strains under sustained load predicted by the three-parameter model was much longer than for the four-parameter model. For woven geotextiles both empirical methods predicted comparable times to failure. Overall, however, both methods predicted time to failure that was much shorter than the normal design life of geotextiles, even at stress levels as low as 30% of ultimate levels.

An extrapolation method, based on a partial rheological model, has been presented by McGown et al. (1984). A related approach uses the extrapolation of isochronous stiffness and time correlation curves (Andrawes et al. 1986). In a more recent paper, Sawicki and Kazimierowicz-Frankowska (1998) have shown that, within sufficient engineering accuracy, a standard rheological model can describe the creep response of many geosynthetics under constant and step-increasing loads.

Another class of models, admittedly more complex than rheological models, is that based on integral techniques. For example, the multiple integral technique suggested by Onaran and Findley (1965) has been found useful in representing the nonlinear viscoelastic behavior of a range of geotextiles and geogrids (Kabir, 1988). According to this technique, for uniaxial creep at some load p

$$\varepsilon = R(t)p + M(t)p^2 + N(t)p^3 \tag{5}$$

For constant loading of geotextiles and polymers, the kernal functions R, M, and N are expected to take on the following form:

$$R(t) = \mu_1 + \omega_1 t^n \tag{6}$$

$$M(t) = \mu_2 + \omega_2 t^n \tag{7}$$

$$N(t) = \mu_3 + \omega_3 t^n \tag{8}$$

where μ_1, μ_2, μ_3, ω_1, ω_2, ω_3 represent temperature-dependent material functions and n is a function of the material that may or may not be a function of temperature. Equations (6)–(8) are then substituted into Eq. (5) to give a single expression for strain. The seven parameters associated with this model are determined by fitting the results of creep tests for at least three different loads (Kabir, 1988).

A related approach has been proposed by Findley et al. (1976), who represented the creep behavior of nonlinear viscoelastic materials by a series of "multiple integrals." However, to effectively use the model, the magnitude of the loading must be known a priori. Thus, if tertiary creep is to be predicted, creep tests to failure must be performed. Using the model of Findley et al. (1976), Helwany and Wu (1992) were able to simulate the creep response of a polypropylene composite, heat-bonded geotextile and a polypropylene nonwoven, heat-bonded geotextile. Stress levels used in the creep tests were not high enough to result in tertiary creep, however, so the assessment of the model was incomplete.

Perkins presented a more rational constitutive model for geosynthetics (Perkins, 2000). In this model, the elastoplastic response combines orthotropic elasticity with a Hill yield criterion with isotropic hardening and an associated flow rule. The creep response is accounted for through a strain hardening form of a power law for uniaxial response. Although Perkins' model is more refined than the simpler models described above, it lacks generality in that it preassumes creep response of the geosynthetic.

7.2 Models Proposed to Simulate Relaxation

Compared to creep models, relatively few formulations have been proposed to simulate the relaxation response of geosynthetics. Koerner et al. (1993) presented the following two-parameter "in-house" formula for stress relaxation of geomembranes.

$$\sigma(t) = ct^{-b} \tag{9}$$

where t denotes time, and b and c are constants. This type of behavior has been referred to as "physical stress relaxation," as opposed to chemical relaxation (Debnath, 1985).

7.3 Models Proposed to Simulate Both Creep and Relaxation

In a recent paper, Sawicki (1998) proposed rheological models for predicting the creep or relaxation response of specific geogrids. However, the models are predicated on the a priori knowledge of the specific type of response. That is, it must be known whether the geogrid will undergo creep or relaxation response; in the course of loading, the response mode cannot change. Thus, Sawicki's models, though more general than the basic rheological models discussed above, still lack true generality.

Zhang and Moore have presented a more general model that accounts for the elastic-viscoplastic response of geosynthetics (Zhang and Moore, 1997). This multi-axial model, which is based on the unified theory of Bodner and Partom (1975), has been shown to realistically simulate various aspects of geosynthetic response with good agreement between numerical predictions and experimental results.

7.4 Concluding Remarks Concerning Modeling

As evident from the overview presented in the previous section, the mathematical modeling of the time-dependent behavior of geosynthetics has typically been realized using formulations specifically designed to simulate creep response, or those specifically designed to simulate relaxation. With the exception of the Zhang and Moore (1997) model, few simple yet robust models appear to have been proposed that account for both creep and relaxation in a robust yet reasonably accurate fashion.

In addition, simple mathematical models, rheological models, and integral techniques all lack one fundamental characteristic that is necessary for their implementation into finite-element computer programs. Namely, using any of the aforementioned approaches, one cannot compute a consistent incremental tangent modulus $E_r = \partial\sigma/\partial\epsilon$.

The above shortcomings manifest themselves in the inability to perform proper finite-element analyses. In particular, consider the approach used by Helwany (1992) in his analysis of a geosynthetically reinforced wall with cohesive backfill. Using an integral technique similar to that described by Eqs. (5)–(8), he states:

> For each time increment Δt, the expected creep strains in all viscoelastic bar elements are calculated. Equivalent nodal creep forces (corresponding to the expected creep strains) are then calculated and applied at the nodal points of each viscoelastic bar element. The response of the structure is then evaluated through regular finite element procedure.

Such an approach is deficient for two reasons: First, it a priori assumes creep response for the reinforcement [a condition that has been shown by Dechasakulsom (2000) not to be true for the particular wall analyzed]. Second, by assuming "expected" creep strains, this approach precludes a consistent finite-element analysis from being performed. In such an analysis, the strains are computed as secondary dependent variables from the displacements (the primary dependent variables) and are not prescribed at the outset.

8 CHARACTERIZATION OF INTERFACES

One of the most important factors in accurately predicting the behavior of reinforced soil structures is the ability to account for relative displacement between the backfill soil and reinforcement and between the structural members (e.g., facing) in contact with the soil. The possible ramifications of failing to model the latter interfaces have been discussed by Kaliakin and Xi (1992), who note that spurious results are very likely in such cases.

The interaction between the soil and the reinforcement and between the soil and the structural members can be modeled by introducing suitable interface elements. The proper kinematic response of such elements (Kaliakin and Li, 1995) is particularly important for geosynthetically reinforced soil structures with cohesive backfill, as they are placed between the soil and reinforcement and thus link these two time-dependent materials. Provided they are robust, standard interface elements should, without modification, be directly applicable to the analysis of geosynthetically reinforced structures with cohesive backfill.

9 CONCLUSIONS

The modeling and finite-element analysis of geosynthetically reinforced soil structures with cohesive backfill have been critically reviewed. The following points pertaining to this subject are particularly significant:

The use of a cohesive backfill has the potential of complicating the problem in that a coupled deformation-pressure formulation may be required. The associated finite-element analysis requires the use of mixed elements, which must be selected judiciously.

In mathematically characterizing the cohesive backfill, the time-dependent behavior of the material must be accounted for. The use of time-independent constitutive models, though convenient and practiced in the past, produces inaccurate results.

When the foundation underlying the structure is soft, the reinforcement will be affected by settlement of the underlying soil. This has the potential of necessitating a geometrically nonlinear analysis. In light of the fact that material nonlinearities must also be accounted for in the analysis, the associated computational effort typically increases rather sharply.

The spatial discretization of the reinforcement is relatively straightforward. Complications may arise if the reinforcement is also used to drain the backfill. In this case, a semicoupled or uncoupled mixed element must be used to represent the reinforcement.

The time-dependent response of the geosynthetic reinforcement must be accounted for in a rational fashion. In particular, the constitutive relation used must be general in scope, thus avoiding the past practice of a priori assuming creep or relaxation response. The latter practice is not consistent with finite-element analyses and typically precludes the determination of a consistent incremental tangent modulus.

Provided that kinematically consistent formulations are used, a standard interface element can be employed in the analysis of geosynthetically reinforced soil structures with cohesive backfill. Failure to account for the interaction between soil and reinforcement and between soil and structural members such as facing can lead to inaccurate and possibly spurious results.

Finally, the general observation that finite-element analysis of geosynthetically reinforced soil structures must accurately simulate the actual or expected construction process likewise holds for such structures with cohesive backfill.

REFERENCES

T Adachi, F Oka. Constitutive equations for normally consolidated clay based on elasto-viscoplasticity. *Soil Foundations* 22(4): 57–70, 1982.

T Adachi, F Oka, M Mimura. Modeling aspects associated with time dependent behavior of soils. In *Measuring and Modeling Time Dependent Soil Behavior*. ASCE Geotechnical Special Technical Publication 61, TC Sheahan, VN Kaliakin, eds. New York: ASCE, 1996.

MM Al-Hussaini, LD Johnson. Numerical analysis of a reinforced earth wall. *Proceedings of the ASCE Symposium on Reinforced Earth*, Pittsburgh, PA, 1978, pp 98–126.

Z Al-Yassin, LR Herrmann. Finite element analysis of reinforced earth walls. *Proceedings of the International Conference on Soil Reinforcement*, Paris, 1979, pp 3–9.

KZ Andrawes, A McGown, RT Murray. The load–strain–time–temperature behaviour of geotextiles and geogrids. *Proceedings of the Third International Conference on Geotextiles,* Vienna, Austria, Vol. III, 1986, pp 707–712.

PK Banerjee. Principles of analysis and design of reinforced earth retaining walls. *J. Inst. Highway Eng.* 22: 13–18, 1975.

DT Bergado, R Shivashankar, MC Alfaro, JC Chai, AS Balasubramaniam. Interaction behaviour of steel grid reinforcements in clayey soil. *Geotechnique* 43(1): 589–603, 1993.

P Bettess. Infinite elements. *Int. J. Numer. Methods Eng.* 11: 53–64, 1977.

P Bettess. More on infinite elements. *Int. J. Numer. Methods Eng.* 15: 1613–1626, 1980.

JC Blivet, M Msouti, Y Matichard, D Levacher, et al. Mechanical behaviour of geotextiles in the design of permanent reinforced structures. In *Earth Reinforcement Practice, Proceedings of the Intl. Symposium on Earth Reinforcement Practice*. Ochiai, ed. Fukuoka, Kyushu, Japan: Balkema, 1992, pp 35–38.

SR Bodner, Y Partom. Constitutive equations for elastic-viscoplastic strain-hardening materials. *J. Appl. Mech.* 42(2): 385–389, 1975.

RI Borja, E Kavazanjian, Jr. A constitutive model for the stress–strain–time behaviour of "Wet" clays. *Geotechnique* 35(3): 283–298, 1985.

JC Chang, RA Forsyth. Finite element analysis of reinforced earth wall. *J. Geotech. Eng. Div, ASCE* 103(GT7): 711–724, 1977.

A Curnier. A static infinite element. *Int. J. Numer. Methods Eng.* 19: 1479–1488, 1983.

S Debnath. Studies on stress-relaxation of styrene–butadiene rubber–mica composites. *Polym. Test.* 8: 109–118, 1985.

M Dechasakulsom. Modeling time-dependent behavior of geogrids and its application to geosynthetically reinforced walls. Ph.D. Dissertation, Department of Civil and Environmental Engineering, University of Delaware, 2000.

G den Hoedt, W Voskamp, CJM van den Heuvel. Creep and time-to-rupture of polyester geogrids at elevated temperatures. *Proceedings of the Fifth International*

Conference on Geotextiles, Geomembranes and Related Products, Singapore, 1994, pp 1125–1130.

JM Duncan, C-Y Chang. Nonlinear analysis of stress and strain in soils. *Soil Mech. Found. Div, ASCE* 96(SM5): 1629–1653, 1970.

RM Ebeling, JF Peters, RE Wahl. Prediction of reinforced sand wall performance. In *Geosynthetically-Reinforced Soil Retaining Walls*. JTH Wu, ed. Rotterdam: Balkema, 1992, pp 243–253.

NA El-Esnawy, AY Akl, AS Bazaraa. A new parametric infinite domain element. *Finite Elem. Anal. Design* 19: 103–114, 1995.

H Eyring, S Glasstone, K Laidler. *The Theory of Rate Process*. New York: McGraw-Hill Book Co., 1941.

WN Findley. 26-year creep and recovery of poly (vinyl chloride) and polyethylene. *Polym. Eng. Sci.* 27(8): 582–585, 1987.

WN Findley, JS Lai, K Onaran. *Creep and Relaxation of Nonlinear Viscoelastic Materials, with an Introduction to Linear Viscoelasticity*. Amsterdam: North Holland, 1976.

JA Finnigan. The creep behaviour of high tenacity yarns and fabrics used in civil engineering applications. *Proceedings of the Intl. Conference on the Use of Fabrics in Geotechnics,* Paris, Vol. 2, 1977, pp 305–309.

CH Fuchs. Influence of adjacent strip footings on associated deformations in granular soils. MCE Thesis, Department of Civil Engineering, University of Delaware, 1999.

MB Helwany. Finite element analysis of geotextile reinforced retaining walls considering creep. In *Geosynthetically-Reinforced Soil Retaining Walls*. JTH Wu, ed. Rotterdam: Balkema, 1992, pp 179–192.

B Helwany, JTH Wu, et al. A generalized creep model for geosynthetics. In *Earth Reinforcement Practice, Proceedings of the Intl. Symposium on Earth Reinforcement Practice*. Ochiai, ed. Fukuoka, Kyushu, Japan: Balkema, 1992, pp 79–84.

LR Herrmann, Z Al-Yassin. Numerical analysis of reinforced earth systems. *Proceedings of the ASCE Symposium on Reinforced Earth*, Pittsburgh, PA, 1978, pp 428–457.

TJR Hughes. *The Finite Element Method, Linear Static and Dynamic Finite Element Analyses*. Englewood Cliffs, NJ: Prentice-Hall, Inc., 1987.

TS Ingold, F Montanelli, P Rimoldi. Extrapolation techniques for long term strength of polymeric geogrids. *Proceedings of the Fifth Intl. Conference on Geotextiles, Geomembranes and Related Products*, Singapore, 1994, pp 1117–1120.

RA Jewell, CJFP Jones. Reinforcement of clay soils and waste materials using grids. *Proceedings of the 10th Intl. Conference on Soil Mechanics and Foundation Engineering, Stockhom,* Sweden, No. 3, 1981, pp 701–706.

MH Kabir. Creep behavior of geotextiles. In *Intl. Geotechnical Symposium on Theory and Practice of Earth Reinforcement*. Yamanouchi, ed. Fukuoka, Japan: Balkema, 1988, pp 111–116.

VN Kaliakin, YF Dafalias. Theoretical aspects of the elastoplastic-viscoplastic bounding surface model for cohesive soils. *Soil Found.* 30(3): 11–24, 1990.

VN Kaliakin, F Xi. Modeling of interfaces in finite element analyses of geosynthetically reinforced walls. In *Earth Reinforcement Practice, Proceedings of the International*

Symposium on Earth Reinforcement Practice. Ochiai, ed. Fukuoka, Kyushu, Japan: Balkema, 1992, pp 351–356.

VN Kaliakin, J Li. Insight into deficiencies associated with commonly used zero-thickness interface elements. *Comput. Geotech.* 17(2): 225–252, 1995.

Kaliakin, VN, Dechasakulsom, M. (2001a). Time-dependent behavior of geosynthetic reinforcement—a review of experimental work. *Report No. 01-1*, Department of Civil and Environmental Engineering, University of Delaware, 2001a Available at http://www.ce.udel.edu/faculty/kaliakin/CEE_Report_01-1.pdf.

Kaliakin, VN, Dechasakulsom, M. (2001b). Time-dependent behavior of geosynthetic reinforcement—a review of mathematical models. *Report No. 01-2*, Department of Civil and Environmental Engineering, University of Delaware, 2001b Available at http://www.ce.udel.edu/faculty/kaliakin/CEE_Report_01-2.pdf.

RM Koerner, Y Hsuan, AE Lord. Remaining technical barriers to obtaining general acceptance of geosynthetics. *Geotext. Geomembr.* 12: 1–52, 1993, (1992 Mercer Lecture).

JS Lai, WN Findley. Elevated temperature creep of polyurethane under nonlinear torsional stress with step changes in torque. *Trans. Soc. Rheol.* 17(1): 129, 1973.

HI Ling, CP Cardany, L-X Sun, H Hashimoto. Finite element study of a geosynthetically-reinforced soil retaining wall with concrete-block facing. *Geosynth. Int.* 7(2): 137–162, 2000.

JMMC Marques, DRJ Owen. Infinite elements in quasi-static materially nonlinear problems. *Comput. Struct.* 18: 199–205, 1984.

Y Matichard, B Lecelerq, M Seqouin. Creep of geotextiles: Soil reinforcement applications. *Proceedings of the Fourth Intl. Conference on Geotextiles*, The Hague, 1990, pp 661–665.

A McGown, KZ Andrawes, KC Yeo, D DuBois. The load-strain-time behaviour of Tensar geogrids. *Proc. Symp. on Polymer Grid Reinforcement*. London: Thomas Telford, 1984, pp 31–36.

H Miki, Y Hayashi, T Takasogo, H Shido. Plane strain tensile strength and creep of spun-bonded non-wovens. *Proceedings of the Fourth Intl. Conference on Geotextiles,* The Hague, Vol. 2, 1990, pp 667–672.

JC Nagtegaal, DM Parks, JR Rice. On numerically accurate finite element solutions in the fully plastic range. *Comput. Methods Appl. Mech. Eng.* 4(2): 153–177, 1974.

DJ Naylor. A study of reinforced earth walls allowing strip slip. *Proceedings of the ASCE Symposium on Reinforced Earth*, Pittsburgh, PA, 1978, pp 618–643.

DJ Naylor, H Richards. Slipping strip analysis of reinforced earth. *Intl. J. Numer. Anal. Methods Geomech.* 2: 343–366, 1978.

R Nova. A viscoplastic constitutive model for normally consolidated clay. In *Deformation and Failure of Granular Materials*. PA Vermeer, HJ Luger, eds. Rotterdan: A.A. Balkema, 1982, pp 287–295 from the IUTAM Symposium, Delft.

F Oka. Elasto/viscoplastic constitutive equations with memory and internal variables. *Comput. Geotech.* 1: 59–69, 1985.

K Onaran, WN Findley. Combined stress creep experiments on a nonlinear visco-elastic material to determine the kernal functions for a multiple integral representation of creep. *Trans. Soc. Rheol.* 9: 299, 1965.

JL Paute, M Segouin. Determination of strength and deformability characteristics of fabrics by dilation of a cylindrical sleeve. *Proceedings of the Intl. Conference on the Use of Fabrics in Geotechnics*, Paris, Vol. 2, 1977, pp 293–298.

SW Perkins. Constitutive model of geosynthetics. *Geotext. Geomembr.* 18: 273–292, 2000.

KM Romstad, LR Herrmann, CK Shen. Integrated study of reinforced earth I: Theoretical formulation. *J. Geotech. Eng. Div, ASCE* 102(GT5): 458–471, 1976.

A Sawicki. A basis for modelling creep and stress relaxation behaviour of geogrids. *Geosynth. Int.* 5(6): 637–645, 1998.

A Sawicki, K Kazimierowicz-Frankowska. Creep behaviour of geosynthetics. *Geotext. Geomembr.* 16(6): 365–382, 1998.

RB Seed, JM Duncan. FE analyses: Compaction-induced stresses and deformations. *J. Geotech. Eng. Div, ASCE* 112(1): 23–43, 1986.

H Sekiguchi. Theory of undrained creep rupture of normally consolidated clay based on elasto-viscoplasticity. *Soil. Found.* 24(1): 129–147, 1984.

CK Shen, KM Romstard, LR Hermann. Integrated study of reinforced earth: II. Behavior and design. *J. Geotech. Eng. Div.*, *ASCE*, 102(GT6): 1967, 577–590.

SC Shrestha, JR Bell. Creep behavior of geotextiles under sustained loads. *Proceedings of the Second Intl. Conference on Geotextiles*, Las Vegas, Vol. III, 1982, pp 769–774.

A Singh, JK Mitchell. General stress–strain–time functions for soils. *J. Soil Mech. Found. Div, ASCE* 94(SMI): 21–46, 1968.

SW Sloan. Plastic collapse calculations using higher-order elements. *Proceedings of the Intl. Conference on Accuracy Estimates and Adaptive Refinements in Finite Element Computations (ARFEC)*, Lisbon, 1984, pp 301–313.

SW Sloan, MF Randolph. Numerical prediction of collapse loads using finite element methods. *Int. J. Numer. Anal. Methods Geomech.* 6(1): 47–76, 1982.

JH Van Leeuween. New methods of determining stress–strain behaviour of woven and non woven fabrics in the laboratory and in practice. *Proceedings of the Intl. Conference on the Use of Fabrics in Geotechnics*, Paris, Vol. 2, 1977, pp 299–304.

DJ Viezee, W Voskamp, G den Hoedt, GH Troost, HM Schmidt. Designing soil reinforcement with woven geotextiles—the effect of mechanical damage and chemical ageing on the long-term performance of polyester fibres and fabrics. *Proceedings of the Fourth Intl. Conference on Geotextiles*, The Hague, Vol. 2, 1990, pp 651–656.

C Zhang, ID Moore. Finite element modelling of inelastic deformation of ductile polymers. *Geosynth. Int.* 4(2): 137–163, 1997.

OC Zienkiewicz, C Emson, P Bettess. A novel boundary infinite element. *Int. J. Numer. Methods Eng.* 19: 393–404, 1983.

OC Zienkiewicz, RL Taylor. *The Finite Element Method, 5th ed. Vol. 1: The Basis*. Oxford: Butterworth Heinemann, 2000.

5

Issue and Nonissue in Block Walls as Implied Through Computer-Aided Design

Dov Leshchinsky
University of Delaware, Newark, Delaware, U.S.A.

1 INTRODUCTION

The Reinforced Earth Company introduced commercial modular wall systems during the 1960s. Both the performance and economics of these reinforced walls made them popular. These walls consisted of large modular precast facing units connected to metallic strips at predetermined vertical and horizontal intervals to produce a coherent reinforced soil system that is both externally and internally stable. During the late 1970s, geosynthetic wall systems were introduced in secondary applications and, during the 1980s, in major applications. The success of the metal strip reinforced wall system resulted in a direct adaptation of its proven design method to geosynthetic walls.

The Federal Highway Administration's Demonstration Project 82 (Elias and Christopher, 1997), also known as Demo 82, provides design guidelines for a variety of mechanically stabilized earth (MSE) walls. It introduces the same computational scheme for all wall systems, including metallic and polymeric reinforcement, using empirical parameters to adjust for the specific properties of each system. Conducting parametric and comparative studies following Demo 82 using hand calculations is tedious. However, utilization of program MSEW (1998), developed as a companion for Demo 82, makes such studies easy and instructive.

The purpose of this paper is to use MSEW software to identify issues and nonissues related to block wall design. The presentation shows that while an issue might be important in metal strip wall design, it is actually not important in geosynthetic block wall, and vice versa. Finally, a practical remedy in design and construction is suggested for the identified issue.

2 NONISSUE (FOR POLYMER REINFORCEMENT)

Consider an example problem taken from the Demo 82 manual (pp. 143–149). That is, wall design height of 7.8 m, traffic surcharge of 9.4 kPa, reinforced soil having $C_u > 7$, $\gamma = 18.8\,\mathrm{kN/m^3}$, $\phi = 34°$ and $c = 0$ retained soil having $\gamma = 18.8\,\mathrm{kN/m^3}$ and $\phi = 30°$ $F^* = 2.0$, Fs(direct sliding) $= 1.5$, eccentricity $<$ L/6, and Fs(pullout) $= 1.5$. For a wall reinforced with metal strips (with panels of 1.5 by 1.5 m) the layout of the reinforcement and data related to resistive pullout length are summarized in Table 1 (see Demo 82 for further details). Large horizontal pressures at the upper portion of the wall combined with low overburden pressure and small interface area of each (ribbed) strip require significant pullout length when compared with the overall strip length (see Fig. 1a and b). In fact, pullout controls the dimensions of the wall structure. Clearly, pullout resistive length is a major design issue in walls reinforced by metal strips.

Consider now the situation for geosynthetic walls where continuous reinforcement is used. To address this issue objectively, a comparison is conducted specifying the same wall geometry, including geosynthetic layers at

Table 1 Example Problem: Layout of Metal Strips (Problem Details Given in Demo 82; Calculations by MSEW Software)

Elevation (m)	S_h (m)	L (m)	K/Ka	F^*	α	T_{max} (kN/m)	Pullout: Fs
0.375	0.75	5.50	1.200	0.67	1.00	37.9	1.75
1.125	0.75	5.50	1.200	0.67	1.00	34.3	1.59
1.875	0.75	5.50	1.206	0.69	1.00	31.3	1.79
2.625	0.75	5.50	1.269	0.85	1.00	28.9	1.51
3.375	0.75	5.50	1.331	1.02	1.00	26.1	1.51
4.125	0.60	5.50	1.394	1.19	1.00	23.0	1.50
4.875	0.75	5.50	1.456	1.35	1.00	19.8	1.58
5.625	0.75	5.50	1.519	1.52	1.00	16.2	1.61
6.375	0.75	5.50	1.581	1.68	1.00	12.1	1.57
7.125	0.50	5.50	1.644	1.85	1.00	9.3	1.60

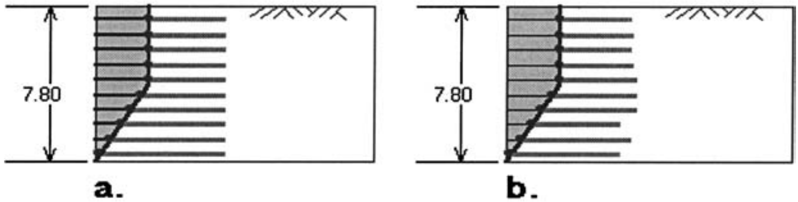

Figure 1 Metal strips wall: (a) as designed (uniform L of 5.50 m; see calculated Fs-pullout in Table 1); (b) length producing Fs-pullout = 1.5 at each elevation (see Table 1 for S_h).

the same vertical spacing as the strips of metal (i.e., 75 cm apart, typically an excessively large spacing in block wall structures).

Figure 2a shows the required layout. Figure 2b shows the length needed to produce a pullout factor with a safety 1.5. Pullout for continuous reinforcement is significantly shorter than that for the strip reinforcement. This is apparent when the required lengths are compared for the same Fs (e.g., Figs. 1b and 2b). Table 2 shows the (conservative) default design data used to assess the geosynthetic pullout data. Note in Table 2 that for uniform reinforcement length, the actual Fs for pullout for the geosynthetic layers is extremely large.

When a typical vertical spacing is specified (say, 40 cm), the pullout resistance is even larger. This resistance is typically large even if the coverage ratio, Rc, drops to as low as 0.5. For continuous reinforcement, changing the interaction coefficient to a low of 0.5 would have marginal effect on the overall required reinforcement length. Clearly, pullout is not an issue for geosynthetic reinforcement. Furthermore, the effort associated with "exact" characterization of interface properties through expensive pullout tests seems to be practically unwarranted. Use of a default length value of 1.0 m in block walls should be sufficient for all practical purposes, even if this value is not ascertained by

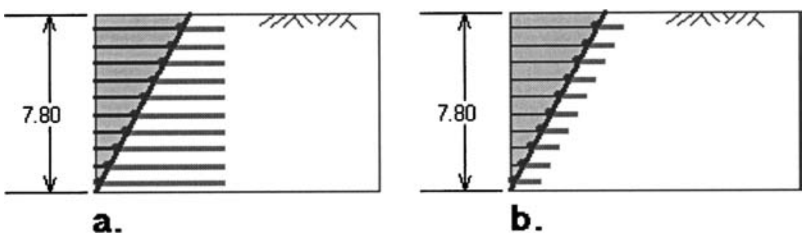

Figure 2 Geosynthetic wall: (a) designed using same geometry, soil, and vertical spacing as metal strip wall (uniform $L = 5.5$ m; $\rho = 28.4$ degrees; see Table 2); (b) length producing Fs-pullout = 1.5 at each elevation.

Table 2 Comparison: Pullout Results for Geosynthetic Wall Having Same Geometry and Vertical Spacing as the Metal Strip Wall in Table 1 (Uniform Length of Reinforcement; See Fig. 1a and 1b)

Elevation (m)	Rc	L (m)	K/Ka	$F*$ $C_i \tan(\phi)$ $[C_i = 0.8]$	α	T_{max} (kN/m)	Pullout: Fs (geosynthetic)	Pullout: Fs (metal strip)
0.375	1.0	5.50	1.0	0.54	0.80	31.6	20.22	1.75
1.125	1.0	5.50	1.0	0.54	0.80	28.6	18.56	1.59
1.875	1.0	5.50	1.0	0.54	0.80	25.6	16.91	1.79
2.625	1.0	5.50	1.0	0.54	0.80	22.6	15.23	1.51
3.375	1.0	5.50	1.0	0.54	0.80	19.6	13.55	1.51
4.125	1.0	5.50	1.0	0.54	0.80	16.6	11.85	1.50
4.875	1.0	5.50	1.0	0.54	0.80	13.7	10.10	1.58
5.625	1.0	5.50	1.0	0.54	0.80	10.7	8.30	1.61
6.375	1.0	5.50	1.0	0.54	0.80	7.7	6.36	1.57
7.125	1.0	5.50	1.0	0.54	0.80	5.7	3.28	1.60

laboratory tests and design computations. It is important to note that this generalization is limited to free draining backfill soil.

3 ISSUE (FOR POLYMER REINFORCEMENT)

Demo 82 requires that the long-term connection strength, reduced by a safety factor, should equal the maximum tensile force in the reinforcement. In many block wall systems, the connection of the geosynthetic to the block is achieved via friction. That is, pullout resistive force at the front end of geosynthetic layers has to be the same as that at its rear end. However, while rear-end pullout resistance is a nonissue, the front-end pullout (i.e., connection strength) can be an issue. It should be pointed out that the front-end frictional resistance is achieved due to the confining pressure of stacked blocks combined with the properties of the geosynthetic–block interface. Contrary to block walls, achieving connection strength for walls reinforced with metal strips is a nonissue.

Table 3 shows the factors of safety at the connection as generated by MSEW software for the original geometry where the layers are spaced at 75 cm. Block data as well as geosynthetic information are marked in the caption of Table 3. Note that T_{ult} used is unrealistically high (it is 115 kN/m). This high strength value was selected because of the large spacing and the desire to examine "failure" only at the facing (i.e., no overstressing of the geosynthetic). While

Table 3 Connection Safety Factors for Geosynthetic Block Wall in Table 2

Elevation (m)	L (m)	Connection force, to (kN/m)	CR_u	CR_s	Connection break, Fs	Connection pullout, Fs	Geosynthetic break, Fs
0.375	5.50	31.6	0.90	0.45	1.49	1.62	1.50
1.125	5.50	28.6	0.90	0.40	1.64	1.61	1.66
1.875	5.50	25.6	0.90	0.36	1.84	1.60	1.86
2.625	5.50	22.6	0.90	0.31	2.08	1.58	2.10
3.375	5.50	19.6	0.90	0.27	2.40	1.56	2.42
4.125	5.50	16.6	0.90	0.22	2.83	1.52	2.86
4.875	5.50	13.7	0.90	0.18	3.45	1.48 (<1.50)	3.48
5.625	5.50	10.7	0.90	0.13	4.41	1.41 (<1.50)	4.46
6.375	5.50	7.7	0.90	0.09	6.13	1.28 (<1.50)	6.19
7.125	5.50	5.7	0.90	0.04	8.22	0.81 (<1.50)	8.31

Note: $T_{\text{ult}} = 115$ kN/m, $RF_d = 1.1$, $RF_{id} = 1.1$, $RF_c = 2.0$, $CR_u = 0.9$, CR_s varies linearly between 0 and 0.9 as blocks confining pressure varies from 0 to 360 kPa; blocks are 20 cm high with average unit weight of 24 kN/m^3.

Table 2 indicates that such large spacing creates no pullout problem, Table 3 shows that connection pullout, especially in upper layers, is a potential problem. Clearly, the calculated Fs for connection break indicate that weaker reinforcement would present a problem as well, albeit at the lower layers. It should be pointed that the connection pullout results are very sensitive to the value of CRs.

Figure 3a shows more realistic layer spacing; i.e., 40 cm apart, 20 layers in total. Table 4 corresponds to this spacing; however, unlike the previous case, it uses a realistic geosynthetic with $T_{\text{ult}} = 65$ kN/m. All other design parameters remain the same. While connection break has improved, layers in the upper 2 m possess low Fs for connection pullout (in the previous case, Table 3, layers in the upper 3 m were deficient in terms of connection pullout). While reducing the tributary area of reinforcement results in smaller connection loads, the problem of insufficient connection strength may still exist, especially at upper layers where confinement provided by the stacked blocks is low.

4 REMEDY (FOR POLYMERIC REINFORCEMENT)

Closely spaced geosynthetic layers (say, every block) significantly reduce the tributary area and thus the connection load. At increments of one block spacing, the problem of insufficient connection strength might be alleviated.

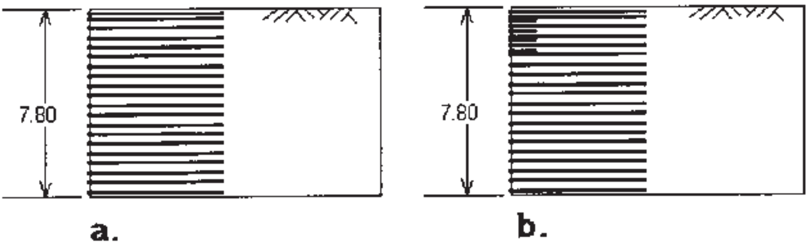

Figure 3 Geosynthetic block wall: (a) layout corresponding to Table 4 (i.e., 40 cm spacing and $L = 5.5$ m); (b) secondary layers, 1 m long, at 20-cm spacing in upper section to improve pullout resistance at connection (see Table 5 for details).

Table 4 Connection Safety Factors for Geosynthetic Block Wall with Half the Spacing and Nearly Half the Geosynthetic Strength Used in Table 3

Elevation (m)	L (m)	Connection force, to (kN/m)	CR_u	CR_s	Connection break, Fs	Connection pullout, Fs	Geosynthetic break, Fs
0.20	5.50	17.2	0.90	0.45	1.54	1.71	1.56
0.60	5.50	16.4	0.90	0.43	1.62	1.71	1.64
1.00	5.50	15.5	0.90	0.41	1.71	1.70	1.73
1.40	5.50	14.7	0.90	0.38	1.81	1.69	1.83
1.80	5.50	13.8	0.90	0.36	1.92	1.68	1.94
2.20	5.50	13.0	0.90	0.33	2.05	1.67	2.07
2.60	5.50	12.1	0.90	0.31	2.19	1.66	2.22
3.00	5.50	11.3	0.90	0.29	2.36	1.65	2.38
3.40	5.50	10.4	0.90	0.26	2.55	1.64	2.58
3.80	5.50	9.6	0.90	0.24	2.78	1.62	2.81
4.20	5.50	8.7	0.90	0.21	3.05	1.60	3.08
4.60	5.50	7.9	0.90	0.19	3.38	1.58	3.41
5.00	5.50	7.0	0.90	0.17	3.79	1.55	3.83
5.40	5.50	6.2	0.90	0.14	4.31	1.51	4.36
5.80	5.50	5.3	0.90	0.12	5.00	1.46 (<1.50)	5.05
6.20	5.50	4.5	0.90	0.10	5.96	1.39 (<1.50)	6.02
6.60	5.50	3.6	0.90	0.07	7.36	1.29 (<1.50)	7.43
7.00	5.50	2.8	0.90	0.05	9.62	1.12 (<1.50)	9.72
7.40	5.50	1.5	0.90	0.02	17.55	1.02 (<1.50)	17.73
7.60	5.50	1.0	0.90	0.01	25.66	0.75 (<1.50)	25.92

$T_{ult} = 65$ kN/m, $RF_d = 1.1$, $RF_{id} = 1.1$, $RP_c = 2.0$, $CR_u = 0.9$, CR_s varies linearly between 0 and 0.9 as blocks confining pressure varies from 0 to 360 kPa; blocks are 20 cm high with average unit weight of 24 kN/m^3.

Unfortunately, such a solution has a cost; typically, it doubles the quantity of geosynthetics.

A more practical solution would be to use short secondary layers. That is, in addition to full-length primary reinforcement (say, at every 40 cm), use intermediate short reinforcement layers (say, 1 m wide at "unused" interface between blocks). Such secondary layers will serve to reduce the tributary area considering the *connection only*. The end result would be an increase in break and pullout factors of safety for the connection. It should be noted that this arrangement would not typically reduce the load carried by the primary reinforcement at the slip surface (T_{max}). Such an arrangement of reinforcement is similar to the use of intermediate layers in steep slopes to improve compaction and erosion control. The increase in overall global stability of the slope due to such layers is normally ignored; however, their increase of superficial stability is effective and significant.

The overall cost associated with the actual installation of secondary layers is not only offset by increasing the connection strength, but also by an improved quality of construction. This is, because intermediate layers are placed, better compaction near the facing is possible without causing misalignment of blocks. Once again, this benefit is completely analogous to the use of intermediate reinforcement in steep slopes where better compaction of the sloping face can be achieved.

Proper "manipulation" of MSEW software allows for assessment of the effects of secondary layers on the connection. If the layers are too short (i.e., typically at higher elevations), the program will indicate that there is no rear-end pullout resistance. However, it will allow these layers to carry some of the connection load. Figure 3b shows a few secondary layers added near the top of the wall. Table 5 presents the resulting factors of safety (note that the geosynthetic and block data in Table 4 were also used for Table 5). Comparing Tables 5 and 4, one realizes that except for the uppermost layer, all connection safety factors have increased significantly. The pullout connection of the uppermost layer, located only 20 cm below the crest, is "hopelessly" small. Bear in mind that traffic load exists in this problem and, hence, the weight of one block would be too small to generate sufficient frictional resistance. Note that *CR*s under 20 cm are negligibly small. However, at extremely low confining pressure, the connection is likely to have pullout strength larger than predicted by pure friction. For example, if due to minor interlocking with stacked blocks *CR*s equal 0.02 for the upper layer, the computed pullout safety factor will increase from 0.75 to about 3.0. MSEW software allows the designer to assess values producing safe structures and thus make an informed judgment.

Alternatively, the MSEW program allows the user to specify a function relating connection loads to the calculated maximum reinforcement force (T_0/T_{max}) versus depth. Currently, Demo 82 recommends a default value of 1.

Table 5 Connection Safety Factors for Geosynthetic Block Wall with Secondary Short Layers for Problem Shown in Table 4

Elevation (m)	L (m)	Reinforcement layer	Connection break, Fs	Connection pullout, Fs	Geosynthetic break, Fs
0.20	5.50	Primary	1.54	1.71	1.56
0.60	5.50	Primary	1.62	1.71	1.64
1.00	5.50	Primary	1.71	1.70	1.73
1.40	5.50	Primary	1.81	1.69	1.83
1.80	5.50	Primary	1.92	1.68	1.94
2.20	5.50	Primary	2.05	1.67	2.07
2.60	5.50	Primary	2.19	1.66	2.22
3.00	5.50	Primary	2.36	1.65	2.38
3.40	5.50	Primary	2.55	1.64	2.58
3.80	5.50	Primary	2.78	1.62	2.81
4.20	5.50	Primary	3.05	1.60	3.08
4.60	5.50	Primary	3.38	1.58	3.41
5.00	5.50	Primary	3.79	1.55	3.83
5.40	5.50	Primary	4.31	1.51	4.36
5.80	5.50	Primary	6.54	1.91	5.05
6.00	1.00	Secondary	10.88	2.86	N/A
6.20	5.50	Primary	11.91	2.78	6.02
6.40	1.00	Secondary	13.17	2.69	N/A
6.60	5.50	Primary	14.71	2.58	7.43
6.80	1.00	Secondary	16.68	2.43	N/A
7.00	5.50	Primary	19.24	2.25	9.72
7.20	1.00	Secondary	22.74	1.99	N/A
7.40	5.50	Primary	27.79	1.62	17.73
7.60	5.50	Primary	25.66	0.75 (<1.50)	25.92

$T_{ult} = 65$ kN/m, $RF_d = 1.1$, $RF_{id} = 1.1$, $RP_c = 2.0$, $CR_u = 0.9$, CR_s varies linearly between 0 and 0.9 as blocks confining pressure varies from 0 to 360 kPa; blocks are 20 cm high with average unit weight of 24 kN/m^3.

However, if there is sufficient data justifying use of smaller connection load, the user can easily adjust the values in the program MSEW. Experience indicates that for closely spaced reinforcement the actual connection loads are significantly smaller than those specified by the default values.

It should be pointed out that connection strength may affect compound stability as well (i.e., slip surfaces extending between the retained soil and the facing). That is, weak connections may provide a "path of least resistance" for failure surfaces potentially resulting in superficial failure (where the blocks and some backfill just roll over) or compound failures where the slip surfaces extend all the way to the retained soil. MSEW software allows for evaluation of such potential failure.

5 CONCLUSION

Using MSEW software and following Demo 82 design guidelines, it is shown that, practically, rear-end pullout of geosynthetic walls is not an issue. However, front-end pullout in block wall systems (i.e., connection pullout) may be an issue. Use of intermediate short layers, as done in reinforced steep slopes, may eliminate or alleviate the problem.

REFERENCES

V Elias, BR Christopher. *Mechanically stabilized earth walls and reinforced steep slopes, design and construction guidelines.* FHWA Demonstration Project 82, Report No. FHWA-SA-96-071, 1997.

MSEW Software. Technical details are displayed at www.GeoPrograms.com.

6

Application of Sliding Block Concept to Geosynthetic-Constructed Facilities

Hoe I. Ling
Columbia University, New York, New York, U.S.A.

1 INTRODUCTION

The sliding block concept has found several applications in geotechnical earthquake engineering. The concept was proposed by Newmark (1965) and Whitman (Marcuson, 1995). A brief review of recent applications of sliding block is given by Ling (2001). This chapter gives an overview of the application to geosynthetic-reinforced soil retaining wall and waste containment liner. In both cases, direct sliding mode of failure was considered. The equations to determine seismic factor of safety, yield acceleration, and permanent displacement are presented. The set of equations for seismic design degenerates to those of static conditions when seismic coefficients are assumed as zero.

In the sliding soil block, earthquake inertia force is considered pseudo-static through a seismic coefficient (Sano, 1916), which is a fraction of the weight of potential sliding soil mass. For combined horizontal and vertical seismic accelerations, Ling (2001) used the functions, k and θ (Fig. 1)

$$k = \sqrt{k_h^2 + (1 \pm k_v)^2} \tag{1}$$

$$\tan\theta = \frac{k_h}{1 \pm k_v} \tag{2}$$

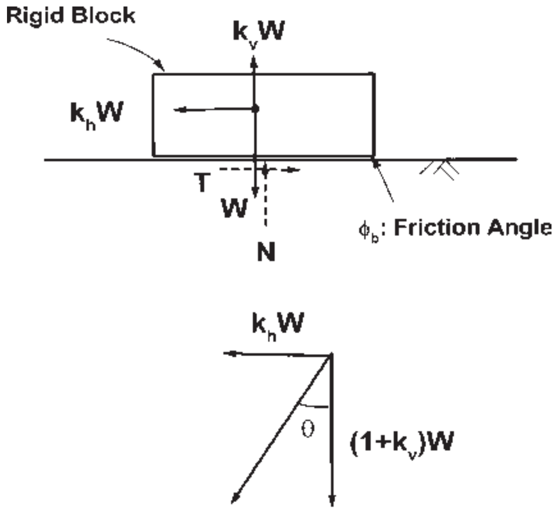

Figure 1 Rigid block subject to earthquake loading.

where k_h and k_v are horizontal and vertical coefficients of acceleration. The vertical acceleration may act upward or downward considering the most critical conditions for design. A typical value of horizontal seismic coefficient may be obtained from the seismic map of Fig. 2 (e.g., AASHTO, 1983).

In using the sliding block concept for permanent displacement analysis, a yield or critical acceleration is defined for the soil mass at sliding where the factor of safety is equal to unity. During seismic excitation, sliding accumulates whenever this yield value is exceeded. Newmark suggested that yielding and thus displacement may be neglected for the reverse direction, which has large yield acceleration. The failure as designated by a factor of safety of unity is momentary. Thus, displacement should be used as the criterion to evaluate earthquake performance. The overview here is based on several publications (Ling et al., 1996, 1997; Ling and Leshchinsky, 1997, 1998; Ling, 2001).

The sliding block concept has been used for practical design of earth dams (Franklin and Chang, 1977; Makdisi and Seed, 1978; Haynes and Franklin, 1984). The idea of permanent displacement limit has also been used for the seismic design of retaining walls (Richards and Elms, 1979; Whitman, 1990). Following the 1994 Kobe earthquake, the methodology has gained wide research in Japan for designing earth structures against high seismic load (e.g., JGS, 1999). This is due to the fact that the seismic design of structures is challenged by a seismic coefficient as large as 0.8 in a Level 2 earthquake (JSCE, 1996). The conventional methodology of design using merely a factor of safety becomes

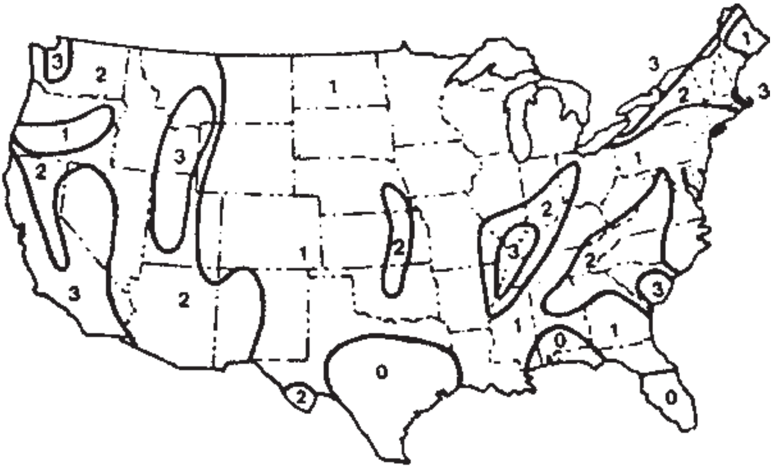

Figure 2 Seismic map. (From AASHTO, 1983.)

impractical for such high seismic loading. Note that an alternative design methodology has also been proposed by Koseki et al. (1998) where Mononobe–Okabe analysis is modified for retaining wall design with the failure plane determined using the peak angle of internal friction, but the strength of the soil is based on the residual value.

2 YIELD ACCELERATION

The concept of yield acceleration can best be illustrated by a rigid block resting on a horizontal plane (Fig. 1). Let W and ϕ_b be the weight of the block and the angle of friction between the block and the plane, respectively. The force equilibrium equations are obtained for the traction T and normal force N:

$$T = k_h W \tag{3}$$

$$N = (1 - k_v)W \tag{4}$$

The interface friction is governed by Coulomb's law:

$$T = \tan \phi_b N \tag{5}$$

When sliding occurs, the coefficient of horizontal acceleration equals the yield value, which is obtained by solving Eqs. (3)–(5):

$$k_{hy} = (1 - k_v)\tan \phi \tag{6}$$

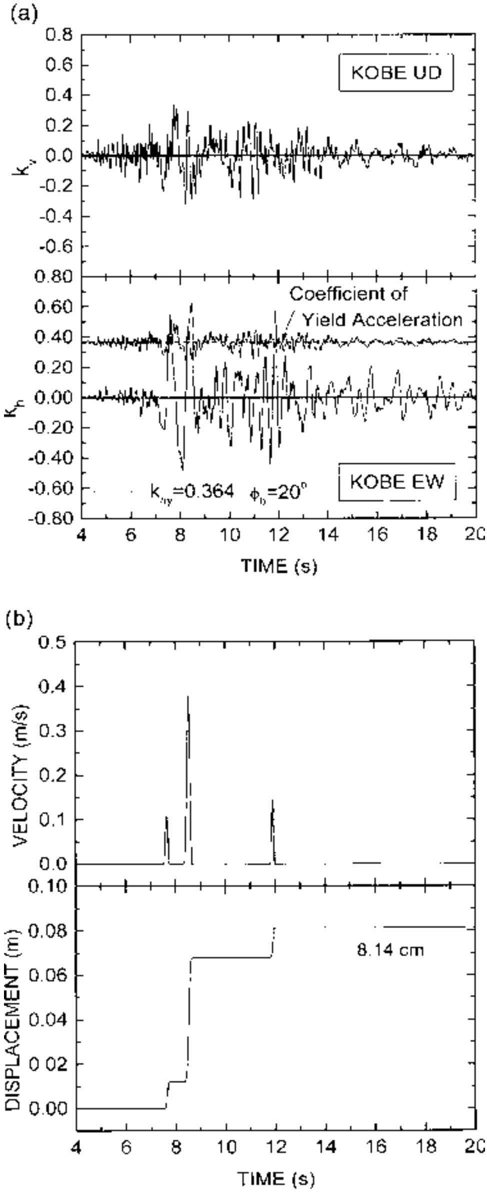

Figure 3 Response of sliding block to Kobe earthquake records: (a) accelerations; (b) velocity and displacement.

where k_{hy} is the yield value of the coefficient of horizontal acceleration. In addition to the angle of friction, the magnitude and direction of vertical acceleration also affect the yield coefficient. If k_v acts downward, the yield coefficient of horizontal acceleration is expressed as

$$k_{hy} = (1 + k_v)\tan\phi \tag{6'}$$

If the earthquake acceleration exceeds the yield acceleration, sliding occurs. The equation of motion is double integrated to give displacement:

$$x = \iint (k_h - k_{hy})g \cdot dt \tag{7}$$

where x is horizontal displacement and g is earth gravity.

Figure 3a shows typical vertical and horizontal accelerations for a block having an interface friction angle $\phi_b = 20°$ when subject to Kobe earthquake records. The peak horizontal and vertical accelerations of the earthquake are $k_{ho} = 0.63$ and $k_{vo} = 0.34$, respectively. The block has a yield value $k_{hy} = 0.364$ when the vertical acceleration is neglected. Figure 3b shows the relationships between velocity and displacement for the rigid block where there are a few spikes of earthquake acceleration that exceeded the yield value. Motion was induced and the permanent displacement was calculated as 8.1 cm.

For different peak values of Kobe earthquake records and yield value of acceleration, the relationships between displacement x and $k_{ho} - k_{hy}$ were determined numerically and are presented in Fig. 4. In design, for a given peak acceleration of the earthquake and knowing the yield acceleration of the block, the permanent displacement can be determined graphically from Fig. 4.

3 REINFORCED SOIL RETAINING WALL

The design of reinforced soil retaining walls encompasses several different components, such as the internal stability that gives the length and strength of geosynthetic layers against rupture and pullout, and the external stability against direct sliding and overturning (Leshchinsky and Boedeker, 1989; Leshchinsky et al., 1995). The procedure of internal stability analysis can be conducted using Rankine/Coloumb analysis or a rigorous log-spiral analysis (Fig. 5). The direct sliding is determined by a two-part wedge analysis (Fig. 6). Note that the most critical acceleration for tieback and direct sliding acts in the downward and upward directions, respectively.

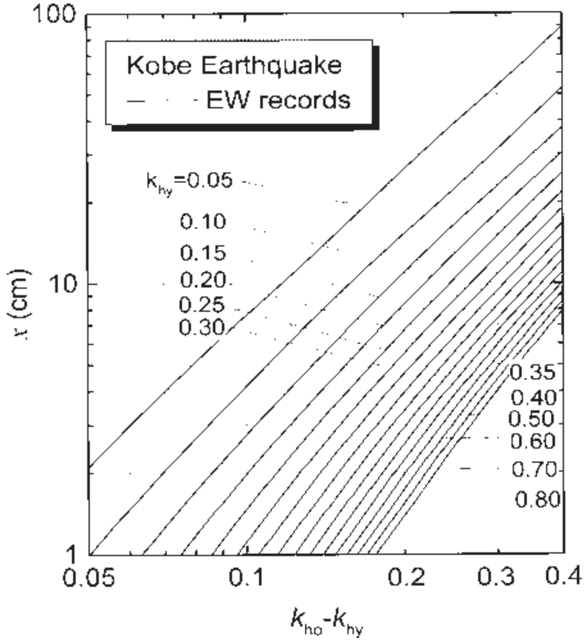

Figure 4 Relationships between permanent displacement, yield, and peak accelerations.

The required strength and lengths of geosynthetic for a design are conveniently expressed using normalized coefficients:

$$K = \frac{\sum t_j}{\frac{1}{2}\gamma H^2} \approx \frac{t_j}{\gamma h_j D_j} \tag{8}$$

$$L_c = \frac{l_c}{H} \tag{9}$$

$$L_{ds} = \frac{l_{ds}}{H} \tag{10}$$

where

γ and H are the unit weight of soil and the wall height, respectively.
h_j is the depth of the jth geosynthetic layer measured from the wall crest.
t_j and D_j are the required geosynthetic tieback strength and tributary area of the jth layer.

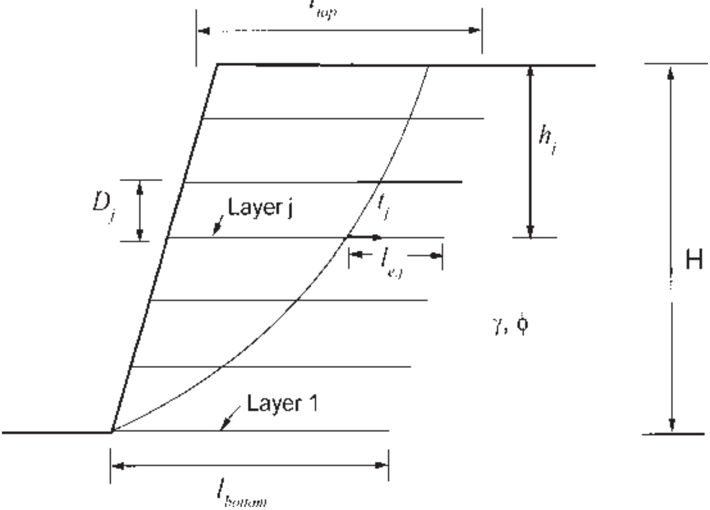

Figure 5 Tieback analysis with log-spiral mechanism.

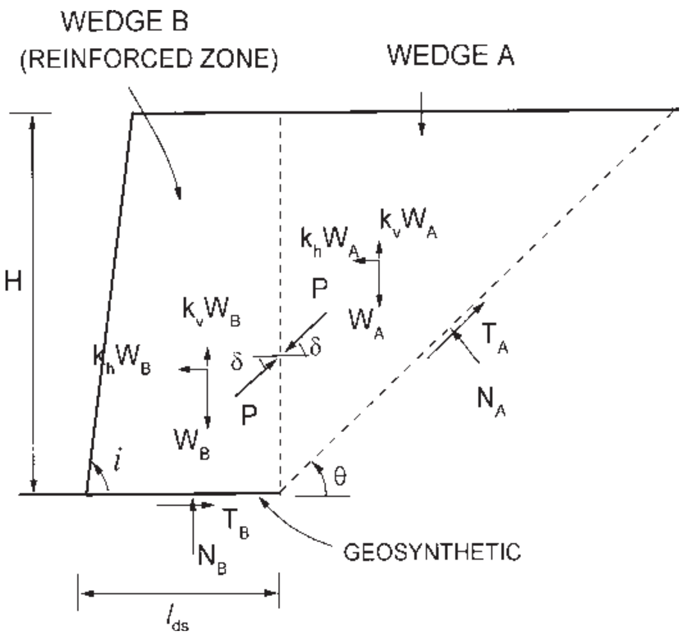

Figure 6 Direct sliding analysis with two-part wedge mechanism.

l_c and l_{ds} are the required length to resist tieback/compound failure and direct sliding, respectively.

t_j is the required strength of the jth layer to ensure local stability.

K is analogous to conventional earth pressure coefficient.

In a design, it is practical to select the required length at the top layer based on L_c and at the bottom based on the greater length of L_c and L_{ds}, whereas length of other layers is obtained by interpolation. The construction may use a constant length, based on the greater value of L_c and L_{ds}, for all geosynthetic layers.

To ensure global stability, where the failure surface extends from the wall face through the reinforced soil zone and into the retained backfill soil, a geosynthetic having allowable strength greater than or equal to that calculated from tieback analysis is specified for each layer. Typically, at the jth layer, the specified geosynthetic has an allowable strength, $t_{j\text{-allowable}}$, larger than the required strength, t_j. It is, thus, practically required that only the bottom m layers be designed against compound failure. That is,

$$\sum_{j=1}^{n} t_{j\text{-allowable}} \geq \sum_{j=1}^{n} t_j \tag{11}$$

The required anchorage length of each layer, $l_{e,j}$, is determined using t_j or $t_{j\text{-allowable}}$, whichever the greater, to prevent pullout failure:

$$l_{e,j} = \frac{t_j \quad or \quad t_{j\text{-allowable}}}{2(1-k_v)\sigma_{v,j} C_i \tan\phi} \tag{12}$$

where ϕ, C_i, $\sigma_{v,j}$ are the internal friction angle, soil–geosynthetic interaction coefficient, and average overburden pressure acting on the jth layer, respectively. C_i is expressed as the ratio of the soil–geosynthetic pullout strength to the soil strength, i.e., $\tan\phi$.

Figures 7a–c show the required geosynthetic strength and lengths for a vertical wall with ϕ ranging from 20 to 45° under static and seismic loadings. The analysis was conducted using the ReSlope program (Leshchinsky, 1995) on a 5-m-high wall having 20 layers of geosynthetics, and the results were normalized. The results for direct sliding were for a coefficient $C_{ds} = 0.8$. $C_{ds} = \tan\phi_s/\tan\phi$ is the interaction coefficient, which expresses the ratio of frictional strength between soil–geosynthetic to that of soil. It is seen that an increase in the lengths and strength of geosynthetic is required following seismic loading. A smaller ϕ also resulted in a longer and stronger geosynthetic. For instance, at ϕ equal to 30°, two times tieback length and strength may be needed when comparing static and seismic designs at $k_h = 0.3$. The difference between the length of static and seismic designs is much larger for direct sliding along the base of the wall. In fact, small soil friction angle and large acceleration may require an excessively long geosynthetic or may render design impossible because equilibrium is not

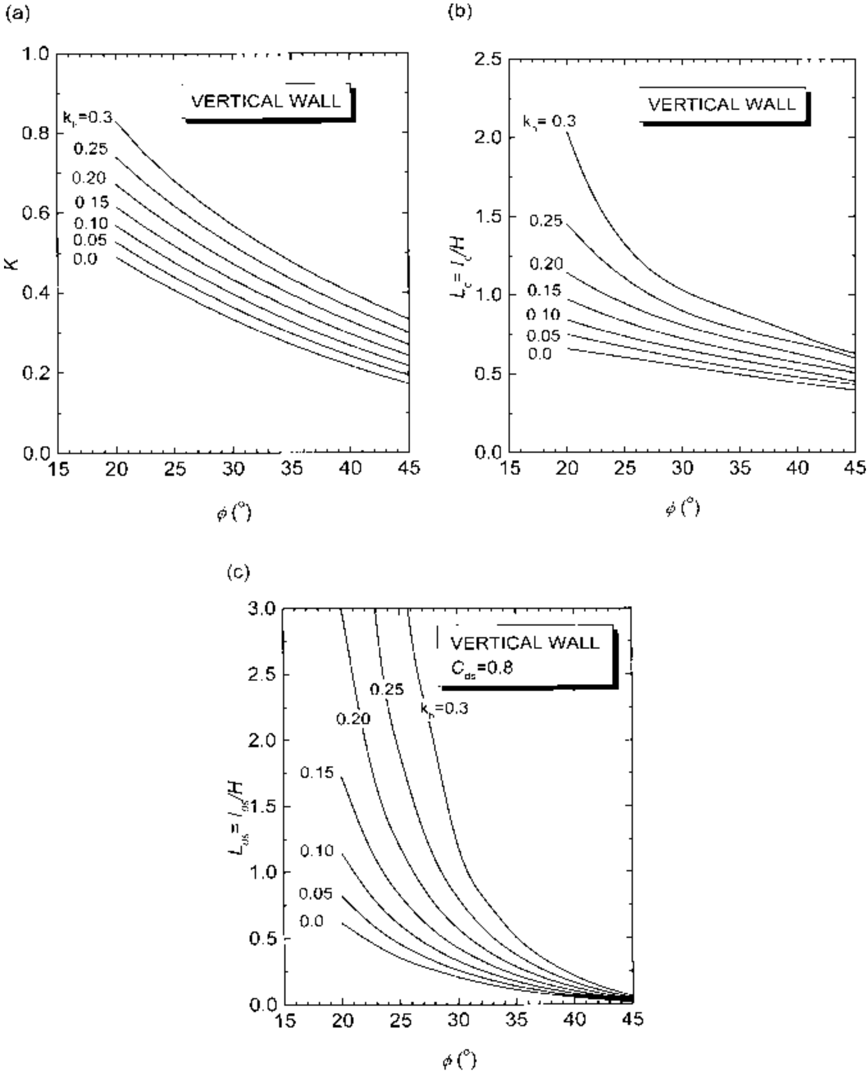

Figure 7 Required strength and length for vertical wall: (a) geosynthetic strength; (b) tieback length; (c) direct sliding length.

attainable. Consequently, a performance-based design should be employed to avoid excessive length of the geosynthetic layer needed to resist direct sliding.

Figures 8a–c show the effects of vertical acceleration for a vertical wall with ϕ equal to 30°. The ratio of vertical acceleration has been considered for

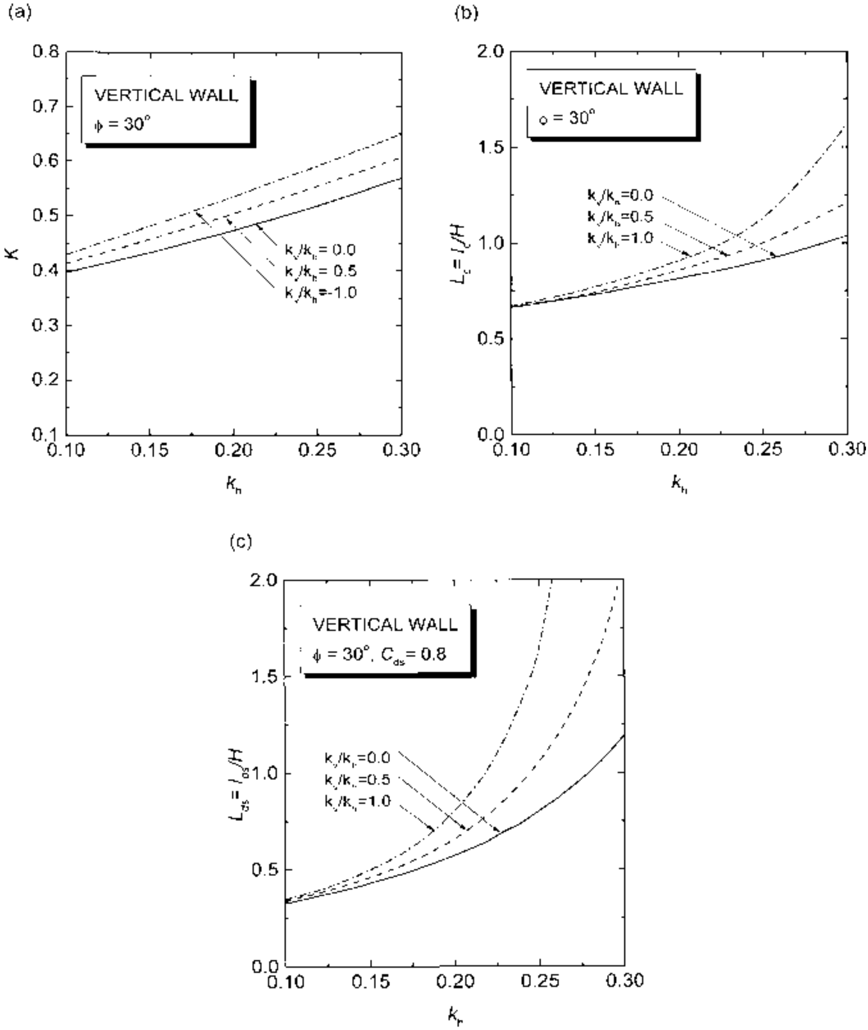

Figure 8 Effect of vertical acceleration on required strength and length for vertical wall, $\phi = 30$: (a) geosynthetic strength; (b) tieback length; (c) direct sliding length.

$k_v/k_h = 0.5$ and 1.0. Note that the most critical direction of vertical acceleration is used in the analysis to obtain normalized values. For tieback length and strength, the most critical acceleration acts downward, whereas it acts upward for direct sliding stability. The effects of vertical acceleration are seen for the strength and lengths. However, the effect is most pronounced in the case of direct sliding with horizontal combined with vertical accelerations.

For direct sliding mechanism, the coefficient of yield acceleration of reinforced soil block is determined as (Ling and Leshchinsky, 1998)

$$k_{hy} = (1 - k_v)\frac{W_B C_{ds}\tan\phi + W_A\tan(\phi - \alpha)\Lambda}{W_B + W_A\Lambda} \tag{13}$$

where

$$\Lambda = \frac{1 - C_{ds}\tan\delta\tan\phi}{1 - \tan\delta\tan(\phi - \alpha)} \tag{14}$$

W_A and W_B are the weights of reinforced soil and potential sliding backfill soil, δ is the interwedge friction angle (equal to relevant values such as ϕ or $\phi/2$). α is the angle of inclination of the most critical failure plane, which may be determined numerically or using the expression of Richards and Elms (1992). For the design where only horizontal acceleration is used, the permanent displacement limit is straightforward, employing Fig. 6.

A comparison is given in Table 1 for a 6-m vertical wall designed statically and seismically with $k_h = 0.4$ and 0.65. The lengths against tieback and direct sliding, and the total reinforcement force, are given. The analysis showed that equilibrium against direct sliding is not attainable for $k_h = 0.65$ and is excessively long for internal stability. However, by allowing a displacement of 6.4 cm, a design can be conducted using $k_h = 0.4$. The required lengths of the geosynthetic become practically acceptable.

4 PERMANENT DISPLACEMENT UNDER VERTICAL ACCELERATION

The vertical acceleration may be required for the design of earth structures, such as in Orange County, California. Under a combined vertical and horizontal acceleration, the equations to determine permanent displacement require k_{hy} and

Table 1 Design of Vertical Wall ($\phi = 35°$, $\gamma = 18\,\text{kN/m}^3$, $C_{ds} = 0.8$, $k_{ho} = 0.65$)

k_h	Tieback length (m)	Direct sliding length (m)	Total reinforcement force (kN/m)	Permanent displacement (cm)
0.0	3.1	0.7	88	—
0.4	6.9	6.6	188	6.4
0.65	22.3	Infinity	346	0.0

therefore k_v, which varies with time. The procedure implies that a separate set of vertical acceleration records is needed in addition to that of horizontal acceleration (Fig. 3a). However, the vertical acceleration may be considered in a simplified manner using a ratio of peak vertical seismic coefficient to peak horizontal seismic coefficient. That is, $\lambda = k_{vo}/k_{ho}$. The vertical acceleration is thus assumed to be in phase with the horizontal acceleration.

For the horizontal block and reinforced soil block, the yield seismic coefficient and displacement correction factors are rewritten as follows for the simplified analysis:

Block sliding along horizontal plane:

$$k_{hy} = \frac{\tan\phi}{1 + \lambda \tan\phi} \tag{15}$$

$$x = (1 + \lambda \tan\phi) \iint (k_h - k_{hy}) g \cdot dt \tag{16}$$

Reinforced soil:

$$k_{hy} = \frac{W_B C_{ds} \tan\phi + W_A \tan(\phi - \alpha)\Lambda}{W_B(1 + \lambda C_{ds} \tan\phi) + W_A[1 + \lambda \tan(\phi - \alpha)]\Lambda} \tag{17}$$

$$x = (1 + \lambda C_{ds} \tan\phi) \iint (k_h - k_{hy}) g \cdot dt \tag{18}$$

Note that Eqs. (16) and (18) are the same since $C_{ds} \tan\phi$ represents the angle of friction of the soil–geosynthetic interface. The simplified approach to include vertical acceleration has been discussed in Ling and Leshchinsky (1998).

5 LANDFILL COVER

Geomembrane is used as liquid barrier in waste containment. It is covered by a layer of cohesive soil as a protection medium. Because of the low frictional resistance between soil and geomembrane, the failure of cover soil typically occurs along the soil–geomembrane interface. It may also occur along the interface of geosynthetics depending on the interface strength. The static stability analysis of landfill cover soil, considering end effect (finite slope), has been presented by Giroud and Beech (1989) and Koerner and Hwu (1991).

In the United States, seismic design of municipal solid waste containment systems became mandatory in 1993 as regulated by the Resource Conservation and Recovery Act Subtitle D. The seismic impact zone, which is defined as an area having a 10% or larger probability that the peak acceleration in lithified earth material will exceed 0.1 g in 250 years, has to be designed against earthquake loading. Figure 9 gives the seismic map typically used for landfill design. Richardson et al. (1995) and Anderson and Kavazanjian (1995) describe in detail the seismic design of landfill.

In this session, the Koerner–Hwu approach is extended to include seismic loading. The approach assumes limit equilibrium analysis for a cover, which is of length and thickness L and H, respectively. These formulations are based on a two-part wedge mechanism with the interwedge force acting parallel to the slope angle, β (Fig. 10). The earthquake inertia force is considered using horizontal and vertical seismic coefficients, k_h and k_v, respectively. Note that the positive vertical acceleration is assumed to act upward. The geometry of landfill cover is referred to Fig. 10.

The factor of safety of the cover soil to resist direct sliding is determined as

$$F_{ds} = \frac{T_A + P + k_v W_A \sin\beta + C_a}{W_A(k_h \cos\beta + \sin\beta)} \tag{19}$$

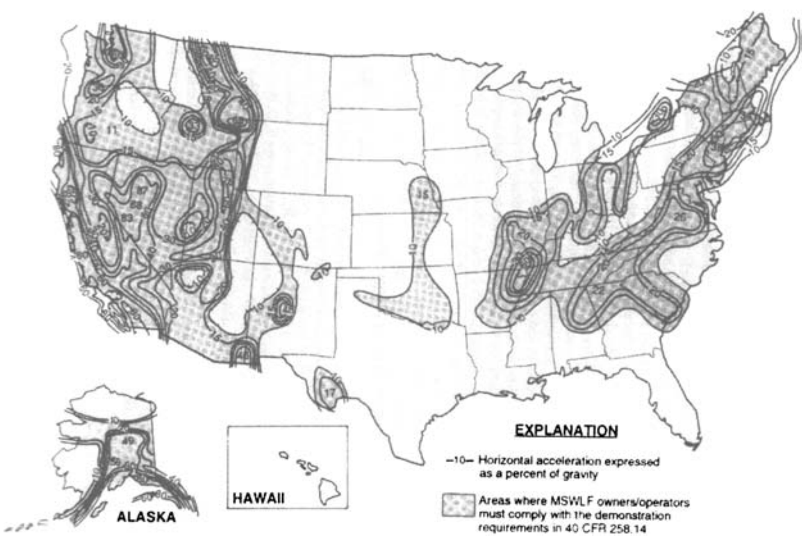

Figure 9 EPA seismic map. (From Sharma and Lewis, 1994.)

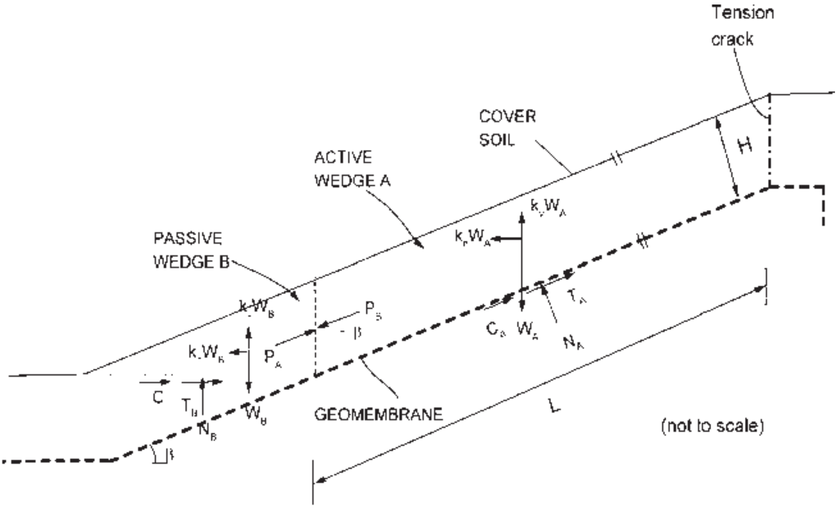

Figure 10 Direct sliding mechanism for landfill liner.

where

$$T_A = C_{ds} \tan\phi\{(1 - k_v)\cos\beta - k_h \sin\beta\}W_A \tag{20}$$

$$P = \frac{W_B\{(1 - k_v)\tan\phi - k_h\} + C}{\eta} \tag{21}$$

$$\eta = \frac{\cos(\phi + \beta)}{\cos\phi} \tag{22}$$

$$W_A = \gamma HL; \quad W_B = \frac{\gamma H^2}{\sin 2\beta}; \quad C = c\frac{H}{\sin\beta}; \quad C_a = c_a L \tag{23}$$

W_A and W_B are the weight of the soil wedges, and c and c_a are the soil cohesion and adhesion between soil and geomembrane, respectively.

From Eq. (19), the coefficient of yield acceleration is determined as

$$k_{hy} = \frac{(1 - k_v)\{W_A\eta(C_{ds}\tan\phi\cos\beta - \sin\beta) + W_B\tan\phi\} + C_a\eta + C}{W_A\eta(\cos\beta + C_{ds}\tan\phi\sin\beta) + W_B} \tag{24}$$

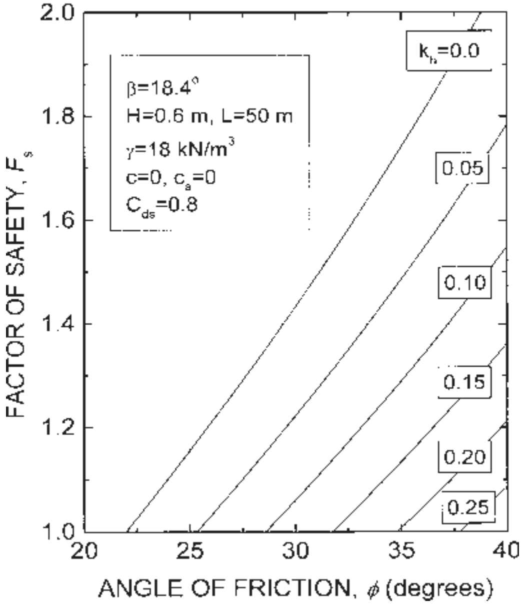

Figure 11 Factor of safety under earthquake acceleration.

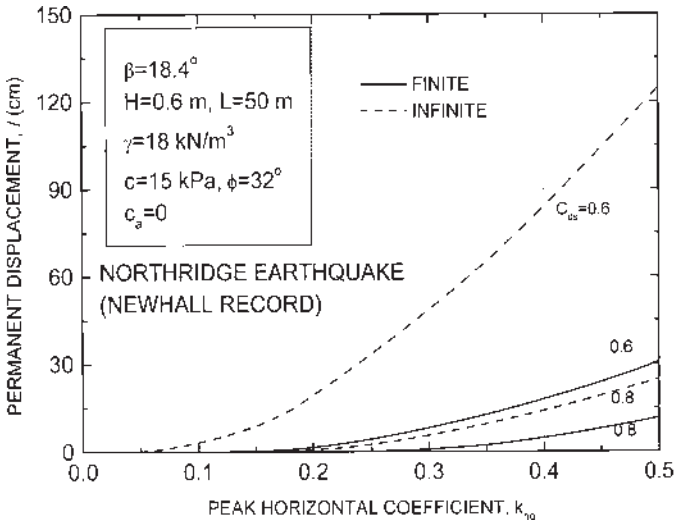

Figure 12 Effects of direct sliding coefficients on permanent sliding.

The displacement along the soil–geomembrane interface is obtained as

$$l = \eta' \iint (k_h - k_{hy}) g \cdot dt \tag{25}$$

where

$$\eta' = \cos\beta + C_{ds}\tan\phi\sin\beta + \frac{H}{L\eta\sin 2\beta} \tag{26}$$

When the end effect is neglected (infinite slope), Eqs. (19), (24), and (22) degenerate to the following expressions, respectively:

$$F_{ds} = \frac{C_{ds}\tan\phi(1 - k_v - k_h\tan\beta) + k_v\tan\beta + c_a/\gamma H\cos\beta}{k_h + \tan\beta} \tag{27}$$

$$k_{hy} = \frac{(1 - k_v)(C_{ds}\tan\phi - \tan\beta) + c_a/\gamma H\cos\beta}{1 + C_{ds}\tan\phi\tan\beta} \tag{28}$$

$$\eta' = \cos\beta + C_{ds}\tan\phi\sin\beta \tag{29}$$

Figure 11 shows the factor of safety of a liner under different values of peak earthquake acceleration. The factor of safety is reduced significantly with an increase in peak acceleration and a reduction in friction angle. The geometries and properties are included in the figure. The yield seismic coefficient are calculated as $k_{hy} = 0.1216$ and 0.037 for a finite and infinite slope when $C_{ds} = 0.6$; and 0.2208 and 0.1428 when $C_{ds} = 0.8$.

The effects of the direct sliding coefficient on the magnitude of sliding are shown in Fig. 12. A low value of coefficient, such as $C_{ds} = 0.6$, gives several times larger displacement than that of $C_{ds} = 0.8$ based on a record of the Northridge earthquake. The end effect of the liner is also shown in the figure.

The parametric studies to look into the effect of other factors are given in Ling and Leshchinsky (1997). It has to be noted that effect of vertical acceleration is not very significant for landfill liner.

6 CONCLUSIONS

Equations for the yield seismic coefficients and permanent displacement were presented for reinforced soil retaining walls and landfill liner considering direct sliding mode of failure. A simplified procedure to include vertical acceleration was presented for yield acceleration and permanent displacement. The permanent displacement would be a more rational criterion for performance-based design under high seismic load.

REFERENCES

AASHTO. *Guide Specifications for Seismic Design of Highway Bridges*. Washington, DC: American Associations for State Highways and Transportation Officials, 1983.

DG Anderson, E Kavazanjian, Jr. Performance of landfill under seismic loading. *Proceedings of the Third Intl. Conference on Recent Advances in Geotechnical Earthquake Engineering and Soil Dynamics*, St. Louis, MO, 1995.

AG Franklin, FK Chang. *Permanent Displacement of Earth Embankments by Newmark Sliding Block Analysis*. Miscellaneous Paper S-71-17. Soil and Pavement Laboratory, U.S. Army Engineer Waterways Experiment Station, Vicksburg, MS, 1977.

JP Giroud, JF Beech. Stability of soil layers on geosynthetic lining systems. *Proceedings of Geosynthetics '89 Conference*. International Fabrics Association, Minneapolis, MN, 1989, pp 35–46.

ME Haynes, AG Franklin. *Rationalizing the Seismic Coefficient Method*. Miscellaneous paper GL-84-13. Waterways Experiment Station, Corps of Engineers, Vicksburg, MS, 1984.

JGS. *Proceedings of 34th Japan National Convention on Geotechnical Engineering*, Tokyo, Vols. 1 & 2, Japanese Society of Geotechnical Engineering, Tokyo, Japan, 1999.

JSCE. Proposal on earthquake resistance for civil engineering structures (Special Task Committee of Earthquake Resistance of Civil Engineering Structures). *The 1995 Hyogoken-Nambu Earthquake Investigation into Damage of Civil Engineering Structures*. Earthquake Engineering Committee, Japan Society of Civil Engineers, Tokyo, Japan, 1996, pp 297–306.

RM Koerner, BL Hwu. Stability and tension considerations regarding cover soils on geomembrane lined slopes. *Geotext. Geomembr.* 10(4): 335–355, 1991.

J Koseki, F Tatsuoka, Y Munaf, M Tateyama, K Kojima. A modified procedure to evaluate active earth pressure at high seismic loads. *Spec. Issue Soils Found.* 209–216, 1998.

D Leshchinsky, RH Boedeker. Geosynthetic reinforced earth structures. *J. Geotech. Eng. ASCE* 115(10): 1459–1478, 1989.

D Leshchinsky. *Design Procedure for Geosynthetic Reinforced Steep Slopes*. Technical Report REMR-GT-120. Waterway Experiment Station, U.S. Army Corps of Engineers, Vicksburg, MS, 1995.

D Leshchinsky, HL Ling, G Hanks. Unified design approach to geosynthetic reinforced slopes and segmental walls. *Geosynth. Int.* 2(5): 845–881, 1995.

HI Ling. Recent application of sliding block theory to geotechnical design. *Soil Dyn. Earthquake Eng.* 21(3): 189–197, 2001.

HI Ling, D Leshchinsky, EB Perry. A new concept of seismic design of geosynthetic-reinforced soil structures: permanent displacement limit. In *Earth Reinforcement*. Ochiai, Yasufuku, Omine, eds. Rotterdam: Balkema, 1996, pp 797–802.

HI Ling, D Leshchinsky. Seismic stability and permanent displacement of landfill cover systems. *J. Geotech. Geoenviron. Eng. ASCE* 123(2): 113–122, 1997.

HI Ling, D Leshchinsky, EB Perry. Seismic design and performance of geosynthetic-reinforced soil structures. *Geotechnique* 47(5): 933–952, 1997.

HI Ling, D Leshchinsky. Effects of vertical acceleration on seismic design of geosynthetic-reinforced soil structures. *Geotechnique* 48(3): 347–373, 1998.

FI Makdisi, HB Seed. Simplified procedure for estimating dam and embankment earthquake-induced deformations. *J. Geotech. Eng. ASCE* 104(7): 849–867, 1978.

WF Marcuson. An example of professional modesty. *The Earth, Engineers and Education*. Cambridge, MA: MIT, 1995, pp 200–202.

NM Newmark. Effects of earthquakes on dams and embankments. *Geotechnique* 15(2): 139–159, 1965.

RJ Richards, DG Elms. Seismic behavior of gravity retaining walls. *J. Geotech. Eng. ASCE* 105(4): 449–464, 1979.

R Richards, DG Elms. Seismic passive resistance of tied-back walls. *J. Geotech. Eng. ASCE* 118(7): 996–1011, 1992.

GN Richardson, E Kavazanjian, Jr., N Matasovic. *RCRA Subtitle D(258), Seismic Design Guidance for Municipal Solid Waste Landfill Facilities*. EPA/600/R-95/051. Washington, DC: U.S. EPA Office of Research and Development, 1995.

T Sano. *Structural Seismic Design of Houses*. Earthquake Disaster Mitigation Committee Report No. 83, 1916, in Japanese.

HD Sharma, SP Lewis. *Waste Containment Systems, Waste Stabilization, and Landfills: Design and Evaluation*. New York: John Wiley & Sons, Inc., 1994.

RV Whitman. Seismic design and behavior of gravity retaining walls. *Proc. Conf. Design Performance Earth Retaining Struct. ASCE*: 817–842, 1990.

7

Failure of an 8-Meter-High Segmental Block Wall in the Northeast United States

C. M. Reith, G. S. Paxson, and A. W. Cadden
Schnabel Engineering Associates, Inc., West Chester, Pennsylvania, U.S.A.

1 INTRODUCTION

This chapter describes the failure, investigation, and remediation of two sections of a geogrid reinforced segmental concrete block retaining wall. This wall was completed in August 1997 and was followed by heavy precipitation in the following fall, winter, and spring. The first failure occurred without any warning about 5 months after construction. The second failure occurred at a different location in the wall about 5 months after the first failure was repaired. The second failure was progressive and exhibited large deformations for several weeks before the collapse occurred.

A geotechnical engineering study was conducted at this site prior to design of the wall, and full time observation and field density testing were performed during fill placement and compaction as the wall was constructed. Field investigations were conducted during the demolition of the first failed section, and a drilling program was used to evaluate the remaining areas of the wall. Standard penetration tests (SPT), in-situ density tests, soil laboratory testing, and a review of construction observation and testing records were performed in an attempt to determine the cause of the failure. No clear single reason for the wall failure was identified during this work. It is believed that the failure occurred as a result of several problems during construction that compounded to cause the failures.

2 WALL DESIGN

The wall is about 175 m long and typically ranges from about 4 m to 8 m high. A loading dock and access drive for a large retail building are located at the top of the wall. The wall was designed using the computer program and methodology developed by the National Concrete Masonry Association (NCMA) for external stability (sliding, overturning, bearing capacity) and internal stability (geogrid overtensioning and pullout). The computer program PCSTABL6 was used to analyze for global and compound failures. In addition, the geogrid and block manufacturer performed independent analyses using similar methodologies to confirm the design.

The project is located in the Piedmont Physiographic Region of the Eastern United States. A geotechnical engineering study conducted by a geotechnical consultant indicated that the on-site soils generally consisted of sandy silts and silty sands derived from weathering of the underlying phyllitic limestone. The wall design was based on using the on-site soils for backfill and specifically required silty sand material with a unit weight of 18.8 kN/m^3, a minimum effective friction angle of 32° and effective cohesion of 0 kPa. A PVC coated polyester geogrid with a long-term allowable design strength of 12.9 kN/m was selected. A coefficient of interaction value of 0.9 was used for the grid on backfill soil. The segmental blocks consisted of dry stack, pinless, concrete masonry units about 0.2 m high with a design offset that achieved about a 6° batter at the wall face. Drainage was provided by a perforated pipe and weep hole system with a blanket drain, and a 1.2-m-thick crushed stone layer behind the block facing.

A variable geogrid reinforcement layout was used with a spacing of about 0.37 m in the lower sections, about 0.55 m in the middle sections, and a maximum spacing of about 0.73 m at the top of the wall. Geogrid lengths typically ranged from 4.3 to 4.9 m, resulting in a height-to-length ratio of at least 0.6. A surface live load surcharge of 12.0 kPa was used to model traffic loading at the top of the wall. The design reinforcement layout with the above parameters resulted in a minimum factor of safety of 1.5 for internal and external stability and 1.4 for global or compound stability. A typical wall section is shown in Fig. 1.

3 FIRST WALL FAILURE

About 5 months after construction of the wall, but prior to opening of the retail store, a section of the wall collapsed. Immediately after the failure, the facing blocks and drainage gravel were piled up at the base of the wall and the reinforced soil mass was standing vertically with lengths of geogrid hanging from the soil. The block facing for the portions of the wall adjacent to the failed section curled outward, away from the wall. A precast concrete stormwater drop inlet was

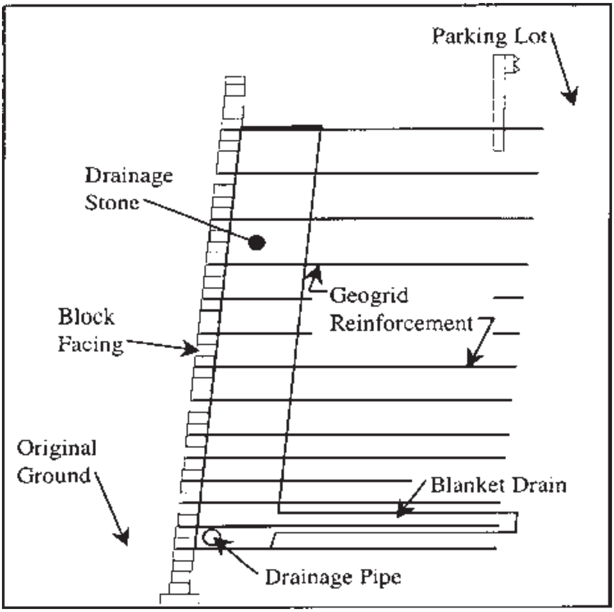

Figure 1 Typical design wall section.

located near the center of the failed area. Photographs of this failure are shown in Figs. 2 and 3.

There was a significant amount of rainfall in the days and months preceding the failure, and it was reported that a large amount of water was released from the fire protection system into the parking lot a few days prior to the failure. The failed and damaged section of the wall was dismantled within a few days and field observations, in-situ testing, and soil laboratory testing were conducted in an attempt to determine the cause of failure and to design the repair. Copies of the daily field reports and in-place density test results during construction were also obtained and reviewed.

Observations and measurements of the wall as it was being dismantled indicated that the wall structure itself was generally constructed as described in the design documents. The geogrid and block units were of the specified type and dimension and appeared to have been located generally at the specified locations and elevations.

Samples collected during excavation were tested in a soils laboratory and fall into two general soil types. The first soil type consisted of a nonplastic, fine to coarse silty sand (SM), with about 20.9 to 44.5% passing the No. 200 Standard Sieve. The second soil type consisted of fine to coarse sandy silt (ML), with

Figure 2 First failure.

slightly more than 50% passing the No. 200 Standard Sieve and moderate to low plasticity. This material did not meet the material classification specified on the design documents.

A modified proctor test (ASTM D1557) was performed on one bulk sample obtained from the failure area. The result of this test indicates that the maximum dry density for this material was about 19.3 kN/m^3 at optimum moisture of about 10.8%. In-place density testing of the soil within the failed reinforced soil zone generally ranged from about 14.0 kN/m^3 to 15.7 kN/m^3 with moisture contents ranging from about 18 to 33%. Given the results of the laboratory tests, the measured densities were calculated to be 73 to 82% of the maximum dry density determined in the laboratory.

A review of daily field reports from construction indicates that the fill was placed and compacted to at least 95% of the maximum dry density in accordance with a modified proctor with resulting field dry densities of at least 16.2 kN/m^3.

During excavation it was noted that the thickness of the stone drainage material behind the block facing was highly variable, ranging from the design thickness of 1.2 m to less than 0.3 m. At several locations thin layers of soil intruded into the drainage material such that water would not be permitted to drain freely to the collection system and outlet pipes at the base of the wall.

Excavation of the stormwater pipe extending from the concrete drop inlet at the failure location revealed that this reinforced concrete pipe was not constructed with rubber gaskets or other sealing materials. Furthermore,

Figure 3 Second failure.

the joints were observed to be open, and the bell of the second pipe section from the inlet was broken, and partially missing. Also, the inlet and pipe were bedded in open graded stone, which may have connected directly with the drainage material behind the wall.

The parties involved generally agreed that the failure was most likely due to hydrostatic pressure buildup from the leaking storm sewer. This was due to the reports of significant amounts of water being introduced into the storm drain system, the location of the failure at the storm drain inlet, and the open joints and crushed stone bedding of the storm drain pipe. The low density of the backfill was noted as an additional factor contributing to the failure. A subsurface exploration program was recommended to evaluate the quality of the backfill in the other areas of the wall. Due to time constraints, the failed section was rebuilt following the original design but using imported dense graded aggregated and a slightly higher-strength grid to account for installation damage due to the size of the rock fragments in the fill.

4 SECOND WALL FAILURE

About 2 months after the repair of the first failed section was complete, several tension cracks were observed in the asphalt pavement located behind other sections of the wall. The contractor sealed these cracks with tar, but they reopened within a few days. The cracks became wider and longer, and movement of the concrete curb was also noticed. However, no bulging of the wall was readily apparent at this time. Again, a monitoring and subsurface investigation program was recommended to evaluate the cause of this movement.

No action was taken initially; however, as the cracks became wider, a vertical displacement became obvious, and the wall face started to bulge outward near the middle and lean in at the top. A subsurface exploration program was conducted by another independent geotechnical consultant, which included performing standard penetration testing (SPT) and obtaining bulk samples and undisturbed Shelby tube samples from several locations behind the wall.

The SPT results indicated that the upper 3 m to 4.5 m of the soil were in a very loose to loose state. In-place density results from the Shelby tubes indicated that the field compaction generally varied from 80 to 90% of the maximum dry density based on the proctor results from the bulk samples obtained in the second study. Direct shear testing on the samples from the Shelby tubes indicated effective friction angles ranging from about 30.5 to 33.7° with an average of 32°.

The cracking and deformation of the ground surface behind the wall continued, and a vertical displacement of about 0.2 m developed at the back of the reinforced zone. The bulging near the middle of the wall and leaning inward at the top continued to progress. The wall finally failed about 5 months after the other section was repaired and about one year after original construction. The failure was similar to the first one, with blocks and drainage gravel piled up at the base of the wall and the reinforced mass still standing. However, the reinforced zone underwent much more movement and exhibited a clear failure surface as was evidenced by the resulting scarp at the ground surface. Photographs of the failure are shown in Figs. 4 and 5.

This failed section was dismantled and rebuilt under the observation of the consultant who performed the second field exploration program.

Figure 4 Second failure—scarp at the ground surface.

Figure 5 Second failure.

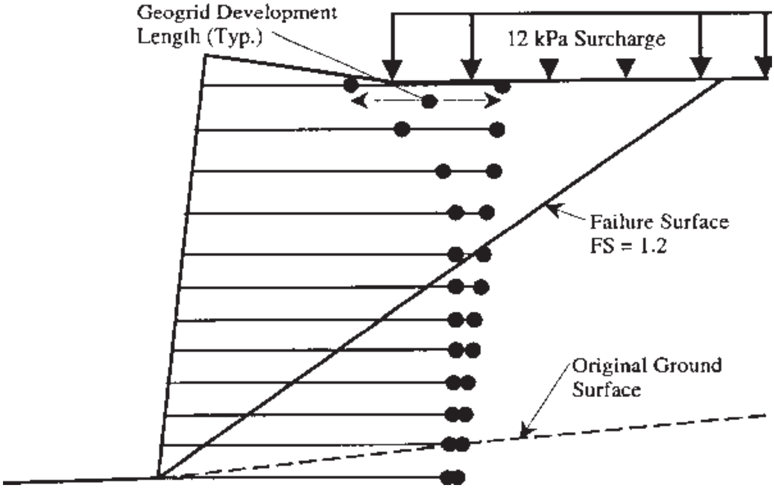

Figure 6 Slope stability output using field data.

5 BACK ANALYSIS

The original wall design was reanalyzed using the data obtained from the field investigation of both collapses in an attempt to determine the cause of the failure. A parametric evaluation was conducted varying the unit weight, effective friction angle, and coefficient of interaction. A compound failure resulted in the lowest factors of safety.

A factor of safety of about 1.17 was estimated using the unit weights measured in the field, the effective friction angle measured from direct shear tests, and a lower coefficient of interaction to account for the high-moisture-content silts. An example output for this case is included in Fig. 6.

The parameters were then varied to get a factor of safety of 1.0. An effective friction angle of 25° was required to achieve a factor of safety of 1.0; however, the failure surface did not approximate the field observed conditions. When a water table was added using a friction angle of 28°, the failure surface more closely approximated the observed field behavior. All of the failure surfaces passed through several layers of the geogrid reinforcement. This indicates that a break or pullout of the grid occurred. There was no evidence of a break in the grids at the base of the wall after failure, and not enough movement occurred to evaluate if the grids pulled out of the back of the reinforced zone. Also, tearing of the grid is not considered to be a probable cause of failure since the creep limited strength was used in the analysis rather than the ultimate strength, which is about 300% higher. An example output for this analysis is included in Fig. 7.

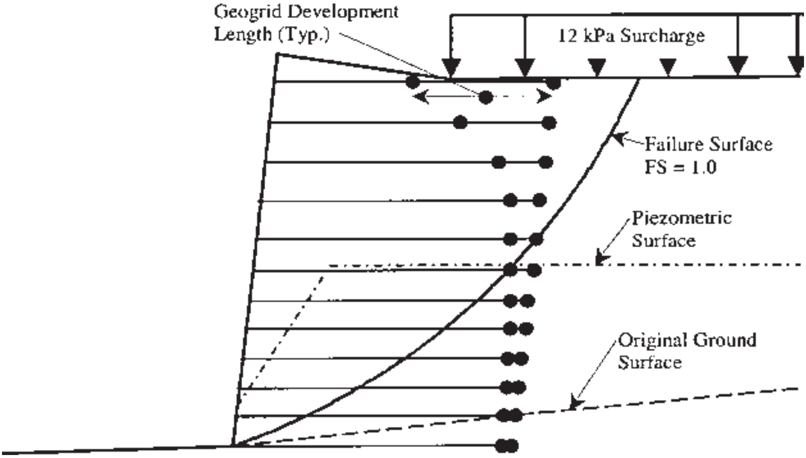

Figure 7 Slope stability output for factor of safety of 1.0.

6 CONCLUSIONS

The first failure occurred rapidly without showing obvious signs of movement. Circumstances surrounding the failure pointed to a buildup of hydrostatic pressure as the primary cause of failure. This hydrostatic buildup was likely due to several construction deficiencies. First, the joints of the storm sewer pipe entering the drop inlet behind the wall were open. Second, the drop inlet and pipe were bedded in crushed stone, which was connected to the drainage material behind the wall facing, causing a "short circuit" for water leaking from the open joints. Finally, significant soil intrusion was observed into the drainage stone behind the facing, reducing the ability to drain water from behind the wall. A second cause of failure, considered important but secondary at the time of failure, was a reduced shear strength from poor compaction and a lower coefficient of interaction due to the saturated silts. Creep movement and possibly differential settlement between the facing and backfill materials most likely caused the facing to fail first, leaving the slightly deformed reinforced mass standing.

The second failure occurred much more slowly and exhibited a classical scarp and obvious deformation at the face prior to failing. Again, this resulted in a facing failure with a much more deformed reinforced soil mass still standing. This failure was likely due to reduced shear strength from poor compaction and a lower coefficient of interaction of the saturated silts.

The in-situ testing performed during tear down of the first failed section indicated that the backfill did not meet the specified degree of compaction. The undisturbed samples obtained during drilling prior to the second failure also indicated that the backfill soils did not meet the projects requirements. However, even though the compaction was less than specified, the laboratory testing showed effective friction angles close to the values used in the original design. Thus, this alone is not considered to be the only cause of failure. The poor compaction resulted in a higher void ratio, which could have affected the permeability. Also, the in-situ moisture contents measured after the wall failure were much higher than those reported during construction.

Several combined construction deficiencies are suspected to have caused the failure. Compaction was performed within the reinforced zone using a small walk behind vibratory sheepsfoot roller. Dry densities measured after the wall failure generally agreed with the dry densities reported during construction. Therefore, the wrong proctor was likely referenced during construction, which showed compaction meeting the specification when in fact the relative degree of compaction was very low. Poor construction of the storm drain introduced additional water into the wall backfill, and the soil intrusion into the drainage stone behind the wall reduced its effectiveness.

REFERENCES

JG Collin,ed. *Design Manual for Segmental Retaining Walls*. Herndon: National Concrete Masonry Association, 1997.

U.S. Department of Transportation, Federal Highway Administration, *PC-STABL6 Users' Guide, Slope Stability Analysis Program*. McLean: Turner-Fairbank Highway Research Center, 1986.

HW Van Aller. *STED 6.5 PCSTABL Editor*. Queenstown: H. W. Van Aller, 1996.

8

Displacement Monitoring at Verrand High Reinforced Soil Structure

G. Sembenelli and P. Sembenelli
SC Sembenelli Consulting, Milan, Italy

1 INTRODUCTION

The Verrand high reinforced soil structure (HRSS) was built within the construction works for a new highway, which will connect the Monte Bianco tunnel with the city of Aosta, in the Italian Alps. The first aim of the structure was providing a stabilizing weight at the toe of a 35° to 40° steep and unstable slope, which forms the left bank of the Dora River. About 10 m above the top of the stabilizing embankment, a shaft foundation of a 30-m-high pier will be placed. The pier is one of the four supports of a 600-m-long bridge.

Additional purposes of the Verrand RSS were the disposal for about 120,000 m^3 of material from nearby tunnel excavations and providing access to construction fronts beyond the embankment.

The slope is basically formed by a glacial till, which can be described as a silty sand matrix containing gravel and large boulders. The glacial till is overconsolidated and slightly cemented. Both effects vanish within the surficial part of the mass, so that the slope can be considered close to limit conditions. The water table daylights about 10 m above the toe of the slope.

2 PROJECT DESCRIPTION

The Verrand Embankment is 37.5 m high and some 150 m long, for a total volume of about 120,000 m^3 (Sembenelli and Sembenelli, 1998). Its geometry is shown in Fig. 1. The lower 27.5 m are reinforced, while the top is a conventional compacted fill, with a 1.5H to 1 V slope, initially designed to be 10 m high and finally brought to 15 m. The volume of the reinforced fill is 50,000 m^3.

The reinforced portion consists of three 9-m-high blocks, with face angle of 60° from the horizontal. The blocks are stepped to create 5-m-wide berms, sloping almost parallel to the riverbed grade. A 5-m-wide service ramp runs on the lower berm and cuts the second and third blocks.

The reinforced soil structure was founded on competent foundation. The surface of the foundation soil, either at the bottom or on the slope, had been stepped to improve interlocking with the new fill.

The toe of the HRSS had to be protected from river action by a cyclopean masonry wall, about 4 m high, founded on a row of micropiles capped by a concrete beam.

Deep and surface drainage systems were key features in the design.

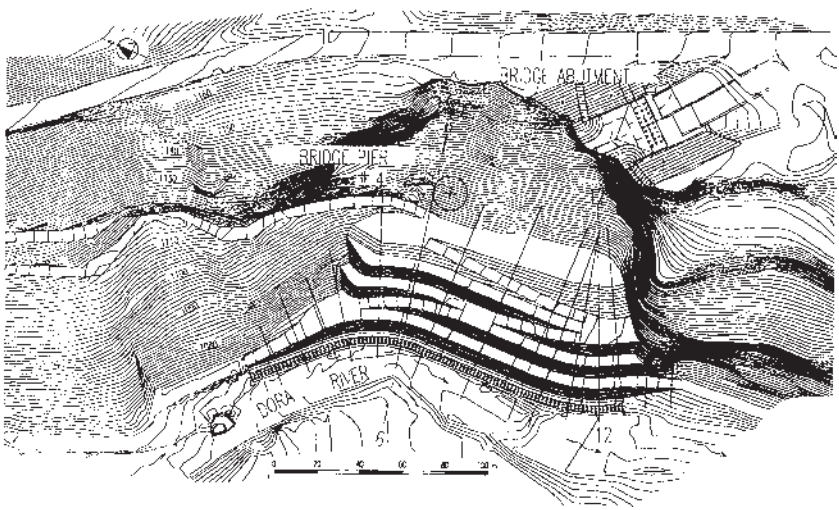

Figure 1 Plan of the Verrand high reinforced soil structure.

3 THE REINFORCED SOIL

The reinforced soil included nonwoven geotextiles reinforcements and a facing system, resulting in a completely grassed surface, once construction completed. The facing system is patented.

The basic element of the selected facing technology are 0.5- or 0.6-m-high, L-shaped forms made by a welded steel wire mesh. Such forms are left in place, after compaction. Each form element is bent to the angle selected for the slope. Short steel tiebacks prevent significative deformation of the wire mesh, during compaction of adjacent lifts. A light woven geotextile is placed inside the form to retain the soil. The fill material is usually spread and compacted in lifts, whose thickness is half the form height. Lifts stop some 0.4 m away from the form. The space between the lifts and the forms is filled with topsoil, to support vegetation. The surface is finally hydroseeded so that it becomes completely and permanently grassed in a short time (Fig. 1).

The reinforcements used at Verrand were anisotropic nonwoven, continuous filament, needle-punched, polyester (PET) fiber geotextiles, of three grades, manufactured by Fritz Landolt A.G., Switzerland. The nominal tensile strengths of the geotextiles were 40, 100 and 120 kN/m, and their main characteristics are summarized in Table 1.

The fill material placed within the reinforced section was well-graded, crushed rock with a relatively large sand and silt fractions, obtained by processing tunnel muck. The material mainly came from tunneling in schists. The tunnel muck was first crushed in order to reduce its maximum grain size to 150–200 mm and then mixed with material obtained from open-air excavations. A relatively high content in sand and silt fines was added to reduce damage to the reinforcements.

The backfill was basically the same material with maximum size in the order of 500 mm.

Table 1 Main Characteristics of Geotextiles FLN-TEXA Used as Reinforcement at Verrand HRSS

		Machine direction		Transverse direction	
Type	Mass [g/m^2]	Strength [kN/m]	Elongation [%]	Strength [kN/m]	Elongation [%]
350	350	48.5	36.8	21.8	37.6
1000	900	115.5	38.3	47.8	36.2
1200	1050	132.7	40.1	55.4	39.6

4 CONSTRUCTION

Construction started in summer 1994 and was completed to the top of the reinforced portion early in September 1996. Conventional fill was then added to the final grade, in the following 2 months. Construction proceeded continuously, except for a stoppage of 1 year, during the summer and winter of 1995. In 1997 the height of the fill was raised 5 more meters, to the present elevation, 5 m higher than the design top elevation. An aerial view of the Verrand Embankment after completion is given in Fig. 2.

In summer 1996, a 600-m^3/s flood (corresponding to an estimated return period of 100 yr) occurred in the Dora River. Although the water level rose to the top of the toe wall, no damages were observed on the reinforced embankment.

Reinforced soil as well as compacted fill were built with a heavy vibrating roller, of class DYNAPAC CA35 (7 static tons on drum). This equipment was

Figure 2 Aerial view of the Verrand high reinforced soil structure after completion.

slightly larger than the specified CA 25 class (5 static tons on drum), and geotextiles survivability had to be checked by full-scale tests.

The tests suggested that the damage is generally not uniformly spread over the reinforcement and that the actual strength retained by the whole reinforcement is 70 to 75% of that of the undamaged material. The corresponding survivability factor of safety to be applied in the Verrand case was selected as $Fd = 1.35$ to 1.45.

5 DESIGN OF THE REINFORCEMENT DISTRIBUTION AND LENGTH

The selection of the reinforcement requirements (force and length) was based on limit equilibrium, reference minimum factor of safety being $Fs = 1.3$ (Christopher et al., 1989; Jewell, 1990). The assumed geotechnical characteristics of the fill material were total unit weight $\gamma = 21\,\text{kN/m}^3$, cohesion $c = 0\,\text{kPa}$, and angle of friction $\phi = 35°$. The strength data were obtained from Triaxial CD tests, on 100-mm-diameter, compacted specimens. Only the fraction finer than 25 mm could be tested, and the measured strength parameters were conservatively reduced when used in stability computations.

The geotextiles tensile strength values were reduced to account for installation damage, long-term durability, and creep. The design strength of the geotextiles was finally assumed to be 27% of the wide-width (200-mm) strength determined according with CNR-UNI (Italian) standards (Cazzuffi et al., 1986).

The length of the reinforcements was selected so that the computed minimum factor of safety for surfaces passing just beyond the reinforcements would be $Fs = 1.3$.

The heaviest reinforcements were located within the lower blocks, not only to fulfill strength requirements but also to provide greater stiffness to the structure. Grade 350 reinforcements were used only locally in the very upper portion of the upper block. Additional reinforcements were introduced at the base of conventional fill to reduce the earth pressure on the reinforced blocks.

6 BEHAVIOR

Since early construction, vertical and horizontal displacements of reference points at cross sections 6 and 12 were monitored by topographic surveying. Long-base extensometers installed on the same cross sections to measure horizontal average strains of the reinforced mass suffered a wrong installation and could not provide reliable and usable readings.

The selected reference points were obtained with special plates, fixed to the wire mesh facing and to the heads of the extensometers. Station points for surveying were set on the opposite bank of the river, at distances not exceeding 100 m. The location of the reference points for cross section 12 are shown in Fig. 3. Plates and extensometers in Section 6 are arranged in a similar way.

Time histories of horizontal and vertical displacements are shown in Fig. 4. Most curves exhibit a sharp rise soon after new fill is added, during construction. As time goes on, the curves smooth toward a horizontal asymptote.

At Section 6, the maximum horizontal displacements is in the order of 70 mm, on the lower plate of the lowest block. The upper blocks exhibit lesser horizontal displacements, in the order of 50 mm. Vertical displacements range between 30 and 45 mm.

At Section 12, the measured horizontal displacements of the lower block are somehow larger, with a maximum in the order of 100 mm. The horizontal displacements of the upper blocks were approximately 50 mm. Vertical displacements are about 70 mm, in the lower block, and 40 mm, above.

Displacement vectors are shown in Fig. 5. The horizontal component generally exceeds the vertical one, throughout the time of observation. The resulting

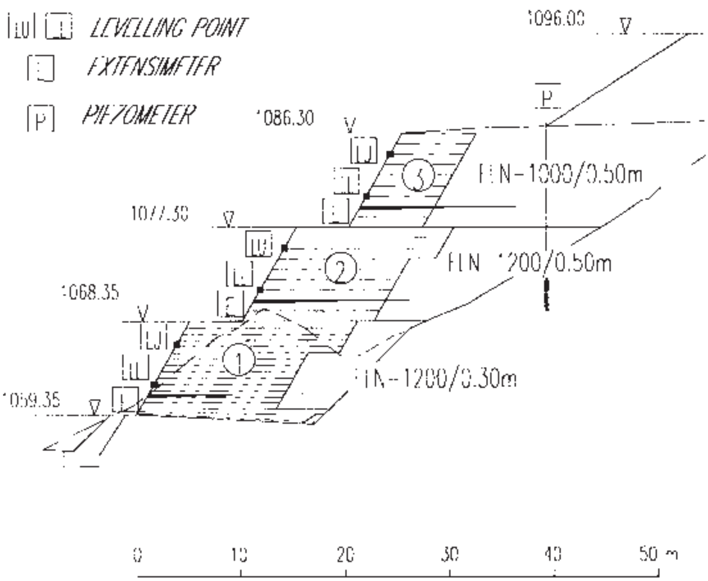

Figure 3 Design cross section 12 with blocks numbering, reinforcements, and instrumentation.

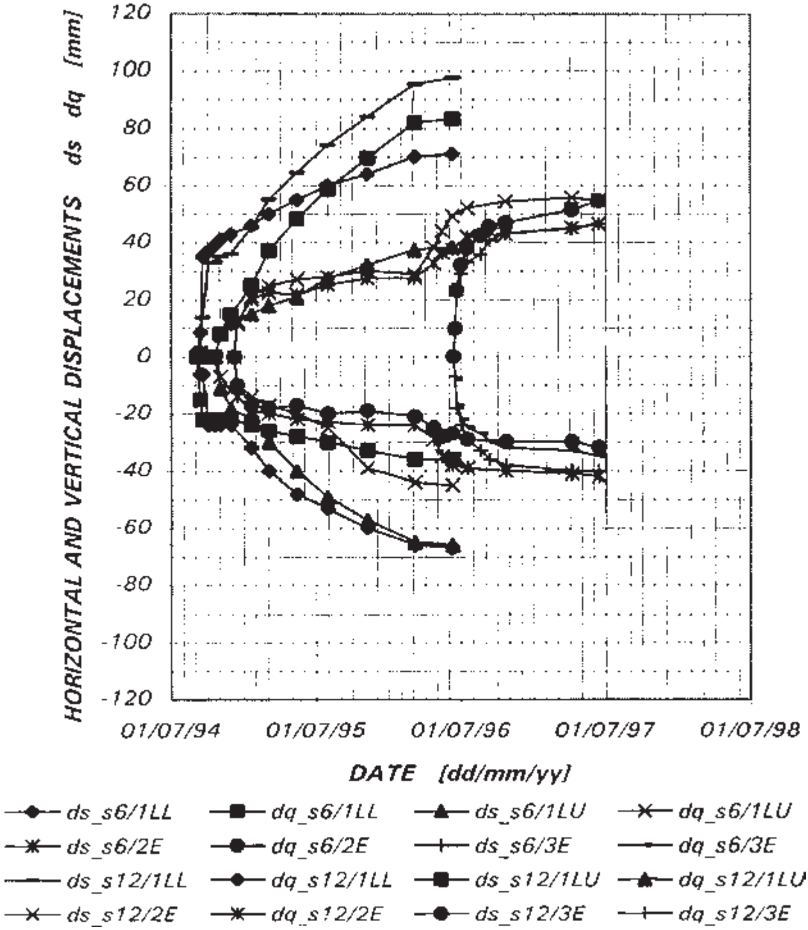

Figure 4 Horizontal and vertical displacements measured on Sections 6 and 12. (See Fig. 3 for key.)

displacement directions dip between 30 and 40° from the horizontal, for all points.

The normalized horizontal displacements, obtained by dividing the displacement by the height of fill above the surveyed point, range between $ds/H = 0.25\%$ to $ds/H = 0.56\%$. As shown in Fig. 6, the values of the normalized displacements are strictly related to the average slope above the point, whose displacements are considered (Sembenelli and Sembenelli, 1998). It is worth noting that normalized horizontal displacements tend toward $ds/H = 0\%$,

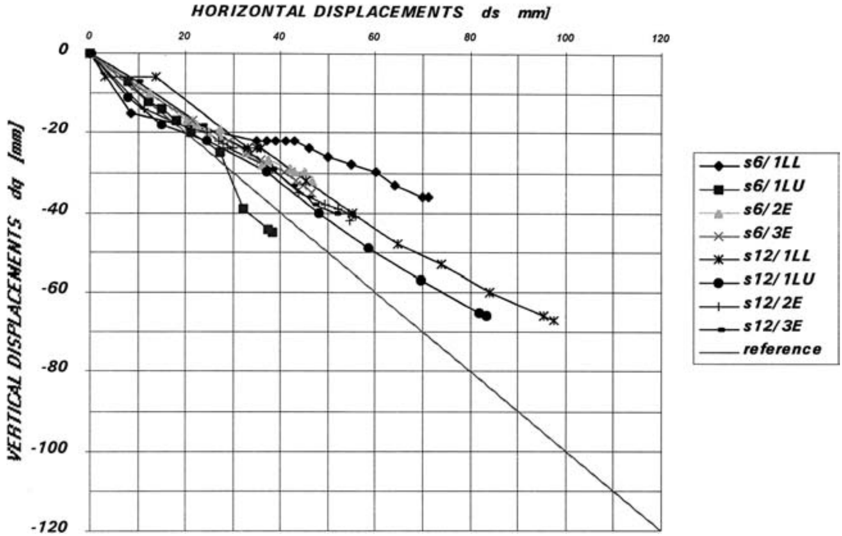

Figure 5 Displacement vectors in a vertical plane measured on Sections 6 and 12. (See Fig. 3 for key.)

when the slope becomes $\beta = 29^\circ$, which roughly equals $45 - \phi/2$ (ϕ = mobilized angle of friction).

7 CREEP AND CONSOLIDATION

From all the evidence, displacements increase during construction and for some time after construction has been completed. This is typical of high structures, for which the effects of the weight of the added fill exceed those of compaction. During this time a flow of strains and stresses moves from the compacted soil to the reinforcements. Because the two components of displacement, vertical and horizontal, are quite similar, no significative volume change are involved in this process, so that it appears to be result of a creeplike deformation. This creep refers to the overall structural behavior of the reinforced soil and is not necessarily linked to the creep of the polymer of reinforcements. The latter would be rather activated by the overall structure deformation, once its displacements and strains exceed a certain yield value. This suggests the need for an advanced prediction of the actual behavior of the structure and of its expected maximum displacement. This may help determine the final strains on the reinforcements and the actual factor of safety.

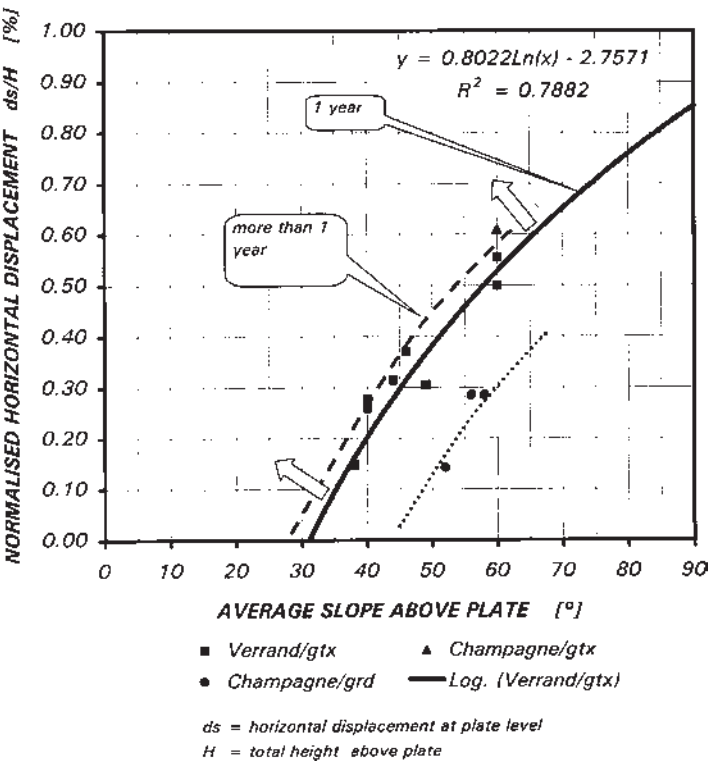

Figure 6 Normalized horizontal displacements versus average slope. (From Sembenelli and Sembenelli, 1998.)

In order to better analyze the data collected at the Verrand Embankment, a plot of the displacement velocity versus time has been drawn, as shown in Fig. 7. A typical curve connecting a series of points is also shown in the diagram. The displacement velocity curve generally lays in the lower part of the cloud of points. The sharp peaks indicate that a new load has been added. It is interesting to note that generally the decay of the curve toward the prepeak values is quite rapid. The prevailing displacement velocity is hence well represented by the lower envelope of the data shown in the figure.

Data obtained from Verrand suggest that the displacement velocity falls from 40 mm/month, during the first month, to about 0.7 mm/month, after 10 months (1 year), and to about 0.01 mm/month, after 100 months (10 years). The above values compare with typical results of rock-fills, for which displacement velocities are 1 to 2 mm/month, after 10 months, and 0.05 to 0.2 mm/month, after 100 months (Parkin, 1991).

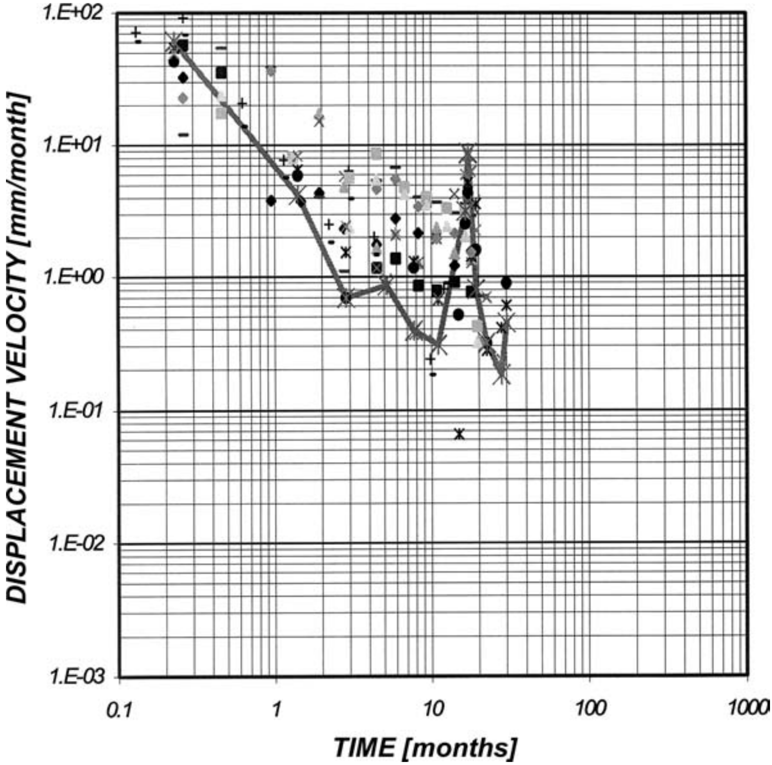

Figure 7 Displacement velocity plot for vertical and horizontal components, measured on Sections 6 and 12.

This suggests that the Verrand HRSS is behaving like a rock-fill embankment and that the transfer of stresses from soil to reinforcement is mainly governed by the fill characteristics. It should be pointed out that the Verrand Embankment envelope is somewhat steeper than the corresponding ones, published for rock-fills in dams. This is likely related to the positive effects of the reinforcements, which reduce the potential for deformation of the mass.

8 OBSERVATIONAL PROCEDURES

From the displacement velocity plot, one can estimate displacements in the order of 15 to 20 mm, in the next 10 years, and below 10 mm, for the following 100 years. This estimate may be affected by the last loading increment, applied just before the last readings. A better estimate would have been possible if the readings could be continued until 1 year after the last load increment, at least.

An attempt was made to use an alternate procedure, developed by Asaoka (1978) for predicting consolidation and creep settlements. Although Asaoka's procedure is generally applied for predictions in clays, the creep behavior observed with the displacement velocity plot suggested that its use can be extended to HRSS of the type of the Verrand Embankment.

The typical plot used in connection with Asaoka's method is displacements at time $t-1$ versus displacements at time t. The typical shape of these curves, upon application of a single loading increment, is a sharp rise followed by a flatter segment, eventually ending against the reference curve $ds(t-1) = ds(t)$.

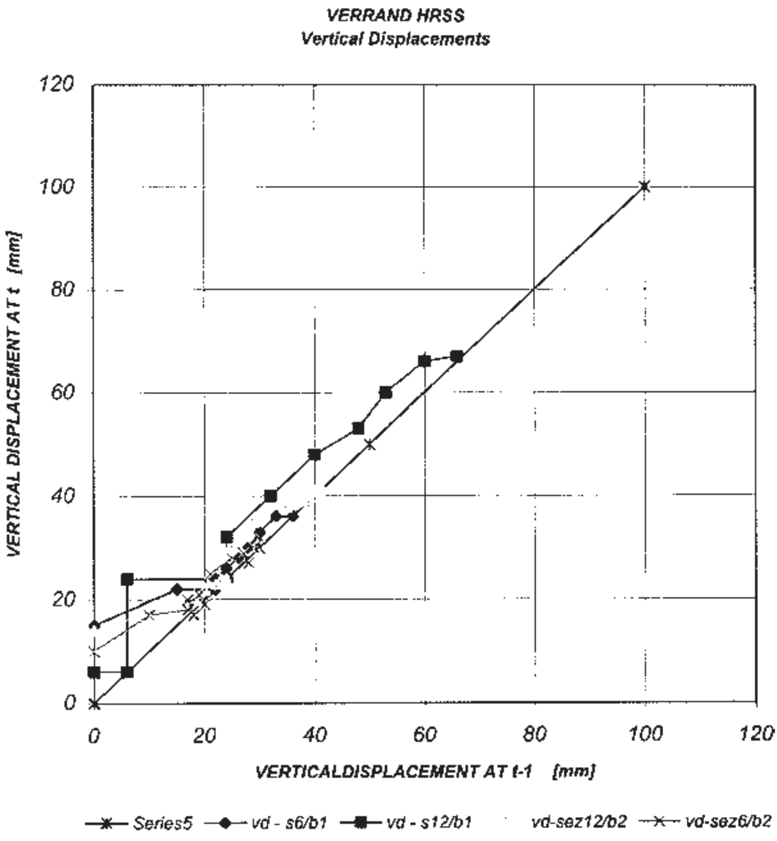

Figure 8 Asaoka's plot for vertical component of displacement, measured on Sections 6 and 12.

The slope of this last segment is related to the coefficient of consolidation governing the process. In case of multiple loading increments, each loading step produces a curve similar to that described above, so that the process as a whole is described by the envelope of all curves.

The $t - 1/t$ displacement curves obtained for the Verrand HRSS are shown in Figs. 8 and 9 for vertical and horizontal displacements, respectively. Both diagrams exhibit the same pattern: A relatively well-defined step, corresponding to the first loading phase, followed by the envelope of small construction increments. All curves turn toward the reference curve soon after the last increment has been applied.

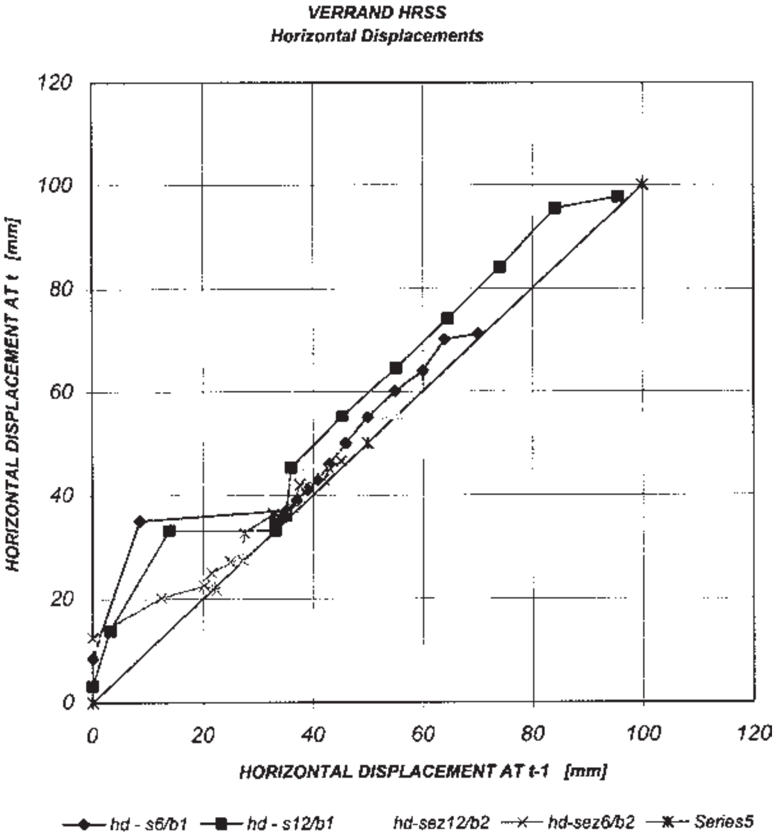

Figure 9 Asaoka's plot for horizontal component of displacement, measured on Sections 6 and 12.

In all cases, the highest displacement gradients occur when filling immediately above the measuring points. Further filling produces additional displacements in a short time, but displacement gradients are, in this case, smaller. It was observed that, whenever some time has delayed from the last previous loading, any additional load produces a sudden reaction of the structure, so that displacements upon loading develop more quickly.

The shape of the displacement curves suggests that the expected displacements in the next 10 and 100 years will be only slightly larger than the present ones. These displacements are actually less than those predictable from the displacement velocity curves.

The discrepancy may be the consequence of the fact that the short-term deformations and creep, both consequences of each loading increment, cannot be separated within the relatively simple operations on the Asaoka's curves. Consideration must also be given to the fact that, after some time, creep displacements between two following readings become smaller than the surveying accuracy. More data are necessary to support this method of interpretating deformation measurements.

9 CONCLUSIONS

Displacement monitoring is a key point in the design of HRSS, on account that the deformation process may take years. The reinforced soil is a material built on site, and its properties can hardly be defined with laboratory testing and analytical tools only. It is important to assess the actual behavior of the structure since early construction phases to make possible a sound prediction of the final displacements.

Displacement velocity plots as well as Asaoka's method are well-established procedures, which appear suitable for describing the behavior of reinforced soil structures, too, especially high structures. A proper theoretical analysis, which could be referred as the pseudo-consolidation of reinforced soils, would require comparing data coming from numerous and different HRSS.

REFERENCES

A Asaoka. Observational procedure of settlement prediction. *Soils and Foundation*, The Japanese Society of Soil Mechanics and Foundation Engineering, 18(4): 87–101, 1978.

D Cazzuffi, E Venesia, M Rinaldi, A Zocca. The mechanical properties of geotextiles: Italian standard and interlaboratory test comparison. *Third Intl. Conference on*

Geotextiles, Geomembranes and Related Products, Vienna, Austria, Vol. 3, 1986, pp 695–700.

BR Christopher, SA Gill, JP Giroud, I Juran, JK Mitchell, J Dunnicliff. Design and construction guidelines for reinforced soil structures. *Report No. FHWA-RD-89-043*, McLean, VA, 1989.

RA Jewell. Strength and deformations in reinforced soil design. *Fourth Intl. Conference on Geotextiles, Geomembranes and Related Products*, The Hague, The Netherlands, Vol. 3, 1990, pp 913–946.

AK Parkin. Creep of rock-fill. In *Advances in Rockfill Structures*. E Maranha das Neves, ed. NATO ASI Series, Series E, Vol. 200, 1991, pp 221–237.

G Sembenelli, P Sembenelli. Experiences with high reinforced soil slopes. *Fifth Intl. Conference on Geotextiles, Geomembranes and Related Products*, Singapore, Vol. 1, 1994, pp 479–482.

G Sembenelli, P Sembenelli. An approach to high reinforced soil structures. In *The Practice of Soil Reinforcing in Europe*. TS Ingold, ed. London: Thomas Telford, 1995, pp 139–152.

G Sembenelli, P Sembenelli. The Verrand high reinforced soil structure. *Sixth Intl. Conference on Geotextiles, Geomembranes and Related Products*, Atlanta, GA, Vol. 2, 1998 pp 619–624.

9

U.K. Case Study: Bluewater Retail and Leisure Destination Reinforced Soil Slopes to Form Steep-Sided New Lakes

J. H. Dixon
Tensar International, Blackburn, U.K.

1 INTRODUCTION

The site is located approximately 30 km east of London and due for completion in early March 1999. Bluewater, developed by Lend Lease, is intended to be the largest and most prestigious retail development in Europe (Fig. 1). It contains 140,000 m^2 of retail space, 13,000 car parking spaces, nearly 12,000 m^2 of leisure space, and has a million trees and shrubs landscaping the area.

The site is located in a former deep chalk quarry. The construction of several lakes was included within an Enabling Works contract, which principally involved bulk filling with approximately three million m^3 of a local silty sand. Two of the lakes, Lakes 1 and 2, were formed with steep sides in order to maximize their water volume and depth for environmental reasons.

Lake sides sloping at 70° to the horizontal and approximately 10 m high were selected. In places these slopes are surcharged by steep highway embankments and landscaping fill under a later contract. The client's consulting engineer, Waterman Partnership, recognized at an early stage the economic and practical advantages of reinforced soil techniques.

Due to significant variations of groundwater level, it was decided to line Lake 1 with a geomembrane in order to retain a constant lake water level. There were concerns about the long-term durability of the geomembrane and in particular its vulnerability to potential damage from burrowing wildlife or boat

Figure 1 Project site.

impact if it were placed on, or close to, the slope surface. It was therefore decided to locate it underneath and up the rear face of the reinforced soil block.

2 DESIGN OF STEEP SLOPES

2.1 Design Brief

The engineer invited Tensar International Ltd. to assist with specialist design support in developing the reinforced soil design beyond the concept stage.

Lake 1, with the geomembrane lining located below the reinforced soil block, presented two unusual reinforced soil design challenges:

1. The potential for sliding of the reinforced soil block over the geomembrane.
2. The combination of the large number of possible water levels (within both the lake and external ground) and various imposed loadings conditions, phased with the subsequent highway and landscaping contracts.

Furthermore, the design brief called for a low-cost durable face with a 120-year life and high security against washout of the fill.

2.1.1 Design Parameters

The fill, which was to be sourced from an adjacent quarry, was a silty fine sand (Thanet Sand). Its design parameters were

$$\phi'_{cv} = 31°, \quad c' = 0, \quad \gamma_{opt} = 19.3\,\mathrm{kN/m^3}, \quad \text{and} \quad \gamma_{sat} = 20.2\,\mathrm{kN/m^3}$$

A series of 30-cm × 30-cm laboratory shear box tests was commissioned to measure the frictional shearing resistance between the various specified geosynthetic materials and this fill.

The selected lining system was 1-mm-thick modified low-density polyethylene (LDPE) geomembrane protected by a 700-g/m^2 polypropylene needle-punched geotextile. The critical interface shearing angle (ϕ_{ls}) for this combination was found to be 20°, for the range of design normal pressures tested.

Two strengths of high-density polyethylene (HDPE) geogrid reinforcement were selected: Tensar 40RE (type 1) and Tensar 80RE (type 2). These are manufactured from extruded sheets and orientated (stretched) in the machine direction. Their Index QC strength measured in accordance with International Organisation for Standardisation, 1993 in the longitudinal direction is 40 kN/m and 80 kN/m, respectively, and rib thicknesses (t_r) 0.7 mm and 1.3 mm and (t_b) 1.9 mm and 3.6 mm, respectively (Fig. 2). Shear tests on these two grid types with the chosen fill material indicated friction angles in excess of 26°. This gives a coefficient of soil interaction:

$$\mu = \frac{\tan 26°}{\tan 31°} > 0.8$$

This is typical for this combination of geogrid and fill type.

2.2 Global Stability

The shear box testing confirmed that the critical potential external failure mechanism for Lake 1 was sliding over the geomembrane lining system. It was

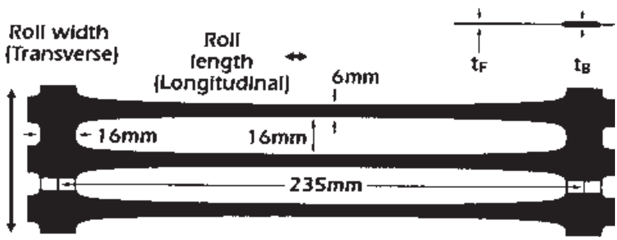

Figure 2 Geometry of the grid reinforcement.

therefore decided to incline the lining at an angle α of approximately 5° below the reinforced soil block. (This equated to a fall of 1.5 m from toe to heel over the width of the block.)

The bottom reinforcement layer remained horizontal and was positioned a minimum distance of 10 cm above the lining system at the face. This ensured that the critical design interface frictional value would not reduce.

The factor of safety against sliding over the inclined geomembrane was calculated by resolving forces about the geomembrane (Fig. 3).

Note: The net mobilizing force (P) is assumed to act on an angle to the rear of the reinforced soil wall $= \square \times \phi'_{ls}$. W = weight of the reinforced soil block, and F and N are the frictional and normal forces acting on the inclined geomembrane.

By resolving forces perpendicular to the geomembrane:

$$W \cos I + : \sin(10^\circ + I) = N \tag{1}$$

By resolving forces parallel with the geomembrane:

$$F = N \tan 20^\circ \tag{2}$$

$$\text{FoS} = \frac{F + W \sin\alpha}{P \cos(10^\circ + \alpha)} \tag{3}$$

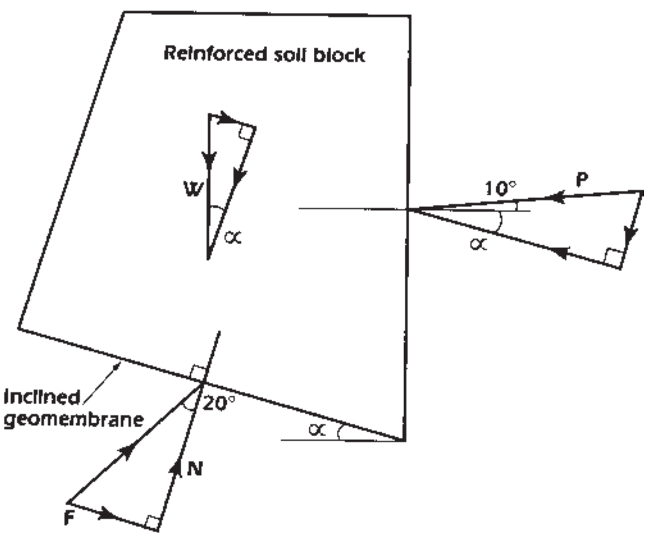

Figure 3 Force resolution on reinforced soil block.

$$\text{FoS} = \frac{[W\cos\alpha + P\sin(10^\circ + \alpha)]\tan 20^\circ + W\sin\alpha}{P\cos(10^\circ + \alpha)} \tag{4}$$

where FoS = factor of safety against sliding over the lining system (i.e., the resisting force divided by the sliding force). FoS for design was specified as 1.5 for the temporary condition and 2.0 for the completed works.

Checks were made for difficult lake conditions: Immediately after construction, after surcharging with the highway embankment, and at final handover. All possible combinations of external and lake water levels were considered. Figure 4 shows the cross section through the north side of Lake 1 and the particular loading condition found to be critical for sliding stability, that is, the condition prior to the placement of landscaping fill and with the lake water level lower than its final design level.

The width of the reinforced soil block is dimensioned to provide sufficient weight (W) to satisfy FoS.

Lakes 1 and 2 were also checked for other external stability conditions, including sliding over the reinforcement.

2.3 Internal Stability of Reinforced Soil Block

The specialist designer's experience of other reinforced soil structures with a similar geometry was that design principles based on the German Institut für Bautechnik (DIBt) would produce a stable and economical solution. Internal

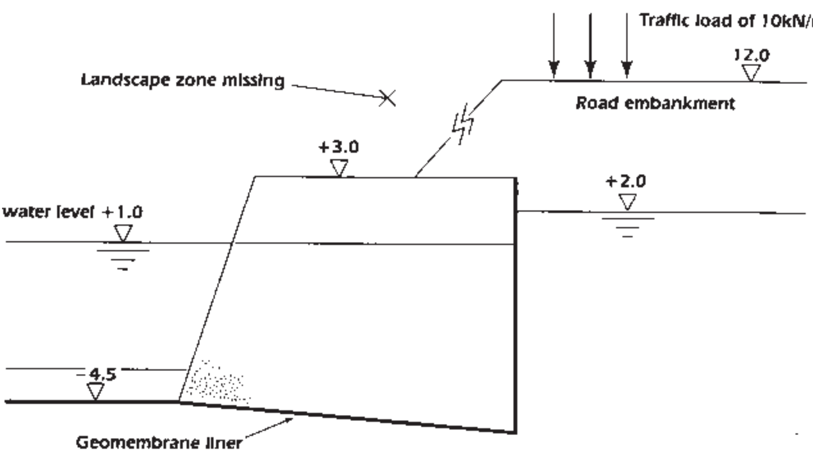

Figure 4 Cross section through north side of Lake 1.

stability calculations take the form of a two-part wedge analysis through the reinforced soil block. A series of two-part wedges is examined with the lower part of the wedge originating at the structure face and passing through the block, and the upper part of the wedge passing up the back face of the reinforced soil block. The active pressure, above that point where the lower part of the wedge cuts the back face of the reinforced soil block, is added to the disturbing forces acting on the two-part wedge to give the total disturbing force. In the case of internal stability, the resultant active force is taken to act on angle equal to the friction angle of the soil block rear face.

Reinforcement must be provided to resist the disturbing force on each two-part wedge by intercepting the wedge being considered. The two-part wedge stability calculation should be carried out from the toe of the structure, the bottom grid layer, at all levels where the grid spacing alters, and at every level where the grid type alters.

The reinforcement design strength is obtained from the creep-limited strength appropriate to the design life and in-soil temperature. Specific partial factors are then applied to take account of such factors as installation damage. Finally, an overall FoS $= 1.75$ is applied to the strength.

The reinforcement layout was derived by analysis with lower part wedge angles (θ) set at 3° intervals (Fig. 5) using the specialist designer's computer program, Winwall (Tensar International, 1995).

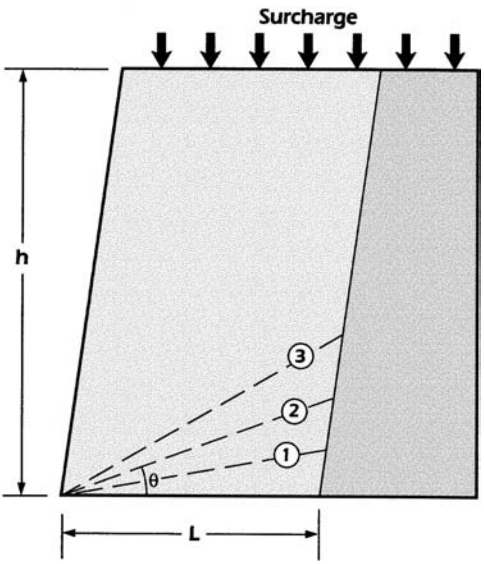

Figure 5 Two-part wedge analysis.

For Lake 1, the critical condition for internal stability was identified as the completed structure fully landscaped under the rapid draw-down condition with the lake empty (perhaps during a future maintenance operation) and the backfill behind the reinforced soil block fully saturated. A typical reinforcement layout for the north side of Lake 1 is shown in Fig. 6. The maximum vertical reinforcement spacing was set at 60 cm.

The road embankment, which is not featured in this paper, formed part of a later contract and was also constructed using Tensar uniaxial HDPE reinforcement and a 60° face, formed by wrapping grids around permanent filled bag formers, which were subsequently planted.

2.4 Face Detail

The face of the reinforced slopes had to be relatively inexpensive while possessing high durability and damage resistance. The engineer ruled out a proprietary segmental concrete block face on the grounds of cost, and instead selected a geogrid wraparound face. With this detail, the horizontal reinforcement layers are extended up the temporarily supported face of the fill and then returned back horizontally and connected with a full-strength joint to the next layer of reinforcement. There was sufficient information on the durability of the specified grids to satisfy long-term serviceability questions (Wrigley, 1987).

The face also had to remain permeable and retain the silty sand fill. Attention was therefore focused on the selection of a geotextile filter to line the wraparound face. It was recognized that any damage or malfunction of this geotextile could lead to a steady washout of fines and ultimately to collapse.

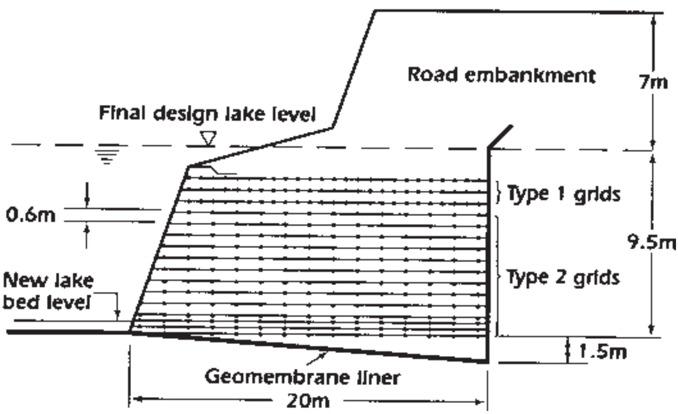

Figure 6 Typical reinforcement layout.

Netlon 813 geotextile (formerly named Netlon 1004R), manufactured by Naue Fasertechnik GmbH, was specified. It has independent certification from the German Federal Waterways Authority (BAW) based on rigorous performance testing with a range of soils including silty sand. These tests assess

Filter performance by filtering a real soil in turbulent conditions and also examining the resultant permeability after impregnation with soil particles
Residual tensile strength following exposure to abrasion (16×5000 revolutions of a rotating drum containing gravel and water)
Puncture resistance in a test replicating rock armor units being dropped on a soil-supported sample

This nonwoven geotextile is manufactured by needle-punching two separate geotextiles, one containing staple (short) fibers of polypropylene and the other, a polyester, to create an integrated 800-g/m^2 duplex material. This efficient double-layer arrangement provides a coarse fiber prefilter that, additionally, interacts with the soil to achieve a degree of mechanical stabilization of soil particles that may otherwise be prone to migration.

Despite this certified evidence of the geotextile's robustness and field experience with similar products under extremely severe test conditions (Dixon and Osborn, 1990), the engineer was concerned about its vulnerability to damage, for example, from accidental impact, burrowing animals, nesting birds, and long-term exposure to ultraviolet (UV) radiation. Unlike some geogrids, there is little or no information available on the long-term life of geotextiles fully exposed to sunlight.

The engineer, therefore, specified an outer grid wraparound face retaining a 15-cm-wide layer of 5–10-cm-sized hard durable fill as cover protection to a geotextile wraparound local to the face of the silty sand fill (Fig. 7).

With the specified grids it is possible to create a full-strength connection between adjacent lengths using an HDPE bodkin (Fig. 8). In a wraparound detail, this bodkin provides a more positive joint than simply relying on a frictional anchorage. Furthermore, when the higher grid length is tensioned during installation, this helps pull the lower wraparound face tight.

3 CONSTRUCTION

3.1 Contract Award

The Enabling Works contract was let by Bluewater Construction Management Team (BCMT) to O'Rourke Civil Engineering Limited in early 1996 following a competitive tendering process. O'Rourke chose to use the specified geosynthetics. They appointed a specialist subcontractor to supply and install the lining system for Lake 1 and opted to construct the reinforced soil slopes themselves.

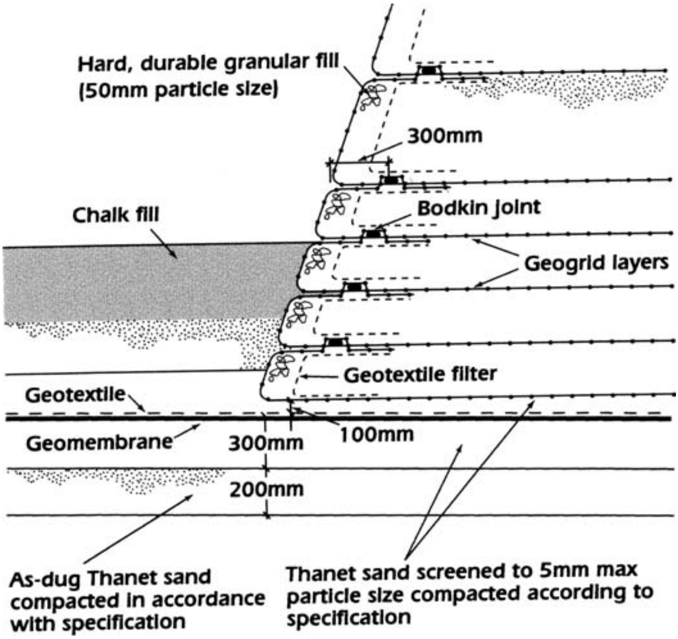

Figure 7 Cross section showing face detail.

3.2 Lake 1: Wraparound Grid Face

Lake 1 is oval in plan with a perimeter slope length of approximately 500 m. Reinforced soil installation began in April 1996. The contractor selected a 2.4-m-high timber formwork system, supported by scaffold tube and fittings,

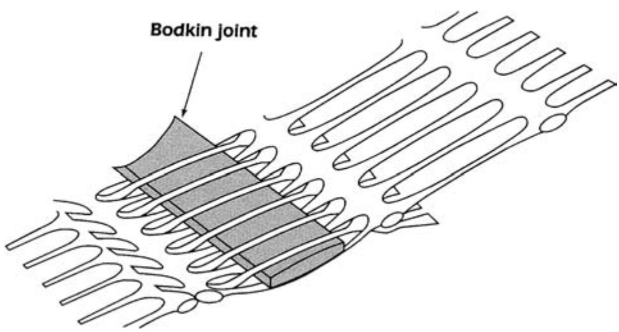

Figure 8 Connection using Bodkin joint.

for temporary support to the grid wraparound face (Fig. 9). A 60-cm-high inner plywood former with lifting holes, tapering in cross section from 20 cm at the top to 15 cm at the bottom, was used to form the inner geotextile wraparound.

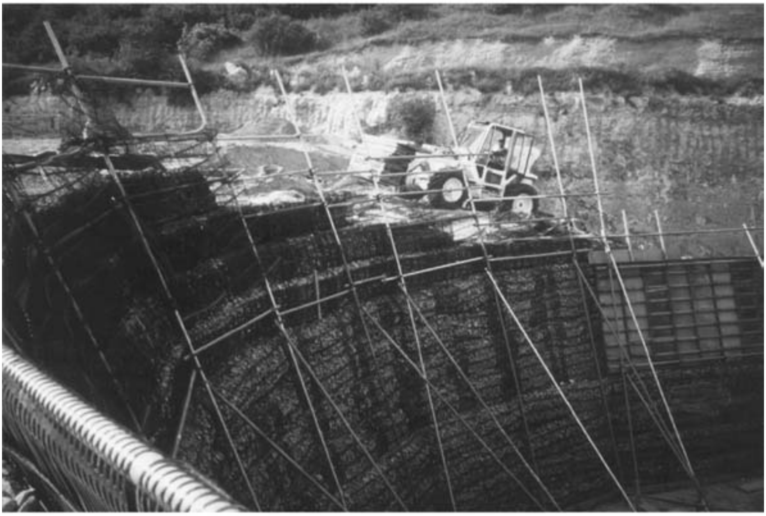

Figure 9 Timber formwork.

The grids were cut to design length on site. Bodkin joints were used to avoid wastage from end of roll off-cuts. These lengths were abutted against the inside face of the shutter and nominally joined by cable ties to avoid any gaps opening during installation. The internal former was then placed against the grid face and the geotextile was wrapped around the internal face of the former. A geotextile overlap of 50 cm was specified. The silty sand fill was placed and compacted in lifts to a depth of 60 cm. This fill was found to have sufficient short-term cohesion that the former could be carefully raised and the resulting void filled, by hand, with coarse material without any slumping of the geotextile face.

The grid wraparound face was next returned over the coarse fill and connected to the next grid layer using a bodkin. The free end of the upper grid was then hand-tensioned using a steel beam.

The face of Lake 1 was slightly reprofiled by local steepening to accommodate 20-cm horizontal ledges at the top of each 2.4-m lift on which the shutter could be seated. The overall slope remained at 70°. (The geomembrane that extended up the rear of the reinforced soil block also required its own temporary shuttering.)

These details resulted in relatively slow outputs of around 40–50 m^2 of completed face area per day using two gangs. In order to improve this, the contractor developed a face detail that replaced the shutter and plywood former with an internal steel mesh former. This was produced by site cutting 5-mm-diameter steel mesh sheets and bending them into "U"-shaped units 60 cm high by 28 cm wide. These units were positioned to act as a permanent face former (Fig. 10) and then filled with the coarse fill. Because the steel mesh aperture was 20 cm by 20 cm, the vertical face of the unit was lined with geogrid Type 1 before filling. The top of the unit was cross braced using steel tiewire.

The geotextile was then wrapped up the rear face of the filled unit and the bulk fill placed behind. The main grid length was then wrapped up the front face of the unit and bodkined and tensioned as normal.

The alternative method proved a little quicker, particularly for the higher levels, although the alignment, while acceptable, was less consistent.

The reinforced soil slopes of the lake are constructed with approximately 60,000 m^2 and 80,000 m^2 of geogrids Types 1 and 2, respectively, supplied in 50-m by 1.3-m rolls. They were constructed in approximately 3 months (Fig. 11).

3.3 Lake 2: Precast Concrete Block Face

The water level of Lake 2 was designed to fluctuate with that of the surrounding chalk aquifer, and so no geomembrane lining was necessary. About half of the slope length of Lake 2 was formed from the existing chalk quarry face.

Reinforced soil construction took place in the winter and spring of 1997. In order to simplify and accelerate installation, the contractor, with assistance from

Figure 10 Face former.

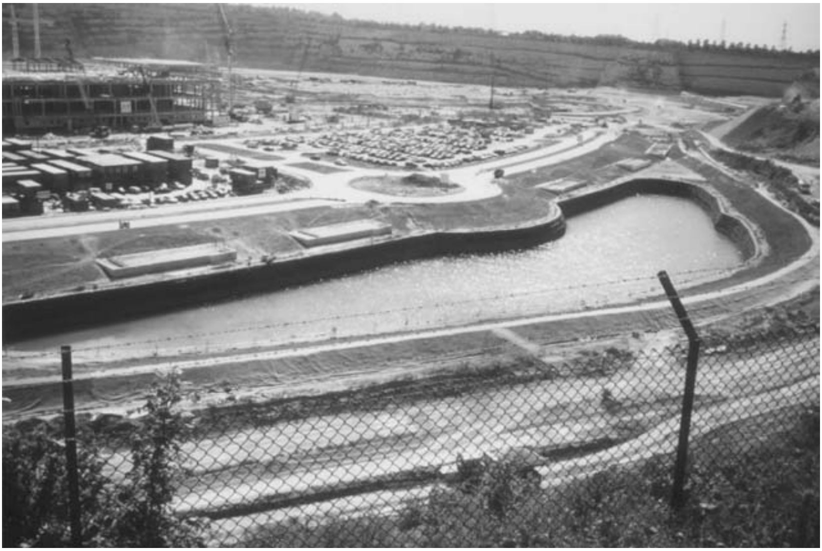

Figure 11 Reinforced soil slope of the lake.

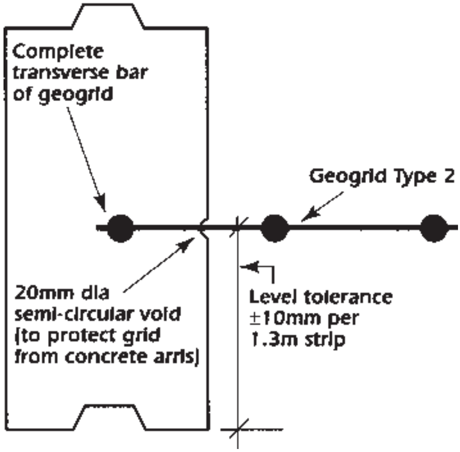

Figure 12 Cross section of typical block.

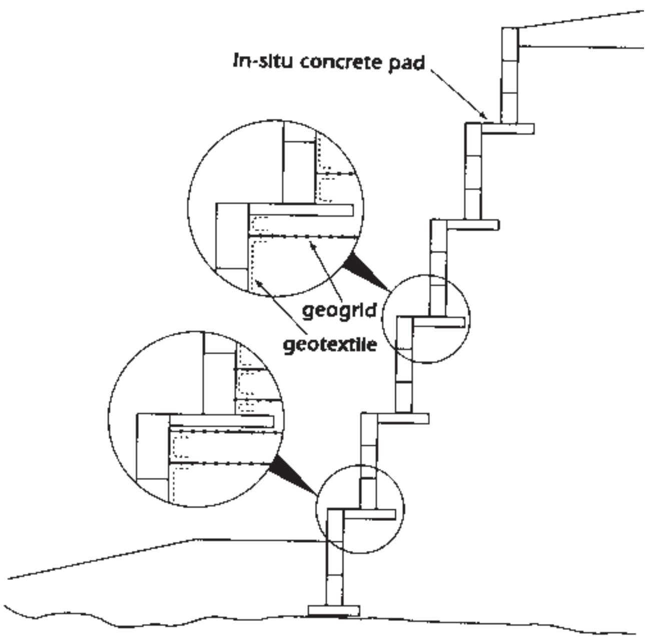

Figure 13 Cross section of stepped vertical face.

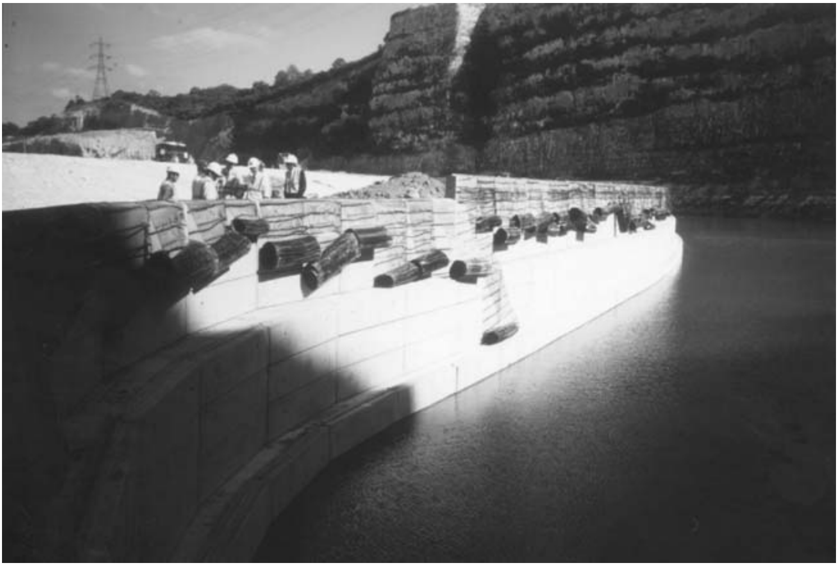

Figure 14 Photo of stepped vertical face.

the grid manufacturer, proposed a radically different face comprising site-cast, ordinary-Portland-cement concrete blocks (with 50-MPa 28-day compressive strength). These blocks were 2.7 m long, 0.6 m high, and 0.3 m wide and contained either one or two layers of "starter" lengths of cast in Type 2 geogrid (Fig. 12). The deeply embedded thick transverse bar of the grid has been shown to provide an anchorage in excess of the design strength of the reinforcement.

HDPE grids have been shown to be unaffected by the highly alkaline environment associated with the concrete embedment (Wrigley, 1987).

This solution was attractive to the contractor, who had already established a batching plant on site and estimated that he could produce blocks at about one third the cost of typical proprietary segmental units.

For simplicity, the blocks were produced with a stepped vertical face, and so the slope profile was amended (Figs. 13 and 14).

These blocks overcame the need for both the shuttering and the coarse fill. The main grid lengths were connected to the starters using bodkins, and the geotextile was used to prevent washout of fines through any small gaps between blocks.

The blocks were cast at a rate of up to 36 per day. Over 1000 blocks, each weighing approximately 1 ton, were required. Installation was much less labor-intensive when compared to Lake 1.

4 CONCLUSION

The Bluewater development is a prestigious, major European project. To the author's knowledge, it includes the first reinforced soil structure designed and constructed over a geomembrane lining. This design solution is rigorous, innovative, and economic.

The three types of facings used for the steeply sloping lakes all exhibited unique features. Each satisfied the design function but required different degrees of installation manpower and time and material costs.

ACKNOWLEDGMENT

The writer is indebted to Lend Lease, BCMT, Waterman Partnership, and O'Rourke Civil Engineering Limited for permission to produce this paper.

REFERENCES

JH Dixon, S Osborn. Field trials to evaluate geotextile puncture resistance. *Proc. 4th Int. Conf. on Geotextiles, Geomembranes and Related Products*. Rotterdam: Balkema, 1990.

International Organisation for Standardisation. *ISO 10319: Geotextiles—Wide Width Tensile Tests*. Geneva: ISO, 1993.

Tensar International. In-house Publication. *Winwall, Version 1.14, In-house Reinforced Wall and Slopes Design Program to Institute für Bautechnik and UK DoT Reinforced Slope Design Method (HA68/94)*, 1995.

NE Wrigley. Durability long-term performance of Tensar polymer grids for soil reinforcement. *Materials Science Technology* 3: 161–172, 1987.

10

State of the Practice: Past, Current, and Future Perspectives of Reinforced Soil Retaining Structures in Turkey

Muhannad Ismeik
Al-Isra University, Amman, Jordan
Erol Guler
Bogazici University, Istanbul, Turkey

1 INTRODUCTION

The concept of reinforced soil was first applied in Turkey with the Web-Soil and reinforced earth technologies. These types of modern technologies were mainly introduced to Turkish engineers with the highway construction, which started as early as the 1970s, but got extensive during the 1980s. The technology—approved by the Turkish Highway Administration and observed by other engineers as being successful and economical—found itself application opportunities on other construction sites. Geosynthetic reinforcements were introduced in the construction of reinforced slopes with the overwrap technique. Both geotextiles and geogrids were used as reinforcing elements for the reinforced slope projects. Most of these applications were used on projects where public visibility was not possible; however, a few exceptions exist. An experimental wall, built in 1993, was the first geosynthetic wall where the backfill consists of lime treated clay. The objective of that wall was to investigate the replacement of granular material with an improved cohesive backfill with emphasis on real measurements and observation of field behavior. The first geosynthetic reinforced segmental retaining wall was constructed during the summer of 1997. It was a project realized for the Highway Administration. It was used to elevate an existing road to pass over a tunnel portal. Generally, this wall was stepping stone for further progress in Turkey with such technology. It is expected that many similar walls will be constructed, with the same fashion, in the near future. A brief summary for every technique used and improvement made in the area is given below under proper headings.

2 WEB-SOIL TECHNOLOGY

The Web-Soil technology uses front panels that are similar in theory to the front panels of the Reinforced Earth technique. On the backside of the panels are special attachments, which allow the connection of band-shaped reinforcement. This band-shaped reinforcement is made of polymer and comes in rolls. So reinforcement is practically woven between the attachments behind the panels and a steel rod located at a certain distance behind the facing. As can be seen from Fig. 1, the depth of the reinforced zone may change according to the design parameters. These types of walls have been extensively used during the construction of the Kinali–Sakarya Highway. The total surface area of the Web-Soil features constructed in this project was approximately 35,000 m^2. The walls were mainly used to support the side wings of approach embankments and as retaining structures. The maximum height to which the Web-Soil wall was constructed was 18 m. However, the majority of the walls were much lower. Ten

Figure 1 Demonstration of the Web-Soil method as used during the construction of the Kinali–Sakarya Highway.

percent of the Web-Soil walls constructed within this project had heights less than 5 m. Fifty percent of the walls were between 5 to 10 m high, constituting the majority. The remaining 40% were higher than 10 m.

3 REINFORCED EARTH WALLS

The reinforced earth technology was used most extensively in Turkey in the late 1980s. A list of the projects is summarized in Table 1. Most of the projects were retaining walls built for the Turkish Highway Administration. However, two municipalities started using this technology. The largest city in Turkey, Istanbul, and the second largest city and the capital of the country, Ankara, have both ordered several reinforced earth walls. The majority of these walls are between 5 to 10 m high. As shown in Fig. 2, the maximum wall height constructed is 23 m and consists of two levels with a small berm in between. Another wall, 18 m high, is seen in Fig. 3. Again, the majority of the walls are constructed as retaining structures or side wings of approach embankments. Where they are used to support side wings of embankments, usually the bridge itself sits on a reinforced concrete structure. However, more recently for some of the cases the reinforced wall was also used as the bridge abutment, as shown in Fig. 4.

Figure 2 A two-step 23-m-height reinforced earth wall (Izmir–Cesme Highway).

Table 1 A List of Reinforced Walls in Turkey

Project	Contractor	Construction year	Surface area (m^2)	Height (m)	Description of the project
Havza Bridge	Bal Is	1990	3253	8	Eight bridge side wings for highway and railroad passes
Gumusova Highway	Bayindir/Astaldi	1990	900	8	Twenty-eight side wing walls
Izmir Cesme Highway	Bayindir	1993	26,000	23	Ten retaining structures and 6 side wing walls
Tarsus Adana Gaziantep Highway	Tekfen	1996	43,000	23	Retaining structures and side wing walls
Pozant Tarsus Highway	Dogus	1993	1680	9	Retaining walls
Ankara Sogutozu Asot Overpass	Metis	1993	3415	13	Retaining walls
Ankara Kazim Karabekir Overpass	Metis	1993	4140	8	Retaining structures and side wing walls
Mamak Cankaya Avenue	Ceylan	1995	43,500	18	Many retaining walls
Bursa Karacabey Avenue	Treko	1995	900	9	Bridge abutments and side wing walls
Istanbul Okmeydani Overpass	Polat	1996	2800	8	Eight bridge abutments and retaining structures
Istanbul Kasimpasa Iplikci Overpass	Kiska	1996	2500	7	Bridge abutment and retaining structures
Istanbul Safakoy Bridge Overpass	Gungen	1996	1611	7	Bridge abutment and retaining structures

Istanbul Pendik Kurtkoy Avenue	Yapisal	1996	2222	14	Retaining walls
Istanbul Cubuklu Overpass	Kurular	1996	1000	8	Retaining walls and bridge abutments
Toprakkale Iskenderun Highway	Nurol	1997	40,000	23	Retaining walls
		Total	180,000		

Figure 3 An 18-m-high reinforced earth wall (Ankara–Mamak–Cankaya Highway).

Figure 4 A reinforced earth wall used as a bridge abutment (Cubuklu Overpass).

4 WRAPPED FACED GEOSYNTHETIC REINFORCED FEATURES

Several features where the facing was established by overwrapping the geotextile reinforcement were constructed. Many of these features had facing inclinations smaller than 70° and consequently are reinforced slopes. All of them were constructed for private owners. The most widely used application for these geosynthetic-reinforced slopes is rehabilitation of landslides or provision of flat areas for structures constructed on potential landslide areas. These applications include mostly housing projects and creation of large storage areas.

5 AN EXPERIMENTAL WALL

In 1992, a three-year research project was developed to construct a full-scale geotextile reinforced retaining wall in Istanbul. This wall project was funded by the U.S. National Science Foundation, the Scientific and Technical Research Council of Turkey, and the Bogazici University Research Fund. The project was unique in its focus on field measurements and was the first known reinforced wall where the backfill consists of lime treated clay. The wall had a trapezoidal face section with upper and lower bases of 8.8 m and 18.2 m, respectively. The wall consisted of 6 layers with a total height of 5.25 m. The upper three reinforcement layers were 3.85 m long, while the lower ones were 2.1 m. Natural clay available at the site was mixed with 4% lime. The selection of this percentage was based on laboratory tests, which indicated that 4% was the optimum mix percentage in terms of strength and permeability characteristics.

The geosynthetic used as reinforcement was a nonwoven, needle-punched, geotextile with a strip tensile strength of 5.9 kN/m and an equivalent opening size of 0.13 mm. No safety factor was applied to this strength. The Federal Highway Administration method (Christopher et al., 1990) was followed for the design of the wall. The wall was designed to fail by rupture under its own weight with a safety factor of slightly less than 1. Throughout the project life, six Glötzl pressure cells were used to measure the vertical pressure within the wall, and five Glötzl pressure cells were used to measure the horizontal stresses. Deformations were measured with a new developed technique, utilizing electronic coils.

An incremental surcharge load of 41 kPa was exerted at the top surface of the wall, which did not bring the wall to failure. Based on the idea that saturation of clay could result in both a significant loss of frictional strength and cohesion, an attempt was made to bring the wall to failure by wetting it. Two large holes were dug into the top surface of the wall and continuously filled with water. During the filling process, the water leaked through the first layer of geotextile material and drained horizontally away from the wall. It was clear that the geosynthetic layer worked as a lateral drain. Therefore, no pore water pressure was developed and reduction in the shear strength was not achieved since no saturation occurred at lower layers. Attempts at bringing the wall to failure ended at this point, and the project was terminated.

The excellent performance of the wall when overloaded showed that the use of lime treated clay in this case study allowed the efficient construction of the wall. This will substantially reduce the cost of similar projects due to the possibility of using available on-site soils instead of having granular material transported to the site. Increased permeability and good structural performance were also observed. Both the instrumentation data, obtained from all sensors, and observations of the actual wall performance indicated that the wall performed its intended function with negligible settlement. This case study proved to be cost-effective and illustrated the importance of drainage.

6 BLOCK FACED GEOSYNTHETIC REINFORCED WALL

The first segmental retaining wall in Turkey, where concrete blocks are used as the facing and the reinforcement is a geotextile, was constructed during the summer of 1997. This wall was constructed under the design and supervision of the second author. Mr. Robert Barrett from the United States was the consultant during design and construction. The project was constructed as part of the Altunizade-Umraniye Highway construction. The highway had interrupted Nurbaba Street, and it had to be elevated to pass over the tunnel portal.

The facing elements were simple building blocks and as the backfill a greywacke was used, as shown in Fig. 5. The reinforcement was a woven geotextile with a tensile strength of 20 kN/m. Though it was the first wall of its kind in Turkey, it included tremendous amounts of complexities. These can be summarized as follows:

1. The exiting road had a mixed cross section, and the retaining structures supporting the fill had deteriorated severely. Therefore, they had to be removed from the side. Due to this fact and the fact that the original ground is sloped, the two sides of the road had to be formed on two different elevations, as shown in Fig. 6.

2. The foundation of the soil was a heavily weathered rock. Its consistency was similar to that of overconsolidated clay. The foundations of the two walls, each on one side of the road, had to be constructed on different elevations. This fact brought up the concern that there can be a stability problem on the slope that is created between the two foundation levels. Special concern and analysis were devoted to the foundation of the wall constructed on the crest of the slope created by excavation.

Figure 5 Placement of the blocks prior to laying of geotextile.

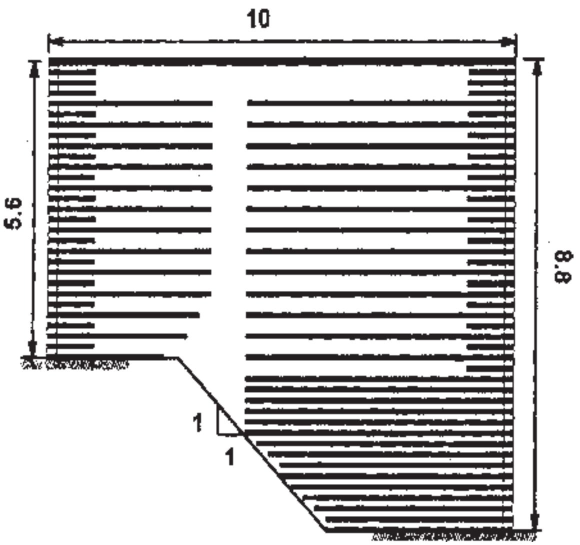

Figure 6 Geometry of the block faced geosynthetic-reinforced wall.

3. Provisions were needed for the utility lines. Four utilities had to pass from underneath the road, namely water, telephone, natural gas, and high voltage electrical power. Because these lines could not be placed side by side, it was not possible to locate the utilities at the center of the road. When the utilities were distributed over the road surface, the reinforcement at the top layers had to be kept short. This problem was solved by considering the top portion as a separate short wall itself, and its effect on the lower layers was considered as a surcharge load.

4. Ladders are needed to provide access to the houses, and they were constructed as part of the reinforced soil wall as illustrated in Fig. 7.

5. At one point the road jumps up onto the tunnel portal. At this point the height of the wall suddenly reduces from 9 m to 1 m, as shown in Fig. 8, and the foundation becomes a rigid structure. To prevent future problems, a joint was provided at this point.

The cost of the whole wall was \$172,000, where the reinforced concrete alternative would have cost \$263,000. So a savings of 35% was achieved.

7 SUMMARY

In Turkey, enough confidence was gained with the concept of reinforced soil technology. Many walls have been successfully constructed without any reported failures. Savings in construction time and cost have been demonstrated when

Figure 7 The ladder provided for pedestrians' access.

Figure 8 Variation of the foundation level toward the tunnel.

compared to reinforced concrete retaining walls. The recently constructed geosynthetic reinforced structure with modular block facing has gone even one step forward and has become very popular. The engineering community of Turkey has admired the easy construction technique, the tremendous cost savings, and the aesthetic advantage of the geosynthetic reinforced modular block faced wall. It is anticipated that similar projects on a wider scale will be constructed in the near future for commercial and governmental projects. The future of the reinforced soil retaining structures in Turkey seems to be promising great success.

ACKNOWLEDGMENT

The assistance of the Turkish Highway Administration and Mr. Inan Unal in providing the required information and photographs is greatly appreciated.

REFERENCE

BR Christopher, SA Gill, JP Giroud, I Juran, JK Mitchell, F Schlosser, J Dunnicliff. Reinforced soil structures, design and construction guidelines, Vols. I & II. Federal Highway Administration, Report No. FHWA-RD-89-043, Washington, DC, 1990.

11

Recent Experiences of Reinforced Soil Retaining Structures in China

Li Guangxin and Wang Zhao
Tsinghua University, Beijing, China

ABSTRACT

The application of a retaining structure reinforced by synthetics has been wildly developed in China. The retaining walls and steeped slopes have been used in many projects, such as the sidewall of a sluice and a highway and the abutment and pier of a bridge. These main cases and related studies on model tests and methods of design and construction are presented in this chapter.

1 INTRODUCTION

The geosynthetics reinforced soil (GRS) retaining structures are composed of reinforced soil and facing structure. Woven geotextile and strip are usually used as reinforcements. A separation technique is in common use in China. The technique is wrapping the geotextile around the face of the wall in the reinforced soil which is connected by strips with facing plate. Between the reinforced soil and facing plate, coarse sand is used as filling material. The facing plate is of a different type, such as modular blocks, full-height concrete plate, concrete blocks, bricks, and shotcrete facing. In most cases, in the retaining walls on-site soil is used as backfill; it even is cohesive or expansive soil. Comparing different gravity walls, the cost of the reinforced wall can be reduced (20–60%).

In the past 10 years, the application of GRS retaining walls in China has developed to include the following:

1. A retaining wall with a height of 35.5 m
2. Reinforced bank with two opposite walls
3. Reinforced soil pier and abutment of bridge
4. Bearing the horizontal pressure on a box foundation

Some related research of tests and design methods includes:

1. Influence of modulus of reinforcement and measurement of earth pressure
2. Properties of fiber-reinforced cohesive soils (FRCS) and centrifugal model tests of FRCS in steep slopes
3. Prevention of frost heave of GRS retaining wall
4. Pullout of geotextile in various directions and stability analysis

The above topics are the focuses of this chapter.

2 EXPERIMENTAL STUDIES

2.1 Stability Analysis of Reinforced Soil Structure in Consideration of Direction of Geotextile

By using the test device shown in Fig. 1, one can conduct a series of pullout tests on geotextile in various directions. In the device, a metal sliding plate can slide along two rails and change its direction, and a top plate with an air bag can apply

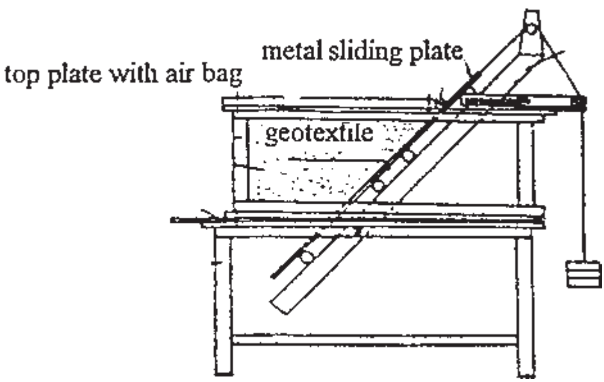

Figure 1 The device of pullout test in various directions.

different normal stresses on the soil. One end of geotextile buried in soil is fixed in the middle of the sliding plate and is pulled out in different directions in tests.

From a series of pullout tests under different normal stresses and different pullout directions, the load-displacement relationship can be expressed as

$$p = \frac{\delta}{a + b\delta} \tag{1}$$

where parameters a and b are functions of the angle between sliding plate and initial orientation of geotextile β, and normal stress σ.

In the stability analysis of the reinforced soil structure, different slip surfaces are chosen, and then their safety factors are calculated by Bishop's method and considering Eq. (1). The slip surface with a minimum safety factor should be the most probable one.

A laboratory model reinforced retaining wall test was performed in a test box with acrylic sidewalls. Vertical load was applied through a rectangular metal strip. Figure 2 shows the shape of the wall in different stages in the test. The safety factor calculated with the proposed method is 1.02, while the one calculated with Rankine's theory is 0.61. Obviously, the former is more reasonable (Wei Yifeng and Li Guangxin, 1996).

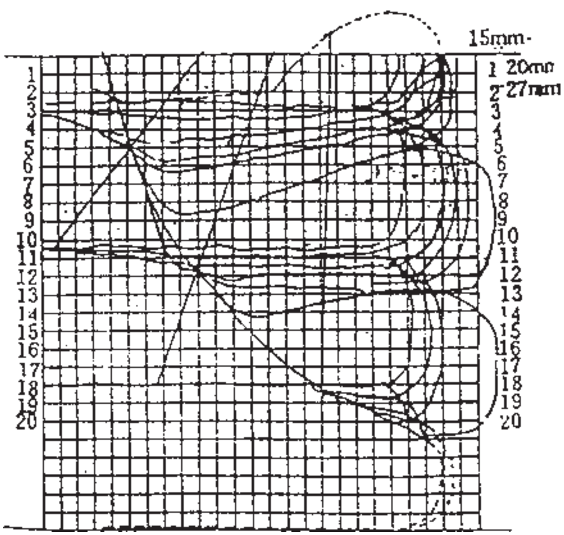

Figure 2 Deformation of geotextile in different test stages.

2.2 Influence of Modulus of Reinforcing Materials on the Stability of a Reinforced Retaining Wall

A model of a reinforced retaining wall is shown in Fig. 3. It consists of a test box with dimensions $940 \times 390 \times 490$ mm, reinforcing materials and backfill, and a steel front facing that can rotate around a hinge connected with a rigid base. The backfill used was gap-graded sand with internal friction angle $\phi = 32°$. The pressure cells and the displacement transducers were employed to measure the load applied on the top of the backfill by jack and horizontal displacement of the top of the front facing, respectively.

Three series of tests are performed in which the model walls with one layer, two layers, and without any reinforcement were used. In these tests of reinforced retaining walls, the three kinds of reinforcing material used were gauze, flexible plastic synthetic, and strengthened window net, which were noted as material A, B, and C, respectively. For material C, the tensile strength is 33 N/mm, the modulus is 5.7 N/mm; for material B, the tensile strength and modulus are 10 N/mm and 0.4 N/mm, respectively; for material A, they are 12.4 N/mm and 2.6 N/mm. The test results with one layer of reinforcement are shown in Figs. 4 and 5. Some conclusions can be drawn from the test results. The deformation and the failure mode of the reinforced retaining wall are significantly affected by the stiffness of the reinforcing material. The retaining wall reinforced by the stiffest material, C, was ruptured brittly. The failure surface consisted of two planes, with the upper one being nearly vertical, and the distance between the failure surface and the front facing tending to $0.3H$, where H was the height of wall. The failure surface of the retaining wall without any reinforcement was almost in conformity

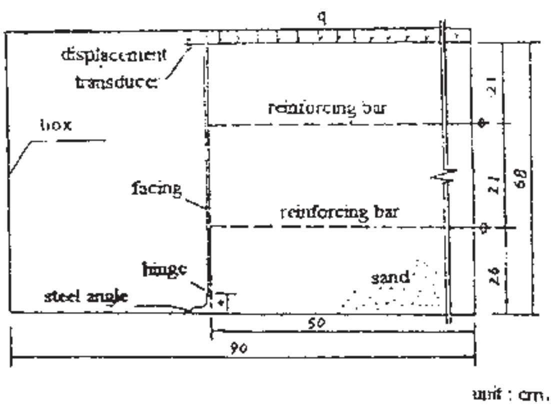

Figure 3 Schematic view of the model test.

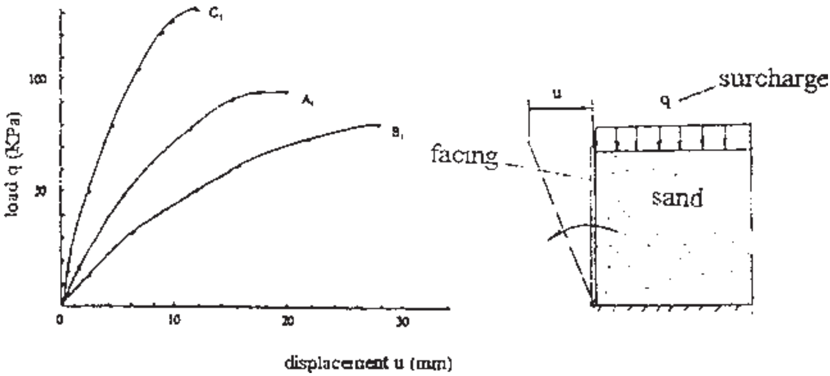

Figure 4 Horizontal displacements of top of front facing when one reinforcement layer was used.

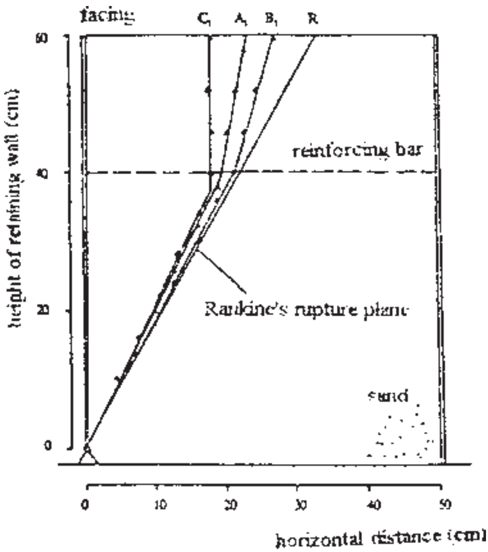

Figure 5 Failure surface of reinforced sand retained wall.

with Rankine's failure surface, namely,

$$\theta_{cr} = 45^\circ + \phi/2 \tag{2}$$

In the cases of reinforcing materials B and A, the failure surfaces, like in that of material C, consist of two planes as well. However, the upper plane is not vertical. The stiffer the reinforcing material is, the more θ_2 tends to 90°.

Based on these test results, a reasonable design method is suggested as follows:

1. For the reinforced retaining wall with far low modulus of reinforcing material, it may be designed using Rankine's theory.
2. For the reinforced retaining wall with a stiff element, it may be assumed that the failure surface consists of two planes. The lower plane is in conformity with Rankine's rupture plane in which $\theta_1 = \theta_{cr} = 45^\circ + \phi/2$, and the upper one is a vertical plane in which the distance from the failure surface to the front facing is $0.3H$.
3. For the reinforced retaining wall with moderate modulus, the lower plane of failure surface is the same as in 2 above, and the inclination angle of upper plane is $(45^\circ + \phi/2) \leq \theta_2?90^\circ$. Here H_1 is the height of the turning point on the failure surface. Then the force equilibrium for upper and lower parts of reinforced earth blocks can be used for calculations, and θ_2, H_1, and the maximum extension of reinforcing element $T_{\max}$ could be obtained by iteration (Lin Yuanzhi and Wang Zhenghong, 1996).

2.3 Tests of Fiber-Reinforced Cohesive Soil

In the 1970s Texsol was researched in France, and then it was used in reinforced steep slopes, retaining walls, and embankments. The three-dimensional randomly distributed continuous fiber-reinforced sand has some advantages in construction, economy, and geotechnical and environmental prosperity. On the other hand, in the practical engineering located in the places short of sand and in some hydraulic engineering, the fiber-reinforced cohesive soil probably will be a kind of useful and economical new material.

A series of tests on fiber-reinforced cohesive soil has been done including drained and undrained triaxial tests, uniaxial extension test, fracture toughness test, thick-wall cylinder test, and hydraulic fracturing test. These tests have indicated that the fiber reinforcement significantly improves geotechnical properties of cohesive soil and increases the plasticity and toughness of soil. The following conclusions can be drawn:

1. Fiber-reinforced cohesive soil has a higher shear strength than an unreinforced one by increasing the cohesion *c*, without significant change of angle of internal friction.
2. Its tensile strength and limit tensile strain increase, and reinforcement changes the failure pattern of cohesive soil extended.
3. Reinforcement increases the fracture toughness of cohesive soil and extends the yield zone of crack tip in a cracked specimen.
4. The hydraulic fracturing test result on the hollow cylinder specimen shows that fiber reinforcement cannot increase the fracturing pressure of cohesive soil, but can make the soil obtain self-seaming ability.

In Fig. 6, the failure patterns of unreinforced and reinforced cohesive soil steep slopes are the results of a model test conducted in centrifuge in Tsinghua University. It is found that fiber reinforcing not only enhances the stability of steep slope, but also changes its failure pattern. For example, in the case of an unreinforced clay slope with dry density 0.00155 g/mm^3, the centrifugal acceleration at failure is 45 g (correspond to 15.7 m high). In the reinforced one with the same dry density, it is 100 g (35 m high). The unreinforced clay steep slope fails abruptly without any noticeable sign before collapse, while the reinforced one fails gradually, which can still bear more loads even after cracks appear. It is also found that there is a family of failure surfaces, rather than only one, in the fiber-reinforced clay slope when failure develops. This phenomenon results from the redistribution of stresses through fiber reinforcing in the slope (Zheng Jiqin et al., 1996; Jie Yuxin, 1998).

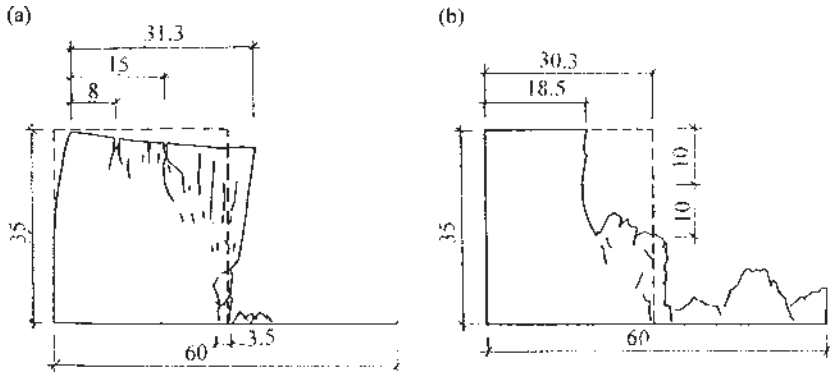

Figure 6 Failure patterns of model steep slopes: (a) reinforced; (b) unreinforced.

2.4 Full-Scale Test Study on Frost Heave of Retaining Wall Reinforced with Geotextile

In the irrigation Area Inner Mongolia Autonomous Region, China, a full-scale test on frost heave of a 2-m-high retaining wall reinforced with geotextile was conducted. In this area, the irrigation system is relatively developed and the irrigation canal forms a dense network. The groundwater table is high in autumn and decreases slowly in winter, with nearly the same rate as that of frost depth penetration. The small and relatively invariant distance between frost penetration and the groundwater table leads to the serious frost damage in hydraulic retaining walls.

The full-scale test wall reinforced with geotextile was southbank of the irrigation canal. The facing panel was made up of reinforced light precast concrete slabs. The retaining wall with a height of 2 m consisted of five geotextile reinforcement layers, each approximately 0.4 m in height. The facing panel was made up of reinforced light precast concrete slabs. The horizontal displacement of the facing panel, the strain of geotextile, and the soil temperature and moisture content were measured during the winter of 1993–1994. Figure 7 shows the schematic diagram of the wall and the measured points on the geotextile.

The test results indicated that the displacement of the facing panel is comprised of the horizontal frost heave of frozen soil and the compressive deformation of unfrozen soil in backfill. It can be observed from Fig. 8 that in the 0–300-mm range from the facing panel, horizontal frost heave occurred; in the 300–900-mm range from the facing panel, the soil was compressed before freezing and then was heaved after freezing; outside that zone the soil was always compressed. Therefore, the horizontal frost heave of backfill was 15–30 mm, while the horizontal displacement of the facing panel measured only 6 mm,

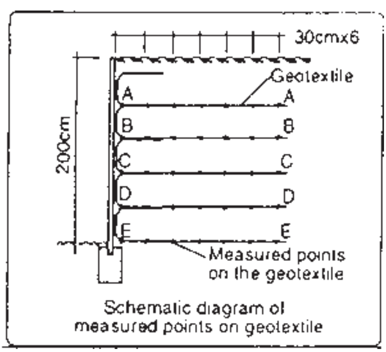

Figure 7 Cross section.

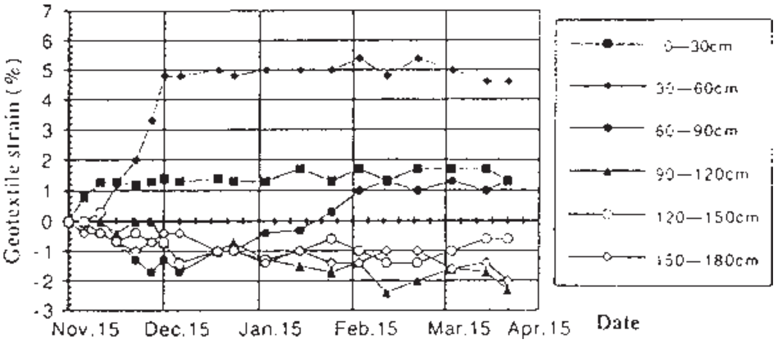

Figure 8 Strain of the geotextile C-C.

because the frost heave was partially counteracted by the compressive deformation of back unfrozen soil.

The experimental study indicated that the in the reinforced wall geotextile applied a restraining pressure to the backfill, and the restraining pressure partially reduced the horizontal frost heave. But it is not necessary that the restraining pressure is as large as or approximate to the "suspended pressure" in order to reduce frost heave. Unfrozen soil will be compressed by the restraining pressure of reinforcement produced by frost heaving of freezing soil, and the frost heave will be partially counteracted by compressive deformation of unfrozen soil. Therefore, under the condition of comparatively small restraining pressure, the frost-heaving displacement of structure can be reduced greatly (Chen Lun et al., 1996).

3 ANALYSIS METHOD

3.1 A New Method for Analysis of Reinforced Earth

Generally, there are two approaches in the analysis of reinforced soil. One deals with soil and reinforcement separately, assuming that they interact with each other through the friction on the interface between them. The other considers the reinforced soil as an anisotropy homogenous composite, so that the interaction force between soil and reinforcement becomes an internal force, which does not appear in the calculation of stress and deformation of the composite. However, in the former approach, at least three constitutive models of soil, reinforcement, and interface are necessary, and many relative parameters have to be used and determined, so the calculation would be very complex when soil is densely reinforced. The shortcoming of the latter approach is that the reinforced soil is anisotropy, which makes its calculation even more difficult. It is also very difficult to determine the parameters of the anisotropy composite in situ by laboratory tests.

A new approach, the equivalent additional stress method, has been used to calculate the reinforced earth. The basic principle of the method is that only the soil skeleton is concerned in the analysis of reinforced soil. The reinforcing material is considered to be an equivalently additional stress acting on the soil skeleton in the direction in which reinforcement is bedded. Namely, only soil elements are used in FEM, and elements of reinforcing material do not appear; their effect is treated as external stress acting on the soil elements. The existing constitutive models of soil can be directly used without equationing any new model. Because the equivalent additional compressive stress acts in the direction in which reinforcement is placed, the anisotropy of reinforced soil can be reasonably described.

The additional stress can be expressed as

$$\Delta\sigma_r = K\varepsilon_r^n \tag{3}$$

where ε_r is the strain of reinforced soil element in reinforcement direction, and parameter K may be determined from $\Delta\sigma_{rf}$ and ε_{rf}, which are the additional stress from reinforcement and strain of sample in the reinforcement direction when the sample fails in a conventional triaxial test. In the case of the layer-built reinforced earth with geotextile, ε_r is the strain of reinforcing material that may be equal to the strain of soil element when the modulus of reinforcing material is not stiff. In addition, K relates to the spaces of geotextile.

By using the equivalently additional stress concept, an FEM program has been composed, and a full-scale model retaining wall, the "Denver Wall", is analyzed. Figure 9 shows the predicted result of the new method, as well as the test results and calculated results with the conventional method (Jie Yuxin, 1998).

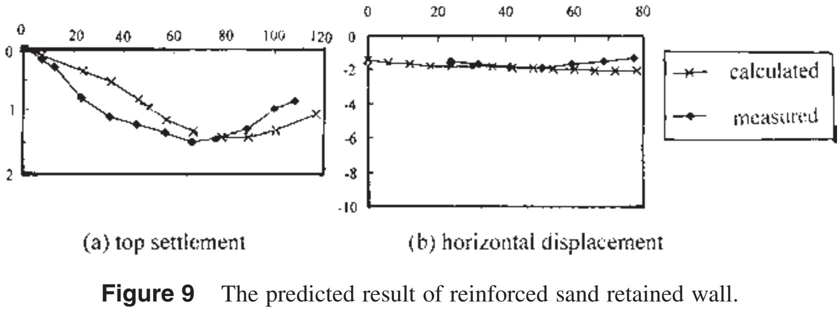

Figure 9 The predicted result of reinforced sand retained wall.

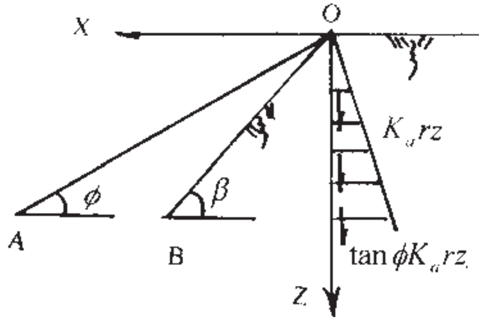

Figure 10 Analysis of sliding surface.

3.2 Consistent Design Method of Reinforced Wall and Steep Slope

3.2.1 Analysis of Earth Pressure

Figure 10 shows a steep slope or wall of cohensionless soil. The slope angle is $\beta(\phi < \beta \leq \pi/2)$. It is well known that the condition of stability of a cohensionless slope is $\beta \leq \phi$. Assume that the same soils are covered on the steep slope to form a slope with angle ϕ; the slope is on limit equilibrium. Analyzing the wedge AOZ with elasticity theory, where Ary's function is a polynomial with three powers and is based on the boundary condition of the wedge (see Fig. 10), the following solution can be obtained:

$$\begin{aligned} \sigma_\gamma &= \tan\phi K_a \gamma x - K_a \gamma z \\ \sigma_z &= \left(\tan^3\phi K_a + \tan\phi\right)\gamma x - \left(1 + \tan^2\phi K_a\right)\gamma z \\ \tau_{\gamma z} &= \tan^2\phi K_a \gamma x - \tan\phi K_a \gamma z \end{aligned} \tag{4}$$

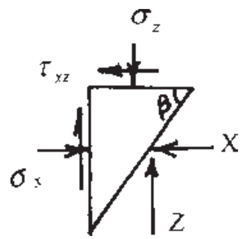

Figure 11 Balance of wedge on OB.

Setting $z = x\tan\beta$ in above equation, the stress on OB can be obtained; then considering the balance of wedge on OB (see Fig. 11), the following equation is obtained:

$$X = \left(1 + \frac{\tan^2\phi}{\tan^2\phi} - 2\frac{\tan\phi}{\tan\beta}\right)K_a\gamma\xi_z = K\gamma\xi_z \tag{5}$$

where $X =$ horizontal pressure acting on the sleep slope OB, i.e., reinforce required by stability of slope OB, while $K =$ horizontal pressure coefficient. Eq. (5) shows that when $\beta = \phi$, $X = 0$; when $\phi = \pi/2$, $X = K_a\gamma z$, namely, active earth pressure.

3.2.2 Prediction of Sliding Surface

Better accuracy of Eq. (5) indicates that wedge analysis of elasticity is applicable. The same analytical methods are used for determining the potential sliding surface of a reinforced slope. Putting reinforced X on the OB (see Fig. 11), based on the balance of wedge BOZ, the stresses in the wedge are obtained. Substituting the stresses to the following equation, the direction of principal stress σ_1 can be obtained:

$$\tan(2\alpha) = -\frac{2\tau_{xz}}{(\sigma_x - \sigma_z)} \tag{6}$$

where $\alpha =$ angle between direction of σ_1 and x-axis.

Because the sliding surface is inclined at an angle $\pm(45^\circ + \phi/2)$ to the direction of the plane acted by σ_1, the sliding surface can be determined.

3.2.3 Design Method

The horizontal earth pressure on the steep slope or wall determines the required tensile strength and the spaces of reinforcements. The length of reinforcement can be calculated based on the position of the sliding surface (Wang Zhao, 1993).

4 CASE HISTORIES

4.1 Retaining Wall with Height of 35.5 Meters

A retaining wall reinforced by parawebs with a height of 35.5 m is one of the highest retaining walls in China. The wall is located in GuYi County for a main highway from Xian to Baotou.

4.1.1 Design and Construction

The retaining wall is composed of three parts; concrete facing plate measuring $1.0 \times 0.4\,m^2$, polypropylene webs with tensile strength of 4 kN per strip and elongation of 2%; and backfill of collapsed soils.

The wall has a vertical face and a platform with a width of 1.4 m at the height of 17.2 m. The design was based on the limit equilibrium method. The subsoil was improved by three rows of piles, whose length was 4.5 m, and the sludge of the top subsoil with a depth of 1.5 m was replaced by lime soil. Considering the elongation of webs, the facing plate was constructed with initial front slope 1:0.01 toward backfill. The sequence of compaction is from the middle of webs to the ends, then to the facing plate. The range of 1.5 m nearby the plate was compacted by a small-sized compactor.

4.1.2 Monitoring

4.1.2.1 Stress of Subsoil. Two rows of pressure cells were pre-embedded on the top of the subsoil. The readings of pressure changed with the height of the backfill (see Table 1). The pressures at the same height of backfill were different. It is due to different positions and good or poor contact with soils.

When the depth of the backfill was more than 22 m, the pressure readings were unchanged.

4.1.2.2 Lateral Deformation of Facing Plate. The lateral deformation was monitored by the attaching strain gauges. Results show that the deformations of plates don't have a regular pattern at the construction period, depending on the looseness or tautness of webs and compaction. When a load on top of the backfill was increased, the maximum lateral deformation appeared in the middle of wall height ($H/2$) toward outside. The deformation of the top plate was slightly toward the backfill. When the load decreased, the deformation could not be restored.

Table 1 Stress of Subsoil

Depth of backfill (m)	Pressure (kPa)
12	120–390
19	204–420
22	380–490

4.1.2.3 The Earth Pressure of Facing Plate. The readings of pressure cells show that the maximum pressure is at the position of $H/2$ much less than $K_0 \gamma H/2$. At the top and bottom of the wall, it reaches zero.

4.1.2.4 Distribution of Stress Along the Webs. The distribution of stress was measured by strain gauges attached on the webs. The maximum stress appeared at the position of $2.0 \sim 2.5\,\mathrm{m}$ from the facing plate. The variety of magnitude was the same as the lateral deformation with the height of wall.

4.1.3 The Economical Effectiveness

The highways on the retaining wall have already run normally for 6 years. Compared to the gravity retaining wall's costs, the cost savings were 50% (Yin Yong, 1992).

4.2 Reinforced Retaining Wall with Two Opposite Facing Plates

The retaining wall has two opposite facing plates (see Fig. 12). The reinforced soils can be divided into three zones—two active zones and a triangle stable zone. The triangle zone and any active zone form the passive zone for another active zone, so that the stability of the walls is improved and the length of reinforcement can be reduced (Wang Zhongsheng, 1992a).

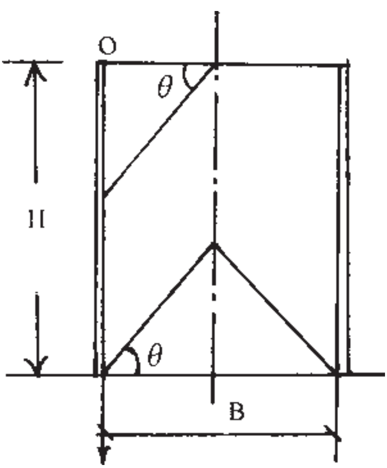

Figure 12 Earth pressure.

Only the active earth pressure on the facing plate is introduced here. Because of symmetry, the active earth pressure of every facing plate can be estimated by Rankine's theory.

$$E_a = \gamma z^2 K_a/2 \quad \text{when} \quad z \le \left(Btg^{\theta}\right)/2 \tag{7}$$

$$E_a = \gamma(z^2 - (z - (Btg^{\theta})/2)^2)K_a/2 \quad \text{when} \quad \left(Btg^{\theta}\right)/2 < z \le H \tag{8}$$

Equation (8) can be simplified to

$$E_a = \gamma\left(B_Z - \left(B^2 tg^{\theta}\right)/4\right))K_a\left(tg^{\theta}\right)/2 \tag{9}$$

where $\gamma =$ unit weight of soil, $K_a =$ active earth pressure coefficient, $B =$ width of retaining structure, $\theta = 45° + \phi/2$, $\phi =$ internal friction angle.

The distribution of earth pressure on the facing can be obtained by the differential of Eqs. (7) and (9):

$$e_a = \gamma z K_a \quad \text{when} \quad z \le (Btg^{\theta})/2 \tag{10}$$

$$e_a = \gamma B\left(tg^{\theta}\right)K_a/2 \quad \text{when} \quad \left(Btg^{\theta}\right)/2 < z \le H \tag{11}$$

Equation (11) shows that the e_a is a constant and equal to e_a from Eq. (10) when $z = (Btg^{\theta})/2$. The e_a is much less than that in direct proportion to z, so that the required tensile strength of reinforcement is much lower.

A reinforced retaining wall with two opposite facing plates is on the bank of the YaLu River (Fig. 13). The maximum height of the wall is 6 m. The thickness of the concrete plate is 120 mm, behind which there are sand cushions

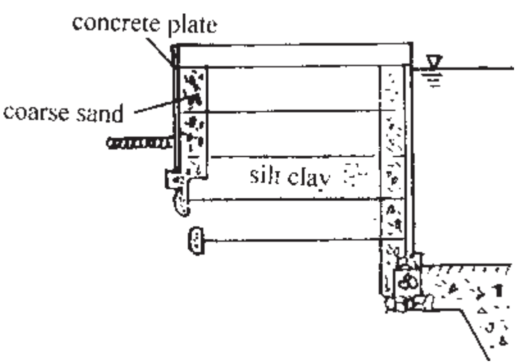

Figure 13 Protection of bank of YaLu River.

with a thickness of 600 mm for filtration and drainage. The backfill of silty clay was reinforced by woven geotextile (Li Changlin and Chen Guanqing, 1992).

4.3 Reinforced Earth Abutment

The Anhui grade separation bridge located in Beijing is composed of 19 bridges, which include 8 round bridges with a height of $2.5 \sim 3.0$ m. Because the spans of bridges are very long and the soft ground with high groundwater level can't bear the gravity wall, the 16 abutments of round bridges are geotextile reinforced earth walls.

4.3.1 Departed Structure

The geotextile reinforced earth with wrapped face was departed from full-high concrete facing and was connected to each other by webs. There was a vertical sand cushion with a thickness of 250 mm between the soft and rigid faces. The reinforced earth (silty clay) was compacted to at least 95% m of $\gamma_{d\max}$. The woven geotextile with a tensile strength of 25 kN/m and elongation of 18% was used as reinforcement with a vertical space of 250 mm. An eccentric load from bridge beams applied the concrete block on the crest of reinforced earth. In order to prevent the differential settlement, anchor rods and blocks were used (see Fig. 14).

4.3.2 Monitoring

The strain gauges were adhered on the webs and the displacement gauges were attached on the outside face of concrete plates. The readings showed that the webs or rigid faceplates bore about one fifth of the earth pressure. When these

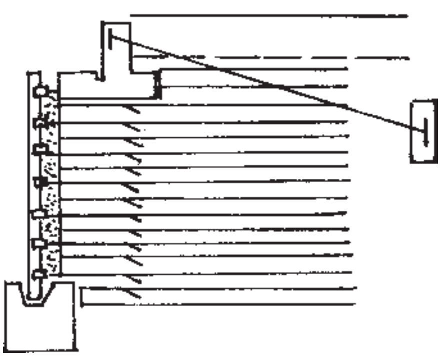

Figure 14 Reinforced earth abutment.

bridges were used, the maximum horizontal displacement of the faceplate was 4.3 mm and the settlement strain of reinforced earth was about 0.5%.

4.3.3 Effectiveness

The 16 abutments were constructed by geotextile reinforced earth, and in all about 0.2 million Chinese yuan was saved compared with the gravity retaining wall. The reinforced earth abutment has the following advantages:

1. Convenient construction and time savings
2. Adequacy to subsoil with low bearing capacity
3. No need for a road concert plate spanned on the concrete block and road embankment, because their settlements are same (Yang Canwen et al., 1990; Luo Baochen and Yu Xijian, 1992)

4.4 A Highway Bridge with Reinforced Earth Pier and Abutment

The bridge is on an arterial highway of Guilingyang Economy Developing zone in Hainan Province. The width of the pavement is 36 m, and the width of canal under the bridge is 22 m (Fig. 15). From geological prospecting, above $\nabla - 3.0$ m is silt clay and sludge, and under $\nabla - 3.0$ m until $\nabla - 9.0$ m is silt

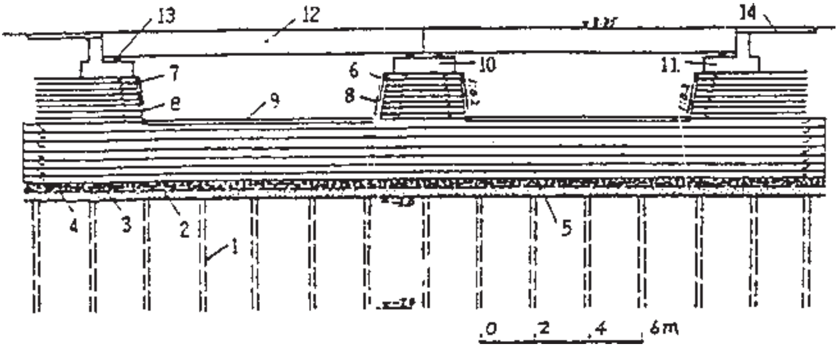

Figure 15 Transverse section of the highway bridge. 1. Nonwoven geotextile-bag sand drains; 2. coarse sand; 3. nonwoven geotextile; 4. crushed stones; 5. reinforced earth mattress (vertical space of woven geotextile: 300 mm); 6. reinforced-earth pier (space: 220 mm); 7. reinforced earth abutment (space: 220 mm); 8. cap of pier or abutments; 9. beams; 10. slabs.

fine sand. Based on a comparison of technology and economy, the geotextile reinforced earth technique was employed in both the abutments and pier, as well as the ground treatment of the bridge.

4.4.1 Design and Construction

The whole project contains four parts; horizontal and vertical drains (see Fig. 15, 1–4); reinforced foundation; reinforced earth pier and abutment (Fig. 15, 6–7); bridge superstructure (see Fig. 15, 9–10). This paper introduces only the third part. The slope-fringe of the pier and abutments is 1:0.2, which is protected by reinforced gunite with a thickness of 80 mm. The soils used in the reinforced earth are all the silty clay with weathered grovels, which are compacted more than three times for each layer by a vibratory compactor with a weight of 11 tons. The degree of compaction of the soils is not less than 96%, and the cement soil whose cement content is 4% is used on the uppermost layers. The allowable beaming capacity of the reinforced earth is 180 kPa and that of the cement soil is 200 kPa, which can meet the requirement of foundation, whose load $p_{\max} = 188$ kPa and $p_{\min} = 39$ kPa. The woven geotextile used in the reinforced earth is the CEF-2006 type made in China with a tensile strength of 40 kN/m on the direction of warp.

4.4.2 Monitoring

After casting the concrete of the caps of pier and abutments, 18 settlement marks have been set up on these caps. According to the observation results from April 1994 to June 1995, it can be seen that the maximum total settlement was 10.4 mm, which included the settlements of reinforced mattress and the settlement of each measuring point basically tending toward stability.

This project employed geotextile and had success. Some advantages can be summarized:

1. The pier abutments and foundation are all the flexible reinforced earth structures and can homogenously spread the loads. The good settlement properties can be obtained as long as the good compacting quality of reinforced earth exists.
2. The construction period is only 2 months, while the time needed by the conventional construction method is more than 3 months.
3. The cost of the whole project is 2.1 million yuan (RMB) and the original conventional method is 3.0 million yuan, so about 0.9 million yuan are saved, or 30% (Zhu Shiao and Cai Duwen, 1996).

4.5 Reinforced Collapsed Soil Retaining Wall

The yellow soil—a kind of collapsed soil—is mainly distributed in the Shanxi Province located in northwest China. There are a lot of storm cracks, which bring trouble to road construction. Many dry bridges have to be thrown across these cracks. Some bridges with a long span are expensive. Three reinforced collapsed soil retaining walls with heights from 11.1 m to 23.1 m have been constructed on the main highway from Xian to Yanan instead of the dry bridges.

4.5.1 Design and Construction

The walls with a face slope of 1:0.05 have been constructed along two sides of highway across the storm cracks. The hexagonal concrete panels with a height of 800 mm and a thickness of 100 mm are connected with parawebs made of polypropylene, whose tensile strength is 4.6 kN per strip and elongation is 6%. The websoil system is designed taking into considerations both Rankine's theory of earth pressure and active zone widens $0.3H$ (H is height of wall). The compaction degree of backfills is required to reach 93% of $\rho_{d\max}$. For the wall with a height more than 15 m, a horizontal platform with a width of 1.25 m should be designed on the level of $H/2$. The platform and surface of the road have to be treated by waterproof materials, such as concrete or asphalt so that the moisture of backfill soil can be maintained. Otherwise, some drainage ditches should be arranged along the upslopes to escape the rains.

4.5.2 Cost-Effectiveness

These retaining walls with a total length of 477 m were completed in 1989. Their good quality has been proven by successful transport service. The total investment was 883,000 yuan compared with the budget of 9,586,000 yuan for dry bridges (Wang Zhongsheng, 1992).

4.6 Retaining Walls in a Foundation Engineering of Pump Station

The Zhijiang pump station for drainage of waterlogging with three pumps of 800 kW is on a silty clay foundation in Huibei Province. The underground water level is very high. When the foundation pit was excavated to a depth of 8 m in November 1993, the severe piping prohibited further excavation. The pit had to be moved a width of foundation apart from the Yangtze River. The former pit should be filled and three concrete pipes with an inner diameter of 2 m had to put on a high compacted soil. In order to prevent the cracks of pipes caused by settlement of filled clay, the added design plan was construction of six "π-type" concrete frames and $6 \times 4 = 24$ piles to sustain pipes. Another problem was that

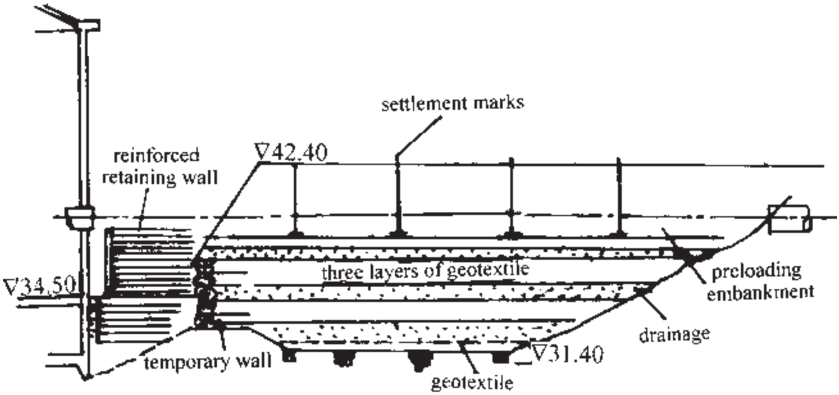

Figure 16 Cross section of foundation pit.

the bearing capacity of the foundation soil was equal to the applied vertical load intensity, so that the pump house can't bear any horizontal earth pressure. The plan included an empty "box-type" concrete retaining wall paralleled to box foundation edge to bear the earth pressure of filled soil. The total budget of frames, piles, and wall was 1,120,000 yuan.

4.6.1 The Scheme of Reinforced Earth

At first, the piping should be stopped and the former pit must be filled. The plan was as follows:

1. Put 900 m^2 of nonwoven geotextile on the bottom of the former pit and cover a thickness of 1 m of sand layer to prevent piping.
2. Control the quality of filled soil as foundation of pipes. However, the wet season in the spring of 1994 made the soil heap up around the pit with a high water content. The modified program was to put two horizontal drain sand layers among the filled soils and construct a preloading embankment (see Fig. 16). Based on the calculation of consolidation, the degree of consolidation can reach 96% until 6 months later when the concrete pipes will be constructed.
3. Construction of three layers of sand mattress reinforced with woven geotextile as the foundation of pipes, under the preloading embankment.
4. The edge of the preloading embankment was a temporary retaining wall reinforced by woven geotextile and wrapped on the wall face by means of soil bags. The temporary wall was the vertical slope for both the preloading embankment and the new foundation pit.

5. Construct a permanent retaining wall reinforced by woven geotextile and wrapped on the wall face by means of mould plates after the buildup of the pump house. When the three pipes are constructed, a brick wall with a thickness of 240 mm was erected to protect the geotextile face of the wall.

4.6.2 Cost-Effectiveness

The project was successfully completed and the pump station run in 1995. It played an important role in the prevention of immense waterlogging hazards in 1996. The cost of the reinforced earth scheme saved 920,000 yuan compared to the budget of the added design plan (Wang Zhao, 1996).

REFERENCES

Chen Lun, Li Guangxin, Huang Wenfeng. Full-scale test studies on prevention of frost damage for retaining wall reinforced with geotextile. Eighth International Conference on Cold Regions Engineering, Fairbanks, AL, USA, pp 724–735, 1996.

Jie Yuxin. A study on geosynthetics-reinforced earth by equivalent additional stress method and tests. Ph.D. thesis, Tsinghau University, Beijing, China, 1998.

Li Changlin, Chen Guanqing. Application of geotextile to hydraulic anchored structures. Proc. 3rd Chinese Conf. on Geosynthetics, pp 87–91, 1992 (in Chinese).

Lin Yuanzhi, Wang Zhenghong. Experimental study on influence of modulus of reinforced retaining wall. '96 Intl. Symp. on Geosynthetics Proc. Shanghai, China, pp 119–126, 1996.

Luo Baochen, Yu Xijian. Geosynthetics reinforced abutment at Anhui gradeseparation bridge in Beijing. A Hundred Case Histories on Application of Geosynthetics, pp 364–368, 1992 (in Chinese).

Wang Zhao. Earth pressure and sliding surface of slope. Proc. Intl. Conf. on Soft Soil Engineering, Guangzhou, China, pp 590–593, 1993.

Wang Zhao, Qiao Zhongshe. The application of geosynthetics to foundation engineering of Zhijiang pump station. Proc. Fourth Chinese Conf. on Geosynthetics, pp 104–107, 1996 (in Chinese).

Wang Zhongsheng. Reinforced collapsed soil retaining wall. A Hundred Case Histories on Application of Geosynthetics, pp 374–378, 1992a (in Chinese).

Wang Zhongseng. Analysis of forces on reinforcement in double facing plates retaining wall. Proc. 3rd Chinese Conf. on Geosynthetics, pp 85–86, 1992b (in Chinese).

Wei Yifeng, Li Guangxin. Pullout tests of geotextile in various directions and stability analysis of reinforced soil structure. '96 Intl. Symp. Geosynthetics Proc. Shanghai, China, pp 7–14, 1996.

Yang Canwen, Yu Xijian, Lau Baohen. Practice and research of geosynthetics reinforced abutment. Proc. 2nd Chinese Conf. on Geosynthetics, pp 318–326, 1990 (in Chinese).
Yin Yong. Reinforced earth retaining wall at Guyi county. A Hundred Case Histories on Application of Geosynthetics, pp 360–363, 1992 (in Chinese).
Zheng Jiqin, Chen Lun, Li Guangxin. Experimental study on fiber-reinforced cohesive soils. '96 Intl. Symp. Geosynthetics Proc. Shanghai, China, pp 25–32, 1996.
Zhu Shiao, Cai Duwen. A highway bridge with reinforced earth pier and abutments. Proc. '96 Int. Symp. Geosynthetics, Shanghai, pp 102–106, 1996.

12

Large-Scale Reinforced Clay Walls Backfilled with Clay at Cheng Kung University

Ching-Chuan Huang, J. F. Wu, B. N. Huang, A. L. Leu, and G. Y. Jean
National Cheng Kung University, Tainan, Taiwan

H. Y. Shan
National Chiao Tung University, Hsinchu, Taiwan

ABSTRACT

A study into the behavior of geosynthetic reinforced walls using clayey soil as the backfill was performed. Two 2.77-m-high full-scale walls, namely, the NCKU walls, were constructed using an alluvial clay containing 98% of fine particles under carefully controlled conditions. Results of the long-term monitoring on the behavior of NCKU walls indicated that cracks or shear planes in the backfill may play important roles in the increase of pore water pressure and the deformation of the wall face during rainfall. In addition to the NCKU walls, a test embankment was also constructed to investigate the infiltration characteristics of compacted clay under practical compaction procedure. Dismantling of the NCKU walls and the test embankment was conducted to investigate the locations of cracks and the water content distribution in the soil. Results of FEM seepage analyses showed that in-plane drainage function of nonwoven geotextile layers may not always be positive to the stability of clay wall. Using an impermeable facing—a rigid concrete panel as used in the RRR method and a geodrain layer close to the top of the wall—is suggested for reinforced clay walls.

1 INTRODUCTION

The utilization of clayey soils as the backfill of a reinforced retaining wall is of environmental and economic significance. A pioneer study on the behavior of 5-m-high reinforced walls using volcanic ash clay (Kanto loam) as the backfill has been performed in Japan since 1982 (Tatsuoka and Yamauchi, 1986). In this study, a nonwoven, low-stiffness geotextile was used as the reinforcing material. A relatively low degree of compaction was obtained because the compaction was conducted under natural water content ($\omega \approx 100\%$). Large deformations were measured for the reinforced clay walls during the long-term monitoring. In this study, Tatsuoka and Yamauchi (1986) found that the nonwoven geotextile may effect degree of compaction and provide drainage function during the rainfall. In the subsequent studies on the reinforced clay wall for railway test embankment (Tatsuoka et al., 1992), relatively stiff geogrid and geosynthetic composite for soil reinforcement were used. In addition, layers of sand filter and cast-in-place rigid RC facing (namely, RRR method) were used to provide drainage and lateral confinement of the soil mass. Consequently, the deformation of the reinforced wall under intensive rainfalls was significantly reduced. Wu (1992) reported a 3-m-high timber-faced steep wall using a clayey sand (classified as SC based on USCS) reinforced with a heat-bonded nonwoven geotextile. In this study, a clayey soil was air-dried, crushed, sieved through a No. 4 sieve (4.76-mm opening), and mixed with silt and sand under carefully controlled conditions. The soil was subsequently mixed with water to achieve a 2% wet optimum water content and was cured in a constant moisture room. The compaction effort was provided by a vibration plate compactor weighted 700 N under 76-mm soil lift to achieve 95% relative compaction of the Standard Proctor test. A reinforced wall backfilled with medium-dense sand (relative density $\approx 67\%$) was also built for comparison purposes. The result of loading tests showed that the ultimate load of the clay wall was larger than the sandy wall. However, a conclusion regarding the feasibility of using clay as the backfill has not been reported. Itoh et al. (1994) also reported a 7.5-m-high steep reinforced wall using a high-plasticity clay (classified as CH based on USCS, approximately on the A-line) formed by weathered mudstone. The compaction was provided by a vibrating roller weighted 70 kN under 0.25-m lift and 4 to 8 passes. In this study, the control of the clod size of clay before compaction, the water content of soil during compaction, and the relative compaction achieved were not reported. Large horizontal and vertical deformations (≈ 0.4 m and 0.6 m, respectively) of the wall face were measured in the five months since completion. Inadequate compaction conditions might account for the large deformation of the wall face. So far, clayey soils have not yet been widely accepted for permanent soil structures because the engineering properties of the compacted clay could be susceptible to various factors. Therefore, a systematic employment of clays as the backfill of reinforced walls requires more studies on the relationship between the performance of reinforced clay walls and the factors that control the quality of the compacted clay. This report covers the design and construction of the reinforced walls, the long-term monitoring, and the results of seepage analyses.

2 CONSTRUCTION OF NCKU WALLS

A 2.77-m-high, 6-m-wide, and 3-m-long reinforced embankment was constructed on a competent ground at the campus of National Cheng Kung University in Tainan City, Taiwan. Two vertical reinforced walls (called NCKU walls hereafter) were constructed as side faces of this test embankment as shown in Fig. 1.

Preliminary studies on the soil properties, the reinforcement strength, and the field compaction methods were conducted. The soil employed was an Alluvial deposit containing 98% fine particles. The soil classification according to the Unified Soil Classification System was CL. Index properties of the clay are summarized in Table 1. Air-dried clay was crushed to produce adequate clod sizes. A vibration plate compactor weighted 780 N and a tamping rammer weighted 700 N were used in the preliminary study on the compaction method.

It was found that using the tamping rammer under an average clod size for about 10 mm, a small life height of 20 mm for water spreading, and a total lift height of 120 mm with 5 passes of compaction under optimum water contents ($\omega_{\text{opt}} \approx 16\%$, lift 17%) resulted in a homogeneous soil mass with 90% relative compaction (R.C.). A smaller lift height of 80 mm with otherwise the same condition resulted in a similar degree of compaction. The results are summarized

Table 1 Index Properties of the Clay Used in the Present Study

Percentage of sand (>0.06 mm) by weight	2.5%
Percentage of silt (0.06–0.002 mm) by weight	79.1%
Percentage of clay (<0.002 mm) by weight	18.4%
USCS	CL
G_s	2.72
LL	31
PL	17
PI	13

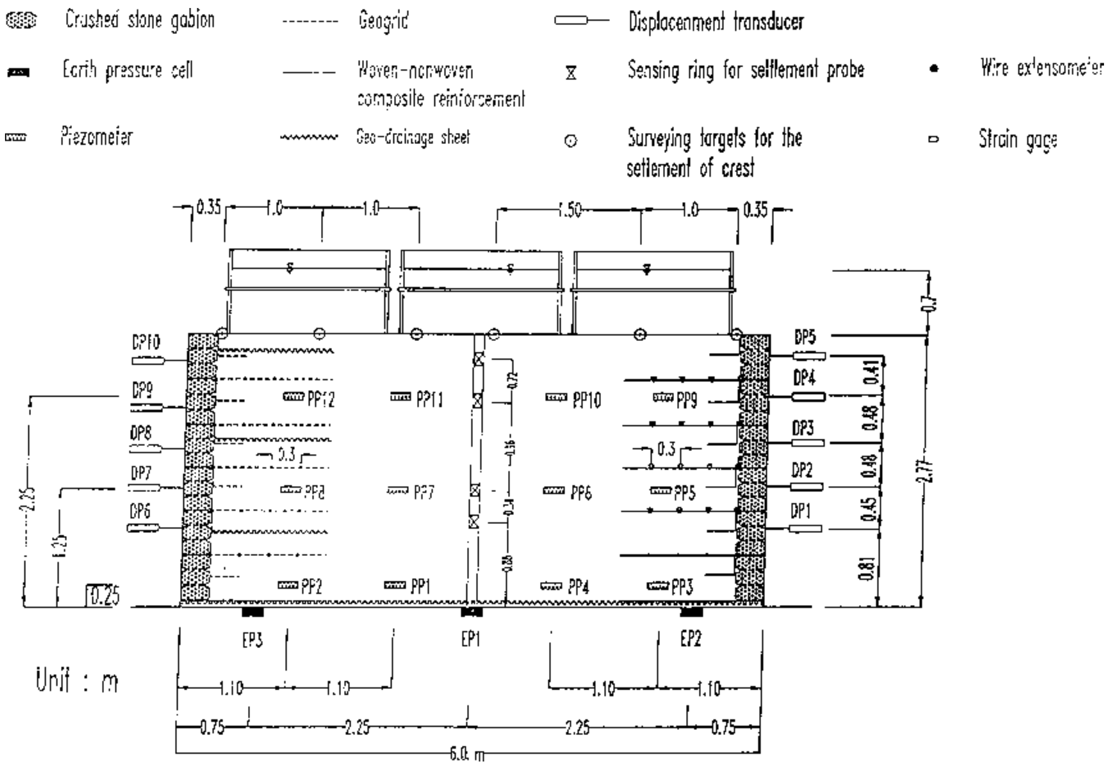

Figure 1 Schemes of the reinforced clay walls (NCKU walls).

in Fig. 2. Compaction under other conditions, for example, using the plate compactor, or increasing the thickness of the soil lift, or increasing the clod size, all failed to obtain a relative compaction of 90% for the clay. Consequently, the specification of compaction as summarized in Table 2 was used for the construction of the test walls.

Triaxial compression tests under the confining pressure ranging between 49 kN/m^2 and 147 kN/m^2 were performed on the compacted soil specimens under R.C. ≈ 90% conditions; the dry unit weight (γ_d) and the water content (ω) were 16.8 kN/m^3 and 15.7% for the in-lab, and 15.9 kN/m^3 and 14.4% for the in-situ specimens, respectively. Strength parameters based on Mohr–Coulomb's failure criterion for the in-lab and in-situ soil specimens are $c' = 43$ kN/m^2, $\phi' = 30°$, and $c' = 26$ kN/m^2, $\phi' = 32.6°$, respectively. The walls at each sides of the embankment were reinforced using different types of reinforcements. For the right-side wall (R-wall), a geosynthetic composite formed by a knitted geotextile layer needle-punched with two layers of nonwoven geotextile was used. For the left-side wall (L-wall), a geogrid with apertures of 20 mm × 20 mm formed by polyester fibers coated with PVC was used. The stress–strain relationships for these two types of reinforcement are shown in Fig. 3. A detailed description on the tensile test and the calibration on the strain gauges attached to the woven–nonwoven composite is reported elsewhere (Huang, 1998).

The side walls of the plane-strain soil container consisted of 3000-mm-long and 100-mm × 150-mm wood studs and 0.5-mm-deep, 0.3-mm-wide, and 3-m-long strip concrete footings. The frames of the side walls were reinforced with wood wales and were further supported externally by struts at two levels as shown in Plate 1. Ten-mm-thick fortified glass was installed on the inner face of the front side wall to form transparent 0.3-mm × 0.3-m windows for measuring the movement of the targets printed on the 0.3-mm-thick rubber membrane sheet. The interface between the membrane sheet and the glass was lubricated with silicone grease to reduce the side wall friction.

Table 2 Compaction Method Used in the Present Study (for a 700 N Tamping Rammer 50–700 mm Stroke, ≈650 vpm)

Maximum clod size of clay	≈10 mm
Water content (%)	16–17
Lift height for water content adjustment	≈20 mm
Thickness before compaction	≈120 mm
Thickness after compaction	≈80 mm
Number of passes	5

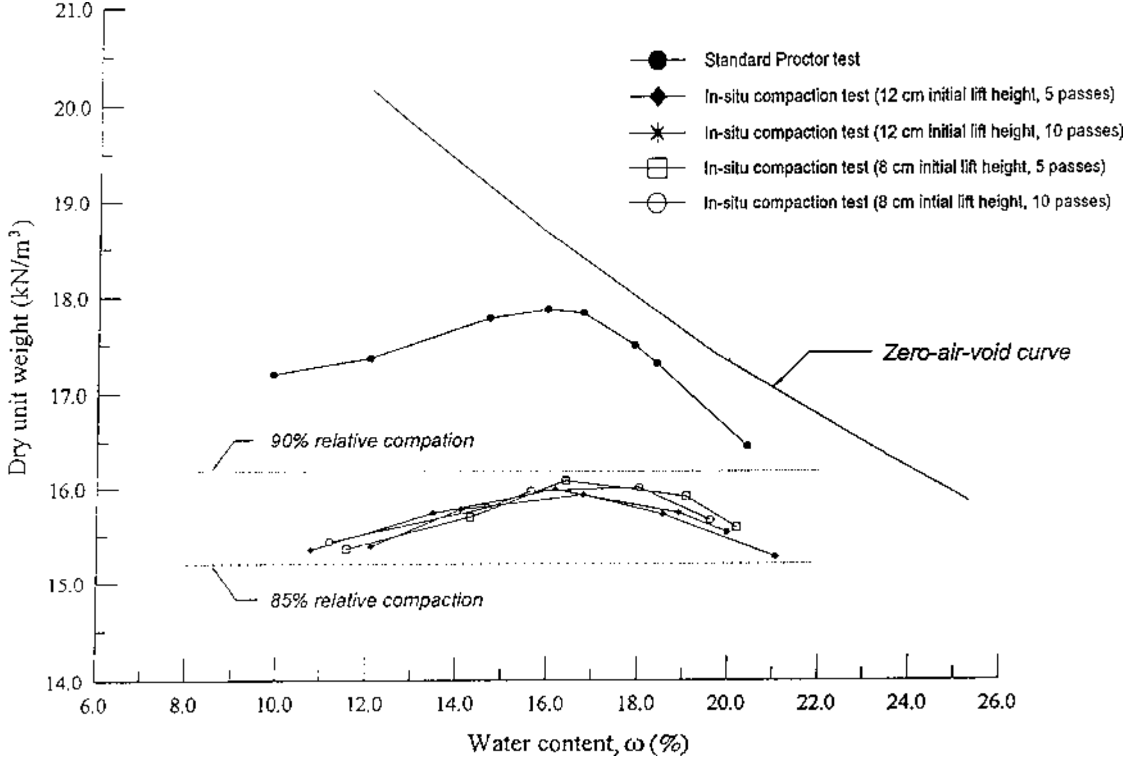

Figure 2 Comparisons of the compaction curves obtained by standard Proctor tests and field compaction tests.

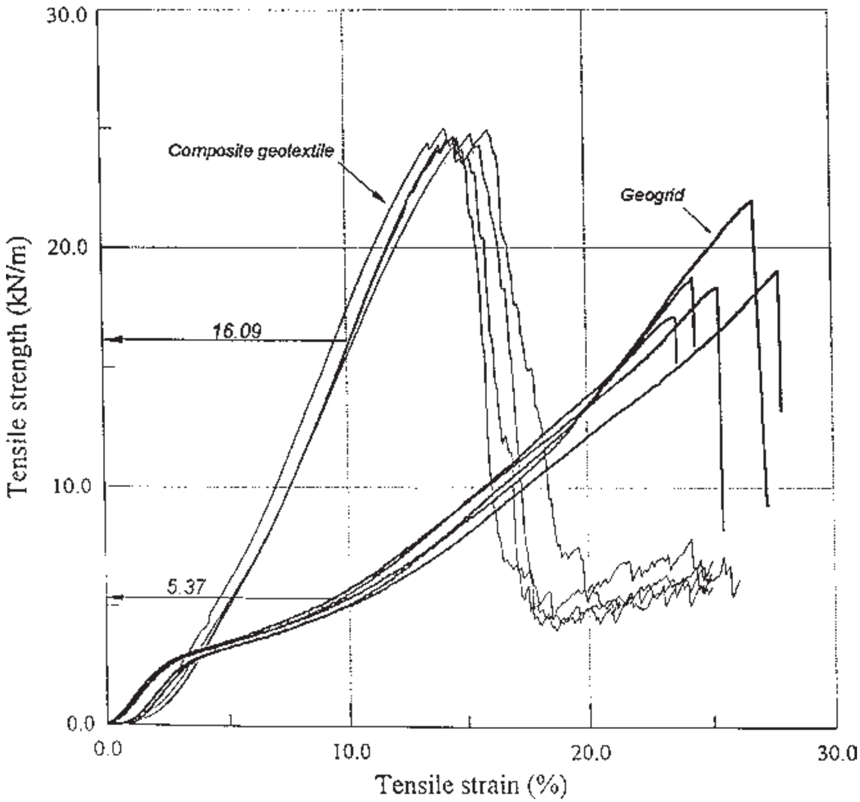

Figure 3 Stress–strain relations for two reinforcements used for the NCKU walls.

The water content for each air-dried, 20-mm-thick layer was adjusted to the optimum water content condition. The spreading of soil and water was repeated for five to six times to form a 120-mm-thick layer for compaction. The soil density and water content were checked using undisturbed block samples during the compaction. The result indicated that the quality control of the compaction work was successful. A schematic view on the monitoring system is also shown in Fig. 1.

The measurement of local tensile strains of reinforcement using Wheatstone bridge has been double-checked using a precision Ohmmeter based on the calibration method reported by Leshchinsky and Fowler (1990). In the present study, the tensile strains measured using these two types of apparatus were practically the same. Temperature effect on the output strain of reinforcement was calibrated; output strain was investigated using a constant-temperature chamber in the laboratory (Guo, 1995).

Plate 1 The completed NCKU walls.

3 CONSTRUCTION OF TEST EMBANKMENT

A 24-m-long, 8-m-wide, and 1.0-m-high test embankment (Fig. 4) was constructed at a port construction site about 20 km from the campus of NCKU using an alluvial clay similar to that used for the NCKU reinforced walls. Prior to the construction, in-lab compaction tests following the procedure of ASTM D698-91 were performed to obtain the compaction curves for the clay. Different clod size distributions were intentionally employed to study the effect of clod size of clay to the compaction curves. Figure 5 shows that the result of compaction was influenced by the size of clod to some extent. Sample 1 was obtained from the standard sample preparation procedure. Larger clod sizes were introduced for samples 2 and 3. It is seen that the samples with larger clod sizes tended to have larger dry densities. However, it is seen from Fig. 5 that the soil sample with larger clod size had a larger permeability coefficient. It is considered that a large clod size might create interparticle planes to facilitate the seepage in the soil mass.

Saturated alluvial clay obtained from the construction site with natural water content of about 22.5% was air-dried on-site for about 47 days. During the air-drying process, the soil was disturbed thoroughly using a backhoe for three times to speed up the drying process. The ready-for-use clay has typical clod size distributions as shown in Fig. 6 and water contents between 7% and 9%. Soil was

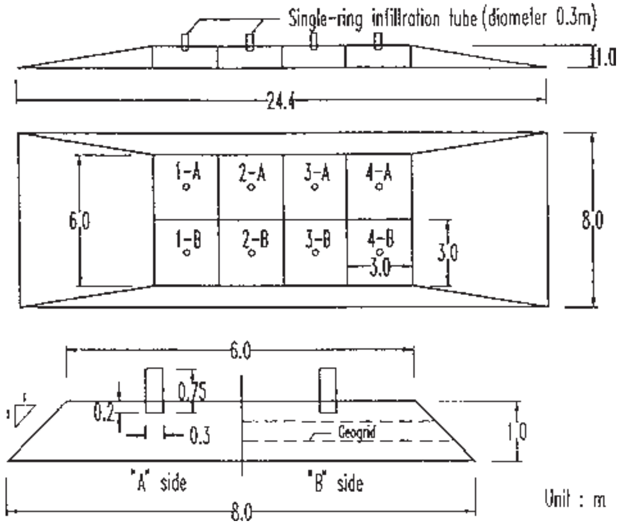

Figure 4 Configuration of the test clay embankment.

leveled by a shovel to form layers approximately 100 mm thick for water spreading. This process was repeated for five times to form a lift height about 400 mm for compaction.

Compaction effort was provided by a steel wheel roller weighted 24 kN and 60.8 kN for the front and the reel wheels, respectively. Field compaction with five passes of the roller was used to achieve 90% of R.C. based on a preliminary field test. The test embankment was divided into eight sections. Sections 1-A and 1-B simulate 3% dry-side compactions; Sections 2-A, 2-B, 4-A, and 4-B simulate the optimum water content compactions; Sections 3-A and 3-B simulate 3% wet-side compactions. No reinforcement was placed in the "A" side, while geogrid sheets spaced at 300 mm vertically was for the "B" side. Measured water contents and relative degree of compaction during construction of the test embankment are summarized in Table 3.

4 STABILITY ANALYSES FOR NCKU WALLS

A modified Bishop's method was used for evaluating the overall stability of NCKU walls. In this method, the interaction between horizontal reinforcement forces and reaction forces on the slice bases is taken into account. The factor of

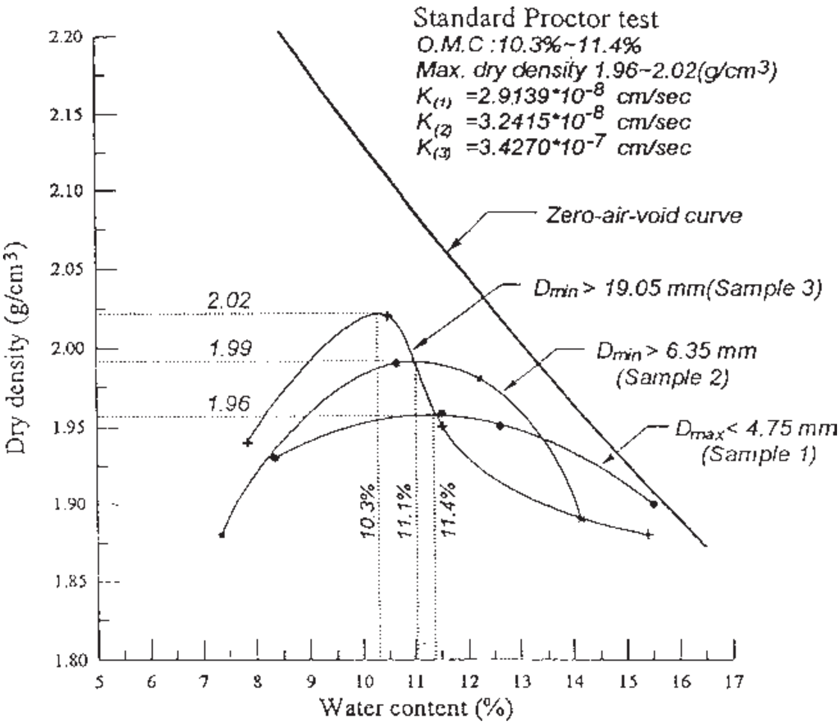

Figure 5 In-lab compaction curves and permeability coefficients of clay with various clod size distributions.

safety is defined as (Fig. 7)

$$F_s = \frac{\Sigma \dfrac{cl_i + [W_i(1 - r_u)]\sec\alpha_i \tan\phi}{(1 + \tan\alpha_i \tan\phi / F_s}}{\Sigma(W_i \sin\alpha_i - T_i \cos\alpha_i)} \tag{1}$$

Table 3 Water Contents and Relative Degree Compaction of the Test Embankment

Section	ω (%) targeted	ω (%) measured	ρ_d (g/cm^3)	R.C. (%)
1	Air-dried	8.5	1.64	83.6
2	11.4	12.6	1.60	81.6
3	14.0	14.5	1.80	91.8
4	11.4	12.7	1.74	88.8

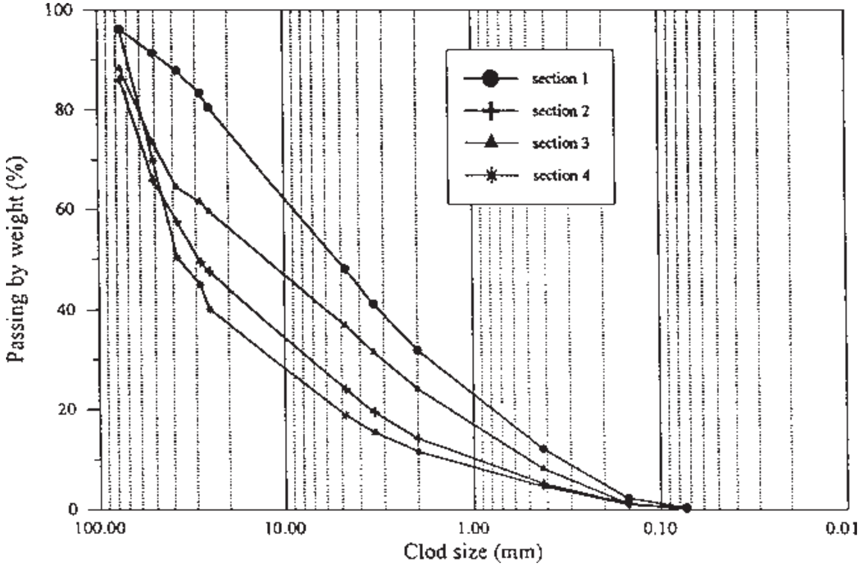

Figure 6 Clod size distribution of the ready-for-use clay.

in which, c, ϕ are the cohesion and internal friction angle of soil; l_i is the length of the slice base; W_i is the self-weight of slice no. i; r_u [$= (u_i b_i / W_i]$ is the pore pressure ratio defined by Bishop (1955); u_i is the pore pressure acting on the base of slice no. i; T_i is the reinforcement force (tension) acting on the base of slice no. i.

A total of 12 cases was investigated. The input parameters and the analytical results are summarized in Table 4. The predicted failure surfaces are also shown in Fig. 7. In cases 1-A through 2-C, the strength parameters for the aforementioned in-laboratory and in-situ soil specimens were used. Note that in these cases the internal friction angles obtained in the triaxial compression tests were multiplied by a factor of 1.1 to simulate the plane-strain condition. In cases 3-A through 4-C, the cohesion of the clay was neglected purposely. Table 5 shows that the cohesion of the compacted clay dominates the stability the clay wall. It also showed that using the tensile strength at 10% of strain, that is, using $F_T = 3.3$ on the ultimate strength ($T_i = 5.37$ kN/m; see Fig.3) of the geogrid, or using a pore pressure ratio $r_u = 0.1$ yielded relatively small reduction in F_s for cases 1-A through 2-C. However, they yielded relatively large reductions for cases 3-A through 4-C in which the cohesion of clay was not considered.

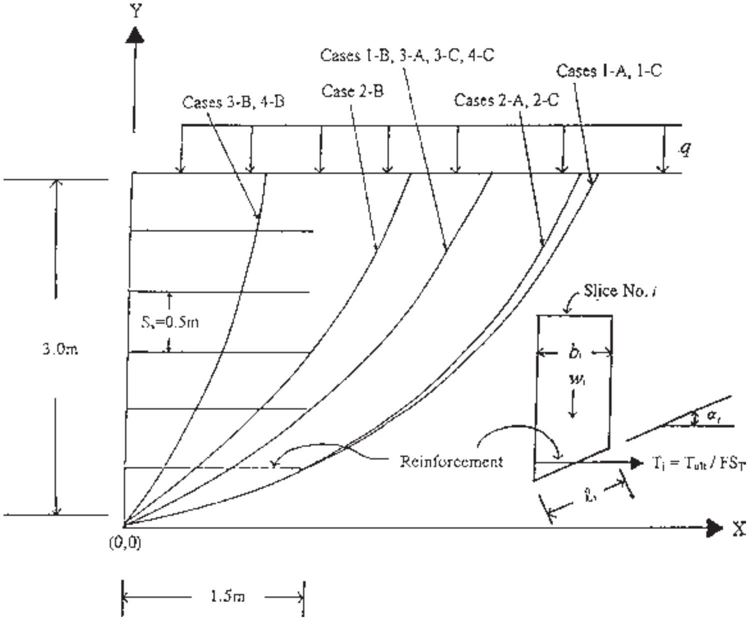

Figure 7 Failure surfaces for L-wall predicted using modified Bishop's method.

Table 4 Results of Slope Stability Analyses for R-Wall Using Modified Bishop's Method Under Various Conditions

No. (strength parameters)	A ($r_u = 0$, $F_T = 1.0$)	B ($r_u = 0$, $F_T = 3.3$)	C ($r_u = 0.1$, $F_T = 1.0$)
1 (c = 43 kN/m^2, $\phi = 33°$)	3.80 *(−0.75, 4.975, 5.014)	3.38 *(−2.375, 5.35, 5.843)	3.66 *(−0.75, 4.975, 5.014)
2 (c = 26 kN/m^2, $\phi = 35.8°$)	2.94 *(−0.625, 4.6, 4.619)	2.50 *(−3.25, 4.975, 5.906)	2.79 *(−0.625, 4.6, 4.619)
3 (c = 0 kN//m^2, $\phi = 33°$)	1.17 *(−2.375, 5.35, 5.843)	0.78 *(−4.75, 3.475, 5.877)	1.04 *(−2.375, 5.35, 5.843)
4 (c = 0 kN/m^2, $\phi = 35.8°$)	1.30 *(−2.375, 5.35, 5.843)	0.87 *(−4.75, 3.475, 5.877)	1.15 *(−2.375, 5.35, 5.843)

For all cases, q = 9.8 kN/m^2, T_{ult} = 17.7 kN/m, $\gamma = \gamma_{sat}$ = 18.1 kN/m^3.
*(X,Y,R): X, Y are the x- and y-coordinates (in meters) for the center of circle, R is the radius (in meter) of the circle, and the origin (0,0) is located at the toe of the wall.

Table 5 Vertical and Horizontal Permeability Coefficients (k_v and k_h) for Undisturbed Sample of Section 3-A

Direction of seepage	ω (%) at saturated	θ^a at saturated	Permeability coefficient (m/day)
Vertical	16.8	0.302	$K_v = 2.158 \times 10^{-5}$
Horizontal	17.8	0.320	$K_h = 1.991 \times 10^{-5}$

[a] $\theta = \omega(1 - n)G_s$; n: porosity (= 0.338); G_s: specific gravity (= 2.72).

For various conditions considered in case A, a maximum F_s is equal to 3.8 for 1-A and a minimum F_s of 1.17 is for 3-A. It inferred that a hidden safety factor was introduced in the design of NCKU walls using current design methods mainly for cohesionless soils (e.g., Koerner, 1998; Jewell, 1991).

5 TEST FOR NCKU WALLS

In the long-term monitoring for about 840 days since completion of the wall, five tests were performed. These tests were

1. Surcharge (6.8 kN/m^2) on the crest of the wall for about 100 days
2. First infiltration test on the crest of wall using 100-mm constant water head for about 50 days
3. Second infiltration test for 23 days using a variable water head method in three 250-mm-deep, 200-mm-wide trench on the top of the wall parallel to the wall face
4. Third infiltration test for 30 days by increasing the depth of trench to 500-mm deep.
5. Fourth infiltration test for 23 days by increasing the depth of trench to 800-mm deep

In addition to these tests, the walls also experienced several heavy rainfalls as shown in Fig. 8. The precipitation was recorded by an automatic weather station at the site of NCKU walls.

6 TEST RESULTS FOR NCKU WALLS

Strains for geosynthetic composite reinforcement at $h = 0.95$, 1.38 m, and 1.89 m were measured immediately after the compaction of one soil layer (120-mm thick) above the reinforcement at $h = 1.89$ m. The increase of overburden on

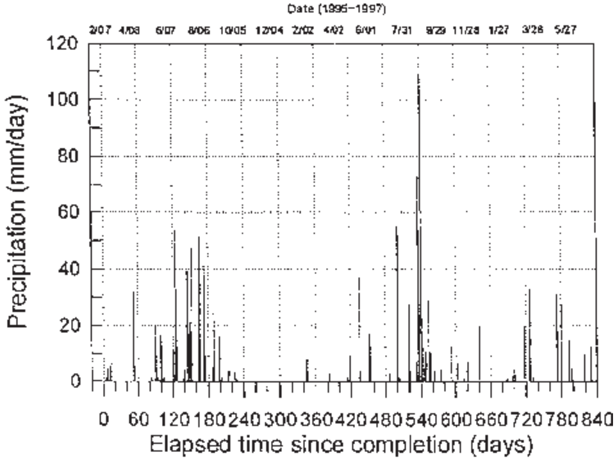

Figure 8 Precipitation recorded by the weather station adjacent to the NCKU walls.

the top of reinforcement for about 0.9 m high hardly increases the tensile strains in the reinforcement (Fig. 9). In fact, small reductions in the tensile strains were measured for lower layers of reinforcement. Based on the tensile strains measurement for the reinforcement at $h = 1.89$ m, the tensile strains developed during the compaction of one lift upon the reinforcement were approximately 1% to 4%, and those due to the subsequent construction from 1.97 m to 2.77 m high were approximately 1.5% to 2%. It means that 40% to 67% of the total strains developed for the whole construction process has been mobilized during the compaction of one layer upon the reinforcement. A similar result has been reported by Schlosser (1990). In this study, 70% to 95% of the total strains that developed during the process of construction were generated during the compaction of one soil layer upon the reinforcement. The smaller value obtained in the present study may be attributable to the relatively smaller compaction energy employed.

The tensile strain increase in 10 months since completion is shown in Fig. 10. The increase of tensile strains for most of the geosynthetic composite reinforcements was not larger than 2%. Because the strain gauges deteriorated very fast, potentiometers with minimum readings of 0.01 mm were connected to steel wires to measure the movement of specific targets attached to the reinforcement. Targets at one end of the steel wire were spaced at 300 mm horizontally for four reinforcement layers in each wall.

The measurement of reinforcement strain using potentiometers restarted at the beginning of the first infiltration test, which was about 11 months (about 330 days) after the completion of the walls. The increment of tensile strains for

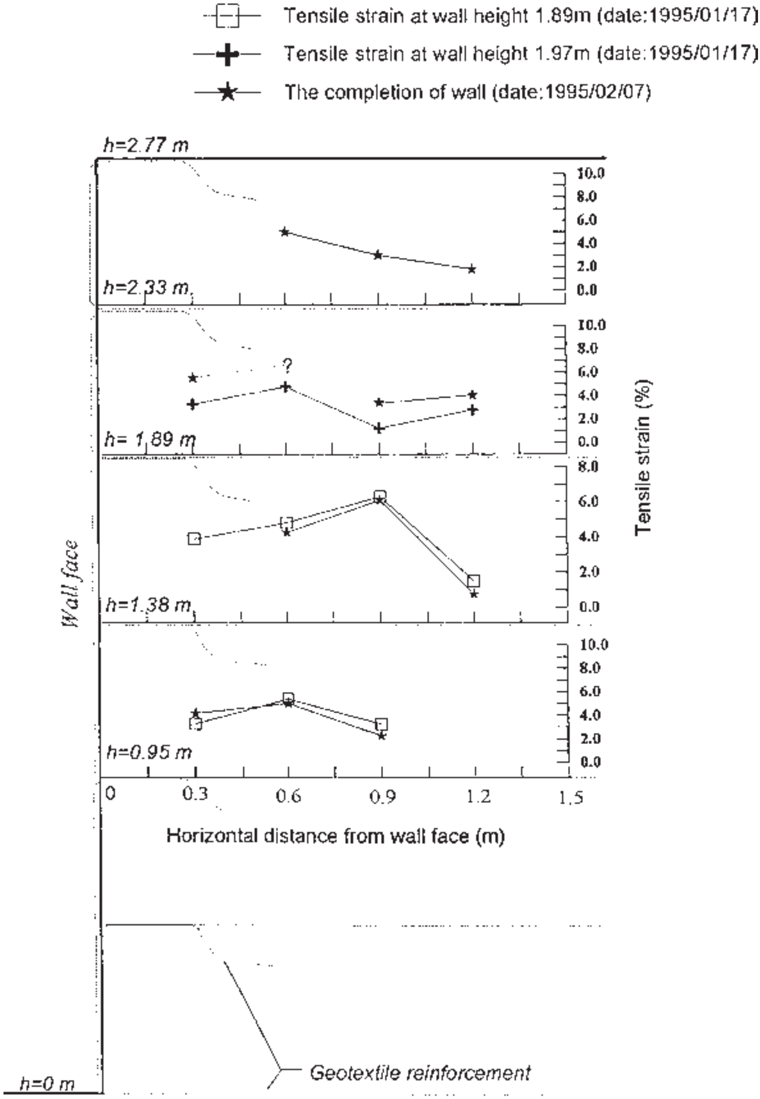

Figure 9 Tensile strain increment measured for the reinforcement during the construction of reinforced walls.

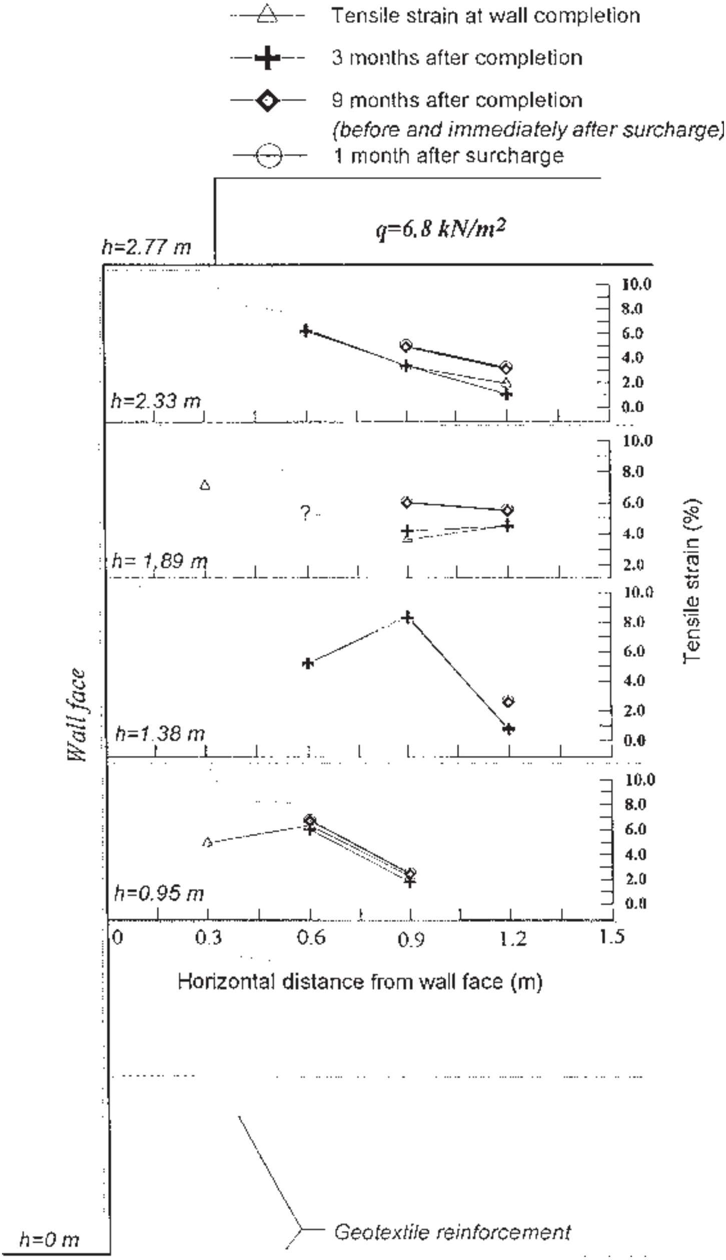

Figure 10 Tensile strain increment measured for the reinforcement during the long-term monitoring.

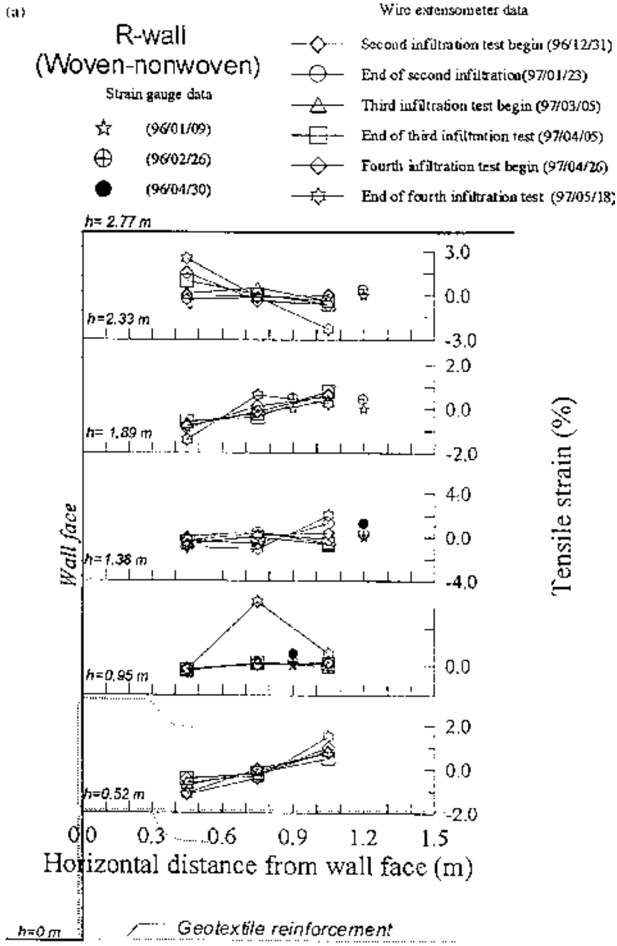

Figure 11 Reinforcement strains measured for second, third, and fourth infiltration tests: (a) R-wall; (b) L-wall.

most of the layers of reinforcement within subsequent 500 days of monitoring were as small as 1% despite the infiltration tests and several intensive rainfalls.

Relatively large strain increments were found for some layers of reinforcement in the R-wall at the end of the fourth infiltration test (Fig. 11a,b). These may indicate the development of a failure surface in the reinforced zone. Figure 12a–c shows the measured pore water pressure for different layers of

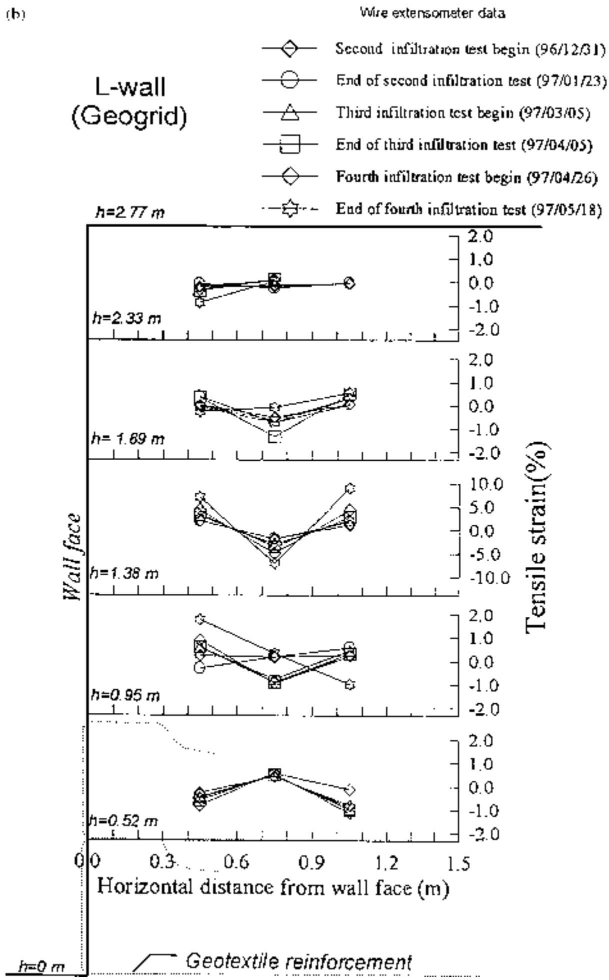

Figure 11 Continued.

piezometers during 840-day monitoring. It is seen that the fluctuations of pore pressure before the end of first infiltration test were small, despite the heavy rainfall between the 120th and 200th days and the constant water head infiltration on the top of the wall for about 50 days. After the first infiltration test, some 5-mm-wide, 350-mm-deep cracks at the crust of the walls were found (Plate 2).

These cracks might account for the responsive pore pressure changes during heavy rainfalls and the 2nd–4th infiltration tests. Figure 13a and b show the movement of facings measured at different levels for the R-wall and L-wall,

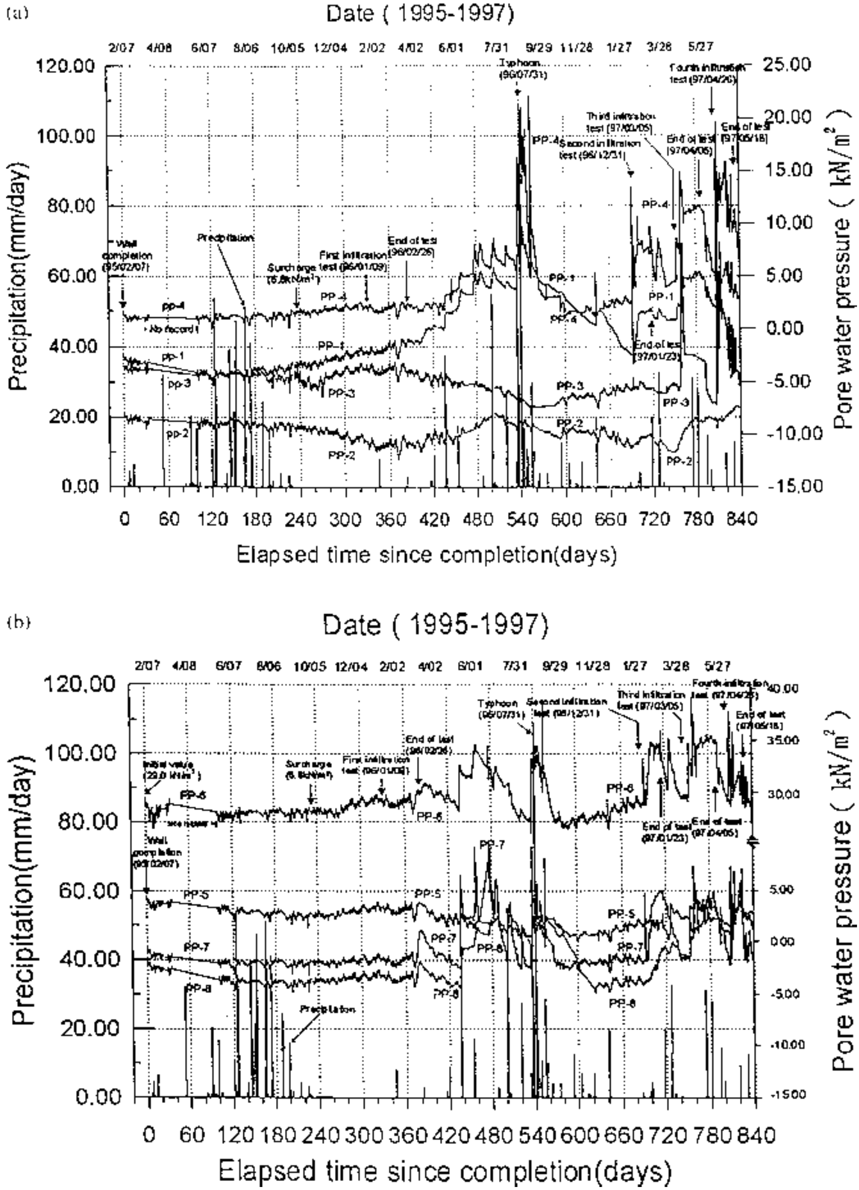

Figure 12 Measured pore pressure for piezometers at (a) lowest layer (0.25 m high); (b) medium layer (1.25 m); (c) highest layer (2.25 m).

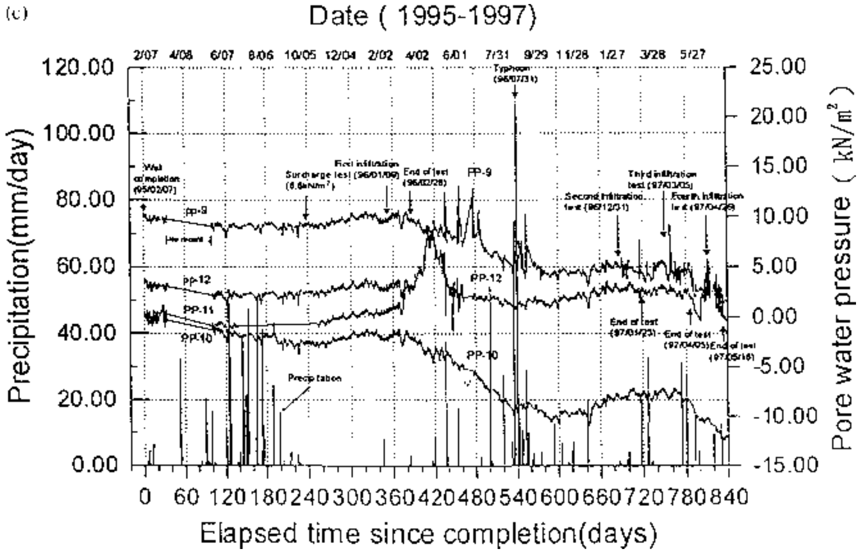

Figure 12 Continued.

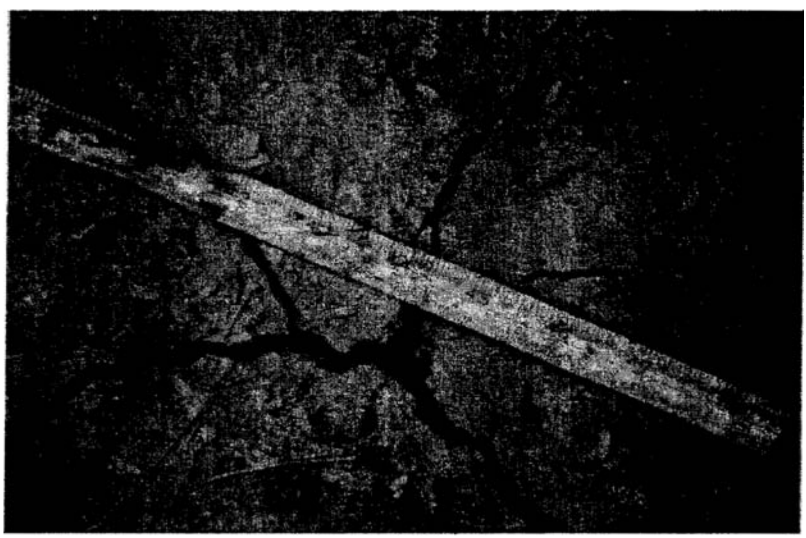

Plate 2 Cracks observed at the top of NCKU walls after first infiltration test.

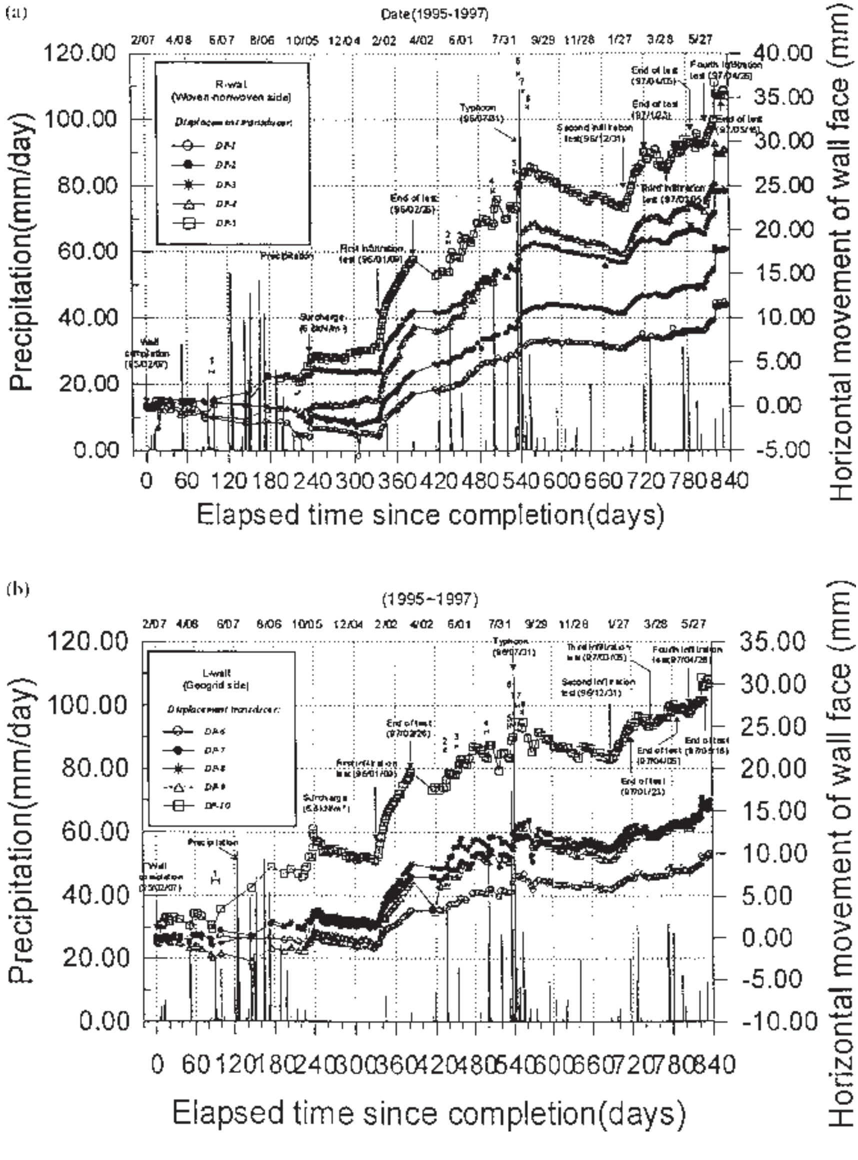

Figure 13 Measured horizontal movements of facing at different heights: (a) R-wall; (b) L-wall.

respectively. The deformation of the wall facing might be a result of the following three mechanisms:

1. Swelling of the soil at the vicinity of facing
2. Water pressure in the tension cracks or shear bands behind the reinforced zone
3. Creep at the soil–reinforcement interface

Because only small and localized cracks parallel to the facing were observed during dismantling of the walls, mechanisms (1) and (3) were most likely to govern the deformation of NCKU walls.

7 TEST RESULTS FOR EMBANKMENT

Infiltration tests were performed on the top of the 1.0-m-high embankment at the center of each section using 300-mm-diameter single-ring infiltrometers immediately after the completion of the embankment. The test arrangement is schematically shown in Fig. 4. The water height versus elapsed time relations obtained in the infiltration tests are shown in Fig. 14a and b. It is seen that the sections under dry-of-optimum compaction (Sections 1-A and 1-B) demonstrated the highest infiltration rates, while those under wet-of-optimum compaction (Sections 3-A and 3-B) showed inconsistent results; that is, Sections 2-A and 2-B showed similar infiltration rates to those compacted under dry-of-optimum (1-A and 1-B), while Sections 4-A and 4-B showed quite small infiltration rates. This inferred that the permeability of clay mass compacted at OMC may vary significantly because of the localized dry-of-optimum zones possibly induced by nonuniform water spreading. The wet-of-optimum sections (3-A and 3-B) consistently showed the lowest infiltration rates in two sides of test.

Relative degrees of compaction (R.C.) for Sections 1 through 4 are summarized in Table 3. It is seen that higher values of R.C. occurred in Sections 3 (about 3% wet-of-optimum), while smaller values of R.C occurred in Sections 2 (optimum water content). Smaller values of R.C. resulted in higher infiltration rates as seen in Fig. 14a and b. For "wetter" conditions (i.e., Sections 3-B and 4-B), the B side demonstrated smaller infiltration rates than the A side. This may be attributable to the soil confinement effect generated by the reinforcing sheets during compaction.

The test embankment was dismantled by cutting through the center of the sections vertically along the long axis of the embankment to measure the distribution of water content on the vertical face of the embankment. A total of 600 samples was taken from eight sections on the vertically cut faces of the embankment. Permeability coefficients at saturated conditions for undisturbed samples from Section 3-A are summarized in Table 5.

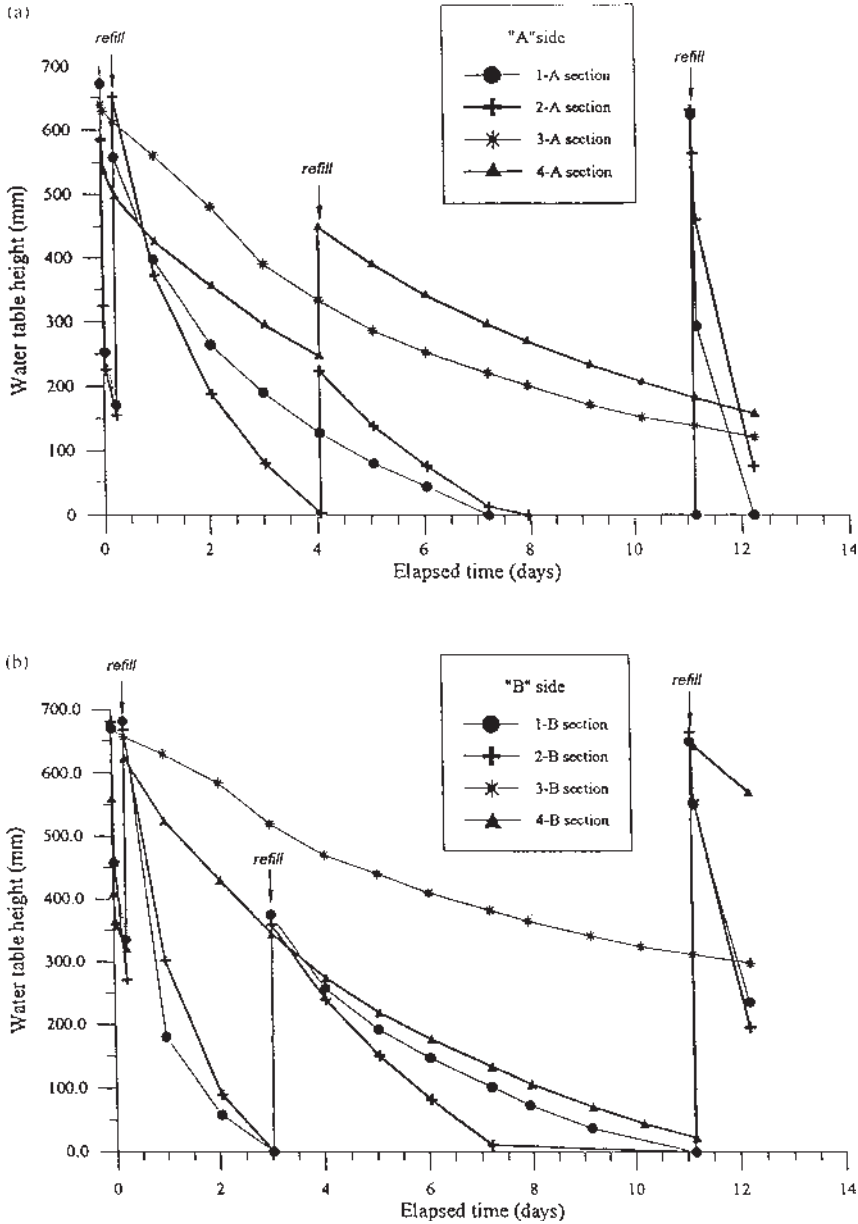

Figure 14 The measured water table heights versus time in the infiltration tests for test embankment: (a) A-side; (b) B-side.

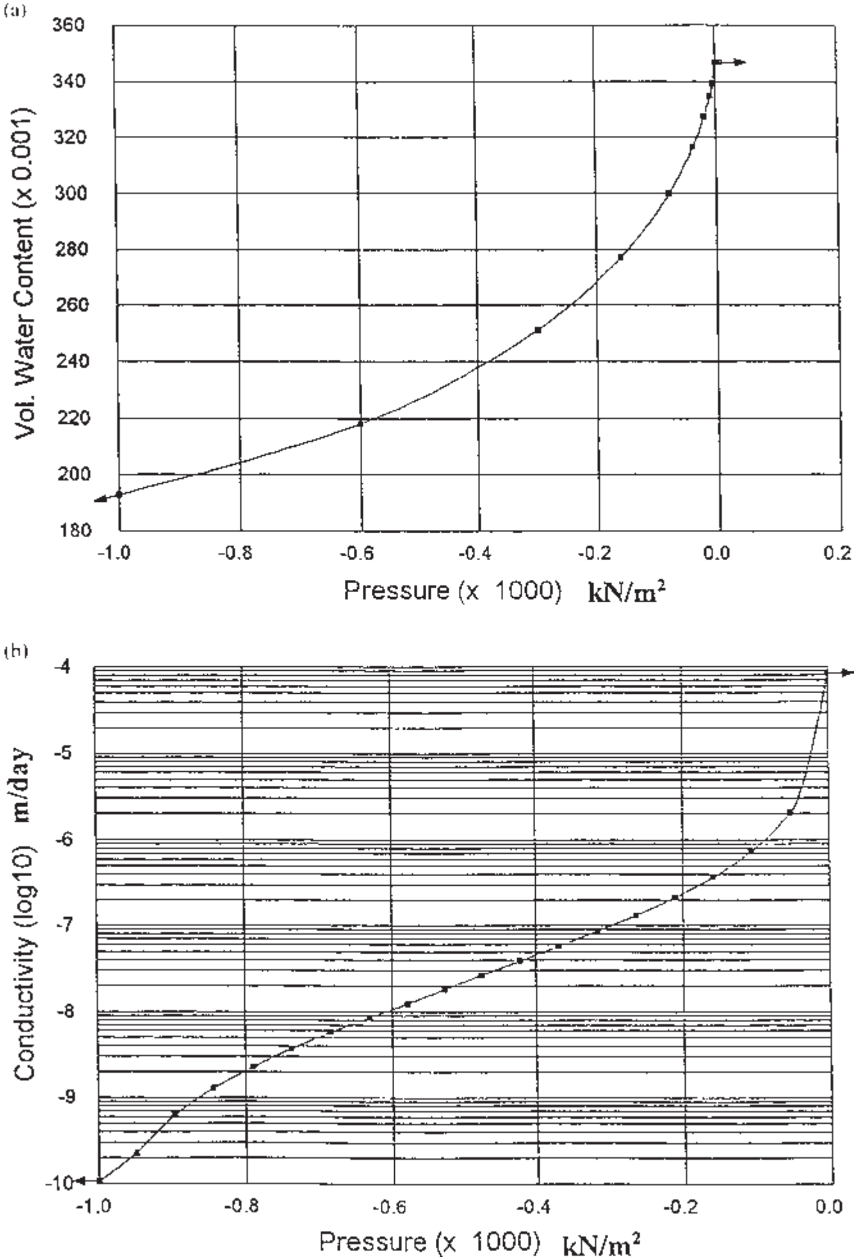

Figure 15 An undisturbed sample from NCKU wall: (a) pore pressure versus volumetric water content; (b) pore pressure versus conductivity in vertical direction.

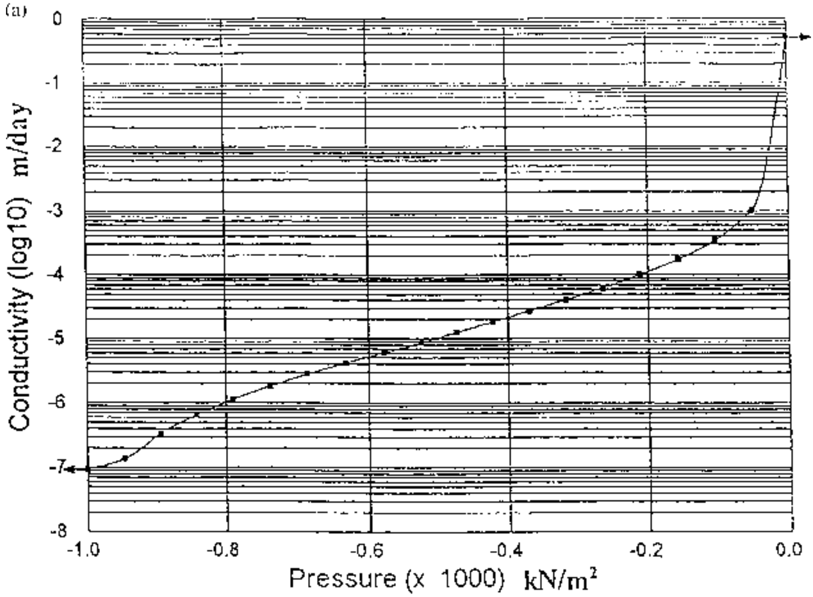

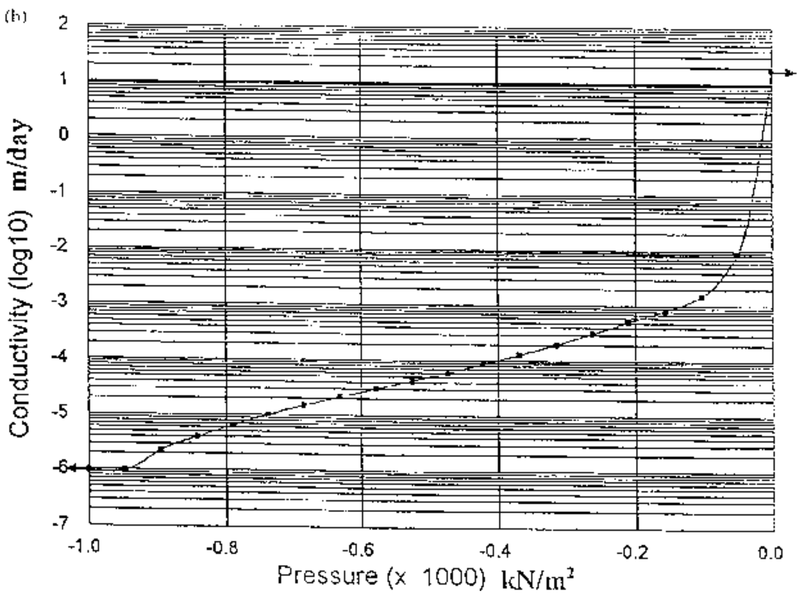

Figure 16 Pore pressure versus in-plane conductivity for the elements, including (a) geosynthetic composite, (b) geodrain, (c) geogrid.

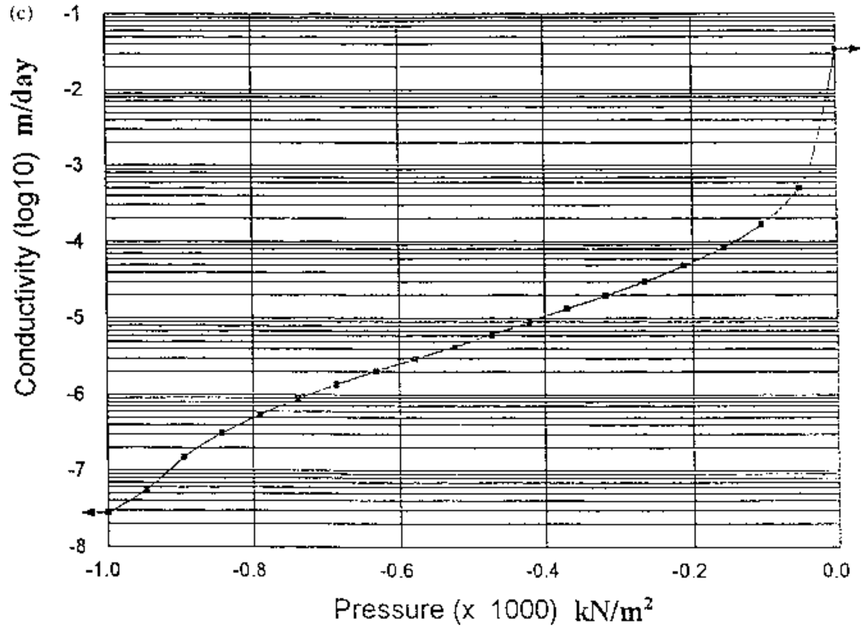

Figure 16 Continued.

8 FEM ANALYSES FOR NCKU WALLS AND EMBANKMENT

The volumetric water content (θ) versus suction relation for undisturbed samples from NCKU walls according to ASTM 3152 is shown in Fig. 15a. The permeability coefficients in the vertical direction (k_v) versus suction relation for NCKU wall based on the equations proposed by Green and Corey (1971) is shown in Fig. 15b. In the present study, the in-plane permeabilities of geosynthetic composite layers, geodrain layers, and geogrid layers were simulated by thin layers of uniform sand, gravel, and fine sand, respectively.

Equivalent permeability coefficients were used for the 50-mm-thick elements including geosynthetics. Example of equivalent in-plane permeabilites for geosynthetic composite, geodrain, and geogrid elements are shown in Fig. 16a, b and c, respectively. The following analyses were performed (Jean, 1998) using an FEM program SEEP/W (SEEP/W, 1994).

1. Infiltration tests using the trenches at the crest of NCKU walls (2nd–4th infiltration tests)

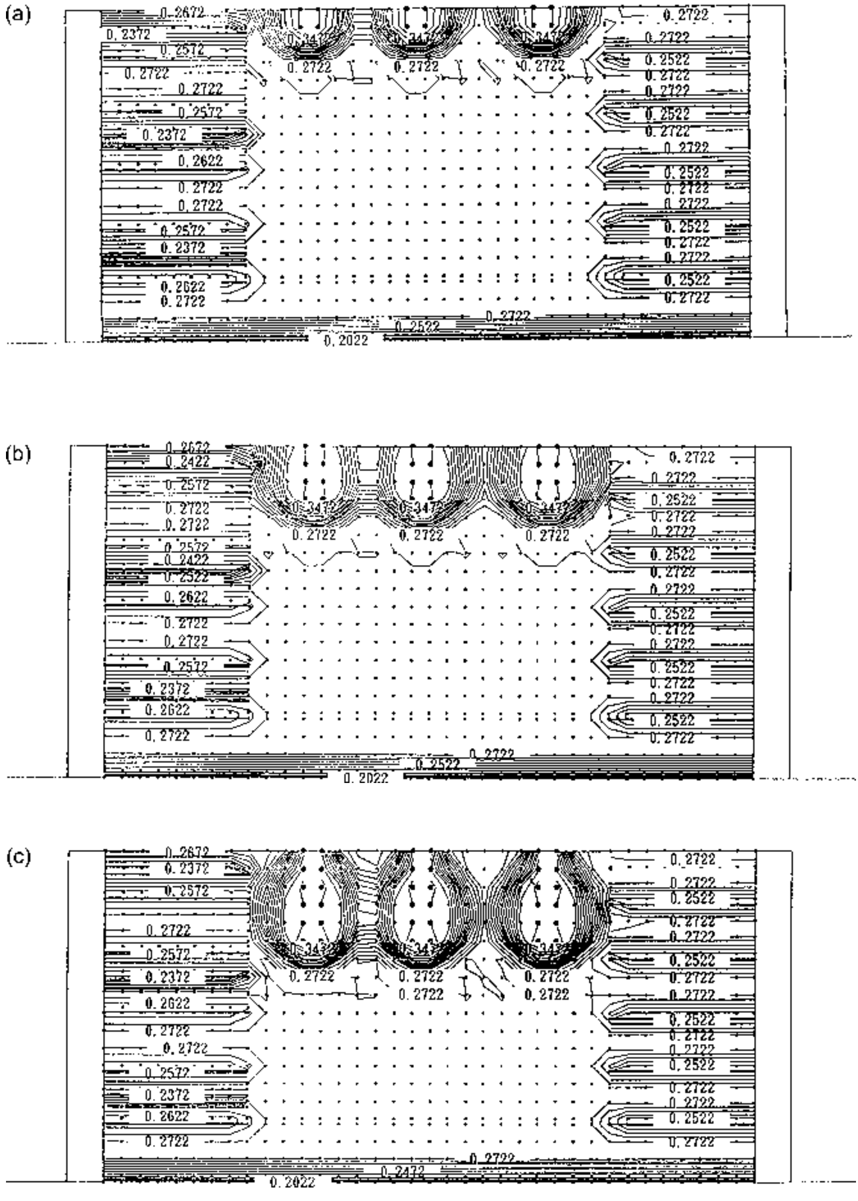

Figure 17 The influenced zones at the end-of-infiltration test in an FEM analysis: (a) second test; (b) third test; (c) fourth test.

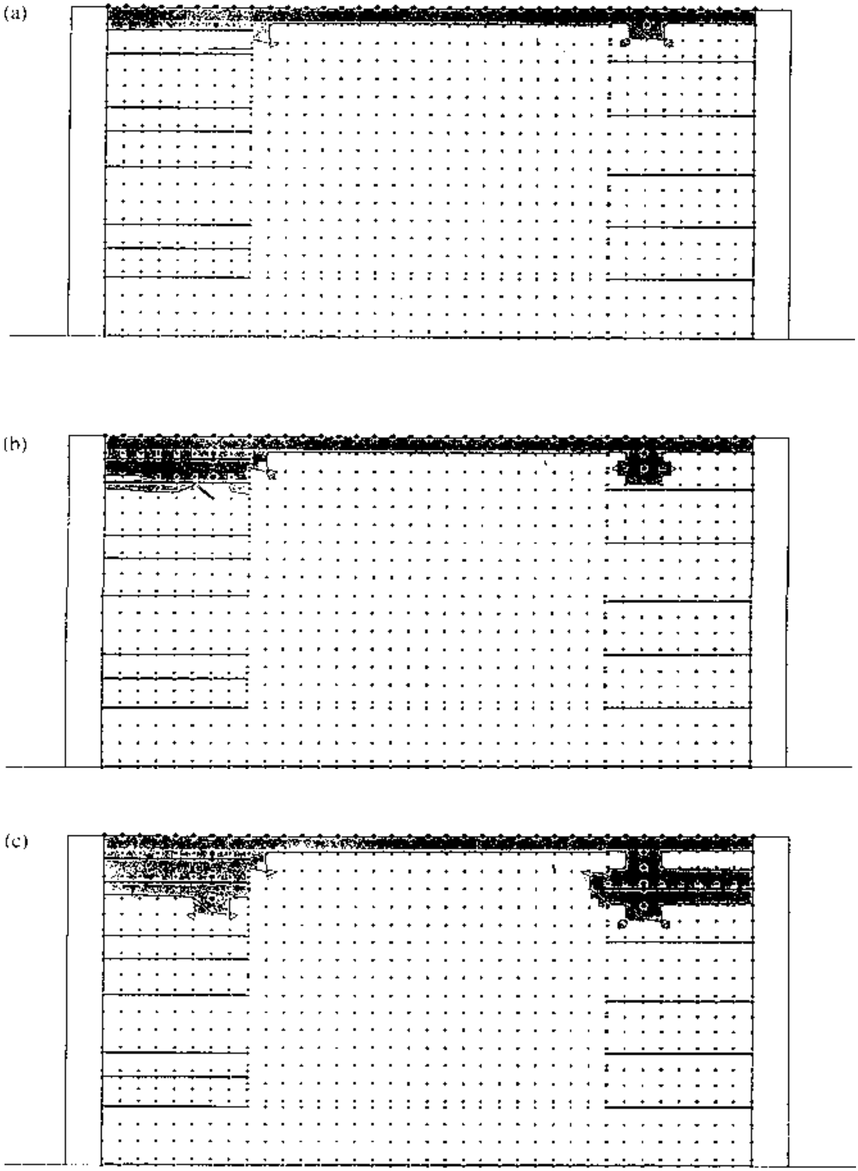

Figure 18 Influenced zones behind the reinforced zones at the end of 10 days assuming zero pore water pressure at the cracks and the crest of walls. Crack depth: (a) 0.15 m; (b) 0.3 m; (c) 0.6 m.

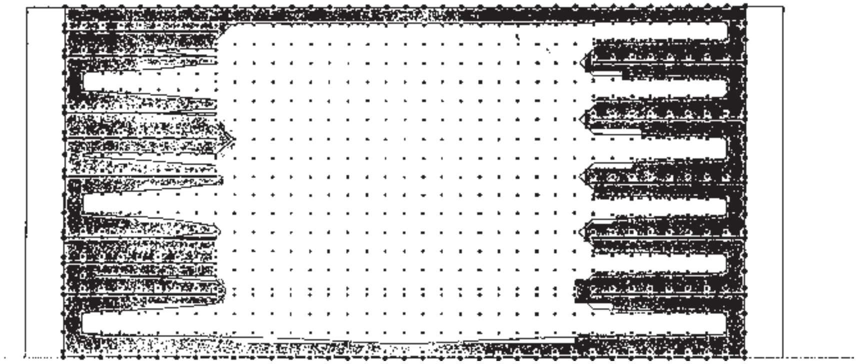

Figure 19 Influenced zones assuming saturated condition (zero pore pressure) at the crest and the side faces of the wall.

2. Infiltration tests performed for 10 days on tension cracks observed for NCKU walls assuming zero pore pressure at the top of the walls and cracks
3. Migrations of saturation fronts in the NCKU walls assuming surfaces of the walls were saturated at wall face during rainfall
4. Back-analysis of the infiltration test result for Section 3-A of the test embankment

Figure 17a–c show the contours of volumetric water content in the backfill of NCKU walls at the end-of-trench infiltration tests. The original volumetric water content at the completion of the walls was 0.27. It is seen that the influenced zones were quite limited. It is also seen that the geosynthetic composite layer played a positive role in lowering the water content in the reinforced zone. In analysis (2), the tension cracks were located immediately behind the reinforced zones as observed in the dismantling of NCKU walls.

The results are shown in Fig. 18a–c. It is seen that the reinforcement layers may have two functions when the tension cracks extend to a certain depth. These two functions include drainage in the horizontal direction and raising the water content in the vicinity of reinforcement layers. The result of analysis (3) is shown in Fig. 19. In this analysis, the boundaries (vertical wall faces and top of the walls) were assumed fully saturated due to a continuous rainfall for 10 days.

It is seen that the reinforcement layers played a negative role because they facilitated the penetration of saturation fronts into the backfill. It is considered

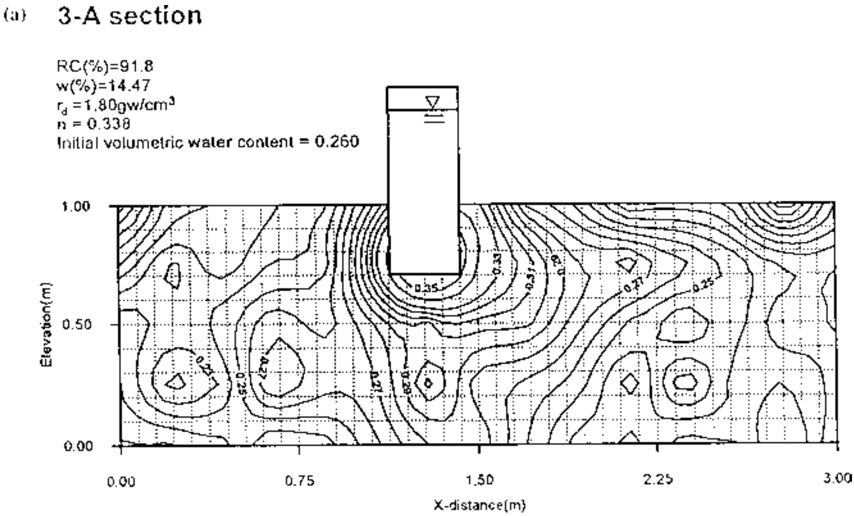

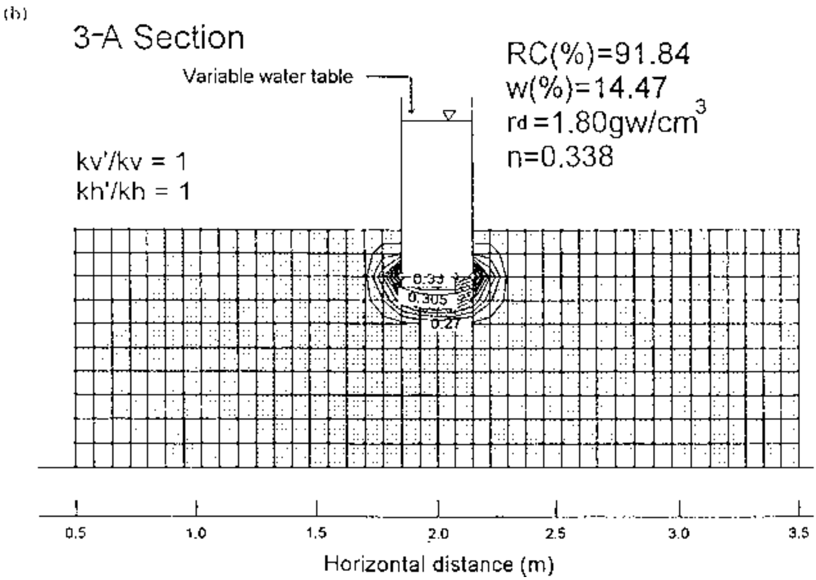

Figure 20 Water content distribution on vertically cut face of Section 3-A: (a) measured; (b) calculated using permeability coefficients obtained in-lab; (c) modified using adjusted permeability coefficients k_h' and k_v'.

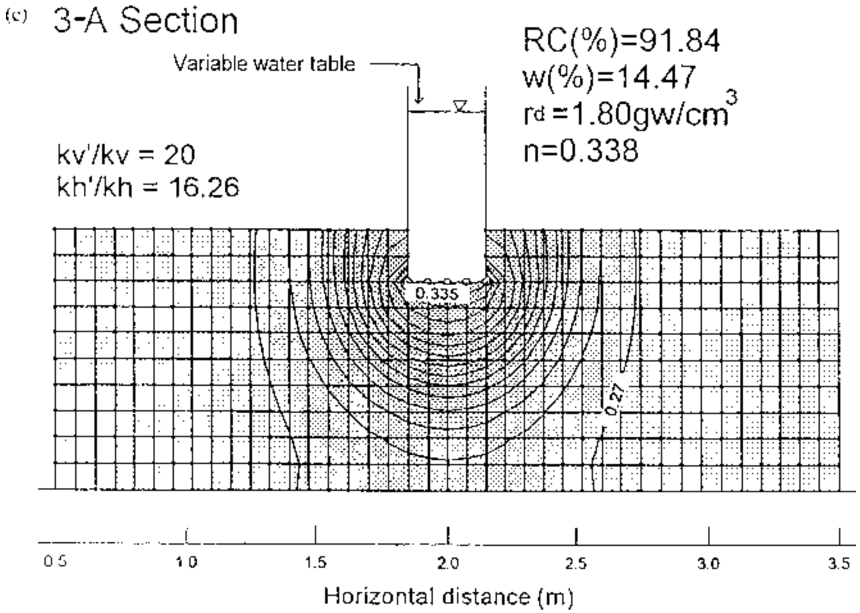

Figure 20 Continued.

that an impermeable facing as used in the RRR method could be an effective countermeasure.

Figure 20a and b show the measured and calculated contours of water contents for Section 3-A of the test embankment at the end-of-infiltration test. It is seen that the influenced zone (the area bounded by the contour of initial volumetric water content $\theta \fallingdotseq 26\%$) was underestimated in the analysis in both vertical and horizontal directions. The underestimation for the extent of influenced zone might result from the unrealistic permeability coefficients obtained in the in-lab permeability test. It is considered that the voids and the bedding planes that control the seepage characteristics of compacted clay in the embankment may not be properly simulated in the in-lab permeability tests. Calibration for the input parameters based on the measured water content distribution on Section 3-A was performed. A trial-and-error process was adopted to modify the calculated values of vertical permeability and horizontal permeability coefficients, k_v' and k_h'. Fig. 20c shows an example of calculated distribution of water content similar to that shown in Fig. 20a. In this case, $k_v'/k_v = 20$, $k_h'/k_h = 16$ (k_v and k_h: the permeability coefficients measured in-lab using undisturbed samples from Section 3-A), in order to obtain a similar pattern of water content distribution to that observed in the field.

9 CONCLUSIONS

Reinforced walls (NCKU walls) that are 2.7 m high were successfully constructed. Long-term monitoring on the behavior of the wall for 840 days was conducted. It was shown that the pore pressure increase in the soil mass had a strong relationship with the development of cracks or shear planes within the compacted clayey backfill. The deformation of the facing was in an overturning mode, and might be caused by the swelling of clay near the facing, the increase of pore water pressure in the tension cracks, or the creep at the soil–reinforcement interface. A 1-m-high test embankment using a compaction method similar to that used in the practice was constructed to investigate the infiltration properties of compacted clay. The results of the infiltration test at the crest of the embankment showed that the infiltration rate for the clay compacted at 3% wet-of-optimum was smaller than those compacted at 3% dry-of-optimum and the optimum water content conditions. It was also shown that the reinforcement sheets may raise the degree of compaction for the clay at 3% wet-of-optimum. FEM seepage analyses for unsaturated soil were performed to investigate the in-situ permeability coefficients in vertical and horizontal directions. It was shown that the permeability tests performed in-lab underestimated the permeability coefficients significantly. Results from FEM seepage analyses for NCKU walls indicated that cracks or shear planes always play a negative role in the stability of the clay wall, while geosynthetic composite layers may play both positive and negative roles depending on the initial pore pressure distributions in the backfill and the boundary of the wall. Using an impermeable facing and an geo-drain layer close to the crest of clay embankment could be an effective measure to mitigate the development of saturated zones in the clayey backfill.

ACKNOWLEDGMENTS

This research is financially supported by the National Science Council, Taiwan, R.O.C. under the contract nos. NSC 83-0209-E-006-022, NSC 85-2611-E006-031, NSC 86-2611-E006-023, and NSC 87-2211-E006-052. The authors appreciate the advice and the strong support from Professor K.S. Su, Department of Civil Engineering, National Cheng Kung University, in setting up the test facility. Grateful thanks are due to the San Lien Development Co., Ltd, for the technical support on the monitoring system. The assistance from Mr F. J. Guo, and Mr J. M. Jang, former graduate students at Cheng Kung University is also acknowledged.

REFERENCES

ASTM. D698-91: Test method for laboratory compaction characteristics of soil using standard effort. 1994 Annual Book of ASTM standards, Vol. 04.08.

AW Bishop. The use of the slip circle in the stability analysis of slopes. *Geotechnique* 5(1): 7–17, 1955.

RE Green, JC Corey. Calculation of hydraulic conductivity: A further evaluation of some predictive methods. *Soil Science Society of America Proc.* 35: 3–18, 1971.

FJ Guo. A study on the tensile strength of a geosynthetic composite. Master thesis of the Dept. Civil Engrg, National Cheng Kung University (in Chinese), 1995.

CC Huang, F Tatsuoka. Stability analysis for footings on reinforced sand slopes. *Soils and Foundations* 34(3): 21–37, 1994.

CC Huang, BN Huang, FY Menq, SR Tsai. Infiltration test on full-scale reinforced clay walls. *Proc. 3rd Int. Symp. Environmental Geotechnology* 1: 885–893, 1996.

CC Huang, BN Huang. Infiltration test on reinforced clay wall and test embankment. Proc. Int. Symp. Earth Reinforcement, IS Kyushu' 96, Fukuoka, Japan, pp 373–378, 1996.

CC Huang. Investigation of the local strains in a geosynthetic composite. Geotextiles and Geomembranes 16: 175–193, 1998.

M Itoh, A Shirasawa, K Kumagai. Well documented case study of a reinforced soil wall. Fifth Int. Conf. on Geotextiles, Geomembranes and Related Products, Singapore, Sept. 1994, pp 255–258, 1994.

GY Jean. Anisotropic seepage analysis for reinforced clay walls. Master thesis, Dept. Civil Engrg, National Cheng Kung University, 1998 (in Chinese).

RA Jewell. Application of revised design charts for steep reinforced slopes. *Geotextiles and Geomembranes* 10(3): 203–233, 1991.

RM Koerner. Designing with Geosynthetics, ed 4. Prentice Hall, Englewood cliffs, New Jersey. 1998.

D Leshchinsky, J Fowler. Laboratory measurement of load-elongation relationship of high-strength geotextile. *Geotextiles and Geomembranes* 9: 145–164, 1990.

SEEP/W. User's Guide, version3, Geo-Slope International Ltd, Calgary, Alberta, Canada, 1994.

F Schlosser. Mechanically stabilized earth retaining structures. Proc. Conf. Design and Performance of Earth Retaining Structures, Geotech. Special Publication, No. 25, ASCE, pp 347–378, 1990.

F Tatsuoka, O Haibara. Shear resistance between sand and smooth or lubricated surfaces. *Technical notes, Soils and Foundations* 25(1): 89–98, 1985.

F Tatsuoka, H Yamauchi. A reinforcing method for steep clay slopes using a non-woven geotextile. *Geotextiles and Geomembranes* 4: 241–268, 1986.

F Tatsuoka, O Murata, M Tateyama. Permanent geosynthetic-reinforced soil retaining walls used for railway. Proc. Int. Symp. Geosynthetic-reinforced Soil Retaining Walls, Denver, CO, 1991, pp 101–130, 1992.

SR Tsai. Measurement on the strains of geotextiles. Master thesis, Dept. Civil Engrg, National Cheng Kung University, Taiwan, 1996 (in Chinese).

JTH Wu. Construction and instrumentation of the Denver walls. Proc. Int. Symp. Geosynthetic-reinforced Soil Retaining Walls, Denver, CO, 1991, pp 21–30, 1992.

13

Geotextile Reinforced Abutments on Soft Foundation

Ennio M. Palmeira and André R. S. Fahel
University of Brasilia, Brasilia, Brazil

Luiz E. P. Campos
Federal University of Bahia, Salvador, Brazil

ABSTRACT

This paper describes the use of geosynthetic reinforced structures in bridge abutments on soft foundation soils. The characteristics of five geotextile reinforced walls constructed on compressible subsoil are presented and discussed. Four of these walls were built on concrete piles with caps, and one was built directly on a sand layer overlaying a soft clay deposit. The designers seem to have aimed for a stiff reinforced mass to distribute stresses to the foundation soil or to minimize differential settlements. Despite rather large vertical or horizontal displacements having been observed in some cases, in general the reinforced structures behaved well. Even in one of the cases where a flood caused severe damage to the reinforced mass, the structure was still able to keep the highway in good operational conditions. These performances enhance the advantages of using flexible retaining structures in problems where severe differential settlements can occur.

1 INTRODUCTION

Geosynthetic reinforced retaining walls and steep slopes have been extensively used in the last two decades. The main reasons for that are its cost-effectiveness, improvements in geosynthetic material properties, design procedures, and better controlled construction techniques. Because they are flexible structures, geosynthetic retaining walls are likely to accept differential settlements rather well. Therefore, its use should be considered when dealing with compressive foundation soil layers, where other solutions might not be appropriate. In these cases geosynthetic reinforced walls may provide a suitable structure in terms of flexibility and savings in maintenance costs due to repairs required by any damage caused by differential settlements (facing damages, for instance). As will be seen later in this chapter, in some cases the settlements may be significant but the structure can still be operational.

This chapter describes the design, construction, and performance of five geotextile reinforced retaining walls used in bridge abutments on soft foundations. These walls were designed and constructed by the geotechnical engineering companies Tecnosolo and Odebrecht, respectively, and were built on soft clay layers with different philosophies to deal with consolidation settlements. The following sections present and discuss the details and performance of these works.

2 SITE AND PROJECT CHARACTERISTICS

2.1 Site Characteristics

The reinforced bridge abutments described in the present work were built in the Linha Verde highway, which is located in the north region of the state of Bahia, Brazil (Fig. 1). This highway is very important for tourism purposes because it runs close to the sea line crossing several cities and sites of natural beauty. The subsoil of the region consists of sedimentary layers with thicknesses reaching up to 25 m. The thickness of the soft layer deposits varies from 1 to 12 m and is particularly thicker close to the rivers crossing the region, where the sedimentation process was more intense. A typical subsoil profile in the region of construction of the reinforced retaining walls shows a layer of very clayey sand, loose to fairly dense, with thicknesses varying between 2 to 5 m, overlaying compressible organic silty clay deposits with thicknesses varying from 2 to 14 m. Values of N from Standard Penetration Tests in the soft soil deposits varied between 0 and 4, and the average undrained strength from vane tests carried out in some sites varied between 10 and 60 kPa, depending on the site. Fig. 2a and b shows the results of field vane tests performed at the sites of

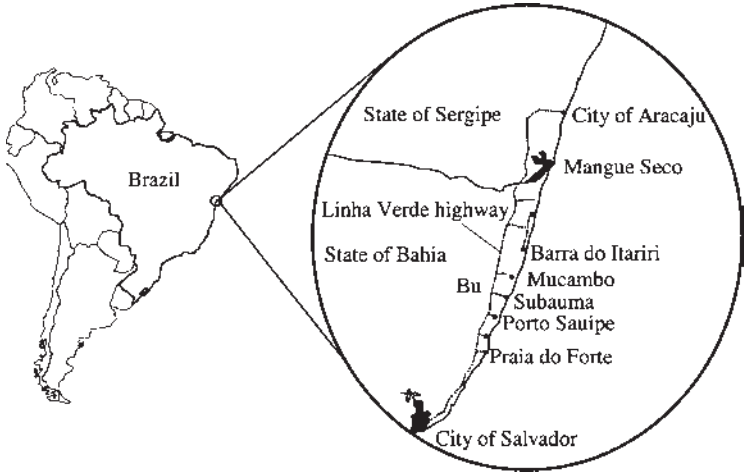

Figure 1 Location of the sites.

the Itariri river and Mucambo river walls. The scatter of the vane test results can be attributed mainly to the organic matter content in the soft clay.

2.2 Case Histories Studied

Five case histories of bridge abutments using geotextile reinforced retaining wall structures were selected. Due to the similarity between the general conditions of the sites, the designers suggested the use of a rather standard cross section for the reinforced embankment. The main characteristics of these case histories are summarized below.

2.2.1 Sauipe River Structure

This structure was 2 m high and was built on a foundation soil consisting of a 4.5-m-thick clayey sand layer overlaying a 5.7-m-thick organic clay layer. A typical cross section of the subsoil and relevant dimensions are presented in Table 1. The main geometrical characteristics of this wall are schematically presented in Fig. 3 and in Table 2. The wall facing units were "L"-shaped and made of concrete in a segmental fashion. The dimensions of the facing units for all structures were the same, being 0.6 m high, 0.55 m wide, 0.09 m thick, and 1.0 m long. The fill material for the Sauipe River structure was a fine silty sand present in the region, and its characteristics are summarized in Table 3. The reinforcement used in this case history was a needle-punched nonwoven geotextile, made of polyester,

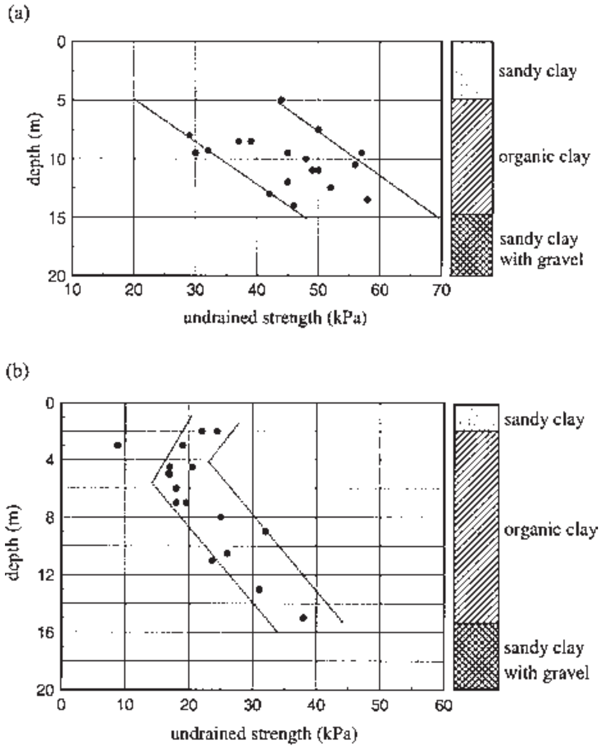

Figure 2 Undrained strength variation with depth from field vane tests: (a) Itarirí structure; (b) Mucambo structure.

commercially available under the name of Bidim OP 30, hereafter referred as geotextile A. The main characteristics of this geotextile are presented in Table 4. The reinforcement layout of the reinforced zone is shown in Fig. 3 and similar layouts were employed in the other case histories to be described later in this

Table 1 Typical Cross Section of the Subsoil for Each Case History

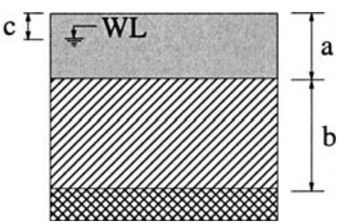

Structure	*a* (m)	*b* (m)	*c* (m)
Sauípe	4.5	5.7	1.5
Subaúma	2.0	3.0	0.6
Bú	2.5	3.6	0.8
Mucambo	2.0	9.5	0.6
Itarirí	1.7	7.8	1.6

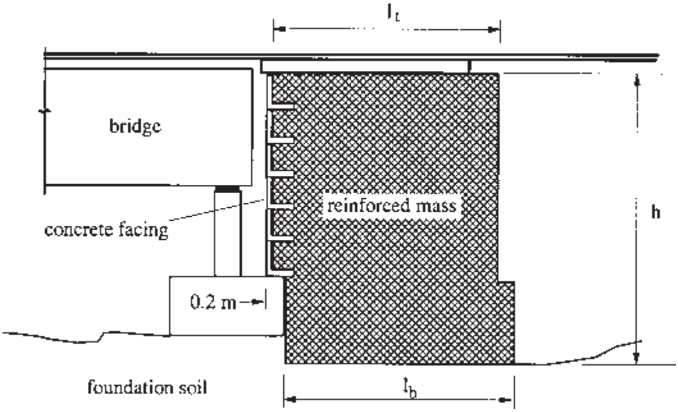

Figure 3 Schematic cross section of Sauipe River reinforced abutment.

work, as commented above. The spacing between reinforcement layers was 0.3 m, and the length of the reinforcement was equal to 3.2 m. It can be observed that the designers heavily reinforced the embankment, aiming for a more uniform settlement distribution.

2.2.2 Bu River Structure

This retaining wall is 7.3 m high and its general characteristics are schematically shown in Fig. 4. Additional information on the reinforcement layout can be found in Table 2. Because of the high compressibility of the foundation soil in this case, the reinforced structure was supported by 0.25-m-diameter piles with caps (1 × 1 × 0.3 m) with 1.25-m spacing distributed in a square pattern. The soil used in the embankment was a clayey sand whose properties are presented in Table 3. The foundation profile (Table 1) shows the presence of a 2.5-m-thick clayey sand layer on a 3.6-m-thick organic silty clay deposit. Nonwoven geotextile A (Table 4) was used as reinforcement in this case. The distribution of reinforcement layers along the wall height was divided in two parts (Fig. 4 and Table 2). In the lower part (up to 2.5 m above the base of the wall) the spacing between reinforcement layers was equal to 0.2 m with a reinforcement length of 8.9 m, while in the upper part of the wall the spacing between reinforcements was equal to 0.3 m with 3.2-m-long reinforcement layers.

2.2.3 Subauma River Structure

The reinforced structure used in the abutment for the crossing of the Subauma River was only 1.75 m high and was also built on 0.25-m-diameter concrete

Table 2 Characteristics of the Reinforced Structures

Structure	Bridge span (m)	h (m)	s (m)	l_t (m)	l_b (m)	n	Foundation treatment[(1)]
Sauípe	80	2.00	0.3	3.2	3.2	7	None
Subaúma	75	1.75	0.2–0.3[(2)]	3.2	3.2	6	Piles
Bú	40	7.30	0.2–0.3[(2)]	3.2	8.9	28	Piles
Mucambo	60	2.70	0.3	5.3	3.25	8	Piles
Itarirí	40	3.80	0.3	3.2	3.2	12	Piles

h = height of the reinforced structures, s = spacing between reinforcement layers, l_t = length of the reinforcement layers in the upper part of the structure, l_b = length of the reinforcement layers in the lower part of the structure, n = number of reinforcement layers. See also Figs. 3–6.

[(1)] Type of solution for load-transference to stronger foundation layers below the reinforced zone.

[(2)] 0.2-m spacing between reinforcements along the lower part of the structure (first 2.5 m from the base) and 0.30-m spacing along the upper part of the structure.

piles with caps (1 × 1 × 0.3 m) with 1.25-m spacing in a square pattern. The reinforced wall layout is schematically shown in Fig. 5. The fill material used was a clayey sand (Table 3). The foundation soil for this wall consists of a 2-m-thick sand layer overlaying a 3-m-thick organic clay (Table 1). The reinforcement type for this structure was a woven geotextile, hereafter referred to as geotextile B, made of polypropelene, with 0.3-m spacing between geotextile layers and with a length of 3.2 m. This reinforcement is commercially available under the name Propex 2004, and its main characteristics are summarized in Table 4.

2.2.4 Itarirí River Structure

The reinforced structure in this case was 3.8 m high and was also constructed on 0.25-m-diameter piles with 1 × 1 × 0.3 m caps with 1.25-m spacing in a square pattern. The reinforced wall layout is schematically shown in Fig. 5. The foundation soil is formed by a 1.7-m-thick top clayey sand layer over a 9.5-m-thick soft to medium organic silty clay, as shown in Table 1. The variation of undrained strength with depth for the soft clay layer is presented in Fig. 2a. Nonwoven geotextile A (Table 4) was also used in this case with a spacing between layers of 0.3 m and a reinforcement length equal to 3.2 m.

2.2.5 Mucambo River Structure

For the crossing of the Mucambo River, a 2.7-m-high geotextile reinforced retaining structure was built as part of the abutment for a 60-m-span concrete bridge. The base of the reinforced structure (3.25 m long) was built on a concrete slab supported by concrete piles (0.25-m-diameter, 1.25-m spacing in

Table 3 Characteristics of the Fill Materials

Structure	Type of soil	G	D_{10} (mm)	D_{50} (mm)	C_u	γ (kN/m^3)	c' (kPa)	ϕ' (deg)
Sauípe	Silty sand	2.66	0.001	0.20	280	19.9	31.8	36.1
Subaúma	Clayey sand	2.64	0.0002	0.21	1350	19.8	29.2	37.8
Bú	Clayey sand	2.66	0.0001	0.25	3000	20.2	16.3	41.1
Mucambo	Sand	NA	NA	NA	NA	18.5	0	29.9
Itarirí	Sand	NA	NA	NA	NA	20.1	4.6	28.1

NA = value not available. c' and ϕ' obtained from drained direct shear tests. γ, c', and ϕ' = specific weight, effective cohesion, and effective friction angle at optimum moisture content, respectively. G = specific gravity of the soil particles, D_{10} and D_{50} = particle diameters corresponding to 10% and 50% passing, respectively, C_u = coefficient of uniformity (= D_{60}/D_{10}).

a square pattern), as shown in Fig. 6. The rest of the embankment was built on the same type of piles and caps ($1 \times 1 \times 0.3$ m) with a layer of geotextile on top (Fig. 6). The soil used in the embankment was a fine sand (Table 3). The foundation soil of this wall is composed by a 2-m-thick layer of clayey sand over a soft organic clay layer with undrained strength typically varying between 10 and 45 kPa along its depth (Fig. 2b and Table 1). Geotextile A (Table 4) was also employed as reinforcement for this structure. The spacing between geotextile layers used was equal to 0.3 m and the reinforcement length was equal to 3.25 m.

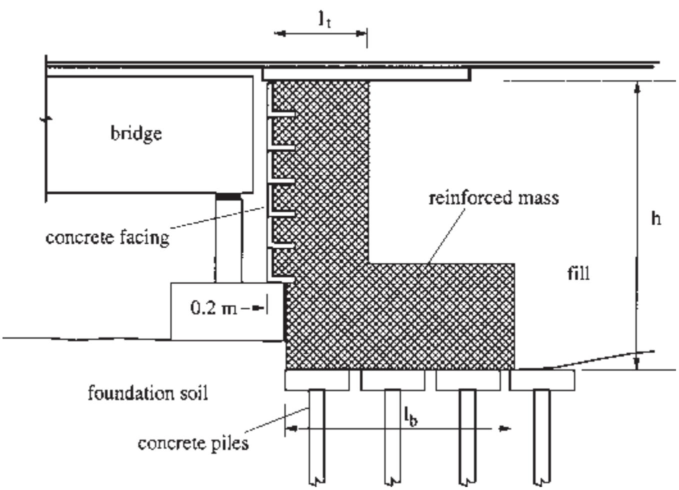

Figure 4 Schematic cross section of the Bu River reinforced abutment.

Table 4 Characteristics of the Geotextiles

Structures	Geotextile code	Geotextile type	μ (g/m^2)	T_{max} (kN/m)	ϵ_{max} (%)	J_{sec} (kN/m)
Sauipe, Bu, Mucambo, and Itarirí	A[(1)]	Nonwoven	300	20[(3)]	45[(3)]	50[(3)]
Subauma	B[(2)]	Woven	138	22[(4)]	15[(4)]	128[(4)]

μ = mass per unit area, T_{max} = tensile strength, ϵ_{max} = tensile strain at failure, and J_{sec} = secant tensile stiffness corresponding to 5% tensile strain.
[(1)] Geotextile A is a nonwoven, needle-punched geotextile made of polyester commercially available under the name of Bidim OP30.
[(2)] Geotextile B is a women geotextile, made polypropilene, commercially available under the name of Propex 2004.
[(3)] Values obtained from wide strip tensile tests according to ASTM D4595.
[(4)] Results from wide strip (20 cm wide) tensile tests conducted under a 2%/min strain rate.

3 PERFORMANCE OF THE REINFORCED STRUCTURES

In general, in spite of the severe conditions of the foundation soil in terms of compressibility, the reinforced structures have behaved well so far. However, some problems caused by consolidation settlements and floods were observed and are discussed below.

The Sauipe reinforced structure was the one presenting the greatest surface settlements. This was mainly due to the fact that this structure was constructed directly on the top sand layer, without piles in the foundation. Therefore, significant vertical stress increments reached the soft clay layer underneath, causing settlements. The maximum settlement observed reached a value of 0.29 m at the wall face decreasing along a length of 21 m away from the wall. The maximum horizontal displacement of the wall crest was equal to 5.5 cm, and the wall face rotated with respect to its crest. The heavily reinforced mass behaved as a rigid body regarding the neighboring soils. This pattern of wall rotation and behavior has also been observed in model tests of geosynthetic walls on soft subgrades (Monte, 1996; Palmeira and Monte, 1997) where the greatest face horizontal displacements occur at the toe of the wall. Figure 7 shows some results presented in Palmeira and Monte (1997) where the rotation of the wall face of one of the model walls can be clearly seen, as commented above. Figure 8 presents a general view of the surface of the highway showing the repairs in the asphalt cap close to the reinforced structures that were required to maintain the road operational after the settlements caused by the foundation soil consolidation.

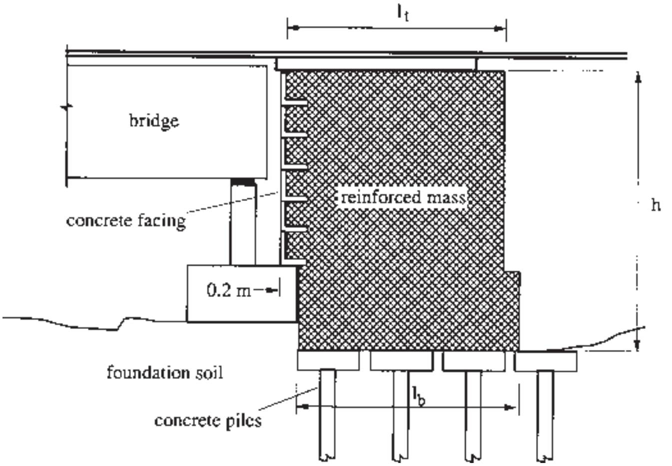

Figure 5 Schematic cross section for Subauma and Itarirí rivers reinforced abutments.

Figure 9 shows some damage to the wall face caused by rotation of the facing elements due to differential settlements. Up to 9 cm relative movement between facing units was observed, as well as some cracks. From these figures it is clear that some improvement of the foundation soil should also have been carried out in this case in order to minimize the development of differential settlements.

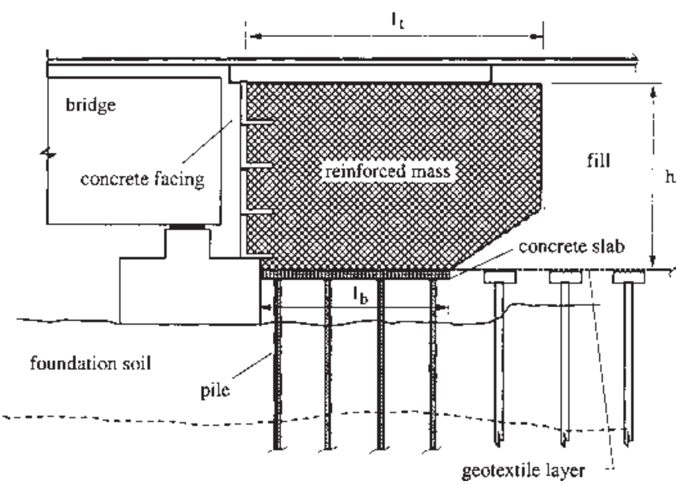

Figure 6 Schematic cross section for Mucambo River reinforced abutments.

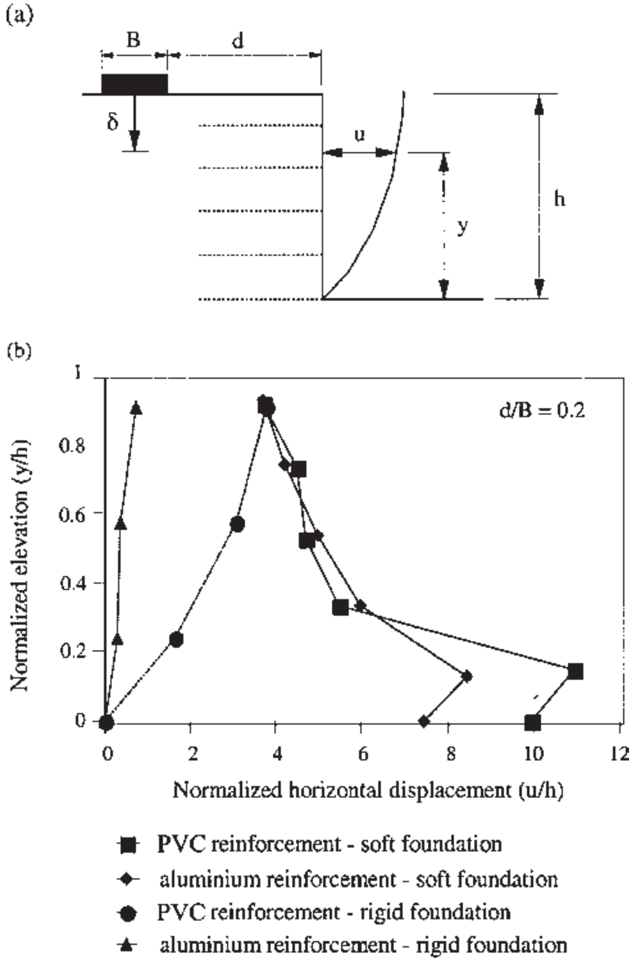

Figure 7 Horizontal displacements of the wall face in model tests on foundations with different stiffness: (a) schematic view of the model tests; (b) normalized horizontal displacement versus normalized elevation. (From Palmeira and Monte, 1997.)

The Subauma and Itariri reinforced structures and the highway surfaces were not affected by any significant settlement of the foundation soil nor showed any significant wall face horizontal displacements. This was certainly due to the low height of these structures and to the use of piles along the reinforced mass base and below the highway embankment.

Figure 8 Repair of the pavement surface at the Sauipe River abutment.

For the Bu reinforced abutment no significant settlement of the highway surface was observed so far. This was the highest reinforced structure (7.3 m high), and this absence of surface settlement can also be credited to the use of piles along the structure base. However, horizontal movements of the wall face were observed, as shown in Fig. 10. The maximum horizontal displacement of the wall occurred at its crest and was equal to 4 cm (approximately 0.55% of the wall height).

A severe damage to the reinforced structure of the Mucambo River abutment was caused by a flood of the river, as presented in Fig. 11. The flood caused the erosion of the fill material below the concrete slab at the base of the reinforced mass. This led to settlements of the rear part of the structure with the collapse of several facing units (Fig. 11). In spite of this severe distortion of the reinforced mass, the highway was still operational with some repairs needed in the asphalt cap, particularly at the edge of the lane immediately above the collapsed facing units, as shown in Fig. 12. This shows that the flexible geotextile reinforced structure was able to sustain large differential settlements and to accommodate them with minor damage to the highway pavement.

Additional studies on the performance of the geotextile reinforced abutments are being carried out (Fahel, 1998) as part of a research program on the behavior of reinforced structures on soft soils at the University of Brasilia, Brazil.

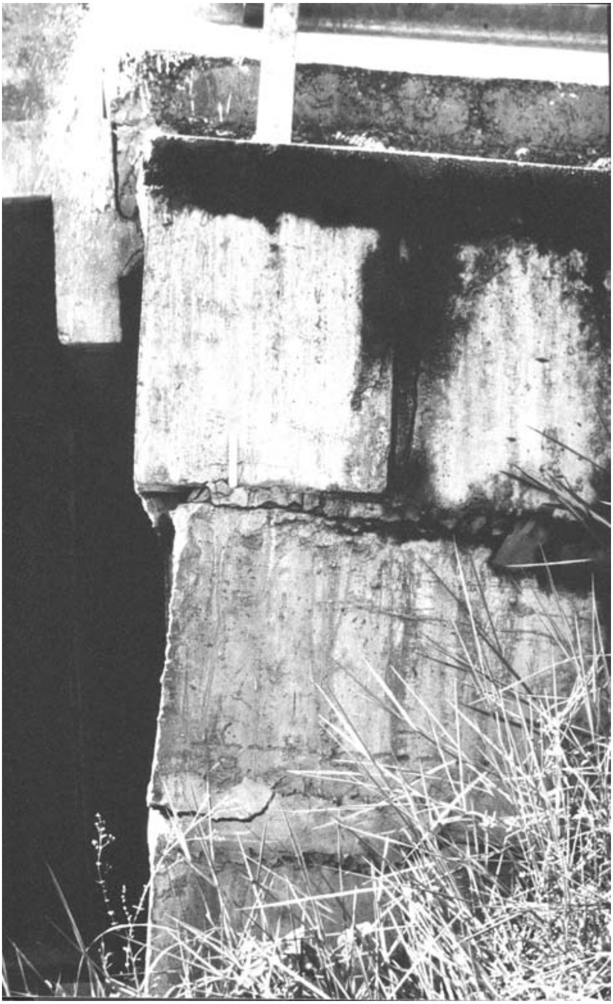

Figure 9 Relative movement and damages of wall facing units in the Sauipe River structure.

4 CONCLUSIONS

The present chapter deals with the performance of geotextile reinforced abutments on compressible foundations. The main conclusions of this work are summarized below:

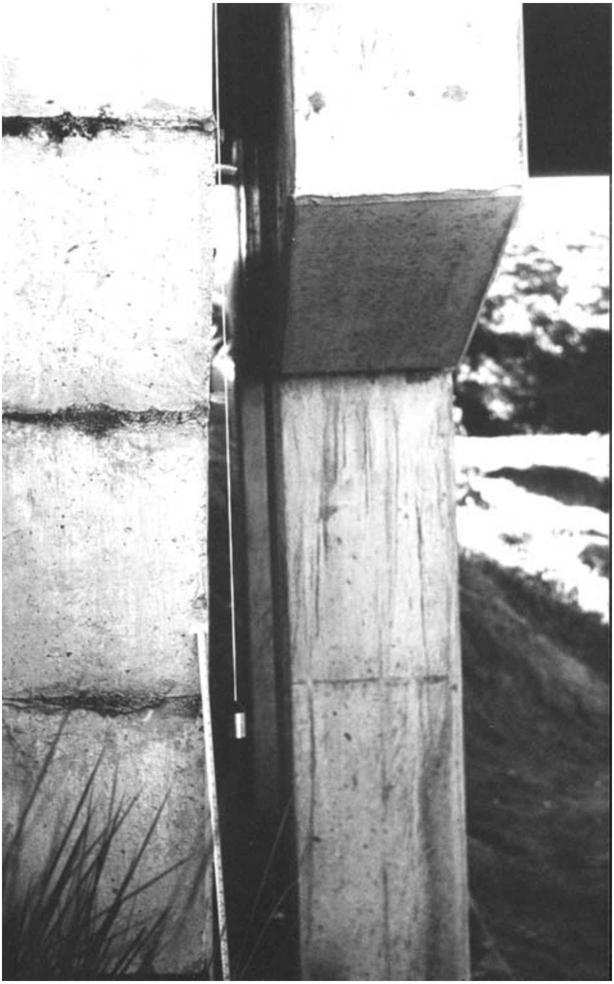

Figure 10 Face movement of the Bu River structure wall facing units in the Sauipe River structure.

1. Despite some large vertical displacements having occurred, in general the geotextile reinforced walls are behaving well so far. In terms of the faces of the walls, only minor damage was observed in the concrete elements in some cases.
2. The structures were heavily reinforced and the aim of the designers with the use of reinforcements in the abutments seems to have been to

Figure 11 Face units collapse in the Mucambo River reinforced structure after a river flood.

obtain a better stress distribution to the foundation soil and to minimize the effect of differential settlements close to the bridge structure. This, however, creates regions with significantly different stiffnesses (reinforced mass and backfill) and if the foundations soil settlements are not prevented by some effective way, damage to the pavement can occur, as was observed in some cases.

3. The use of piles with caps along the base of the structures improved their performances and no damage or noticeable vertical displacements were observed where this solution was employed.
4. The Sauipe River reinforced structure was placed directly on a layer of sand overlaying the soft clay. The thickness of this sand layer was not enough to prevent significant stress increments to reach the soft soil deposit. Therefore, large vertical displacements were observed in this structure that caused some damage to the highway pavement that had to be repaired. Since then no additional repair was necessary. However, repairs may still be required in the future due to further settlements caused by the consolidation of the soft clay.
5. The Mucambo River structure had its lateral face severely damaged by a flood. Even with the erosion of part of the backfill soil and loss of some facing elements, the reinforced mass was still able to sustain the large differential settlements that took place and only minor damage was observed in the highway.

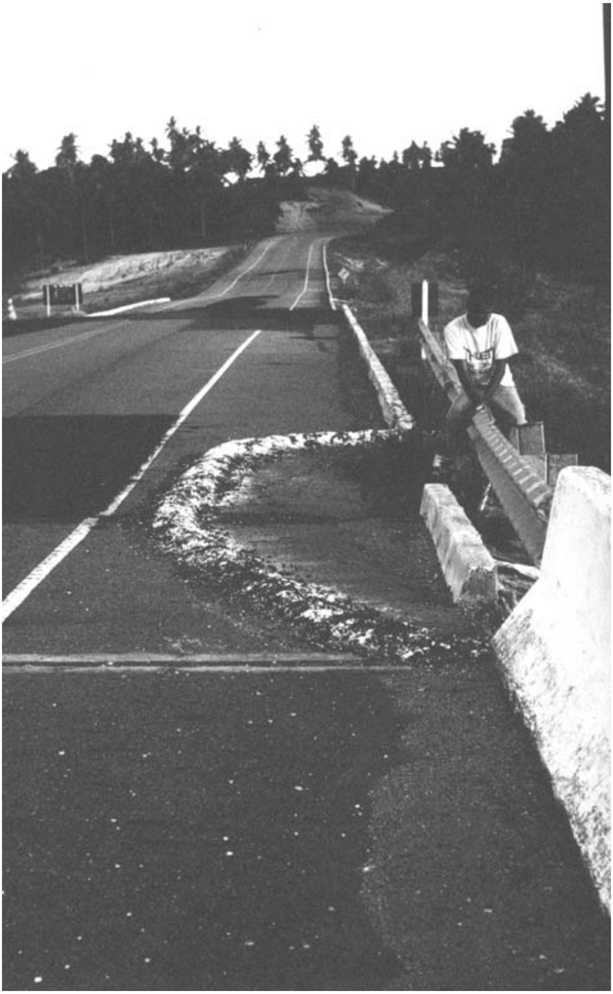

Figure 12 Damage to the lane in the Mucambo River structure.

6. The performance of the structures described in this work shows the potentials of the use of flexible geosynthetic reinforced retaining structures in problems where large differential settlements may occur. Nevertheless, further research is required for a better understanding of the behavior of reinforced abutments on soft subgrades.

ACKNOWLEDGMENTS

The authors are indebted to the following persons and institutions that made this work possible: Evangelista C. Fonseca, Federal University of Bahia Geotechnical Laboratory, Tecnosolo S.A., DERBA/Bahia State Highway Department, University of Brasilia, Bidim-BBA Geosynthetics, Amoco Geosynthetics, and CAPES/Brazilian Ministry of Education.

REFERENCES

A Fahel. The performance of some geotextile reinforced structures of bridge abutments on soft soils. M.Sc. Thesis, University of Brasilia, Brasilia, Brazil, in progress, 1998 (in Portuguese).

LM Monte. A study on the mechanisms of failure and deformation of reinforced retaining walls on soft subgrades. M.Sc. Thesis, University of Brasilia, Brasilia, Brazil, 1996 (in Portuguese).

EM Palmeira, LM Monte. The behaviour of model reinforced walls on soft soils. Geosynthetics '97, Long Beach CA, 1:73–84, 1997.

14

Geosynthetic Reinforcement in the Mitigation of Pipeline Flotation

Yoshiyuki Mohri
National Research Institute of Agriculture Engineering, Tsukuba, Japan

Toshinori Kawabata
Kobe University, Kobe, Japan

Hoe I. Ling
Columbia University, New York, New York, U.S.A.

ABSTRACT

This chapter describes a series of experiments where geosynthetic reinforcement was used with the pipeline buried at a shallow depth. The geosynthetic was used to confine the materials around the pipe. It was observed that the resistance to flotation increases with the additional resistance offered by the overburden weight when the geogrid confines the gravels in place. A simple force equilibrium equation between the overburden weight and buoyancy is suggested for design.

1 INTRODUCTION

The geosynthetic reinforcements are being used effectively to tensile reinforce soil structures, such as foundations and slopes (Koerner, 1998). The mechanism of reinforcement has been revealed through laboratory as well as field testings. Many successful field constructions implied feasibility of extending geosynthetic reinforcement to other important applications.

The uplift behavior of pipe has been studied, for example, by Trautmann et al. (1985). The behavior of buried pipelines is affected by the groundwater. The buoyancy of the water acts on the pipes so that a minimum depth of burial is required. The designs conducted by considering force equilibrium between the prism load and buoyancy are costly. The cost is accelerated if the diameter of the pipes is larger because a deeper excavation is involved. To reduce the cost, the burial depth of the pipe has to be minimized.

This paper deals with the flotation of pipelines where geosynthetics are used to mitigate flotation. Full-scale tests were conducted, and the results are reported and discussed herein.

2 MATERIALS

A large test pit available at the National Research Institute of Agricultural Engineering (NRIAE) was used for the experiment. The test pit measured 3 m by 5 m and was 3 m deep. This test pit was constructed to allow the control of water table in it.

The full-scale pipe model was used in the tests. The inner diameter and thickness of the pipe were 110 cm and 1.32 cm, respectively. It was manufactured from fiberglass reinforced plastic mortar. Its gross weight was 1.27 kN/m. The pipe was 290 cm long, to fit the width of the test pit.

The flotation of pipe model was mitigated by confining the backfill material using a geosynthetic reinforcement. The sand, gravel, and soil cement were used as backfill materials. The sand, gravel, and soil cement had a dry unit weight $\gamma_d = 14.75$ to $15.52\,\mathrm{kN/m^3}$, $19.61\,\mathrm{kN/m^3}$ and $15.14\,\mathrm{kN/m^3}$, respectively.

A polypropylene biaxial geogrid was used. Its aperture size was 2.8 cm (machine direction) by 3.3 cm (cross-machine direction). The mass per unit area was $550\,\mathrm{g/m^2}$ and the strength was 46 kN/m.

3 TESTING PROGRAM

Table 1 and Fig. 1 give the details and cross section for the five cases of testing. Test 1 was conducted as a control case where the backfill soil was not treated. Tests 2 and 3 used gravel as the backfill material. In tests 4 and 5, the soil cement was used. The testing procedure is illustrated in Fig. 2.

In the test without geogrid, first the pipe model was placed on the foundation in the test pit. A vibratory compactor was used. The backfill soil was

Table 1 Description of Testing Models

Test	Descriptions
1	Control model. Sand as backfill material.
2	Sand as backfill. Geosynthetic reinforcement was used.
3	Gravel as backfill. Geosynthetic reinforcement was used.
4	Geosynthetic was used as reinforcement with a soil cement block (30 cm thick) above the spring line.
5	Geosynthetic was used as reinforcement with a soil cement block (30 cm thick) 30 cm below the spring line.

constructed in increments where each layer was of 10-cm thickness. In all tests, the cover soil reached 70 cm above the crown. At the completion of backfilling, the water was introduced into the test pit.

The behavior of the pipe was measured as the water table reached the ground surface. It was confirmed that the pipe did not move with the rise of the water table. The water table was then lowered to the spring of the pipe. The soil above the pipe was removed at 10-cm increments until the pipe floated. The critical overburden height of the soil cover was thus determined.

For tests 2 to 5, the geogrid was wrapped from the crown to the spring of the pipe model. The length of the geogrid extended from the spring was about the radius of the pipe.

Figure 3 shows the test where the geogrid was installed around the pipe in the test pit. The backfill sand, gravel, or soil cement was placed on the grid. The strain gauges were attached to both surfaces of the geogrid. The locations of strain gauges in each test are shown in Fig. 4. The load cells were installed in the ground and at the pipe to measure the load acting on them.

4 CRITICAL HEIGHT OF SOIL COVER

The results are summarized for each case of testing:

Test 1. When the overburden height was reduced from 70 cm to 30 cm, the pipe floated. The cracks were observed in the soil along the longitudinal direction of the pipe model. They occurred at a distance d apart, where d is equal to the pipe diameter. The volume of the soil enclosed between the cracks was lifted when the pipe floated. The ground surface after lifting up is shown in Fig. 5.

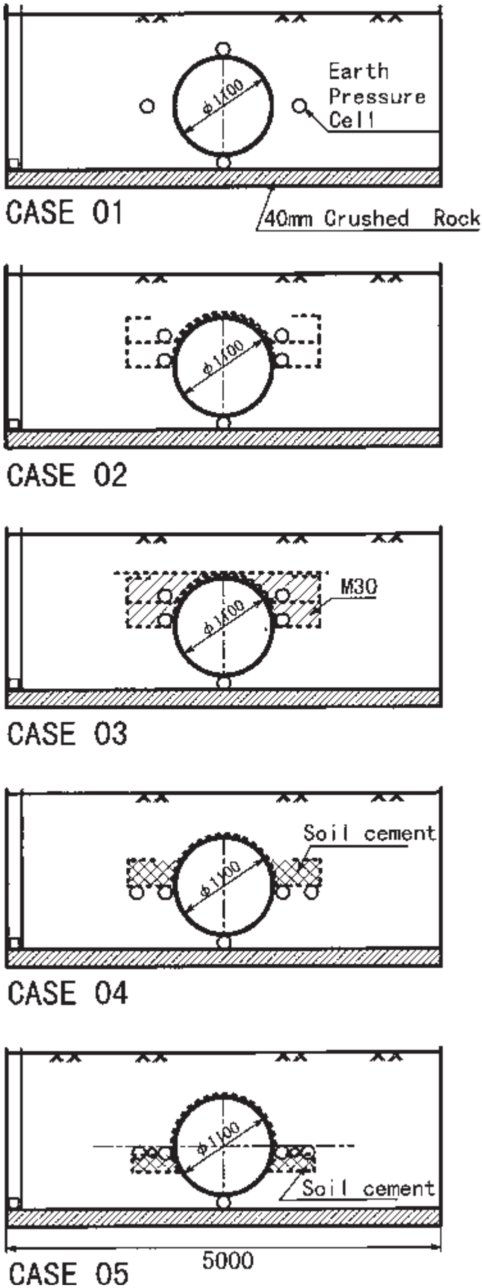

Figure 1 Cross section of model tests.

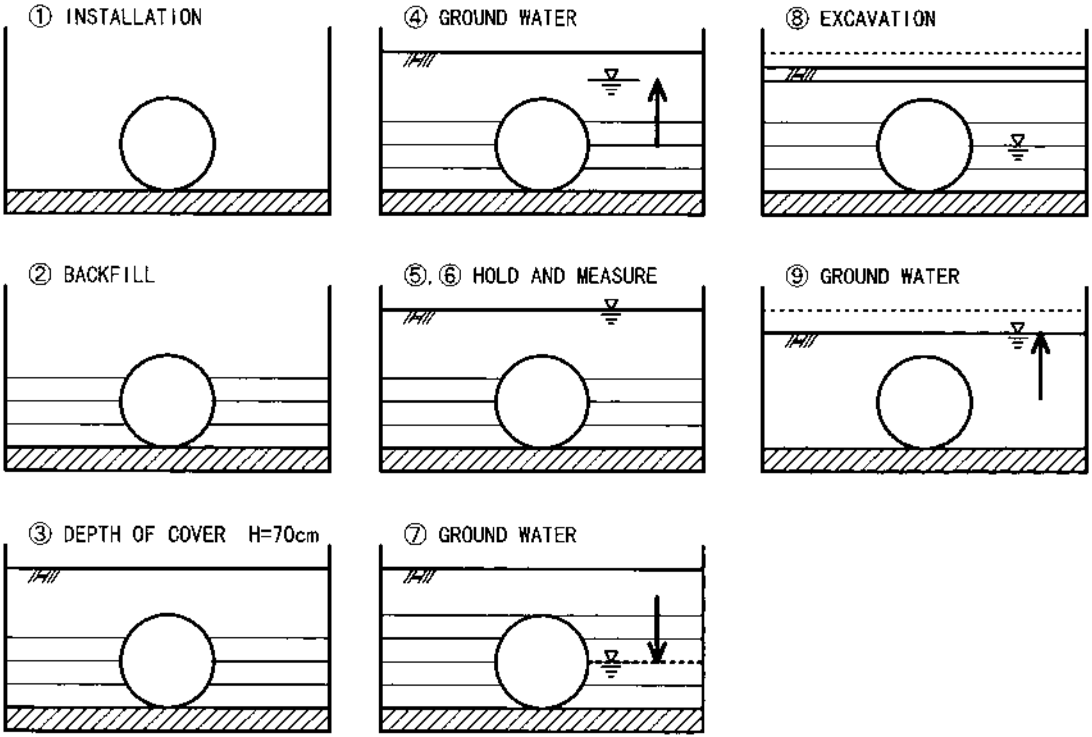

Figure 2 Construction procedure.

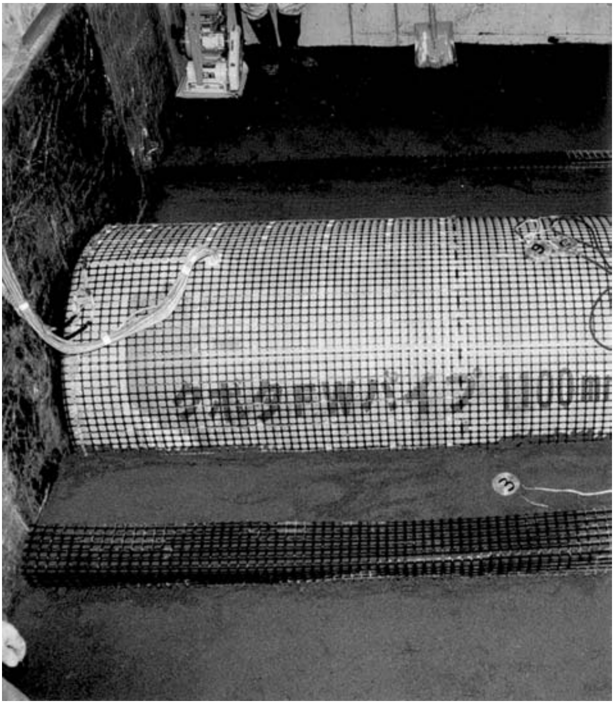

Figure 3 Installation of geogrid.

Test 2. In this model, because the backfill soil was confined by the geogrid, additional resistance to flotation was expected. The pipe floated when the overburden height was reduced to 20 cm. The failure surfaces as observed were similar to those of test 1. The speed of flotation was smaller than that of test 1.

Test 3. The resistance of pipeline to flotation was enhanced by the use of gravel and geogrid. The pipe floated when the overburden height was reduced to zero. The cracks along the longitudinal direction of the pipe developed in a manner different from tests 1 and 2. The cracks were observed along the boundaries between the gravel and original foundation. The grid floated with the surrounding gravel. The speed of flotation was smaller than the previous two tests.

Test 4. The soil cement, 30 cm thick, was placed on the geogrid along its length. The flotation was observed when the thickness of the overburden soil layer was equal to zero. The effect of mitigation was similar to test 3, where gravel was used with geogrid.

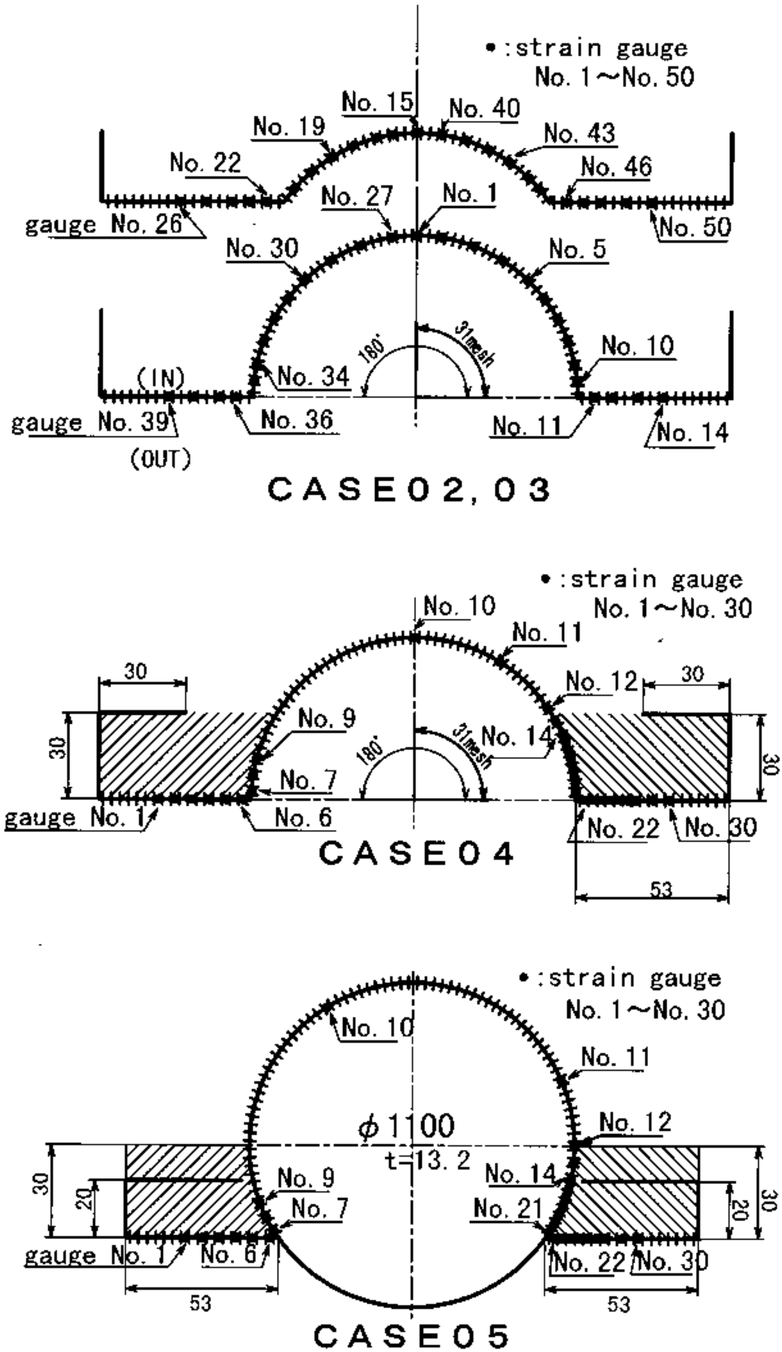

Figure 4 Location of strain gauges.

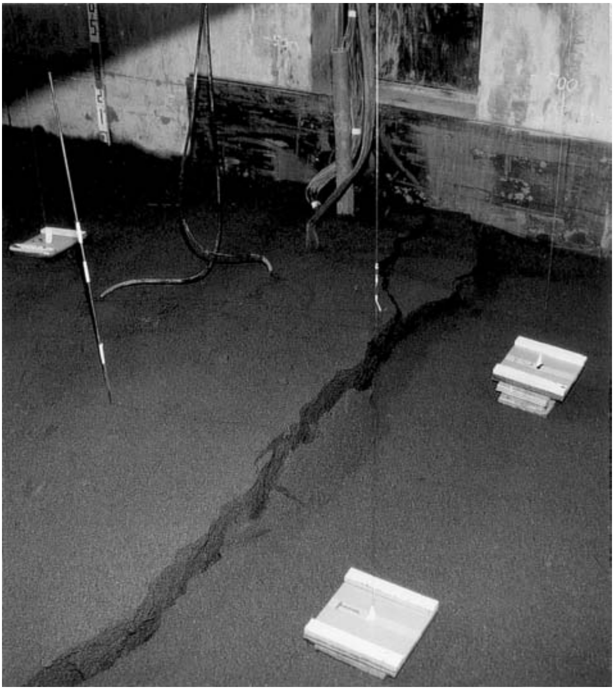

Figure 5 Ground surface after pipe flotation.

Test 5. The soil cement was at an elevation 30 cm shallower than that of test 4. The pipe did not float until the excavation reached 20 cm below the crown of the pipe. The soil cement block acted as an "anchor" and offered a greater resistance to flotation.

5 FLOTATION

Figure 6 shows the flotation of pipe model and ground with time. The locations of measurement points at the ground surface are shown in Fig. 2. The two points were at a distance 81 cm from the pipe center.

In tests 1 and 2, the movement of the ground surface was very little until the pipeline floated. In test 3, with the presence of gravel, the ground surface was affected when the pipe started to float gradually. In tests 4 and 5, the soil cement block moved as an integrated body with the backfill soil. The backfill soil above the soil cement was lifted together.

It was also observed that the void space formed below the pipe, as it floated, was filled by the sand flowing in from the surrounding ground.

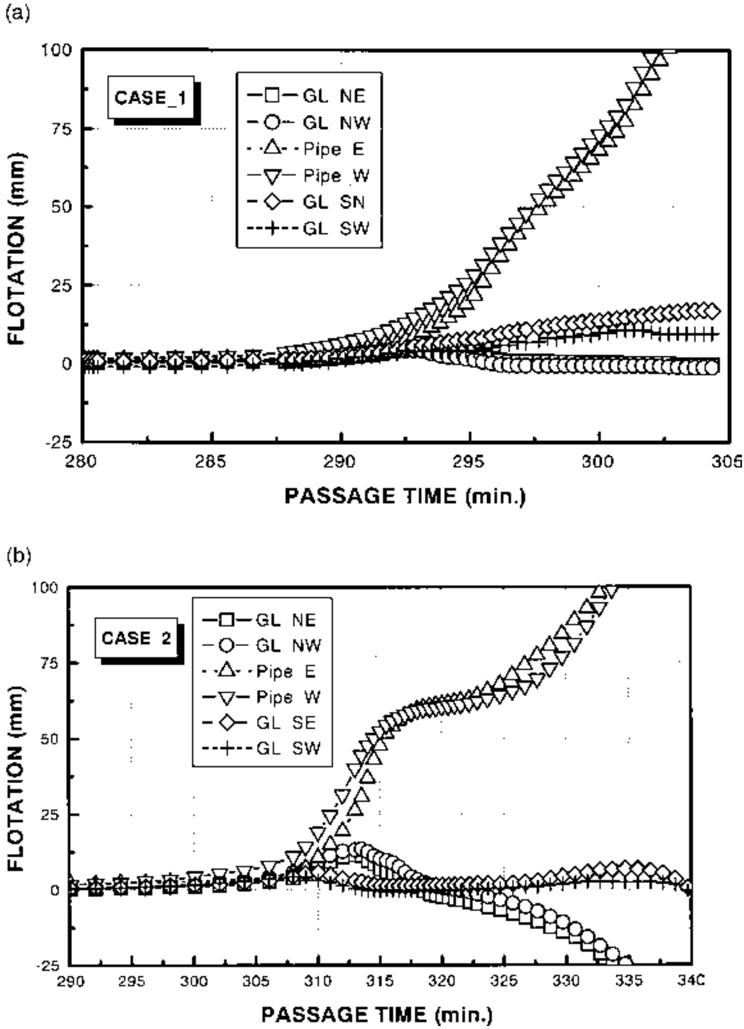

Figure 6 Flotation of pipe and ground surface versus time: (a)–(e) tests 1–5.

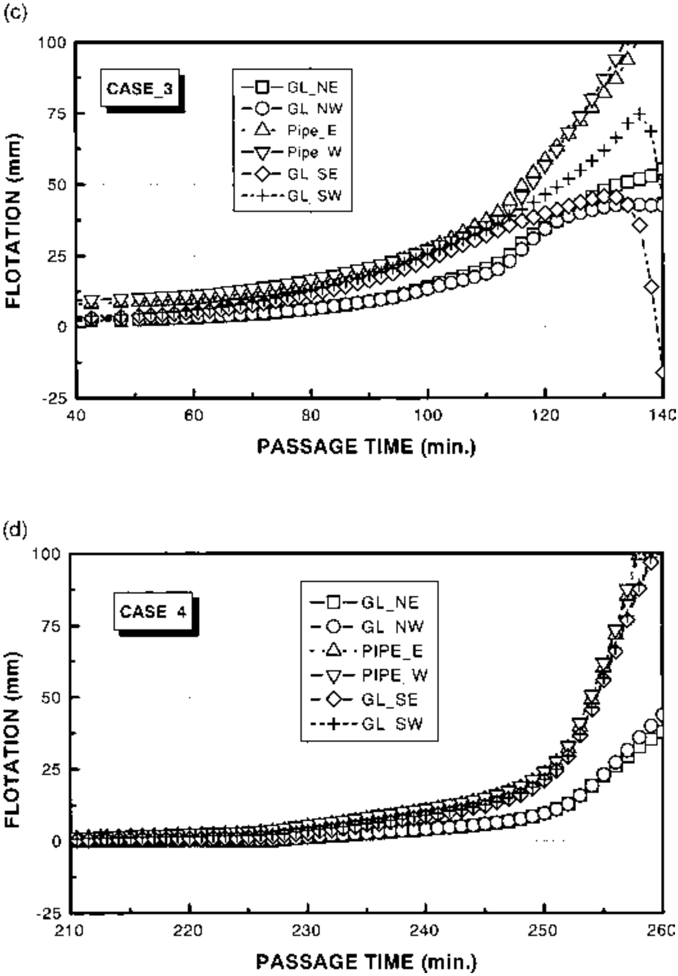

Figure 6 Continued.

The ground surface was lifted 10 to 20 cm in tests 2 and 3. In tests 4 and 5, where soil cement was used, the ground surface settled for over 20 cm. In test 5, where the soil cement was installed below the springline, the surface settled very slowly. Thus the flowing-in of the surrounding sand was prohibited.

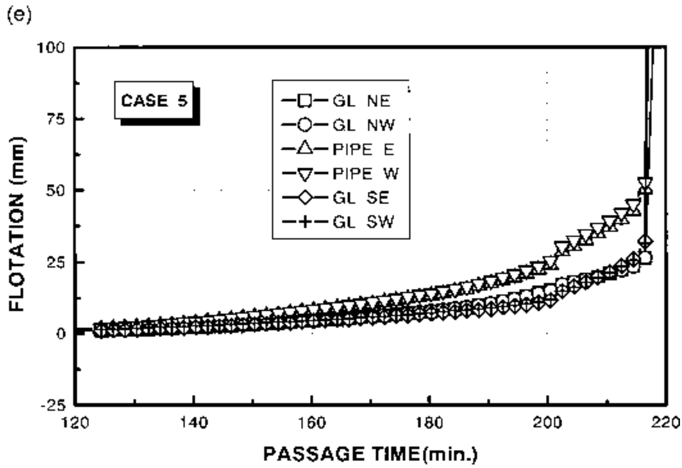

Figure 6 Continued.

6 STRAIN IN GEOGRID

Figure 7a shows the strain measured in the upper surface (marked as IN) of geogrid and its relation with the uplifting of the pipe. The compressive strain is shown for the portion of geogrid that was bent and located close to the pipe. The strain developed at strain gauge No. 22 and distributed toward the length of geogrid. The tensile strain was measured for the lower surface of geogrid (marked as OUT). Again, the tensile strain propagated from strain gauge No. 22 outwards. The peak strain increased with the distance of uplifting.

The strain gauge readings indicated that the geogrid was not under pure tension, but also subjected to bending moment. The bending moment in the geogrid was the greatest around the vicinity of the pipe. Figure 7b shows the strain measured at the lower surface of geogrid in test 2. Similar to the upper surface, the tensile strain in the geogrid increased with the distance of uplifting, and distributed toward the end of geogrid. The layer in between the grids was subject to the same behavior.

Figure 8 shows the results for test 3, where gravel was used. The compressive strains were recorded in the lower surface of geogrid, whereas its upper surface was under tension. Thus by confining the backfill in between the grid layer using gravels, an opposite pattern of strain development was noticed.

Figures 9 and 10 show the results when the soil cement was used. The geogrid at the lower portion was not subject to any strains. The portion of the grid near the pipe was under tension.

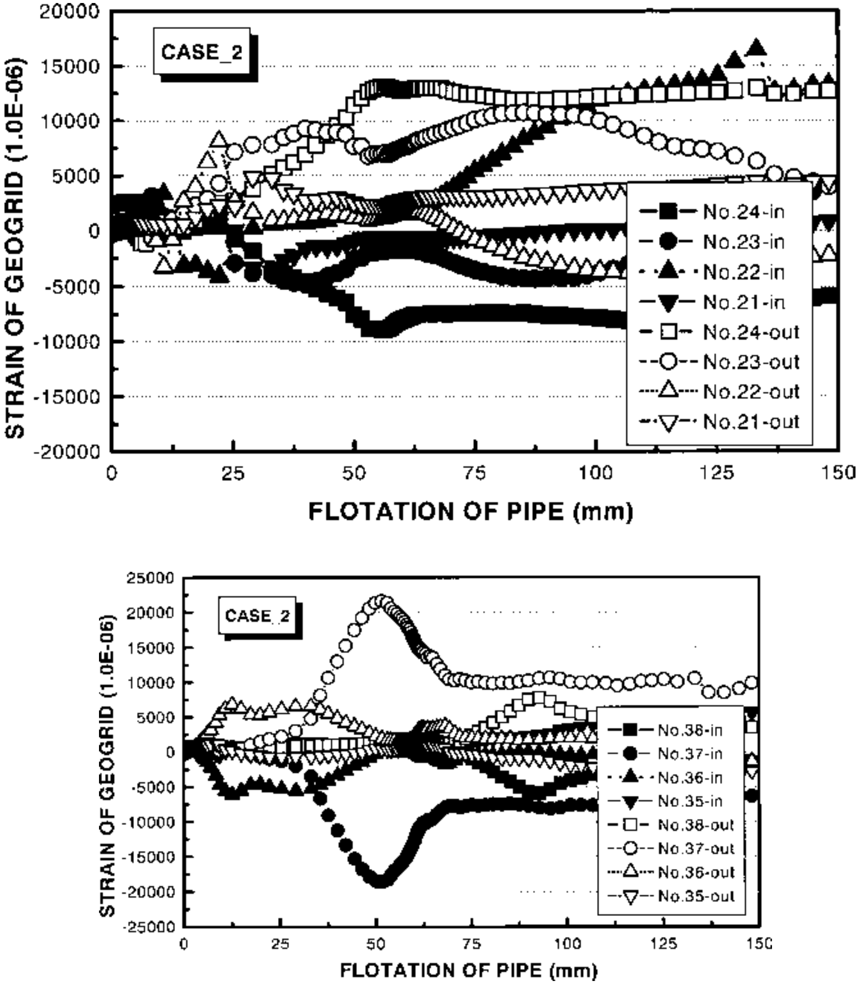

Figure 7 Strain in the geogrid versus pipe flotation—test 2: (top) strain gauges 21–24; (bottom) strain gauges 35–38.

7 DEFORMATION OF GEOGRID

The deformation of the geogrid is schematically illustrated in Fig. 11. The geogrid behaved as a cantilever beam when the pipe was uplifted. The backfill soil above the geogrid acted as the resisting load against flotation. When the sand was used, and if the geosynthetic has a large aperture, such as in this study,

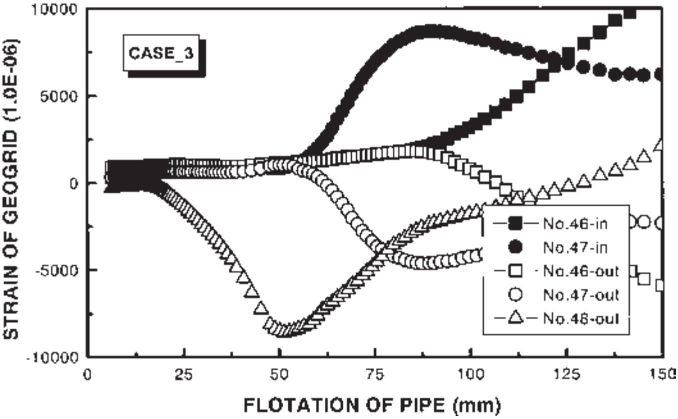

Figure 8 Strain in the geogrid versus pipe flotation—test 3.

adequate retention of sand was not possible. If the sand is loose, it contributes less toward the bending resistance while confined by the geosynthetic. When the soil cement was used above the geogrid, the flexural rigidity was increased. The effects of using gravel had been illustrated in test 3. Thus, the geogrid shall not only be considered as tensile reinforcement, but also functioned as an anchor.

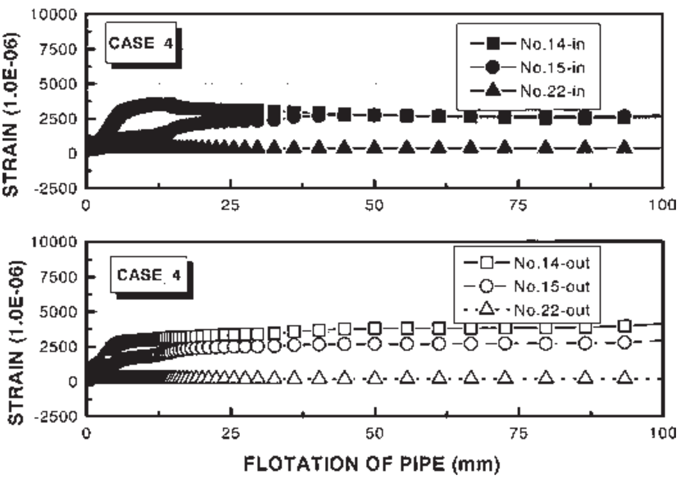

Figure 9 Strain in the geogrid versus pipe flotation—test 4.

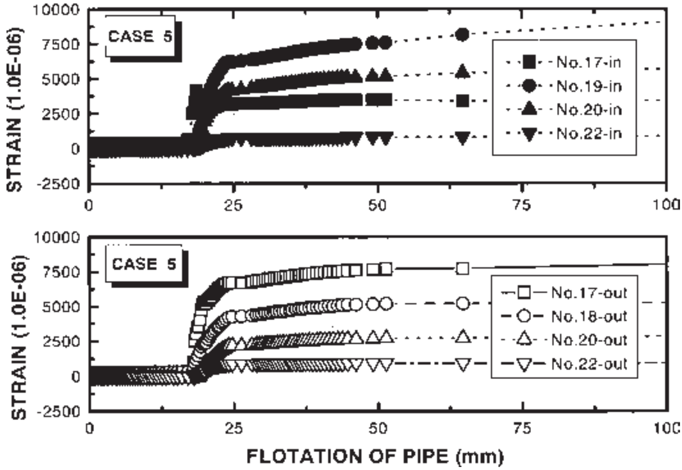

Figure 10 Strain in the geogrid versus pipe flotation—test 5.

8 LOAD ACTING ON THE PIPE

The relationships between buoyancy and counterweight of the pipe are shown in Table 2.

The resisting force includes the contribution of dead load of regions A, B, and C of the backfill material and the deadweight of the pipe (Fig. 12).

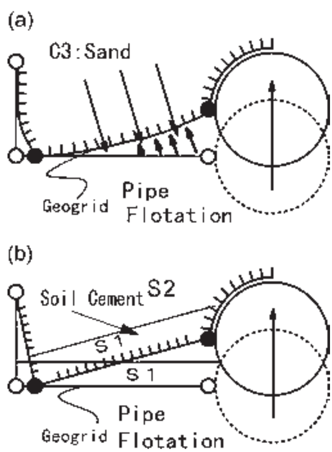

Figure 11 Deformation of geogrid.

Table 2 Resisting Forces and Buoyancy

Test	*H* (cm)	*H* (cm)	*A* (kN/m)	*B* (kN/m)	*C* (kN/m)	*W* (km/m)	*T* (kN/m)	*U* (kN/m)	Uplifting
1	40	—	4.73	0	0	1.27	6.00	9.77	No
	30	—	3.82	0	0	1.27	5.09	9.77	Yes
2	30	56.3	3.43	4.32	2.30	1.27	11.32	9.77	No
	20	56.3	2.62	1.32	1.54	1.27	9.74	9.77	Yes
3	10	56.3	2.02	4.05	0.86	1.27	11.20	9.77	No
	0	56.3	1.11	7.05	0	1.27	9.43	9.77	Yes
4	10	30.0	1.99	2.58	3.07	1.27	8.91	9.77	No
	0	30.0	1.09	2.58	2.23	1.27	7.16	9.77	Yes
5	−10	30.0	0.52	2.11	3.18	1.27	7.08	9.34	No
	−20	30.0	0.24	2.11	2.49	1.27	6.11	8.59	Yes

A: Weight for Region A. *B*: Weight for Region B. *C*: Weight for Region C. *W*: Weight of pipe. $T = A + B + C + W$: total resisting forces. *U*: Uplifting force.

The overburden weight contributes significantly to tests 2 and 3 when compared to test 1. For tests 4 and 5, the overburden load was not present when the soil above the crown was fully excavated, yet the resistance to flotation was large. That is, the soil cement block acted as anchor so that the shear resistance of soil played a major role.

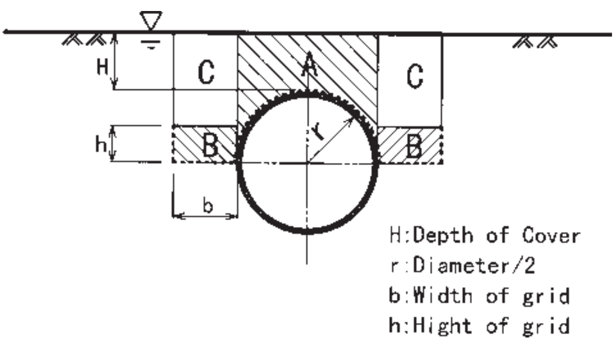

Figure 12 Resisting forces in stability calculation.

9 CONCLUSION

The experimental study of pipe flotation has been conducted using a 110-cm-diameter pipe. It was shown that the geogrid can be used effectively to reduce flotation of pipelines with the gravels and soil cement acting as backfill material. An integrated body was obtained when the geogrid was placed above the pipeline. The soil above the geogrid contributed additional overburden weight. The geosynthetic functioned as not only tensile reinforcement, but its bending stiffness also played a role.

REFERENCES

RM Koerner. *Designing with Geosynthetics*, Fourth Ed., Prentice Hall, 1998.

CH Trautmann, TD O'Rourke, FD Kulhawy. Uplift force-displacement response of buried pipe. *J. Geotechnical Eng, ASCE* 111(9): 1061–1076, 1985.

15

Practice and Research of Geosynthetic Reinforced Soil Walls in Australia

Sik-Cheung Robert Lo
University of New South Wales, Sydney, Australia

ABSTRACT

The practice and research of GRS walls in Australia are presented here. The discussion on GRS wall practice is restricted to projects under the jurisdiction of state road authorities (SRAs). GRS walls for SRA projects have a relatively short history. However, innovative forms of GRS walls have been used in a number of milestone projects. This attests to the cost-effectiveness, versatility, and strength of GRS walls.

1 INTRODUCTION

The construction of major geosynthetic reinforced soil (GRS) walls in Australia dates back probably to the mid-1980s. For example, GRS walls with a height up to 6.6 m were constructed as traverse walls at the Mulwala Ammunition Factory located in the state of New South Wales. The impact of partial damage (and sabotage) to GRS walls was also studied (Greet, 1986). However, the construction of GRS walls for the state road authorities (SRAs) and state rail authorities has a relatively short history; it only began in 1991. The acceptance of GRS walls by the SRAs has special significance, as the SRAs standards and performance requirements are seen to be high. Since 1991, GRS walls have been gaining wide market acceptance. The highest GRS wall built to date has a maximum height of about 19 m. A number of GRS abutment walls supporting bridge decks have been successfully constructed. A GRS wall in wraparound construction was also used effectively in the construction of a temporary wall (that was dismantled subsequently) at the Great Western Highway west of Sydney. However, the design practice for GRS walls is, at the time of writing, by no means standardized. There is no Australian Standard specific for the design and construction of reinforced soil walls. The draft Australian Standard on Reinforced Soil Walls (DR-91271, 1991) evolved into a draft Australian Standard on Earth Retaining Structures (DR-96405, 1996), still under revision at time of writing. The latter is a broad-based document that contains some references to the principles for the design of GRS walls. Hence, the design practice differs between states. Within a state, the design practice for projects under the jurisdiction of the local government may differ from that under the jurisdiction of the SRAs. This paper is focused on GRS walls under the jurisdiction of the road authorities of the eastern states (Queensland, New South Wales, and Victoria). Research in GRS walls is often linked to specific requirements of Australia or specific projects. In the latter case, some of the research outcomes may not be published in the public domain.

2 OVERVIEW

GRS walls for the SRAs are often built with a "hard" near-vertical surface. Either articulated precast concrete panels or modular blocks have been used as the facing. Both high-density polyethylene (HDPE) and high-tenacity polyester reinforcements, in either strap or grid form, have been used successfully. Although fine-grain soils can be used as the fill material in the reinforced zone, it is not uncommon that a granular fill (with less than 15% fine content) is required by an SRA. Hence, the term "select fill" is often used to designate fill material in the reinforced zone.

The construction of reinforced soil wall for the SRAs was often based on the design and construct contract. This means a specialist GRS contractor is responsible for both the design and construction of the GRS walls at an agreed price. As such, GRS walls have to compete with reinforced soil (RS) walls based on metallic reinforcement system and conventional retaining walls on cost-effectiveness. This contract system encourages innovation and cost-effective design. However, the implementation of such a form of contract for the construction of retaining walls is not easy, because the design requirements, being part of the contract document, will be subject to both contractual and technical interpretation. Although the GRS wall design requirements can be varied during construction, any change in design requirements constitutes a contractual variation (and possible contractual disputes). Hence, studies have been undertaken in an attempt to develop a model for specifying design requirements. The design requirements may be prescribed in detail, and this is the current practice of the SRA of New South Wales; or a broad-based (and brief) design specification may be used, which is the current practice of the SRA of Victoria. In the latter case, the specialist GRS contractor will, as part of his tender bid, provide a more comprehensive set of design methods and criteria. The SRA of Queensland has adopted a somewhat intermediate approach. The SRA of Western Australia, until 1997, only allowed steel soil reinforcement, although a brief draft document on the design requirements of RS walls for a range of reinforcement systems is currently under consideration. The road authorities of other states, to the best of the author's knowledge, do not have design specifications for GRS walls. This somewhat justifies restricting the scope of reference of this paper to the three eastern states of Australia.

Although the "best" approach in specifying design requirements in a design and construct contract for GRS walls is still being debated, the ability of GRS walls to gain market share under such a design and construct contractual system attests to its cost-effectiveness. Indeed, GRS walls have been adopted in a number of milestone projects in Australia. It is pertinent to note that GRS walls are well adapted to a design and construct contract. Because geosynthetic reinforcements are normally manufactured in rolls, the reinforcement length and grade are not constrained by the logistics of prefabrication (which is often the case for metallic reinforcement). It is not uncommon to have GRS wall sections that utilize different reinforcement grades at different spacing and of different length, as shown in Fig. 1 for a GRS wall constructed in the state of Queensland. Geosynthetic reinforcement only has to be cut to the design length during installation; hence the cost and time impact of any design changes as a result of deviations from expected site conditions is also smaller.

3 DESIGN

A range of design methods has been used for the design of GRS walls in Australia. The term "design methods" includes the calculation model(s) for assessing actions (such as maximum reinforcement tension) and the methodology for assessing resistance (such as the long-term design strength of geosynthetic reinforcement). The design methods can be either specified by the SRA or proposed by the specialist GRS wall contractor as part of the tender. In either case, the design methods form part of the contractual agreement once the contract is awarded.

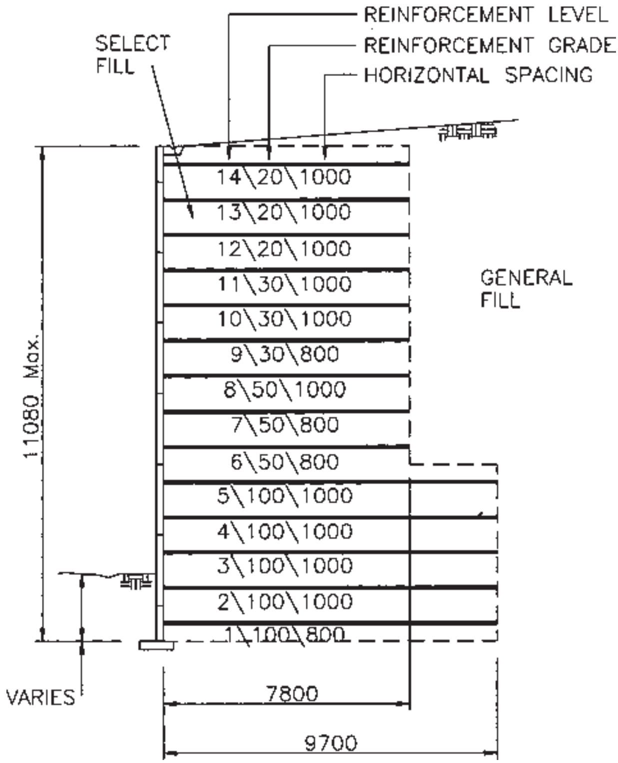

Figure 1 GRS wall section that utilizes different reinforcement grades at different spacing and of different length.

3.1 Calculation of Actions

Before 1996, the design methods were often specified with reference to international design documents such as the FHWA Design Guidelines (Christopher et al., 1990), BS 8006 (1995), BE3/78, or British Board of Agrément Certificate. In general, simple calculation models have been used in assessing actions (such as reinforcement tension) although sophisticated, nonlinear stress analysis based on either finite-element analysis or the so-called FLAC (Fast Lagranian Analysis of Continua) analysis has sometimes been used for unusual or innovative wall configurations. A complete formulation of FLAC is contained in Cundall and Board (1988) although a brief explanation is presented in the appendix. The differences in reinforcement tension predicted by different simple calculation models for static loading are generally small, with the possible exception of BE3/78, which can give considerably higher reinforcement tension for an abutment wall supporting a sill beam.

Because Australia is not located in a seismically active zone, seismic design methods receive comparatively less attention. Earthquake conditions may not be explicitly considered in the design of pre-1995 GRS walls; and most post-1995 GRS walls are designed for a k_h-value in the range of 0.08 to 0.10 (with $k_v = 0$) using the calculation model recommended in FHWA design guidelines (Christopher et al., 1990). In most cases, these low seismic coefficients only have a slight influence on the design outcomes.

3.2 Long-Term Designed Strength of Geosynthetics Reinforcement

However, different design documents can give significantly different long-term capacity of geosynthetic reinforcement. This led to some concern on whether different RS systems are evaluated with a common benchmark. The road authority of New South Wales put a significant effort into developing its own design specification for GRS. The document, referred to as R57 (1988), is based on partial factors. R57 attempts to serve the following two apparently conflicting criteria:

1. It has to encourage effective design and allow for innovations.
2. It has to be a contractually enforceable document.

The document was also written with a holistic approach in an attempt to harmonize the different activities (ground investigation, soil testing, design, construction, and quality assurance) of the "whole design process." It was also written to ensure full compatibility with the closely related construction specification referred to as R58 (1997). The geotechnical calculation models closely follow that of BS 8006 (1995) but with the following modifications:

1. The reinforcement tension and active pressure are calculated with the critical state friction angle, ϕ_{cv} (together with a partial material factor of unity), in lieu of the peak friction angle.
2. The restriction on the minimum width of a reinforced block is relaxed.
3. A more liberal approach was adopted in the calculation of the pullout resistance.
4. The requirement on the overall limit equilibrium is stated in a more specific manner. In particular, a noncircular potential slip surface intersecting some of the reinforcements is explicitly stated as one of the potential failure modes to be considered.

R57 has sometimes been criticized as an excessively detailed document. However, it can also be argued that until an enforceable and truly performance-based specification is developed, a detailed design specification is needed to avoid “contractual misinterpretation.”

The more debatable aspect of R57 is the methodology used to assess the design strength of the reinforcement (at the end of the design life of the GRS wall). Following the philosophy of BS 8006 (1995), the relevant equations for design against reinforcement rupture are

$$T^{*} \leq T_{dr} \tag{1}$$

$$T_{dr} = \frac{T_B}{f_m} \tag{1a}$$

where T^* is the factored reinforcement tension (which are generally calculated with partial load factors of 1.25 on dead load and 1.50 on live load), T_{dr} is the design strength for reinforcement rupture, T_B is the base strength of the material at the prescribed design life, and f_m is the partial factor for reinforcement strength. T_B is derived by extrapolation of sustained load test data presented by the specialist GRS wall contractor (or geosynthetic manufacturer) as illustrated in Fig. 2.

A test duration of at least 1 year is required. Based on available data, the ratio T_{dr}/T_{uo}, where T_{uo} is the tensile strength as measured in a quick tensile test,

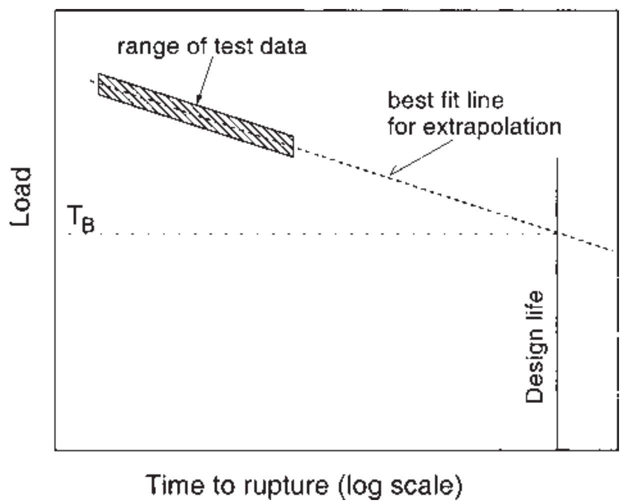

Figure 2 Long-term strength of geosynthetic reinforcement by stress rupture method.

was found to be significantly less than unity. For high-tenacity polyester, it is generally in the range of 55–70%. For HDPE, it is in the range of 33–45%. Note that f_m takes into account both uncertainties in material strength and loss in cross-sectional area. The former is due to manufacturing variability and error in extrapolating test data to a 100-year design life. The latter is due to construction damage along with chemical degradation due to the ambient environment.

The above procedure gives T_{dr} as a fraction of the tensile strength measured in a quick tensile test. There have been debates on the extent of conservatism inherent in the method used to assess T_{dr}, the long-term design strength. Deriving T_B by the stress rupture method inherently implies a load duration effect. This, in conjunction with Eq. (1), implies that the geosynthetic reinforcement will be adequate to carry T^*, the factored reinforcement tension, for the specified design life. However, T^*, being a factored value, will not occur throughout the entire design life. Indeed, it will only occur for short durations. As such, GRS walls may have been designed with an extra margin of conservatism. Alternative design methodologies based on the so-called residual strength method (Greenwood, 1996; Lo, 1997) have been debated but have not been adopted due to the perceived lack of adequate data.

3.3 Modular Block Walls

In Australia, modular block walls are commonly referred to as segmental block walls. The connection between the blocks and reinforcement is commonly achieved by sandwiching the reinforcement between two blocks. Dowel pins may also bear against the transverse member of a geogrid, hence providing additional connection strength. The practice for SRA projects in New South Wales is to assess the connection strength based on short-term pullout test data provided by the specialist GRS contractor or the block manufacturer. The pullout test results can be idealized as consisting of two segments, as illustrated in Fig. 3.

The connection strength manifested in the first segment, which manifests dependence on vertical stress, represents reinforcement pulling out between the blocks. As such, the as-measured strength of the first segment is taken as the long-term strength. The connection strength manifested in the second segment is independent of the vertical stress. It represents the limiting connection strength due to reinforcement rupture. This limiting connection strength, however, is only about 50–70% of the T_{uo}. This reduction is believed to be due to the nonuniform-clamping action from the blocks. Some work has been done on developing more effective connections, but such design, at the time of writing, has not yet been used in SRA projects in NSW. To account for the reduction in rupture strength with load duration, this limiting strength (from segment 2) is reduced by the factor T_{dr}/T_{uo}, where T_{uo} is the short-term tensile strength of the reinforcement.

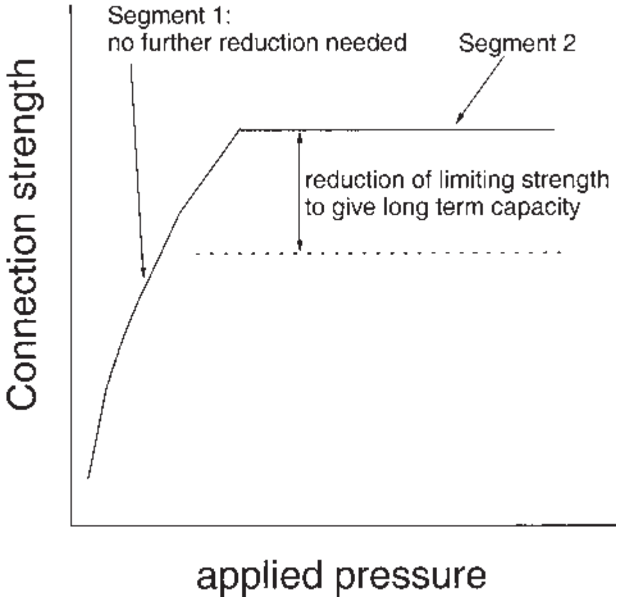

Figure 3 Connection strength of modular block facing.

4 RESEARCH AND DEVELOPMENT

Research and development activities of geosynthetic reinforced soil walls are largely driven by the immediate needs of industry. Research projects are in the form of special laboratory testing, calibration of design rules by nonlinear stress analysis of innovative wall configurations, instrumentation and back analysis of GRS walls. As such, some of the research works are reported under the "Case History" section.

4.1 Pullout Resistance

4.1.1 Fly Ash as Select Fill

Fly ash is often considered as a waste material. However, it may be used in the construction of GRS walls because the concern about its corrosive potential to metallic soil reinforcement is no longer applicable. In order to study the suitability of fly ash as the select fill, a series of large-scale pullout tests on a range of geosynthetic reinforcements was reported in Hausmann and Clarke (1994). Fly ash from the Vales Point Power Station, which had a grading varying from sandy silt to silty sand, was used in this study. The test results unambiguously suggested that fly ash can be used as a select fill material.

4.1.2 Pullout Resistance of Polyester Straps

Significant efforts have been made in studying the pullout resistance of high-tenacity polyester straps for the Freyssisol (formerly known as Websol) GRS wall system. A typical cross section of the polyester strap, formerly known as Paraweb, is shown in Fig. 4.

It is available in five different grades, but the overall dimensions of the straps are approximately the same for all five grades. Due to the high load-carrying capacity of the strap and its relatively small perimeter, the pullout resistance often controls the reinforcement length at low overburden stress. A large-scale pullout apparatus that utilizes a flexible sleeve near the front wall was used in this study. The pullout resistance as measured on a pullout box can be expressed as

$$R_p = \alpha F \sigma_0 p L_p \tag{2}$$

where α is a scale correction factor, F is the basic parameter characterizing interface strength, σ_0 is the applied pressure, p is the perimeter, and L_p is

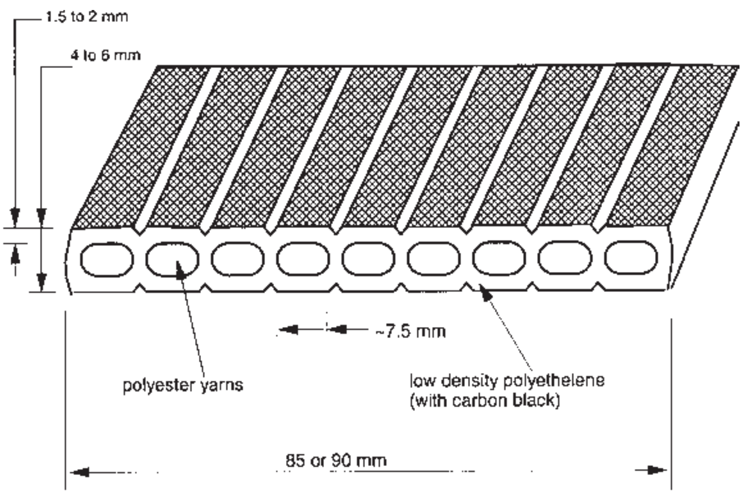

Figure 4 Cross section of Paraweb.

the anchored length. For a pullout box that utilizes a sleeve, L_p is the embedded reinforcement length minus the sleeve length. For a pullout box of adequate large scale, the value of αF so measured may be considered as representative of the field condition, with σ_0 being taken as the average overburden stress at the reinforcement level. Because pullout box testing alone will not yield separate values of α and F, the test results were interpreted simply in terms of the friction factor, f, defined by $f = \alpha F$.

A set of typical test results for a well-compacted granular soil is presented in Fig. 5. The test results unambiguously show that f is dependent on σ_0, the test pressure. The trend manifested in Fig. 5 was also representative of test data for other well-compacted granular soils (Lo, 1998). The f-value decreased with a reduction in test pressure and can exceed tan ϕ, where ϕ is the peak friction angle of the material. This observation can be explained by the constrained dilatancy hypothesis as detailed in Lo (1998). During reinforcement pullout, the soil in the vicinity of the strap is subject to considerable shearing. For a well-compacted granular soil, shearing will lead to volumetric dilation. However, the volumetric dilation of the soil elements in the vicinity of the strap will be contained by the surrounding soil. This interaction locally increases the normal stress, σ_n, acting directly on a strap to a value in excess of σ_0, the test pressure or overburden stress acting on the surrounding soil. This local increase in normal stress,

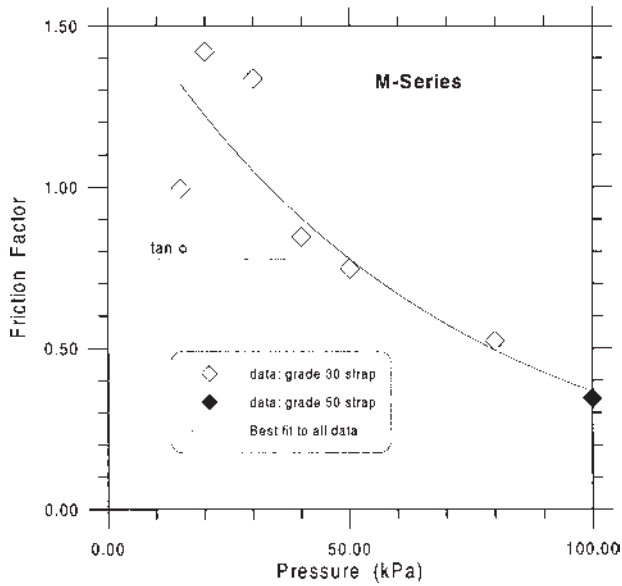

Figure 5 Variation of friction factor with applied pressure.

$\Delta\sigma = \sigma_n - \sigma_0$, is not explicitly modeled in Eq. (2) and hence its effect on the test results leads to an increase in the f-value. The magnitude and effect of $\Delta\sigma$ are most significant at low test pressure, which can then explain the increase in f with a reduction in test pressure. The detailed analysis is contained in Lo (1998). The constrained dilatancy hypothesis was also used by Milligan and Tei (1998) in modeling the pullout resistance of a soil nail. It is pertinent to note that the soils used in this testing program were from active construction sites. As such, the findings are considered to be representative of Australian conditions and hence have been incorporated in the design of Freyssisol walls for SRA projects.

4.2 Tied Back-to-Back Walls

Finite-element analyses have been used to develop and calibrate design rules for innovative forms of GRS walls. A notable example of this approach is the development work related to tied back-to-back GRS for the Dutton Park section of the Dutton Park to Port of Brisbane Rail Link. This project includes 1650 m^2 of reinforced soil walls for supporting an elevated section of the railway. About 80%

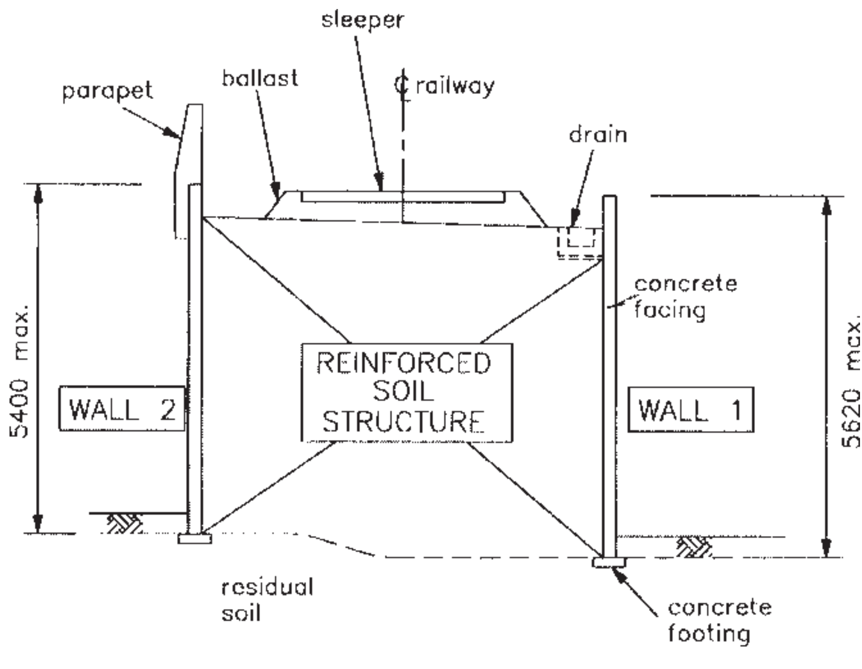

Figure 6 General arrangement of RSW.

of the reinforced soil walls consists of two walls aligned parallel at a distance of 6 m apart (see Fig. 6).

The small distance between the two zones led to overlapping of the two reinforced zones. FHWA design guidelines (Christopher et al., 1990) suggest that the two walls be designed independently with overlapping of reinforcements. A possibly more effective approach is simply to connect the two walls with the same reinforcement. Such a wall configuration is referred to as a tied back-to-back (abbreviated as TBB) reinforced soil wall. However, FHWA design guidelines suggest that the reinforcement tension of a TBB wall can be considerably higher than that predicted by a conventional calculation model and that there can be difficulties in constructing a TBB wall. The final design adopted was a TBB wall that utilized high-tenacity polyester straps as the reinforcing

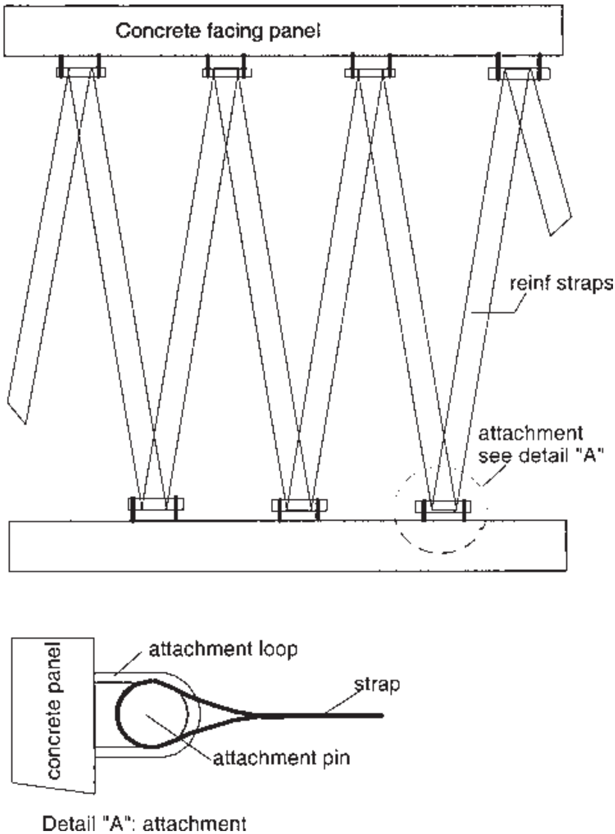

Figure 7 Layout of reinforcing strap for TBB wall.

system This reinforcement system overcame the construction difficulties by running the straps between the two walls in a zigzag fashion as shown in Fig. 7. However, the conventional calculation model may be neither applicable nor conservative because of the TBB configuration. The heavy setback surcharge from the railway loading further complicated the design. Hence, a series of nonlinear finite-element analyses was conducted to study the behavior of a TBB wall and to develop simple design rules (Lo et al., 1996). The results of the analyses unambiguously showed that the higher reinforcement tension would occur for the metallic reinforcement system, but would not be applicable to the proposed geosynthetic reinforcement system. This is because of its extensibility. It is pertinent to note that both the reinforcement tension and horizontal displacement profile were not sensitive to the choice of soil models and soil parameters. As such, simple conservative design rules were established. The cost-effectiveness of the TBB Freyssisol wall was also demonstrated in a subsequent project, the Y-Link Railway project, which involved the construction of GRS walls up to 8.5 m in height supporting the elevated section of a railway track.

4.3 Measurement of Soil Temperature

The temperature in the select fill affects the stress rupture curves and hence the value of T_{dr}. It may also have an effect on the hydrolysis of polyester reinforcement if the soil temperature is significantly higher than 20°. The temperature in the reinforced zone of a GRS wall located in Western Sydney was monitored by the SRA of New South Wales for several months during 1994. The monitoring period included all the summer months and extended into early winter. Thermocouples were installed at various distances from the wall facing, starting at a distance of about 300 mm. In addition to having thermocouples installed in the GRS wall, a benchmark thermocouple was also installed to measure the shaded air temperature at the GRS wall location. Continuous temperature logging was undertaken. The test data indicated that maximum soil temperature at about 300 mm from the facing was 35°, decreasing to 26° at 1 m from the facing. The temperature at about 300 mm from the facing was also close to the air temperature. The maximum soil temperature relative to the latitude and the coastal location of Sydney may appear to be high relative to the data presented by Yeo and Pang (1996). However, the black asphalt pavement of this wall may increase the soil temperature. It is also important to note that the data reported by Yeo and Pang (1996) were based on two readings per day, whereas the RTA data gave a daily maximum because of continuous data logging. This fact needs to be considered in assessing the influence of measured soil temperature on the long-term capacity of geosynthetics.

5 CASE HISTORIES

5.1 GRS Walls Constructed with Fine-Grain Soils

One possible advantage of the GRS wall is that the select fill does not have to comply with tight grading requirements. As such, fine-grain soils may be used in the construction of a GRS wall to achieve cost savings. The use of a crushed shale in the construction of a GRS wall supporting the on- and off-ramps of a major interchange in Western Sydney was reported by Won et al. (1994). The maximum wall height is about 8 m. The soil reinforcement is a high-tenacity polyester strap known as Paraweb. The select fill was compacted to near-maximum dry density (as determined by standard Proctor test), and the foundation material was competent. The wall was instrumented with

- Load bolts to measure reinforcement tension, noting that only the load bolts of the lowest level of reinforcement survived the construction
- Earth pressure cells to measure foundation stress
- Extensometers at three levels to measure internal displacements
- Survey points to measure horizontal wall displacements

The monitoring until 1994 showed that a facing panel bulged out by 100 mm although the horizontal displacements of other instrumented panels were typically less than 50 mm. Since then, the lateral movements of certain wall panels have continued at a slow rate. The as-measured reinforcement tension was significantly lower than the designed value but also manifested a slow increase with time. Although the causes of the higher wall deflection are a matter of debate, compaction of fine-grain soil at a moisture content on the dry side of optimum will lead to a high matrix suction that may dissipate with time. This matrix suction can be modeled by an apparent cohesion that reduces with time. The effects of a reduction of apparent cohesion with time can be studied by conducting a FLAC analysis of a “fictitious” GRS wall as shown in Fig. 8.

The dimensions of this wall were chosen to ensure adequate overall stability. The reinforcement was modeled as elastic and with high interface parameters to suppress pullout failure. Hence the wall could not have any form of internal stability. Both the general and select fill were modeled by the Mohr–Coulomb elastic-plastic model following a nonassociative flow rule (dilatancy angle $= 0$). For the purpose of this exercise, a friction angle of 30° was assumed for both the general and select fill. The reinforcement was assigned an elastic axial stiffness of 1000 kN/m. The construction of the wall was modeled in a layer-by-layer manner, and an apparent cohesion of 60 kPa was assumed in the analysis to represent the initial matrix suction. As such, the analysis is a total stress analysis. Dissipation of matrix suction after completion of construction was then simulated by a progressive reduction in apparent cohesion via time stepping.

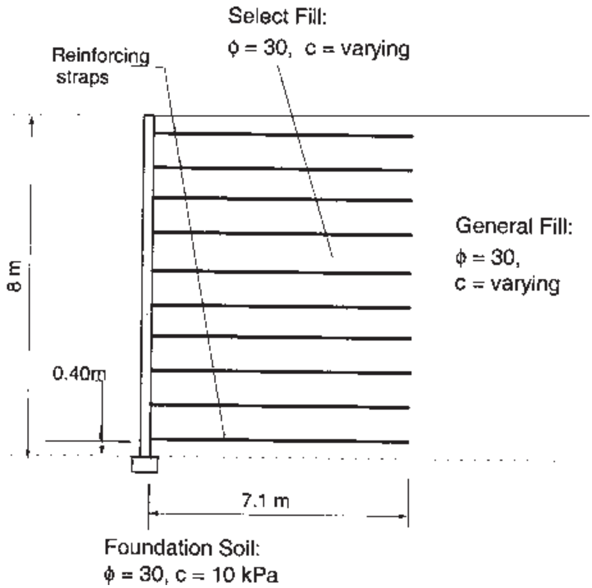

Figure 8 Fictitious GRS wall.

For simplicity, Young's modulus was maintained constant at 25 MPa. FLAC is well suited to modeling the effects of reduction in strength parameters. The foundation soil (7 m thick) was assigned constant strength parameters of $\phi = 30°$ and $c = 10$ kPa, with Young's modulus increasing from 25 MPa near foundation level to 55 MPa. Hence the foundation can offer significant restraint against movement. The predicted changes in reinforcement tension and horizontal wall deflection with time are presented in Fig. 9a and b. Both horizontal wall deflection and reinforcement tension increased with a reduction in apparent cohesion. This analysis illustrates that significant delayed wall movement could occur when the select fill is a well-compacted fine-grain soil. This fictitious wall analysis illustrates the possible development of delayed movement that may need to be considered in the design.

5.2 Multitier Modular Block Wall

Modular block walls may be constructed to a higher height using a stacked wall arrangement. This type of GRS wall was used to support the end span of a major bridge structure as shown in Fig. 10. The GRS wall consists of four tiers. Each tier has a height in the range of 2.2 to 2.95 m, and the setback distance between tiers is 2.0 m. A bridge sill beam sits on the top tier, thus giving a total wall height

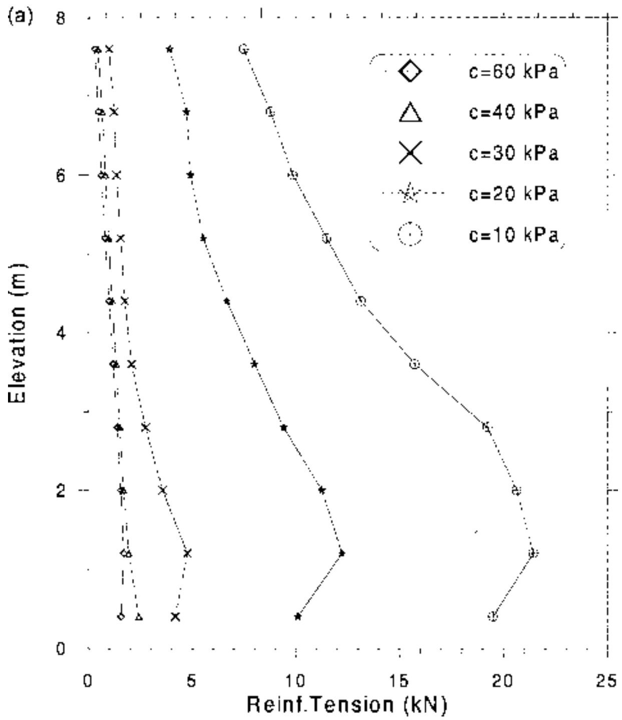

Figure 9 (a) Increase of reinforcement tension; (b) increase in wall displacement due to dissipation of apparent cohesion.

of about 12 m. The overall dimensions of a facing block are 315 mm deep by 200 mm high. HDPE geogrids were used as the soil reinforcements. The ground conditions consist of 1 to 3 m of loose silty sand overlying 7 to 10 m of medium-dense silty sand. Sandstone bedrock is at approximately 13-m depth. The loose sand layer contains pockets and/or lenses of soft silty clay. These silty clay pockets/lenses, although not located accurately, were considered to have only a slight influence on the overall behavior of the foundation material but may lead to some differential settlement. A GRS wall was considered to be most suitable in accommodating such a differential settlement. In view of the loose and somewhat variable nature of the top layer of the foundation soil, the top 1 m was replaced with compacted sand over the front 7 m as shown in Fig. 10.

The wall was designed with both limit equilibrium analysis and FLAC analysis. In the FLAC analysis, referred hereafter as the initial FLAC analysis, the soil was modeled with the Mohr–Coulomb elastic-plastic model (with nonassociative flow rule), whereas the modular block facing was modeled by

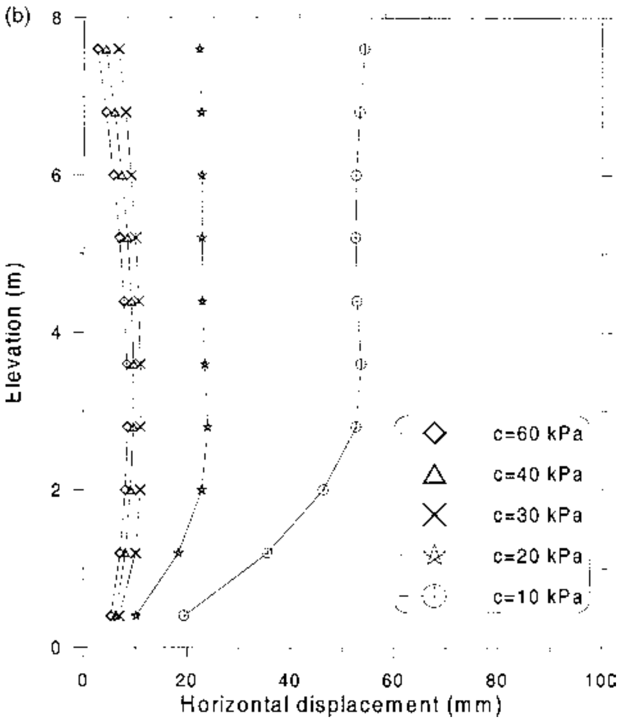

Figure 9 Continued.

elastic beam elements. The stresses due to self-weight of soil were analyzed as a single stage. The reinforcement layout adopted was conservative relative to the outcome of these analyses. Construction began in mid-1993. The wall was instrumented with

- Horizontal profile gauges (HPG-1 to HPG-3 of Fig. 10) to give near-continuous settlement profile and settlement plates to give spot settlement.
- Inclinometers (I-1 to I-3 of Fig. 10) to monitor horizontal displacements.
- Loads bolts and strain gauges were installed at the same level as the horizontal profile gauges to monitor reinforcement tension.
- Earth pressure cells to monitor vertical stress at foundation level.

Details of the initial design, construction, and monitoring of this multitier abutment are reported in Won et al. (1996). It is pertinent to note that the initial FLAC analysis yielded a rather unusual variation of reinforcement tension.

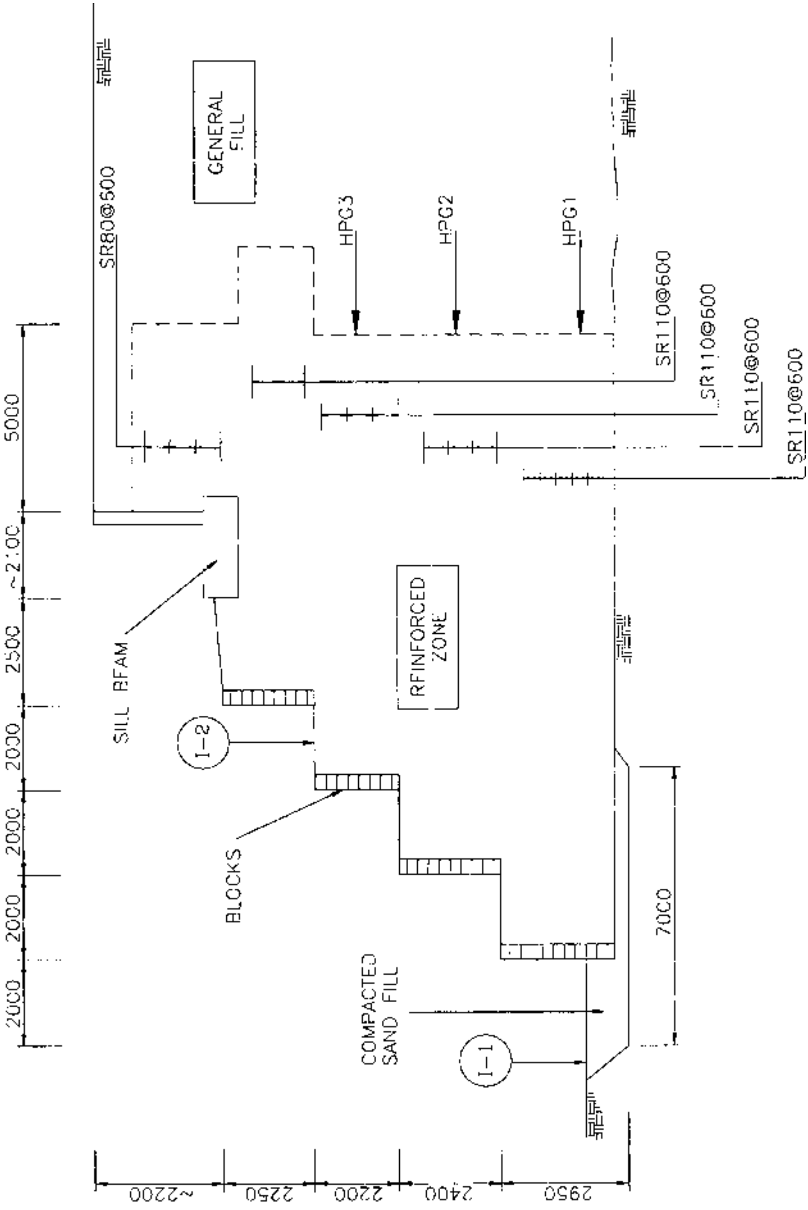

Figure 10 General arrangement of multitier GRS wall.

Some reinforcement levels had two peaks in the reinforcement tension, with de-tensioning between the two peaks. Such a pattern was also reflected in the load bolt readings.

However, field measurements indicated significant settlement and significant horizontal displacements. Some of the field measurements taken mid-December 1996 are presented as Fig. 11 (for settlement profiles) and as Fig. 12 (for horizontal displacements at I-2).

The settlement profiles presented in Fig. 11 were relative to their respective set of initial readings, which were taken about a month after filling began. Comparison with readings from settlement plates indicated that the settlement at HPG-1 could be about 10 mm higher than that presented. The I-2 inclinometer was installed a few days after the job began, and initial readings were taken two weeks after the job began. However, the inclinometer tube was extended with wall construction. As such, some of the horizontal displacement that occurred during wall construction was not fully registered. The magnitude of this error was considered to be low (10 to 20 mm). Although the initial FLAC analysis can predict the high settlement by assuming low, but tenable, values for Young's modulus for soils, the significant horizontal movements were not predicted. Furthermore, the as-measured settlement profile showed a peak near the rear end of the reinforced zone, and the initial analysis did not predict this feature. A series of additional analyses was conducted to investigate the status of this GRS wall. The final assumptions in the analysis were

1. The construction sequence was modeled closely in a layer-by-layer manner.
2. The soil was modeled as an elastic–plastic material with the elastic behavior given by the Duncan–Chang nonlinear elastic equation.
3. The modular block facing was modeled as 2D elements with horizontal no-tension joint planes.

To improve the Duncan–Chang model (which only gives a variation of tangential Young's modulus with stress), Poisson's ratio was taken as dependent on stress with the following equation:

$$\nu = 0.3 + 0.2\sqrt{S} \geq 0.495 \tag{3}$$

$$S = \frac{r_f(1 - \sin\phi)(\sigma_1 - \sigma_3)}{2c\cos\phi + 2\phi_3\sin\phi} \tag{3a}$$

The parameters adopted in the analysis are given in Table 1.

Equations (3) and (3a) ensure that unrealistically large volumetric strain will not occur (by giving $\nu \rightarrow 0.5$ as Young's modulus approaches zero).

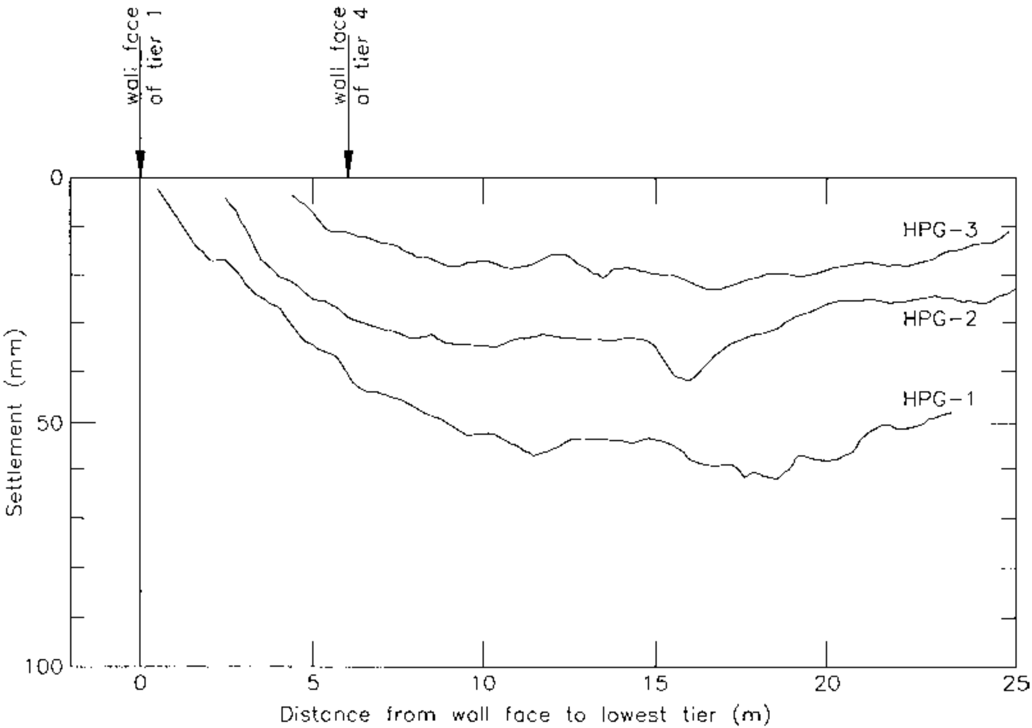

Figure 11 As-measured vertical displacement profile.

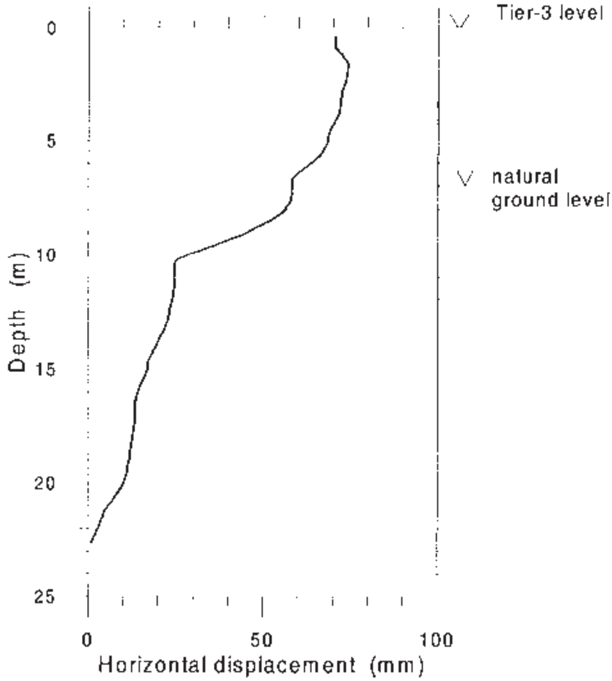

Figure 12 Measured horizontal displacement at I-2.

Table 1 Soil Parameters

Parameter	Fill	Foundation soil: Loose sand	Foundation soil: Medium sand
ϕ (deg)	33	30	33
c (kPa)	10	0	0
K	800	400	600
n	1	1	1
r_f	0.9	0.9	0.9

K, n, and r_f are nondimensional parameters for the Duncan–Chang model.

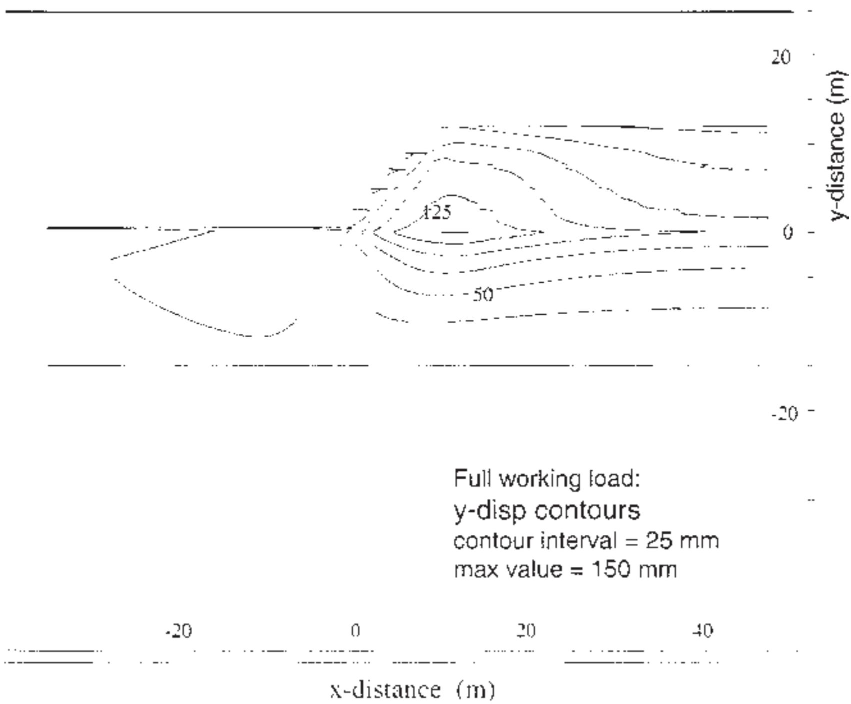

Figure 13 Predicted vertical displacement contours.

Minimum Young's moduli of 5 MPa for fill and 1 MPa for foundation soil were also coded in to prevent numerical problems when the state of a soil element soil changed from an elastic to a plastic. The subsurface conditions adopted in the analysis corresponded to that of a "worst scenario", and the soil parameters adopted were considered to be conservative. The predicted vertical and horizontal displacements are presented in Figs. 13 and 14, respectively. The predicted displacements were significantly higher than the monitored value. The maximum predicted settlement at foundation level was 150 mm, but the maximum measured settlement was about 70 mm. The maximum horizontal deflection at tier 3 was 150 mm, but the measured value was 75 to 85 mm. This is somewhat expected, partly because of "worst-scenario" assumptions made and partly due to the nature of a Duncan–Chang model. More importantly, the improved analysis was able to give the "unusual" settlement profile, and both settlement and horizontal displacements were predicted to be significant.

The analysis was continued by progressively reducing the strength parameters until a collapse was detected. As explained in Appendix A,

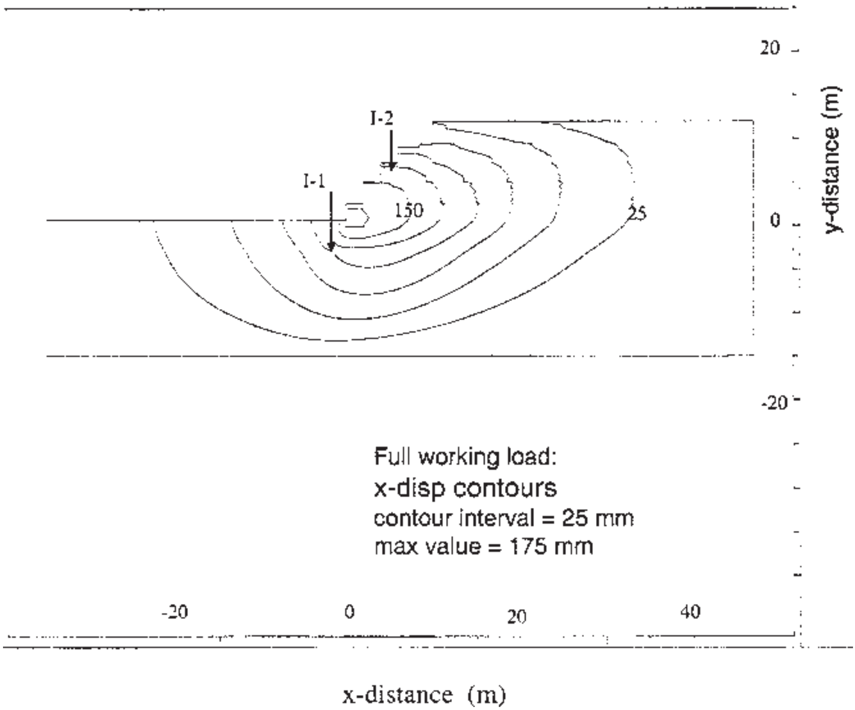

Figure 14 Predicted horizontal displacement contours.

the numerical scheme of FLAC enables the analysis to proceed to collapse without "ill-conditioning." Collapse was detected when the friction angle of the foundation soil was reduced to 21°. Noting that "worst-scenario" assumptions were made in the analysis, and that the predicted behavior at working conditions was more severe than that observed, one can conclude that the GRS wall has an adequate safety margin.

5.3 M2 Motorway

The M2 motorway is a 20-km road corridor that connects the northwestern suburbs of Sydney to 10 km northwest of the Sydney Harbour Bridge. The project is based on the design and construct contract system and was completed in May 1997. This road corridor traverses forested bushland by means of bridges and RSW embankments. All the wall structures, including abutment walls that support bridge decks, are GRS walls. The facing was constructed from articulated precast concrete panels, with a standard area of about 3.1 m^2 per panel.

The Paraweb high-tenacity polyester straps (Fig. 14) were used exclusively as the reinforcing elements. Crushed sandstone excavated from the route was used as the select fill. The use of GRS walls for the M2 project has been seen as a milestone that marks the cost-effectiveness, versatility, and strength of GRS walls. A total of 30 GRS walls, with a total wall facing area of about 23,000 m^2, was constructed under a fast-track contractual agreement. The fast-track nature of the project means that the precasting of up to 80% of the panels was carried out before the individual wall designs were completed. The design and construction

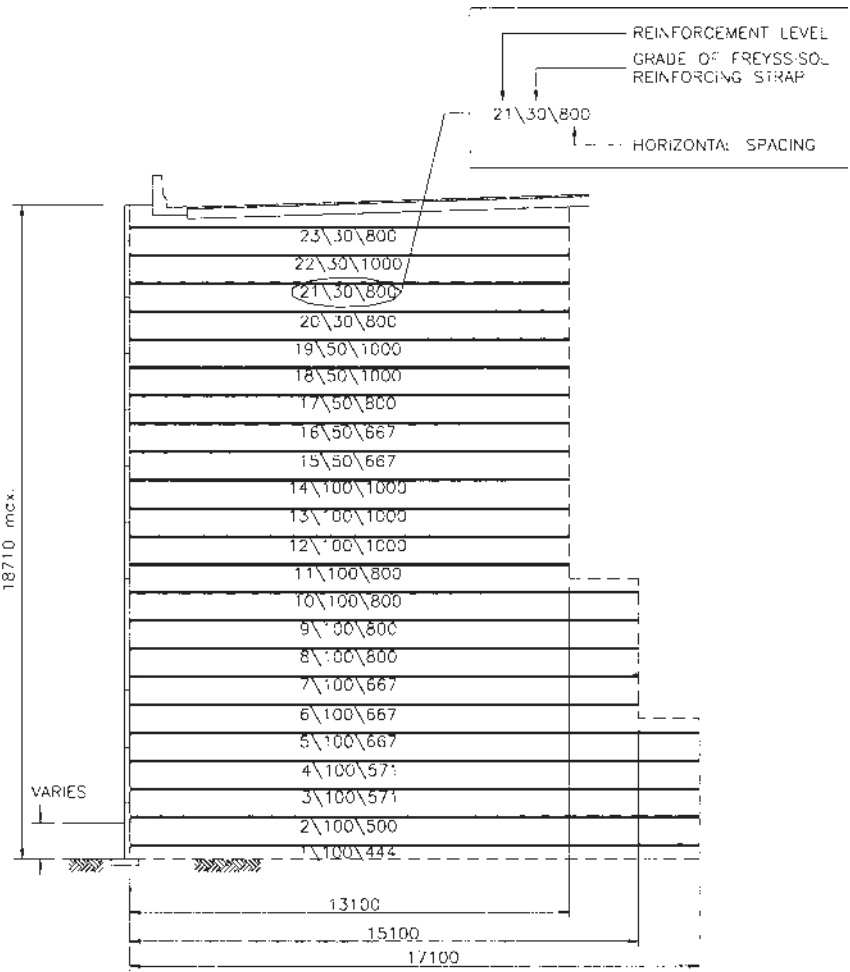

Figure 15 Tallest GRS wall for M2.

of the GRS walls were conducted under a quality assurance system. This means that there were a number of check/hold points in both the design and construction processes. The success of this project under such a demanding contractual environment attested to the effectiveness of GRS walls. The tallest GRS wall for the M2 project was 18.71 m. It was founded directly on sandstone bedrock, but the possible presence of weak horizontal bedding joints was considered in the design. This wall section is a stepped wall (see Fig. 15) constructed from three different grades of reinforcing straps and utilizing six different horizontal spacings. A number of abutment walls that directly support bridge decks were constructed. One such wall section is shown in Fig. 16. The sill beam is about 25.7 m in length. The design vertical loadings from the bridge deck are 8400 kN and 2460 kN for dead and live load respectively. The top 2 to 2.5 m of in-situ material below the foundation level were replaced by crushed sandstone compacted to a target dry density of 18.5 kN/m^3. This layer is underlain by sandstone bedrock. An inverted tee-shape sill beam contributed to minimizing the end rotation of the bridge deck (due to the tilt of the sill beam). It is important to backfill behind and against the sill beam before placement of bridge beams.

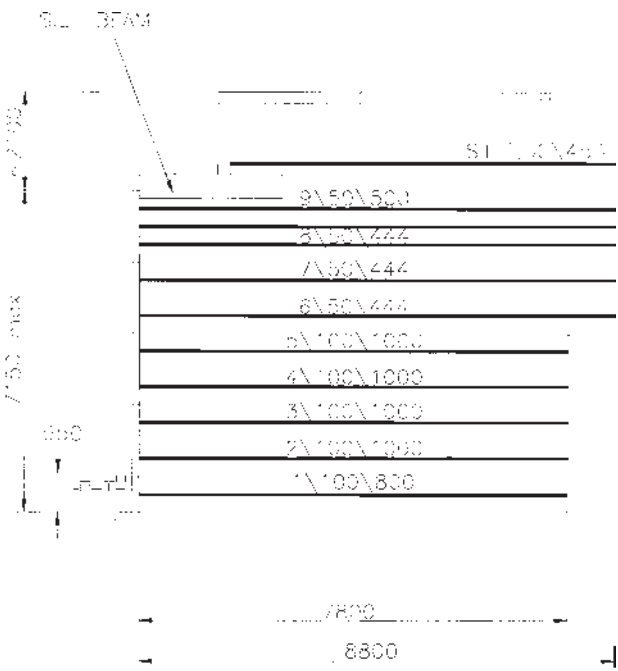

Figure 16 GRS wall supporting bridge deck.

This requirement was reflected in both nonlinear finite-element analysis and observations during construction. The postconstruction movements of the abutment walls have been monitored for a liability period before full payments were released to the GRS wall contractor. It is the author's understanding that the payment was fully released, thus verifying satisfactory performance, although the monitored results have not yet been released.

5.4 Modular Block Walls

Modular block walls are relatively popular in the state of New South Wales because of their cost-effectiveness and aesthetic appeal. Both HDPE and high-tenacity polyester geogrids have been used. In New South Wales (probably also in Australia), the first modular block wall for the SRA was constructed in1992 at Gosford (a coastal town located about 50 km north of Sydney). The wall is up to 3.1 m high. Crushed sandstone was used as the fill material, and the blocks were laid with a small setback of 1(H) in 8(V). Since then, a number of modular block walls have been constructed for several milestone projects. As reported in Won (1994), the applications range from road widening to foreshore protection (as sea walls). The wall height is generally limited to 4 m. Setbacks in laying the blocks may or may not be specified. The reinforcement density is generally one layer every two to three blocks. In the case of an abutment wall, the bridge deck is supported independently by piers, with the exception of the wall described in Section 5.3. Multitier walls, also referred to as terrace walls, have been used to achieve higher heights. A recent example is the widening of the F6 freeway (from 4 to 6 lanes) at Wollongong, a coastal city about 75 km south of Sydney. A multitier wall was used to achieve, more effectively, a higher retained height of about 6 m. The tallest section of this wall is presented in Fig. 17.

The reinforcement content of this type of wall is often governed by overall stability, with the potential slip surface passing through some of the reinforcement layers. As such, the reinforcement distribution is often close to uniform, and additional conservatism is exercised in the design.

6 CONCLUSION

In Australia, the construction of GRS walls for SRA projects has a relatively short history. However, GRS walls have gained market acceptance, despite being under a very demanding contractual system. This attests to the cost-effectiveness, versatility, and strength of GRS walls.

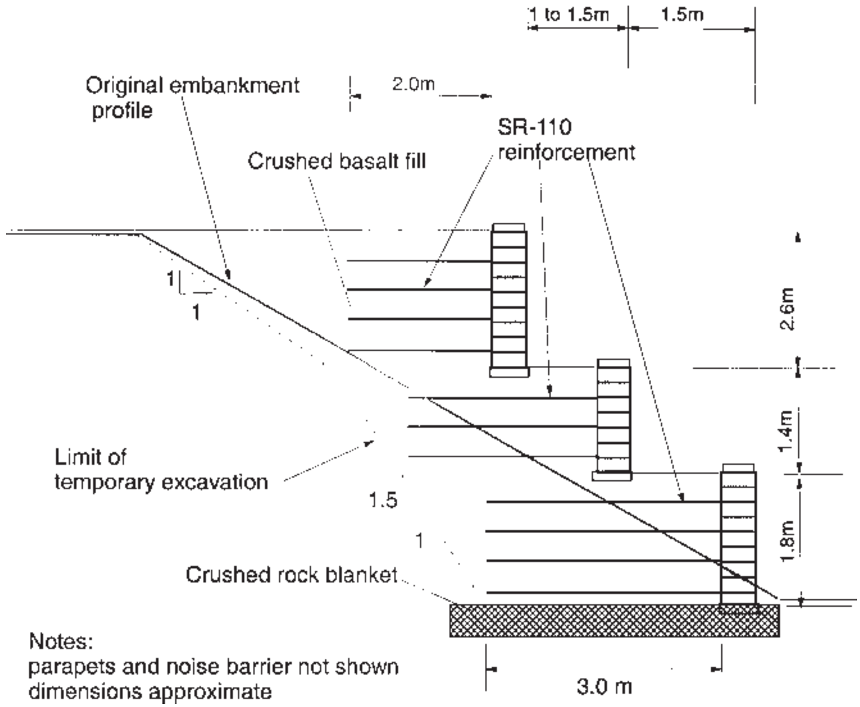

Figure 17 Modular block wall for widening of F6 freeway.

APPENDIX: FLAC ANALYSIS

FLAC analysis is based on a program called FLAC, a two-dimensional finite-difference code for engineering mechanics computation. Materials are discretized into elements in a manner similar to finite elements. However, a mix discretization scheme (Marti and Cundall, 1982) is used to improve modeling of plastic flow and collapse. The solver is based on an explicit time marching scheme, iterating between the equations of motion and material (constitutive) behavior. The full equations of motion are used, and pseudo-damping is used to bring a stable static system to a state of near-zero velocity. The numerical process needs to be user-controlled by specifying the number of iterations or the maximum out-of-balance nodal force. These control parameters needs to be assessed on a problem-by-problem basis. Because the solution scheme does not involve matrix inversion, it is effective for incremental nonlinear analysis, including modeling of construction sequence and changing of material parameters. Furthermore, the collapse of a system due to load application or reduction in material strength can be captured. In addition to a suite of built-in material models, complicated material behavior can be readily implemented using either macros or user-defined functions.

ACKNOWLEDGMENTS

Many engineers, from different sectors of the profession, contributed to the preparation of this paper. The opinions expressed in this paper are, however, solely those of the author.

REFERENCES

BS 8006. Strengthened/reinforced soils and other fills. British Standards Institution, 1995.

BE3/78. Reinforced and anchored earth. Retaining walls and bridge abutments for embankments. Dept. of Transport, UK, 1978.

BR Christopher, SA Gill, I Juran, F Achlosser, JK Mitchell, J Duncliffe. Reinforced Soil Structures, Vol. 1, Design and Construction Guidelines. Federal Hwy Administration, FHWA-RD-89-043, 1990.

P Cundall, M Board. A microcomputer program for modeling strain-strain plasticity problems. *Proc. 6th Intl. Conf. in Numerical Methods in Geomechanics* 3: 2101–2108, 1988.

DR-91271. Strengthened/reinforced soils. Draft Australian Standard, 1991.

JH Greenwood. Designing to residual strength of geosynthetics instead of stress rupture. *Geosynthetics Intl.* 4(1): 1–10, 1996.

N Greet. Geosynthetic reinforced structure. B.E. thesis, University College, UNSW, 1986.

MR Hausmann, J Clarke. Flyash-geosynthetic interaction. Fifth Intl. Conf. on Geotextiles, Geomembranes and Related Products, Singapore, Sept. 1994, pp 433–436, 1994.

S-CR Lo. Discussion of designing to residual strength of geosynthetics instead of stress rupture. *Geosynthetics Intl.* 4(6): 673–675, 1997.

S-CR Lo, S-Q Li, M Gopalan, Z Gao. Analysis and design of a tied back-to-back geosynthetic reinforced soil wall. *Geotechnical Engr. SE Asian Geotechnical Society.* 27(1): 37–50, 1996.

S-CR Lo. Pull-out resistance of polyester straps at low overburden stress. Geosynthetics Intl. 5(4), Dec. 1998.

J Marti, PA Cundall. Mixed discretization procedure for accurate solution of plasticity problem. *Intl. J. Numerical and Anal. Methods in Goemechanics.* 6: 129–139, 1982.

GWE Milligan, K Tei. The pullout resistance of model soil nails. *Soils and Foundations*, 1998.

R57. Design of reinforced soil walls. QA Specification R57, Road and Traffic Authority of New South Wales, Australia, Edition 1, Rev-4, Aug 1998.

R58. Construction of reinforced soil walls. QA Specification R58, Road and Traffic Authority of New South Wales, Australia, Edition 1, Rev-1, Mar 1997.

GW Won. Use of geosynthetic reinforced structures in highway engineering. Ground Modification Seminar No. 3, University of Technology, Sydney, Sept. 1994.
GW Won, MR Haussmann, E Jankulovski. Performance of Websol soil wall bridge abutment in Sydney, Australia. *Fifth Intl. Conf. Geotextiles, Geomembranes and Related Products*, Singapore, Sept. 1994, pp 433–436, 1994.
GW Won, T Hull, L De Ambrosis. Performance of a geosynthetic segmental block wall structure to support bridge abutments. *Proc. Intl. Symposium on Earth Reinforcement*, Fukuoka, Japan, Nov. 1996, pp 543–548, 1996.
KC Yeo, PLR Pang. Review of design temperature for reinforced fill slopes in Hong Kong. *Proc. Intl. Symp. on Earth Reinforcement*, Kyushu, Japan, Nov. 1996, vol 1, pp 289–26.

16

Geosynthetic Reinforced Containment Dike Constructed over Soft Foundation: Numerical Analysis

Hoe I. Ling and Dongyi Yue
Columbia University, New York, New York, U.S.A.

V. N. Kaliakin
University of Delaware, Newark, Delaware, U.S.A.

1 INTRODUCTION

Geosynthetics have been used to strengthen the embankment constructed over soft foundation (e.g., Fowler, 1982; Schimelfenyg, 1994; Sandiford et al., 1996). This chapter describes the results of numerical analysis of a containment dike over soft foundation that used an anisotropic bounding surface soil model and coupled stress-flow analysis.

In order to meet the long-term needs for the disposal of dredged material at Wilmington Harbor, the Wilmington Harbor South Disposal Area (WHSDA) was constructed in the period from 1985 to 1990. The WHSDA containment structure consisted of an approximately 9,000$'$ (3-km) earthen dike within the Delaware River. Fig. 1 shows the location of the containment dike.

The foundation was composed of extremely soft soil and was located below the water table. Innovative construction techniques, including the use of

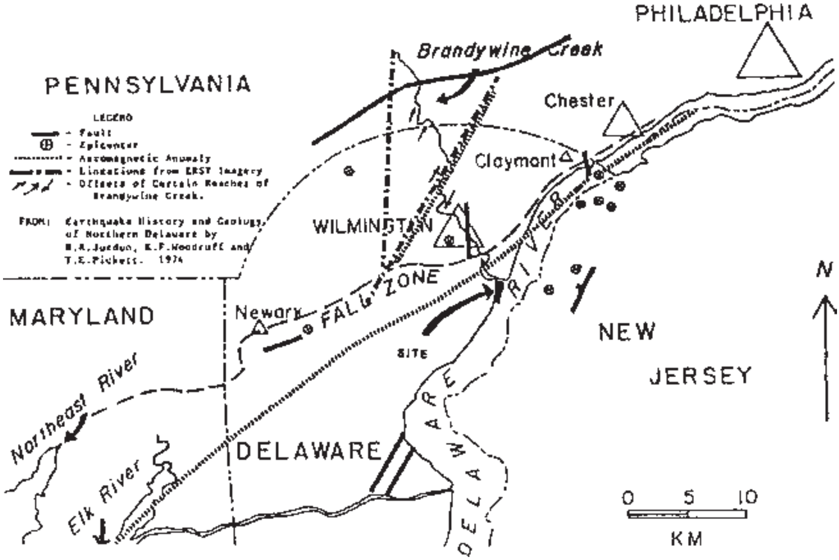

Figure 1 Location of Wilmington Harbor South disposal site.

geotextile and wick drains, were adopted to improve the performance of the dike and its foundation. Wick drains were installed to accelerate consolidation. The dike was constructed in several phases and was instrumented to monitor the performance during the period of construction and also after construction. It was hoped that the results of this instrumentation would provide valuable information for future construction of similar structures.

In order to solve the sophisticated initial-boundary-value problem, an anisotropic bounding surface model (Yue, 2001; Ling et al., 2002) was incorporated into a two-dimensional finite-element program (SAC-2, Herrmann and Kaliakin, 1987) for the analysis. SAC-2 utilizes a coupled stress-flow analysis based on Biot's theory. It has been used for geotechnical analysis of similar problems (such as Poran et al., 1988; Kaliakin et al., 1990). A set of comprehensive field results was compared with the results obtained from numerical prediction.

2 FOUNDATION AND SOIL PROPERTIES

Figure 2 shows a typical cross section of the containment dike and associated foundation profile. It was identified based on the boring logs and laboratory soil testings conducted by the U.S. Army Corps of Engineers (USACE, 1985) and

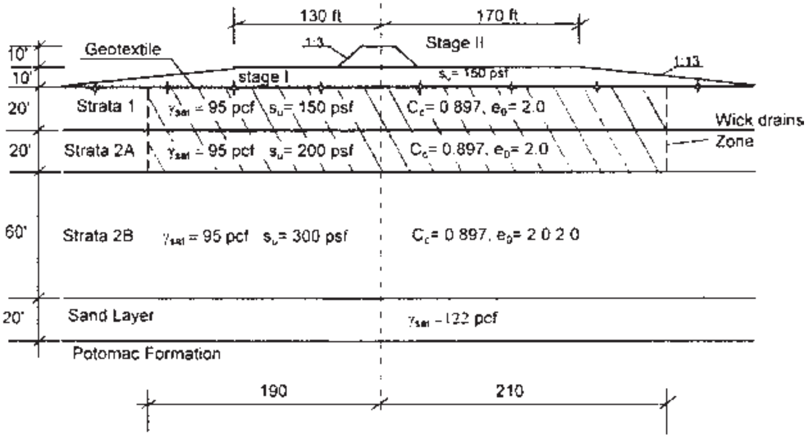

Figure 2 Soil profile and properties.

Duffield Associates (1994). The recent or Holocene Age deposits consisted of very soft, dark gray, highly plastic clayey silts and silty clays of 25′ to 100′ (8.3 to 33 m) thick, overlying a relatively thin 5′ to 20′ (1.7 to 6.7 m) thick sand layer of the Pleistocene Age Columbia formation. These sediments were underlain by the Cretaceous Age Potomac formation that consisted of variegated silt and clays containing highly variable interbedded sand and gravel layers.

Table 1 summarizes the results of soil testing for the foundations based on standard classification, consolidation, permeability, triaxial compression, and unconfined compression tests. The design cross section incorporated the greatest thickness of compressible clay encountered in the soil boring. These compressible clays were separated into three strata, Strata 1, 2A, and 2B, based on the soil properties. The parameters used for each stratum are included in Fig. 2.

3 CONSTRUCTION AND INSTRUMENTATION

The dike was constructed in two stages. Stage I consisted of hydraulic placement between March 1987 to December 1988 for the whole embankment. The fill provided a platform to install the wick drains and geotechnical instrumentation. The final dike was constructed in Stage II. It started in late December 1988 and was completed in April 1990. Generally, Stage II was constructed one half to one year after completion of Stage I construction.

Table 1 Summary of Soil Test Results*

Stratum no.	Elevation	PI	Class USCS	Test type†	Shear properties c (tsf)	ϕ (°)	q_u (tsf)	Consolidation data p_c (tsf)	p_0 (tsf)	C_c	Other
1	−10.5 to −12.5	31	MH	TC/UU	0.22	0		0.8	0.6	0.897	$k = 3.15\text{e-}7$ ft/min‡
1	−40.5 to −42.5	47	CH	UC	—	—	0.38	1.3	0.7	0.863	$k = 3.35\text{e-}7$ ft/min‡
1	−13.0 to −15.0	53	CH	UC	—	—	0.03	—	—	—	—
1	−17.0 to −19.0	64	CH	UC	—	—	0.15	—	—	—	—
1	−19.0 to −21.0	33	CH	UC	—	—	0.15	—	—	—	—
1	−11.5 to −13.5	42	CH	UC	—	—	0.05	—	—	—	—
1	−15.5 to −17.5	47	CH	UC	—	—	0.14	0.1	0.15	0.897	—
1	−17.5 to −19.5	34	CH	TC/CU	0	19.5	—	—	—	—	$c' = 0$ $\phi' = 38°$
1	−21.5 to −23.5	50	CH	UC	—	—	0.2	—	—	—	—
1	−1.0 to −3.0	47	CH	UC	—	—	0.09	—	—	—	—
1	−5.0 to −7.0	56	CH	UC	—	—	0.1	0.1	0.16	0.93	—
1	−7.0 to −9.0	62	CH	TC/CU & UC			0.28	—	—	—	$c' = 0$ $\phi' = 32.5°$
2	−38.0 to −40.0	42	MH	UC	—	—	0.46	—	—	—	—
2	−17.0 to −19.0	52	MH	—	—	—	—	—	—	—	$k_h = 5.9\text{e-}6$ ft/min $k_v = 3.9\text{e-}6$ ft/min
2	−26.0 to −28.0	43	CH	TC/CU & UC	0.1	1705	0.22	0.3	0.4	0.831	$k = 1.95\text{e-}6$ ft/min‡
2	−36.0 to −38.0	31	CH	—	—	—	—	—	—	—	$k_h = 3.0\text{e-}5$ ft/min k_v 5.9e-6 ft/min
2	−22.0 to −24.0	33	CH	—	—	—	—	—	—	—	$k_h = 9.3\text{e-}5$ ft/min $k_v = 5.9\text{e-}6$ ft/min
2	−42.0 to −44.0	36	CH	—	—	—	—	—	—	—	$k_h = 1.4\text{e-}6$ ft/min $k_v = 5.9\text{e-}7$ ft/min
2	−22.0 to −24.0	55	CH	TC/CU & UC	0.1	15.5	0.2	—	—	—	$c' = 0$ $\phi' = 32.5°$

2	−32.0 to −34.0	42	CH	—	—	—	—	—	—	—	$k_h = 6.3\text{e-}5$ ft/min
											$k_v = 2.3\text{e-}5$ ft/min
2	−21.0 to −23.0	31	CH	—	—	—	—	—	—	—	$k_h = 1.7\text{e-}5$ ft/min
											$k_v = 7.5\text{e-}6$ ft/min
2	−37.0 to −39.0	53	CH	TC/CU & UC	0.15	18.5	0.33	0.6	0.55	0.897	$k = 1.8\text{e-}6$ ft/min‡
2	−22.0 to −24.0	48	CH	UC	—	—	0.2	—	—	—	—
2	−28.5 to −30.5	40	CH	UC	—	—	0.15	—	—	—	—
2	−50.5 to −52.5	38	CH	UC	—	—	0.39	—	—	—	—
2	−68.5 to −70.5	35	CH	TC/CU & UC	0.04	0	0.06	—	—	—	—
2	−88.5 to −90.5	40	CH	UC	—	—	0.1	—	—	—	—
2	−28.5 to −30.5	30	CH	TC/UU	0.2	0.5	—	—	—	—	—
				TC/CU	0.05	25	—	—	—	—	—
2	−48.5 to −50.5	29	MH	TC/UU	0.5	0	—	—	—	—	—
2	−68.5 to −70.5	30	MH	TC/CU	0.4	11.5	—	—	—	—	$c' = 0$ $\phi' = 32.5°$

* Data taken from USACE (1985).
† TC = triaxial compression. UC = unconfined compression. UU = unconsolidated undrained. CU = consolidated undrained.
‡ Permeability obtained from consolidation test.

A high-strength woven geotextile, manufactured from polyester, was installed under the embankment/foundation to tensile-reinforce the foundation and also acted as separator. The wick drains extended approximately 40′ (13.3 m) into the foundation to accelerate consolidation of the top portion of foundation soil, that is, Strata 1 and 2A. The wick drains were 4″ (10 cm) wide and 0.25″ (0.64 cm) thick. They contained plastic cores to allow free vertical flow of pore water and were covered by a geotextile.

The instrumentation scheme included 42 settlement plates, 3 inclinometers, and 25 piezometers along the critical riverward portion of the dike. The measured settlement ranged from 1.5″ to 10″ (13.8 to 25.4 cm) along the centerline and between 4″ and 4.5″ (10.2 to 11.25 cm) along the dike exterior slope 5 years after construction. Most lateral movements were detected during construction. The piezometric reading leveled off following completion of construction.

A total of 66 strain gauges were installed in the geotextile along the three terminals (each having 22 strain gauges). The total strains in the geotextile ranged from 1.8 to 3.0% in the fill direction and 1.9 to 3.1% in the wrap direction. The geotextile continued to creep after construction. About half of the instruments were still functioning 3.5 years after construction.

4 FINITE-ELEMENT ANALYSIS

The anisotropic bounding surface elastoplastic model (Yue, 2001; Ling et al., 2002) was incorporated into a general-purpose finite-element program SAC-2 (Herrmann and Kaliakin, 1987) for the analysis. This version of model requires 12 input parameters. A material subroutine describing the proposed model was coded to provide SAC-2 with the material matrix to deal with the anisotropic clays. The numerical scheme of implementation is in principle similar to that outlined by Herrmann et al. (1987).

The containment dike and foundation soil were idealized as plane strain based on the assumptions that the curvature of the embankment could be neglected and the three-dimensional configuration of the wick drains could be idealized as two dimensions through a separate procedure as described subsequently. Figure 3 shows the mesh for finite-element analysis. It consisted of 175, 21, and 46 elements for the foundation, fill and geotextile, respectively.

The construction stages were simulated using the incremental construction option of the program. A total of 1800 days and 132 increments, with a time step of 10–15 days per increment, was included in the analysis. Considering the extremely poor drainage conditions of the soft clays, Stage I was treated as instantaneous loading through the fill elements at the beginning of calculation, and the wick drains were assumed to take effect at the very beginning (time $t = 0$). Consolidation was allowed for a year until Stage II was initiated.

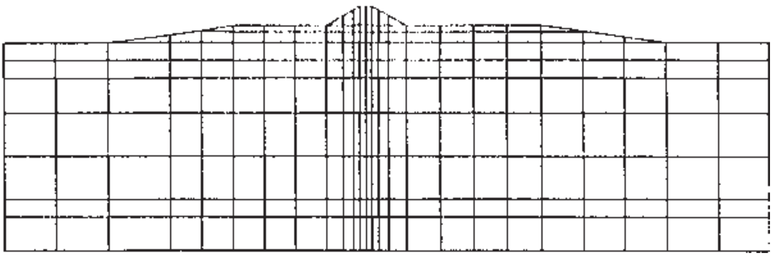

Figure 3 Finite-element mesh.

Linear elastic material and plane strain mixed elements were selected to model the dike and sand layer of foundation. The mixed element implemented in SAC-2 has four nodes to represent the displacement and pore pressure. The geotextile was modeled through the elastic membrane element to account for the large deformations. The clays (Strata 1 and 2) were characterized using the proposed anisotropic bounding surface elastoplastic model. The material parameters for sand, fill, and geotextile are summarized in Table 2. The material parameters for clays are given in Table 3. Due to a lack of information on the laboratory tests, some of the model parameters were estimated from the typical values based on the sensitivity studies (Yue, 2001). Note that the same set of parameters was used for the three soil strata.

The wick drain was modeled following the methods proposed by Poran et al. (1988). A more comprehensive procedure of modeling was also proposed by Amirebrahimi and Herrmann (1993); the essence of this method is to transform the axisymmetric problem into its equivalent plane strain idealization by conducting water flow analysis using the finite-element method. The two simulations, which used different permeability coefficients but the same loading conditions, were considered to be equivalent when the difference of the average excess pore pressure, resulting from the two simulations at some particular time, was within an acceptable range. The equivalent coefficients of permeability

Table 2 Material Properties of Sand, Fill, and Geotextile

Material	Elastic modulus	Poisson ratio	Thickness
Sand	28,000 kPa	0.3	20′
Stage I fill	14,400 kPa	0.3	10′ (3.3 m)
State II fill	28,000 kPa	0.3	10′ (3.3 m)
Geotextile	1400 kN/m	—	100 mil

Table 3 Anisotropic Model Parameters for Strata 1 and 2

Parameters	Values
λ	0.36
κ	0.04
ν	0.20
M_c (M_e)	1.20 (1.02)
R	3.4
C	0.4
s	2.0
Ψ_1	5.0
Ψ_2	1.0
Ψ_3	5.0
W	2.0
A_0	1.0

adopted in the two-dimensional plane strain analysis are summarized in Table 4. This equivalent model produced results within 5% error with the actual axisymmetric idealization at 90, 180, and 360 days after load application (20 kPa as step loading at $t = 0$). The sand layer and dike fill were assigned a relatively high coefficient of permeability—namely 200 m/day—to simulate free drainage.

The initial stress states for the several soil layers in the underlying strata were calculated using the given unit weights for saturated soils (see Fig. 2), the thickness of the layers and coefficient of earth pressure at rest K_0, which was assumed as 0.6 for all clay layers.

For the purpose of comparison of the proposed model with the isotropic bounding surface model of Kaliakin and Dafalias (1990a,b), a finite-element analysis was also conducted by assuming the clays to be isotropic and time-independent by taking the material constant A_0 to be 0.0. Table 5 summarizes the parameters for above two cases of analysis.

Table 4 Coefficients of Permeability of Foundation

Coefficient of permeability ($\times 10^{-3}$ m/day)	Strata 1		Strata 2A		
	With drains	No drains	With drains	No drains	Strata 2B
Vertical	3.8	3.8	3.8	3.8	0.61
Horizontal	4.2	1.7	4.2	1.7	0.61

Table 5 Isotropic Model Parameters for Strata 1 and 2

Parameters	Isotropic, time-independent	Isotropic, time-dependent
λ	0.36	0.36
κ	0.04	0.04
ν	0.20	0.20
M_c (M_e)	1.20 (1.02)	1.20 (1.02)
R	2.0	2.0
C	0.4	0.4
s	2.0	2.0
Ψ_1	5.0	5.0 (h_2)*
Ψ_2	1.0	2.0 (m)*
Ψ_3	5.0	5.0 (h_c)*
W	2.0	1.0 (w)*
A_0	0.0	1.0 (a)*
n	—	2.0
V	—	7.9E + 9 (kPa.min)
S_v	—	1.6

* See Kaliakin and Dafalias (1990a,b) for definitions.

5 RESULTS AND DISCUSSION

Figures 4 and 5a–d compare the settlement and horizontal displacement at some representative locations between the analysis and field measurements. The settlement was for the point at a depth approximately 3.3 m below the surface and 1.8 m to the left of the centerline of the dike. The horizontal displacement distribution was for the vertical line at 6.7 m to the left of the centerline. Due to the simplified method used to simulate the water flow, it required another set of finite-element analysis to obtain the curve of pore pressure response with time.

The results of comparison showed that the agreement between model prediction and measurements is satisfactory. However, the analysis under-estimated the horizontal displacement, especially for the isotropic model. The difference between the anisotropic model and field measurements could be partially attributed to the idealization of three-dimensional to two-dimensional configuration. Also, the difference between designed and constructed cross section contributed to the difference. Moreover, the recorded deformation was large, whereas the analysis assumed small strain deformation.

The results also showed that the anisotropic bounding surface model gave a better prediction than the isotropic version of model. Anisotropy played an important role in determining the response of the foundation under embankment loading. Ladd et al. (1994) have indicated that the conventional isotropic version

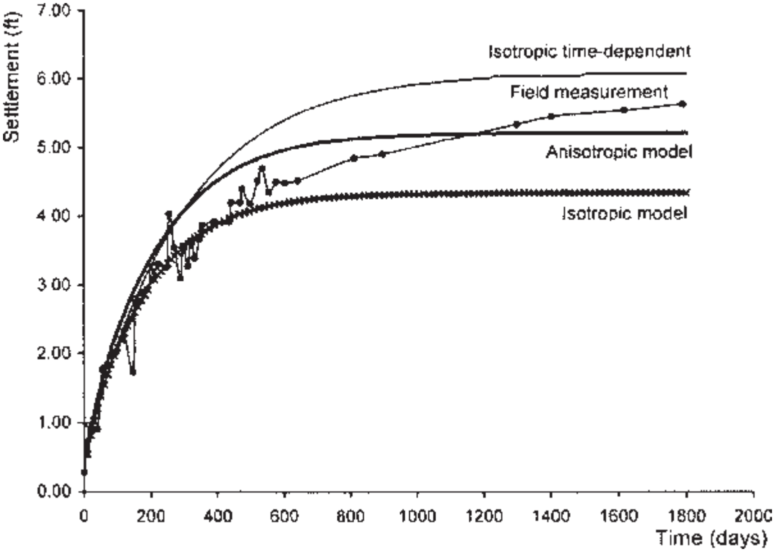

Figure 4 Comparison of analyzed and measured settlement.

of a modified Cam-clay model is incapable of predicting the lateral deformation of foundation beneath an embankment.

The measured results showed that the settlement was still in progress, whereas the time-independent version of model did not predict the creep behavior. Thus, the time-dependent version of the proposed model should be incorporated into the analysis following the refinement of numerical scheme.

6 SUMMARY AND CONCLUSIONS

A waste containment dike constructed over soft clay foundation was analyzed. A set of field instrumentation results was compared to the results of analysis. The comparison showed that the agreement between the analysis and measurements was satisfactory. However, the analysis underestimated the horizontal displacement, especially for the isotropic model. The importance of simulating the anisotropic behavior of soils was highlighted in this analysis.

The results of this study, as summarized here, should be considered as an initial attempt to the application of the anisotropic version of bounding surface model to embankment constructed over soft foundations. The time-dependent version of the proposed model should be incorporated into the analysis following the refinement of the numerical scheme.

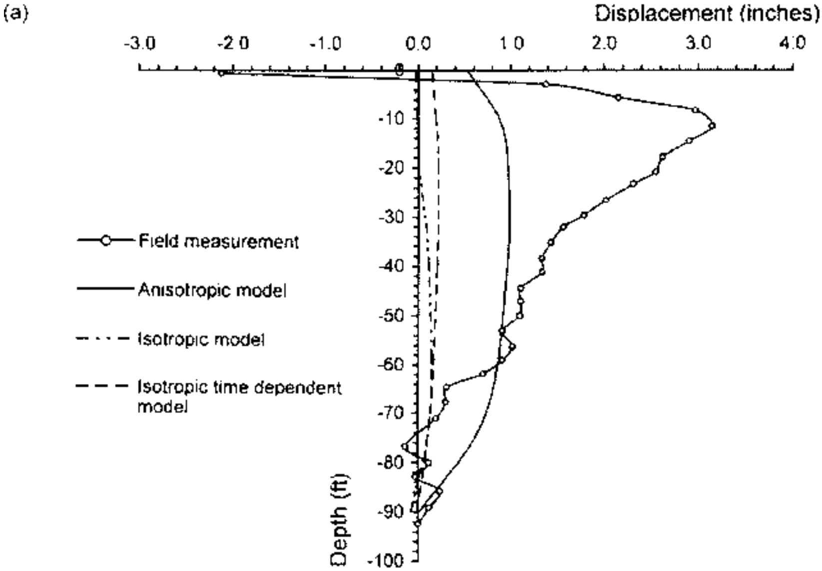

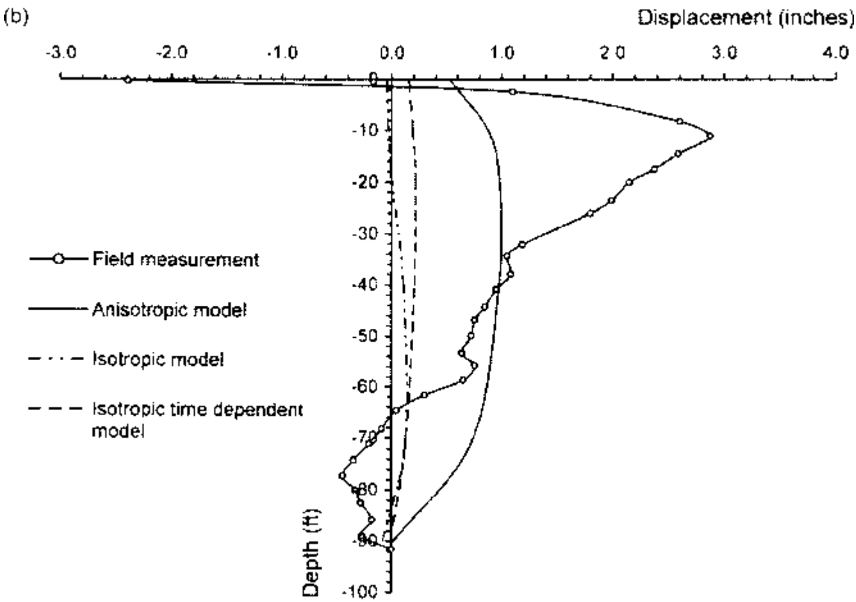

Figure 5 Comparison of horizontal displacement: t = (a) 480 days, (b) 540 days, (c) 920 days, (d) 1080 days.

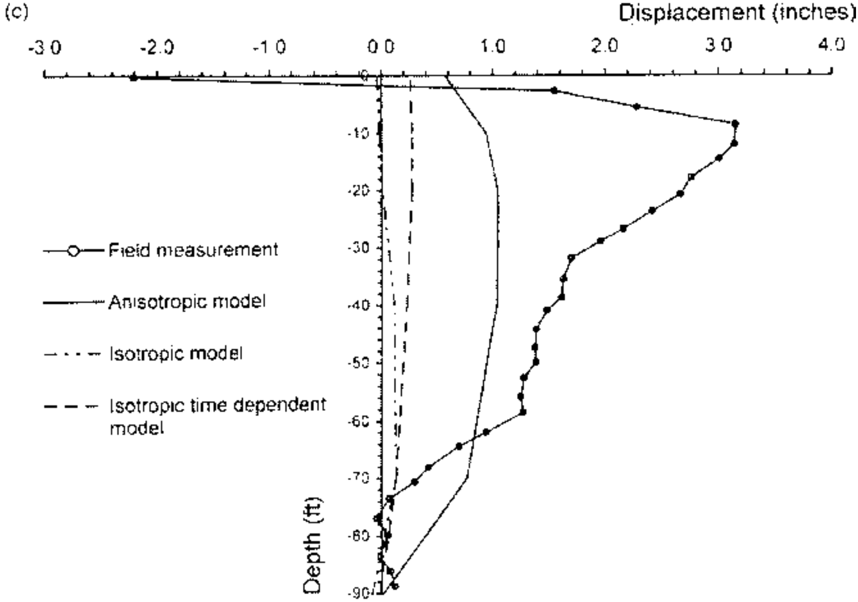

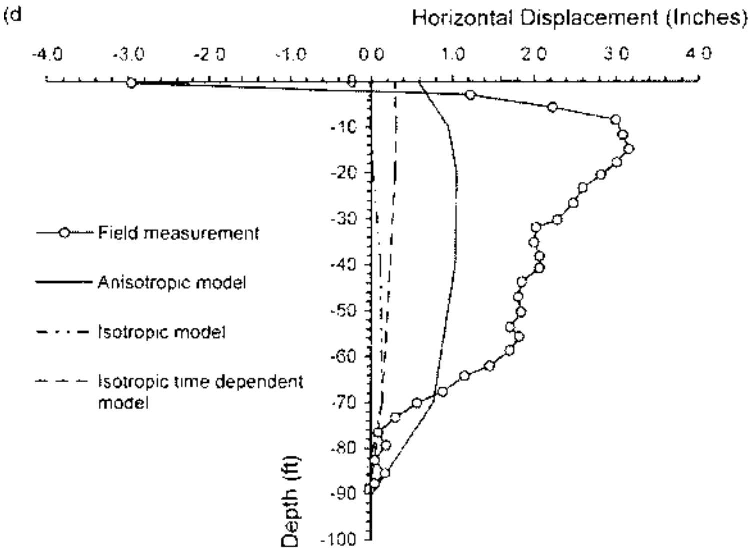

Figure 5 Continued.

REFERENCES

AM Amirebrahimi, LR Herrmann. Continuum model and analysis of wick-drained systems. *Intl. J. Numerical and Analytical Methods in Geomechanics* 17: 827–847, 1993.

Duffield Associates, Inc. Summary Report: Wilmington Harbor South Disposal Area. Prepared for U.S. Army Corps of Engineers, Philadelphia District, 1994.

J Fowler. Theoretical design considerations for fabric reinforced embankments. *Proc. 2nd Intl. Conf. on Geotextiles*, Las Vegas, pp. 665–676, 1982.

LR Herrmann, VN Kaliakin, YF Dafalias. Computer Implementation of the Bounding Surface Plasticity Model for Cohesive Soils. Department of Civil Engineering Report, University of California at Davis, 1983.

LR Herrmann, VN Kaliakin. User's Manual for SAC-2, A Two-Dimensional Nonlinear Time-Dependent Soil Analysis Code Using the Bonding Surface Elastoplasticity-Viscoplasticity Model, Department of Civil Engineering Report, University of California at Davis, 1987.

LR Herrmann, VN Kaliakin, CK Shen, KD Mish, ZY Zhu. Numerical implementation of plasticity model for cohesive soils. *J. Engineering Mechanics*, ASCE 113(4): 500–519, 1987.

VN Kaliakin, KK Muraleetharan, YF Dafalias, LR Herrmann. Foundation-response predictions below caisson-retained island. *J. Geotechnical Engineering* 116(9): 1291–1308, 1990.

VN Kaliakin, YF Dafalias. Theoretical aspects of the elastoplastic-viscoplastic bounding surface model for cohesive soils. *Soils and Foundations* 30(3): 11–24, 1990a.

VN Kaliakin, YF Dafalias. Verification of the elastoplastic-viscoplastic bounding surface model for cohesive soils. *Soils and Foundations* 30(3): 25–36, 1990b.

CC Ladd, AJ Whittle, DE Legaspi, Jr. Stress-deformation behavior of an embankment on Boston blue clay. *Vertical and Horizontal Deformation of Foundation and Embankments*, ASCE pp. 1730–1759, 1994.

HL Ling, D Yue, VN Kaliakin, NJ Themelis. An anisotropic elasto-plastic bounding surface model for cohesive soils. *J. Engineering Mechanics*, ASCE 128(7):748–758, 2002.

CJ Poran, VN Kaliakin, LR Hermaan, KM Romstad, DF Lee, CK Shen. Prediction of trial embankment behavior Hertfordshire County Councils—Stanstead Abbotts. *Proc. Prediction Symp. on a Reinforced Embankment on Soft Ground*, RH Bassett and KC Yeo, eds, King's College London, 1988.

RE Sandiford, S Law, G Roscoe. Application of geosynthetics in the construction of an overrun area at La Guadia Airport. *Geotextiles and Geomembranes* 14: 193–200, 1996.

P Schimelfenyg, J Fowler, D Leshchinsky. Fabric reinforced containment dike, New Bedford superfund site. *Proc. 4th Intl. Conf. on Geotextiles, Geomembranes and Related Products*, Balkema, Rotterdam, pp.149–154, 1994.

U.S. Army Corps of Engineers. *Design Memorandum: Wilmington Harbor South Disposal Area Development*. U.S. Army Corps of Engineers, Philadelphia District, 1985.

D Yue. An isotropic and time-dependent bounding surface model for clays and its application to a containment dike constructed over a soft foundation. *D. Eng. Sci. Thesis*, Columbia University, 2001.

17

Post-Earthquake Investigation of Several Geosynthetic Reinforced Soil Retaining Walls and Slopes During Ji-Ji Earthquake of Taiwan

Hoe I. Ling
Columbia University, New York, New York, U.S.A.

Dov Leshchinsky
University of Delaware, Newark, Delaware, U.S.A.

ABSTRACT

This chapter gives an overview on the application and seismic performance of geosynthetic- reinforced soil structures in Taiwan. Taiwan has an unique topography and geotechnical conditions that render a less conservative and more challenging design compared to that of North America, Europe, and Japan. The Ji-Ji (Chi-Chi) earthquake of 1999 gave an opportunity to examine the behavior of reinforced soil structures. The performance of several modular block reinforced soil retaining walls and reinforced slopes at the vicinity of the fault was evaluated. Reinforced structures performed better than unreinforced soil retaining walls. The failure cases were highlighted, and the cause of failure was identified. The lack of seismic design consideration could be a major cause of failure. The compound failure mode, the inertia force of the blocks, and the connection stiffness and strength relative to the large dynamic earth pressure were among major items that warrant further design consideration.

1 REINFORCED SOIL APPLICATIONS IN TAIWAN

Taiwan is an island country of 360,000 km^2 with over 21.9 million people (ROC, 2000). The main island is densely populated (606 persons/km^2), ranked second in the world. More than 70% of the island is composed of slopes and mountains. Reinforced soil retaining walls and reinforced slopes have gained wide popularity in Taiwan over recent years because of the many large-scale housing and industrial development projects located at the slopes and hillsides.

Chou (2000) gave an overview of the recent development of geosynthetic reinforced soil structures (GRSS) in Taiwan. There are several unique features for GRSS constructed in Taiwan compared to the technology that has been developed and established in North America, Europe and Japan:

1. The topography and geotechnical conditions of Taiwan are quite different from the rest of the world. Many recent constructions are located along the slopes and mountains. While GRSS constructed in the United States, Europe, and Japan are mostly near vertical and for a height of less than 10 m, some of the reinforced slopes in Taiwan are over 30 to 40 m, usually with a series of walls stacking over each other (multiple walls).
2. The on-site soil is usually used as backfill material. The cost of granular sand is relatively high at its scarcity. Disposal of on-site soils and transportation of granular soils to the construction site, typically in the mountains, are difficult and costly.
3. A wraparound facing structure is commonly used for reinforcing slopes. The wall face is usually finished with a vegetated facing.
4. For reinforced soil retaining walls, the modular block facing structure is most popular. The height is typically between 2 and 10 m.
5. Geogrids comprise more than 95% of the applications in reinforced soil structures for economic reasons. There are several local geogrid manufacturers in Taiwan. The geotextiles and metallic reinforcements are not popular.
6. The designs of GRSS are typically provided by the manufacturers. There is a lack of geotechnical consideration for certain specific applications.

The reinforced soil technology has not been adopted widely by the public sectors compared to the private developers, such as for residential and industrial facilities. So far, three sets of design manuals are available by the highway and railway authorities, and the Society of Civil Engineers. The design manual for the highway (Chen et al., 1990) is an adopted version of the FHWA and AASHTO documentation. The version for the railway structures (Chou et al., 1996) is based on the reinforced soil technology developed by the Japan Railway Technical Research Institute. A design and construction manual is also issued by the Taipei Society of Civil Engineers (Chou et al., 1998).

In this paper, the performance of several geosynthetic reinforced soil structures during the 1999 Ji-Ji earthquake is reported. The causes of failure are identified and suggestions leading to design improvement are made.

2 SEISMIC DESIGN

The seismic design of reinforced soil structures is typically done using a pseudo-static approach. A seismic coefficient is used to express the earthquake inertia force as a percentage of the dead weight of the potential failure soil mass. There are a few design procedures proposed in recent years, as briefly mentioned below.

Ling et al. (1996, 1997) and Ling and Leshchinsky (1998) proposed a pseudo-static analysis considering the internal (tieback) and external (compound failure and direct sliding) stabilities of the reinforced soil structures. The procedure is an extension of the design procedure proposed by Leshchinsky (e.g., Leshchinsky et al., 1995). The result of study is compiled in the form of design charts and also available for computerized design (Leshchinsky, 1997, 1999). The authors then extended the procedure for a permanent displacement analysis.

From a series of parametric studies, the authors concluded that in the event of a large earthquake, external stability, typically by direct sliding, may govern the design. That is, a longer geosynthetic length is required for design in addition to a stronger reinforcement in resisting the earthquake inertia force. The proposed procedure was verified with 8 case histories for the 1994 Northridge earthquake ($M = 6.7$), the 1995 Kobe earthquake ($M = 7.3$), the 1993 Kushiro-oki earthquake ($M = 7.8$) and the 1987 Chiba-ken Toho-oki earthquake ($M = 6.7$). Among all these cases, only the Tanata Wall of Kobe earthquake was relevant for the verification of permanent displacement.

The effect of vertical acceleration on the performance of geosynthetic reinforced soil structures was also studied by Ling and Leshchinsky (1998). Vertical acceleration increases the required reinforcement length and force. It was also concluded that the vertical acceleration may reduce the stability, especially for direct sliding mode, if the corresponding horizontal component of acceleration is very large.

A separate seismic design procedure was proposed by Bathurst and Cai (1995) and Bathurst and Alfaro (1997). The procedure was based on an extension of Mononobe–Okabe analysis. The procedure was subsequently adopted for the design of modular block walls for the National Concrete Masonry Association (NCMA, Collin, 1997).

The design manual issued by the Federal Highway Administration (FHWA) has also included seismic design procedure (Christopher et al., 1990; Elias and Christopher, 1996) and has been made available for computerized design (Leshchinsky, 1999). FHWA procedure was centered for the reinforced soil structures with metallic reinforcements.

The previous earthquakes that occurred in the United States and Japan had proved that geosynthetic reinforced soil structures are durable to minor and major shakings (Elihau and Watt, 1991; Collin et al., 1992; Sandri, 1997; White and Holtz, 1997; Tatsuoka et al., 1995, 1997). However, most reinforced soil structures were subject to minor shaking except for the 1995 Kobe earthquake. The reinforced soil structures found around the Kobe area had a rigid facing, which is different from most geosynthetic reinforced soil retaining walls available in other parts of the world. Moreoever, the modular block reinforced soil retaining walls, an increasingly popular structure in North America, were not constructed in Japan. Thus, the 1999 Ji-Ji earthquake in Taiwan provided an opportunity to evaluate the seismic performance of geosynthetic reinforced soil structures, particularly the modular block walls.

3 JI-JI (CHI-CHI) EARTHQUAKE AND PERFORMANCE OF REINFORCED SOIL STRUCTURES

The Chi-Chi earthquake occurred on September 21, 1999, at 1:47 a.m., with a magnitude of 7.3. More than 2200 people were killed, and devastating damage was recorded. The main shock was recorded at 23.87°N, 120.75°E in central Taiwan, at a depth of 7 km (Lee, 1999). The rupture surface observed at the Chelungpu fault extended for more than 85 km, with a vertical displacement of 1 to 6 m (Fig. 1). The maximum horizontal peak ground acceleration was recorded for over 1 g. The ratio of vertical to horizontal acceleration was large. For example, at station TCU129, 13.5 km from the epicenter, the E–W, N–S, and vertical (U–D) accelerations were 983 gal, 611 gal, and 335 gal, respectively.

Seismic design is conducted for the buildings and highway structures in Taiwan. The main island is divided into 4 main seismic zones: I-A, I-B, II, and III (Fig. 2). The respective accelerations used for design are 0.33 g, 0.28 g, 0.23 g, and 0.18 g. It is obvious that the recorded accelerations, such as that at station TCU129, far exceeded the design values.

The investigation on the performance of several geosynthetic reinforced soil structures was conducted on January 28 and 29 around central Taiwan. Although most severely damaged buildings have been demolished, many soil

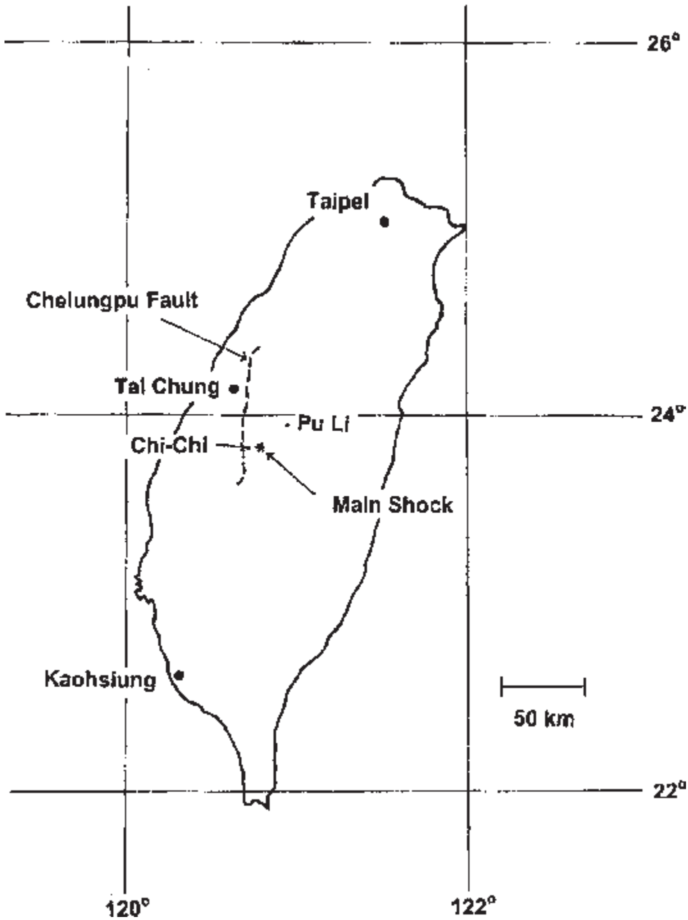

Figure 1 Location of epicenter and fault. (Information from CIA and CWB, Taipei.)

structures were still unrepaired or undergoing repair. A total of six reinforced soil structures was investigated and reported herein. Among these structures, two were geosynthetic reinforced slopes whereas four others were geosynthetic reinforced soil retaining walls with modular block facing. The locations of these structures are marked as ■ in Fig. 3. They were located around Tai Chung City, Chung Hsin New Village (the capital for former Taiwan Provisional Government), and Pu Li. The locations are at a distance of 1 km or less from the fault, except for Pu Li.

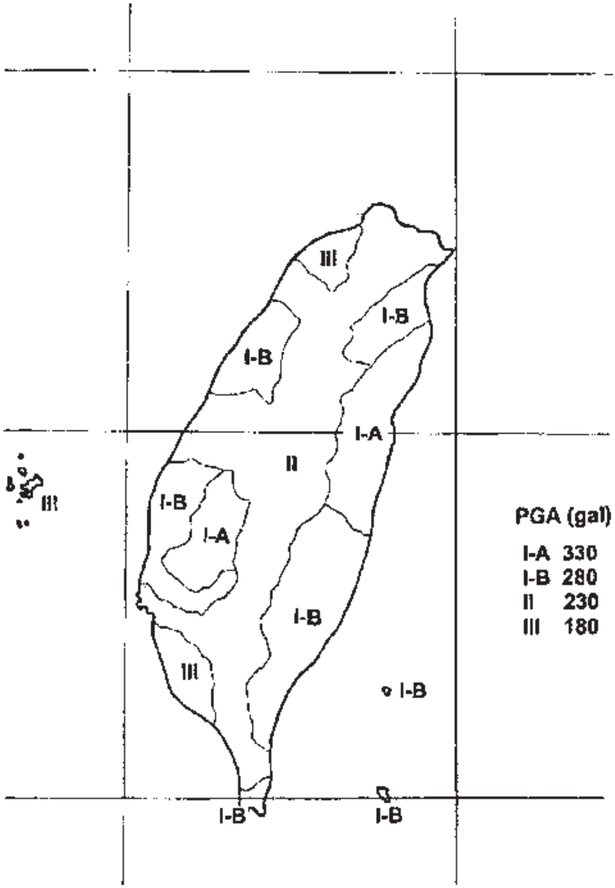

Figure 2 Seismic design zones in Taiwan. (After NCREE, 2000.)

4 MODULAR BLOCK GEOSYNTHETIC REINFORCED SOIL RETAINING WALLS

4.1 Ta Kung Housing Development Site, Tai Chung

This development site is located along the mountains. The housing development project had been abandoned prior to the Ji-Ji earthquake. Large cracks and settlements were found along the slopes (Figs. 4a and b), which indicated that part of the slope failed under seismic excitation due to loss of global stability. There was almost no obvious structural damage to the frames of the buildings, except for some of the foundations and slabs that were damaged by significant

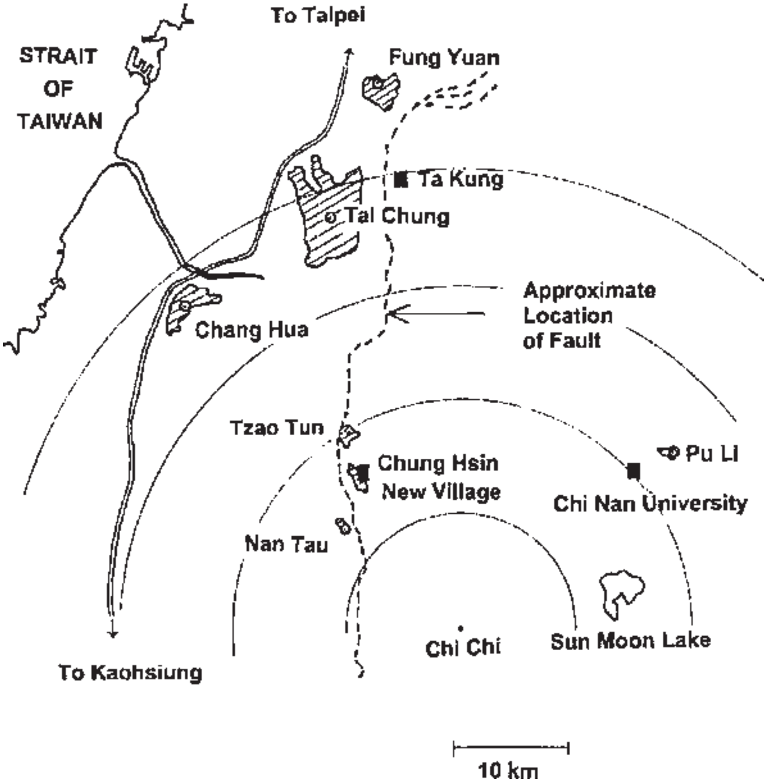

Figure 3 Major sites of investigation.

displacement resulting from the earthquake (Fig. 4a). Figures 5a and b show conventional reinforced concrete retaining walls that exhibited cracks along the horizontal and vertical construction joints, respectively. Figure 5c shows a typical case of structural failure of the reinforced concrete retaining wall.

A modular block retaining wall was constructed at this residential site (Fig. 6). The wall was 5 m high (24 blocks) at its tallest point, and accessibility to the bottom of this wall was not possible during the time of investigation. To the right of the structure is an unreinforced modular block retaining wall that collapsed. The height of this unreinforced wall was 2.4 m (12 blocks), and a failure surface was observed 2.2 m behind the wall. Note that the reinforced concrete wall, which was attached to one of the ends of this modular block wall, tilted significantly.

The geosynthetic reinforced retaining wall is found on the left of the structure. The modular block reinforced retaining wall failed at two locations.

(a) (b)

Figure 4 Ta Kung housing development site: (a) failure of slabs and foundation; (b) rupture surfaces along the slope.

(a) (b)

(c)

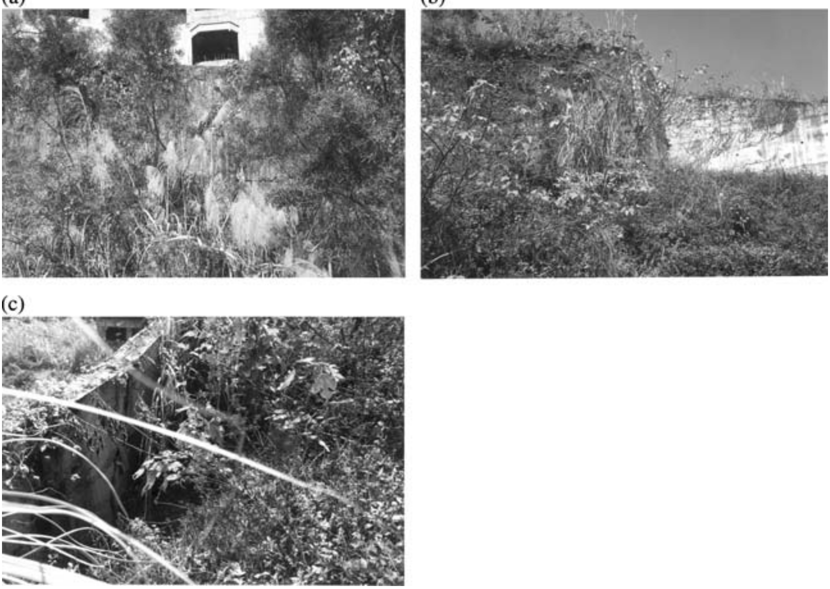

Figure 5 Failure of reinforced concrete retaining walls in Ta Kung housing development site: (a) horizontal crack, (b) separation of walls; (c) structural failure of wall.

Figure 6 Ta Kung housing development site: (a) geosynthetic reinforced soil retaining wall; (b) large settlement and failure surface behind GRS-RW; (c) deformation of modular blocks along the top of the wall; (d) collapse of GRS-RW.

At one location close to the top of the wall, the blocks displaced outward, resulting in the exposure of the connection pins (Fig. 6c). At the other location, the wall collapsed with the blocks fallen apart (Fig. 6d). It can be seen from the pictures that good-quality backfill material, gravel, was used. The reinforcement was a polyester geogrid. Because of the problem of accessibility, information related to the spacing of geogrid was not obtained directly, though it is expected to be 3 or 4 blocks based on Taiwanese design practice. It has to be mentioned that behind the wall, a very large settlement of over 2 m was observed. The large settlement damaged the foundation slab of the building (Figs. 4a and 6b). The distance from the major crack to the wall was between 15 and 20 m.

4.2 Ta Kung Roadway 129, Tai Chung City

Along the earthquake-affected areas, the stone walls, reinforced concrete walls, and tie-back walls are widely used to retain the slopes. There were many failure cases for the conventional retaining walls. Geosynthetic reinforced soil retaining walls, with a modular block facing, were constructed at several locations along Roadway 129. At one location, failure of a 3.4-m-high modular block

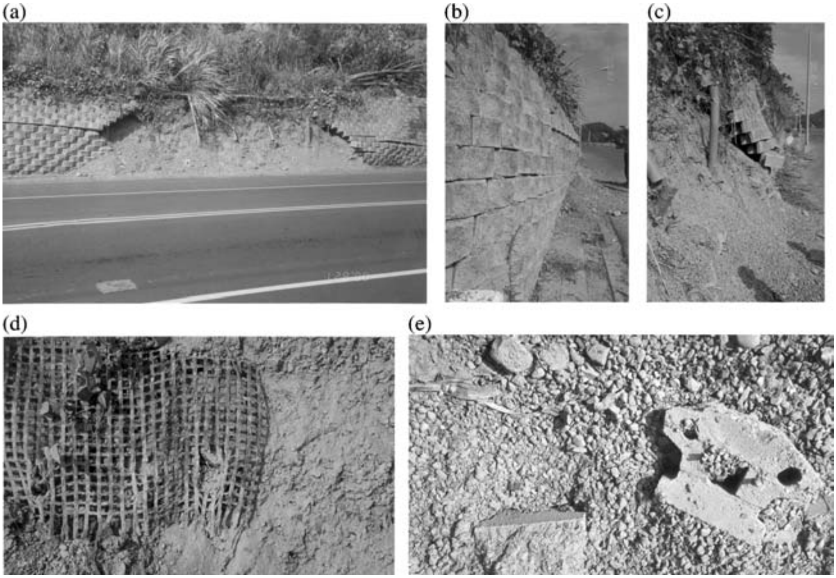

Figure 7 Ta Kung Roadway 129 geosynthetic reinforced soil retaining wall: (a) front view of collapsed section; (b) side view; (c) backfill soil; (d) geogrid reinforcement; (e) block with the connection pins.

geosynthetic reinforced retaining wall was found (Fig. 7). The wall was constructed with four-block reinforcement spacing. Figure 7b shows the largely deformed portion of the wall. The modular blocks were buried under the backfill soil (Fig. 7c). The backfill material is a silty sand. A polyester geogrid was used (Fig. 7d). Figure 7e shows the block used as facing for the reinforced soil retaining wall.

Figure 7b shows that the largest horizontal displacement was at a height of 8 blocks (1.6 m) from the bottom of the wall. This point of maximum displacement varied along the length of the wall. However, failure could be initiated from the bottom of the wall, at the region where the blocks totally collapsed, because of excessive displacement. A major crack was observed at a distance 5.6 m behind the wall. A minor crack was also formed at about 2.5 m behind the wall, which corresponded to the length of geogrid reinforcement. In Taiwan, the length of geosynthetic reinforcement is typically selected as 70% of the wall height for modular block reinforced soil retaining walls.

Note also that the transverse rib of the geogrid reinforcement was torn at the location of the connection pins (Fig. 7d). Some of the pins were bent and yielded because of the movement of the blocks. The results indicated that the transverse stiffness and strength of geogrid, as well as that of the pins, are required to keep the modular blocks in place under large dynamic earth pressure induced by the earthquake.

4.3 Chung-Hsin Stadium, Chung Hsin New Village

Modular block reinforced soil retaining walls were used extensively around Chung-Hsin Stadium. Two walls were affected by the earthquake.

The first wall was located along the side of the stadium, of height 2 m or less (Fig. 8a). A series of lampposts was installed very close to the wall. It was observed that the blocks dislocated around the location of the lampposts (Fig. 8b). The connection pins were seen through the spacing between the blocks. The deformations were due to the movement of the foundation of the lamppost. The post deflected inward and thus pushed the foundation outward to the wall. The problem could be avoided by installing the post at a distance away from the wall, or with a deeper foundation.

The second wall was located behind the stadium, 3 m high (Fig. 9a). At the crest of the wall, two cracks were observed. The first crack was about half a meter from the block, whereas the second crack was more than 2 m from the block. The blocks moved away from the backfill for over 30 cm. This wall collapsed at the lower corner. A close view of the bottom corner appears in Fig. 9b. Note that the length of reinforcement at the corner is likely less than normal because of the limited space available behind the wall. The reinforcement used was a polyester geogrid, with a vertical spacing of 3 blocks. Thus, the top layer had a spacing

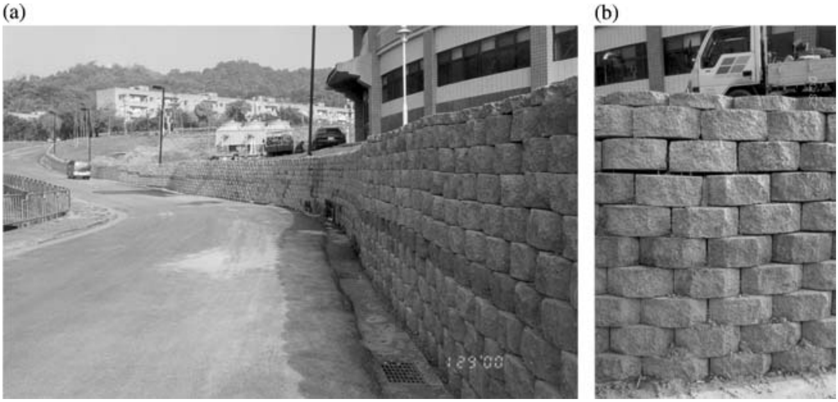

Figure 8 Chung Hsin Stadium: (a) geosynthetic reinforced soil retaining wall along the side of the stadium; (b) the gap exposing the connection pins at the location of lamppost.

(a) (b)

Figure 9 Chung Hsin Stadium: (a) geosynthetic reinforced soil retaining wall behind the stadium; (b) closer view of the failure section.

of 5 blocks or 1 m. The first crack should correspond to the sliding surface of the top backfill soil layer.

4.4 Chung Hsin Nai Lu Shi Park, Chung Hsin New Village

The park is located near Chung Hsin Stadium. Two reinforced soil structures were constructed opposite to each other in this park. Both structures were composed of three stacked walls (Fig. 10a). Part of the structure facing west collapsed, whereas the structure facing east was stable. The collapsed portion of the wall was unreinforced and was supported at the back by the H-steel piles. Note that some of the blocks were also damaged structurally (Fig. 10b). The portion of the wall at the second level, which was reinforced, remained stable (Fig. 10c). In this stable wall, the first reinforcement layer was placed 2 blocks from the base, followed by 4-block, 3-block, and 5-block spacings, as marked by the dry leaves in the picture.

This case history demonstrated the earthquake resistance of the reinforced soil retaining wall compared to the unreinforced wall. The difference in

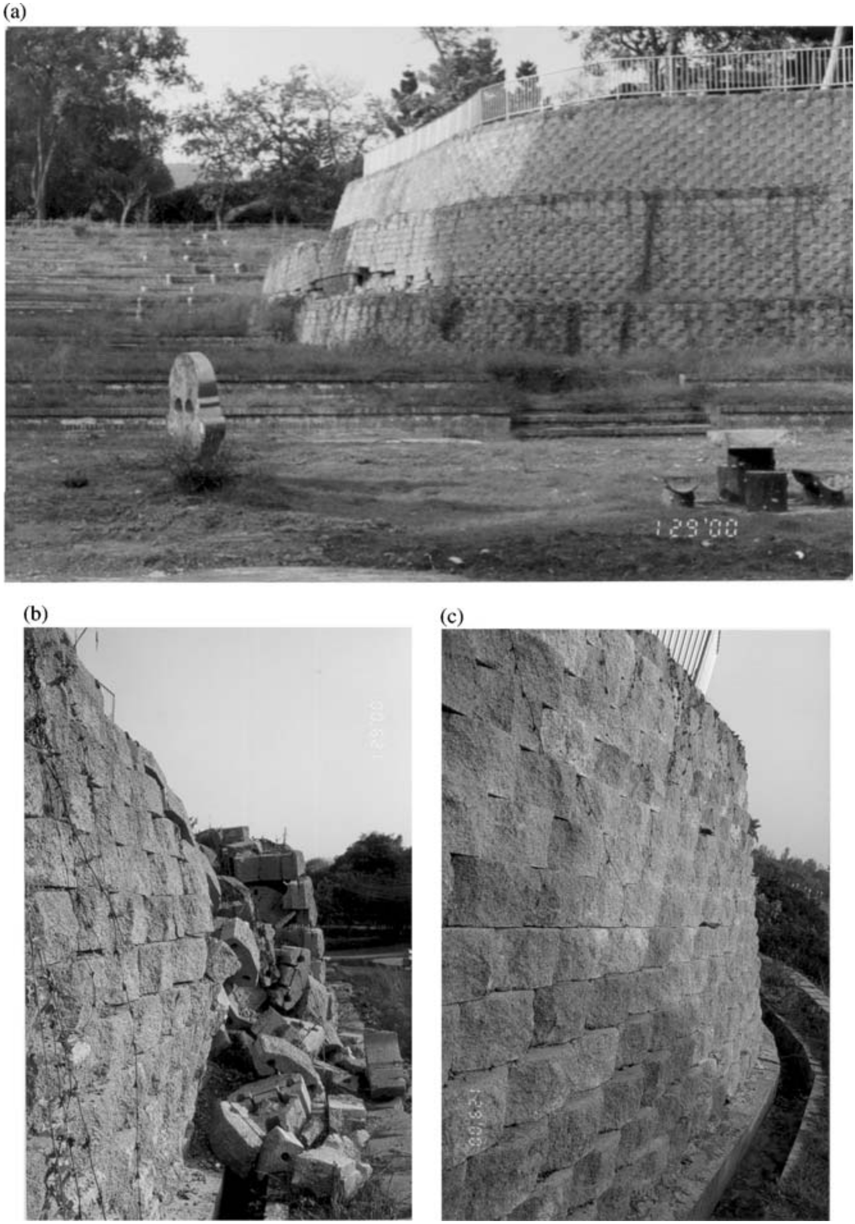

Figure 10 Chung Hsin Nai Lu Shi Park: (a) overall view of geosynthetic reinforced soil retaining wall; (b) collapse of unreinforced section of the wall; (c) the reinforced section (the leaves indicating location of reinforcement layers).

performance between the walls facing east and west could be related to the acceleration characteristics of the earthquake.

5 REINFORCED SLOPES

5.1 Chi-Nan University, Pu Li

Pu Li was the most severely damaged town by the earthquake. It is located about 25 km from the epicenter. The reinforced slope, 40 m tall, was located at the front gate of National Chi-Nan University, facing east. The geogrids were used as reinforcement, and the slope was backfilled by on-site soil, which was a silty clay. The slope had a wraparound facing. The reinforced structure was constructed by stacking a series of reinforced slopes, with a reinforcement spacing of 1 m. The reinforced slopes, after failure, is shown in Figs. 11a (side view) and 11c (front view).

The backfill soils and concrete structures from the slope moved for more than 10 m and buried the road. The security office was damaged (Fig. 11b).

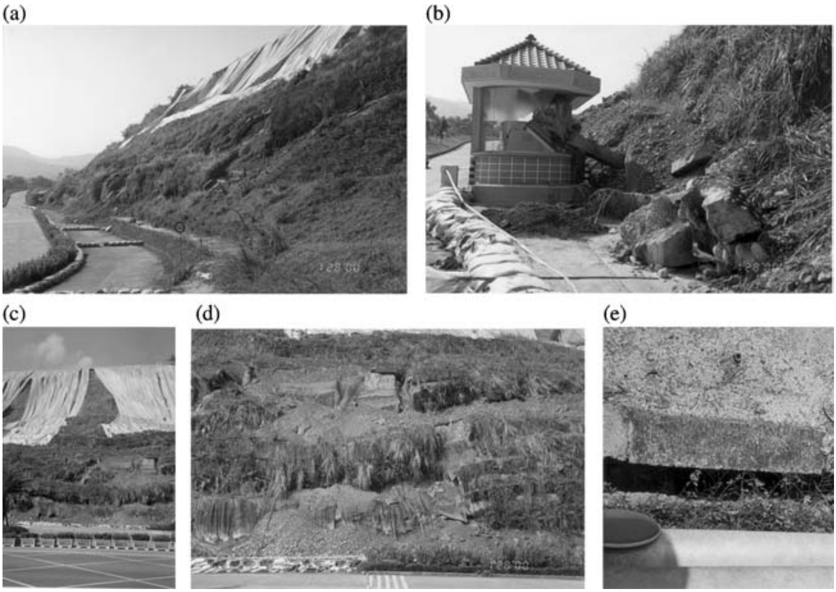

Figure 11 Chi-Nan University geosynthetic reinforced slope: (a) side view of failure; (b) damaged security office; (c) front view of failure; (d) close view of failure showing the reinforcement and backfill soil; (e) settlement of concrete pavement along the foot of slope.

A close view of the slope is shown in Fig. 11d, where the reinforcements are seen to pull out of the slope. Note that the concrete pavement around the site, at the foot and crest of the slope, deformed excessively (Fig. 11e).

It is, however, not certain if the failure of this reinforced structure was attributed to the seismic excitation alone. Excessive deformation of this reinforced slope was reported previously following an excavation at the foot of the slope in 1994 (Chou, 2000). The original configuration of this reinforced slope and the configuration after failure in 1994 are shown in Fig. 12 (Huang, 2000).

5.2 Nai Lu Housing Development Site, Chung Hsin New Village

A 35-m-high reinforced structure, located near Chung Hsin New Village, remained stable after the earthquake. The structure was composed of six multiple reinforced slopes, facing south-west. The slope has a wraparound facing and was fully vegetated (Fig. 13a). The details of this reinforced slope were given by Chou et al. (1994). It was the tallest reinforced soil structure at the time of completion of construction. Note that the road pavement along the slope suffered significant damage (Fig. 13b).

Figure 14 shows the configuration of this structure. The slope was constructed on a V-shaped valley having an inclination of 2(V):1(H) backfilled

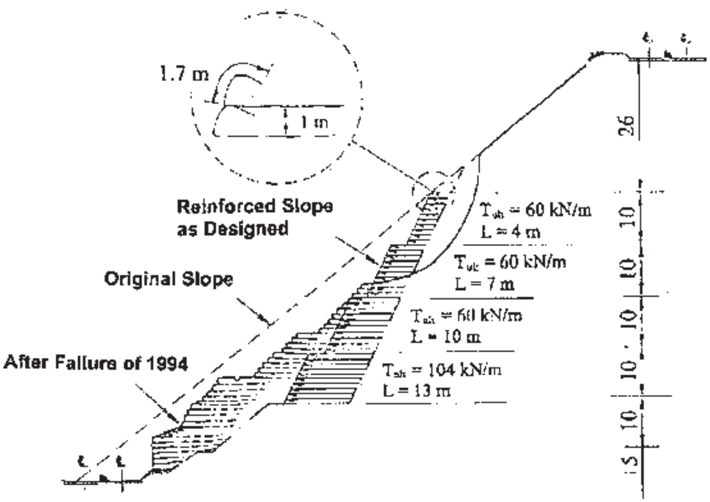

Figure 12 Configuration of Chi-Nan University before and failure of 1994. (After Huang 2000.)

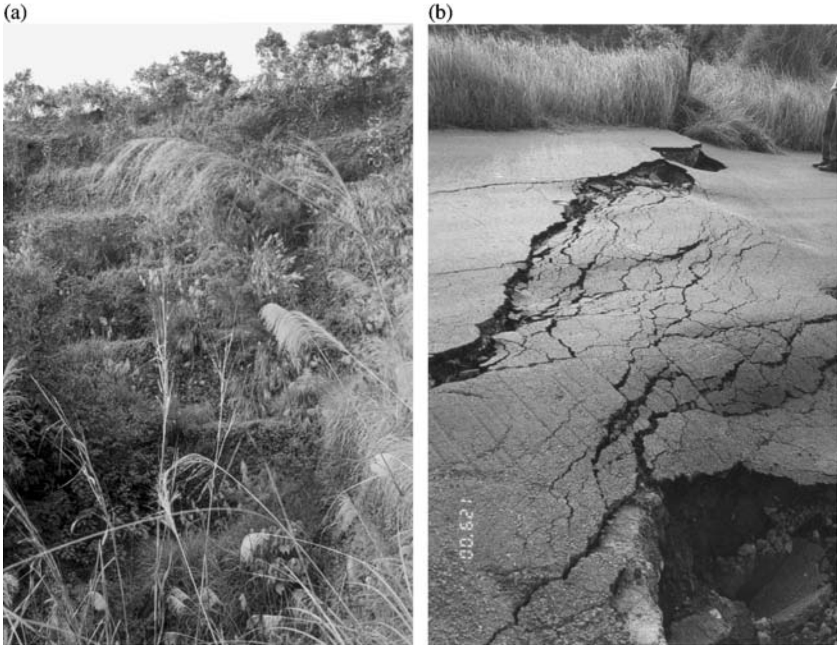

Figure 13 Nai Lu housing development site: (a) stable geosynthetic reinforced slope with vegetated facing; (b) severely cracked pavement along the road to the slope.

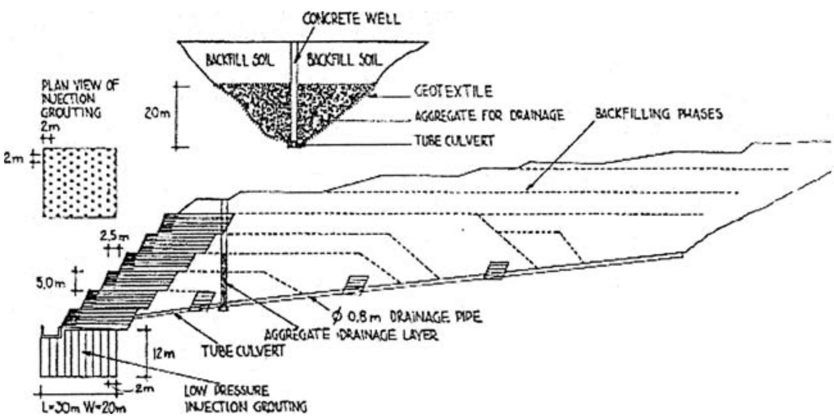

Figure 14 Cross-section of Nai Lu housing development site. (From Chou et al., 1995.)

with on-site soils. The slope was designed for seismic stability with a seismic coefficient of 0.15. An HDPE geogrid was used. The spacing of reinforced slope was 50 cm, and the reinforcement was 18.5 m long with an overlapping length of 2.5 m.

Note that the width of this slope was less than that of Chi-Nan University and the orientation was different as well. This reinforced slope behaved as an archlike structure when viewed along its width (see Chou et al., 1994). The end effects could have improved the stability.

6 CONCLUSIONS

The Ji-Ji earthquake caused some damage to the geosynthetic reinfoced soil structures in Taiwan. A few modular block geosynthetic reinforced soil retaining walls and reinforced slopes were damaged. Some of the lessons learned from the post-earthquake investigation are as follows:

1. Taiwan is located in a seismically active region, but it is not clear if seismic design was conducted for most reinforced soil structures. While the design of geosynthetic reinforced soil structures is believed to be very conservative in other parts of the world, the design conditions are more severe in Taiwan because of the topography and economic reasons, such as the use of on-site backfill soil and above-normal-height stacked walls and slopes.
2. The seismic design of reinforced soil structures has gained attention worldwide only in recent years. However, most of the seismic design procedures do not incorporate compound failure analysis. The cracks behind the wall indicated that a few of the structures suffered compound failure or did not have adequate global stability.
3. The failure of modular block reinforced soil retaining walls could be attributed to a lack of professional design as seen by arbitrary spacings used in several of the reinforced soil retaining walls, and with a mixture of unreinforced and reinforced retaining walls within a common structure.
4. The connection between the modular blocks and reinforcement is vital for a satisfactory performance of the structure under high seismic load. The strength and stiffness of the pins, and that of the reinforcement in the transverse direction, should be large enough to sustain the dynamic earth pressure since the collapse of the blocks led to failure of the wall.
5. The inertia of the modular blocks led to excessive deformation under seismic excitation. The structures, such as the lampposts, should not be installed at the vicinity of the modular block walls.

6. For the sites where reinforced and unreinforced soil retaining structures were found, a better performance was achieved for the reinforced soil structures.

The information obtained from the post-earthquake investigation is invaluable for the verification and improvement of seismic design procedure. A post-earthquake analysis will soon be available in a Ling and Leshchinsky study called *Failure Analysis of Module-Block Reinforced Soil Walls During Earthquake* (submitted, 2003).

ACKNOWLEDGMENTS

The material is based upon work supported by the National Science Foundation (Grant no. CMS-0084449) with Dr Richard J. Fragaszy as the Program Director. Any opinions, findings, and conclusions or recommendations expressed in this material are those of the authors and do not necessarily reflect the views of the National Science Foundation. The source of all seismic information included in this paper was from the Seismology Center, Central Weather Bureau (CWB), Taipei, Taiwan.

REFERENCES

RJ Bathurst, Z Cai. Pseudo-static seismic analysis of geosynthetic-reinforced segmental retaining walls. *Geosynthetics Intl.* 2(5): 787–830, 1995.

RJ Bathurst, MC Alfaro. Review of seismic design, analysis and performance of geosynthetic-reinforced walls, slopes and embankments. In *Earth Reinforcement*. H Ochiai, N Yasufuku, K Omine, eds. Rotterdam, The Netherlands: Balkema, 1997, pp 887–918.

RJ Bathurst, Z Cai, M Alfaro, M Pelletier. Seismic design issues for geosynthetic reinforced segmental retaining walls. In *Mechanically Stabilized Backfill*. JTH Wu, ed. Rotterdam, The Netherlands: Balkema, 1997, pp 79–97.

R-H Chen, et al, eds. *Technical Manual for Reinforced Soil Structures*. Taiwan Area National Expressway Engineering Bureau, Ministry of Transportation and Communications (in Mandarin), 1990.

NNS Chou. Latest development of reinforced soil retaining structures in Taiwan. In *Proc. Symp. on Latest Development of Reinforced Soil Retaining Structures, Taipei*. NNS Chou, GC Fang, eds. 2000, pp 26–45.

NNS Chou, JHC Hew, P Rimoldi. 35 m-high geogrid-reinforced slope: New heights and innovative construction. *Proc. 5th Intl. Conf. on Geotextiles, Geomembranes and Related Products*: 473–478, 1994.

NNS Chou, et al, eds. *Study on Reinforced Soil Structures for High-Speed Railways, Bureau of Taiwan High-Speed Rail*. Ministry of Transportation and Communications (in Mandarin), 1996.

NNS Chou, et al, eds. *Design and Construction Manual for Reinforced Soil Structures*. Taipei Society of Civil Engineers (in Mandarin), 1998.

BR Christopher, SA Gill, JP Giroud, I Juran, JK Mitchell, F Schlossser, J Dunnicliff. *Reinforced Soil Structures, Vol. 1. Design and Construction Guidelines*. FHWA-RD-89-043, Federal Highway Administration, U.S. Dept. of Transportation, 1990.

JG Collin. *Design Manual for Segmental Retaining Walls*, 2nd ed; Herndon, VA: National Concrete Masonry Association, 1997.

JG Collin, VE Chouery-Curtis, RR Berg, Field observations of reinforced soil structures under seismic loading. In *Proc. Intl. Symp. on Earth Reinforcement*. H Ochiai, H Hoyashi, J Otani, eds. Rotterdam, The Netherlands: Balkema, 1992, pp 223–228.

U Eliahu, S Watt. Geogrid-reinforced wall withstands earthquake. *Geotechnical Fabric Report*, March, Industrial Fabric Association International, pp. 8–13, 1991.

V Elias, BR Christopher. *Mechanically Stabilized Earthwalls and Reinforced Soil Slopes Design and Construction Guidelines*. FHWA-SA-96-071, Federal Highway Administration, U.S. Dept. of Transportation, 1999.

C-C Huang. Performance of reinforced soil structures during Ji-Ji and Hanshin earthquakes, and slope reinforcement method of Japan High Speed Railways after the earthquake. In *Proc. Symp. on Latest Development of Reinforced Soil Retaining Structures, Taipei*. NNS Chou, GC Fang, eds. (in Mandarin), 2000, pp 70–102.

WHK Lee. Report #1 on the Chi-Chi (Taiwan) Earthquake, U.S. Geological Survey, Menlo Park, CA, 1999.

D Leshchinsky. ReSlope. *Geotechnical Fabric Report* 15(1), Industrial Fabrics Association International, pp. 40–46, 1997.

D Leshchinsky. Putting technology to work: MSEW and ReSlope for reinforced soil structure design. *Geotechnical Fabric Report* 17(3), Industrial Fabrics Association International, pp. 34–38, 1999.

D Leshchinsky, HI Ling, G Hanks. Unified design approach to geosynthetic reinforced slopes and segmental walls. *Geosynthetics Intl.* 2(5): 845–881, 1995.

HI Ling, D Leshchinsky, EB Perry. A new concept of seismic design of geosynthetic-reinforced soil structures: Permanent displacement limit. In *Earth Reinforcement*. H Ochiai, N Yasufuku, K Omine, eds. Rotterdam, The Netherlands: Balkema, 1996, pp 797–802.

HI Ling, D Leshchinsky, EB Perry. Seismic design and performance of geosynthetic-reinforced soil structures. *Geotechnique* 47(5): 933–952, 1997.

HI Ling, D Leshchinsky. Effects of vertical acceleration on seismic design of geosynthetic-reinforced soil structures. *Geotechnique* 48(3): 347–373, 1998.

HI Ling, D Leshchinsky. Failure Analysis of Modular-Block Reinforced Soil Walls During Earthquakes. Submitted, 2003.

NCREE. National Center for Research on Earthquake Engineering, 2000.

ROC. The Republic of China at a glance. Governmental Information Office, Republic of China http://www.gio.gov.tw/info/nation/en/glance/, 2000.

D Sandri. A summary of reinforced soil structures performance in the Greater Los Angeles area after the Northridge Earthquake. In *Mechanically Stabilized Backfill*. JTH Wu, ed. Rotterdam, The Netherlands: Balkema, 1997, pp 433–442.
F Tatsuoka, M Tateyama, J Koseki. Behavior of geogrid-reinforced soil retaining walls during the Great Hanshin–Awaji earthquake. In *Proc. 1st Intl. Symp. on Earthquake Geotechnical Engineering*. K Ishihara, ed. 1995, pp 55–60.
F Tatsuoka, J Koseki, M Tateyama. Performance of reinforced soil structures during the 1995 Hyogo-ken Nambu earthquake. In *Earth Reinforcement*. H Ochiai, N Yasufuku, K Omine, eds. Rotterdam, The Netherlands: Balkema, 1997, pp 979–1008.
D White, RD Holtz. Performance of geosynthetic-reinforced slopes and walls during the Northridge California earthquake of January 17, 1994. In *Earth Reinforcement*. H Ochiai, N Yasufuku, K Omine, eds. Rotterdam, The Netherlands: Balkema, 1997, pp 965–972.

18

Model Tests of Seismic Stability of Several Types of Soil Retaining Walls

Junichi Koseki and Fumio Tatsuoka
University of Tokyo, Tokyo, Japan

Kenji Watanabe, Masaru Tateyama, and Kenichi Kojima
Railway Technical Research Institute, Tokyo, Japan

Yulman Munaf
University of Missouri–Rolla, Rolla, Missouri, U.S.A.

ABSTRACT

In order to establish a practical and relevant design procedure to evaluate the seismic stability of different types of soil retaining walls against high seismic loads, a series of irregular shaking tests was conducted on retaining wall models of six different types. In some tests, after the first failure plane was formed in the backfill, the second failure plane was formed at higher seismic loads. This can be explained by considering the effects of strain localization in the backfill soil and associated postpeak reduction in the shear resistance from peak to residual values along a previously formed failure plane. Such behavior has not been observed in the tilting tests and the sinusoidal shaking tests that were conducted on the same models in the previous study. In the present series of tests, reinforced soil retaining wall models with a full-height rigid facing exhibited ductile behavior compared to conventional-type retaining wall models such as gravity-type, leaning-type, and cantilever-type ones. The tilting of the conventional type retaining wall models was associated with the concentration of subgrade reactions at the wall toe, which resulted in local soil failure due to a loss of bearing capacity. Under similar conditions, tensile force in the reinforcements of the reinforced soil retaining walls was mobilized effectively to

resist against the tilting displacement. Comparisons are also made on the resultant force of normal earth pressures and the critical seismic coefficient at the ultimate overall wall failure condition.

1 INTRODUCTION

The 1995 Hyogoken-Nambu earthquake caused serious damage to a number of soil retaining walls (RWs) for railway embankments, as reported by Tatsuoka et al. (1996). Based on field investigations and back analyses on the performance of the damaged RWs, Koseki et al. (1996, 1999) showed that there is a large difference between the seismic coefficients $(k_h)_{\text{design}}$ used in the current design for RWs and the ratios of the highest peak horizontal ground accelerations to the gravitational acceleration estimated at the damaged RWs.

Tatsuoka et al. (1998) argue that some factors for the above difference include (1) the use of conservative soil strength in the design, (2) positive aspects of dynamic effects arising from the ductility and flexibility of RWs that are not considered in the pseudo-static approaches, and (3) the use of a global safety factor larger than unity. Because of the above factors, it is difficult to accurately predict the stability or performance of RWs during such a severe seismic event as the 1995 Hyogoken-Nambu earthquake when following the current seismic design procedures. It is suggested that the currently used $(k_h)_{\text{design}}$-values should be increased appropriately to avoid such collapse of RWs as observed during the earthquake. At the same time, it is also suggested to increase the $(k_h)_{\text{design}}$-value to a larger extent in the order of (1) gravity type RWs, (2) cantilever reinforced concrete RWs, and (3) geosynthetic reinforced soil RWs having a full-height rigid facing.

Many researchers, including Ichihara and Matsuzawa (1973), Sakaguchi (1996), and Matsuo et al. (1998), conducted model tests to study seismic behavior of RWs. Based on the results from these investigations, several different methods have been proposed to predict the stability of RWs during earthquakes for both conventional RWs and geosynthethic reinforced soil-type RWs. In engineering practice, the limit equilibrium method by the pseudo-static approach is the most widely used to analyze the seismic stability of RWs (e.g., Seed and Whitman, 1970; Bathurst and Alfaro, 1996; Ling et al., 1997; RTRI, 1997).

The different seismic performances of different types of RWs have not yet been fully investigated, particularly experimentally. The possible limitations of the pseudo-static approach have not yet been fully understood, either. In the present study, therefore, a series of relatively small-scale model shaking tests was conducted on the different types of RWs to observe their different performances during irregular shaking. They were compared with the behaviors observed during a series of tilting tests and sinusoidal shaking tests conducted on the same types of RW models, as reported by Koseki et al. (1998a, 1999).

2 MODEL RETAINING WALLS

2.1 Types of Model Walls

The cross sections of six different model retaining walls are shown in Fig. 1. The models were 600 mm in width (Fig. 2). They were three conventional RWs (cantilever type, gravity type, and leaning type) and three types of reinforced soil RWs with a full-height rigid facing having different arrangements of reinforcement layers (reinforced soil wall type 1, type 2, and type 3).

The total height of the conventional walls was 530 mm, while that of the reinforced soil walls was 500 mm. The bottom width at the base of the cantilever- and gravity-type walls was 230 mm, while it was reduced to 180 mm for the leaning-type wall. To adjust the dead load of the gravity- and leaning-type walls, extra weights were added nearly at the center of gravity of these walls. For the reinforced soil wall type 1, 10 layers of reinforcement strips having a length of 200 mm were horizontally placed in the backfill sand. The length of the top and fourth reinforcement layers was increased to 800 mm and 450 mm, respectively, for the reinforced-soil wall type 2 in order to increase the stability against overturning failure, as is the common practice in Japan. To study effects of the length of reinforcement layers, the length of all the reinforcement layers was increased to 350 mm for the reinforced soil wall type 3.

To measure the response of each retaining wall during static tilting and shaking of the sand box, a number of displacement transducers and accelerometers were installed. The transducers were arranged in such a way that the response among different types of walls could be easily compared.

Shear load in the vertical direction and normal lateral load acting on the backface of the wall were measured with a number of small two-components loadcells that were set on the back of wall, as shown in Fig. 2. The working principle of the loadcells is explained in Tatsuoka (1988). For the cantilever, gravity, and leaning types, the earth pressures acting on the base of wall were also measured in the similar way. By using a piece of sponge covered by a Teflon sheet and smeared with silicone grease, as shown in Fig. 2, the friction between the side of the wall and the side wall of the sand box was reduced, and the sealing between them was also achieved.

3 MATERIALS USED TO CONSTRUCT MODEL WALLS

The facing and base parts of the model walls were made of wooden blocks. To form a rigid structural body for the facing, the wooden blocks were stacked and reinforced with vertical steel bars having a diameter of 10 mm together with

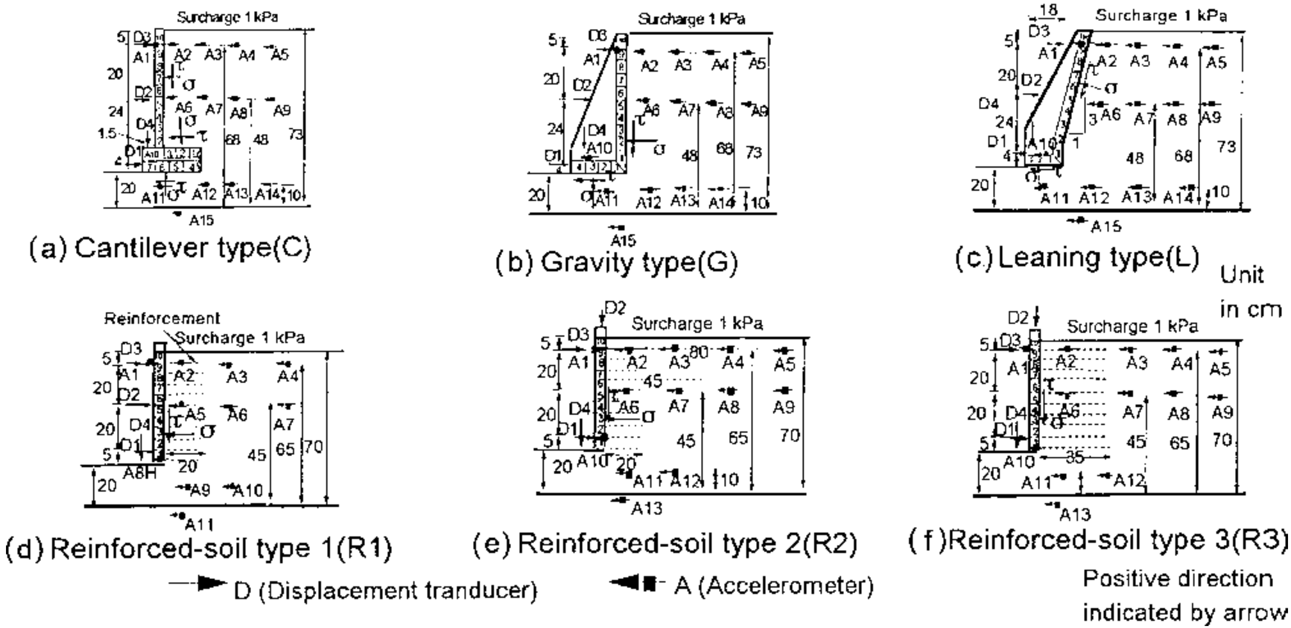

Figure 1 Cross sections of model retaining walls.

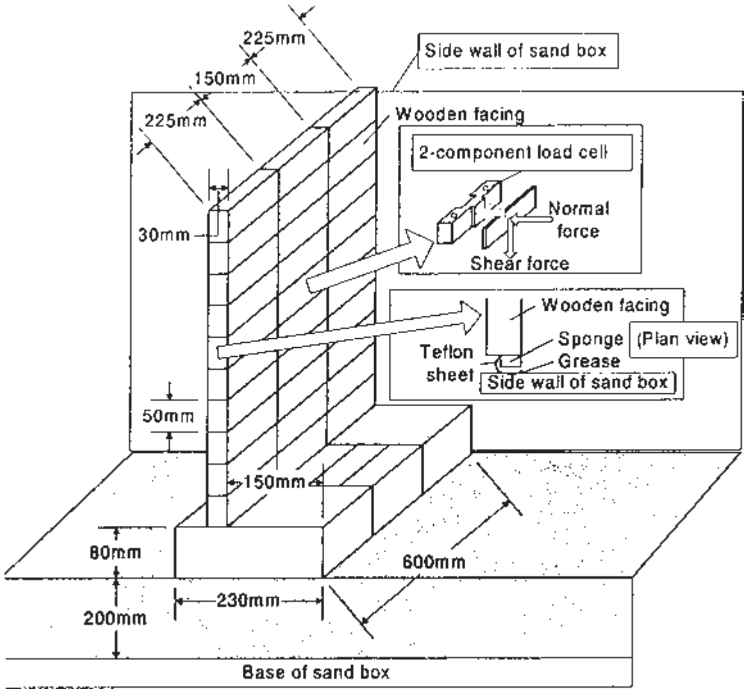

Figure 2 Details of typical wall model.

horizontal L-shape metals. To reinforce the base, metal plates having a thickness of 10 mm were inserted at its middle level. The surfaces of the facing and base parts in contact with the backfill and subsoil layers were made rough by gluing sandpaper.

For the reinforced soil RW models, a grid of phosphor-bronze strips was used as the model reinforcement. To form a model grid reinforcement layer, strips having a thickness of 0.1 mm and a width of 3 mm were soldered to each other at an interval of 50 mm in the longitudinal direction, in parallel with the side wall, and 100 mm in the transverse direction, in parallel with the facing, as shown in Fig. 3. To effectively mobilize friction between the reinforcement and the backfill, sand particles were glued on the surface of the strips. The details of the model wall and reinforcement configurations are described in Koseki et al. (1998a).

4 BACKFILL AND SUBSOIL MATERIAL

Air-dried Toyoura sand, having $e_{\max} = 0.977$, $e_{\min} = 0.605$, $G_s = 2.64$, $D_{10} = 0.11$ mm, and $D_{50} = 0.23$ mm, was used to form the backfill and subsoil

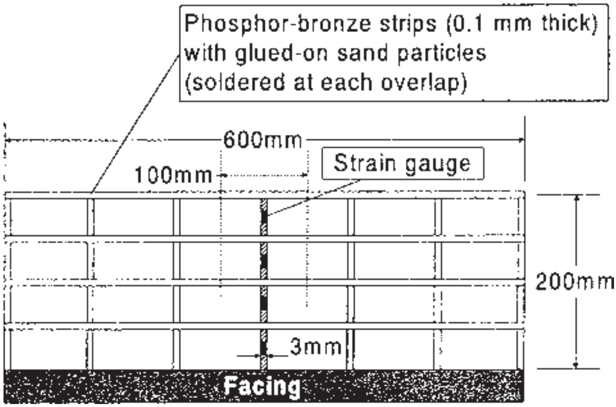

Figure 3 Plan of model reinforcement layer.

layers. In order to evaluate the shear resistance angle of the batch of sand used in the model tests, a series of plane strain compression (PSC) tests was performed. The specimens were prepared by air pluviation to obtain the same density as in the model tests. The PSC tests were performed at constant low confining pressure of 9.8 kPa so as to simulate the low stress level in the model tests. It should be noted that the direction of the major principal stress σ_1 is normal to the bedding plane direction in these PSC tests.

Figure 4 shows the relationships between the principal stress ratio σ_1/σ_3 and the axial strain ϵ_1. The peak angle of internal friction ϕ_{peak} was equal to, on average, 51°, mobilized at an axial strain of about 2%. The residual angle of friction ϕ_{res} was calculated to be 43° based on the lowest principal stress ratios in the postpeak regime.

5 TEST PROCEDURES

5.1 Model Construction

Models were constructed in a sand box (1400 mm high, 2600 mm long, and 600 mm wide in the inner dimensions) using a sand hopper with an inner volume of about 0.0315 m^3 having a 600-mm-long slit. To prepare as homogeneous as possible sand layers at a target void ratio of 0.650, the falling height of sand, the traveling speed of the sand hopper, and the opening width of the slit were basically kept constant at 800 mm, 2.5 m/min, and 1 mm, respectively. However, to adjust the surface height of each layer, when needed, the traveling speed and the opening width of the slit were changed in ranges of 1–3 m/min and 1–3 mm, respectively. Based on preliminary tests, it was confirmed that these changes result in a variation of void ratio ranging between 0.625 and 0.675.

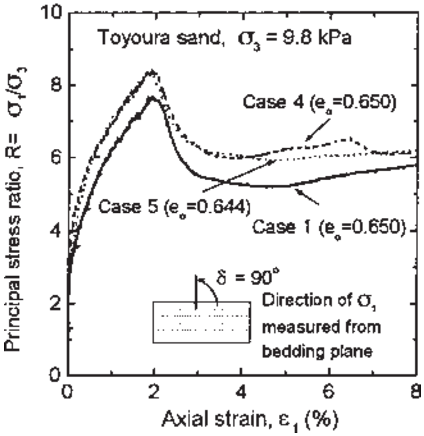

Figure 4 Results from plane strain compression tests on Toyoura sand.

To observe the deformation and displacement of sand layers, horizontal layers of black-dyed Toyoura sand having a thickness of 10 mm were prepared at a vertical spacing of 50 mm in a width of about 30 mm both adjacent to the transparent side wall and at the center of the backfill.

After the subsoil layer was prepared, the sand located beneath the bottom of the model retaining wall was trimmed to have a level surface, and then the model wall was carefully placed. The backfill layer was then prepared in the same way as the subsoil layer. For the reinforced soil walls, a temporary steel frame was used to support the wall during preparation of the backfill, which was removed before applying seismic loads. Each reinforcement layer was placed horizontally on the temporary level surface of the backfill when the height of the backfill became the respective specified level.

After finishing the filling of sand, the surface of the backfill was trimmed to the prescribed geometry, and a surcharge of 1 kPa was applied by placing lead shots on the surface of the backfill to simulate such a structure as the railway ballast fill. To separate sand from the lead shots, 0.2-mm-thick rubber membranes were placed between them.

5.2 Seismic Load Application

Seismic loads were applied by shaking the sand box horizontally with an irregular base acceleration. A strong motion that was recorded as N-S component at Kobe Marine Meteorological Observation Station during the 1995 Hyogoken-Nanbu earthquake was employed as the base acceleration (Fig. 5a). Its amplitude and

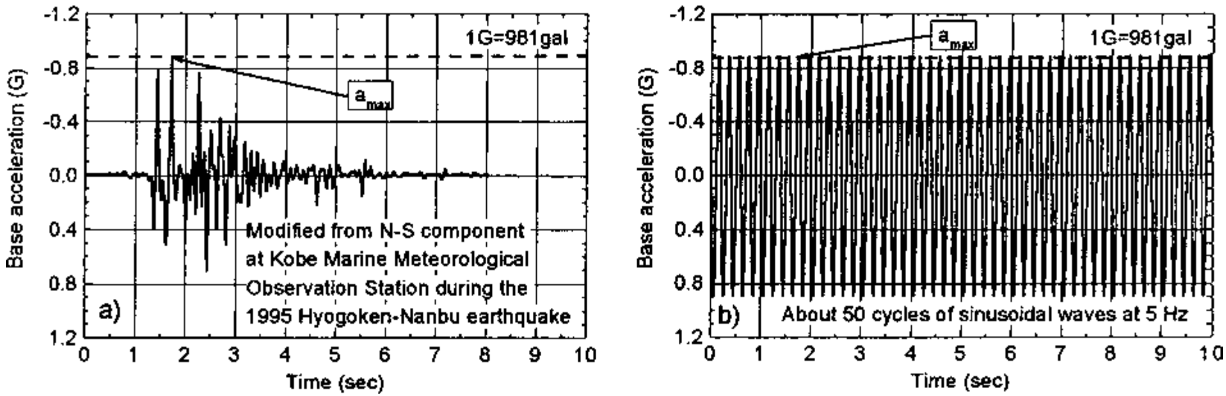

Figure 5 Typical time histories of base accelerations: (a) irregular shaking; (b) sinusoidal shaking.

time scale were adjusted so that the base acceleration has a prescribed maximum amplitude with a predominant frequency of 5 Hz. Each model was subjected to several shaking steps, where the maximum amplitude of the base acceleration was initially set to 100 gal and increased at increments of 100 gal. Shaking was terminated when the wall displacement became considerably large. During shaking, the deformation of the wall and the surrounding sand layers was monitored up to the ultimate failure state through the side wall of the sand box by means of a digital video camera. Stresses acting on the facing, displacements of the wall, response accelerations of the wall and the backfill, and tensile forces acting in the reinforcements were also recorded.

Results from these irregular shaking tests were compared with the previous test results (Koseki et al., 1998a, 1999), where seismic loads were applied either by tilting the sand box to simulate pseudo-static loading conditions or by shaking the sand box with a sinusoidal base acceleration at a frequency of 5 Hz (Fig. 5b). In the tilting tests, the sand box was tilted continuously at a rate of approximately 1.0°/min until a considerable displacement of the wall was observed. Based on the pseudo-static approach, the observed seismic coefficient k_h in the tilting tests was defined as

$$k_h = \tan\theta \tag{1}$$

where θ is the tilting angle of the sand box. In the sinusoidal shaking tests on the cantilever-type wall model, the amplitude of the base acceleration was initially set to 25 gal and increased at an increment of 25 gal. For the other models, the initial base acceleration was set first to 50 gal, and the increment was also doubled to 50 gal in order to minimize possible effects of the previous shaking history on the behavior at the subsequent loading stages. At each acceleration level, the same amplitude of base acceleration was maintained for about 10 sec. In this study, effects of previous shaking histories on the test results were assumed to be insignificant. The observed seismic coefficient k_h in the shaking table tests was defined as

$$k_h = a_{\max}/g \tag{2}$$

where $a_{\max}$ is the single amplitude of maximum base acceleration at the active state (i.e., when the inertia force of the backfill is acting outward) for each shaking step, and g is the gravitational acceleration.

6 TEST RESULTS AND DISCUSSIONS

6.1 Failure Pattern

Figure 6 shows the residual displacement of the wall and the residual deformation of the backfill, which were observed at the end of irregular shaking step when a

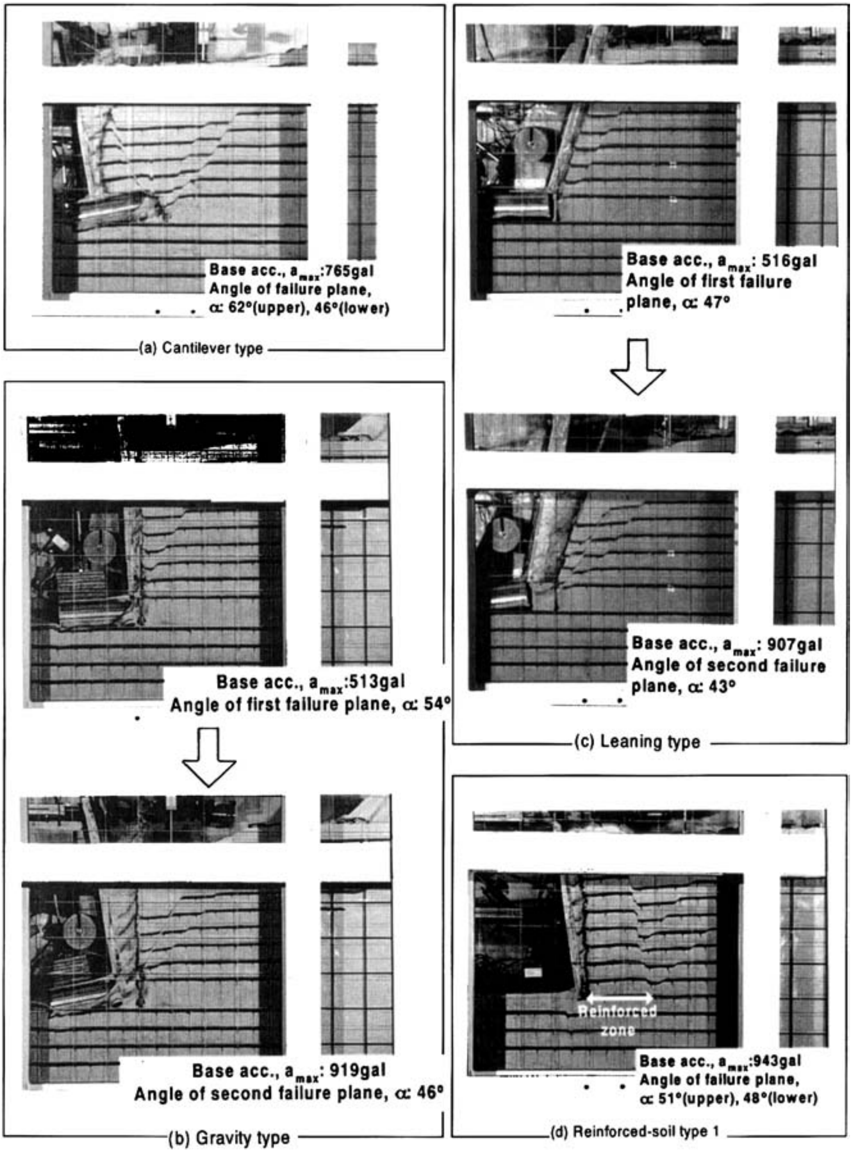

Figure 6 Residual deformations observed at the end of irregular shaking step when failure plane was formed in the backfill.

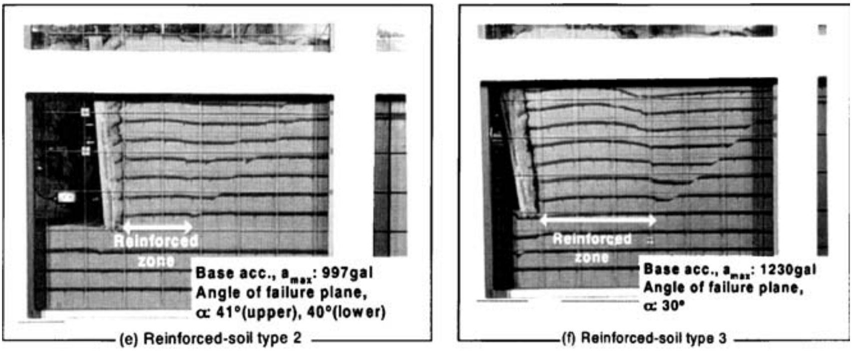

Figure 6 Continued.

failure plane was formed in the backfill. For all the RW models, the major failure pattern of the walls was overturning, which was associated with bearing capacity failure in the ground beneath the wall toe for the cantilever-, leaning-, and gravity-type RWs. For these conventional-type RWs, two differently inclined failure planes (plus a vertical failure plane starting from the heel of the wall in the case of the cantilever-type wall) developed in the unreinforced backfill.

In particular, for the leaning- and gravity-type RWs, the first failure plane developed much earlier than the second failure plane (Fig. 6b and c). This progressive formation of multiple failure planes can be explained by considering the effects of strain localization in the backfill soil and associated postpeak reduction in the shear resistance from peak to residual values along a previously formed failure plane, as schematically shown in Fig. 7 and described in detail by Koseki et al. (1998b). Such behavior was not observed in the tilting tests and the sinusoidal shaking tests, where localized shear displacements were accumulated in the backfill only along a single failure plane. These different behaviors are due possibly to the difference in the duration of peak load conditions. Note also that, for the cantilever-type wall, two failure planes were formed almost simultaneously during the irregular shaking test.

For the reinforced soil RWs, as seen from Fig. 6d–f, a two-wedge failure mechanism, as assumed in the current seismic design practice in Japan (refer to Fig. 8; Horii et al., 1994, for the details), was observed. However, no failure plane could be observed at the bottom of the front wedge in the reinforced zone (i.e., along segment OP in Fig. 8). This was possibly because the development of the shear band was relatively small along this part, which could not be identified as no dyed sand layer crossed the shear band. Importantly, the front wedge did not behave as a rigid body, but it exhibited simple shear deformation along horizontal planes. Similar behavior was observed in the tilting tests and the sinusoidal

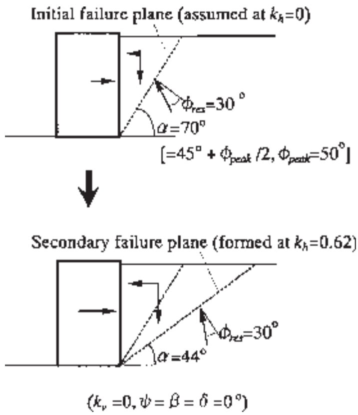

Figure 7 Progressive formation of multiple failure planes predicted by considering effects of strain localization in backfill. (After Koseki et al., 1998b.)

shaking tests (Koseki et al., 1998a). This factor is not considered in the current seismic design practice. This behavior suggests that the horizontally placed short reinforcement layers cannot effectively resist such simple shear deformation of the reinforced backfill. A modification of the design procedure is being attempted to evaluate the residual deformation of the wall due to this simple shear deformation of the reinforced backfill (Horii et al., 1998).

It should be noted that the two failure planes observed in the unreinforced backfill of the reinforced soil wall types 1 and 2, as shown in Fig. 6d and e, were

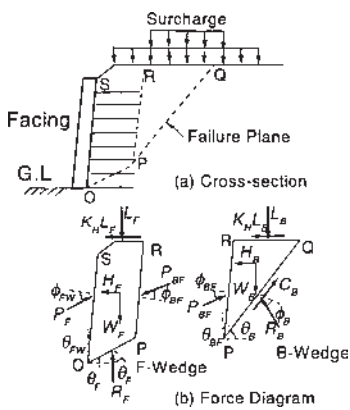

Figure 8 Two-wedge failure mechanism assumed in current seismic design of reinforced soil retaining walls with rigid full-height facing. (After Horii et al., 1994.)

formed almost simultaneously during irregular shaking. In particular, for the reinforced-soil type 2 (Fig. 9), the upper failure plane developed from the heel of the backfill zone reinforced with short reinforcement layers and stopped somewhere below the longest reinforcement layer located near the backfill surface. On the other hand, as shown in Fig. 9, it is very likely that the lower failure plane reached the surface of the backfill. This inference is supported by the observed amount of wall displacements at the moment when failure planes were formed. The location of the lower failure plane was governed by the existence of the longest reinforcement layer.

6.2 Angle of Failure Plane

The angle of failure plane α defined from the horizontal direction was evaluated by carefully removing the backfill surrounding the central layers of black-dyed Toyoura sand. The angle was taken at the failure plane developing from the bottom of the back wedge in the backfill (i.e., in the unreinforced zone for the reinforced soil walls). For the leaning- and gravity-type RWs in the irregular shaking tests, as shown in Fig. 6b and c, the formation of the deeper (second) failure plane and associated deformation of backfill located above it slightly changed the angle of the shallower (first) failure plane that has been previously formed. In these cases, the α-values of the shallower failure planes were corrected to those for the initial wall configuration (before deformation). In so doing, it was assumed that the initial failure plane was formed at the same time at the side wall and at the center part of the backfill.

In Fig. 10, the values of the failure plane angle α are plotted versus the seismic coefficients $(k_h)_{fp}$ for the shaking step when the respective failure plane was formed. For comparison, results from the static tilting tests and the sinusoidal

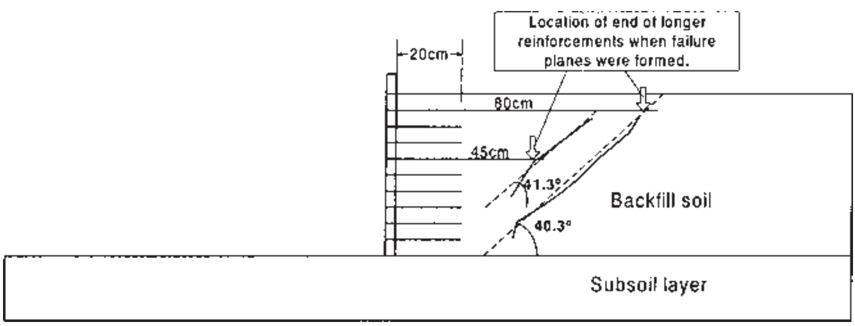

Figure 9 Comparison of locations of failure planes and longer reinforcement layers for reinforced soil retaining wall type 2.

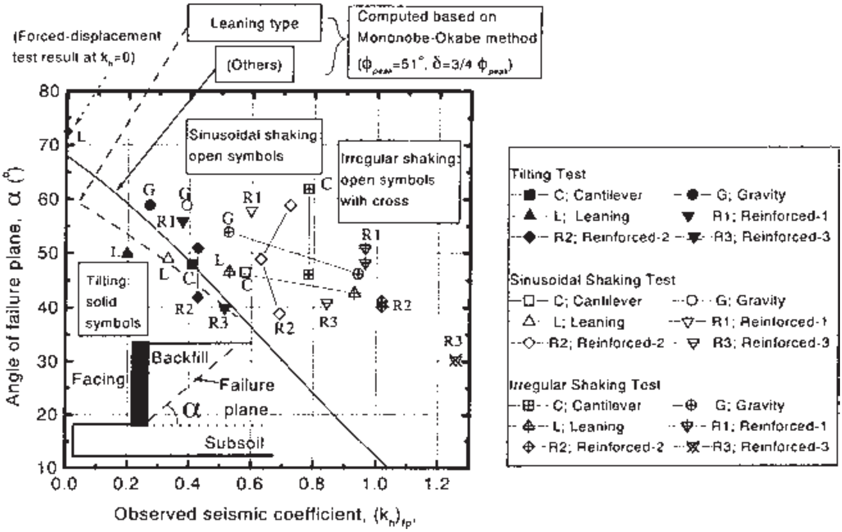

Figure 10 Relationships between angle of failure plane and seismic coefficient when respective distinct failure plane was formed.

shaking tests are also shown as well as the theoretical relationships based on the Mononobe–Okabe method (Okabe 1924; Mononobe and Matsuo, 1929). In computing the theoretical relationships, the shear resistance angle ϕ of the backfill and subsoil layers was set equal to ϕ_{peak} ($=51°$) obtained from the PSC tests mentioned above, and the frictional angle δ at the interface between the backfill and the wall facing with sandpaper was set equal to $3/4\phi_{\text{peak}}$. The reason for the latter setting will be explained later.

The following trends of behavior can be seen from Fig. 10:

1. In the tilting tests, the observed relationships between α and $(k_h)_{fp}$ were close to the respective theoretical relationship, irrespective of the wall type.
2. In the sinusoidal shaking tests, the value of α for each RW was generally similar to the one observed in the tilting tests, while the value of $(k_h)_{fp}$ was larger than the one in the tilting test. The latter difference depended on the RW type, generally larger for the reinforced soil RWs than for the three conventional RWs.
3. In the irregular shaking tests, the value of $(k_h)_{fp}$ was largest among the three types of loading conditions, and the value of α was generally smaller than the ones observed in the tilting and sinusoidal shaking tests.

In the two types of shaking tests, the failure plane angle α was not directly linked to $(k_h)_{fp}$. It is likely that the difference in the $(k_h)_{fp}$ between the tilting and shaking tests are due to the dynamic effects. As shown in Fig. 11, for each RW, the horizontal displacement $(d_{\mathrm{top}})_{fp}$ measured at the moment of the formation of a failure plane at a distance of 5 cm below the top of the wall depended on the loading conditions. It was larger in the two types of shaking tests than in the tilting tests. This would be due to the following mechanism:

1. In the static tilting tests, the loading condition by which strain tends to localize in a certain location continues for the largest duration among the three types of test. For this reason, a shear band is easiest to develop with the smallest deformation outside the shear band in the backfill, resulting in the smallest displacement and the lowest $(k_h)_{fp}$ at the moment of shear band formation.
2. The opposite would be the case with the shaking tests using irregular waves. Larger deformation outside the shear band in the backfill is required before the development of a distinct shear band at a fixed location, because the loading condition varies by time and space due to different dynamic loading levels with effects of amplification/attenuation and phase lag of response accelerations.

Further investigations are required on the above issues.

It can be also seen from Fig. 11 that the value of $(k_h)_{fp}$ is generally larger for the reinforced soil RWs than for the three conventional RWs.

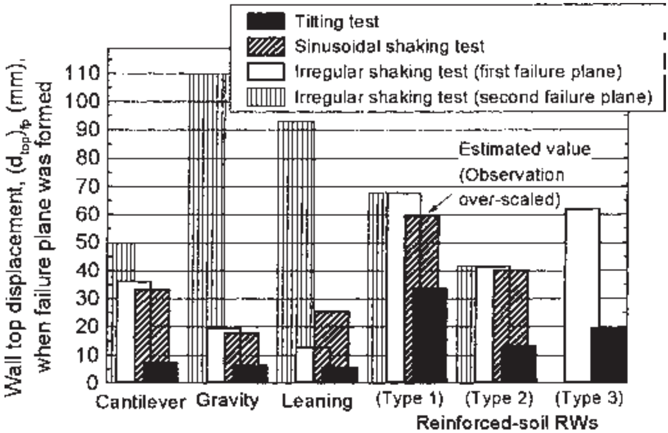

Figure 11 Comparison of wall top displacements when a distinct failure plane was formed.

6.3 Residual Displacement of Wall

Relationships between the seismic coefficient k_h and the horizontal displacement d_{top} measured at a distance of 5 cm below the top of the wall are shown in Fig. 12. For the shaking tests, the values of d_{top} at the end of each shaking step are plotted. In the sinusoidal shaking tests as well as the tilting tests, after exceeding about 25 mm, which corresponds to about 5% of the total wall height, the d_{top}-value increased very rapidly, soon resulting into the ultimate overall wall failure.

In the early steps of irregular shaking tests up to a k_h-value of about 0.5, the d_{top}-value accumulated in a similar manner among different types of RWs. When the k_h-value exceeded about 0.5, however, the rate of increase in the d_{top}-value became larger for the three conventional-type RWs than for the three reinforced soil-type RWs. Such different extents of ductility that depend on the RW type will be discussed in the next two sections.

6.4 Reaction Force from Subsoil

Relationships between the reaction force from the subsoil and the horizontal displacement d_{top} near the top of wall are shown in Fig. 13 for gravity-type RW in irregular shaking tests. The reaction forces were evaluated from the data measured with loadcells when the base acceleration inducing outward inertia force became its maximum in each shaking step. These reaction forces include

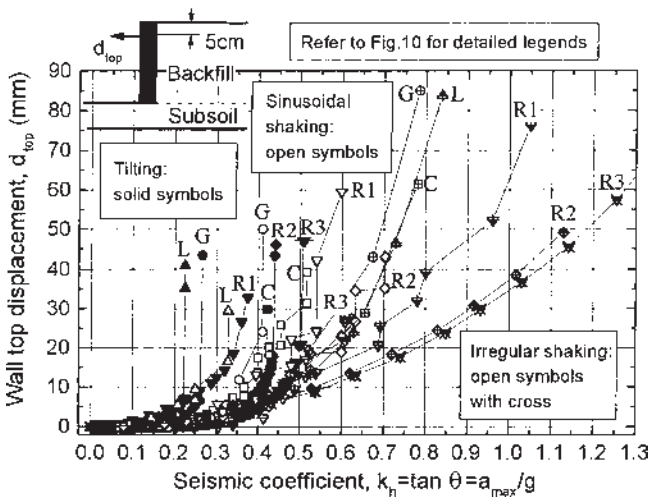

Figure 12 Accumulation of residual horizontal displacement near the top of wall.

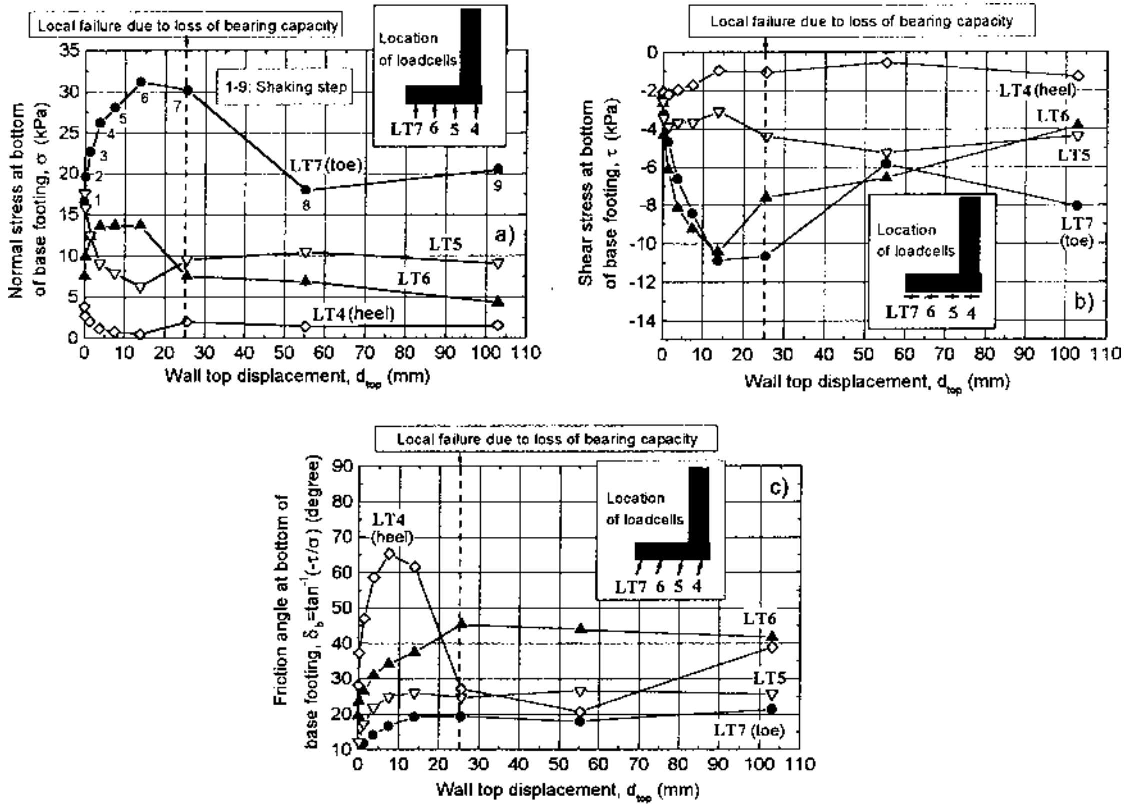

Figure 13 Measured reactions from subsoil for gravity-type retaining wall; (a) normal stress; (b) shear stress; (c) friction angle.

initial values measured before starting shaking. The d_{top}-values were evaluated at the same moment as the reaction forces were evaluated. In the early shaking steps, the normal stress measured at the toe of wall base (with loadcell LT7 in Fig. 13a) increased rapidly. It suddenly decreased, however, after showing a peak state (at the d_{top}-value of around 20 mm), suggesting a local failure due to loss of bearing capacity. After this peak state, the d_{top}-value accumulated rapidly. The normal stress measured at a location next to the toe of wall base (LT6) showed a similar trend, while its peak value was much smaller than that of LT7. On the other hand, the normal stresses measured near the heel of wall base (LT4 and LT5) decreased in the early shaking steps, followed by a slight increase with the occurrence of the local failure near the toe of wall base.

As shown in Fig. 13b, the shear stresses measured near the toe of wall base (LT6 and LT7) increased in the early shaking steps. They decreased after the d_{top}-value exceeded about 20 mm. Such a change of the shear stresses is linked with that of the corresponding normal stresses. As shown in Fig. 13c, therefore, the mobilized friction angle computed from the normal and shear stresses measured at LT6 and LT7 became nearly constant after the d_{top}-value exceeded about 20 mm. Similar behavior was observed with the loadcell LT5. On the other hand, the mobilized friction angle δ_b at the heel of wall base (LT4) increased very rapidly in the early shaking steps. This is because the normal stress decreased to be nearly zero, as shown in Fig. 13a, so the measured values of δ_b became rather unreliable.

The effects of the local failure due to a loss of bearing capacity at the wall toe can be clearly seen in Fig. 14, where the resultant normal reaction force from subsoil is plotted versus the relative location of its application *D*/*W*, where *D*

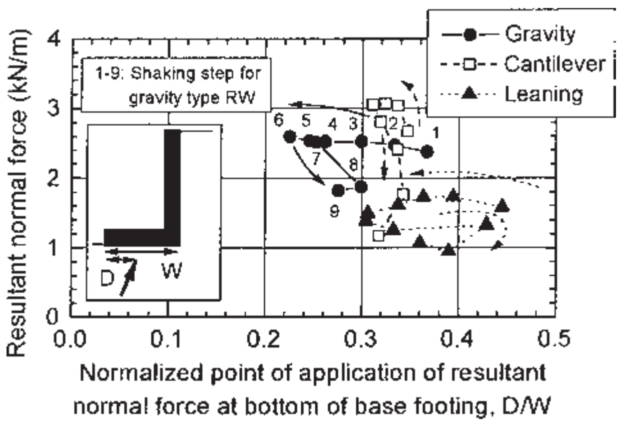

Figure 14 Relationships between resultant normal reaction force from subsoil and relative location of its application.

denotes the distance between the application point of the resultant force and the edge on the wall toe, and W is the width of the wall base. The numeral shown next to every data point for gravity-type RW indicates the sequential order of the shaking steps, which is indicated in Fig. 13a as well. In the early shaking steps, the application point of the resultant force gradually moved toward the wall toe, accompanied with only a slight increase in the amount of the resultant force. After the occurrence of the local failure at the 6th and 7th shaking steps for gravity-type RW, the resultant force decreased suddenly, and its application point moved back toward the wall heel. These behaviors seem to be reasonable, considering a gradual increase in the overturning moment due to horizontal inertia force of the wall and earth pressures, followed by a loss of bearing capacity near the toe of wall base at the 6th and 7th shaking steps.

The same trend of behavior as mentioned above can be seen in Fig. 14 with leaning-type RW. With cantilever-type RW, however, the reduction in the D/W-value before the local failure was to a much lesser extent than the other RWs, which would be due to mobilization of a large shear stress acting along the vertical failure plane developing from the wall heel (Fig. 6a) that reduced the overturning moment.

6.5 Tensile Force in Reinforcement Layers

As mentioned before in Fig. 12, the rate of accumulation of the d_{top}-value did not increase rapidly with the three types of reinforced soil RWs in irregular shaking tests. In relation to this, relationships between the tensile force in reinforcement layers, which include initial values measured before starting shaking, and the wall top displacement d_{top} for these RWs are shown in Fig. 15. The tensile forces when the base acceleration-inducing outward inertia force became its maximum in each shaking step are evaluated from the data measured with strain gauges that were attached to reinforcements at a horizontal distance of 2.5 cm from the facing. For all types of reinforced soil RWs, the tensile force increased with the increase in the d_{top}-value, not showing such a sudden drop as observed in the reactions from subsoil for gravity-type RW (Fig. 13). This may explain the ductile behavior of reinforced soil RWs.

It can also be seen from Fig. 15 that the tensile force in the uppermost layer was largest with reinforced soil type 2 RW having the longest reinforcement, while it was smallest with reinforced-soil type 1 RW having the shortest reinforcement. In particular, the former value increased at a large rate even when the d_{top}-value was relatively small, while the latter value increased only after the d_{top}-value exceeded about 20 mm. These different behaviors may suggest that extension of the upper enforcement layer, such as the case with reinforced soil type 2, may result in concentration of the mobilized tensile force in the extended

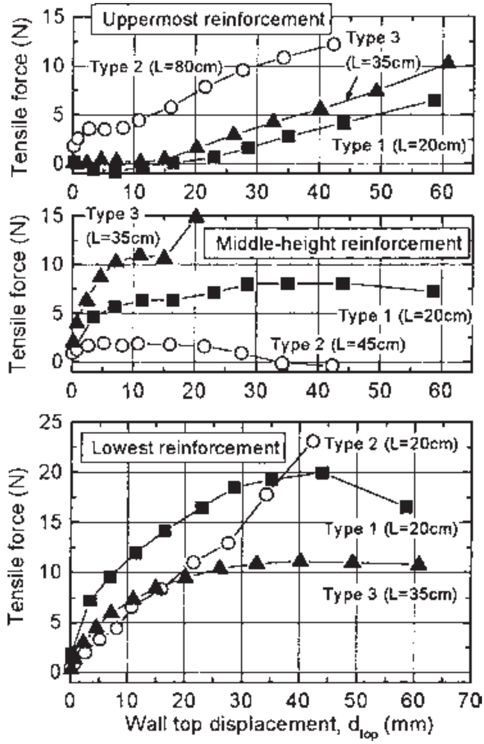

Figure 15 Tensile forces in reinforcement layers measured at a distance of 2.5 cm from facing of reinforced soil RWs in irregular shaking tests.

reinforcement, since it can effectively resist against the overturning moment acting on the facing.

In relation to the above, the tensile force in the middle-height layer was not large with reinforced soil RW type 2, although the length of the reinforcement at the same height was largest among the three reinforced soil RWs. This may be caused by the concentration of the mobilized tensile force in the extended uppermost reinforcement. It should be noted that, with reinforced soil type 3 RW, the tensile force was mobilized relatively rapidly at the middle-height reinforcement. In contrast to these behaviors, with reinforced soil type 1 having the shortest reinforcements, the tensile force was rather effectively mobilized at the lowest reinforcement. The height of reinforcement where the tensile force is the most effectively mobilized may depend on the arrangement of reinforcements.

Horizontal distributions of tensile forces in the three reinforcement layers at different heights measured at every two shaking steps are shown in Figs. 16–18. For the type 1 RW with shorter reinforcements having an even

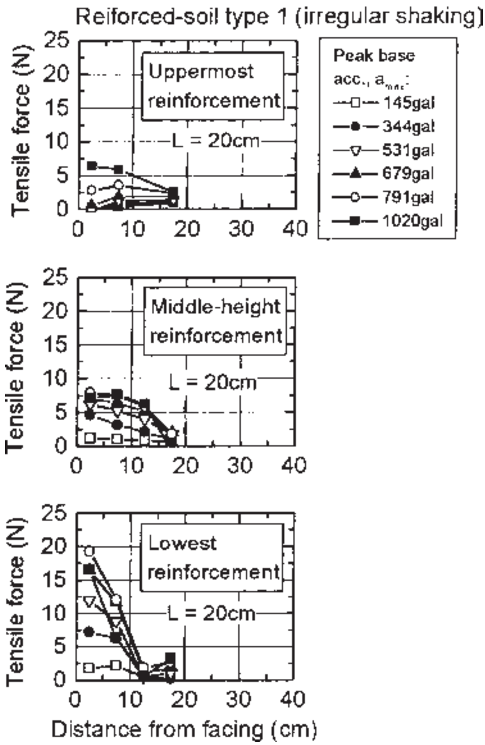

Figure 16 Horizontal distribution of tensile forces in reinforcement layers for reinforced soil retaining wall type 1.

length of 20 cm (Fig. 16), the tensile forces increased rather linearly with approaching the facing. On the other hand, for the type 3 RW with longer reinforcements having an even length of 35 cm (Fig. 18), the tensile forces measured in a region apart from the facing did not increase largely, suggesting that the frictional resistance between the reinforcement and the backfill was not fully mobilized in this region. It should be noted that, for the type 3 RW, the data measured in the middle-height reinforcement near the facing showed a remarkable increase at the shaking steps at $a_{max} = 913$ and 1119 gal. This peculiar behavior may be due to an unexpected drifting that was possibly caused by excessive bending at the location where the strain gauge was attached.

For type 2 RW having partly extended upper reinforcement layers (Fig. 17), the tensile force in the lowest reinforcement having a length of 20 cm showed similar behavior to that of the type 1 RW. On the other hand, tensile forces of the uppermost and the middle-height reinforcements that were extended to a length

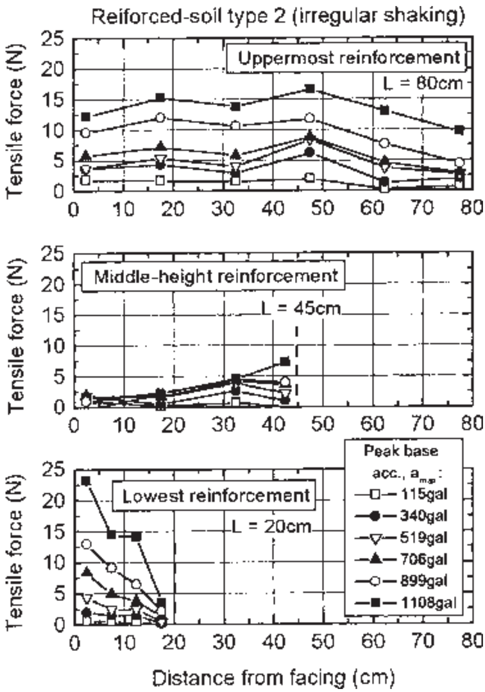

Figure 17 Horizontal distribution of tensile forces in reinforcement layers for reinforced soil retaining wall type 2.

of 80 cm and 45 cm, respectively, showed different behaviors from others. The tensile force of the uppermost reinforcement was constantly large, showing a reduction with approaching its tip, while the tensile force of the middle-height reinforcement was very limited. These behaviors suggest that the extended uppermost reinforcement mobilized the frictional resistance near its tip, while the middle-height reinforcement that was extended to a lesser extent did not mobilize the frictional resistance effectively. Such different degrees of mobilization of frictional resistance may be linked to the different locations of these reinforcements relative to the failure planes as typically shown in Fig. 9.

If it can be assumed that the frictional angle at the interface between the reinforcement and the backfill is equal to the simple shear peak friction angle of the backfill, $\phi_{ss} = \arctan(\tau/\sigma)_{\max}$ along a horizontal failure plane, which is estimated to be 38° as shown later, the frictional resistance mobilized on both sides of the reinforcement having a width of 3 mm over its full length (= 200 mm; refer to the hatched zone in Fig. 3) for reinforced soil type 1 will become about 0.8 N, 3.8 N, and 6.8 N for the uppermost, middle-height, and lowest reinforcements,

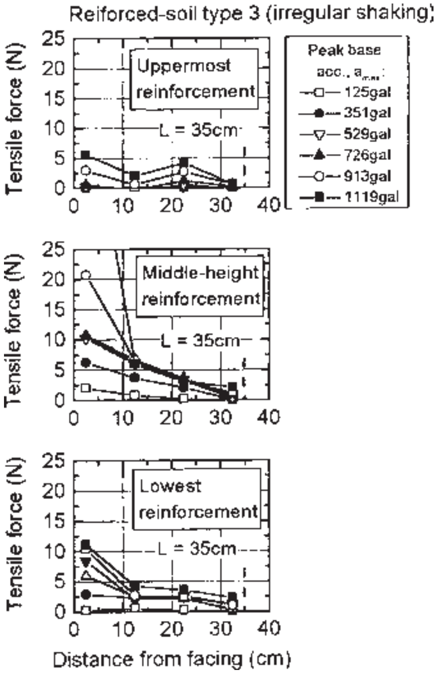

Figure 18 Horizontal distribution of tensile forces in reinforcement layers for reinforced soil retaining wall type 3.

respectively. As seen from Fig. 16, these values are much smaller than the peak values measured near the facing, suggesting the effectiveness of the grid shape in developing the tensile force in the reinforcements. On the other hand, if the effect width of the reinforcement is assumed to be 100 mm, which is equal to the horizontal interval of the reinforcements that connected to the facing (Fig. 3), the computed frictional resistance will become about 25 N, 125 N, and 225 N for the uppermost, middle-height, and lowest reinforcements, respectively. These values are substantially larger than the peak values measured near the facing (Fig. 16). Future investigations are required to establish a procedure to quantitatively evaluate the mobilized tensile force in the reinforcements, including actual geogrids used in practice.

6.6 Resultant Force of Normal Earth Pressures

Relationships between the resultant force P_a acting normally on the facing from the backfill and the seismic coefficient k_h are shown in Fig. 19. Those measured during the tilting tests and the sinusoidal shaking tests are also shown. The P_a-values are evaluated by integrating normal stresses measured with loadcells along the depth of the facing, which include initial values measured before the start of shaking or tilting. For each irregular or sinusoidal shaking step, the P_a-value was defined under three different conditions; i.e., when either one of P_a-values itself, the wall top displacement d_{top} or base acceleration (on the negative side, inducing outward inertia force) becomes respective peak state. The k_h-values are evaluated based on Eqs. (1) and (2). Note that for the tilting tests, the measured values of the normal stresses at tilted conditions were corrected for the effects of the sand box inclination by a factor of $1/(\cos\theta)$, where θ is the tilting angle.

In Fig. 19a–c, theoretical relationships based on the Mononobe–Okabe method are shown, while in Fig. 19d–f, those based on limit-equilibrium stability analysis assuming the two-wedge failure mechanism, as shown in Fig. 8, are presented. In obtaining these relationships, similarly to the case with Fig. 10, the shear resistance angle ϕ of the backfill was set equal to ϕ_{peak} ($=51°$) and the frictional angle δ at the interface between the backfill and the wall facing with sandpaper was set equal to $3/4\phi_{\mathrm{peak}}$. For comparison, the residual condition of $\phi = \phi_{\mathrm{res}}$ ($=43°$) and $\delta = 3/4\phi_{\mathrm{res}}$ was also employed in the calculation.

For the cantilever-type RW, the resultant forces measured at the backface of the wall cannot be directly compared to the calculated values, because the calculated resultant forces are those acting on the vertical failure plane in the backfill, which was actually observed to develop from the heel of the wall base (Fig. 6a). Therefore, the resultant force P_a acting on this vertical failure plane was estimated from the measured values of the normal force P_{a1} acting on the backface of the facing and the shear force T acting on the top of the wall base from the backfill as

$$P_a = P_{a1} + T - k_{h1} \times W \tag{3}$$

where $k_{h1} \times W$ is the horizontal inertia of the soil block located above the wall base and separated by the vertical failure plane from the remaining part of the backfill (i.e., W is the weight of this soil block, and k_{h1} is the measured horizontal response acceleration a_b of this soil block divided by the gravitational acceleration g for the shaking table tests); T and $k_{h1} \times W$ are defined positive when they act in the direction toward the facing (i.e., at the active state). In this case, theoretical relationships with $\phi = \delta = \phi_{\mathrm{peak}}$ and $\phi = \delta = \phi_{\mathrm{res}}$ are added to the figure, since the frictional angle δ at the vertical failure plane can be assumed equal to ϕ.

It can be seen from Fig. 19 that, in general, the P_a-values measured in the tilting tests were larger than those measured in the sinusoidal or irregular shaking tests. In a broad sense, the results from tilting tests were comparable with the theoretical ones, except for the leaning-type RW. It should be noted, however, that the direct comparison of the measured values with those calculated by the Mononobe–Okabe or its equivalent method is valid at the active failure state in

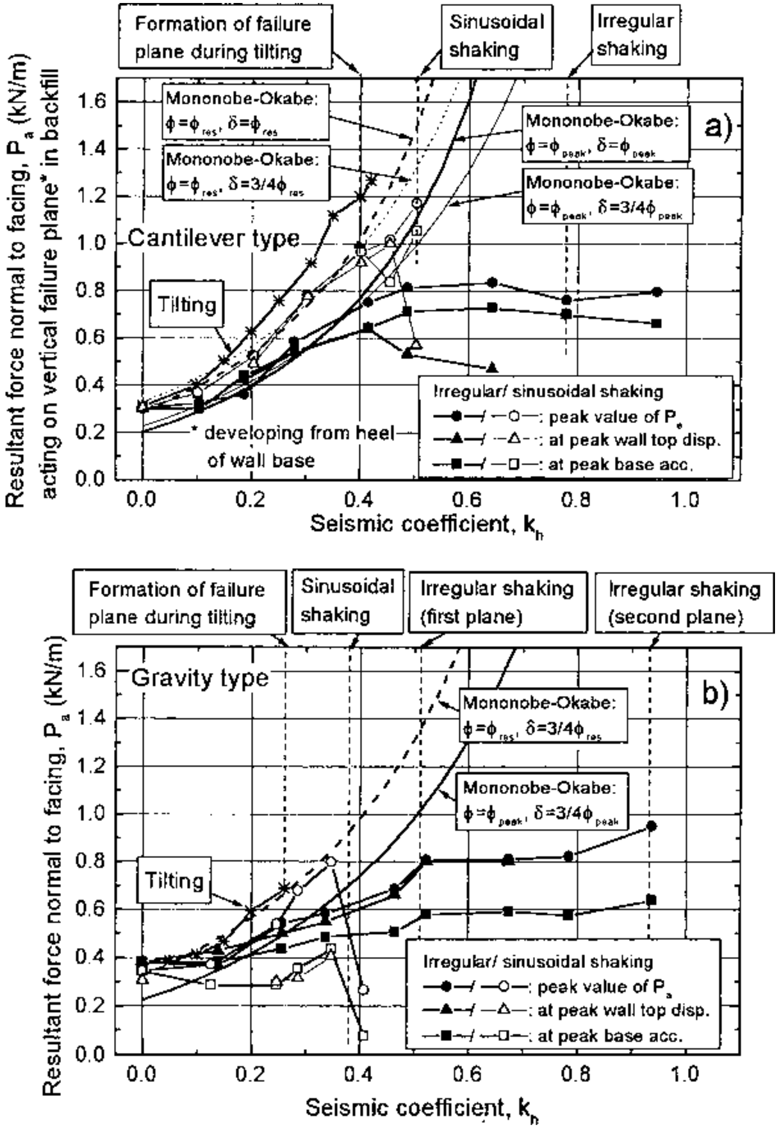

Figure 19 Relationships between resultant normal force acting on facing from backfill and seismic coefficient.

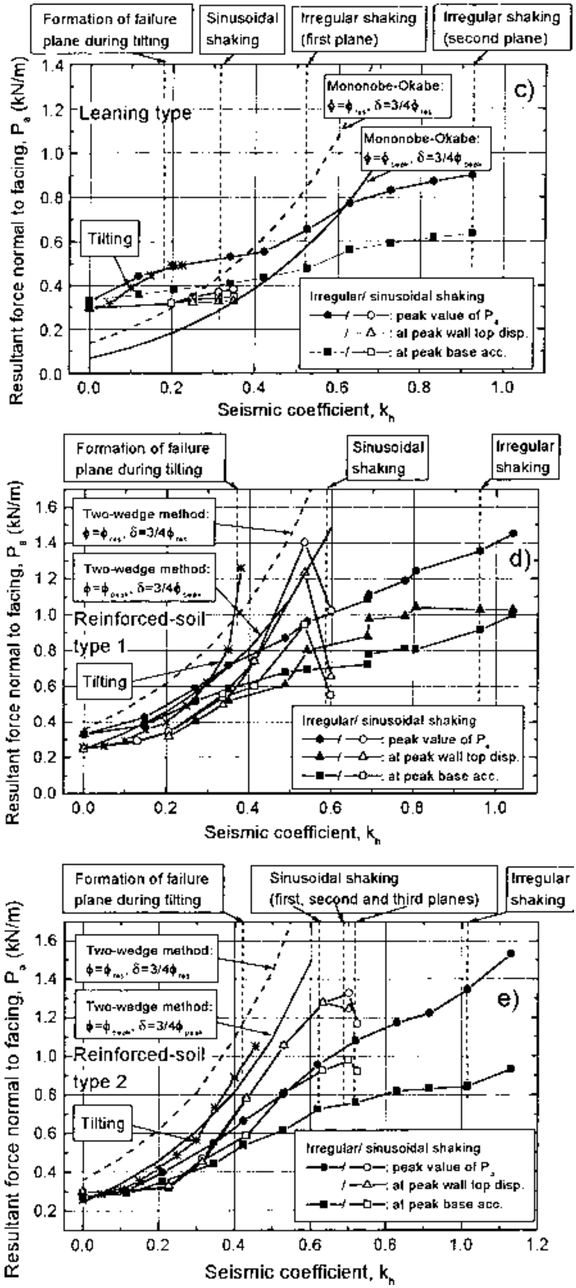

Figure 19 Continued.

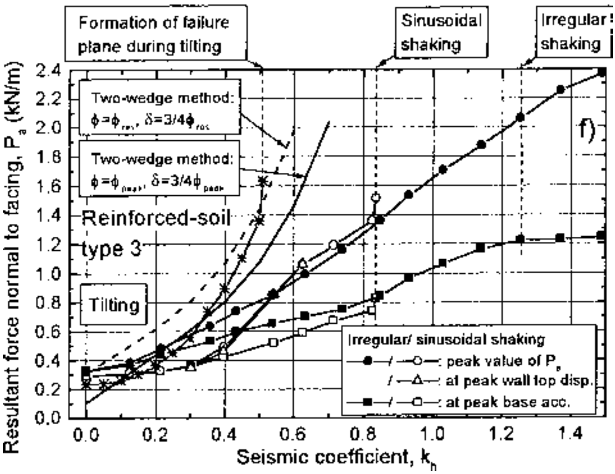

Figure 19 Continued.

the backfill. The active failure state could be defined as the state either when the failure plane is about to develop (for $\phi = \phi_{peak}$), or after the failure plane has developed in the backfill, where the ϕ-values have dropped to ϕ_{res}.

Phase difference in the shaking tests in the vertical distribution of horizontal response accelerations of backfill would be one of the reasons for the different P_a-values from the tilting tests. In addition, as discussed by Tatsuoka et al. (1998), different from the case of tilting tests, the earth pressure acting on the back of the facing in the shaking tests is controlled largely by an interaction between dynamic response of the backfill and the wall structure. In fact, the P_a−values defined under the three different conditions as mentioned above were, in general, different from each other.

In Fig. 20, the peak horizontal response acceleration $(a_h)_{max}$ in the backfill-inducing outward inertia force was compared with the peak base acceleration a_{max} in the irregular shaking tests. The $(a_h)_{max}$-values were evaluated based on the records of an accelerometer located near the mass center of the soil wedge (in the unreinforced zone for reinforced soil RWs; i.e., the B-wedge shown in Fig. 8b) above the failure plane. With the increase in the shaking level, the $(a_h)_{max.}$-value became gradually smaller than the a_{max}-value. In particular, after the failure plane was formed in the backfill, the rate of increase in the $(a_h)_{max}$-value was significantly reduced, or even the increase stopped temporarily, due possibly to sliding of the soil wedge along the failure plane.

For gravity-type and reinforced soil-type 1 RWs, results from sinusoidal shaking tests are also shown in Fig. 20. Note that, using 20 cycles of sinusoidal waves, these shaking tests were additionally conducted on limited types of RWs. By reducing the number of cycles from 50 to 20, it was attempted to observe their behaviors at higher seismic loads after the formation of the failure plane. In these tests, a noticeable amplification of the response acceleration took place before the formation of the failure plane, in contrast to the attenuation in the response

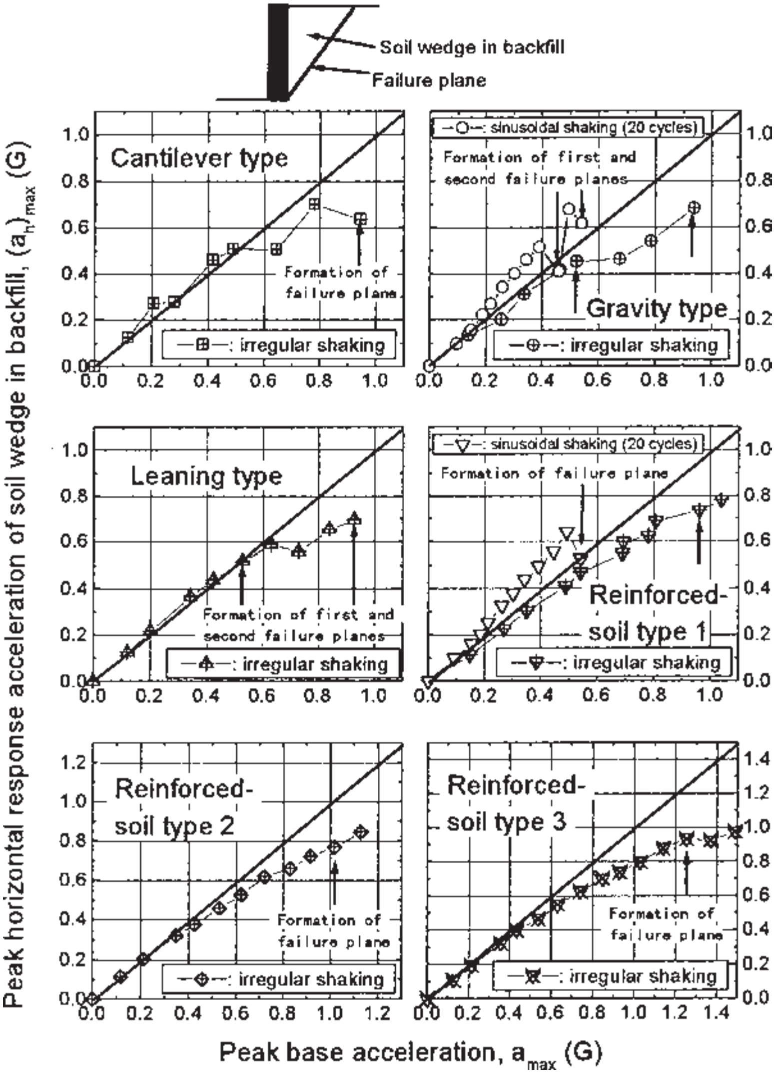

Figure 20 Relationships between peak horizontal response acceleration.

observed in the irregular shaking tests. On the other hand, after the formation of the failure plane, a sudden reduction in the backfill and peak base acceleration response acceleration took place in the sinusoidal shaking tests, which may also be due to the sliding of the soil wedge along the failure plane.

It should also be noted that the horizontal response of the soil wedge above the failure plane was accompanied by its vertical response, as typically shown in Fig. 21. In this case, the first failure plane had been already formed in the backfill during the previous shaking steps, and several large cycles of horizontal base acceleration induced a relatively large response of the soil wedge not only in the horizontal but also in the vertical directions. The peak horizontal response acceleration was mobilized after a certain phase lag after the peak base acceleration, and, as mentioned above, the $(a_h)_{max}$-value was smaller than the a_{max}-value. When the outward inertia force was acting on the soil wedge, it was also subjected to vertical upward inertia force (i.e., downward acceleration) in the beginning, which was reversed into the downward inertia force (i.e., upward acceleration) in the later stage.

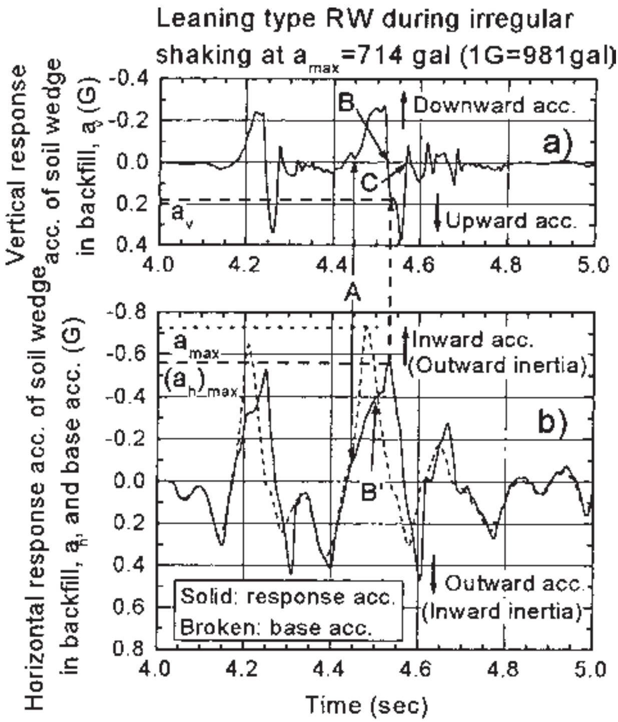

Figure 21 Typical response accelerations of soil wedge above failure plane for leaning-type RW during irregular shaking.

This peculiar behavior could be explained qualitatively by considering the sliding of the soil wedge along the failure plane as follows:

1. The broken curve in Fig. 21b is the base acceleration. When the soil wedge started sliding (after point A in Fig. 21), its horizontal response acceleration became smaller than the base acceleration. At the same time, it slid down along the failure plane with negative (downward) vertical acceleration (between points A and B in Fig. 21a).
2. Since reversal of the base acceleration took place, the sliding of the soil wedge was terminated eventually (at point C in Fig. 21a). Before the termination, the sliding movement was decelerated with positive (upward) vertical acceleration (between points B and C in Fig. 21a).
3. The point B′ in Fig. 21b is the point after which the horizontal response acceleration of the soil wedge became larger than the base acceleration (i.e., when the relative horizontal acceleration of the soil wedge to the base was reversed). It was slightly different from the point B (when the vertical acceleration of the soil wedge was reversed) in Fig. 21a, possibly because the horizontal response acceleration in the underlying nonsliding soil mass was not equal to the base acceleration. Similarly, the point that corresponds to the point C in Fig. 21a (after which the horizontal response acceleration of the soil wedge became equal to the base acceleration) could not be clearly defined in Fig. 21b.

In the case with Fig. 21, the peak horizontal response acceleration was mobilized while the sliding movement was decelerated (between points B and C in Fig. 21a). In some of the other cases, however, the peak horizontal response acceleration was mobilized while the sliding movement was accelerated (between points A and B in Fig. 21a).

In Fig. 22, correction for the effects of horizontal and vertical responses of the soil wedge during the irregular shaking was made on the seismic coefficient k_h and the measured resultant force P_a respectively; the k_h-value was evaluated from the $(d_h)_{\max}$-value; the P_a-value was obtained at the moment when the $(a_h)_{\max}$-value was mobilized, and it was corrected by dividing with a factor of "$1 + a_v/g$", where a_v is the vertical acceleration of the soil wedge obtained at the same moment as above (defined as positive when it induces downward inertia force). The corrected relationships are represented by using open symbols in Fig. 22. For reference, measured relationships between uncorrected k_h- and P_a-values that were obtained at the moment when the base acceleration became its peak (i.e., when the $a_{\max}$-value was mobilized) are plotted by using solid symbols, and the aforementioned theoretical relationships are also shown. It can be seen that, by making a correction to the response of the soil wedge, the measured relationships became much closer to the theoretical ones, in particular, in the region at high seismic loads.

In summary, the experimental data support the overall trend of the Mononobe–Okabe method. However, the detailed quantitative evaluation of the Mononobe–Okabe method was not possible, because of the delicate nature of dynamic earth pressures. It is readily seen that the reinforced soil RWs could stand without exhibiting ultimate failure against earth pressures that were much higher than those acting on the conventional-type RWs.

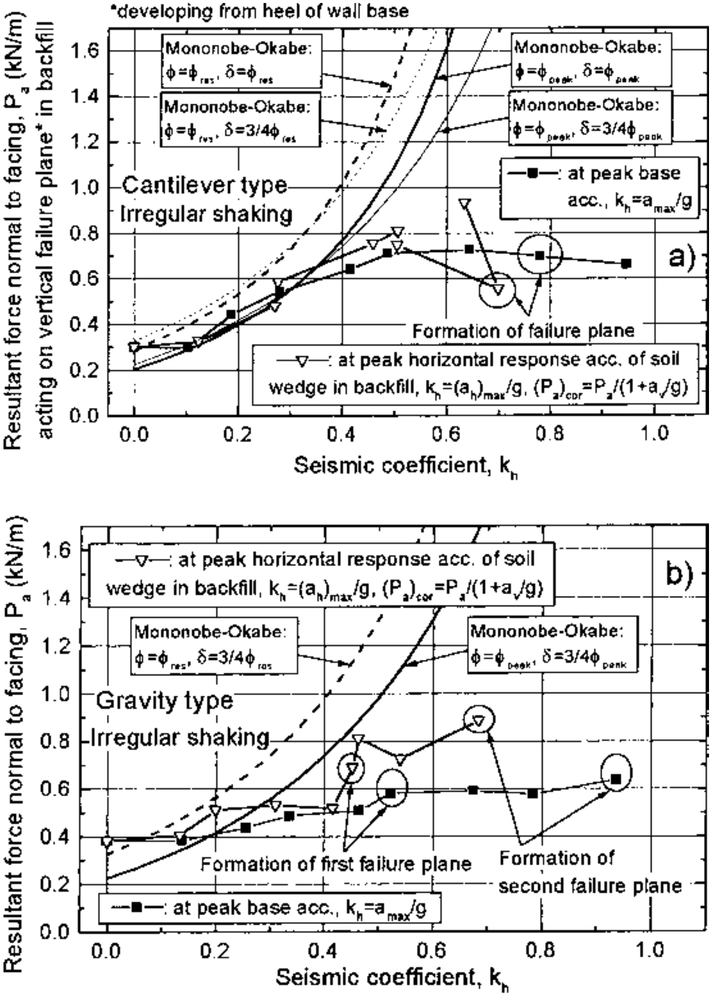

Figure 22 Effects of correction for response of soil wedge on relationships between resultant normal force acting on facing from backfill and seismic coefficient.

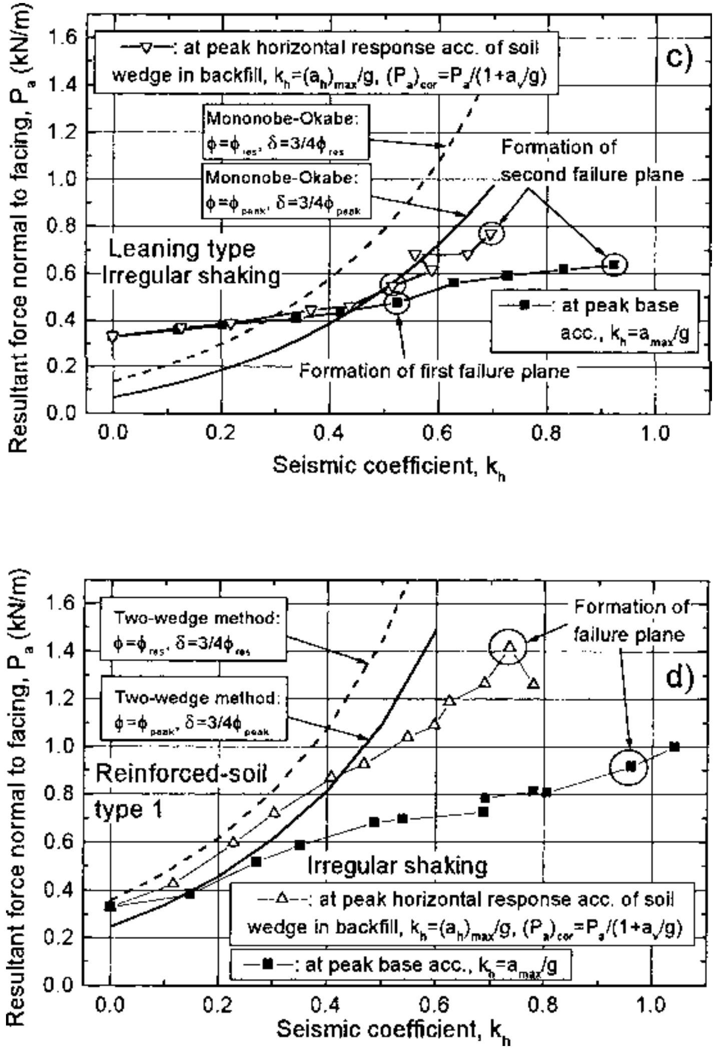

Figure 22 Continued.

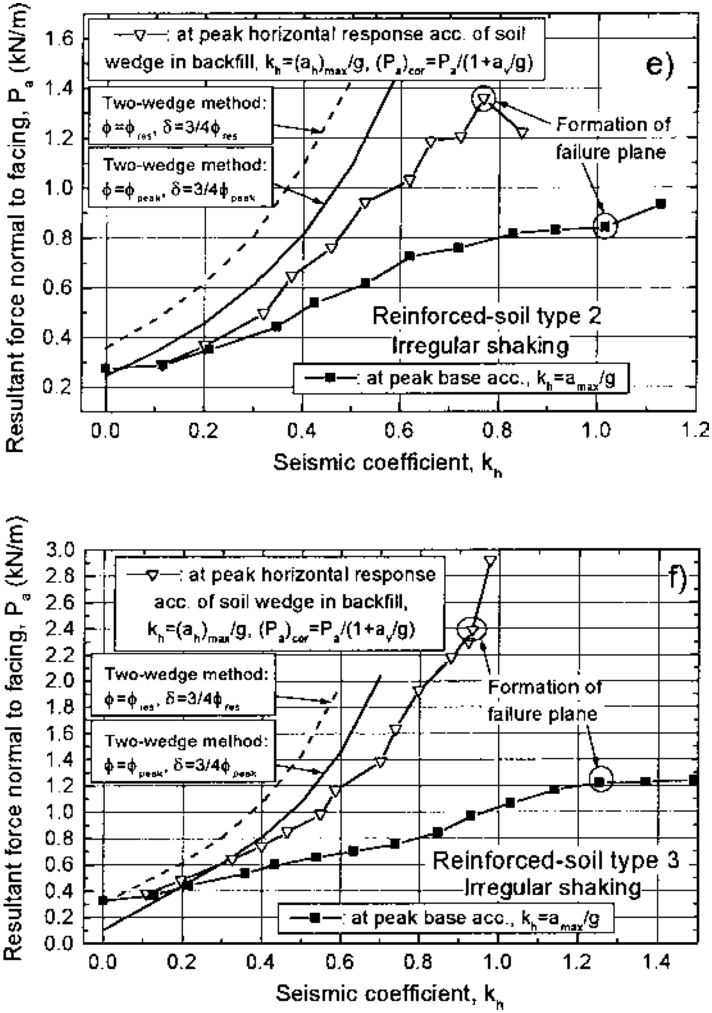

Figure 22 Continued.

7 COMPARISONS WITH RESULTS FROM STABILITY ANALYSIS

7.1 Calculation of Critical Seismic Coefficients

Safety factors against overturning, sliding, and bearing capaity failure of the RW models were evaluated based on a limit equilibrium-based pseudo-static approach.

For each test, the critical seismic coefficient $(k_h)_{cr}$ was defined at the state when the calculated safety factor became equal to unity. Theoretical lateral earth pressures acting on the backface of wall were calculated by the Mononobe–Okabe method (Okabe, 1924; Mononobe and Matsuo, 1929) assuming a single soil wedge for the conventional walls and by the two-wedge method for the reinforced soil-type walls, as described by Horii et al. (1994). In both methods, earth pressures due to the self-weight of the backfill were assumed to be hydrostatically distributed along the wall height, and those due to the surcharge applied at the top of the backfill were assumed to be uniformly distributed. This assumption of hydrostatic distribution was employed because it was broadly used in the current practice to design soil retaining walls in Japan.

The theoretical safety factors against overturning were obtained by assuming that overturning occurred around the toe of the base part of the wall. The bearing capacity for the conventional walls was evaluated by assuming the subsoil thickness to be sufficient to cause boundary-free subsoil failure, despite the fact that the actual thickness of subsoil layer was limited to 200 mm. On the other hand, the ultimate failure of the reinforced soil-type walls due to the bearing capacity failure was not considered; in other words, the maximum allowable vertical contact load at the bottom of the facing was set equal to the bearing capacity of the subsoil layer (RTRI, 1997).

For the cantilever wall having a wall base overlain by the backfill, a virtual vertical backface was assumed within the backfill, and the portion of the backfill located above the wall base and between the back face of facing and the virtual backface was regarded as a part of the wall.

As mentioned before, the shear resistance angle ϕ of the backfill and subsoil layers was set equal to ϕ_{peak} $(=51°)$ obtained from the PSC tests mentioned above.

It is very likely that the friction angle along the bottom face of the rigid base is equivalent to the simple shear angle of friction $\phi_{ss} = \arctan(\tau/\sigma)_{\max}$ along the horizontal failure plane. The ratio of the simple shear peak friction angle ϕ_{ss} to the peak angle of $\phi_{\text{peak}} = \arcsin\{(\sigma_1 - \sigma_3)/(\sigma_1 + \sigma_3)_{\max}\}$ from the PSC tests having the vertical σ_1 direction, both obtained for air-pluviated Toyoura sand, is around 3/4 (Tatsuoka et al., 1991). Considering the effect of the sandpaper glued on the surface of the wall base, therefore, the frictional angle δ_b at the interface between the subsoil and the wall base was assumed equal to $3/4\phi_{\text{peak}}$ $(=38°)$ in the calculation of safety factor against sliding.

Similarly, with ignoring the effects of strength anisotropy, the frictional angle δ_w at the interface between the backfill and the wall facing with sandpaper was set equal to $3/4\phi_{\text{peak}}$. For the cantilever-type wall, the δ_w-value along the assumed virtual vertical backface was also set equal to $3/4\phi_{\text{peak}}$, because with δ_w set equal to ϕ_{peak}, the safety factor equal to unity could not be obtained until the seismic coefficient became unrealistically large.

Dynamic effects in the shaking table tests, such as an amplification and a phase lag between the response and the base accelerations, and effects of progressive failure were not considered in these evaluation procedures of RW stability.

7.2 Observed Critical Seismic Coefficients

The observed critical seismic coefficients $(k_h)_{\mathrm{ult}}$ at the ultimate overall wall failure condition were obtained based on the relationships between the seismic coefficient k_h and the horizontal displacement d_{top} measured at a distance of 5 cm below the top of the wall (Fig. 12). As previously mentioned, in the sinusoidal shaking tests and the tilting tests, after exceeding about 25 mm, which corresponds to about 5% of the total wall height, the d_{top}-value increased very rapidly, soon resulting into the ultimate overall wall failure. The values of $(k_h)_{\mathrm{ult}}$ are, therefore, defined as those when the d_{top}-value exceeded 5% of the wall height.

7.3 Comparison Between Observed and Calculated Critical Seismic Coefficients

Figure 23 shows the relationships between the observed values of $(k_h)_{\mathrm{ult}}$ for the ultimate overall wall failure and the calculated values of $(k_h)_{\mathrm{cr}}$ against external instability obtained for the observed major failure pattern (i.e., overturning or bearing capacity failure). For each case, the calculated value of $(k_h)_{\mathrm{cr}}$ against

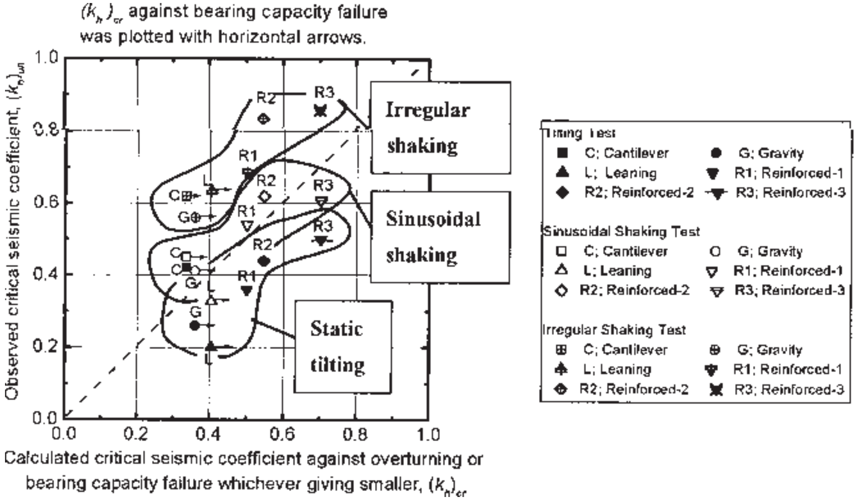

Figure 23 Comparison of observed critical seismic coefficients to calculated ones against overturning or bearing capacity failure.

bearing capacity failure for conventional-type RWs was plotted when it was smaller than that against overturning.

It should be noted that, for the reinforce soil RWs, the bearing capacity failure was not considered in the calculation of $(k_h)_{\mathrm{cr}}$, since the wall can maintain its stability even when the load acting at the bottom of the facing reaches the bearing capacity of the subsoil, as demonstrated by a large-scale shaking test on a similar model of reinforced soil RW (Murata et al., 1994). It should be kept in mind that the bearing capacity for the conventional RWs was evaluated by assuming that the subsoil thickness was sufficient to cause boundary-free subsoil failure despite the fact that the actual thickness of the Toyoura sand layer was only 200 mm. Therefore, the safety factors against bearing capacity failure may have somehow been underestimated. In Fig. 23, this inference is indicated by arrows directing right shown next to the data points for the cantilever- and gravity-type RWs.

The following trends may be seen from Fig. 23:

1. The base width was the same, equal to 230 mm, among the gravity- and cantilever-type RWs and the reinforced soil-type 1 RW (if the reinforced backfill is regarded as a part of the base). On the other hand, for the leaning-type RW, the base width was 180 mm, whereas the width between the top of the back face and the toe of the base was wider, equal to 330 mm. Despite the above conditions, in the tilting tests, the reinforced soil-type 1 RW and the cantilever RW exhibited larger values of $(k_h)_{\mathrm{ult}}$ than the leaning-type and gravity-type RWs. In the sinusoidal and irregular shaking tests, the reinforced soil-type 1 RW was more stable than all the conventional-type RWs (L, G, and C). These results are, in a broad sense, consistent with the full-scale field behavior observed during the Hyogoken-Nambu earthquake (Tatsuoka et al., 1996), suggesting a relatively high seismic stability of reinforced soil RWs having a full-height rigid (FHR) facing.
2. In the tilting tests, the ratios $(k_h)_{\mathrm{ult}}/(k_h)_{\mathrm{cr}}$ were generally lower than unity, perhaps except for the cantilever-type RW. This result suggests that the conventional pseudo-static approaches using the peak soil strength ϕ_{peak} obtained under plane strain conditions with the σ_1 direction normal to the bedding plane direction overestimate the stability of RW. This overestimation is possibly because the effects of progressive failure associated with strain softening properties are not considered in the pseudo-static approaches.
3. In the sinusoidal shaking tests, the ratios $(k_h)_{\mathrm{ult}}/(k_h)_{\mathrm{cr}}$ were generally larger than unity, except for the leaning-, and reinforced soil-type 3 RWs. These ratios were larger than those observed in the tilting tests. In the irregular shaking tests, the ratios $(k_h)_{\mathrm{ult}}/(k_h)_{\mathrm{cr}}$ were larger than those

observed in the sinusoidal shaking tests. In addition, these ratios were different among the different types of RWs.

4. These facts suggest that the dynamic stability of RWs is not totally controlled by "peak base acceleration"/g, but also by other dynamic factors such as the duration of peak lateral force acting on the backface of wall, phase lag and amplification of response acceleration, dynamic ductility and flexibility of RWs, and dynamic shear deformation of backfill, especially for the reinforced soil-type RWs with longer reinforcements. Effects of those dynamic factors should not be ignored for proper seismic stability analysis of RWs.
5. In the sinusoidal and irregular shaking tests, the observed values of $(k_h)_{\mathrm{ult}}$ were similar between the reinforced soil-type 2 RW having a couple of long reinforcement layers at high levels in the backfill and the reinforced soil-type 3 RW having moderately long same-length reinforcement layers. On the other hand, the total amount of reinforcements was smaller with reinforced soil-type 2 RW. When reconstructing existing slopes to vertical reinforced soil-type RWs having an FHR facing, the use of relatively short reinforcements at low levels is preferred to minimize the amount of slope excavation. Based on the test results described above, using several long reinforcement layers at high levels, as reinforced soil-type 2 RW, can be recommended to effectively increase its seismic stability.

Figure 24 compares the respective calculated critical seismic coefficient $(k_h)_{\mathrm{cr}}$ against sliding with those against overturning and bearing capacity failure. With cantilever- and gravity-type RWs, the $(k_h)_{\mathrm{cr}}$-value against overturning (solid symbols) was larger than that against bearing capacity failure (open symbols), and in the following comparison, therefore, the latter value was employed.

For leaning-type and reinforced soil-type 3 RWs, the calculated value of $(k_h)_{\mathrm{cr}}$ against sliding failure was marginally smaller than the respective value against overturning or bearing capacity failure. On the other hand, for the other RWs, the calculated values of $(k_h)_{\mathrm{cr}}$ against sliding failure were larger than those against overturning or bearing capacity failure, whichever was smaller. For leaning-type RW, the above result is consistent with the fact that the observed failure mode consisted not only of overturning but also of sliding (Fig. 6c). Such behavior can be also seen from Fig. 25, where the residual overturning angle of the facing at the end of each shaking step is plotted versus the residual sliding displacement, which were evaluated from records of two displacement transducers set near the top and bottom parts of the facing. It should be noted, however, that these $(k_h)_{\mathrm{cr}}$-values against sliding should be treated with caution, because these values are too sensitive to the friction angle at the interface between the wall base and the subsoil layers (except for the reinforced soil-type RWs).

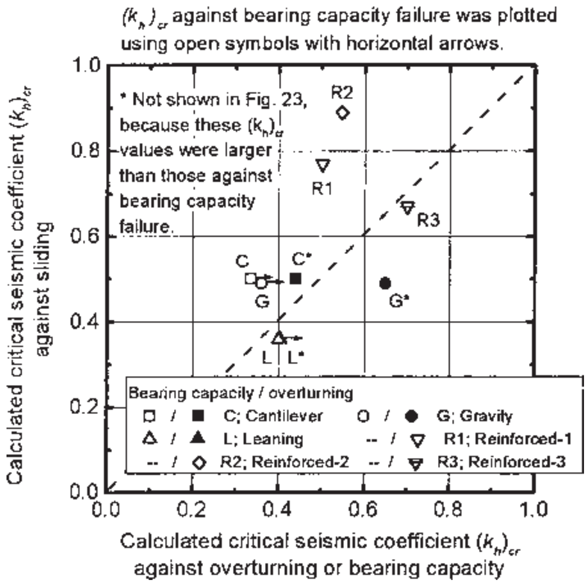

Figure 24 Comparison of calculated critical seismic coefficients against sliding, overturning, and bearing capacity failures.

It can be seen from Fig. 25 that, for reinforced soil-type 3 RW, the amount of sliding displacement relative to the overturning angle was not significant, although its value of $(k_h)_{\mathrm{cr}}$ against sliding was marginally smaller than that against overturning (Fig. 24). In relation to this, it should be kept in mind that, for the reinforced soil-type walls, the reinforced backfill is assumed to behave as a rigid body in evaluating the safety factors discussed above. It was observed in the tests, however, that overturning of the wall was associated with noticeable simple shear deformation of the reinforced backfill (Fig. 6d–f). Therefore, it can be inferred that, when following the current design procedures that does not consider such simple shear deformation, seismic stability of reinforced soil-retaining walls with relatively long reinforcements could be overestimated against the overturning mode of failure. This inference is consistent with the results that, with reinforced soil-type 3 RW having longer reinforcements, the ratios $(k_h)_{\mathrm{ult}}/(k_h)_{\mathrm{cr}}$ in the sinusoidal and irregular shaking tests were smaller than the respective values with reinforced soil-type 1 RW having shorter reinforcements (Fig. 23).

It can be also seen from Fig. 25 that, for reinforced soil-type 2 RW, the amount of sliding displacement relative to the overturning angle was largest among the three types of reinforced soil RWs. This may suggest that using several long reinforcement layers at a high level will improve the seismic

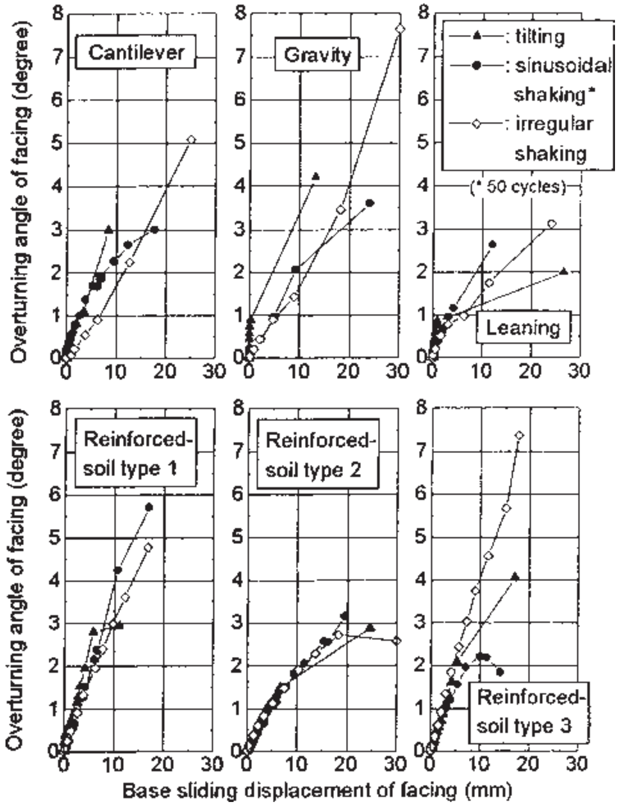

Figure 25 Relationships between residual overturning angled of facing and residual sliding displacement.

stability against overturning mode of failure to a larger extent than that against sliding mode of failure. However, such behavior could not be rationally evaluated by the current design procedures, as can be seen from Fig. 24.

8 CONCLUSIONS

The major conclusions obtained from the present study are summarized below:

1. In the irregular shaking tests on leaning-type and gravity-type RWs, after the failure plane was formed in the backfill, the second failure plane was formed at higher seismic loads. This can be explained by

considering the effects of strain localization in the backfill soil and associated postpeak reduction in the shear resistance from peak to residual values along a previously formed failure plane.

2. The angle of failure plane observed in the tilting tests was consistent with that calculated by the Mononobe–Okabe method using ϕ_{peak} and the seismic coefficient $(k_h)_{fp}$ at which the failure plane was initially formed. The value of ϕ_{peak} was evaluated by conducting plane strain compression tests on the backfill material. In the sinusoidal and irregular shaking tests, however, the observed failure plane angle was not directly linked to the $(k_h)_{fp}$-values, and the amount of wall displacement measured at the moment of the formation of the failure plane was larger than that in the tilting tests.
3. At high seismic loads in irregular shaking tests, reinforced soil-type RWs showed more ductile behavior than conventional- (cantilever-, gravity-, and leaning-) type RWs. When the model walls started tilting, concentration of subgrade reactions at the toe of conventional-type RWs resulted into a local failure in the subsoil, leading to the loss of bearing capacity. On the other hand, under similar conditions, tensile force in the reinforcement of the reinforced soil RWs could be mobilized effectively to resist against the wall movement.
4. The resultant forces of normal earth pressures measured in the tilting tests were in a broad sense, comparable with theoretical ones based on the Mononobe–Okabe or its equivalent method. On the other hand, the resultant forces measured in the sinusoidal and irregular shaking tests were smaller than those measured in the tilting tests. However, by making corrections for the horizontal and vertical response accelerations of soil wedge in the backfill, the measured values became much closer to the theoretical ones, in particular, in the region at high seismic loads.
5. In the static tilting tests, the observed critical seismic coefficient at the ultimate overall wall failure was smaller than that calculated by the Mononobe–Okabe method using ϕ_{peak}. This is possibly due to the effects of progressive failure with strain softening in the backfill, which are not considered in the calculation.
6. For the same type of RW, the observed seismic coefficient at the ultimate overall wall failure was largest in the irregular shaking tests, while it was smallest in the tilting tests. This is possibly affected by several dynamic factors, which are not considered in the calculation, such as different duration of the peak seismic load, phase lag and amplification of response acceleration, dynamic ductility and flexibility of RWs, and dynamic shear deformation of backfill.
7. It was demonstrated that by extending several upper reinforcements the seismic stability of reinforced soil walls could be improved more

effectively than by extending all the reinforcements moderately. On the other hand, effects of shear deformation of the reinforced backfill, which are not considered in the current design procedures, cannot be ignored, in particular for reinforced soil RWs with longer reinforcements.

ACKNOWLEDGMENTS

The authors appreciate the assistance of Mr. T. Sato, Research Associate at the Institute of Industrial Science, for offering thoughtful suggestions during preparation of the model; Dr. S.J.M. Yasin, formerly at the University of Tokyo, for helping to conduct plane strain compression tests; Mr. H. Kimura and Mr. S. Ebisawa at RTRI for their assistance in conducting the tilting and shaking table tests; Mr. K. Horii, of Integrated Geotechnology Institute Limited, for his great help in performing the stability analysis of the reinforced soil-type RWs.

REFERENCES

RJ Bathurst, MC Alfaro. Review of seismic design, analysis and performance of geosynthetic reinforced walls, slopes and embankments. *Earth Reinforcement*. ?? Ochiai et al., eds. Vol. 2. The Netherlands: Balkema, pp 887–918, 1996.

K Horii, H Kishida, M Tateyama, F Tatsuoka. Computerized design method for geosynthetic-reinforced soil retaining walls for railway embankments. *Recent Case Histories of Permanent Geosynthetic-Reinforced Soil Retaining Walls*. F Tatsuoka, D Leshchinsky, eds. The Netherlands: Balkema, pp 205–218, 1994.

K Horii, M Tateyama, J Koseki, F Tatsuoka. Stability and residual deformation analyses of geosynthetic reinforced earth retaining wall with rigid facing due to large earthquakes. *Proc. of 13th Geosysthetics Symposium*, Japan Chapter of International Geosysthetics Society (in Japanese), pp 260–269, 1998.

M Ichihara, H Matsuzawa. Earth pressure during earthquake. *Soils and Foundations* 13(4): 75–86, 1973.

J Koseki, M Tateyama, F Tatsuoka, K Horii. Back analyses of soil retaining wall for railway embankments damaged by the 1995 Hyogoken Nanbu earthquake. *The 1995 Hyogoken-nanbu Earthquake—Investigation into Damage to Civil Engineering Structures*, Committee of Earthquake Engineering, Japan Society of Civil Engineers, pp 101–114, 1996.

J Koseki, Y Munaf, F Tatsuoka, M Tateyama, K Kojima, T Sato. Shaking table and tilt table tests of geosynthetic-reinforced soil and conventional retaining wall. *Geosynthetics Intl.* 5(1–2): 73–96, 1998a.

J Koseki, F Tatsuoka, Y Munaf, M Tateyama, K Kojima. A modified procedure to evaluate active earth pressure at high seismic loads. *Soils and Foundations,* Special Issue on Geotechnical Aspect of the January 17, 1995, Hyogoken-Nambu Earthquake No. 2: 209–216, 1998b.

J Koseki, Y Munaf, M Tateyama, K Kojima, K Horii. Back analyses of case histories and model tests on seismic stability of retaining walls. *11th Asian Regional Conf. on Soil Mechanics and Geotechnical Engineering* 1: 399–402, 1999.

HI Ling, D Leshchinsky, EB Perry. Seismic design and performance of geosynthetic-reinforced soil structures. *Geotechnique* 47(5): 933–952, 1997.

O Matsuo, T Tsutsumi, K Yokoyama, Y Saito. Shaking table tests and analyses of geosynthetic-reinforced soil retaining walls. *Geosynthetics Intl.* 5(1–2): 97–126, 1998.

N Mononobe, H Matsuo. On determination of earth pressure during earthquake. *Proc. World Engineering Congress,* Tokyo 9: 177–185, 1929.

O Murata, M Tateyama, F Tatsuoka. Shaking table tests on a large geosynthetic-reinforced soil retaining wall model. *Recent Case Histories of Permanent Geosynthetic-Reinforced Soil Retaining Walls*. F Tatsuoka, D Leshchinsk, eds. The Netherlands: Balkema, pp 259–264, 1994.

S Okabe. General theory on earth on pressure and seismic stability of retaining wall and dam. *J Japan Society of Civil Engineers* 10(6): 1277–1323, 1924.

Railway Technical Research Institute. Design standard for railway foundations/soil retaining structures (in Japanese), pp 132–135, 1997.

M Sakaguchi. A study of the seismic behavior of geosynthetic reinforced walls in Japan. *Geosynthetics Intl.* 3(1): 13–30, 1996.

HB Seed, RV Whitman. Design of earth retaining structures for dynamic loads, *ASCE Specialty Conf. on Lateral Stresses in the Ground and Design of Earth Retaining Structures*, pp 103–147, 1970.

F Tatsuoka. Some recent developments in triaxial testing systems for cohesionless soils. *Advanced Triaxial Testing of Soil and Rock*, ASTM STP 977, pp 7–67, 1988.

F Tatsuoka, M Okahara, T Tanaka, K Tani, T Morimoto, MSA Siddiquee. Progressive failure and particle size effect in bearing capacity of a footing on sand. *Geotechnical Engineering Congress 1991*, ASCE, Geotechnical Special Publication, No. 27, 2:788–802, 1991.

F Tatsuoka, M Tateyama, J Koseki. Performance of soil retaining walls for railway embankments. *Soils and Foundations*, Special Issue of Soils and Foundations on Geotechnical Aspects of the January 17, 1995, Hyogoken-Nanbu Earthquake, pp 311–324, 1996.

F Tatsuoka, J Koseki, M Tateyama, Y Munaf, K Horii. Seismic stability against high seismic loads of geosynthetics reinforced soil retaining structures. *Proc. 6th Intl. Conf. on Geosynthetics*, Vol. 1, Atlanta, pp. 103–142, 1998.

19

Performance of Geosynthetic Reinforced Soil Wall and Reinforced Earth Wall Subject to Blast Loading: Experimental and Numerical Study

Soon Hoe Chew, Siew Ann Tan, G. P. Karunaratne, and Chiew Chiat Ng
National University of Singapore, Singapore

ABSTRACT

Earth structures are often used in military and civilian applications to protect personnel and property from accidental detonation of stored explosives, munitions, and ammunition plants. The advantages of reinforced soil structures lie in their cost-effectiveness, rapid construction, and minimal use of occupied ground area and high tolerance for differential settlements. They are also able to impede the propagation of a blast at ground level and absorb high levels of energy due to their high damping properties and great tolerance for deformation before collapse. In using geosynthetics as facings and reinforcements, the reinforced soil structures not only can absorb fragments from cased weapon explosion, but also are not subjected to brittle fracture like concrete after blasting and hence minimize the dispersal of flying debris. They are also resistant to multiple blasting.

A geosynthetics reinforced soil (RS) wall and a Reinforced Earth® (RE) wall with precast concrete facings were constructed and subjected to multiple blasts, and their extent of damage was recorded and studied. After a series of blasts, the concrete facings of the front of the RE wall collapsed and the soil mass slid out and down the front. There were obvious pullout failures of the metal reinforcement strips as well as tension failure at the joints of the panel facings and reinforcements. However, the geosynthetics facing of the RS wall only suffered superficial damage due to high temperature and direct fragment impact. Comparing the failure modes of RS and RE walls, it was obvious that flexible facing units such as the geosynthetics wrap around type of facing can be effectively used for protective blast-resistant soil structures.

Evidence of the good performance of the RS wall also obtained from the dynamic earth pressure measurements made in the reinforced soil mass, clearly showing the very high efficiency of blast energy dissipation from the rapid decay and large reductions of earth pressures measured in the wall. Pressure reductions of more than 90% were achieved when comparing peak dynamic lateral earth pressures measured at 0.5 m and 3.5 m from the blasted front of the wall.

A numerical simulation of the blast event of the RS wall was made using the dynamic module of PLAXIS version 7.2. The various soil parameters' influence on wall performance were investigated by comparing FEM calculations with the measured earth pressures in the wall. Some preliminary recommendations were made for suitable selection of soil dynamic parameters for good simulation of the RS wall subjected to blast loadings. With an appropriate choice of parameters, the observed field response of the RS wall was successfully simulated with dynamic FEM, and the pressure dissipation calculated in the dynamic FEM analysis matched well with the field measurements for two blast events.

1 INTRODUCTION

Reinforced soil structures are often used in military and civilian applications to protect personnel and property from accidental detonation of stored explosives, munitions, and ammunition plants. The advantages of reinforced soil structures lie in their cost-effectiveness, rapid construction, and minimal use of occupied ground area and high tolerance of differential settlements. They are able to impede the propagation of an explosive blast at ground level and absorb high levels of energy due to their high tolerance for large deformation before collapse. However, the dynamic response of these structures to short-duration impulsive excitations resulting from above-ground explosions is rarely studied and less well understood. Therefore, a geosynthetics reinforced soil (RS) wall and a Reinforced Earth® (RE) wall with precast concrete facings were constructed and tested in a collaboration research project between the National University of Singapore and the Ministry of Defense of Singapore for application in protective defense structures. The walls were subjected to multiple blasts, and their extent of damage was recorded and studied. Various instruments such as strain gauges, total pressure cells, and accelerometers were used to record response during the tests. The field data were analyzed and compared to numerical FEM calculations.

The main objective of this test is to study the dynamic behavior of RS and RE walls when subjected to multiple blasts of various magnitudes. The effectiveness of residual soil in reducing the blast pressure and ground shock as well as the effectiveness of geosynthetics in reinforcing the soil wall are the main interests of this test. Comparisons are made between the performance and failure modes of RS and RE walls. A brief account of this comparative study was presented by Ng et al. (2000), at ASCE GeoDenver 2000.

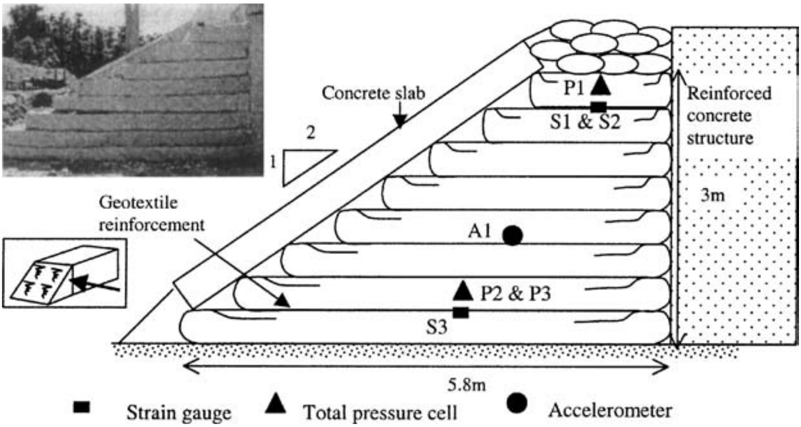

Figure 1 Front elevation of RS wall facing blast with instrumentation plan (not to scale).

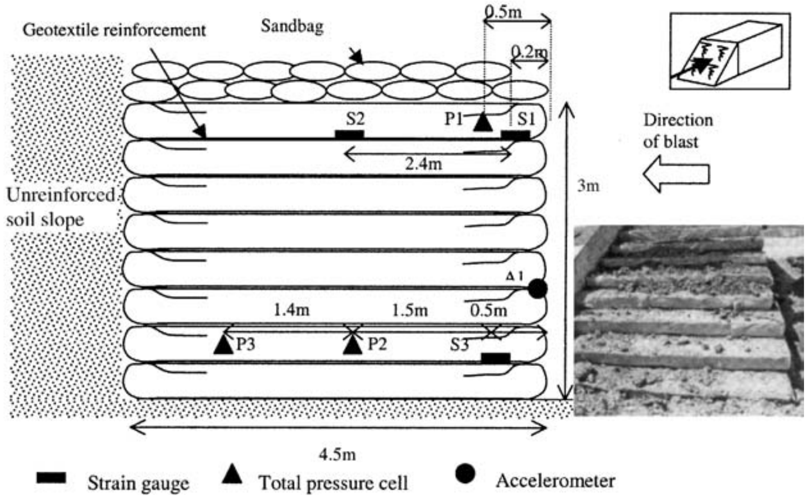

Figure 2 Side elevation of RS wall with instrumentation plan (not to scale).

2 DEVELOPMENT, INSTRUMENTATION, AND CONSTRUCTION OF FULL-SCALE TEST WALL

Figures 1 and 2 show the front and side views of the RS wall with the instrumentation plan. The RS wall rests against a reinforced concrete structure without any connection. It has one vertical face along side with one of the sides of the reinforced concrete shelter and another side sloping down from the top of the reinforced concrete structure. As a result, the vertical face of the RS wall has a triangular shape with a height of 3 m and base width of 5.8 m. The length of the wall in the slope direction was 4.5 m. A reinforced concrete slab 0.8 m thick was to be placed on the sloping side of the RS wall. Both facing and reinforcement for the RS wall were geotextile-type PEC200 (Polyfelt). PEC200 is composite geotextile, which has woven high-strength polyester (PET) yarns on a mechanically bonded polypropylene (PP) nonwoven base. The technical specification of the geotextile PEC200 is shown in Table 1. The polyester yarns provide the required strength and the polypropylene base is the geotextile layer providing for filtration, drainage, and separation function. This type of geotextile was chosen for this project mainly because it has a very high strength and is suitable for reinforcement in poorly draining soil, typical of local tropical residual soils.

The front and side views of the reinforced earth wall are shown in Figs. 3 and 4. The height of the front face of the RE wall is 3.75 m, and the width of

Table 1 Technical Data of Geotextile Type PEC200 Manufactured by Polyfelt

Properties	Unit	PEC200
Type of product	—	Composite geotextile
Material	—	Mechanically bonded PP nonwoven/ high-strength PET yarns
Orientation of reinforcement	—	Unidirectional
Tensile strength (MD*/CD†)	KN/m	200/14
Elongation at break (MD*/CD*)	%	13/60
Tensile strength (MD)		
at 2%	kN/m	30
at 3%	kN/m	45
at 5%	kN/m	72
at 10%	kN/m	168
Long-term design strength (120 years) (MD)	kN/m	85.1
Thickness	mm	2.9
Mass	g/m^2	580

Data provided by Polyfelt.
* M.D. = Machine direction in weaving.
† C.D. = Cross-machine direction perpendicular to machine direction.

the front wall is 4.1 m. The wall is sloping down from the front face of the wall to the back at a slope of 1:2. A reinforced concrete slab 0.8 m thick was also placed on the sloping top of the RE wall, similar to the RS wall. Precast reinforced concrete panels and ribbed metal strips are used for the facings and reinforcements, respectively, for the construction of the RE wall. Table 2 shows the specifications of the reinforced concrete facing panels and metal reinforcement strips used for the construction of the full-scale reinforced earth wall at the test site.

Strain gauges, total pressure cells, and accelerometers, similar to those used by Richardson (1976), were installed in the full-scale RS wall to measure tensions in the geotextile, horizontal earth pressure in the backfill and acceleration in front of the RS wall, respectively. The strain gauges, total earth pressure cells, and accelerometers were monitored dynamically during blast events. The instrumentation program was intended to provide a field dynamic response of RS wall for comparison with earlier numerical results by other researchers, and with FEM simulations later. No instrumentation was provided for monitoring

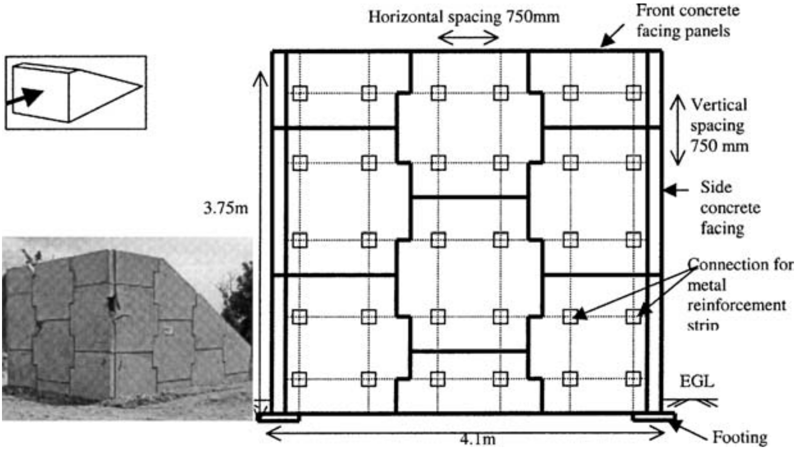

Figure 3 Front elevation of RE wall facing blast (not to scale).

the response of the RE wall during both static and dynamic conditions due to severe time and financial constraints in the project. The dynamic response of the RE wall was monitored and compared to the RS wall based on visual observations and photo survey.

Tropical residual soil in Singapore was used in the tests. Several laboratory tests were conducted to obtain the properties of the soil. All the properties tests for the residual soil were conducted as per British Standard BS 1377 (1990).

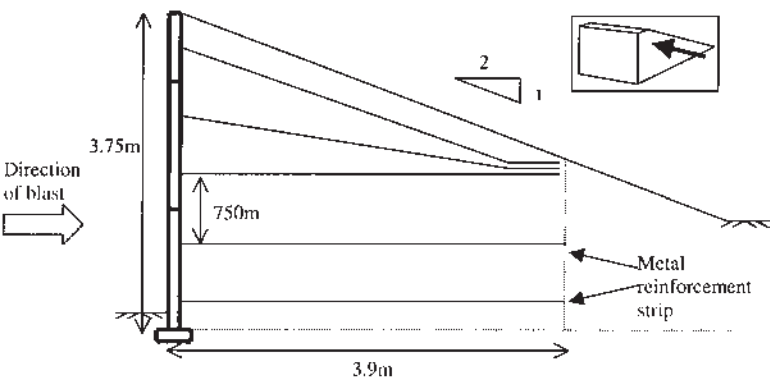

Figure 4 Side elevation of RE wall (not to scale).

Table 2 Technical Data of the Reinforced Concrete Facing Panels and Metal Reinforcements Strips

Properties of reinforced concrete facing panels	
Panel thickness	140 mm
Compressive strength of reinforced concrete	28 MPa (medium-strength concrete)
Density of reinforced concrete	2320 kg/m^3
Size of panel	1.5 m × 1.5 m
Properties of metal reinforcement strips	
Type of strip	Ribbed strip
Type of metal	ASTM A-572, Grade 65 (high-strength, low Alloy Columbium-Vanadium steels of structural quality)
Strength (T'_{Ult})	415 MPa
Strip thickness	4 mm
Strip width	50 mm

Data provided by Reinforced Earth® Company.

The particle size distribution of the soil is shown in Fig. 5, and the properties of the residual soil are summarized in Table 3.

3 TEST PROCEDURES

A series of blasts was detonated at various locations around the RS and RE walls. However, for discussion in this chapter detonation events MD5-E2, MD5-E3, MD11-E2, and MD11-E3 were referred to for comparison of performance

Table 3 Properties of Residual Soil

Particle density	2.65
Moisture content	24.1%
Liquid limit	67%
Plastic limit	26%
Plastic index	41%
Coefficient of consolidation (at $U = 90\%$)	1.88×10^{-7} m^2/sec (or 6 m^2/yr)
Coefficient of permeability	1.61×10^{-9} m/sec

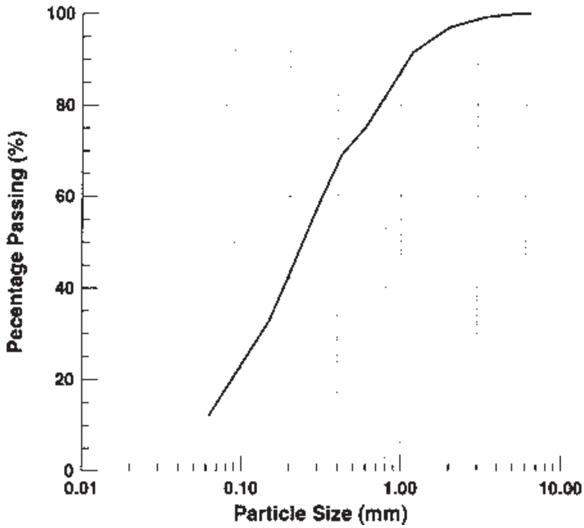

Figure 5 Particle size distribution of residual soil in Singapore.

between RS and RE walls, as these detonation events were similar in charge mass and distance from the respective walls. The details of these detonation events are shown in Table 4. After every detonation event, sketches and photographs recorded visual observations of the RS and RE walls. Digital signals were also recorded during these detonation events for the RS wall. The performance of RE and RS walls during blast loading was compared based on visual observation records. Detonation events MD5-E1 and MD11-E1 were not referred to when comparing the performance of the two walls as the charge mass and locations

Table 4 Detonation Events for Main Test

Detonation event		
MD5-E1	300-kg bar charge	15 m away from the front of RS wall
MD5-E2	100-kg bare charge	5 m away from the front of RS wall
MD5-E3	100-kg cased charge	5 m away from the front of RS wall
MD11-E1	7.5-kg bare charge	5 m away from the front of RE wall
MD11-E2	100-kg bare charge	5 m away from the front of RE wall
MD11-E3	100-kg cased charge	5 m away from the front of RE wall

were not similar. Furthermore, these two detonation events were either some distance from the wall or too small a detonation charge, and did not cause significant deterioration to the walls. The instrumentation results for detonation events MD5-E1 and MD5-E2 will also be presented and discussed here.

4 COMPARISONS BETWEEN PERFORMANCE OF RS AND RE WALLS SUBJECT TO BLAST

Schematic sketches based on visual observations and photographic records illustrating the conditions of RS and RE walls after the their respective detonation events are discussed here for comparisons between performance of RS and RE walls.

Figure 6 shows the condition of the RS wall after detonation events MD5-E1 and MD5-E2. A slight inward compression of the wall can be observed. On the facing, some area of the geotextile facing has melted from the extremely high temperatures of the explosion. At certain areas of the geotextile facing, fragments

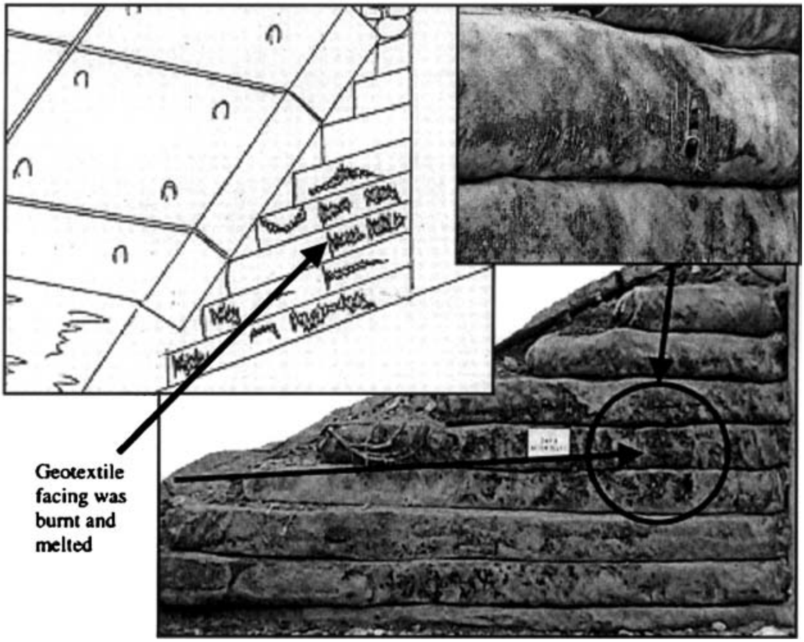

Figure 6 Condition of the RS wall after detonation event MD5-E2.

from the blast cut the PET yarns and the PP base of the geotextile. Spiral-shaped holes were formed behind the geotextile facing at all those areas where the geotextile were torn. Small pieces of blast fragments were found embedded in the holes. Hence it was concluded that the reinforced soil was effective in absorbing the blast fragments. Some soil mass fell out to the front of the RS wall from the areas where the geotextile facing was torn.

Figure 7 shows the condition of the RS wall after detonation event MD5-E3. The areas of melted geotextile facing increased and the extent of melting deteriorated further. The areas of geotextile cut by blast fragments also increased, and the degree of damage was more severe than the conditions after the previous detonation event. More soil mass and some of the sandbags placed at the top of the RS wall fell out to the front of the RS wall. Despite the above deterioration, the RS wall stood up vertically except that some soil mass fell out from the torn facing area. In addition, there was slightly more compression on the facing.

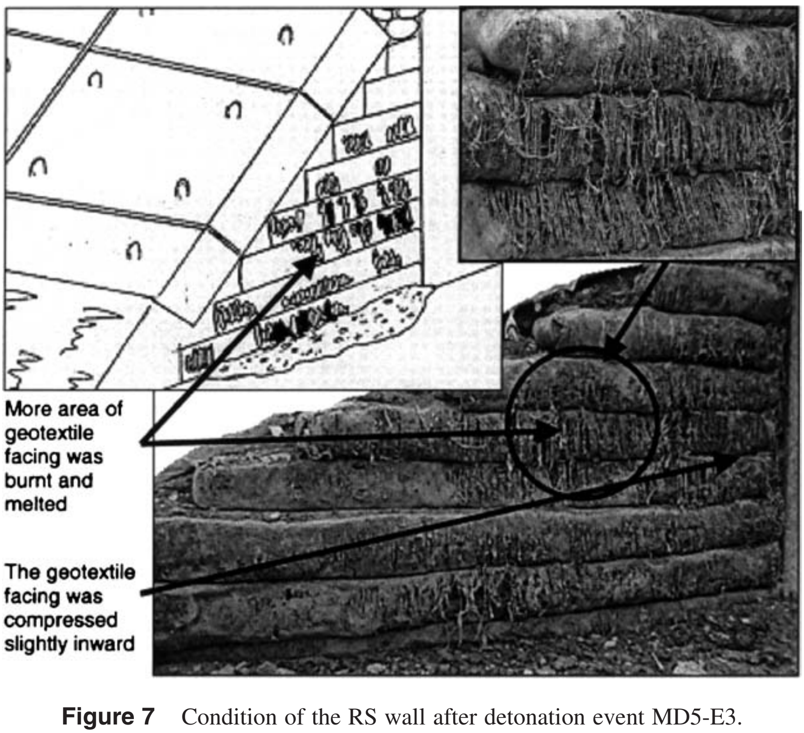

Figure 7 Condition of the RS wall after detonation event MD5-E3.

Figure 8 shows the conditions of RE wall after detonation events MD11-E1 and MD11-E2. Chipping off and spalling occurred at some areas of concrete panel facings. There were also through holes and crack lines on the concrete panel facings. The side panels of the RE wall bulged out with the maximum deflection of approximately 12 cm at the mid-height of the wall. The first column of side panels at both sides bulged out slightly while the rest of side panels remain undisturbed.

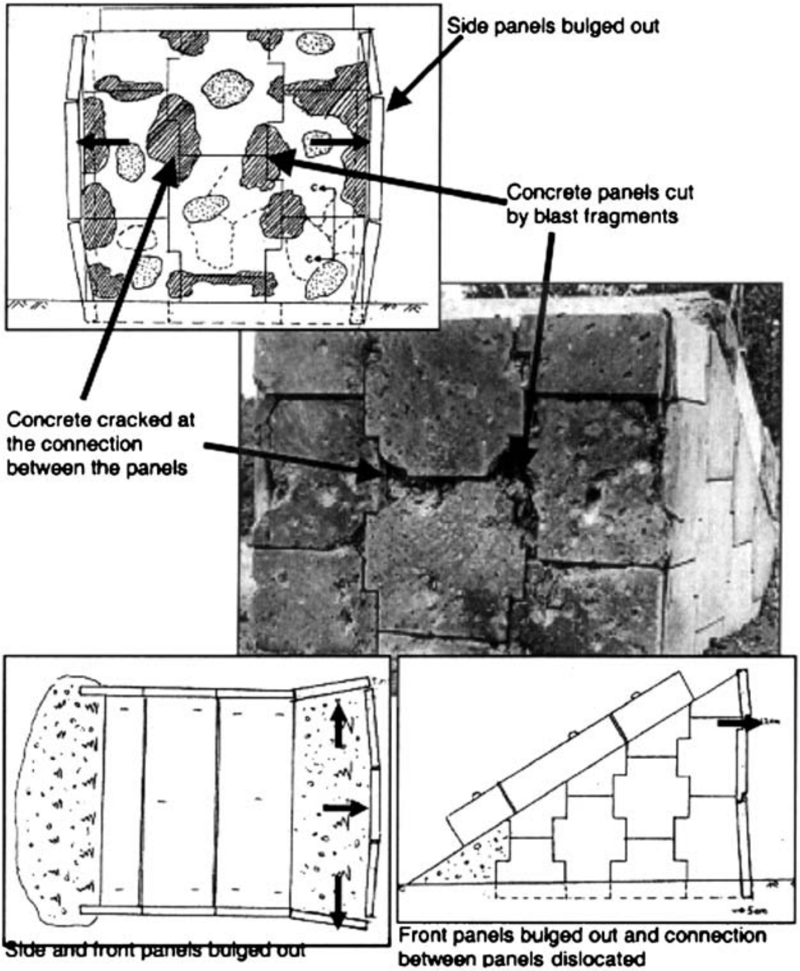

Figure 8 Condition of the RS wall after detonation event MD11-E2.

The front concrete panels bulged out slightly at the center of the wall when seen on plan view. The front concrete panels deflected outward as seen on the side view.

The overall picture of deformation of the RE wall after detonation event MD11-E2 suggests that the interaction between the blast wave and the RE wall was as follows. When the blast wave arrives at the front of the RE wall, the incident blast wave of compressional nature pushed the front concrete panels inward as the concrete panels were hard and rigid. As the concrete panels were pushed inward, the soil behind the concrete panel facings was compressed. The soil mass behind the front concrete panel facings was vertically confined by the concrete slab on top and laterally confined by the concrete panels at both sides. During undrained dynamic loading, the volume of soil mass remains unchanged because there can be no dissipation of excess pore water pressure. Therefore, the soil mass expanded laterally when it was compressed from the front. As a result, the first column of the side concrete panels was pushed outward. Based on diffraction theory of blast wave loading on structures, after the shock wave strikes the front wall of the structure, the shock front reaches the rear edge of the structure and starts spilling down toward the bottom of the back wall. The concrete panels were similar to rigid concrete wall. Hence, the back of the front concrete panel facings began to experience increased pressures as soon as the shock front had passed beyond and enveloped it through the diffraction process. Consequently, the front concrete panels were pushed outward by this diffracted wave. Therefore, there was significant outward displacement of the front concrete panels.

Figure 9 shows the condition of the RE wall after detonation event MD11-E3. The front panels of the RE wall collapsed, and the soil mass behind the wall spalled out. The soil mass and the concrete panels fell out to the front of the wall. The reinforcement strips at the upper layers were pulled out extensively from the soil mass by the concrete panels that fell outward. Some of these reinforcement strips were pulled out completely from the soil mass and rest on top of the soil mass in front of the wall. These reinforcement strips were still firmly attached to the concrete panels that fell out, as the connections between the reinforcement strips and the concrete panels were still intact. However, the concrete panels were detached from the reinforcement strips for the lower layers. Unlike the upper layers, the connections between the reinforcement strips and the concrete panels, which were anchored into the concrete panel, were separated from the concrete panels. The connections and the reinforcement strips remained in the soil mass, while the concrete panels broke up and fell outward to the front.

The mechanism of the blast wave interaction with the RE wall was similar to the previous detonation. When the incident blast wave first struck the wall front, it pushed the front panels inward and caused the soil mass to be compressed. This was not damaging to the wall. But after the incident blast wave

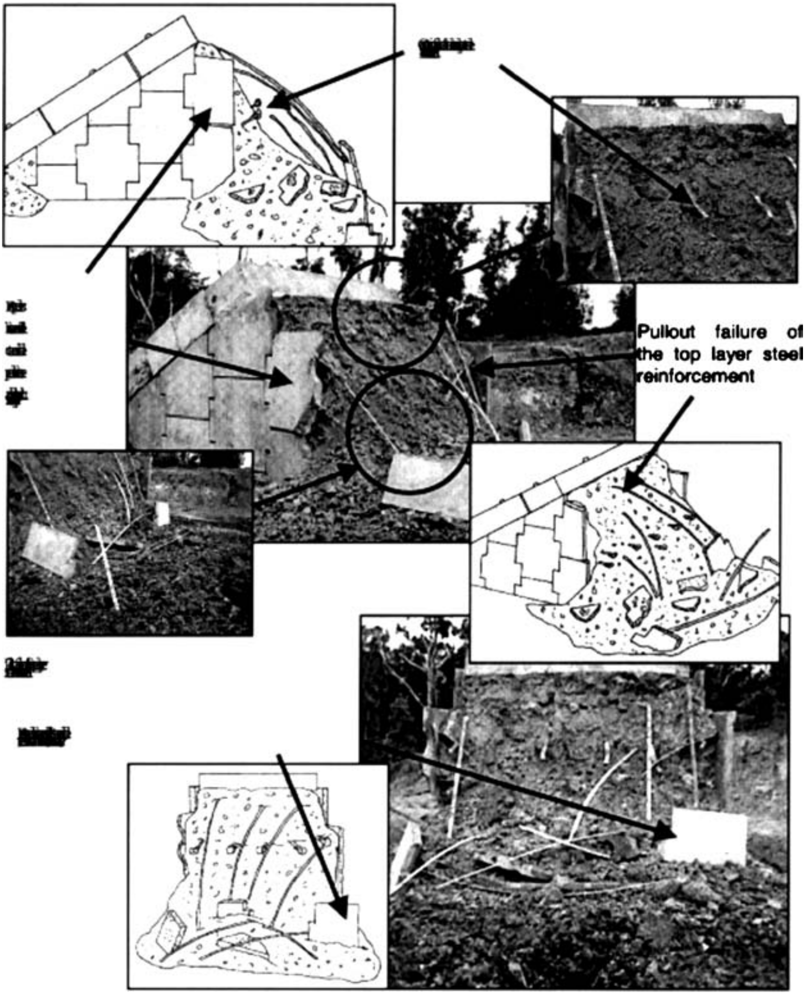

Figure 9 Condition of the RS wall after detonation event MD11-E3.

had enveloped the wall, a diffracted wave was developed at the back of the front panels. Hence the pressure acting on the back of the front panels increased. During detonation event MD11-E2, the front panels were already displaced outward to some extent, and the connection joints were already weakened. Furthermore the reinforced concrete panels might have been cracked during detonation event MD11-E2. The magnitude of both incident and diffracted waves was similar to the previous detonation event as the blasts were of similar intensity and at the same distance from the wall. As a result, the diffracted wave, which caused the pressure to increase on the back of the front panels, pushed the front panels further out. When the concrete panels were pushed further outward, reinforcement strips at the upper layers suffered pullout failure as the dynamic force acting on the back of the concrete panels was greater than the pullout resistance of the reinforcement strips attached to the respective concrete panels. The pullout resistance of the reinforcement strips for the lower layers was higher due to larger overburden pressure. This pullout resistance was higher than the punching shear strength of the concrete.

Therefore, the dynamic forces acting on the back of the front panels were less than the pullout resistance of the reinforcement strips at the lower layers; these reinforcement strips did not suffer pullout failure. However, the tension developed in the reinforcement strips at the time when the dynamic force was acting was greater than the punching shear strength of the concrete. As a result, the connections between reinforcement strips and the concrete panels were sheared away from the concrete panels by the large tension force in the reinforcement strips. Some of the concrete panels were broken apart because weakened crack lines had already developed in the concrete panels during detonation event MD11-E2.

In summary, the RS wall performed better as a blast-resistant structure when compared to the RE wall. This was due to the different behavior of the facing and reinforcement materials used for the reinforced soil structures when subjected to blast loading. The different behavior of these two wall systems is based on the observations of the field trial results.

The comparisons of different behavior of the two different wall systems were based on detonation events MD5-E2 and MD5-E3 for the RS wall, MD11-E2 and MD11-E3 for the RE wall of similar dimensions. The charge type (bare or cased), charge weight (100 kg), and distance (5 m) of the detonation point from the walls for these detonation events were the same. The acceleration and incident blast pressure on the front of the walls were as high as 5000 g and 200 kPa, respectively, as suggested by the measurements made in the RS wall.

After detonation event MD5-E2, some areas of geotextile facing melted and some areas of the geotextile facing were cut by the blast fragments, and the fragments were eventually stopped in the soil mass. There was similar observation at the RE wall after detonation event MD11-E2 as the blast fragments cut through the concrete panel facings, drilled a hole of conical shape into the soil, and eventually stopped at the base of the holes. This showed that both wall systems were effective in absorbing the blast fragments. However, the RE wall has a distinct disadvantage having hard and brittle reinforced concrete panel facings. When the blast fragments cut through the concrete panels, it caused the concrete to fracture and concrete debris to fly out at high speed, which can be deadly to human occupants. However, no flying debris was produced when blast fragments cut the geotextile facing.

During detonation event MD5-E2, all strain gauges in the RS wall did not register any significant changes. In addition, there was also no significant deformation of the RS wall. This implies that the geotextile reinforcement was not subjected to additional dynamic strain during and after detonation. However, there was extensive outward deformation of the RE wall front and side panels after detonation event MD11-E2. Hence it may be deduced that additional tension developed in the reinforcement strips during and after detonation. This comparison implies that the stability of the RE wall was greatly affected by the blast loading whereas the stability of the RS wall was not much affected. This difference in the behavior of the two wall systems was mainly due to the different facing materials. Geotextile facing was flexible and porous enough for the blast wave to pass through, whereas the concrete panel facing was like a rigid wall where the wave diffraction process would occur when the blast waves envelop the wall and pass around it. The diffracted wave caused the pressure on the back of the wall to increase and pushed the wall outward to the front.

After detonation event MD5-E3, larger areas of geotextile facing were melted and cut by fragments, but there was still no significant deflection or bulging of the RS wall facing. However, after detonation event MD11-E3, the front panels of the RE wall collapsed and the soil mass behind the RE wall fell out. The reinforcement strips at the upper layers were pulled out extensively from the soil mass by the concrete panels that fell outward. At the lower layers, the connections between the reinforcement strips and the concrete panels, which were anchored into the concrete panel, were sheared away from the concrete panels. This clearly illustrates the disadvantage of using rigid concrete panels as facing material compared to flexible facing material such as geotextile. Another distinct advantage of geotextile sheet reinforcements compared to metallic strip reinforcements is that the larger contact area of geotextiles with the soil made dynamic pullout failure less likely in the RS wall as compared to the RE wall. Thus the RS wall gave a better composite reinforced structure than the RE wall.

5 INSTRUMENTATION RESULTS FOR THE RS WALL

Figure 10 shows the accelerometer (A1) and total pressure cells (P1 to P3) responses during detonation event MD5-E1. The accelerometer A1 registered a peak instantaneous acceleration of approximately 20,000 g at about 20 milliseconds after the detonation. The total pressure cells P1, P2, and P3 registered peak dynamic pressure (compressive) of approximately 160 kPa, 110 kPa, and 10 kPa, respectively, at about 35 milliseconds after the detonation. The response of the total earth pressures with time for all the total pressure cells

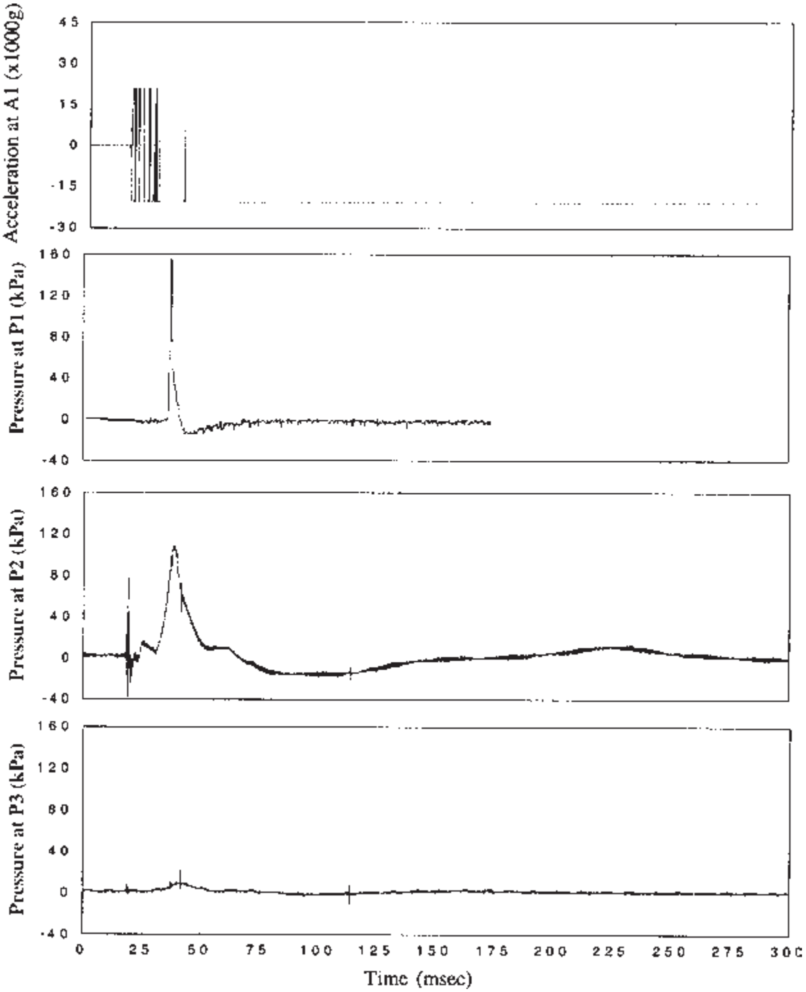

Figure 10 Accelerometer (A1) and total pressure cells (P1 to P3) response during detonation event MD5-E1. Time shown is after triggering of detonation.

during blast was similar to the free-field pressure–time history measured separately. When the blast wave front arrived at the RS wall, the total earth pressure rose almost instantly to its peak value. Then, the incident pressure decayed gradually to the ambient pressure during the positive phase duration.

This was followed by a negative phase with duration longer than the positive phase duration and characterized by a pressure below the ambient pressure.

The dynamic pressure registered was highest at P1 ($\approx$160 kPa), followed by P2 ($\approx$120 kPa) and P3 ($\approx$10 kPa). This variation of dynamic pressure at different total pressure cells may be due to different depths behind the facing of the RS wall where the total pressure cells were installed. The depth behind the facing of RS wall for total pressure cells P1, P2, and P3 was 0.5 m, 2 m, and 3.4 m, respectively. The largest dynamic peak total pressure was recorded at P1, which was closest to the facing of the RS wall, followed by P2, which was farther away behind the facing of RS wall, and P3, which was farthest away behind the facing of RS wall. Although total pressure cell P1 was not at the same elevation as P2 and P3, the dynamic pressure was not affected because the blast wave front was likely a uniform plane when it reached the RS wall. This shows that the peak dynamic pressure due to the detonation of a 300-kg charge of TNT 15 m away can be effectively reduced from approximately 160 kPa to 10 kPa by a soil mass of thickness roughly equal to 3.5 m. Furthermore, the RS wall can withstand a peak acceleration of about 20,000 g without much deterioration. Hence, with the use of a geotextile reinforced soil wall, the blast incident pressure can be reduced significantly and yet the wall was stable and can be subjected to multiple blasts.

At the construction stage and one week after complete construction, strain gauges of geotextiles in the RS wall registered stains from 1% to 3% in geotextiles layer 2, 5, and 8, for both machine and cross-machine direction. For all the blast events in the field, these strain gauges registered additional strains of less than 0.2%, with the larger strains near the blast front of the RS wall. From the instant of blasting and the next 200 ms, the strain gauges did not register any significant changes. This shows that the geotextile reinforcement was not subjected to additional tension during blast, which implies that the factor of safety from static design for the geotextile reinforcement in the RS wall is adequate.

Figure 11 shows the accelerometer (A1) and total pressure cells (P1 to P3) responses during detonation event MD5-E2. The accelerometer A1 registered a peak instantaneous acceleration of approximately 5000 g about 20 milliseconds after the detonation. Although the detonation was closer to the RS wall, this acceleration was lower than that for detonation event MD5-E1 because the charge mass was smaller, only 110 kg compared to 300 kg of event MD5-E1.

The total pressure cells P1, P2, and P3 registered peak dynamic pressures (compressive) of approximately 110 kPa, 50 kPa, and 8 kPa, respectively, about 35 milliseconds after the detonation. The response of the total earth pressures with time for all the total pressure cells during blast was similar to the free-field pressure–time history. Again, the results of this event shows that the peak

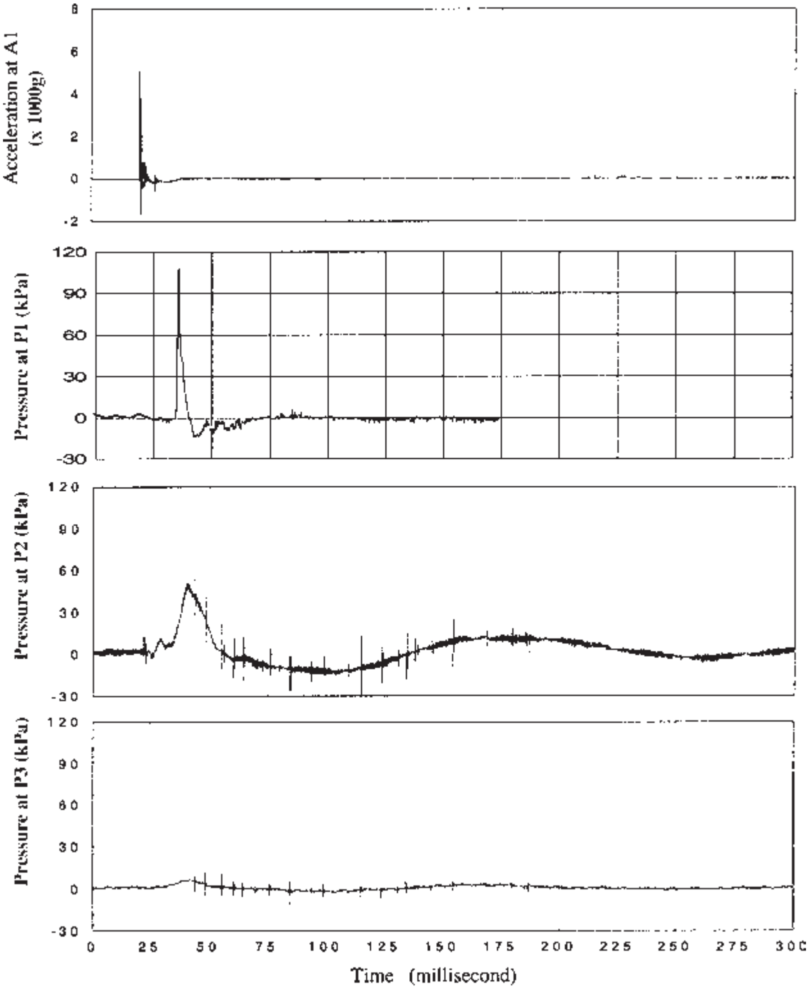

Figure 11 Accelerometer (A1) and total pressure cells (P1 to P3) response during detonation event MD5-E2. Time shown is after triggering of detonation.

dynamic pressure due to the detonation of a 110-kg charge of TNT 5 m away can be effectively reduced from approximately 110 kPa to 8 kPa by a soil mass of thickness roughly equal to 3.5 m. No strain gauge registered any significant changes because the geotextile was not subjected to additional strain during blast.

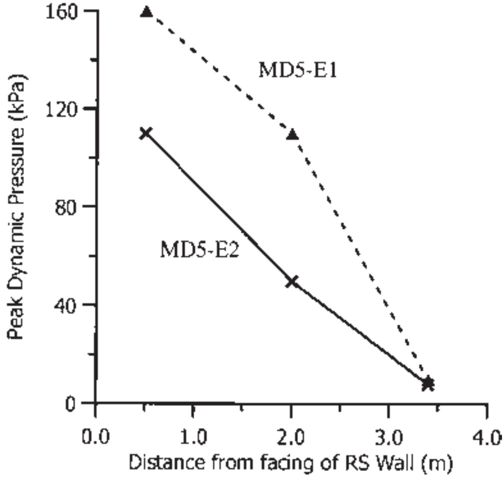

Figure 12 Variation of peak dynamic pressure with distance from the facing of the RS wall.

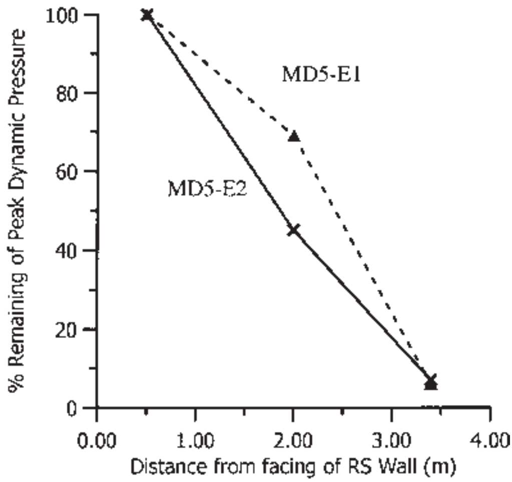

Figure 13 Variation of percentage remaining of peak dynamic pressure with distance from the facing of the RS wall.

Figures 12 and 13 show the variation of peak dynamic pressure and percentage remaining of peak dynamic pressure, respectively, with the distance from the facing of the RS wall for detonation events MD5-E1 and MD5-E2. The peak dynamic pressure was reduced from approximately 160 kPa to 10 kPa for event MD5-E1 and from approximately 120 kPa to 8 kPa for event MD5-E2. The percentage remaining of the peak dynamic pressure at a distance of 3.5 m from the facing of the RS wall was 6% and 7%, respectively, for events MD5-E1 and MD5-E2. In other words, the percentage reduction of the peak dynamic pressure at a distance of 3.5 m from the facing of RS wall was 94% and 93%, respectively, for events MD5-E1 and MD5-E2.

6 FEM MODELING OF RS WALL SUBJECT TO BLAST LOADING

This section presents detail of the finite-element modeling of the geotextile reinforced soil wall shown in Fig. 2 using PLAXIS (version 7.2), a two-dimensional finite-element program. The blast loading response of the wall was simulated using the newly implemented Dynamic Module in the program. Tan et al. (2000) briefly reported this FEM blast study. There are very few published reports on numerical modeling of RS walls subject to blast loadings, among which is the work of Yogendrakumar et al. (1992, 1993). Their study concluded that for the flexible RS slope structure examined, little additional dynamic strains

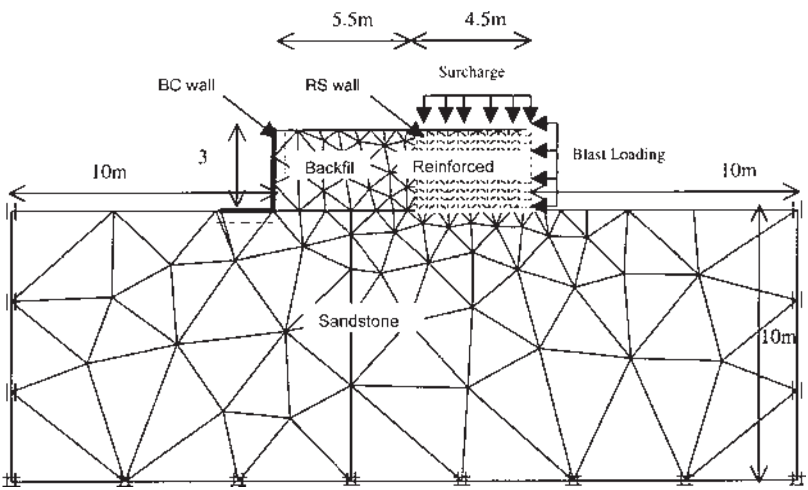

Figure 14 FEM geometry of the geotextile reinforced soil wall.

in the reinforcements were produced, and there was significant reduction of dynamic and permanent soil slope deformation when subjected to explosive blast loadings. This is in good agreement with the findings of the present study.

The FEM geometry of the geotextile reinforced soil wall model is shown in Fig. 14. The height of the wall is 3 m, and the depth of reinforcement is 4.5 m. The vertical distance between the geotextile reinforcement is 0.3 m. A surcharge of 19.6 kN/m^2, due to the weight of the concrete slab, was applied on top of the RS wall. The facing of the wall was wrapped around with the geotextile reinforcement. The boundaries are far enough such that they will not influence the results, and viscous boundaries are imposed on the left and bottom limit of the FEM model. It is assumed that the RC (reinforced concrete) wall would behave elastically in dynamic events. Hence, an axial stiffness, EA, and a flexural rigidity, EI, of an equivalent wall thickness of 140 mm are specified in this model. The elastic modulus of the RC wall is assumed to be equal to 25 Mpa.

Singapore tropical residual soil found at the test site was used as backfill material for the reinforced soil wall. The soil behind the reinforced soil was also Singapore residual soil but with slightly different soil properties due to a lower level of soil compaction. The material model used for both soil types is the Mohr–Coulomb model. The properties of these two Mohr–Coulomb soil models are shown in Table 5. The dynamic elastic modulus of the soil is generally considerably larger than the static elastic modulus, since dynamic loadings are usually fast and cause very little deformations. In this study, the estimate of the dynamic elastic modulus of the reinforced soil is back calculated from the p-wave velocity in the soil based on the field test results, using the following equation (Hunt, 1984):

$$v_p = \sqrt{\frac{E(1-\nu)}{\rho(1+\nu)(1-2\nu)}} \qquad (1)$$

Assuming typical value of Poisson's ratio (ν) of 0.4 and typical soil density (ρ) of 1.8 kNs^2/m^4 (Hunt, 1984) and the measured p-wave velocity, v_p, from field approximately equal; to 300 ms^{-1}, the calculated E is equal to 220,000 kPa.

Table 5 Properties of Mohr–Coulomb Soil Model

Type	γ_{dry} (kN/m^3)	γ_{wet} (kN/m^3)	E_{ref} (kN/m^2)	k'_x/k'_y (m/ms)	c_{ref} (kN/m^2)	ϑ (°)	Ψ (°)	R_{inter}
Reinforced soil	16	20	2.2×10^5	1.1×10^{-5}	25	35	0	Vary
Backfill	17	20	2.2×10^{-5}	1.1×10^{-5}	30	38	0	Vary

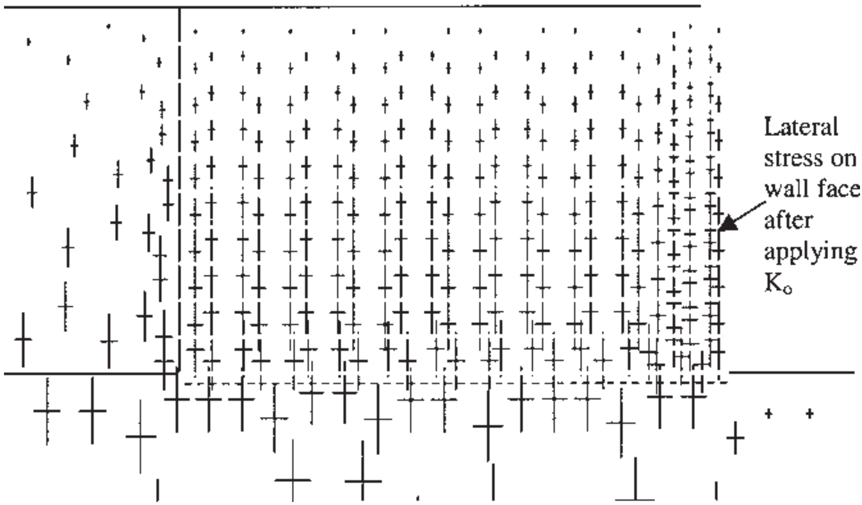

Figure 15 Initial stress condition of the reinforced soil wall after K_0 procedure.

The value of v_P measured from the field test and the calculated values of E are consistent with the published data (Hunt, 1984). The geotextile used in the model has an equivalent axial stiffness (EA) value of 1200 kN/m, estimated as the 10% secant modulus of the PEC geotextile used.

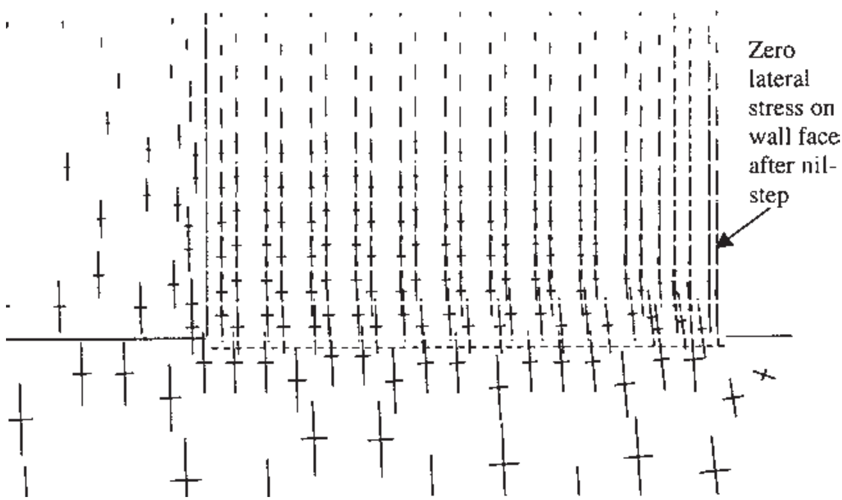

Figure 16 Initial stress condition of the reinforced soil wall after nil-step.

The initial stress in the soil mass was generated using the K_0 procedure, where the horizontal effective stresses were computed as K_o times of the vertical effective stresses. As the RS wall was constructed above ground level; the water table is at depth of 10 m below ground level; the GWT is placed at the base of the FEM model. After the initial stress in the soil was generated using the K_0 procedure, there were unbalanced forces in the soil near to the vertical free surface. Hence, a nil-step was implemented to zero out the unbalanced forces. Figs. 15 and 16 show the principal stresses of the soil generated with the K_0 procedure before and after the nil-step. After the nil-step, the horizontal stresses near the free surface of the wall were reduced to zero. The equilibrium stress conditions of the soil after the nil-step of Fig. 16 are now used as the initial stress condition of the wall prior to the blast loading.

Dynamic analysis of two blast events of different blast magnitudes was carried out. The dynamic analysis option was selected in the calculation step when applying the blast loading on the wall. In the dynamic analysis, the time span is in milliseconds. The blast pressure acting on the wall was simulated by applying a uniformly distributed load on the wall front, which increases in magnitude instantaneously to its peak value and then gradually decreases to zero after a short duration (Yogendrakumar and Bathurst, 1993). The magnitude of the uniformly distributed load was made to vary with time by applying a total multiplier of varying magnitude with time based on the input text file. Fig. 17 shows the blast pressure–time histories for the two events, MD5-E1 with peak

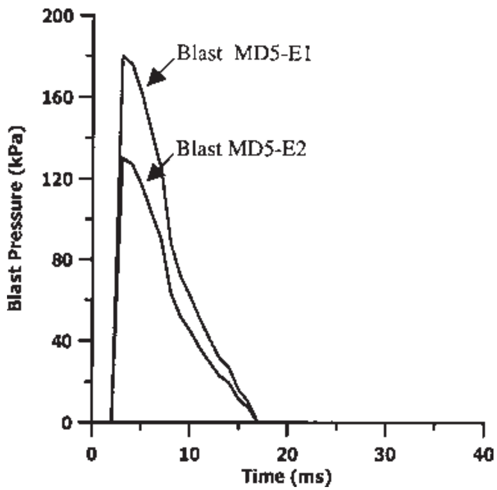

Figure 17 Blast pressure–time histories for the blast events MD5-E1 and MD5-E2, with peak pressures of 180 kPa and 130 kPa, respectively.

Table 6 Manual Setting Values for Iterative Procedure Used in Analysis

Parameter		Manual setting value	Default value
Rayleigh damping coefficient	α	0.01	0
	β	0.01	0
Newmark time integration factor	α	0.25	0.25
	β	0.5	0.5
Viscous boundary condition	C1	2	1
	C2	2	0.25

pressure of 180 kPa, and MD5-E2 with peak pressure of 130 kPa. The blast loadings were assumed to be a plane compressional impulsive wave imposed as a time-varying pressure on the whole vertical front of the RS wall, as shown in Fig. 17. The blast pressure–time history acting on the boundary of the reinforced soil wall was determined by means of approximate method based on the empirical charts and equations proposed by Bulson (1997) and Baker (1983).

The computation time of the dynamic analysis was continued for 40 ms even though the duration of blast loading was only 15 ms. This is to ensure that the system returns to an equilibrium state after the blast. A special type of viscous dynamic boundary conditions was imposed on the left and bottom end of the FEM model to account for the fact that in reality the soil is a semi-infinite medium. This viscous boundary can absorb the increments of stresses on the far end boundaries caused by dynamic loading, which would otherwise be reflected inside the soil body and disturb the results. In the dynamic analysis, the settings

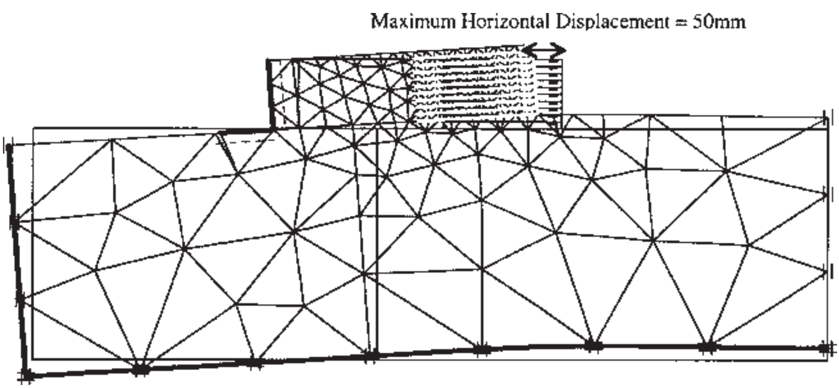

Figure 18 Typical deformed mesh of the model after the blast loading (scale up 20 times).

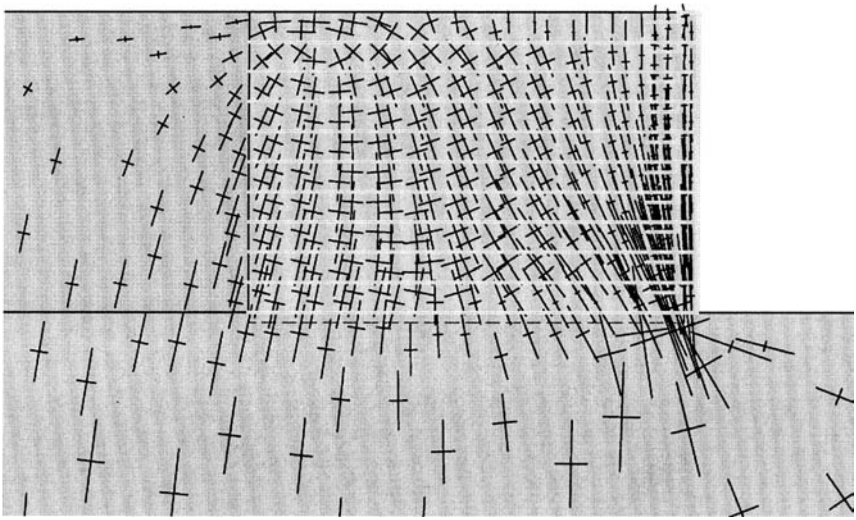

Figure 19 Typical total stress state of the model at the end of blast loading impulse.

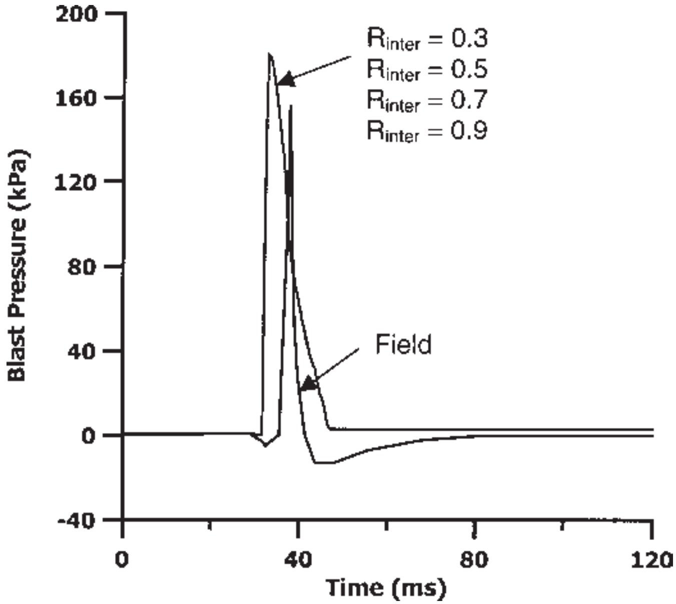

Figure 20 Horizontal stress variation with time during blast event MD5-E1 for location P1.

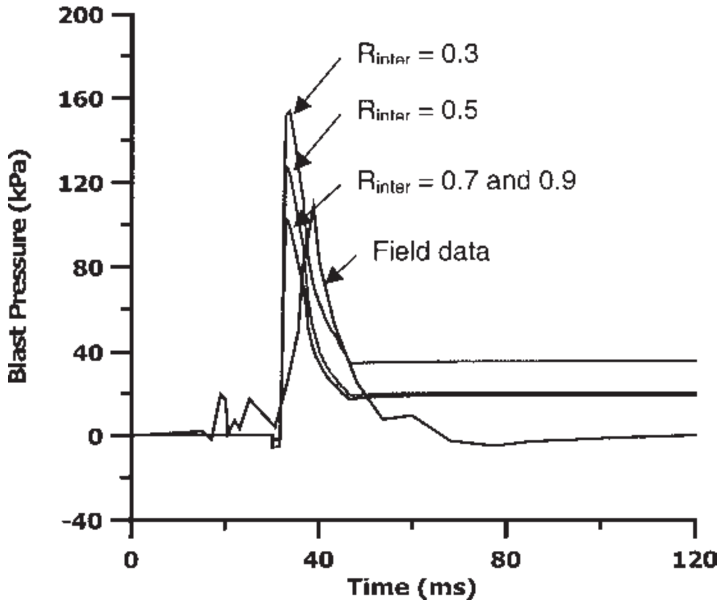

Figure 21 Horizontal stress variation with time during blast event MD5-E1 for location P2.

for the iterative procedures were set manually, instead of adopting the default values. Table 6 shows the values used for the iterative procedure settings, selected after a series of parametric studies was made to obtain reasonably good agreement between measured and computed pressures at P1 and P2.

Hence, the sequence of the calculation steps used in the analysis is as follows:

Phase 0: Generate initial stress condition using K_o procedure.
Phase 1: Nil-step (staged construction) to zero unbalanced forces.
Phase 2: Apply slab weight on top of the reinforced soil wall (total multiplier).
Phase 3: Nil-step (staged construction) to zero unbalanced forces.
Phase 4: Dynamic analysis (total multiplier).

Figs. 18 and 19 show the typical deformed mesh and total stress state of the model, respectively, after blast loading. The maximum horizontal displacement at the top front end of the RS wall is computed to be 50 mm, which consistent with field observations. From Fig. 19, it is seen that the impulsive blast wave produced a rotation of principal stresses near the top of the RS wall, while

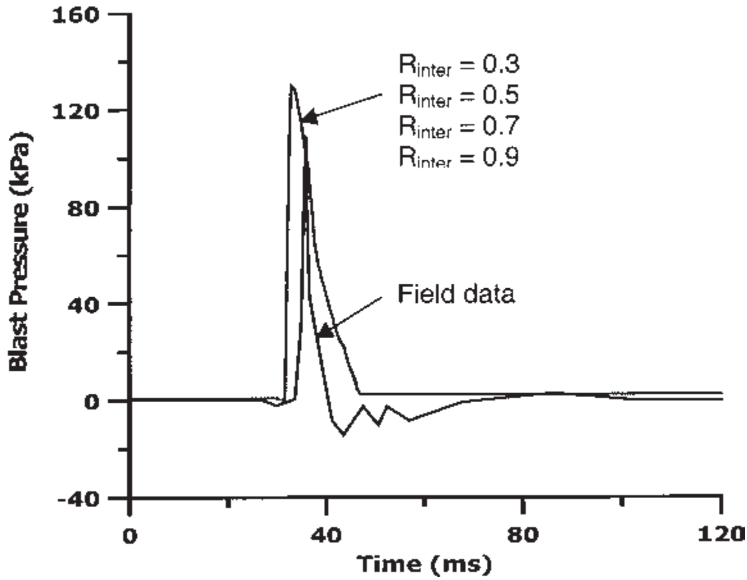

Figure 22 Horizontal stress variation with time during blast event MD5-E2 for location P1.

a significant increase of lateral pressures occurs deeper down the RS wall with little rotation of principal stresses.

Figs. 20 and 21 show the horizontal stress variation with time during blast event MD5-E1 from FEM and field results for locations P1 and P2, respectively. Figs. 22 and 23 show the horizontal stress variation with time during blast event MD5-E2 from FEM and field results for locations P1 and P2, respectively.

Figs. 20 and 22 show that for the dynamic pressure response at location P1, the numerical results obtained from PLAXIS Dynamic Analysis program generally agree with the field instrumentation results. The peak pressure at location P1 from the numerical results is slightly higher than the field instrumentation results. The peak dynamic pressures at P1 are approximately 175 kPa and 156 kPa, as observed from numerical and field instrumentation results, respectively, for blast event MD5-E1. The peak dynamic pressures at P1 are approximately 130 kPa and 110 kPa, as observed from numerical and field instrumentation results, respectively, for blast event MD5-E2. Nevertheless, the dynamic pressure responses at P1, as observed from numerical and field instrumentation results for both events, are almost similar. The dynamic pressure responses for different responses for different values of interface reduction factor (R_{inter}) are similar, which means that dynamic pressure response at location P1 is

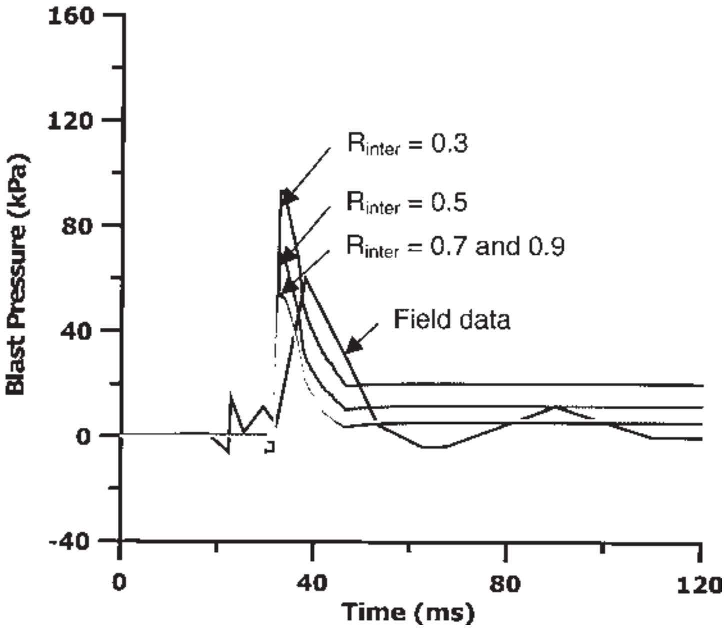

Figure 23 Horizontal stress variation with time during blast event MD5-EA2 for location P2.

less dependent on R_{inter}, as this location is far from the base of RS wall (0.3 m from the top and 0.5 m from the front of the RS wall). Both PLAXIS and field results show that the dynamic pressure in the soil dissipates to zero after blast.

Figs. 21 and 23, however, show that the dynamic pressure response at location P2 is highly dependent on R_{inter}, as this location is very close to the base of the RS wall (0.3 m from the bottom and 1.5 m from the front of the RS wall). The peak dynamic pressure varies from approximately 90 kPa to 50 kPa when R_{inter} varies from 0.3 to 0.9. However, there is not much difference between the peak dynamic pressures when R_{inter} changes from 0.7 to 0.9. PLAXIS results show residual stress in the soil at location P2, whereas field results show small residual stress after blast. This could be due to the fact that the total pressure cells in the field were unable to measure residual stress in the soil after the blast, due to loss of contact with the soil after blast. This residual stress in the soil at location P2 also varies with R_{inter}. It varies from approximately 20 kPa to 7 kPa when R_{inter} varies from 0.3 to 0.9. Again, there is not much difference between the residual stresses when R_{inter} changes from 0.7 to 0.9. As observed from Figs. 21 and 23, the appropriate value of R_{inter} to be used should be about 0.5 to 0.7, which are reasonable values obtained from pullout tests for the PEC200 geotextile used with Singapore tropical residual soil.

7 CONCLUSION

From the field and photographic comparison, it is observed that the RS wall was more suitable to be used as a blast-resistant structure as compared to the RE wall. This was due to the different behavior of the facing and reinforcement materials used for the reinforced soil structures when subjected to blast loading and also the different mechanisms of interaction between the blast wave and the RS and RE walls.

After the blast, some areas of geotextile facing melted and some areas were cut by the blast fragments, which eventually stopped in the soil mass. There was similar observation for the RE wall after blast as the blast fragments cut through the concrete panel facings, drilled a hole of conical shape into the soil, and blast fragments are embedded at the end of the holes. This showed that both wall systems were effective in absorbing the blast fragments. However, there is a disadvantage of the RE wall with rigid reinforced concrete panel facings, which can produce high-speed flying concrete debris dangerous to human occupants. On the other hand, no hard flying debris was produced when the geotextile facing was cut by the blast fragments.

During the blast, no strain gauge in the RS wall registered any significant changes, with additional peak strain of less than 0.2%. In addition, there was only small horizontal inward depression of the RS wall, estimated to be about 50 mm at maximum. This implies that the geotextile reinforcement was not subjected to additional dynamic strain during and after the blast. However, there was extensive outward deformation of the RE wall front and side panels after the blast. Hence it can be deduced that large additional tension developed in the reinforcement strips during and after detonation. This comparison implies that the stability of the RE wall was greatly affected by the blast loading whereas the stability of the RS wall was not much affected. This difference in the behavior of the two wall systems was mainly due to the different facing materials. Geotextile facing was porous enough for the blast wave to pass through whereas concrete panel facing was like a rigid wall where the wave diffraction process would occur when the blast wave enveloped the wall and passed around it, inducing a net outward pressure on the back of the wall. The diffracted wave caused the pressure on the back of the wall to increase and pushed the wall outward.

At the end of several detonation events, more exposed areas of geotextile facing of the RS wall were melted and cut by fragments, but there was still no significant deflection or bulging of the RS wall facing. However, the front panels of the RE wall collapsed and the soil mass behind the wall spalled out.

The reinforcement strips at the upper layers were pulled out extensively from the soil mass by the concrete panels that fell outward. At the lower layers, the connections between the reinforcement strips and the concrete panels, which were anchored into the concrete panel, were pulled out from the concrete panels. This clearly illustrates the disadvantage of using rigid concrete panels as facing material compared to flexible facing material such as geotextile. Hence, it can be concluded the RS walls are more suitable for blast-resistant structures than RE walls.

From the instrumentation program, the dynamic pressure recorded by the total pressure cells installed in the RS wall showed that the peak incident pressure in the soil, at a distance of about 3 m from the front of the wall, can be effectively reduced to approximately 10% of its value at the front of the wall for all blast events recorded. The instrumented data gave convincing proof of the efficient dissipation of blast wave energy as it propagates into the depth of the RS wall, making it a very efficient protective structure against blast loadings. Furthermore, the RS wall can withstand a peak acceleration of about 20,000 g without any deterioration. Hence, with the use of the geotextile reinforced soil wall, the blast incident pressure can be reduced significantly and yet the wall was stable even after several multiple blastings of similar intensity.

The dynamic response of the RS wall structure was studied using the new PLAXIS Dynamics Module (version 7.2). Despite the difficulty of modeling the exact details of the problem, a simplified 2D FEM model of the RS wall produced results that matched reasonably well in trend with the field measurements of the lateral stresses at two different locations of the RS wall, for the blast events MD5-E1 and MD5-E2. With appropriate choice of soil dynamic and model parameters, the FEM analysis clearly showed the importance of interface factors for the soil response near the base of the wall. For the stress point close to the wall base, the interface element plays a very crucial role to model realistic soil slippage between the RS wall and the original ground, which is reflected in the matching of the stress response for this location P (0.3 m from wall base). Though exact matching is not possible, the overall trend of stress increase and dissipation with the blast loading is adequately shown in the calculations. For interface factors of about 0.5 to 0.7, good agreement with measured response of soil pressures near the base of the wall can be achieved. Thus dynamic FEM programs like PLAXIS are capable of realistically modeling the dynamic response of reinforced soil wall subjected to blast loading.

ACKNOWLEDGMENTS

The authors would like to acknowledge gratefully the support of LEO, Ministry of Defence, and Singapore in this collaborative research and permission to publish these results. Special thanks are due to Mr. Lim Chee Hiong, Deputy Director (Technology) of LEO, and Mr. Koh Tong Chia, Senior Manager of DCD, LEO, for their support, encouragement, and comments on this paper. Special thanks also go to Associate Professor Lee Fook Hou, Director of the Center for Protective Technology (CPT), National University of Singapore (NUS), for assistance and support in this research.

REFERENCES

WE Baker. *Explosions in Air*, 1st ed., 1983.

PS Bulson. *Explosive Loading of Engineering Structures*, 1st ed., E & FN Spon, 1997.

RE Hunt. *Geotechnical Engineering Investigation Manual*. New York: McGraw-Hill, 1984.

CC Ng, SH Chew, GP Karunaratne, SA Tan, SL Loh. Flexible and rigid faced mechanical stabilized earth walls subject to blasting. *ASCE STP no. 103*, GeoDenver 2000, JG Zornberg, BR Christopher, eds, pp 332–336, 2000.

G Richardson. *The seismic response of reinforced earth walls*. Ph.D. Thesis, University of California, Los Angeles, 1976.

SA Tan, SH Chew, CC Ng. Plaxis practice: Modeling of a reinforced wall subject to blast. *Plaxis Bulletin no. 9*, July 2000.

N Yogendrakumar, RJ Bathurst, WD Liam Finn. Dynamic response analysis of reinforced soil retaining wall. *J. Geotechnical Eng.* 18(8): 1158–1167, 1992.

M Yogendrakumar, RJ Bathurst. Numerical simulation of reinforced soil structures during blast loads. *Transportation Research Record* 1336: 1–8, 1993.

20

Shaking Table Tests of Embankment Models Reinforced with Geotextiles

S. Tani
National Research Institute of Agricultural Engineering, Tsukuba, Japan

S. Ihara
Kumagai-gumi Co. Ltd., Tokyo, Japan

Y. Yokota
Maeda Kousen Co. Ltd., Fukui, Japan

Y. Okabe
Tokyo Soil Research Co., Tsukuba, Japan

ABSTRACT

Large earthquakes have caused damage to soil structures such as earth dams, river dikes, and reclamation dikes. To prevent this, the reinforcement of soil structures with geotextiles has been attempted. This chapter describes the behavior of embankments reinforced with geotextiles (continuous fibers, geogrids) in shaking table tests using embankment models. The shaking table tests used small- and large-scale models constructed with sand. The test results confirmed that reinforcement with geotextiles greatly decreases settlement even if embankments and foundations were constructed with loose sand. Some results of the shaking table tests of models reinforced with continuous fibers

were analyzed by using the finite-element method and compared with the test results.

1 INTRODUCTION

Many soil structures such as earth dams, reclamation dikes, and farm roads have been damaged by earthquakes. Surveys of damaged soil structures showed that 200 earth dams were damaged by the 1983 Nihon-Kai Chubu earthquake, while 1300 earth dams were damaged by the Hyogoken-Nambu earthquake. Foundation ground and embankments are especially prone to heavy damage if liquefaction occurs. Reinforcement of these soil structures is necessary to improve earthquake resistance. Embankment models (earth dam, reclamation dike) reinforced with (1) continuous fibers, (2) geogrids, and (3) foundation improvement with cement were subjected to shaking table tests to determine their effectiveness.

2 REINFORCEMENT WITH CONTINUOUS FIBERS

This section reviews shaking table tests that were conducted on embankments constructed with loose sand and reinforced with continuous fibers to investigate the safety of this method during earthquakes. The method uses continuous fibers and covers the embankment surface with a mixture of continuous fibers and sand.

2.1 Mechanical Properties of Reinforced Sand

Prior to the shaking table test, the mechanical properties of sand reinforced with continuous fibers were investigated. The tests used two types of sand: A and B. A was used in the mechanical tests, and both A and B in the shaking table tests. Table 1 and Fig. 1 show the physical characteristics of the two sand types. The mechanical tests were drained triaxial compression and cyclic triaxial tests. The fibers mixed with the sand were polyester, with characteristics as shown in Table 2. Both tests used 10-cm-diameter and 20-cm-high specimens. The specimens were a compacted mixture of constant-weight ratio of fibers to sand. Fibers were mixed in, at a ratio of 0.2% of the dry weight of the sand. The density of specimens. ρ_d, was 1.52 (t/m^3).

The effective reinforcement was about 1% axial strain, and the difference between the principal stress of the unreinforced and reinforced sand increased as shown in Fig. 2.

Table 1 Sand Properties

Sand	Specific Gravity Gs	D_{50} (mm)	u_s	Maximum and minimum void ratio*		Compaction properties**	
				e_{max}	e_{max}	$\rho_{d\max}$ (t/m^3)	ω_{opt} (%)
A	2.72	0.26	1.96	0.96	0.615	1.61	17.2
B	2.70	0.18	1.20	–	–	1.59	19.8

* JSE(T26-1981).
** JISA1210(1.1.a).

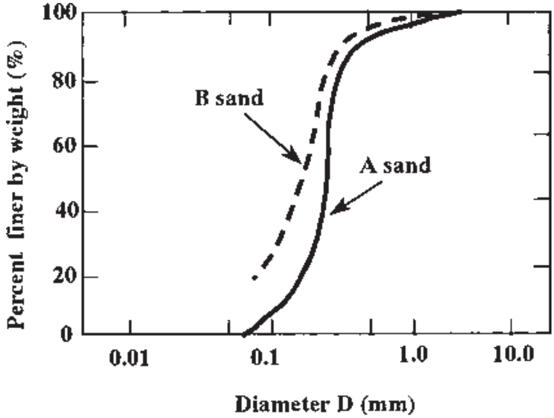

Figure 1 Grain size distribution (sands A and B).

Table 2 Fiber Properties

Standard	Tensile strength
Polyester	4.53(gf/denier)
150(denier*)	56.2(kgf/cm^2)
30(filament)	36(%)

* 1 denier = 1 g/9 km.

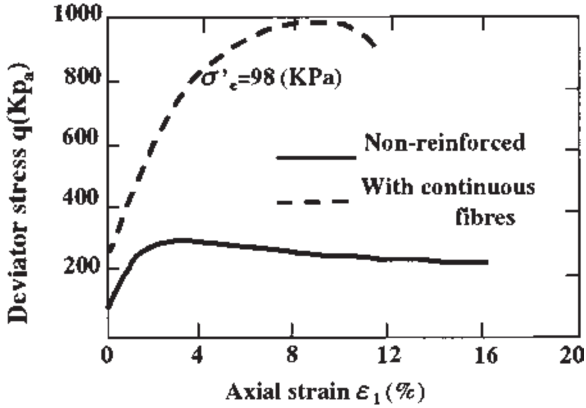

Figure 2 Triaxial test results.

The strength parameter of the unreinforced sand was $c = 3.0$ kPa and $\phi' = 38°$, white that of the reinforced sand was $c' = 107$ kPa and $\phi' = 42°$. The effect of the reinforcement mainly showed in c', and the difference, $\Delta c'$, was 104 kPa. Test results are shown in Fig. 3. There are only small differences in the number of cycles, but the stress ratio of the reinforced sand is 35% greater than that of the unreinforced sand with 20 cycles, the number generally used to determine liquefaction strength. The results of the mechanical tests clearly show that reinforcement with continuous fibers is effective.

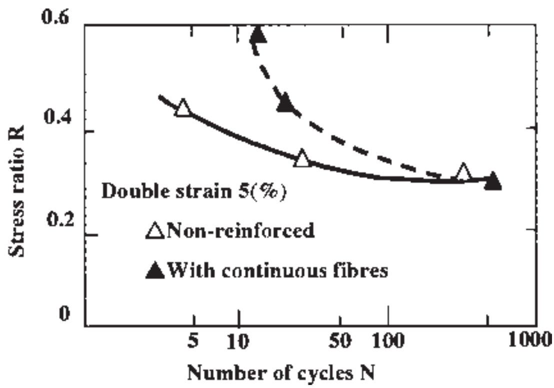

Figure 3 Undrained cyclic strength of unreinforced and reinforced specimens.

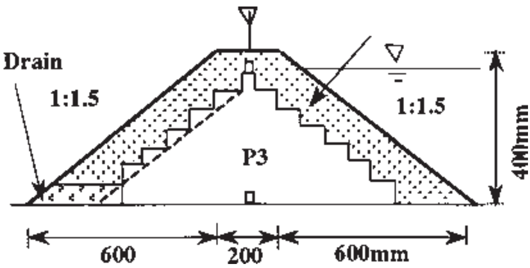

Figure 4 Small-scale shaking table test model.

2.2 Shaking Table Test

The shaking table tests were performed to determine the effectiveness of reinforcement in embankment structures. The shaking table tests were of two types: a small-scale model test of embankments and a large-scale model test of foundations and embankments.

2.2.1 Small-Scale Shaking Table Model Test

Two types of sand, A and B, were used in the tests as shown in Table 1. The model in Fig. 4 was constructed in a small box (68 cm high, 40 cm wide, 230 cm long). Sand A was used in the (a), (b), and (c) tests in Fig. 5, and sand B in the (a) and (c) tests. With sand A, reinforcement with dense sand was tested to determine whether the effect in Case (c) was due to the continuous fibers or the dense sand. In Case (a), the relative densities of sands A and B, the D-value ($\rho_d/\rho_{d\max}$), were about 80%. The reinforced portions in (b) and (c) are hatched parts in Fig. 4. In (b), the sand was well compacted, and in (c), the sand was compacted and reinforced with continuous fibers, 0.2% of the dry weight of sand. The relative density of the sand in the reinforced portion, the D-value, was above 85%.

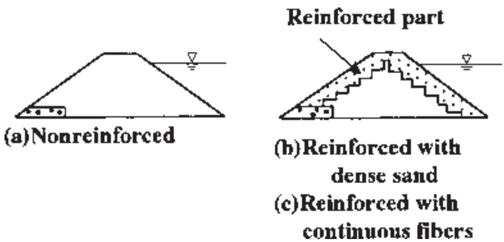

Figure 5 Case of small-scale shaking table test.

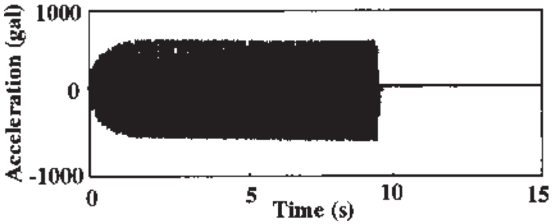

Figure 6 Input wave form at acceleration 650 gal.

A sine wave with a frequency of 10 Hz was imposed for 10 sec. The acceleration was increased in stages to about 100, 200, 400, and 600 gal. Figure 6 shows the input wave at 650 gal; crest settlement was very small up to 400 gal. However, at the maximum acceleration of 600 gal, both the crest settlement and pore water pressure increased greatly, and the model without reinforcement collapsed.

Figure 7 compares the settlement of the crest (D2) with sand A with and without reinforcement. Five seconds after loading, the settlement with continuous-fiber reinforcement was approximately one tenth that without reinforcement, and about one third of the case reinforced with dense sand. Figure 8 compares the crest settlement with sand B. After loading for 10 sec the settlement of the case reinforced with continuous fibers was about one fifth of the unreinforced case.

Figure 9 shows a comparison of the acceleration (A10) of specimen A, the pore water pressure (P3), and the amount of settlement of the crown. In the case of reinforcement, there was almost no increase in the pore water pressure 3 sec after loading, but after 7 sec there was a rise in all cases to the respective effective overburden pressures. The acceleration response of unreinforced materials decreased in about 1 sec, but in the reinforced materials, an increase in acceleration response was seen for about 4 sec. Specimen B showed similar

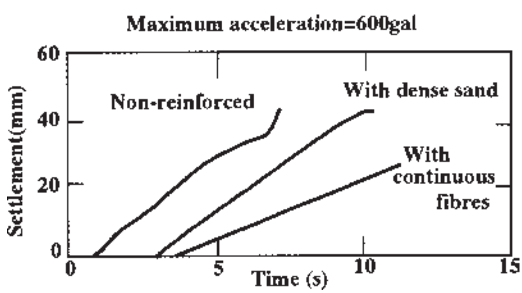

Figure 7 Settlement at crest D2 (sand A).

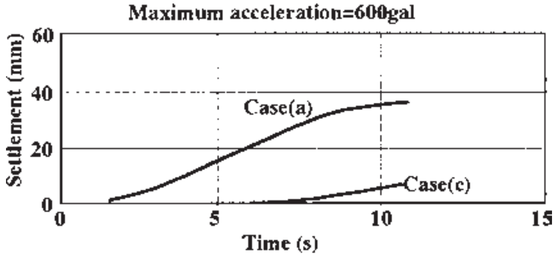

Figure 8 Settlement at crest D2 (sand B).

results. This indicates that reinforcing embankments with the continuous system can increase acceleration response, greatly reduce settlement, and increase seismic resistance.

Next, the results of the large-scale model tests will be detailed.

2.2.2 Large-Scale Shaking Table Model Tests

The model in Fig. 10 was constructed on the large-scale shaking table (1.5 m high, 2.8 m wide, 5.5 m long). The model was about one tenth of an earth dam where 1.5-m settlement occurred at the Mid Japan Sea earthquake in 1983. The grain size of the sand in the earth dam was very similar to that used in the shaking

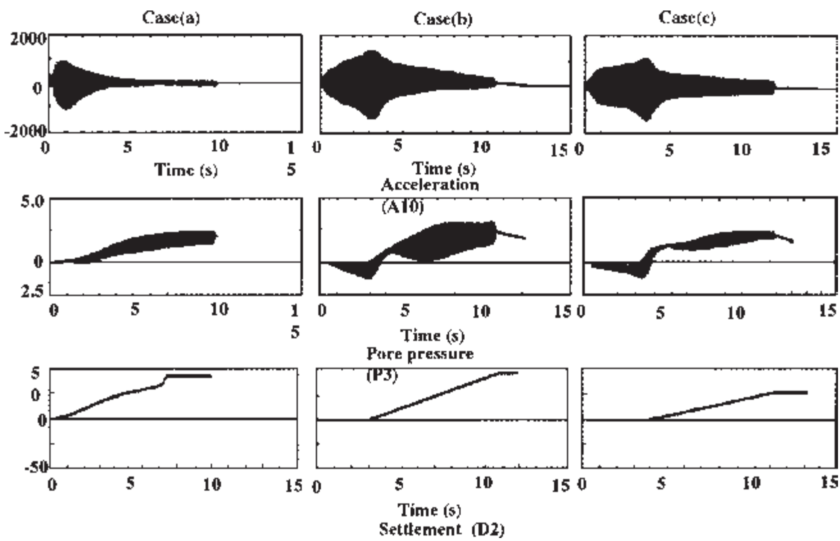

Figure 9 Observed records with time (sand B).

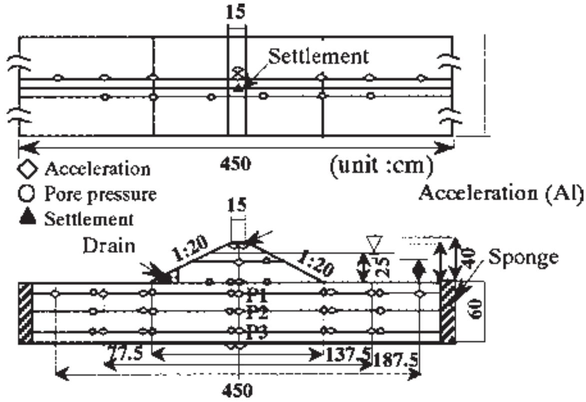

Figure 10 Large-scale shaking test table.

table test. Fig. 11 shows the three tests: (1) without reinforcement of either the dam or foundations [Case (a)]; (2) reinforcement of only the dam with continuous fibers [Case (b)]; and (3) reinforcement for the dam with continuous fibers and the foundations with model sheet piles [Case (c)].

An outline of the model and the arrangement of instruments are shown in Fig. 10. The foundations were made by depositing wet material in the shaking box with 30-cm-deep water. The dam was also constructed by placing formwork and depositing wet material in the forms filled with water like the foundations. The relative density was about 50%. The reinforcement of the dam in Case (b) consisted of two fibers from a four-hole nozzle bundled into eight fibers, which were pushed out by high-pressure water and mixed with sand injected through a hose via a hopper. The reinforced parts were compacted with a small vibrator, and the continuous fibers comprised 0.2% of the dry weight of the sand. In Case (e), a sheet pile model of 15-cm-thick acrylic plate was installed placed from the top of the dam wall to the base of the foundations in Case (b).

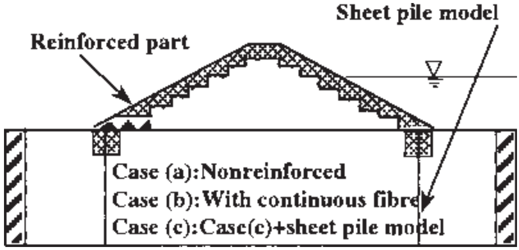

Figure 11 Case of the large-scale shaking table test (sand A).

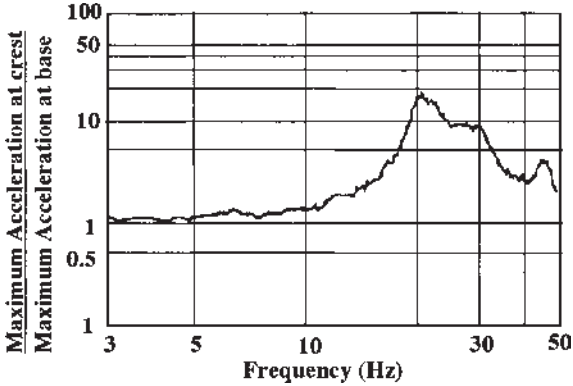

Figure 12 Resonant curve [Case (a)].

A 3-Hz sine wave was imposed for 10 sec, and the maximum input acceleration was 150 and 250 gal. Figure 12 shows the resonant curve of the crest in Case (a) (without reinforcement) with an input sine wave of 20 gal. The response increased about 16 times with a frequency of 22 Hz. With a maximum input acceleration of 150 gal, the crest settlement was 30 mm in Case (b), but there was little settlement in Case (b) and (c). At the maximum input acceleration of 250 gal, loading for 10 sec resulted in crest settlement of more than 70 mm in Case (a), but only 40 mm in Case (b) and about 26 mm in Case (c), as shown in Fig. 13. In Case (b), the crest settlement was 60% less than without reinforcement. In Case (c), the settlement decreased less because the sheet pile moved and was of no use; however, settlement was still 40% less than without reinforcement and 60% less than Case (b). The effectiveness of reinforcement together with sheet piles may have been very good.

Figure 14 shows the input wave of 250 gal, and response acceleration at A1 Case (a) appears in Fig. 15. Figure 16 shows the pore water pressure at P12 in the three cases. The pore pressure started to increase immediately in Case (a), but there was little increase until about 3 sec of loading with (b) and (c). This was

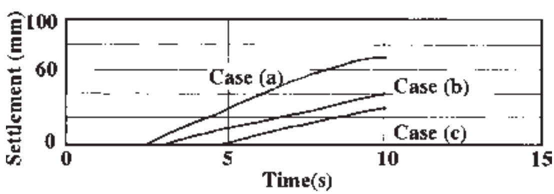

Figure 13 Settlement at crest (max acc. = 250 gal, D1).

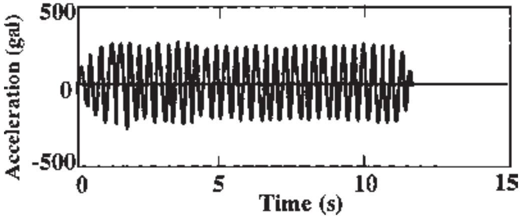

Figure 14 Input wave form at acceleration 250 gal.

caused by the reinforcement preventing an initial increase in pore water pressure and less settlement of the crest. When the pore water pressure increased to the effective overburden pressure, settlement with reinforcement did not increase as rapidly as without reinforcement. This would indicate that reinforcement with continuous fibers or together with sheet piles may greatly decrease settlement of existing embankments on liquefiable foundations.

Though the results from the models cannot be applied directly to actual structures, this method may offer an advantageous construction method providing earthquake resistance for existing earth structures.

2.3 Analysis of the Shaking Table Tests

The effectiveness of reinforcement with continuous fibers was confirmed by the shaking table tests, and the following is an analysis of the effectiveness by simulation of the large shaking table test. The dynamic analysis program "DIANA-J2" was used.

2.3.1 Method of Analysis

The constitutive low used in the analysis was the Densification model, which uses Endochoronick equations to show an increase in pore water pressure. The model assumed a total strain, ϵ, given by the effective strain, ϵ', and the autogenious

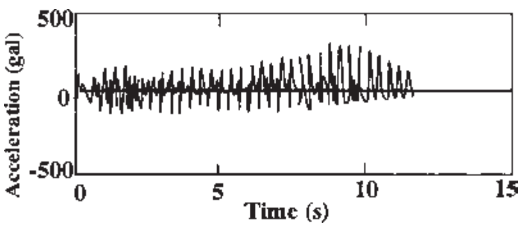

Figure 15 Acceleration at A1 [Case (a)].

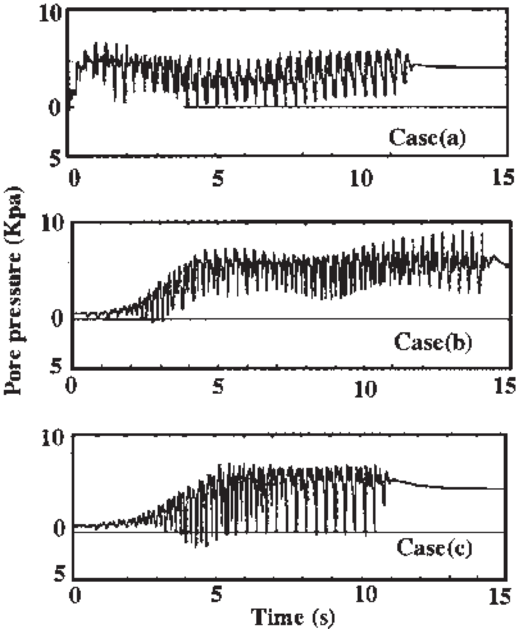

Figure 16 Pore pressure at P12 [Case (a), (b), (c)].

volumetric strain ϵv. The autogenious volumetric strain is defined by the following equation by use of the empirical parameters A and B, and the damage parameter κ. A plane strain model divided into 280 elements was used in the analysis (Fig. 17). Table 3 shows values used in the analysis and the parameters of the Densification model.

Total strain $\epsilon = \epsilon' + \epsilon_v$

Autogenious volumetric strain ϵ_v: $= A/B \ln (l + B\kappa)$

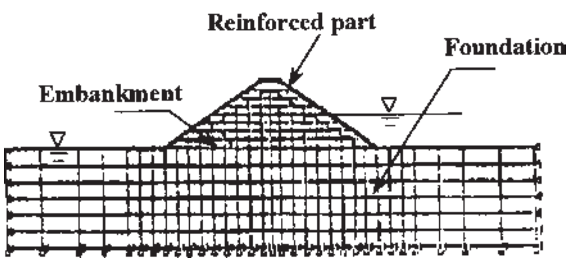

Figure 17 Finite-element model for the analysis.

Table 3 Material Parameters for the Analysis

Parameter		Foundation	Embankment	Reinforced part
ϕ		37.6	37.6	43.4
c (kgf/cm^2)		0.03	0.03	1.08
Endochoronic parameter	γ	3.0	3.0	3.0
	A	103	0.039	0.0151
	B	74.5	34.3	19.2
Poisson's ratio $\nu = 0.35$				

2.3.2 Analytical Results

The results of the shaking table test at the maximum input acceleration of 250 gal were compared with the analytical results. Figure 18 shows the time history of pore water pressures in the unreinforced test and in the analysis in each part for (1) lower body (P1), (2) foundation center (P2), and (3) lower foundation (P3).

Figure 19 shows the time history of pore water pressure (P2) in Case 2. The pore water pressure in both cases increased to the effective overburden pressures, while the calculated values increased earlier than the test values. Figure 20 shows the settlement of the crest. After a 10-sec loading, the test indicated a settlement of about 70 mm in the unreinforced case, but this was reduced by 60%, to about 40 mm in reinforced case. This verifies the effectiveness of reinforcement with continuous fibers.

The analysis shows the settlement in unreinforced case reduced by about 85% in the reinforced case. Here the reinforcement due to continuous fibers is qualitatively confirmed. The effectiveness may depend on the restraint from the top, with an increase in apparent cohesion of the part reinforced with continuous

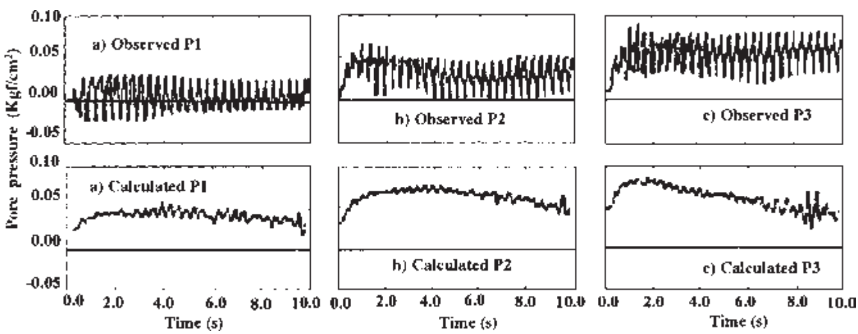

Figure 18 Observed and calculated excess pore water pressure P2 in the unreinforced model tests.

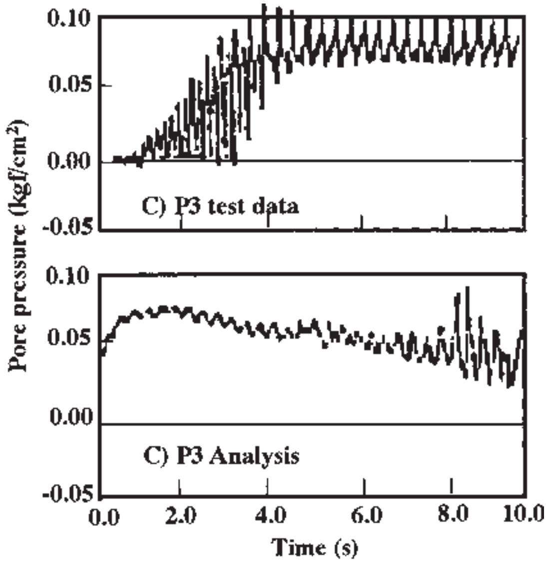

Figure 19 Observed pore pressure (Case 2).

fibers (deformation mode after loading in Fig. 21). In the analysis, lower body foundations were almost completely liquefied. The main deformation occurred within 4 sec of loading. In the tests, the deformation continued after liquefaction of the ground, but this was not the case in the analysis.

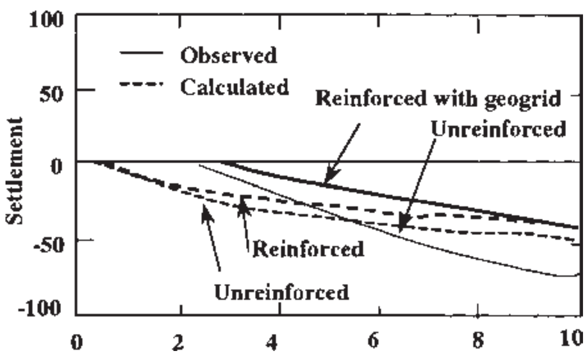

Figure 20 Comparison between the observed and calculated settlement at crest DV1.

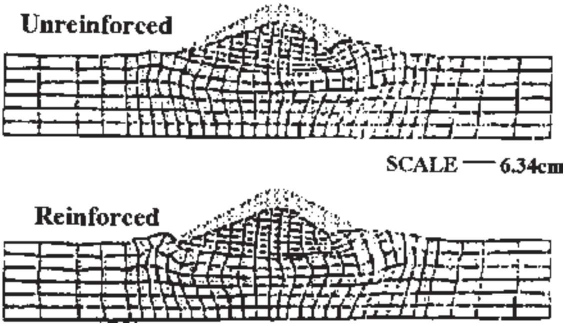

Figure 21 Calculated deformation mode after loading.

3 REINFORCEMENT WITH GEOGRIDS

The effectiveness of geotextiles (geogrid, sheet) was investigated with the shaking table tests using the large- and small-scale models assuming a reclamation dike with a reservoir.

3.1 Reclamation Dike Model

3.1.1 Small-Scale Model

In the small-scale shaking table test, the embankment was constructed with rock on the upper stream side and loose sand on down stream. Sand C (Fig. 22) was used in the test. Figure 23 shows an outline of the small-scale model and the arrangement of instruments. The model was 2 m long, 43.3 cm high, and 40 cm wide. Table 4 shows the properties of the geogrids, which were placed

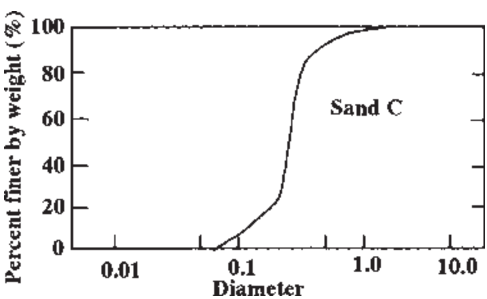

Figure 22 Grain size distribution curve (sand C).

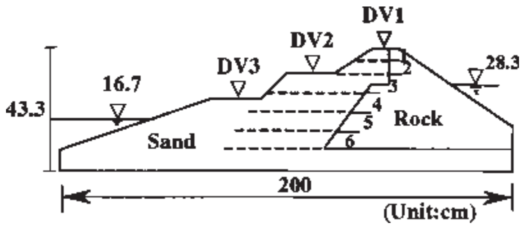

Figure 23 Small-scale shaking table test model reinforced with geogrids.

horizontally in the embankment. The numbers 0, 3, 4, or 6 were used to clear differences in reinforcement effectiveness.

The model was constructed by depositing wet sand with underwater deposition to obtain the required density. The input wave was a 3-Hz sine wave, and the maximum input acceleration was about 220, 350, or 450 gal. Resonance tests prior to the shaking test established no resonance frequency between 1–50 Hz. As the model was relatively small, geogrids with low rigidity were used in consideration of scale effects.

The density of the rock portion was 1.90 t/m^3, and the relative density of the sand portion was Dr = 40–50%. Table 5 and Fig. 24 show the settlement of the berm (DV2) to evaluate the reinforcement effectiveness. The unreinforced portion collapsed at 220 gal, while the reinforced portion with three sheets of geogrid collapsed at 355 gal. The test results show that the reinforcement with geogrids was effective in preventing settlement.

Table 4 Properties of Geogrid

Mesh size (mm)	Strength (kg/m)	Open area ratio (%)
6 × 6	530	62

Table 5 Test Results in the Small Scale Shaking Table Test

Case	Reinforced part (In Fig. 23)	Settlement at DV2		
1	0	220 gal	35	460
2	1, 2, 3	42	64	–
3	1, 2, 3, 4	0.1	10	21
4	1, 2, 3, 4, 5, 6	0.4	10	21

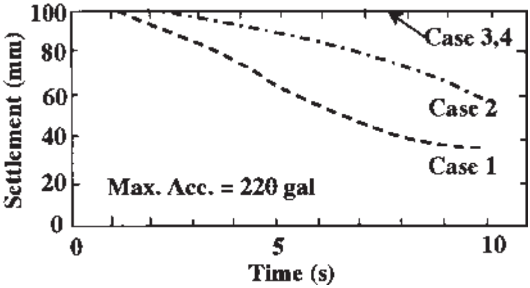

Figure 24 Settlement (DV2) at berm.

The reinforcement effectiveness with three sheets is appreciable, but four sheets of geogrid is more effective. The test results of Cases 3 and 4 with 460 gal show that there was no difference in the effectiveness with four and six sheets of geogrid. The fourth sheet of geogrid was located between the saturated and unsaturated zones of the embankment. The test indicated that the reinforcing effect of geogrids in the saturated zone was small.

3.1.2 Large-Scale Model

Experimental method and results: Figure 25 is a depiction of the large-scale model. The rock zone was created by using gravel, and in the area adjoining the sand foundation, sheeting was installed and overlain by a mixture of sand and gravel. With that, let us examine the results of the experiments. Figures 25 and 26 show two cases—Case 1, in which there was no reinforcement, and Case 2, in which reinforcement was provided by sheets. The sandy section of the dam had a relative density of 50%. The sheet was installed as shown in Fig. 26.

The modeling for Case 3 was done in the same way as for Case 1. The geogrids were anchored in the rock zone and installed as shown in Fig. 27.

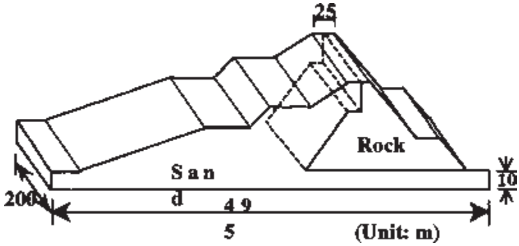

Figure 25 Large-scale land reclamation model (Case 1).

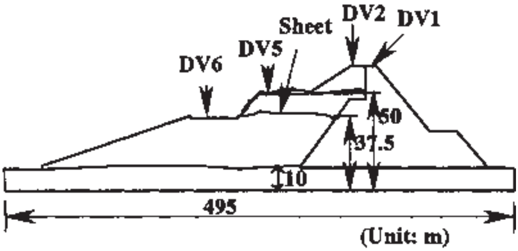

Figure 26 Large-scale land reclamation model (Case 2).

To understand the effect of reinforcement, let us look at Table 6, which compares the maximum settlement of each case at the time of 300-gal input.

Both Cases 2 and 3 showed slightly less settlement than Case 1, but looking at DV2 in Case 2, we can see that there was a large amount of settlement for the reinforced model. For Case 1, when the acceleration was at 320 gal, rupture occurred. Conditions during this rupture included considerable settlement of the sandy foundation around the crest and the occurrence of cracking. Here, the reinforcing material i.e., sheets moved downstream as the sandy foundation became fluid, affecting the area around the crest.

In Case 3, the original shape was kept more intact than in Case 1 for acceleration of 320 gal. However, rupture did occur at 440 gal. In the sandy section, there was not much settlement in the cases of nonreinforcement and reinforcement by geogrids, while there was quite an increase in settlement with sheeting. This was the result of either very little effectiveness of the sheet when there was liquefaction, or increased settlement in the central (sandy) section of the crest. Looking at the berm (DV5), more sand flowed from the upper section of the dam when there was liquefaction than in the case of nonreinforcement (DV6), meaning that the mechanism of "settlement" was very complex. Therefore, we cannot evaluate the reinforcement effect from the settlement at this location.

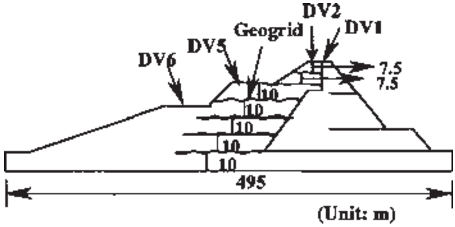

Figure 27 Large-scale land reclamation model (Case 3).

Table 6 Settlement After Loading

Case	Crest (gravel) DV1	Crest (sand) DV1	Berm	Berm
1 (unreinforced)	92	38	68	26
2 (sheet)	45	127	45	10
3 (Geogrid)	36	28	24	37

We can from the above information that in the model tests, sheeting had very little reinforcing effect, while geogrids were able to reduce the deformation throughout the embankment to a considerable degree. Although it is difficult to quantify the reinforcement effects in an actual dike based on the model experiment, we can at least say that, quantitatively speaking, there should be a large reinforcement effect.

For structures which might undergo liquefaction due to saturation of the embankment and foundation, we can conclude that geogrids would be a significant way to increase strength. Since a large amount of money was required to conduct the large-scale shaking table tests, only Case 2 was considered here, but from the results of the small model experiment in 3.1.1, we can see that geogrids played a major role in reinforcing the upper section of the dam. Therefore, even if we reduce the number of geogrids in Case 2 by half, we should still be able to expect some strengthening effect. Under actual conditions, this can help reduce costs (due to fewer geogrids being used), which in turn should help to bring this method into practical use.

Next, the effects of seismic resistance of geogrids used in an embankment were investigated in a shaking table test that used a model dike. The results indicated that geogrids were effective in seismically strengthening structures whose embankments (sometimes including foundations) were vulnerable to liquefaction. Furthermore, reinforcement can be especially effective if it is focused on saturated sections.

4 COMPARISON OF REINFORCED EMBANKMENT MODEL TESTS WITH GEOGRID AND SOIL IMPROVEMENT

The Nihonkai–Chubu earthquake of 1983 caused damage to about 200 earth dams, while the Hyogo–Nambu earthquake damaged about 1300 dams. Among the dams that were most damaged (collapsed or severely incapacitated), some earth dams probably ruptured due to liquefaction, and their foundations were restored after the earthquake using cement-type materials. This section examines two earth dam models that were employed to compare the seismic strengthening

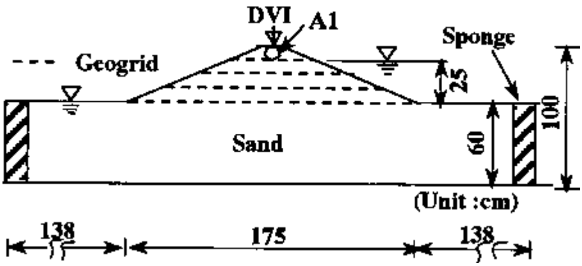

Figure 28 Large-scale shaking table test model.

effects of geogrids and foundation improvement with cement during shaking table tests. It should be noted that a series of tests was conducted in which different shaking tables were used, so this should be taken into account when making comparisons.

4.1 Model 1

4.1.1 Test Procedures and Results

Figure 28 depicts the large-scale model and the arrangement of measuring instruments. The model was built on a 1:10 scale of an actual earth dam that was damaged by the Nihonkai–Chubu earthquake. The model was 4.51 m in total length, 1 m high, and 2.8 m wide.

Shaking table tests were conducted for two cases: reinforced and unreinforced embankments.

In the large shaking table tests, the reinforcement effect of geogrids in the embankment section was considered for a model whose foundation and embankment were composed of loose sand. In the large-scale model, there was a resonance point at around 24 Hz. The relative density of the sandy section was Dr = 50%. Figure 29 shows a comparison of crest settlement (DV1). Here we can see that such settlement was constrained to about 40% of that which occurred in the tests shown in Fig. 13. In addition, deformation was more uniform in the reinforced model than in the unreinforced one, and there was almost no occurrence of cracking in the former.

Figure 29 also compares settlement and acceleration for two cases at representative locations. Although there was little difference in acceleration on the plus side, there was a noticeable difference on the minus side. The factor responsible for this phenomenon is not well understood.

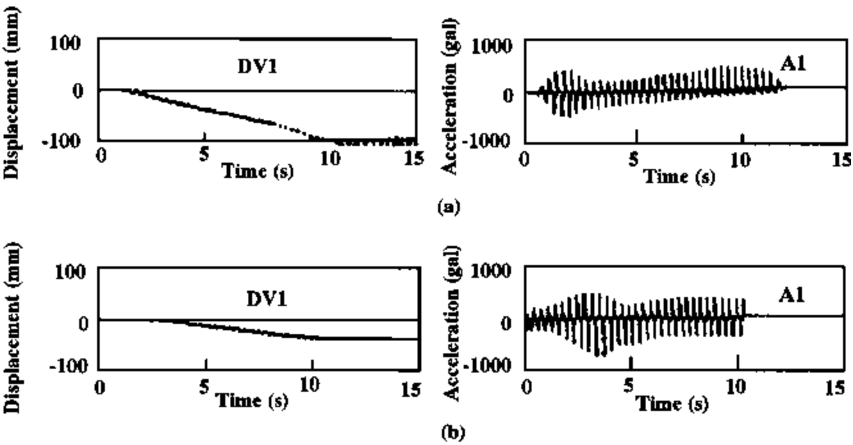

Figure 29 Observed displacement and acceleration at crest: (a) nonreinforced; (b) reinforced with geogrid.

From the above information, it was confirmed that in both the large- and small-scale models, geogrid reinforcement helped reduce crest settlement of embankments.

4.2 Model 2

4.2.1 Test Procedures

The model dam used in this test was a 6-m-high uniform-type earth dam that failed during the Hyogoken–Nambu earthquake. Figure 30 shows the state of

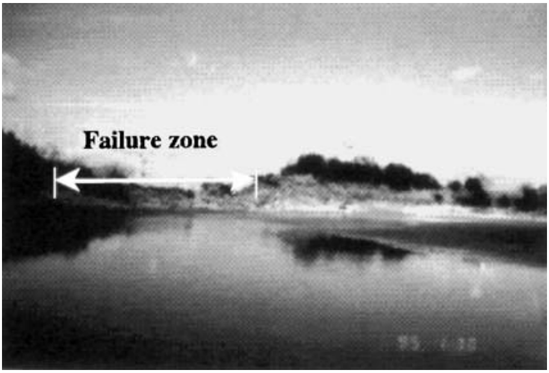

Figure 30 Damage to an earth dam caused by the Hyogoken–Nambu earthquake.

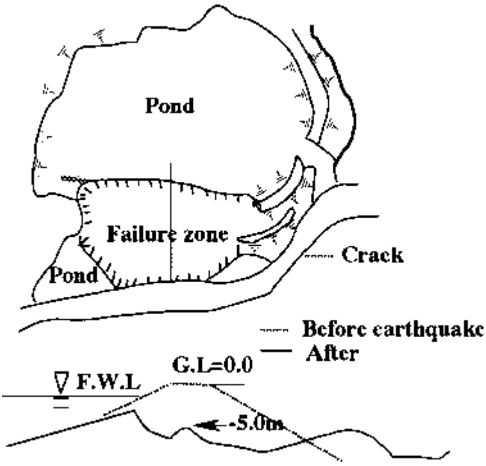

Figure 31 Damage to an earth dam caused by liquefaction.

damage to this dam, which was completely destroyed, in the central area. Boring surveys conducted after the earthquake suggested that since both body of the dam and its foundation were mainly composed of fine sand with an *N*-value of less than 5, the damage was caused by liquefaction (Fig. 31). To make a comparison with geogrid reinforcement and to confirm the reinforcement effects in a model experiment of foundation improvement, find sand similar to that used in the actual dam was used to construct a 1:10 scale model, which was then subject to shaking table tests. The model dam was divided into two models of 4.5 m in length, 2.8 m in width and were simultaneously subjected to seismic vibration.

Test were conducted for the following cases:

C1-1: Nonreinforced embankment.
C1-2: The foundation of the embankment was improved with cement-type materials.
C1-3: The embankment was reinforced with geogrids.

Diagrams of each of three cases are shown in Fig. 32.

The sand used in the model experiment had a particle size distribution that was almost exactly the same as the fine sand that was the main component of the body and foundation of the destroyed earth dam. Specifications were sand content of 94%, uniformity coefficient of 2.5, maximum particle diameter of 4.75 mm, $e_{\min} = 0.627$, and $e_{\max} = 0.957$. The relative density of each model was approximately $\mathrm{Dr} = 60\%$. The foundation was improved with cement-type

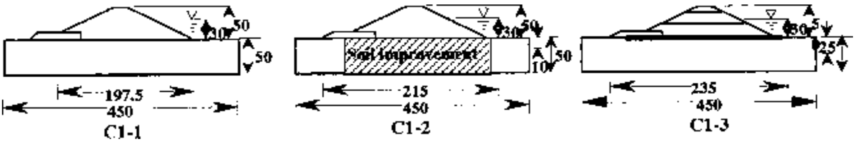

Figure 32 Earth dam model 2.

materials, and, considering that this was a model experiment, these materials were added at a rate of 60 kg/m^3, and the unconfined compression strength of the samples was $qu = 500–700$ kgf/cm^2. It was difficult to improve the foundations in the earth dam model, so the improved section was constructed separately and incorporated into the model. Loading in each case was conducted for 7 sec under sin wave and 3-Hz conditions. The maximum input acceleration was targeted as stepwise loads of 100, 200, 300, and 400 gal. Pore water pressure, acceleration, and displacement were measured.

4.2.2 Experimental Results

The states of deformation at 300 gal for C1-1, C1-2, and C1-3 are shown in Figs. 33, 34, and 35, respectively. Massive deformation occurred in the foundation and embankment of the unreinforced C1-1, but there was almost none in the embankment of C1-2, whose foundation had been improved. Deformation in C1-3 was about the same as that in C1-1, but many cracks appeared on the surface of the C1-1 embankment, while almost no cracking occurred on the C1-3 embankment, which showed a generally "smooth" deformation.

As acceleration increased in the geogrid-reinforced model, more of the acceleration was transferred to the upper section than in the unreinforced model, so it appears likely that geogrids did little to reduce settlement. Figure 35 shows total settlement of the crests of C1-1, 2, and 3 after vibration. Here we can see that there was almost no settlement in C1-3, whose foundation had been improved.

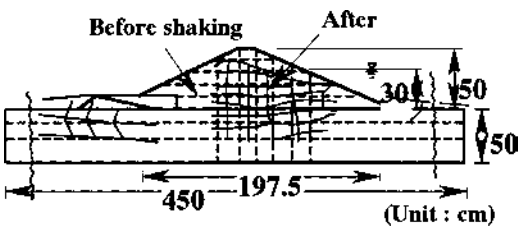

Figure 33 Displacement of earth dam model 1 (C1-1, 300 gal).

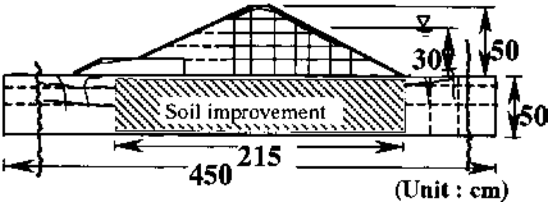

Figure 34 Displacement of earth dam model 1 (C1-2, 300 gal).

In the embankments reinforced with geogrids, settlement could not be reduced after exceeding 300 gal, but geogrids did play a major role in preventing the occurrence of cracking.

Although it was impossible to quantitatively evaluate the seismic strengthening effect, qualitative assessments indicated that it would be possible to improve farm roads and earth dams of high seismic resistance by improving their foundations. Furthermore, a reinforcement effect was seen even if only part of the foundations was improved, indicating that it was possible to undertake efficient reconstruction to meet the objectives of this study.

In reinforced embankments containing geogrids, it was not possible to reduce settlement once 300 gal had been exceeded, but geogrids did play a major role in preventing the occurrence of cracking. A model was constructed of the previously mentioned earth dam that was destroyed in the Hyogoken–Nambu earthquake, and the reinforcement effects of geogrids were compared to those of foundation improvement. Foundation improvements made during the restoration of an actual earth dam showed a noticeable improvement in the dam's strength, proving the effectiveness of the proposed method.

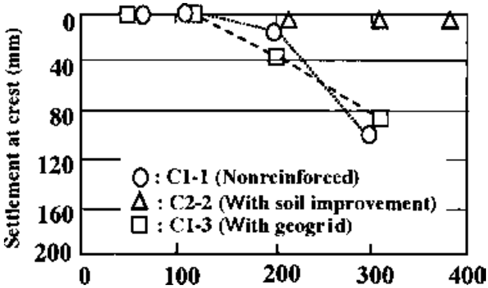

Figure 35 Relationship between crest settlement and input maximum acceleration (earth model 1).

5 CONCLUSION

This paper has examined the reinforcement effects on reinforced embankments structures such as dams, and reclamation dikes using (1) continuous fibers, (2) geogrids, and (3) improvement foundation with a cement by using shaking table tests. The following results were obtained.

(1) When the embankment surface was reinforced with continuous fibers, and subjected to a maximum acceleration of at least 250 gal, the acceleration response value of the embankment increased, but it became possible to greatly reduce settlement. Even when pore water pressure increased, the increase in settlement was far less dramatic with the reinforced model than the unreinforced one. The use of a sheet pile in conjunction with this method further improved the reinforcement effect. Because there was a scale effect with the model tests, we could only do a qualitative evaluation, but we should nonetheless be able to expect a large decrease in settlement, Finite-element analysis also confirmed that there was a reinforcement effect.

(2) Using a model of a planned reclamation dike, the effectiveness of geogrid reinforcement was examined. Although geogrids did have a reinforcing effect, sheeting had almost none, and a rather large amount of deformation occurred. It is also believed that sheeting had little effect in the saturated zone.

(3) In the earth dam model reinforced by geogrids and foundation improvement, the maximum acceleration sin wave of the shaking table showed a decrease in settlement up to 200 gal, but once 300 gal was reached, the settlement volume was the same as in the unreinforced model. A likely reason for this was the reinforcement effect of the geogrids on the embankment caused the acceleration response to increase. Therefore, geogrid reinforcement was effective until a maximum input acceleration of 200 gal (standing wave), but this effect decreased above 200 gal.

Because these conclusions have been made based on limited experimental data, it will be necessary to subject the results to various types of analyses.

REFERENCES

M Fukuoka, S Tani, T Yamashita, S Ishihara, Y Takano. Stability of a retaining wall reinforced by continuous fibers during an earthquake. *4th Intl. Conf. on Geotextile*, pp 27–32, 1990.

S Tani, S Takano, Y Yokota. Shaking table tests of embankment models reinforced with geotextiles. *Earthquake Engineering, Tenth World Conf.*, pp 1317–1322, 1992.

S Tani, M Nakashima, H Suzuki, Y Okabe. Shaking table tests of embanking using geotextille and soil improvement. *The 32nd Japan Natl. Conf. on Soil Mechanics and Foundation Enginering* (in Japanese), pp 1039–1040, 1997.

21
Centrifuge Modeling of Seismic Performance of Reinforced Earth Structures

Jiro Takemura
Asian Institute of Technology, Bangkok, Thailand

Akihiro Takahashi
Tokyo Institute of Technology, Tokyo, Japan

1 INTRODUCTION

Centrifuge model testing has been widely recognized as one of the most versatile research tools in geotechnical engineering. This physical modeling technique shows its advantage in simulating behavior of soil structures in which the self-weight of soils plays important roles. For examples, stress–strain relationships of soils normally have a strong stress dependency and shear stresses in the soil structures are mainly caused by the weight of soils, especially for slopes, excavations, and retaining structures. In addition to these advantages, as small-scale model tests, the centrifuge model tests can be carried out relatively easier than the large-scale gravity models, so that the centrifuge model tests can provide very useful information, such as failure and deformation mechanisms and earth pressures acting on the structures, which are sometimes crucial in design models, for many conditions we must consider.

Because of these features, centrifuge model testing has been applied in the research on the performance of reinforced earth structures from the early era of earth reinforcement. Bolton and Pang (1982) conducted more then 70 centrifuge tests on the vertical retaining walls reinforced with metal strips and discussed the limit states of this type of wall and applicability of various analyses to evaluate the collapse limit state using observed failure types (friction failure and tension failure) and other data such as vertical stresses on the base of reinforced portion and tensions of the strips. Shen et al. (1982) used the centrifuge model tests to confirm the shape of the failure plane assumed in a stability analysis on the cut reinforced with soil nailing. These two centrifuge model tests are good examples showing the high potential of centrifuge modeling; namely, it can provide very useful information about the behavior of soil structures, for which very limited information is available under the conditions assumed in some design methods.

Earth reinforcement technology has a relatively long history compared with the time since centrifuge modeling has been applied to this type of structure. However, many aspects still exist for many for which the centrifuge can contribute to earth reinforcement technology. The performance of reinforced soils during an earthquake is one of the typical examples about which very few reliable field records are available in the literature. Although intensive field observations conducted after previous large earthquakes have provided useful data on the seismic performance of various structures, the data are normally limited in the final figures after the earthquakes, not including responses of structures during the earthquakes and accurate input ground motions. From the study on the damage of soil retaining walls for railway embankments after the 1995 Hyogoken-Nanbu earthquake, Tatsuoka et al. (1996) reported that geogrid reinforced soil retaining walls performed very well even in one of the most severely shaken areas, while gravity-type retaining walls showed a low stability against strong seismic motion. Nishimura et al. (1996) also concluded from the investigation of the geogrid reinforced soil walls after the 1995 Hyogoken-Nanbu earthquake that the geogrid reinforced soil wall could have a much higher seismic resistance than that predicted by two methods based on the pseudo-static limit equilibrium approach. Tatsuoka et al. (1996) concluded in their report that the performance of the geogrid reinforced soil wall observed in their investigation would foster confirmation and development of aseismic design procedures. In order to develop more rational design procedures and confirm the applicability, observing the behavior of the reinforced soils under well-controlled or recorded shaking motion, which can be done by physical modeling, is most important.

The following sections outline advantages of centrifuge modeling in the study of reinforced earth structures especially for the seismic performance, as well as some limitations to this technique. As an example of the application, centrifuge model tests on the vertical geogrid reinforced wall are described, and results and discussions on the tests are presented.

2 CENTRIFUGE IN STUDY OF EARTH REINFORCEMENT

2.1 Principles of Centrifuge Modeling

The behavior of soil structure highly depends on its stress conditions (σ,τ), which are mainly caused by the self-weight of the soil. For example, the strength of soil τ_f and the shear stress τ on a possible slip plane in a slope are functions of the normal stress σ.

$$\tau_f = c + \sigma \tan\phi \tag{1}$$

$$\tau = f(H, \beta, \gamma, etc.) \tag{2}$$

where c and ϕ are the cohesion and internal friction angle, respectively, and H, β, and γ are the slope height, angle, and unit weight of soil as shown in Fig. 1.

The behavior of the slope depends on the mobilized strength or factor of safety defined by the following equation:

$$F_s = \frac{\tau_f}{\tau} \tag{3}$$

Therefore, this nondimensional number (F_S) should be properly represented in a model in order to simulate the prototype behavior in it. However, confining stresses (or overburden pressures) as well as shear stresses of soil in a small-scale model under the ordinary gravity field (1 g) are very small compared with its prototype, which causes an erroneous behavior between the model and the prototype.

Provided that the soil in a 1/N-scale model has the same properties as that in the prototype, which means $c_m = c_p$, $\phi_m = \phi_p$, and $\gamma_m = \gamma_p$, the safety

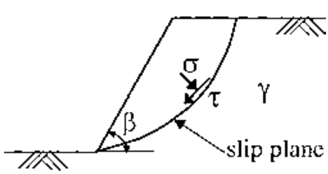

Figure 1 Slope and possible failure surface.

factor of the model slope (F_{sm}) can be given by Eq. (4).

$$F_{sm} = \frac{\tau_{fm}}{\tau_m} = \frac{c_m + \sigma_m \tan\phi_m}{\tau_m} = \frac{c_p + \frac{\sigma_p}{n}\tan\phi_p}{\frac{\tau_p}{n}} = \frac{nc_p + \sigma_p \tan\phi_p}{\tau_p}$$

$$\geq \frac{c_p + \sigma_P \tan\phi_p}{\tau_p} = F_{sp} \tag{4}$$

Here m and p denote model and prototype, respectively.

For the model with saturated clay, in which $\phi_u = 0$ can be assumed in the undrained condition. Eq. (4) becomes

$$F_{sm} = nF_{sp} \tag{5}$$

For the model with cohesionless dry sand, the following relation is derived;

$$F_{sm} = F_{sp} \tag{6}$$

Equations (4) and (5) clearly show that it is very difficult to simulate a large deformation or failure in a small-scale model under a normal gravity field. The discrepancy in F_s in the $1/N$-scale model and the prototype can be solved by subjecting the model to an inertial acceleration of intensity N times the earth's gravity, because the stresses at a homologous point in the model become identical with those in the prototype, i.e., $\sigma_m = \sigma_p$, $\tau_m = \tau_p$. This stress similitude is the basic scaling law of centrifuge modeling.

From Eq.(6), the small-scale gravity model seems to give similar behavior of the prototype for cohesionless soils. However, Eq. (6) is derived under the conditions that strength parameters are identical between the model and prototype, which can hardly be assumed for soils, because soil behavior is a function of stress level and stress history. For example, the peak angle of the internal friction of soil of a given density decreases as the applied effective stress increases due to the suspension of dilation. This again proves the necessity of the stress similitude in the small-scale model.

2.2 Advantages and Limitations of Centrifuge Modeling

2.2.1 Advantages of Centrifuge Modeling

As detailed scaling laws and applications of centrifuge technology in geotechnical engineering field have already been given in various sources, such as Schofield (1980) and Taylor (1995), specific advantages and limitations of centrifuge modeling for reinforced earth structures are outlined in this section.

Bolton and Pang (1982) give the following reasons as the justification for performing centrifuge tests rather than simpler conventional model tests of a reinforced earth wall:

1. By creating an equality of stress in the model with that in a typical field-scale wall, the proper dilatancy of the soil is reflected; the sand in conventional small models dilate extremely strongly, and this must distort failure mechanism;
2. By enhancing soil stress, the requirements for the reinforcement are similarly increased, so that the additional stiffness created by strain gauges and lead wires is insignificant for the already substantial ties;
3. Because the materials are thicker, the strength of the joints can be more easily controlled and the impact of local imperfections is reduced.

Reason (1) is the main advantage of a centrifuge explained in the above section. Regarding the advantage from reason (1), someone may argue that from Eq. (6) a proper simulation of the behavior of the prototype consisting of cohesionless soil would be possible in a small-scale gravity model, if the dilatancy of the prototype soil can be created by modifying the relative density of the soil. Even if it is possible, there are considerable difficulties in modeling the reinforcement, which are mentioned in reasons (2) and (3). Table 1 shows the

Table 1 Scaling Factors in Centrifuge Model

Parameter (dimension)	Scaling factor (*m/p*)
Acceleration (L/T^2)	$\lambda_a = N$
Length (L)	$\lambda_L = 1/N$
Area (L^2)	$\lambda_A = 1/N^2$
Soil density (M/L^3)	$\lambda_\rho = 1$
Force (ML/T^2) $=$ (F)	$\lambda_F = 1/N^2$
Stress (F/L^2)	$\lambda_\sigma = 1$
Particle size (L)	$\lambda_P = 1$
Permeability (L/T)	$\lambda_k = N$
Cohesion (F/L^2)	$\lambda_c = 1$
Stiffness (F/L^2)	$\lambda_E = 1$
Time: inertia (dynamic) (T)	$\lambda_{Ti} = 1/N$
Time: laminar flow (T)	$\lambda_{Tf} = 1/N^2$
Time: creep (T)	$\lambda_{Tc} = 1$
Reinforcement tensile force (F)	$\lambda_{Rs} = 1/N^2$ ($1/N^*$)
Reinforcement strain	$\lambda_{R\epsilon} = 1$

* Per unit length.

scaling factors in the centrifuge model. The scaling factor on the tensile strength of reinforcement λ_{Rs} ($S_{\mathrm{Rm}}/S_{\mathrm{Rp}}$) is $1/N^2$. As the model reinforcement width is also reduced by $1/N$, the scaling factor on tensile strength as well as the elongation rigidity of reinforcement per unit width become $1/N$ in the centrifuge. While in the small-scale gravity model, λ_{Rs} ($S_{\mathrm{Rm}}/S_{\mathrm{Rp}}$) is $1/N^3$ for one reinforcement and $1/N^2$ for per unit width, because the scaling factor on force in the gravity model is $1/N^3$. $1/N^2$ times smaller strength and elongation rigidity per unit width in the model reinforcement than those in the prototype causes the problems in the model as explained in reasons (2) and (3).

The above-mentioned advantages of the centrifuge models are relative ones to the small-scale gravity models. In addition, the centrifuge models can be more easily and economically conducted than the large-scale model. This advantage is very crucial in the study of the mechanical behavior of soil structures affected by many factors. The reinforced earth slopes and walls have many conditions, which also include many factors or variables, as shown in Table 2.

Therefore, a large number of tests are required in order to investigate the effects of these factors under well-controlled test conditions. Mitchell et al. (1988) conducted 38 centrifuge tests on reinforced soil walls and discussed the effects of reinforcement extensibility, type of facing, compressibility of foundation, and surcharge. Satoh et al. (1998) reported a series of centrifuge

Table 2 Conditions and Factors Considered in the Performance of Reinforced Earth Wall

Conditions	Factors or variables
Soil	Cohesionless soil
	Cohesive soil
	Density
Reinforcement	Type (grid, metal strip, etc.)
	Strength
	Extensibility
	Length
	Spacing
	Construction sequence
Wall or slope	Slope angle
	Facing
Foundation	Compressibility
External load	Self-weight or height of wall
	Surcharge
	Seismic force (k_h, k_y, frequency)

model tests on seismic performance of steep geogrid-reinforced embankments with three different facing types and showed the effectiveness of increasing facing stiffness and number of reinforcements on reducing the face permanent displacement. They also discussed the effect of soil density and length of geogrid to reduce the shear deformation of the reinforced earth.

2.2.2 Limitations of Centrifuge Modeling

As a physical model, the precise replication of all details of the prototype is almost impossible, even in the centrifuge model, and some approximations have to be made in the modeling process. The influence of the nonuniform acceleration field in the centrifuge models is one typical example of scale effects (Schofield, 1980; Taylor, 1995). The particular examples relevant in the centrifuge modeling on reinforced earth are (1) construction effects and (2) particle size effects.

Construction Effect. As the reinforced soil structures are relatively flexible compared to rigid gravity-type walls, reinforcement and soils in the reinforced earth might be subject to relatively large strains during construction. These strains are highly dependent on the construction sequence and affect the mechanical properties of the reinforced soil, especially mass stiffness. Furthermore the construction procedure is the main process of external loading in the static stability problem of this type of structure. However, it is very difficult to build the reinforced earth structures in-flight by the same manner as in actual practice. Therefore, the reinforced earth model is first made on a laboratory floor under a 1-g field and then centrifugation is applied to the model.

Satoh et al. (1995) showed the comparison of mobilization of tensile strains or forces in geogrids between a centrifuge model and field tests, as shown in Fig. 2.

Figure 2a is the relationship between the tensile strains in the model geogrids and the centrifugal acceleration observed in the centrifuge model with a height of 40 cm. Similar relationships observed in the field tests are shown in Fig. 2b, where horizontal and vertical axes are tensile forces in the geogrids and height of embankment, respectively. In the centrifuge model, the strains of all geogrids increased linearly with increasing centrifugal acceleration from the beginning. While in the field test where actual construction was conducted, of course there was no mobilization of strain of the geogrid until it was installed, and furthermore the strain mobilization of the lower grid was affected by the installation of the upper grid. In the centrifuge modeling on static problems, centrifuge acceleration is often used to simulate the external load and increased up to when clear failure occurs (Table 3).

This technique can give us useful information about the failure height as well as failure mechanism on a reinforced earth slope with various conditions. With different centrifugal acceleration at failure and the difference in the loading

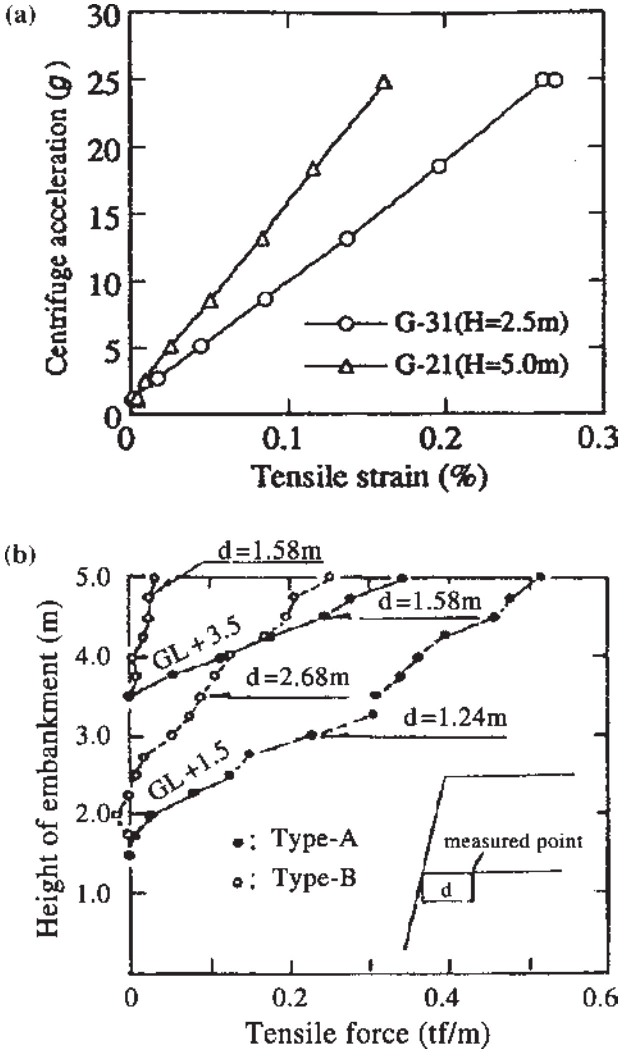

Figure 2 (a) Relationship between centrifuge acceleration and tensile strain in geogrid. (b) Increase in tensile force of geogrid with increasing height of embankment in field test. (From Satoh et al., 1995.)

history, however, it is rather difficult to yield quantitative discussions on the performance.

In order to avoid the uncertainty in the increasing centrifugal acceleration during the loading process, Matichard et al. (1988) and Davies and Jones (1988)

Table 3 Types of Loading to Reinforced Earth and Methods Simulating Loadings

Type of loading	Simulating methods	Examples of previous studies using methods
Construction of wall	Increasing centrifugal acceleration	Bolton and Pang (1982) Shen et al. (1982) Mitchell et al. (1988)
	Removal of temporary support under constant centrifugal acceleration	Davies and Jones (1998) Matichard et al. (1988)
Surcharge from the top	Supplying water into box with flexible base	Mitchell et al. (1988)
	Hydraulic piston with loading plate	Taniguchi et al. (1988)
Seismic force	Tilting methods	Taniguchi et al. (1988)
	Shaking table	Satoh et al. (1998) Takahashi et al. (1999) Takahashi et al. (2001)

removed temporary supports in front of the reinforced slopes under a constant centrifugal acceleration field. Also, applying external loads like surcharge and seismic force to the model reinforced earth structures with reasonable static stability under a constant acceleration is the most appropriate situation where controlled initial conditions and loading conditions can be specified. However, it should be noted that even in this type of test the effect of construction sequence is inevitably included in the initial conditions of reinforced soil as shown in Fig. 2.

Particle Size Effects. If the same soil as the prototype is used in the model, the difference of the scaling factors between the model dimensions and soil particle size cannot be avoided, as shown in Table 1. The effect is called "particle size effect," which should be considered when the particle size would be significant compared with model dimensions and local effects of soil particles would influence the behavior of soil, such as shear band formation in a small model (Tatsuoka et al., 1991). These conditions may most probably occur in the pullout failure of geogrid reinforcement. If the dimensions of the geogrid are precisely reduced in the model, the sand particle size becomes relatively large compared to the typical dimensions of the geogrid, like the opening size and thickness. To answer the question about the particle size effects, Satoh et al. (1995) conducted pullout tests in dense Toyoura sand using real geogrids and a reduced-size model geogrid made by the same procedure as the real one. They obtained similar relationships between the pullout forces normalized by the elongation rigidity of the geogrid and the observed strains in the model and the real geogrids under the same vertical pressures. From these observations they confirmed the similarity of pullout resistance between the model and the prototype. Zimmie at al. (1994) evaluated the dynamic geosynthetic interface friction in the centrifuge using a shaking table and found the obtained interface frictions agreed well with those reported in the literature. Although some research shows less particle size effects on the performance of reinforced earth structures, the available data are still limited, which requires more research on the effect.

Other Effects Especially for Shaking Tests. Measurement in the detailed behavior of the model is one of the other difficulties especially for shaking tests using small-scale models under high centrifugal accelerations. In the small-scale model, not only particle size but also sensor size may affect the behavior; even it is difficult to instrument the sensors in it. Therefore, in order to conduct fully instrumented centrifuge model tests, a relatively large-scale model under small centrifugal accelerations is normally adopted, which is only available for a large shaking table on centrifuge. In other words, middle-size tests using 1-g shaking tables may provide better information about the detailed behavior including deformation, earth pressures and accelerations in the ground, and tensile strains of the reinforcements than small-scale centrifuge tests, although there are limitations in the similitude of 1-g models explained above. For example, Koseki et al. (1998) give very interesting results about the seismic performance of reinforced earth walls under strong earthquakes from shaking table and tilting tests. Using the observed results, they discuss the applicability of current design methods against strong seismic motions like the 1995 Hyogoken-Nanbu earthquake.

Applying seismic forces is also one of the difficult and challenging parts in the simulation of earthquake motions under high centrifugal acceleration fields. Now many shaking tables are available in many centrifuge research centers all over the world, especially in Japan (Kimura, 2000), but they are very limited in multidirectional shakers (Shen et al., 1998; Takemura et al., 2002). As many analytical researchers have pointed out, the effects of vertical motion on the seismic stability of reinforced earth, for example, Cai and Bathurst (1996), Ling et al. (1997), further development of the multi-directional shaker on centrifuge will expand the applicability of centrifuge modeling on this problem. But not only a very sophisticated centrifuge shaking table but also simple tilting tests are very useful to show the applicability of the pseudo-static approach in the seismic design of reinforced earth by the combination of shaking table tests, which was actually done with a 1-g test by Koseki et al. (1998).

3 CENTRIFUGE MODEL TEST ON THE SEISMIC PERFORMANCE OF A GEOGRID REINFORCED SOIL WALL

This section describes centrifuge model tests on seismic performance of geogrid reinforced soil wall done at the Tokyo Institute of Technology and presents some results and discussions on the tests as an example of the application of centrifuge modeling to this type of problem.

3.1 Test Procedures and Conditions

3.1.1 Test Procedures and Model Preparation

T.I.T. Mark II Centrifuge and servo-hydraulic type shaker (Takemura et al., 1989) were used in the tests. An aluminum model container with inner sizes of 450 mm in width, 150 mm in breadth, and 250 mm in height was used. Rubber sheets were placed at both sides of the container for absorbing stress waves from the side boundaries. The model setup used is shown in Fig. 3.

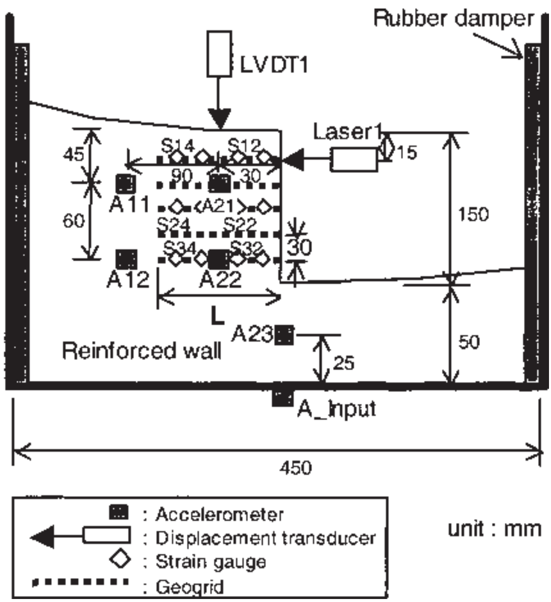

Figure 3 Model setup for centrifuge tests. (From Takahashi et al., 2001.)

Table 4 Mechanical Properties of Inagi Sand

Specific gravity G_s	2.66
Mean grain size D_{50} (mm)	0.20
Uniformity coefficient C_u	3.2
Modulus of deformation E_{50} (kPa)	$1.0 \times 10^{3*}$, 2.6×10^{3}†
Apparent cohesion c	4.2^{*}, 6.8†
Internal friction angle ϕ (deg.)	33^{*}, 35†

* $\rho_d = 1.40$ Mg/m^3; $w_0 = 26\%$.
† $\rho_d = 1.48$ Mg/m^3; $w_0 = 26\%$.

Model grounds were made with Inagi sand, whose initial water content (w_0) is 26–27%, with dry density (ρ_d) of 1.40 and 1.48 Mg/m^3. Basic properties of Inagi sand are given in Table 4.

The internal friction angle (ϕ) of the sand was obtained from triaxial compression tests under a drained condition, and cohesion (c) was back-calculated from the failure height observed in a centrifuge test on a nonreinforced vertical slope.

Model geogrids used in the test were a glass fiber-made fly-guard (Fig. 4), whose properties are listed in Table 5. The opening of the grids was 2.5 by 2.5 mm. Typical pullout test results are given in Fig. 5. The tensile strain of the geogrid when the pullout force reached its peak was about 0–3%. To support the vertical face of the wall, aluminum facing plates were adopted. One piece of geogrid was attached to one plate, and these plates were hinged to each other (Figs. 4 and 6).

In the preparation of the model ground, a static compaction technique was adopted in order to control the density of the moisture sand with the installation of model geogrids. Inagi sand with an initial water content of 26–27% was first compacted statically layer by layer using a bellofram cylinder and a loading rigid plate to form the base foundation. After completion of the base foundation, a temporary spacer was placed at the portion in front of the earth wall to secure l-D static compression of the soil in the wall part as done in the preparation of the base foundation. The model geogrid was placed on each compacted layer, and optical markers for displacement measurement were also placed at the front

Table 5 Material Properties of Model Geogrid

Mass per unit area	1.1×10^{-2} (0.56) kg/m^2
Tensile strength T_f	7.0 (350) kN/m
Elongation at break ϵ_f	8.0%

In parentheses, prototype scale under 50 g.

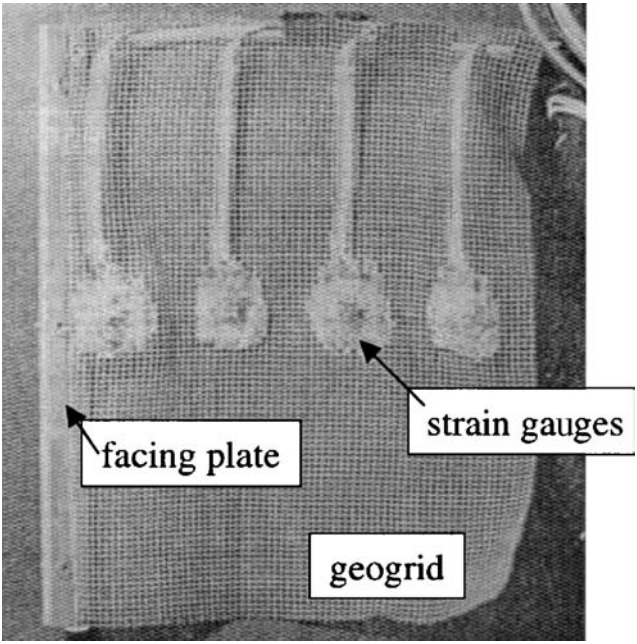

Figure 4 Model geogrid instrumented with strain gauges.

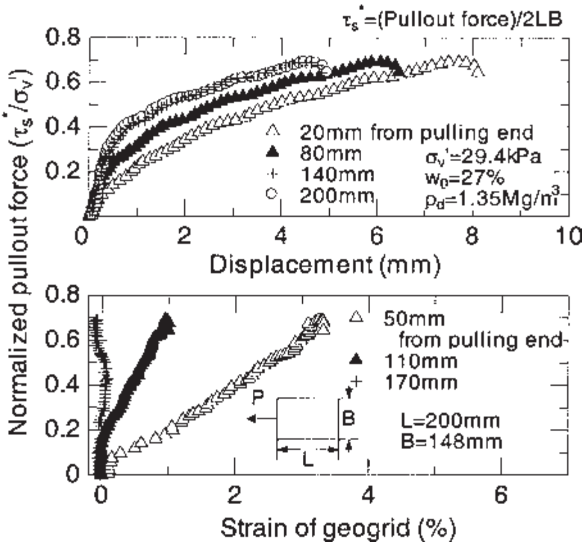

Figure 5 Typical pullout test results. (From Takahashi et al., 2001.)

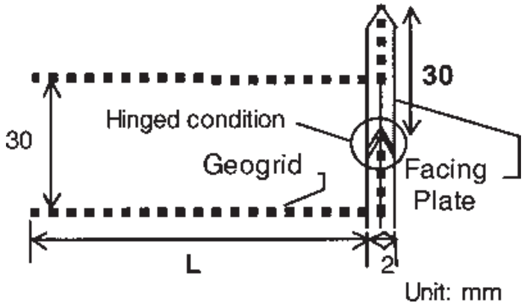

Figure 6 Schematic drawing of model facing plate. (From Takahashi et al., 2001.)

surface of the ground. This compaction of the wall part was continued up to the top level of the reinforced soil wall.

Having prepared the model, the container was set on the shaking table mounted on the centrifuge and the centrifugal acceleration was increased gradually up to 50 g. Confirming the rate of settlement due to the centrifugation was negligible, shaking tests were conducted by inputting sinusoidal waves with a frequency of 100 Hz, which is equivalent to 2 Hz in the prototype scale, to the shaking table. Four waves with different conditions were input to each model. Typical time histories of the input sinusoidal waves are shown in the prototype scale in Fig. 7. During the shaking tests, acceleration and displacement of the earth wall and the tensile strain of the geogrid were measured at the locations shown in Fig. 3. Photographs were taken before and after shaking to observe the displacement of targets on the front surface of the reinforced soil.

3.1.2 Test Conditions

Results of seven centrifuge tests with different conditions are shown. The height of the reinforced soil wall was fixed for all tests, namely 150 mm, 7.5 m in the prototype scale. The length of geogrids (L), spacing (s), and dry density (ρ_d) are the variable parameters in the tests. The effects of each parameter on the permanent deformation and dynamic response of reinforced earth wall were studied. Table 6 gives the test conditions The first letter in the test code means the density, namely "L" and "D" are $\rho_d = 1.40\,\mathrm{Mg/m^3}$ and $1.48\,\mathrm{Mg/m^3}$, respectively. One tenth of the first number after the letter in the code corresponds to the length of the geogrid in the prototype scale and one hundredth of the second number grid spacing. The natural frequencies measured using a random wave with small intensity before shaking tests were around 140 Hz and 180 Hz for the model $\rho_d = 1.40\,\mathrm{Mg/m^3}$ and $1.48\,\mathrm{Mg/m^3}$ respectively, which are 2.8 Hz and 3.6 Hz in prototype scale. The measured natural frequency was not dependent on

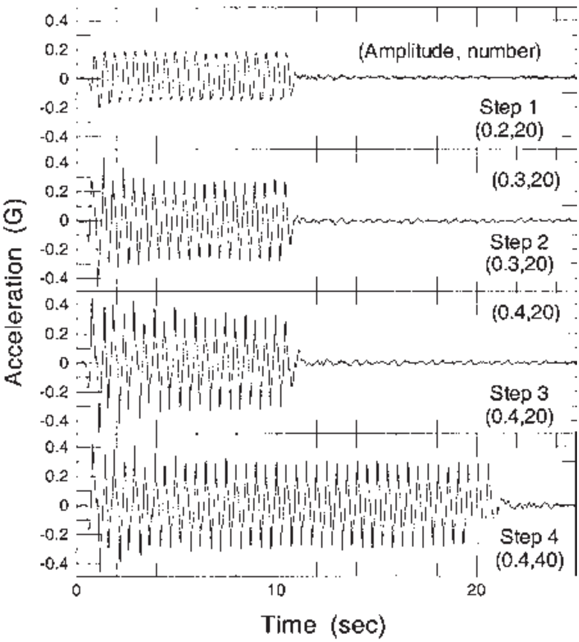

Figure 7 Input wave time history: D60–150. (Modified from Takahashi et al., 2001.)

Table 6 Test Conditions

Test code	Dry density *rd* (Mg/m^3)	Grid length *L* (m)	Grid spacing *s* (m)	Remarks
L60-075	1.4	6	0.75	
L45-075	1.4	4.5	0.75	
D60–150	1.48	6	1.5	*
L60–150	1.4	6	1.5	*
D45–150	1.48	4.5	1.5	*
L45–150	1.4	4.5	1.5	
D20–150	1.48	2	1.5	

* Strain gauges were provided on model geogrids.

the reinforcement conditions (L, s) in the tests. All test results are given in prototype scale in the following section.

3.2 Test Results and Discussions

3.2.1 Permanent Deformation of Reinforced Soil Wall

Observed deformations of the soil wall due to the four steps of shaking are shown in Fig. 8. These deformations were obtained from the in-flight photographs taken before and after shaking, as shown in Fig. 9. In D20–150 with the shortest length of geogrids, the failure mode was the circular type and the failure line was across the geogrid reinforced zone at the lower portion of the wall. Except for D20–150, although the magnitudes of displacement differed for different conditions, deformation modes were of the two-part wedges type in all cases. That is

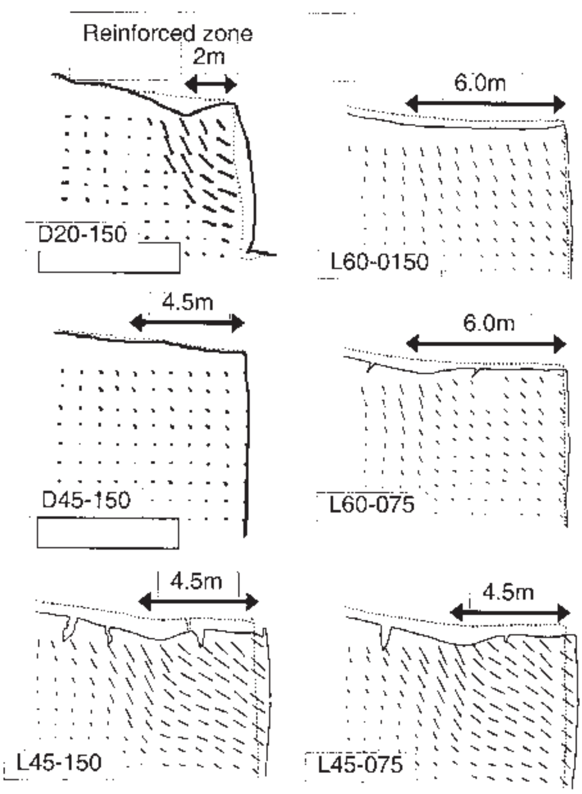

Figure 8 Observed deformation of reinforced earth wall.

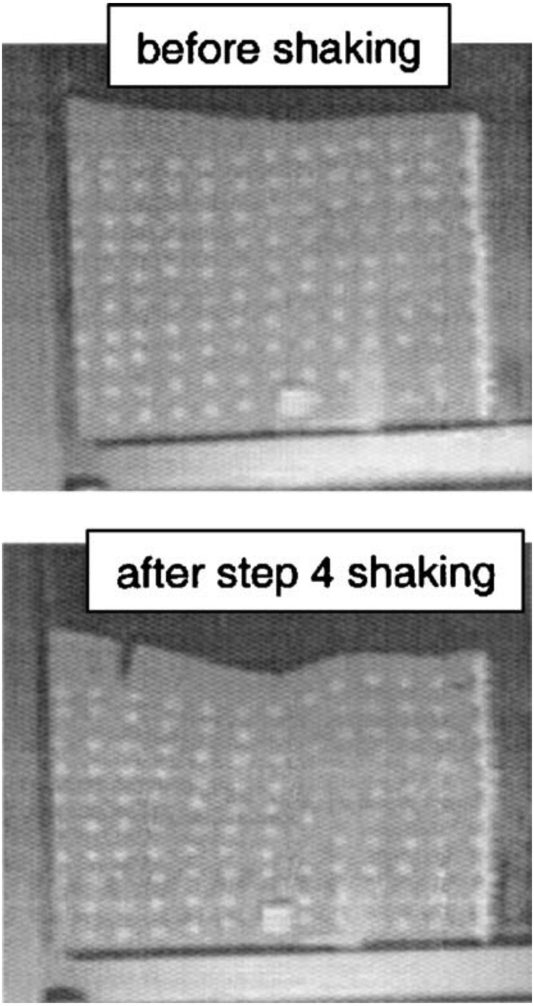

Figure 9 In-flight photos of reinforced earth wall: L45-075.

a triangle active failure behind the reinforced soil accompanied by the horizontal translational displacement of the reinforced zone. In the reinforced zone a relatively large shear deformation was observed at the lower portion. Takahashi et al. (1999) discuss more details about the deformation pattern of the reinforced soil.

Time histories of settlement of the shoulder of the soil slope, Ll, in L45–150 are shown in Fig. 10. The settlement gradually accumulated with time

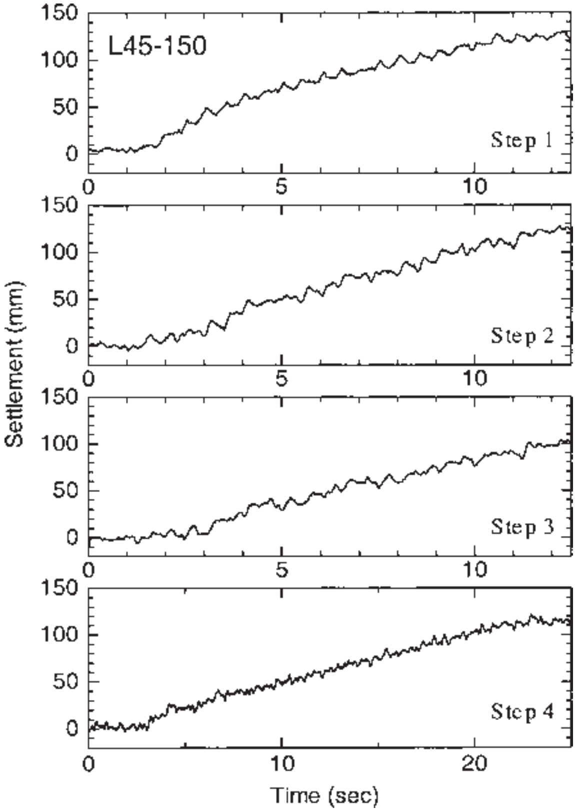

Figure 10 Time history of settlement at L1: L45 – 150. (Modified from Takahashi et al., 2001.)

without showing any dramatic increase, even against the largest input waves. This ductile dynamic behavior is one of the great advantages of this type of wall against large earthquakes as many researchers point out, for example, Tatsuoka et al. (1996) and Koseki et al. (1998). But it should be noted that no apparent pullout failures and breakage of geogrids were observed in the test conditions.

Figure 11 shows incremental and total permanent horizontal displacements of the wall faces at the height of 6.75 m (Laser1) and incremental and total settlements of the walls at the shoulder of the wall (LVDT1). The accumulation of the permanent displacements decreased as the length of the geogrids and the dry density of the soil increased. As shown in Fig. 8, for the loose cases ($\rho_d =$ 1.4 Mg/m^3), the large translational movement occurred in the reinforced zone with the geogrid of $L = 4.5$ m, while for the dense cases ($\rho_d =$ 1.4 Mg/m^3) with

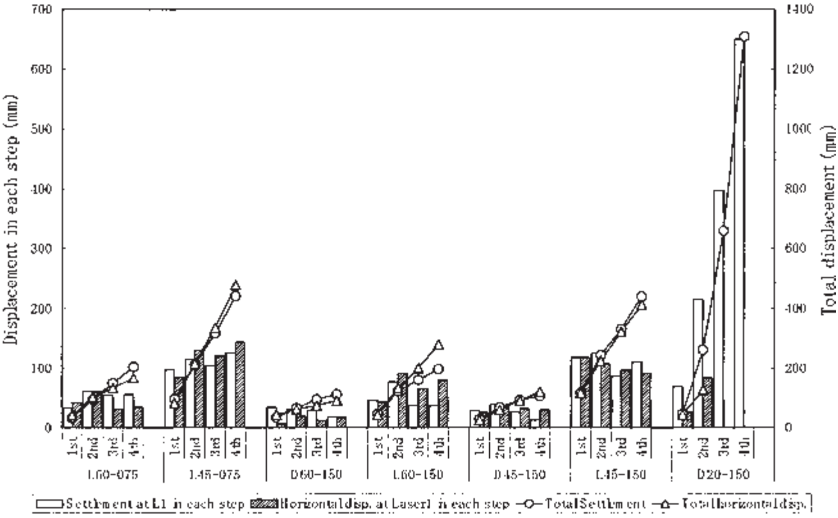

Figure 11 Permanent displacement of reinforced earth wall.

the same length this large translational movement could be prevented. Although the increase of seismicity and number of waves increased with the shaking step, the incremental permanent displacements in the step did not apparently increase with the number of step, except for D20–150. Some cases even showed better seismic performance, that is, the decrease in the incremental displacement with the shaking number. This type of good seismic performance or ductile behavior could not be observed in D20–150 with the shortest geogrid length, in which a different failure mode from the other tests was observed. The effect of the spacing between geogrids could not be clearly seen in the permanent displacements. Particularly in L45–150 and L45–075, where large translational movements occurred in reinforced zone, there was not much difference in the settlement and horizontal displacements.

3.2.2 Tensile Strain of Geogrids

Figure 12 shows observed distributions of the residual strain of geogrids at different elevations $z = 6.75$, 3.75, and 0 m, for each shaking step of D60–150 and L60–150. These two cases had the same reinforcement conditions but different dry densities. Positive values in the figure represent elongation of the grids. Irrespective of the density of the soil, the larger residual strain of geogrids was observed at the lower portion. Paying attention to the accumulation of the residual strain of the grids at the lower portion, large strain was observed along

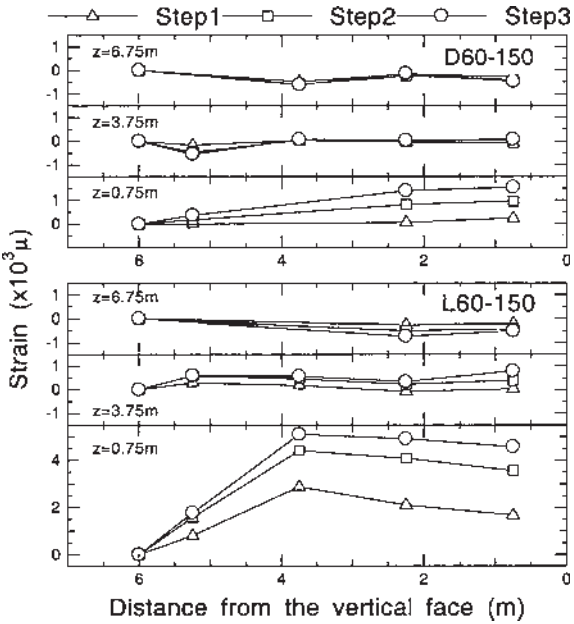

Figure 12 Residual strains of geogrids: D45–150, L60–150. (Modified from Takahashi et al., 2001.)

the geogrids in the first step for L60–150, while in D60–150 the residual strain in the first step was very small and gradually increased backward from the face with the following shaking number. This tendency is probably associated with the progress of the permanent deformation of the reinforced soil wall and indicates that the slight lack of the compaction of the soil, $\Delta\rho_d = 0.08\mathrm{Mg/m^3}$ in this case, may result in the large permanent deformation of the wall.

From Fig. 12 it seems that the contribution of the lower geogrids is greater than the upper ones to the seismic performance of the reinforced earth. However, the very important role of the upper geogrids can be confirmed form Fig. 13, which shows the time history of tensile strains observed in the step 3 shaking of D60–150. Although overburden stresses on the geogrid surfaces were smaller in the middle and top geogrid than the bottom one, strain amplitudes of the former two portions were larger than the latter portion. The large amplitudes imply that the geogrid resisted well against the cyclic shear forces during shaking. Koseki et al. (1998) and Satoh et al. (1998) point out the importance of the reinforcement at the upper portion of the wall.

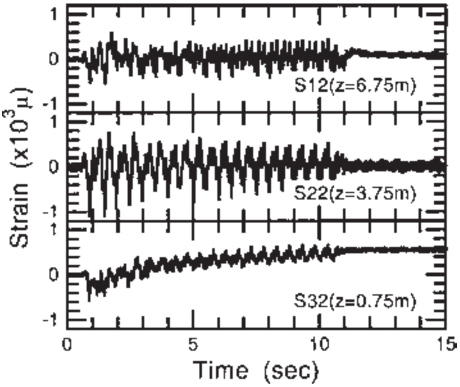

Figure 13 Example of time history of tensile strains of geogrid: D60–150.

3.2.3 Acceleration Responses and Stress–Strain Relationships of Reinforced Soils

Figure 14 shows partial time histories of the acceleration at A21, A22, and A23 in step 2 shaking for D60–150 and L60–150. The points of A21 and A22 were located in the reinforced zone, and the point of A23 was in the base. The phase lag between the acceleration of A21 and A22 in the latter was larger than that in the former. This fact implies that the relatively large deformation of the reinforced zone occurred in the case with the small dry density. This difference is induced by not only the natural frequency of the reinforced soil wall, but also the deformation characteristic of the wall.

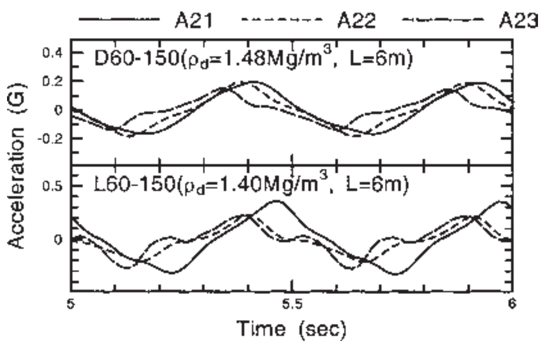

Figure 14 Acceleration time histories: D60–150, L60–150. (Modified from Takahashi et al., 2001.)

Generally, the effect of the reinforcement can be seen when the tensile strains of the geogrid increase with the deformation of the reinforced soil. To gain insight into the relationship between the effect of the reinforcement and the deformation of the soil, mean stress–strain relationships of the reinforced zone were calculated from the acceleration records. The applied method for the stress–strain calculation was proposed by Koga et al. (1990) and is briefly summarized in Fig. 15. The used acceleration records were measured at A21, A22 and A23. The records were filtered for cutting out frequencies of less than 0.4 Hz and greater than 10 Hz; thus no residual strain was included in the results. The calculated stress–strain relationships in step 3 shaking are shown in Fig. 16 for the cases of D60–150, L60–150, D45–150, and L45–150. From the stress–strain relationships, it can be seen that the secant shear modulus becomes larger and the amplitude of strain becomes smaller as the length of geogrids and the dry density of the soil increase.

The secant shear modulus in Fig. 16 was the slope of the approximated line of stress–strain relations calculated by the least-squares method. The secant shear modulus is plotted against the permanent horizontal displacement of the wall face near the top of the wall at the height of 6.75 m in Fig. 17. In all cases, the secant shear modulus decreased with the permanent lateral displacement of the soil wall. However, the secant shear modulus increased when the permanent displacement of the soil reached a certain level. These turning points in the variation of the shear modulus with the displacement of the reinforced soil should be the points where the strained reinforcement showed its effectiveness in preventing the further deformation of the wall discussed in Figs. 10 and 11. These points varied according to the compaction level of the soil. There are differences in the horizontal displacement of the facing top at the turning point between two soils with different densities. These were about 1% of the wall height for

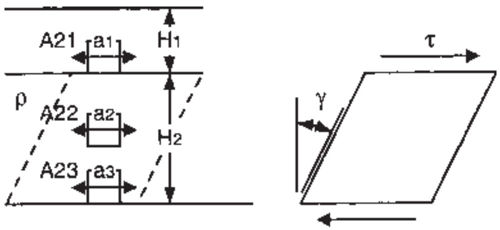

$$\tau = \rho H_1 a_1 + \rho \frac{H_2}{2} a_2, \quad \gamma = \left(-\iint a_1 + \iint a_3\right) / H_2$$

a_i: acceleration, ρ: density, H_i: thickness of layer

Figure 15 Calculation of shear stress and strain from acceleration records. (Modified from Takahashi et al., 2001.)

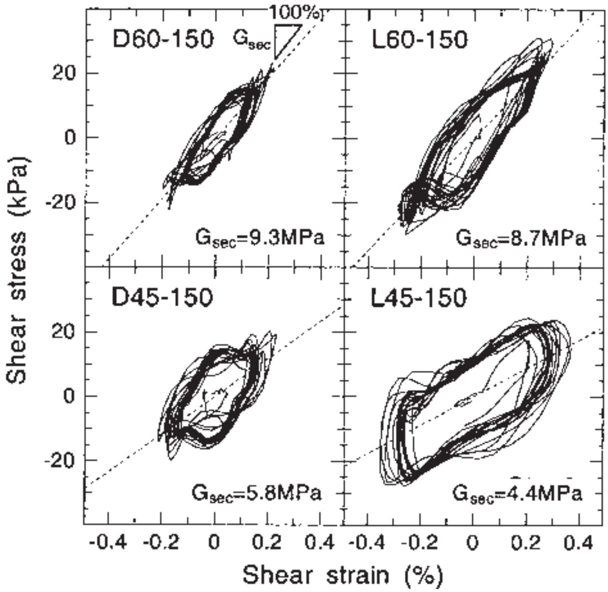

Figure 16 Relationship between shear stress and strain of reinforced zone. (Modified from Takahashi et al., 2001.)

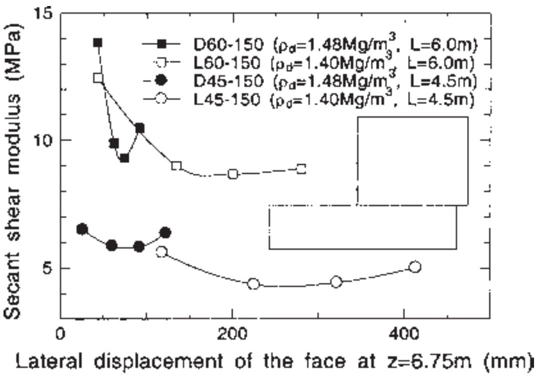

Figure 17 Variation of shear modulus with lateral displacement of facing. (Modified from Takahashi et al., 2001.)

the larger density soil and 3–4% of the wall height for the small density soil, even though the difference of the dry density was about 5%. However, it should be noted that the large horizontal movement of the facing top was caused by both deformation and horizontal translation of the reinforced zone. The cases with lower density showed the larger horizontal translation (Fig. 8) but also showed the larger increase in the residual tensile strains of geogrids as shown in Fig. 12, which clearly implies that the geogrids functioned well in preventing the further deformation of reinforced zone. From these observations it can be said that because the large deformation or failure in the reinforced zone, as seen in D20–150, was prevented, the large horizontal translation occurred instead for the cases with the low density.

4 SUMMARY

This chapter has outlined the advantages and limitations of the centrifuge model tests as a physical modeling on the performance of a reinforced soil structure. Centrifuge model tests on the seismic performance of a geogrid reinforced vertical soil wall done at the Tokyo Institute of Technology are also presented. Because of the small size and high acceleration circumstances, the centrifuge modeling technique has some limitations, both theoretically and technically, which should be taken into account in interpreting the test results. However, as the previous research–including the example presented here–has shown, the centrifuge model tests can provide very useful information, such as failure and deformation mechanisms and even more complicated interaction between soils and reinforcement during earthquakes under well-controlled conditions. Therefore, utilizing the advantages and compensating for the limitations by cooperating with other techniques, such as relatively large-scale gravity models, and analytical and numerical methods, the authors strongly believe that centrifuge modeling will be able to contribute to the further development of technology for earth reinforcement.

REFERENCES

MD Bolton, PLR Pang. Collapse limit state of reinforced earth retaining walls. *Geotechnique* 32(4): 349–367, 1982.

Z Cai, RJ Bathurst. Seismic-induced permanent displacement of geosynthetic-reinforced segmental retaining walls. *Can. Geotechnical J.* 33: 937–955, 1996.

MCR Davies, AM Jones. Stability of a steep excavation retained by soil nails. *Proc. Centrifuge* 98(1): 773–778, 1998, Tokyo, Balkema.

T Kimura. Development of geotechnical centrifuge in Japan. *Proc. Centrifuge* 98(2): 945–954, 2000, Tokyo, Balkema.

Y Koga, O Matsuo. Shaking table tests of embankments resting on liquefiable sandy ground. *Soils and Foundations* 30(4): 162–174, 1990.

J Koseki, Y Munaf, F Tatsuoka, M Tateyama, K Kojima, T Sato. Shaking and tilt table tests of geosynthetic-reinforced soil and conventional-type retaining walls. *Geosynthetics Intl* 5(1): 73–96, 1998.

HI Ling, D Leshchinsky, EB Perry. Seismic design and performance of geosynthetic-reinforced soil. *Geotechnique* 47(5): 933–952, 1997.

M Matichard, JC Blivet, J Garnier, P Delmas. Etude en grandes deformation d'ourages de soutenement reinforces par geotextile. *Proc. Centrifuge* 88: 273–282, 1988, Paris, Balkema.

JK Mitchell, M Jabber, CK Chen, ZK Hua. Behavior of reinforced soil walls in centrifuge model tests. *Proc Centrifuge* 88: 259–271, 1988, Paris, Balkema.

J Nishimura, T Hirai, K Iwasaki, Y Saitoh, M Morishima, H Shintani, S Yoshikawa, H Yamamoto. Earthquake resistance of geogrid-reinforced soil walls based on a study conducted following the southern Hyogo earthquake. *Proc. Intl. Symp on Earth Reinforcement* 1: 439–444, 1996, Kyusyu, Balkema.

M Satoh, Y Shamoto, JM Zhang, K Hayashi. Aseismic evaluation of geogrid-reinforced embankments with steep slope using centrifuge modeling. *Proc. JSCE* 523/III-32: 151–161, 1995, (in Japanese).

M Satoh, Y Shamoto, JM Zhang. Aseismic evaluation of geogrid-reinforced embankments. *Proc. Centrifuge* 98(1): 761–766, 1998, Tokyo, Balkema.

AN Schofield. Cambridge geotechnical centrifuge operations. *Geotechnique* 30(3): 225–268, 1980.

CK Shen, Y Kim, S Bang, JF Mitchell. Centrifuge modeling of lateral earth support. J. of GTE. *ASCE* 108 GT9: 1150–1164, 1982.

CK Shen, XS Li, CWW Ng, PA Van Laak, BL Kutter, K Cuppel, RC Tauscher. Development of a geotechnical centrifuge in Hong Kong. *Proc. Centrifuge* 98: 13–18, 1998, Tokyo, Balkema.

A Takashashi, J Takemura, J Izawa. Dynamic behavior of vertical geogrid-reinforced soil during earthquake. *Proc. Intl. Symp. on Slope Stability Eng* 2: 991–996, 1999, Matsuyama, Balkema.

A Takahashi, J Takemura, T Shimomura. Seismic performance of reinforced earth wall with geogrid. *Proc. Intl. Conf. SMGE.* 2: 1265–1268, 2001, Istanbul.

J Takemura, T Kimura, N Suemasa. Development of earthquake simulators at Tokyo Institute of Technology. *Technical Report, No.* 40: 41–60, 1989.

J Takemura, A Takahashi, Y Aoki. Development of horizontal-vertical 21 shaker in a centrifuge. *Proc. ICPMG* 02: 163–168, 2002, St. John's, Balkema.

E Taniguchi, Y Koga, I Morimoto, S Yasuda. Centrifuge model tests on reinforced embankments by non-woven fabric. *Proc. Centrifuge* 88: 253–258, 1988, Paris, Balkema.

F. Tatsuoka M. Okahara, T. Tanaka, K. Tani, T. Morimoto, and M.S.A. Siddiquee. Progressive failure and particle size effects in bearing capacity of a footing in sand ASCE Geotechnical Eng. Cong. 1991, Vol II (Geotechnical Special Publication 27). 788-802 1991

F. Tatsuoka, M. Tateyama, and J. Koseki. Performance of soil retaining walls for railway embankments. Soils and Foundations, Special Issue on Geotechnical Aspects of the Jan. 17, 1995 Hyogoken-Nambu Earthquake, 311-324, 1996

RN Taylor. *Geotechnical Centrifuge Technology*. Blackie Academic & Professional, 1995.

TF Zimmie, D Anirban, MB Mahmud. Study of geosynthetic interface friction. *Proc. Centrifuge* 94: 301–306, 1994, Boulder, Balkema.

22

Performance and Analysis of Arifiye Overpass Reinforced Earth Walls During the 1999 Kocaeli (Turkey) Earthquake

C. Guney Olgun and James R. Martin II
Virginia Tech, Blacksburg, Virginia, U.S.A.

ABSTRACT

Following the August 1999 earthquake in Kocaeli, Turkey ($M_W = 7.4$), the authors performed field investigations in the affected area to document the performance of improved soil sites and mechanically stabilized embankments. The seismic performance of a pair of conventional reinforced earth walls constructed of steel strips and compacted granular backfill is described here. The walls performed well, suffering only minor damage, despite being subjected to severe ground shaking and large ground displacements. Static and dynamic numerical analyses were performed to investigate the factors contributing to this performance. The analyses were successful in predicting the observed wall behavior. The results suggest that conventionally designed reinforced earth walls perform relatively well during strong ground shaking and that displacement may be the controlling criterion as opposed to shear failure/collapse.

1 INTRODUCTION

An earthquake of magnitude $M_W = 7.4$ struck northwestern Turkey on August 17, 1999, resulting in widespread destruction and loss of life. Peak accelerations of up to 0.4 g were measured in areas near the fault. Following the earthquake, the authors traveled to Turkey to document the field performance of improved soil sites and mechanically stabilized embankments (MSE) in the affected area. Five soil improvement sites were studied in detail, and more than 10 MSEs were investigated. The findings indicated that improved soil sites and MSE walls performed well in most cases. Of particular significance was the performance of two reinforced earth (RE) walls located at the site of the Arifiye Bridge overpass. These walls performed well and suffered little damage despite being subjected to strong ground shaking and large ground displacements.

The Arifiye Bridge is located along the Trans European Motorway about, 10 Km south of the town of Adapazari, as shown in Fig. 1. The site is located at the zone of energy release, as the surficial fault rupture passed directly beneath the site. The bridge, which was constructed in 1988 and destroyed in the 1999 earthquake, consisted of four simply supported spans resting on approach abutments and three mid-span pier supports. The two wing walls of the northern approach abutment were constructed using conventional reinforced earth (RE)

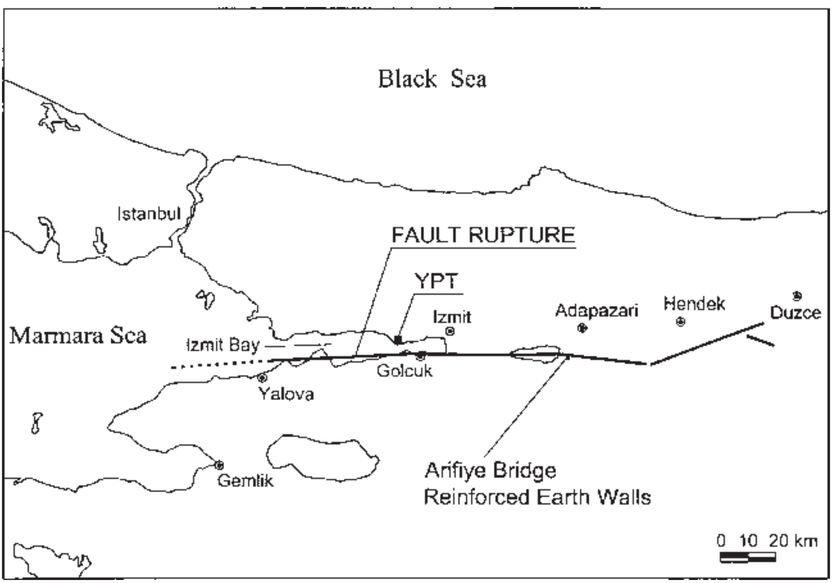

Figure 1 Setting of the Kocaeli earthquake (August 17, 1999).

with steel strips and compacted granular backfill. The abutment was supported on piles, and the RE walls and approach fills rested on a thin layer of fill overlying natural ground.

Four spans of the bridge collapsed in a “sawtooth” manner due to lateral displacements of the peirs and abutments, along with inadequate beam seat widths. However, the RE walls remained intact and experienced relatively little damage. In fact, the minor damage that occurred was associated with the settlement/partial collapse of a culvert that ran beneath the wall and caused a loss of foundation support beneath one section of the wall. This resulted in separation and loss of interlocks between some of the lower wall panels, which, in turn, caused some minor spillage of backfill material. The damage was not at all associated with internal shearing mechanisms of the walls.

Because there are few data regarding the seismic field performance of RE walls, the authors recognized the importance of this site and documented the behavior, including measurements of wall displacements and fault-related ground movements. The subsoil conditions and construction plans for the walls were also obtained during the investigation. These data made it possible for the authors to perform numerical analyses to predict the observed wall behavior. This chapter provides a description of the RE walls and their seismic performance, along with the methodology and results of a detailed numerical analysis. The study is thought to provide important insight into RE behavior under seismic loading and yield data that can be used to improve our predictive capabilities and design procedures.

2 CASE STUDY: ARIFIYE BRIDGE OVERPASS

The Arifiye Bridge overpass, which was constructed in 1988 and destroyed in the 1999 earthquake, consisted of four simply supported spans resting on approach abutments and three mid-span pier supports. The site is located along the Trans European Motorway at the zone of energy release, as the surficial fault rupture passed directly beneath the site; see Fig. 1. A schematic of the site developed from an aerial photograph taken by the authors is shown in Fig. 2.

The wing walls of the northern approach abutment were constructed using reinforced earth (RE). The RE walls were 10 m high and of conventional design, consisting of square, interlocking reinforced concrete panels as facing elements. The panels were 150 cm × 150 cm in the frontal area, and the reinforcing elements were ribbed, galvanized steel strips with a cross section of 40 mm × 5 mm. Typically, four strips were used per panel at a horizontal spacing of 75 cm. The backfill soil was of good quality, consisting of sand and gravel that was compacted in lifts during wall construction. A cross section of the maximum section of the double-walled abutment is given in Fig. 3. The abutment

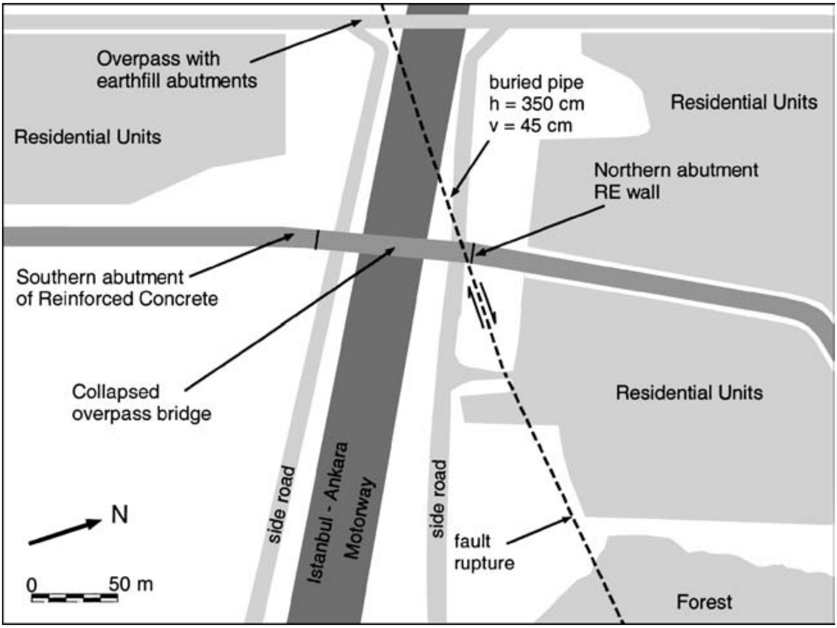

Figure 2 Plan view of Arifiye overpass and the fault rupture trace.

was supported on piles, and the RE wing walls and approach fills rested on 1 m of fill overlying natural ground. As can be seen, the foundation soil originally had a moderate slope that was leveled for construction. The base of the left wall is 75 cm higher than the right wall. A reinforced concrete culvert of 4.8 m width passed beneath the RE wall. The culvert is located in a creek channel that runs beneath the site.

2.1 Subsoil Conditions

The Arifiye wall site is situated within a deposit of Quaternary alluvial sediments. Soil borings obtained from State Highway Directorate, along with CPTs and shear wave velocity measurements performed for this study, indicate the presence of alternating layers of medium clay and medium sand with the water table at a depth of about 5 m. A typical CPT that extends to a depth of 25 m is shown in Fig. 4.

It can be seen that the upper 8 m of the profile consist of 1 m of fill underlain by a 2 m-thick medium clay layer that is underlain by a 1 m-thick medium-dense sand stratum. A loose silty sand layer is found between

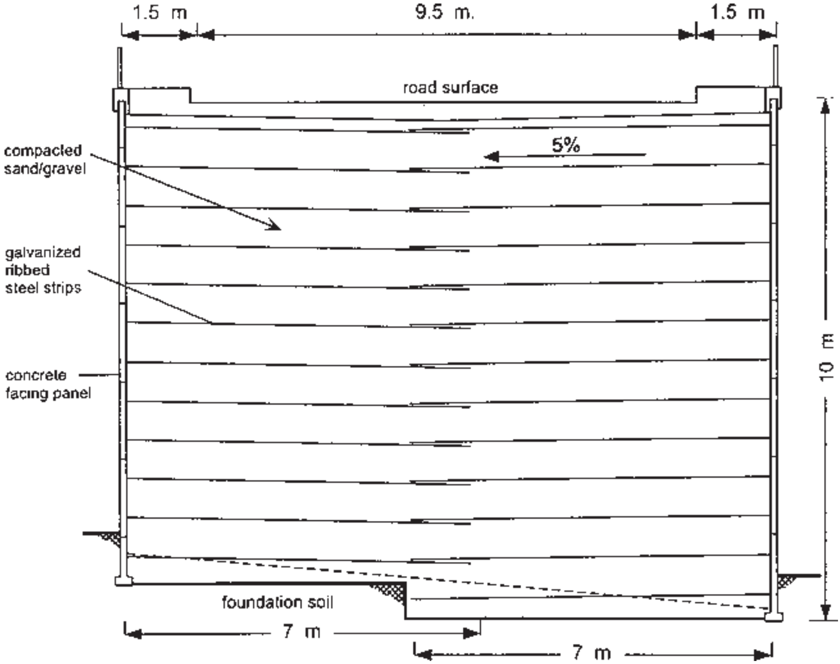

Figure 3 Cross section of the Arifiye reinforced earth walls.

the depths of 5 m and 8 m. A medium clay stratum extends from the depth of 8 m down to 25 m, where the CPT was terminated. The shear wave velocities increase gradually with depth and average about 150 m/s throughout the 25 m profile. It should be noted that based on the CPT resistances and shear wave velocities, the upper medium-dense and silty sand layers found between the depths of 3 m and 8 m are susceptible to liquefaction under moderate to strong ground shaking.

2.2 Observed Field Performance

Field reconnaissance for the Arifiye Bridge site was performed a few days following the earthquake. The closest accelerometer was located about 10 km away in Adapazari, where the maximum accelerations were measured at 0.4 g. The soil conditions at the bridge site, however, are different than those found at Adapazari, and less localized amplification would be expected. It is thought that the accelerations at the Arifiye Bridge were probably closer to those near Izmit, in the range of 0.3 g. In addition to significant shaking, ground

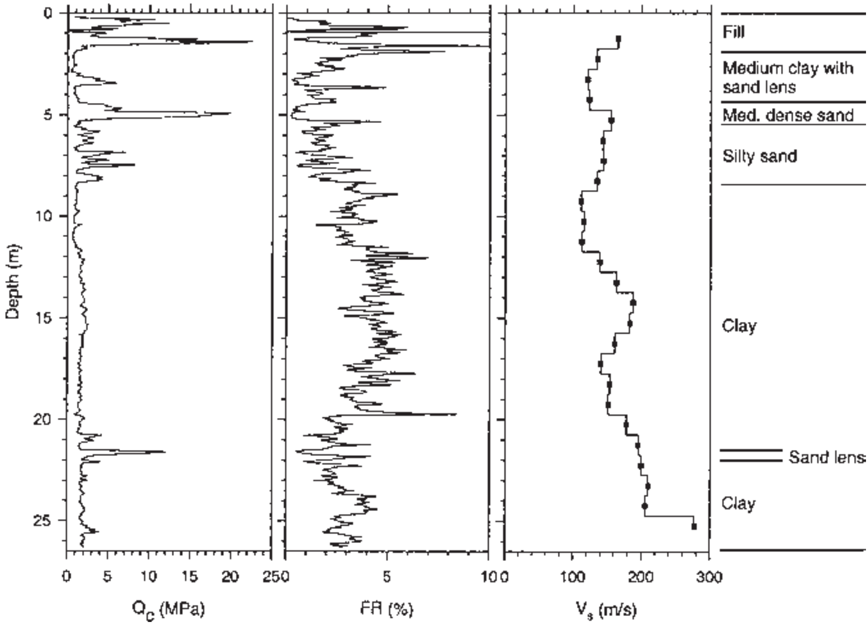

Figure 4 Subsoil profile from SCPT soundings.

displacements within a few meters of the RE walls were large, as the surficial fault rupture passed between the northern abutment and the center pier (see Fig. 2). Maximum horizontal and vertical ground displacements near the northern abutment were estimated at 350 cm and 45 cm, respectively. These movements were inferred from the measured displacement of a buried pipe that was ruptured by the fault about 50 m from the wall. Four spans of the bridge collapsed in a "sawtooth" manner due to lateral displacements of the piers and abutments, along with inadequate beam seat widths.

In addition to fault-related lateral movement, up to 25 cm of vertical movement occurred in the section of the wall overlying the culvert. The culvert appears to have settled during the earthquake, probably due to the presence of soft and/or liquefiable creek bed sediments that were noted above. The resulting differential wall settlement caused the facing panels to become separated and misaligned, which allowed spillage of some backfill material. The maximum out-of-plane panel displacement was about 10 cm. The differential wall movement may have also been related to the fact that the culvert created a discontinuity in foundation conditions beneath the wall.

The most notable overall observation was the relative lack of significant damage to the RE walls despite being subjected to strong ground shaking and large displacements. In stark contrast to this behavior, a conventionally constructed approach embankment located about 250 m from the RE wall suffered heavy damage during the earthquake, experiencing settlements of more than 1 m. The good performance of the RE walls is thought to be particularly meaningful in demonstrating the seismic stability of conventionally constructed walls of this type.

3 NUMERICAL ANALYSES

Numerical analyses were performed to provide insight into the Arifiye Bridge RE wall behavior and to calibrate our numerical model for a series of parametric analyses to be performed later. The commercially available program FLAC (fast Lagrangian analysis of continua) was used for these analyses. FLAC uses an explicit finite-difference scheme to solve static and dynamic problems. Although some aspects of RE wall behavior are three-dimensional, the aspects important to this study are captured with two-dimensional analyses, and thus the two-dimensional version of FLAC (FLAC2D) was used and a plane strain condition was assumed.

The FLAC program offers several structural elements such as cable elements, beam elements, and pile elements to represent structural members in geotechnical engineering problems. Interface elements are provided to define the interaction of the structural elements with the immediate media around (Itasca Consulting Group, 2000).

For this study, cable elements were utilized to model the strip reinforcements. Cable elements are defined by their axial strength and axial stiffness properties as well as the interface characteristics between the cable and the surrounding media. Facing panels were modeled using beam elements where the flexural stiffness properties are formulated. Interface elements are used to define the connectivity between the facing panel and the backfill soil.

The analyses considered the pre-earthquake condition of the wall by modeling the wall construction in a static condition, as well as a dynamic phase that stimulated earthquake shaking. The static analysis was accomplished in stages stimulating the sequence of construction, followed by the dynamic phase where the model was excited with a recorded acceleration time history from the 1999 Kocaeli earthquake. Details of the analysis procedure and results are discussed below.

4 MODEL GEOMETRY AND INPUT PARAMETERS

A cross section of the highest portion of the double-wall reinforced earth approach embankment was modeled in two dimensions assuming plane strain conditions, as shown in Fig. 3.

At this maximum wall section, the wall is 10 m high and steel strips with a cross-sectional area of 40 mm × 5 mm and length of 7 m were used. Design drawings indicate that the reinforcements were placed with a horizontal-to-vertical grade of 5%. Four strips were used per panel in most cases, although five strips were used per panel for the two lower panels of the maximum wall section being modeled. The embankment is 12.5 m wide, resulting in a 1.5 m reinforcement overlap at the wall center for the cross section considered. As shown in Fig. 3, the reinforcements were not connected at the overlap zone.

For modeling purposes, the cross section was discretized into zones of sizes 18.75 cm × 18.75 cm; see Fig. 5. Thus, the analyzed cross section was divided into 67 zones in the horizontal direction and 53 zones in the vertical direction. This discretization provided sufficient accuracy to capture the stresses and displacements in the soil and reinforcements, while keeping computation time

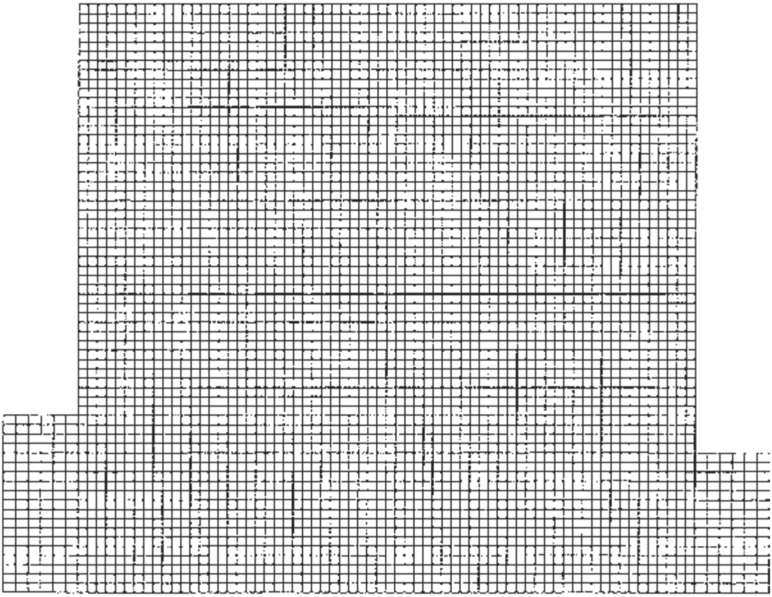

Figure 5 Finite-difference grid used in the static and dynamic analyses.

within practical limits. The asphalt pavement and other structural elements on the top of the wall were not incorporated into the analysis.

The foundation soil and the backfill were modeled using the Mohr–Coulomb model built into the FLAC code. This is an elastoplastic model with a nonassociated flow rule in which the yield surface is defined by the Mohr–Coulomb shear strength criteria. The stress–strain relationship is linear elastic below yielding, and the material attains plastic flow at yielding (Itasca Consulting, 2000). The foundation soil was defined to have a cohesion of 150 kPa, $\phi = 40°$, and a shear modulus of 15,000 kPa. The backfill was assigned a $\phi = 40$ and a cohesion of zero. The stiffness of the backfill was stress level-dependent, and these properties were updated during the analyses at each lift placement. Tangential values of bulk and shear modulus were defined to incrementally follow a hyperbolic stress strain relationship (i.e., Duncan and Chang, 1970; Duncan et al., 1980). In this model, tangential Young's modulus, E, and Bulk modulus, B, are defined as

$$E = \left[1 - \frac{R_f(1 - \sin\phi)(\sigma_1 - \sigma_3)}{2 \cdot (c\cos\phi + \sigma_3 \sin\phi)}\right] K \cdot p_a \left(\frac{\sigma_3}{p_a}\right)^n$$

$$B = K_b \cdot p_a \left(\frac{\sigma_3}{p_a}\right)^m$$

where

K, n: Young's modulus number and exponent.
B, m: Bulk modulus number and exponent.
c, ϕ: Shear strength parameters.
σ_1, σ_3: minor and major principal stresses.
p_a: atmospheric pressure.

Parameters typical of those used in previous numerical studies were selected to define the stress-level dependency of the backfill (Adib, 1988; Schmertmann et al., 1989), as summarized in Table 1.

Interface elements were used to model the connectivity between the backfill soil and the facing panels. In FLAC a contact logic is defined between each side of the interface by the use of normal and shear springs. The interface can be defined between adjacent soil surfaces along discontinuities, or between soil media and structural elements. The shear strength of the interface is defined by Mohr–Coulomb strength parameters. The shear strength of the soil/facing panel interfaces were assigned $\phi = 30°$. Normal and shear spring stiffnesses of these interfaces were defined to be 1.0×10^6 kN/m^2/m and 5.0×10^3 kN/m^2/m, respectively.

Table 1 Model Parameters of the Backfill

Unit weight (kN/m^3)	19.6
Young's modulus number, K	500
Young's modulus exponent, n	0.5
Bulk modulus number, K_b	300
Bulk modulus exponent, m	0.4
Unload modulus number, K_u	800
Failure ratio, R_f	0.80

Steel strips were defined using cable elements in FLAC. Cable elements have a built-in feature that allows the user to define the element connectivity to the soil media without using interface elements. For this project, the shear strength of the reinforcement soil interface is defined to have $\phi = 35°$. The elastic modulus of the steel reinforcements, the cross-sectional area, and the perimeter of the strips were scaled per the actual reinforcement spacing, as recommended by Donovan et al. (1984). This scaling was performed to average out the discrete effect of the reinforcement and convert the system into an equivalent homogenous force system throughout the unit wall width.

5 STATIC ANALYSIS AND RESULTS

A static analysis was used to model the pre-earthquake conditions by simulating wall construction. This phase was important because static equilibrium stresses within the backfill and the reinforcing strips play a major role in the dynamic behavior of mechanically stabilized earth wall systems. Because the wall is built in compacted soil lifts, compaction-induced stresses were modeled in the analyses. It is likely that reinforcement forces especially in the upper layers will be affected by the compaction effort. This is generally true for earth retention systems with inextensible reinforcements (comparably stiffer reinforcements and facing panels) where the structure does not have as much flexibility to deform laterally.

The static analysis was performed by modeling the sequential construction stages used for the walls (as indicated by the actual wall construction plans obtained). Lifts of 37.5 cm thickness (corresponding to two zone levels in the finite difference grid) were placed in stages. The following sequence was followed for each lift placement stage:

1. The lift was placed (by switching the model properties of the corresponding soil zones from null to Mohr–Coulomb), and the system was brought to equilibrium under this additional load,

2. Stiffness and strength values were recalculated under the new stress state,
3. To simulate compaction, a surcharge load of 20 kN/m^2 (tapered to a smaller value near the wall face) was applied at the top of the recently placed lift of soil and the system again brought to equilibrium, and again the stiffness and strength properties were updated,
4. The load was removed and once again the system brought to equilibrium and the strength/stiffness properties were updated.

End-of-construction reinforcement forces calculated during the numerical simulation of wall construction are shown in Fig. 6.

Maximum reinforcement forces at each elevation per unit width (into the page) are presented. For benchmarking purposes, boundary lines are shown in the figure that correspond to reinforcement forces from active and at-rest earth pressures, respectively. These bounds represent the upper and lower bounds used in conventional RE wall design (in general, static design guidelines utilize an approach where the reinforcement forces are determined by computing lateral earth pressures, assumed to be somewhere between active and at-rest, within a given tributary area). Examining the figure, one can see that the maximum

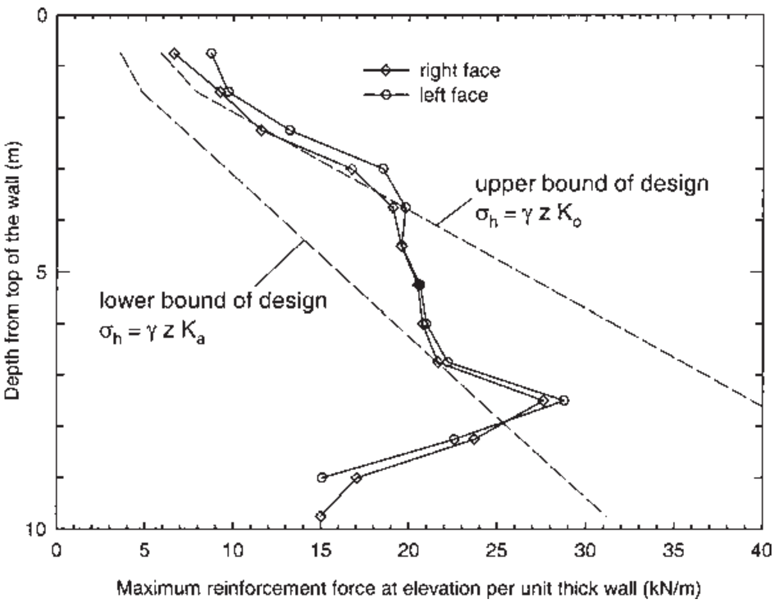

Figure 6 Maximum reinforcement forces following the construction simulation relative to the upper and lower bounds that would be used for static design.

reinforcement forces fall between the active and at-rest bounds in the upper two thirds (6.5 m) of the wall. In the lower third of the wall, however, the maximum reinforcement forces fall below the lower bound. Although not a focus of the present study, it is beneficial to explain this behavior. Design guidelines are based on idea that the horizontal pressures within a certain tributary area are carried by the corresponding reinforcements. Assumed horizontal stresses are based on simple earth pressure theories that assume rigid-plastic behavior. The actual stress deformation pattern within the wall, however, is different and more complicated. Also, sharing of stresses among the reinforcements is more complicated than is assumed by the simple tributary area concept. Lower sections of the wall do not have the same mobility to deform as the upper portions of the wall. These differences result in a decrease in the forces taken by the lower elevation reinforcements, and an increase in the reinforcements in the upper levels (relative to the design values). Other factors that affect the maximum reinforcement forces include the connection of the reinforcement to the facing panel, relative movement between the facing panel and the backfill soil, and passive pressures due to soil retained on the outside of the wall. For instance, the approximate 1 m of wall embedment (see bottom portion of wall in Fig. 3) resulted in a further decrease of reinforcement forces near the bottom of the wall.

6 DYNAMIC ANALYSIS AND RESULTS

A dynamic analysis that stimulated earthquake shaking was carried out following the static analysis. Stiffness of the backfill and the foundation soil were calculated from the end-of-construction stress states based on the above-mentioned relationships. Likewise, the shear strength of the backfill and foundation soil followed the Mohr–Coulomb criteria described above. For these dynamic analyses, deformations are assumed linear-elastic below yielding, and plastic flow is assumed at the yielding stress.

The east–west component of the acceleration time history recorded at the YPT (Yarimca, Petkim) Station during the Kocaeli earthquake was used in the analysis. The YPT Station is about 40 km from the Airfiye site and located on ground conditions similar to those at Arifiye. The acceleration record was baseline-corrected, and frequencies above 15 Hz were removed by low-pass filtering. This processing was needed to ensure that the input motion can be transmitted within the finite-difference grid without being distorted (Kuhlemeyer and Lysmer, 1973). An additional filtering process was performed to attain a zero displacement at the end of the record (these corrections are necessary to minimize errors for displacement-based numerical methods). Acceleration and velocity time histories of the record after filtering are shown in Fig. 7.

It can be seen that the peak ground acceleration reaches 0.27 g and peak ground velocity reaches approximately 0.5 m/s. The input acceleration motion was applied at the base of the model. Free-field boundary conditions were assumed at the sides of the model using the free-field boundary feature built in FLAC. This enabled truncation of the sides of the model close to the wall faces while still maintaining the condition of vertically propagating shear waves.

For the dynamic analysis, several key parameters were monitored throughout the duration of ground shaking. Of primary interest were the displacements along both faces of the wall and the wall centerline, and the maximum forces along the length of the reinforcements. The deformed shape of the grid at the end of shaking is shown in Fig. 8.

It can be seen that the wall settled along the centerline and bulged laterally near the base. A predicted maximum permanent lateral deformation of 16 cm occurred about one third of the wall height above the base. This prediction agrees well with the actual measured peak lateral displacement of 10 cm that occurred near the bottom of the wall. Displacements for both faces of the wall were monitored versus time during the analysis at many locations; see Fig. 9.

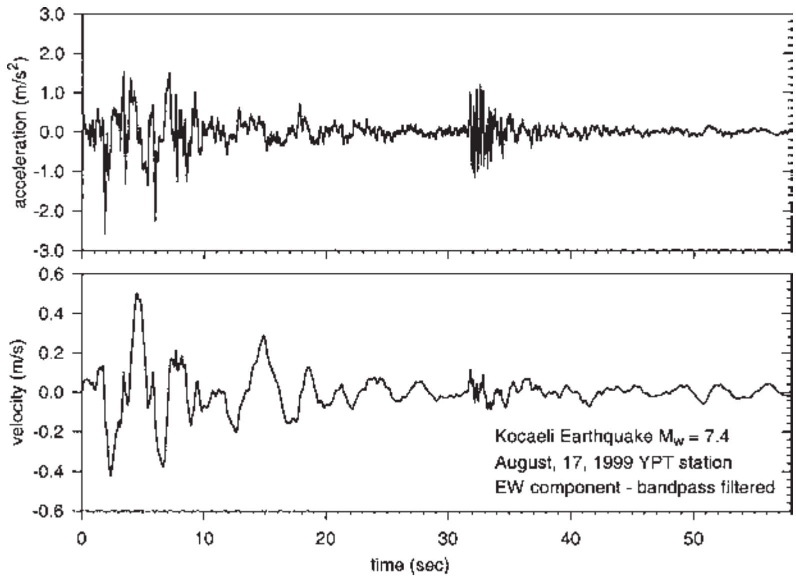

Figure 7 Acceleration and velocity time history used in the analyses—Kocaeli earthquake YPT Station EW component (record above is bandpass filtered and baseline corrected).

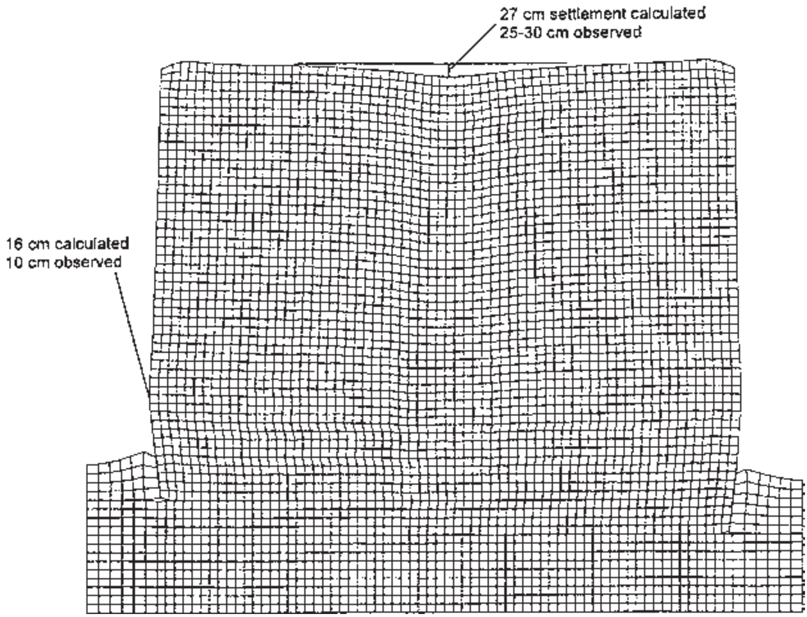

Figure 8 Deformed shape of the finite-difference grid after shaking (no exaggeration) and comparisons between predicted and observed displacements.

The results are provided Figs. 10 and 11 in the form of displacement time histories for the right and left wall faces, respectively. As expected, the time histories suggest that the majority of the deformations developed during the stronger ground shaking (initial 10 sec). The predicted top-of-wall settlement (along the centerline) was 27 cm, due primarily to the lateral deformation of the system. This settlement prediction is consistent with the observed settlement that was estimated in the rang of 25–30 cm.

The predicted maximum reinforcement forces that developed during shaking are presented in Fig. 12. The values shown are the maximum forces per unit wall width (1 m into the page). It can be seen that the predicted reinforcement forces are relatively high at the lower levels of the wall, at almost 150 kN/m. This dynamically induced value exceeds the reinforcement design values (for static design) by a factor of more than 2.

Finally, it was noted in the analyses that no slip surface or failure wedge developed in the backfill, although enough vertical and horizontal displacement occurred to present potential serviceability problems for the walls. The predicted settlement of the overlying roadway was substantial, for instance. Also,

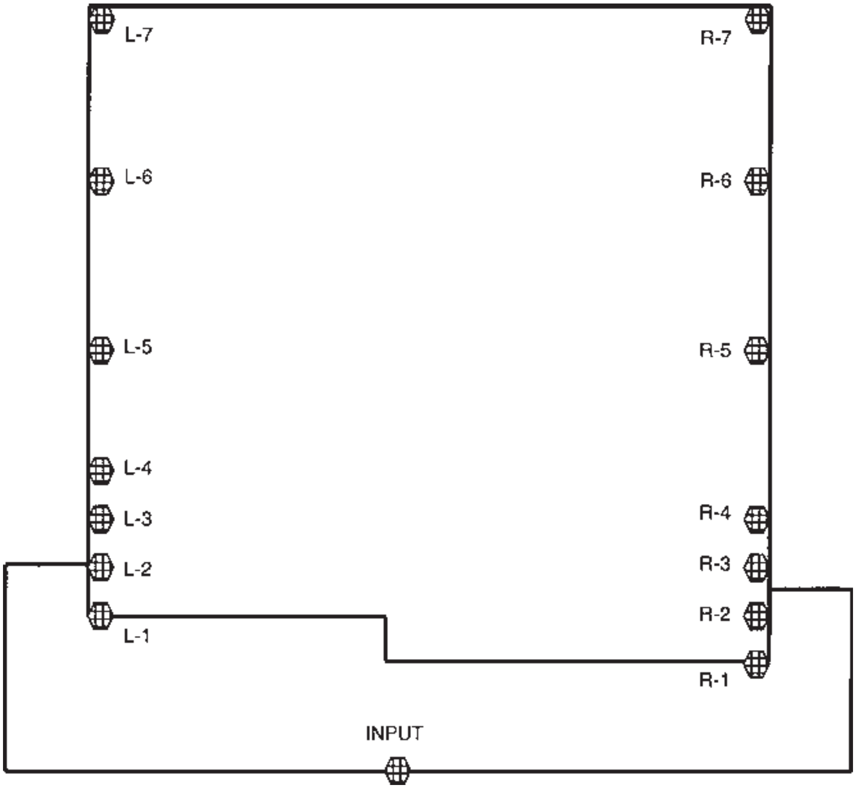

Figure 9 Locations where displacement time histories were calculated during the dynamic analysis.

the analyses indicated that it is likely that enough out-of-plane movement of the facing panels would occur to allow spillage of the backfill long before a pronounced slip surface would develop. Thus, in terms of the overall seismic performance of RE walls, the numerical analyses suggest that displacement is likely to be the controlling criterion as opposed to shear failure.

7 SUMMARY AND CONCLUSIONS

Following the August 1999 Kocaeli, Turkey, earthquake ($M_W = 7.4$), the authors performed investigations in the affected area to document geotechnical field performance. The study focused on the performance of improved soil sites and

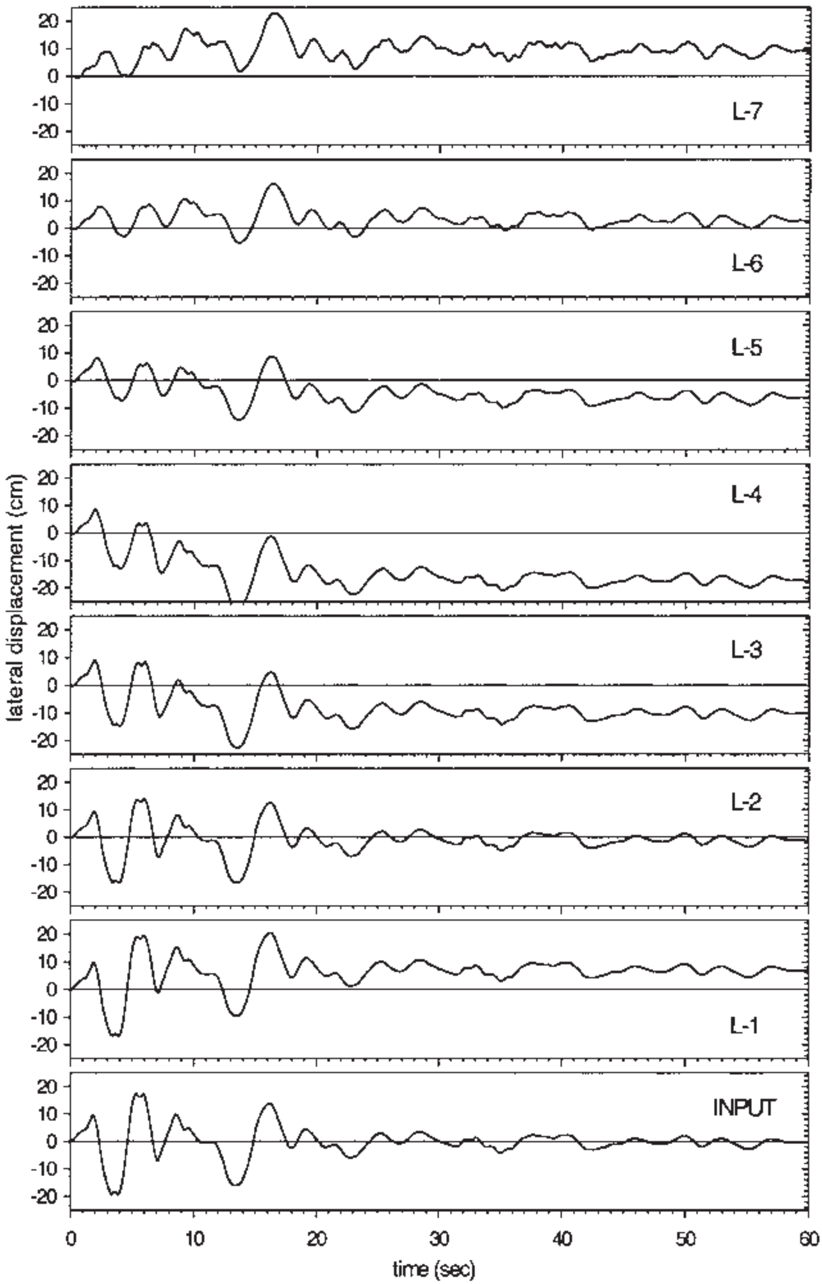

Figure 10 Displacement time histories along the left face of the wall (see key in Figure 9). Predicted maximum displacement was 16 cm, and the actual displacement was 10 cm.

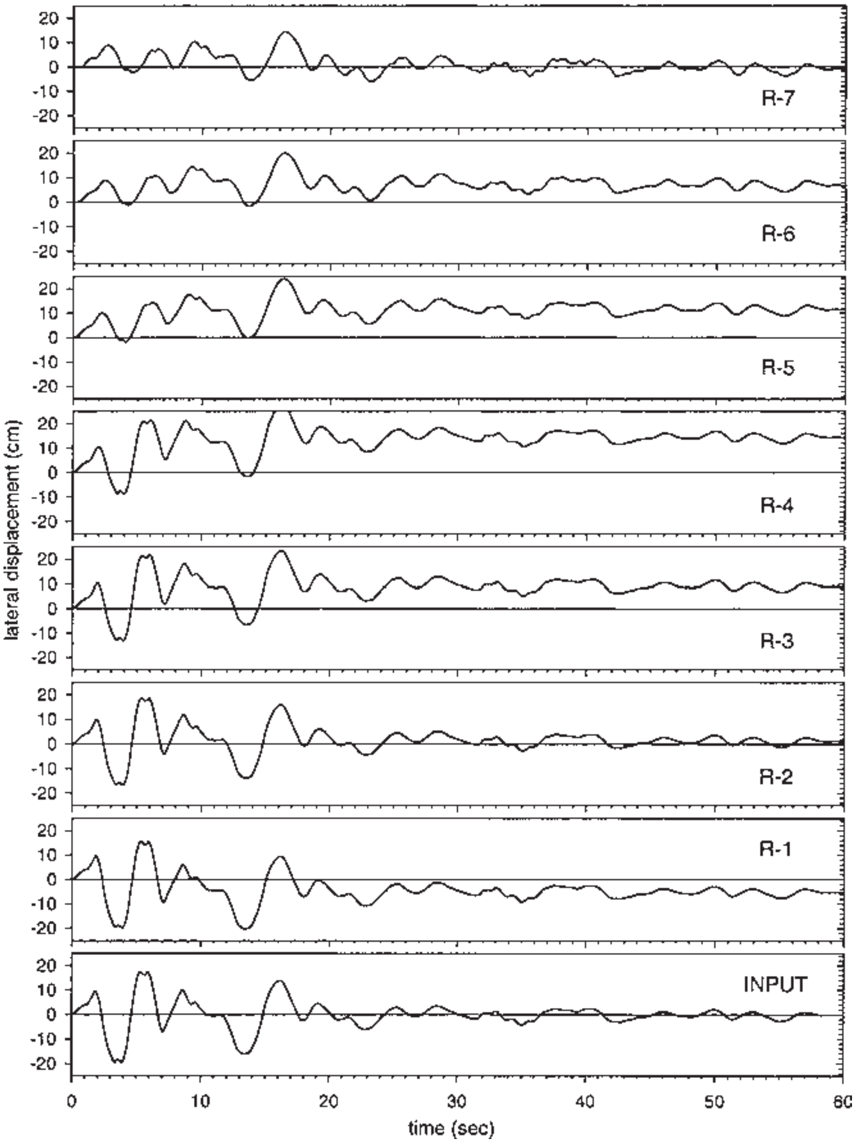

Figure 11 Displacement time histories along the right face of the wall. Predicted maximum displacement was 16 cm, and the actual displacement was 10 cm. (See key in Figure 9.)

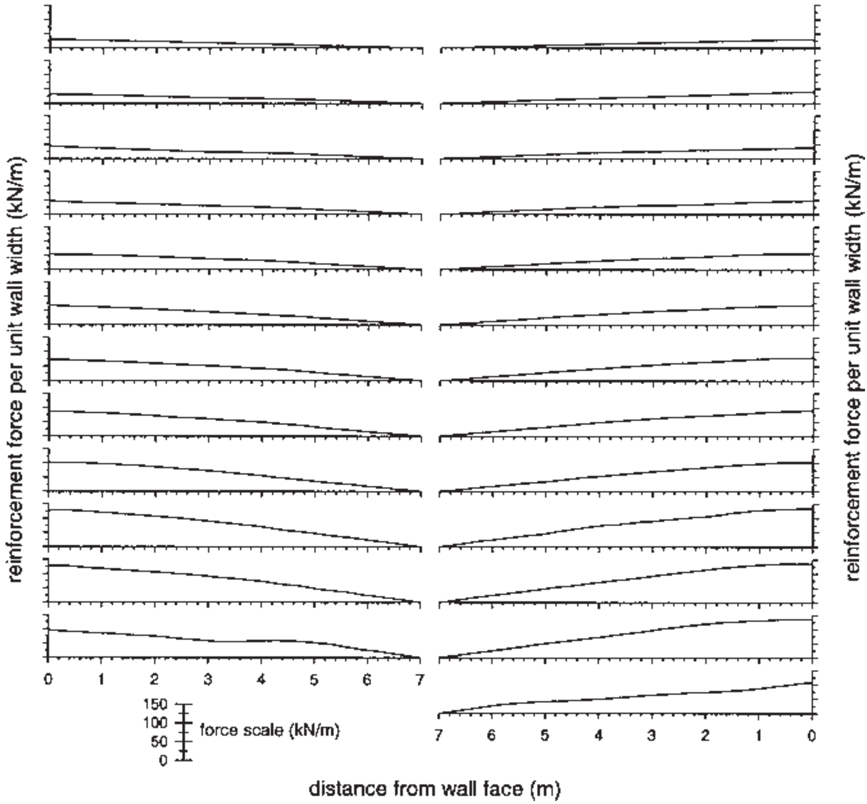

Figure 12 Computed maximum reinforcement forces that developed along the strip during shaking.

mechanically stabilized embankments (MSEs). Of particular significance was the performance of two reinforced earth (RE) walls located at the site of the Arifiye Bridge overpass. These walls, constructed of steel strips, concrete facing elements, and compacted granular fill, performed well and suffered little damage despite being subjected to ground shaking and large fault-rupture related ground displacements nearby. Numerical analyses were performed to investigate the factors contributing to this performance. Both the field documentation of the walls as well as the numerical analyses provided important insight into RE wall behavior under seismic loading.

The principal findings from the study are as follows:

1. The RE wall system at the Arifiye Bridge overpass is an important case history that highlights the seismic performance of reinforced earth

walls. The walls, constructed of steel strips and compacted select backfill, performed well despite being shaken with ground accelerations $>0.3\,g$ in an M7.4 event and being subjected to fault-related ground displacements of 350 cm that occurred almost adjacent to the wall. An unreinforced earthen embankment about 250 m from the wall suffered heavy damage, settling more than 1 m.

2. Following the earthquake, the maximum permanent lateral movement of the RE facing panels was about 10 cm, and this occurred at about one third the wall height above the base. The settlement along the centerline of the double-wall system was estimated at 25–30 cm, primarily due to the lateral building of the system.
3. The earthquake-induced RE wall deformation pattern and displacement magnitudes were successfully predicted using the computer code FLAC assuming two-dimensional, plane strain conditions. The predicted deformation pattern was one of significant settlement along the double-wall centerline, and lateral bulging with peak displacements occurring at about one third the wall height above the base. This predicted deformation was consistent with the observations. In terms of the displacement magnitudes, a maximum lateral wall displacement of 16 cm was predicted, compared to an observed value of 10 cm. The predicted settlement along the centerline of the double-wall system was 27 cm, consistent with the observed value of 25–30 cm. The static analysis was conducted using a Mohr–Coulomb soil model and hyperbolic soil stiffness criteria, and the dynamic analysis assumed an elastoplastic model that assumed linear behavior up to the yield stress, and plastic behavior beyond this value.
4. Pre-earthquake stress conditions determined during a static analysis that simulated wall construction were important in terms of correctly estimating the final earthquake-induced stresses and forces in the RE system.
5. Permanent vertical and lateral displacements probably developed during the strong part of shaking (first 10 sec), as indicated by predicted displacement time histories calculated for different locations and elevations along the walls.
6. The numerical analysis indicate that the earthquake shaking significantly increased the forces in the steel reinforcement strips, especially in the lower third of the walls. Maximum reinforcement forces reached values about two to three times those existed at the end of construction at the upper and lower elevations, respectively. Even though these numbers indicate that the some of the steel strips reached their yield strength and some slip probably took place, the system integrity was maintained by a large margin.

7. Displacement is likely to be controlling criterion for the seismic performance of RE walls, as opposed to shear failure or collapse. From a seismic standpoint, RE walls behave as flexible systems. In the numerical analyses, no slip surface or failure wedge developed in the backfill, although enough settlement and horizontal displacement occurred to present potential serviceability problems for the walls. The predicted settlement presented a potential problem for the overlying roadway. Similarly, the analyses predicted that it is likely that enough out-of-plane movement of the facing panels to allow backfill spillage would occur before a pronounced slip surface can develop.
8. Well-designed conventionally constructed RE walls (steel strips and compacted select fill) with good foundations tend to perform well under strong ground shaking.

ACKNOWLEDGMENTS

We would like to express our sincere appreciation to Dr. Turan Durgunoglu of Bogazici University, Istanbul, and Turhan Karadayilar, Canan Emrem, and Serdar Elgun of Zetas Earth Technology Co. and Murat Ozbatir of Reinforced Earth Turkey for their cooperation during the reconnaissance and site investigations performed for this study. Financial support for this study was provided by the National Science Foundation (NSF), Division of Civil and Mechanical Systems, under grant no. 0085281 and by the Earthquake Engineering Center for Southeastern United States (ECSUS) of Virginia Tech.

REFERENCES

ME Adib. Internal lateral earth pressure in earth walls. Ph.D. thesis. Berkeley: University of California, 1988.

K Donavan, WG Pariseau, M Cepak. Finite element approach to cable bolting in steeply dipping VCR slopes. *Geomechanics Application in Underground Hardrock Mining*: 65–90, 1984.

JM Duncan, C-Y Chang. Nonlinear analyses of stress and strain in soils. *Soil Mechanics and Foundations Division, ASCE* 96(5): 1629–1653, 1970.

JM Duncan, P Byrne, KS Wong, P Mabry. Strength, stress-strain and bulk modulus parameters for finite element analyses of stresses and movements in soil masses. Report No. UCB/GT/80–01. Berkeley: Department of Civil Engineering, University of California, 1980.

Itasca Consulting Group, FLAC – Fast Lagrangian Analysis of Continua. User's Manuals for Version 4.0. Minneapolis, MN: Itasca Consulting Group, Inc., 2000.

RL Kuhlemeyer, J Lysmer. Finite element method accuracy for wave propagation problems. *Soil Mechanics and Foundations Division, ASCE* 99(5): 421–427, 1973.

GR Schmertmann, SH Chew, JK Mitchell. Finite element modeling of reinforced soil behavior. Department of Civil Engineering, University of California, Berkeley, Report no. UCB/GT/89-01, 1989.

23

Dynamic Simulation of the Reinforced Slope Failure at Chi-Nan University During the 1999 Chi-Chi Earthquake

Nelson N. S. Chou and Chia-Cheng Fan
Genesis Group/Taiwan, Taipei, Taiwan

ABSTRACT

A reinforced slope, 60 to 80 m high and 180 m long, located at the entrance of the National Chi-Nan University in Pu-Li collapsed during the 1999 Chi-Chi earthquake. Although the Chi-Chi earthquake was the most severe earthquake during the past 100 years in Taiwan, geologic conditions at the site and some design deficiencies may also play roles in the failure of the reinforced slope. Dynamic simulation of the reinforced slope using the FEM software PLAXIS was conducted. The result shows that the slip surface took place along a thin layer of clayey material. The reinforced slope with a low ratio of reinforcement length to height is blamed for the instability of the slope. In addition, the low strength of recompacted backfill of a previous failed slope may also cause failure.

1 INTRODUCTION

The Chi-Chi (also known as Ji-Ji in English) earthquake, with a Richter scale of 7.3, hit the central part of Taiwan at 1:47 a.m. on September 21, 1999. The earthquake caused devastating damage to campus buildings and reinforced slope failure at the National Chi-Nan University in Pu-Li, which is approximately 20 km northeast from the epicenter of Chi-Chi. This chapter analyzes the mechanism of the failure in terms of design aspects, seismic intensity, geological condition, and so forth. In addition, dynamic simulation of failure during the earthquake was performed using the finite-element software PLAXIS.

2 DESCRIPTION OF THE COLLAPSED REINFORCED SLOPE

The collapsed reinforced slope is on the middle part of a cut slope, which is 60 to 80 m high. The collapsed area covers an alignment 180 m long. Pictures of the collapsed reinforced slope induced by the earthquake and topographic condition are shown in Figs. 1 and 2, respectively. The failed area is also shown in Fig. 2. The reinforced slope itself is arranged in four tiers, 10 m high for each tier. The profile of the reinforced slope prior to and after the Chi-Chi earthquake is shown in Fig. 3. According to the field investigation, tension cracks were identified at the overlap portion of the reinforcement, and backfill overflowed between overlaps.

Reinforcements of the reinforced slope at each tier are different in length. The reinforcement is 4 m long on the top level of the reinforced slope and increases gradually to 13 m long on the bottom level of the reinforced slope, as shown in Fig. 3. Vertical spacing of the reinforcement 1 m, and the overlapping length of reinforcement for wraparound is 1.7 m. Some of the reinforcements for wraparound were pulled out at the site.

2.1 Previous Slope Failure at the Site

Previous slope failure at the site took place during construction of the reinforced slope in 1995. Shown in Fig. 4 is the collapsed slope in 1995. A failure plane with hard yellowish clayey material on the back of the reinforced slope can be clearly identified at the site. The clayey material has a thickness of 2 to 3 m according to the field investigation of the failed slope and is considered as a weak plane for the slope. The weak plane has a slope angle of 30° to 35° toward east and is N30°E in strike. In other words, the failed slope is considered a dip slope. The slope failure, in 1995 was induced

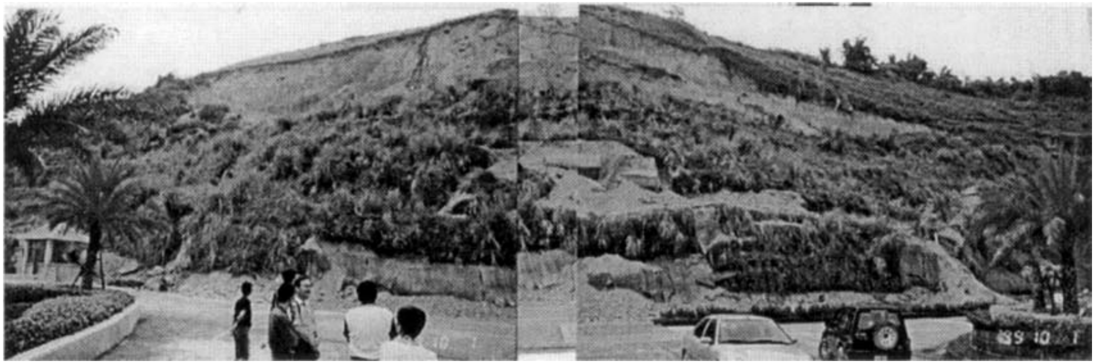

Figure 1 The failed reinforced slope after the Chi-Chi earthquake.

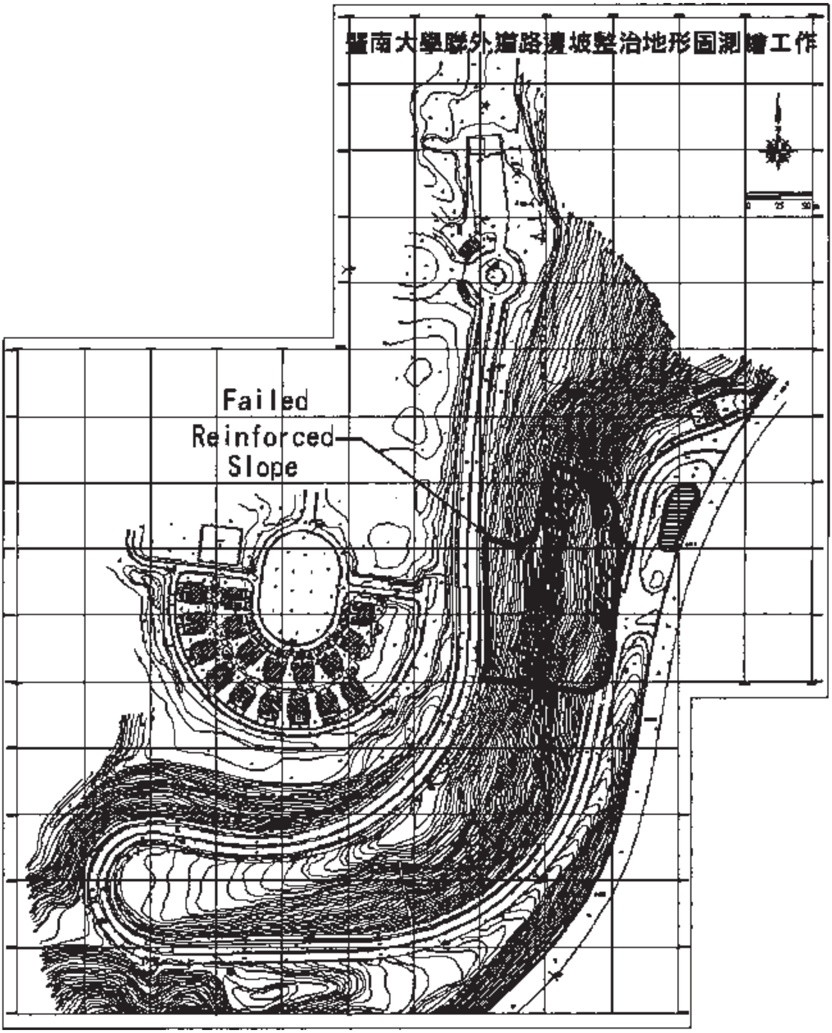

Figure 2 Topography of the site.

by excavation on top of the slope for construction of the road connecting the Chi-Nan University and Route 21. Nevertheless, the reinforced slope was reconstructed in accordance with the original design. The link between the failure that occurred in the earthquake and that in 1995 will also be studied.

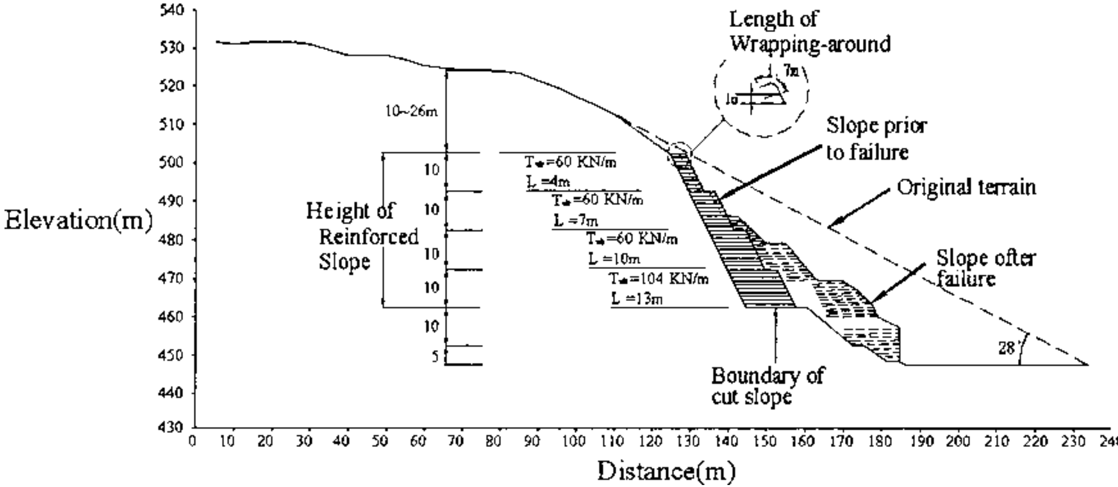

Figure 3 Slope profile prior to and after the earthquake.

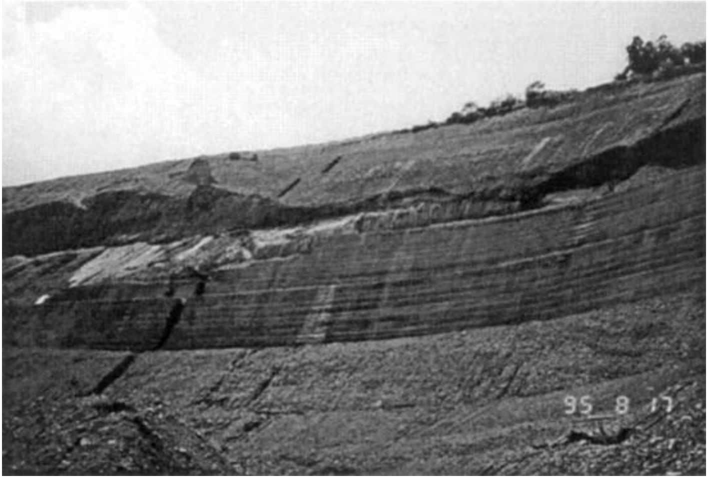

Figure 4 Failure of the reinforced slope during construction in 1995.

3 CHARACTERISTICS OF THE CHI-CHI EARTHQUAKE

The Chi-Chi earthquake with a record high of 989 gal in acceleration (E–W direction) hit the central part of Taiwan on September 21, 1999. Seismic information recorded at the Nan-Kuan elementary school, which is the closest seismograph station to the site, in Pu-Li shows that the peak accelerations for north–south east–west, and vertical directions are 368.4, 585.94, and 270.18 gal, respectively. The time history recorded at this station is shown in Fig. 5.

4 GEOLOGICAL CONDITIONS AT THE SITE

The site is around the rim of Pu-Li basin, a geographic center in Taiwan. The geology at the site is composed of a thick layer of gravel mixed with soil underlain by sandstone embedded with shale. The gravel stratum, however, is embedded with a thin layer of hard clay at a given depth based on the boring investigation. The geological profile at the site of the reinforced slope is shown in Fig. 6. Descriptions and engineering properties of the geological deposits at the site up to a depth of 80 m are as follows:

1. Top soil: brown; tens of centimeters of 2 m in thickness.

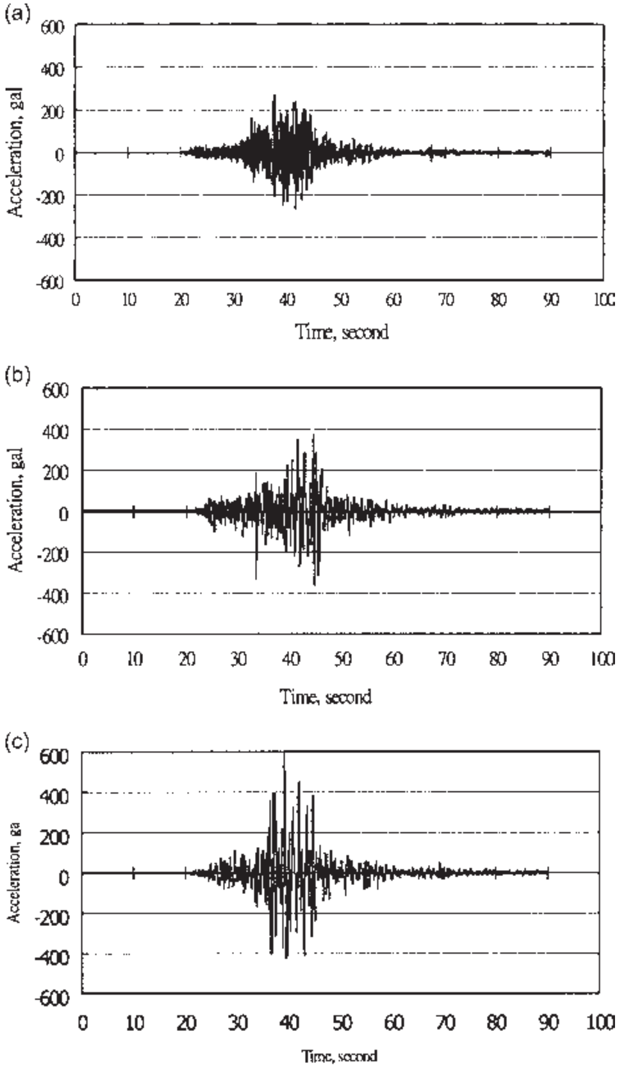

Figure 5 Time history recorded at Nan-Kuan Elementary School, Pu-Li, Nan Tou, during the 1999 Chi-Chi earthquake: (a) vertical; (b) north-south, (c) east-west.

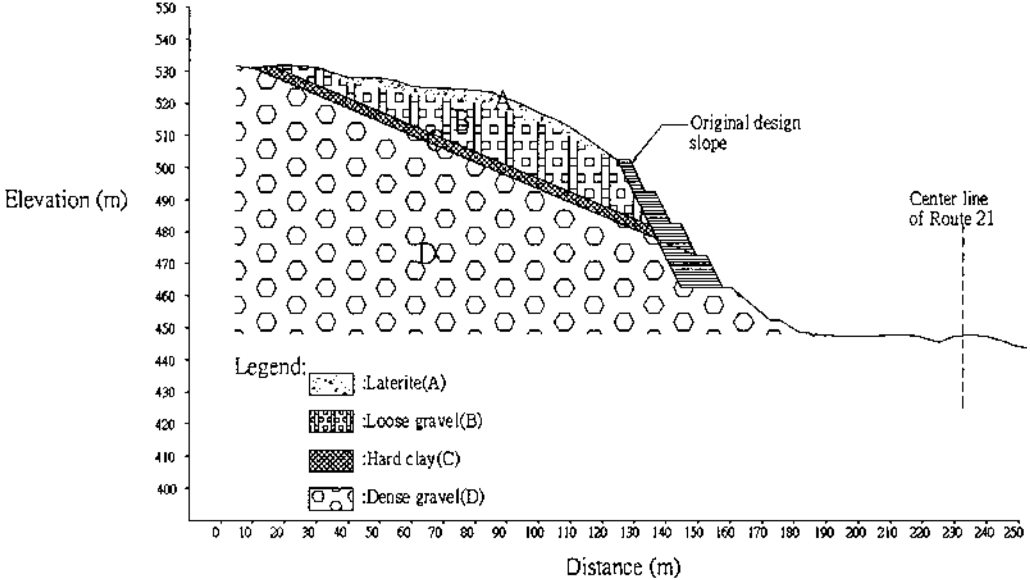

Figure 6 Geological profile at the site of the reinforced slope.

2. Loose gravel deposit: mixed with laterite; 3 to 10 cm in diameter; round.
3. Hard clay: brown; clayey material; 2 to 3 m in thickness; sloping; weak plane with dip angle of 30° to 35° east; strike of the weak plane is approximately N30°E.
4. Dense gravel deposit: mixed with soil with low plasticity; round to subround; gravel size is larger than that in loose gravel deposit.

The hard clay, forming a weak plane with slope angle of 30° to 35° toward east, was first identified at the site during the slope failure in 1995. The weak plane was considered a dip slope for most of the reinforced slope. The groundwater level at the slope area is approximately 55 m to 60 m below the ground surface based on the boring results.

5 DYNAMIC SIMULATION OF THE REINFORCED SLOPE

Dynamic simulation of the reinforced slope subjected to seismic forces is conducted to better understand the process of the failure. The computer program PLAXIS (Plaxis, 1998), which is based on the finite-element method, is used for the dynamic simulation of the reinforced slope during the earthquake. The time history of acceleration, shown in Fig. 5, recorded at the Nan-Kuan elementary school in Pu-Li during the Chi-Chi earthquake is used for the seismic source in

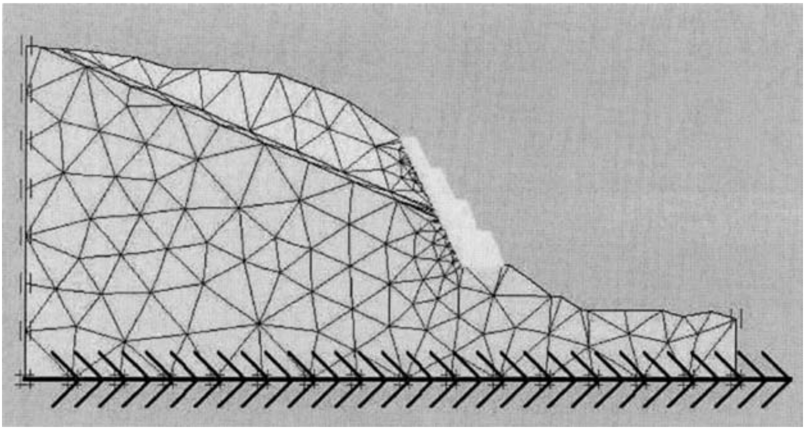

Figure 7 Finite-element mesh for dynamic simulation of the reinforced slope during the 1999 Chi-Chi earthquake (Remark: The arrow symbol shown on the bottom of the mesh is the source of the seismic force).

Table 1 Properties of the Geological Deposits Used in Finite-Element Analysis

	Dry unit weight (kN/m^3)	Unit weight (kN/m^3)	Friction angle (degrees)	Cohesion (kPa)	Young's modulus (kPa)	Poisson's ratio	Shear modulus (kPa)	Shear wave velocity (m/sec)
Backfill	16	20	30	48	35,000	0.3	15,380	97
Loose gravel deposit	17	20	39.4	40	30,000	0.27	11,780	82
Clayey material	18.8	20	30	48	30,000	0.33	11,280	77
Dense gravel deposit	19	21	39.4	70	50,000	0.3	19,230	100

the analysis. Time history of the acceleration in the east–west direction is taken as the seismic input since orientation of the slope is approximately in the direction of north–south.

Properties of the geological deposits used in the finite-element analysis are listed in Table 1. Cohesion of the gravel and backfill, however, are greater than those discussed previously due to the need to maintain the stability of the slope in the gravity loading, which is imposed on the slope to generate initial stress condition in the soil mass. The Mohr–Coulomb constitutive model is used for the geological deposits. The finite-element mesh generated for the reinforced slope and its surrounding area in shown in Fig. 7. The number of nodes, elements, and stress points are 829, 370, and 1110, respectively. Forty layers of reinforcements are input in the finite-element mesh to simulate the reinforced slope. The seismic source is located on the lower boundary of the finite-element mesh. The seismic force lasts for about 90 sec. The groundwater level is not considered in the analysis. Animation of the slope subjected to seismic forces can be created when the calculation is completed. A deformed mesh, however, at four different time steps is illustrated in Fig. 8. In addition, principal directions of displacement of the mesh at different time steps are shown in Fig. 9. The result shows that deformation of the whole soil mass takes place as of the commencement of the earthquake. However, the soil mass above the weak plane starts to move at a greater scale compared to that below the weak plane at approximately the 36th second in the record shown in Fig. 5. The soil mass above the weak plane continues to move downward along the weak plane. In the meantime, the reinforced slope also deforms significantly.

Questions may be raised regarding whether the slope failure initially results from the collapse of the reinforced slope itself or if the weak plane is the primary factor to blame. Fig. 10 shows a vector of the acceleration developing in the slope at different time steps during the earthquake. The result shows that the acceleration at the reinforced slope is much greater than that at other areas. Thus, it hints that the reinforced slope may collapse earlier than other areas in the slope. However, the dynamic simulation conducted herein may not clearly give insightful details about this issue. Nevertheless, failure mechanism of the reinforced slope are summarized and discussed in next section.

6 FAILURE MECHANISM OF THE REINFORCED SLOPE INDUCED BY THE CHI-CHI EARTHQUAKE

According to the field investigation, the location of the slip surface in the Chi-Chi earthquake is close to that which took place in 1995 (Genesis Group/Taiwan, 2000). Thus, the reinforced slope may fail through the backfill during the Chi-Chi earthquake rather than through the existing gravel stratum, which is undisturbed.

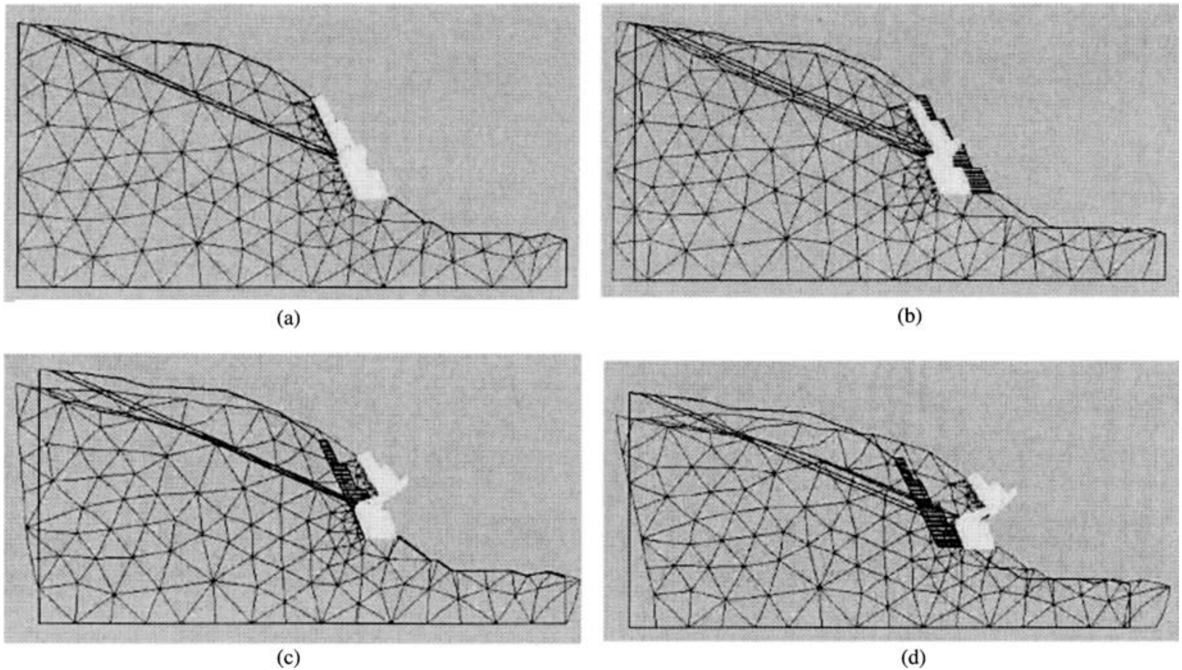

Figure 8 Deformed mesh at different time steps during the 1999 Chi-Chi earthquake: (a) 20th second; (b) 40th second; (c) 60th second; (d) 90th second.

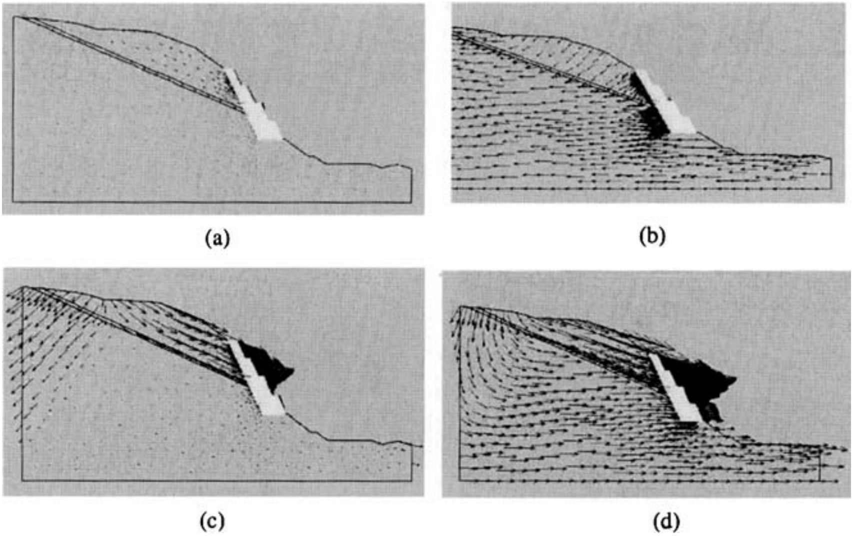

Figure 9 Principal direction of displacement of different times steps during the 1999 Chi-Chi earthquake: (a) 20th second; (b) 40th second; (c) 60th second; (d) 90th second.

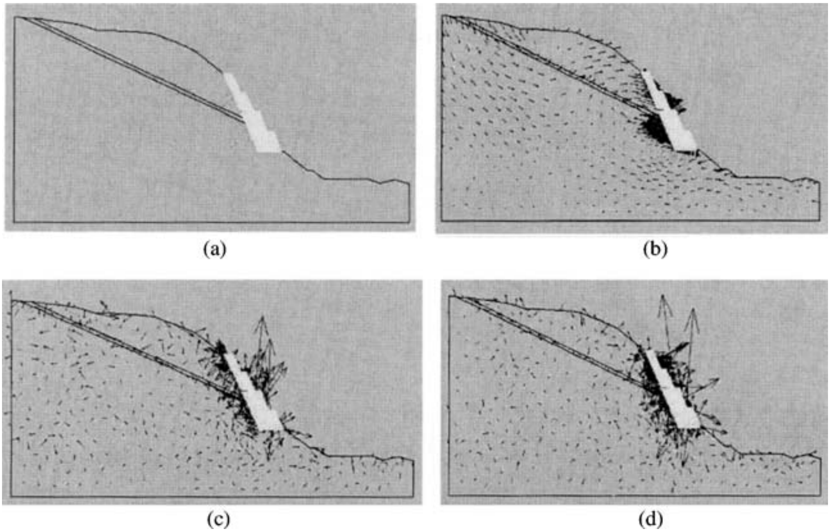

Figure 10 Acceleration in the slope at different time steps during the 1999 Chi-Chi earthquake: (a) 20th second; (b) 40th second; (c) 60th second; (d) 90th second.

Major factors, however, playing a role in the failure of the reinforced slope are summarized as follows:

1. The peak acceleration on the east–west direction is up to 0.58 g, which is much greater than the local earthquake-resistant design criterion ($a_{\max} = 0.23$ g).
2. Soil placed on the back of the reinforced slope was recompacted materials since the slope collapsed in 1995. The strength of backfill on the back of the reinforced slope is less than that of existing gravel stratum. Slope instability may occur much easier in the unreinforced backfill than in the undistributed gravel stratum in the seismic condition.
3. The geologic weak plane locating on the up slope of the reinforced slope may have a direct link with the failure of the reinforced slope during the earthquake. The weak plane is considered as a trigger for the failure of the reinforced slope. Soil mass above the weak plane moves along the plane during the Chi-Chi earthquake.
4. The reinforcement length of the reinforced slope is short compared to the height of the reinforced slope. Reinforcements of the reinforced slope at each tier are different in length. The reinforcement is 4 m long on the top tier of the reinforced slope and increases gradually to 13 m long on the bottom tier of the reinforced slope. The reinforced slope, however, is as high as 40 m. The ratio of average reinforcement length of height of reinforced slope at the failure site is just 0.2, which is much lower than normally acceptable ratios in practice (i.e., 0.6 to 1.0). Thus, the stability of the reinforced slope at the failure site may be on the margin of critical condition in normal condition. The Chi-Chi earthquake may be just the trigger blamed for the failure of the reinforced slope.

7 CONCLUSIONS

The study of a failed reinforced slope, with a height of 60 to 70 m, induced by the Chi-Chi earthquake is conducted in this chapter. The reinforced slope itself is arranged in four tiers, which is 10 m high for each tier, and is located on the middle part of a cut slope. The slope angle of the reinforced slope is 60°. Field investigation, survey, geologic exploration, laboratory tests, and dynamic simulation of the reinforced slope are carried out. Although the Chi-Chi earthquake has been the most severe earthquake during the past 100 years in Taiwan, geologic conditions at the site and some design aspects may also have played a role in the failure of the reinforced slope. Dynamic simulation of the reinforced slope during the earthquake clearly shows that the slip surface takes place along a thin layer of clayey material, which caused the slope failure in 1995. The reinforced slope with a low ratio of reinforcement length to height of the slope may be critical to the stability of the slope. In addition, the recompacted backfill on the up slope of the reinforced slope may also decrease the overall stability of the slope.

REFERENCES

Genesis Group/Taiwan. *Investigation of Failure of the Reinforced Slope at the National Chi-Nan University During the Chi-Chi Earthquake*, interim report, 2000.

BV Plaxis, *PLAXIS: Finite Element Code for Soil and Rock Analyses*, RBJ Brinkgreve, PA Vermeer, eds., 1998.

C-L Cheng. Ground dislocation caused by the Chi-Chi earthquake. *Proc. Failure Investigation for Chi-Chi Earthquake in 1999*, Tainan, Taiwan, IV-1–IV-22, 1999 (in Chinese).

24

A Compact Probabilistic Representation of the Chi-Chi Earthquake Ground Motion

A. W. Smyth
Columbia University, New York, New York, U.S.A.

S. F. Masri
University of Southern California, Los Angeles, California, U.S.A.

C. H. Loh
National Center for Research on Earthquake Engineering, Taipei, Taiwan

ABSTRACT

A previously developed procedure to condense nonstationary random excitation data to perform analytical random vibration response studies is used to investigate the 1999 Chi-Chi (Taiwan) earthquake, recorded ground motions. An ensemble of free-field ground motion records from the main earthquake event collected from locations near the Chelungpu fault were used to create the second, order statistics of the earthquake excitation. Using the compaction procedure, the covariance matrix of the excitation process was spectrally decomposed by the Karhunen–Loeve expansion. The dominant eigenvectors, that is, those with the largest eigenvalues, represent the dominant energy time histories in the random process and can be used to characterize the dominant features of the earthquake process. Second-order descriptions of the transient dynamic response of discrete systems to the compact form of the earthquake process are obtained. This type of result can be used to facilitate

improved design standards for civil structure and to perform reliability studies. A comparison is made of the preliminary results of this study and those obtained from a similar analysis performed on an ensemble of ground motions from the 1994 Northridge earthquake.

1 INTRODUCTION

Given the proliferation of dense seismic arrays around the world, it is possible to glean statistical information about the characteristics of major seismic events and their potential effects on structural designs. An analysis procedure developed by Masri et al. (1990), and later generalized in Smyth (1998) and Masri et al. (1998) for the representation and transmission of random excitation processes, provides a new tool to characterize strong ground motions from large data sets. For details of this analytical compaction, representation, and transmission procedure, the reader is referred to Masri et al. (1998). In summary, the method involves two main stages of compaction of the random excitation data. The first stage is based on the spectral decomposition of the covariance matrix by the orthogonal Karhunen–Loeve expansion. The dominant eigenvectors are subsequently least-squares fitted with orthogonal polynomials to yield an analytical approximation. This compact analytical representation of the random process is then used to derive an exact closed-form solution for the nonstationary response of general linear multidegree-of-freedom dynamic systems.

2 THE ENSEMBLE OF CHI-CHI EARTHQUAKE GROUND MOTION DATA

An ensemble of Chi-Chi earthquake ground motion data was gathered from the extensive seismic network in Taiwan. Specifically, these are records from stations denoted by "TCU" distributed around the Taichung region (in the west coast of the central part of Taiwan) and also records from stations denoted by "HWA," which are from the Hwa-Liang area (east coast).This Chapter presents the results from the 51 TCU stations. Because the records come from a specific geographic region relative to the Chelungpu fault, they are treated as statistically representing the ground motion in that region. It is probably judicious not to mix records from areas that are too varied. A map of the TCU seismic sensor locations in Taiwan is shown in Fig. 1.

A representative sample of some of the time histories used to create the ensemble are shown in Fig. 2. The data was downsampled from the original

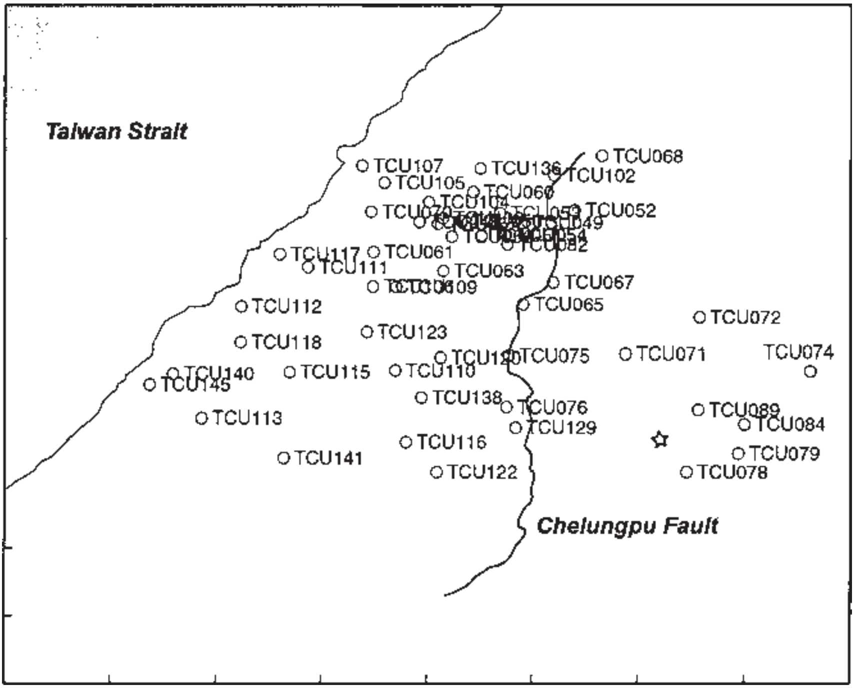

Figure 1 Map indicating the TCU ground motion recording sites relative to the Chelungpu Fault and the Chi-Chi earthquake epicenter.

200 Hz to 50 Hz so that simulations could be run relatively quickly on standard desktop PCs. The duration of the records used to create the ensemble was 60 sec, thus yielding records with 3000 samples. Each of the records was synchronized by a trigger level of 0.1%g in horizontal acceleration at a given station. All three directions of acceleration were included in the ensemble for demonstration purposes. The covariance matrix of the data ensemble is shown in Fig. 3. The nonstationary character of the data set is clearly visible. Using the Karhunen–Loeve expansion, the data was spectrally decomposed. The convergence rate of the 153 nonzero eigenvalues is shown in Fig. 4.

3 CONDENSATION AND ANALYTICAL APPROXIMATION OF EXCITATION DATA

The first stage of the data compaction procedure cited earlier involves the K–L expansion and truncating the series representation to include the most dominant

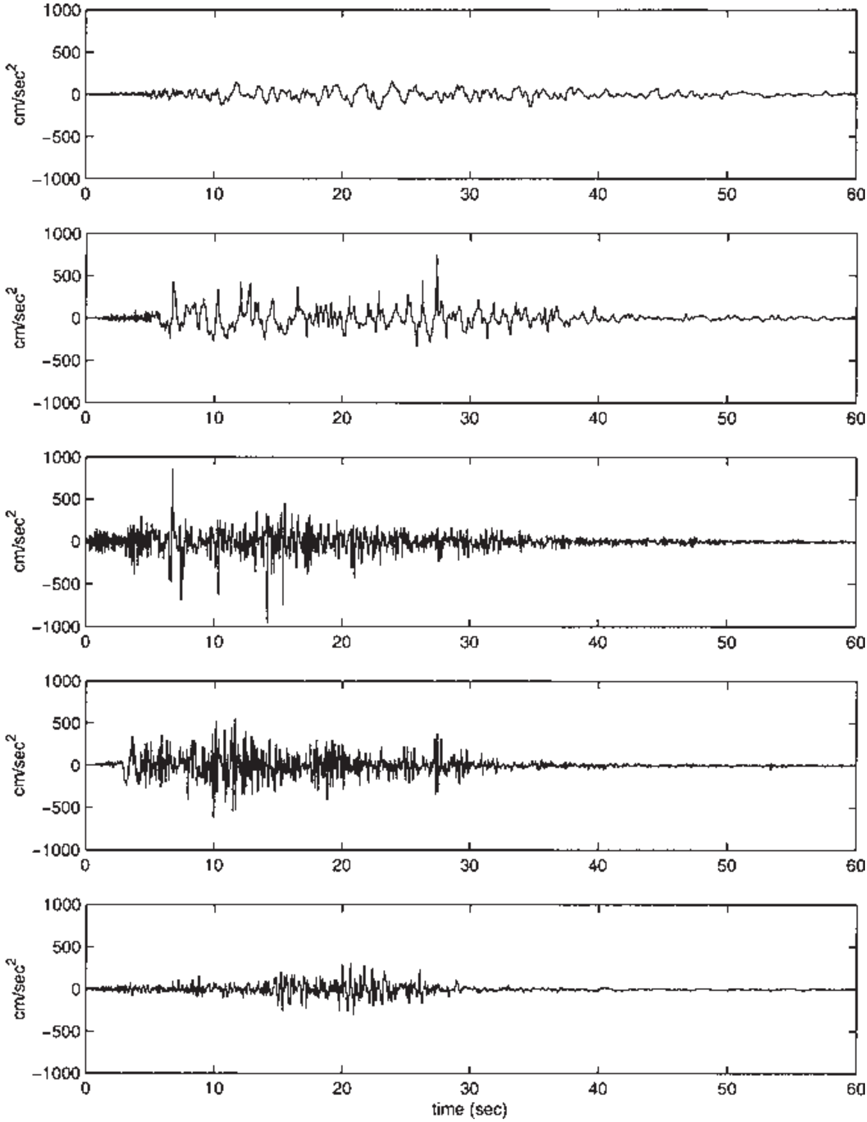

Figure 2 Samples of the TCU recorded ground motion accelerations from the Chi-Chi earthquake.

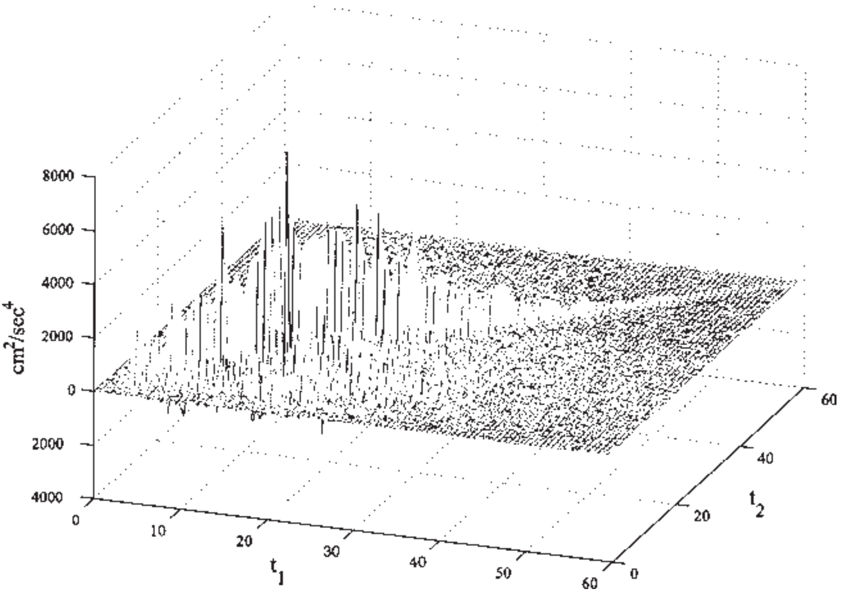

Figure 3 Input covariance matrix of the ground motions from the TCU stations (using 1% and trigger level).

eigenvectors. It was decided that the dominant 60 eigenvectors would constitute the truncated series representation of the covariance matrix. From the eigenvalue convergence rate shown in Fig. 4, it is clear that the first 60 eigenvalues represent a substantial fraction of the input process energy (about 85% of the total input energy). From past experience, the convergence rate improves substantially for large numbers of records, and therefore the ratio of the number of eigenvectors to be included in the truncated series versus the number of data records used to create the ensemble decreases considerably for a given level of energy error. The second stage in the condensation procedure involves the fitting of the eigenvectors with analytical orthogonal polynomial functions (in this case Chebyshev polynomials). Given that the eigenvectors represented 60 sec of relatively high-frequency content, the order of Chebyshev polynomial fitting was chosen to 400. In the case of the 20-sec-duration Northridge data set (Masri et al., 1998) a 200-order fit was deemed sufficient. Fig. 5 shows the fit comparison for the three most dominant eigenvectors. Notice in this figure that for the second and third eigenvectors, which have a substantial high-frequency content, that the 400-order fit is not as good as for the first eigenvector. Therefore, some of

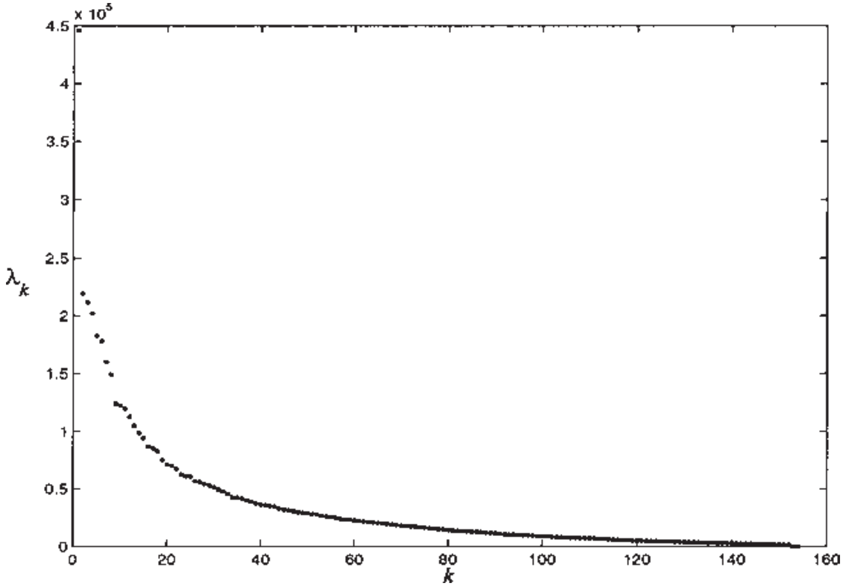

Figure 4 Convergence of the eigenvalues of the covariance matrix composed of the input accelerations.

the higher-frequency energy is being removed from the excitation process, and this would affect results of response simulations for systems with natural frequencies in that range. For a complete discussion and error analysis of the truncation and fitting procedures, see Masri et al. (1998).

4 ANALYTICAL TRANSIENT RESPONSE SOLUTION

Once the excitation process has been condensed into an approximate analytical form, one can quickly obtain the second-order probabilistic description of the transient response of linear multidegree-of-freedom systems (Smyth, 1998). For simple illustration purposes a single-degree-of-freedom system with a natural frequency of 1 Hz and 5% critical damping is considered for response analysis to this excitation process. This example could simplistically represent the dominant modal response of a multistory building. From the closed-form analytical response solution, the response covariance matrix, shown in Fig. 6, is obtained. The diagonal of this matrix represents transient mean-square response of

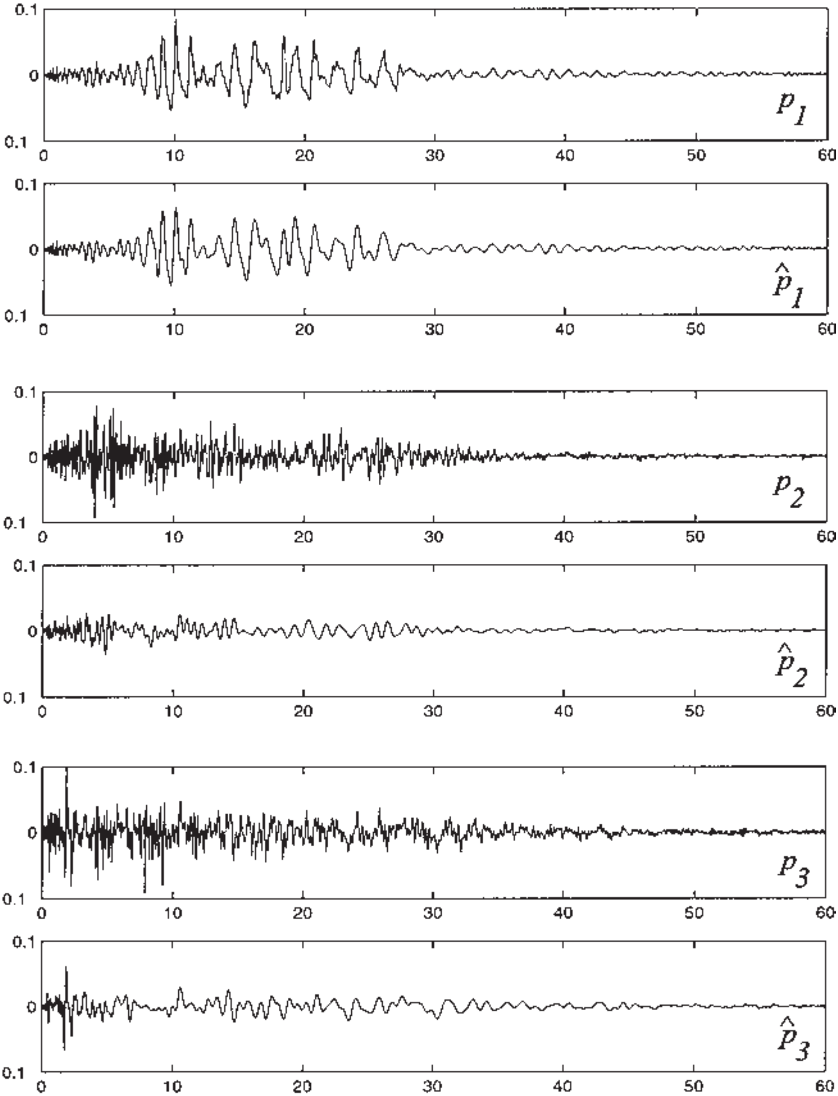

Figure 5 Comparison of the first three analytically approximated $\hat{p}_k$ and the exact eigenvectors p_k of the excitation process covariance matrix. These are ordered corresponding to the magnitude of the corresponding eigenvalue; that is, p_1 represents the eigenvector with the most energy.

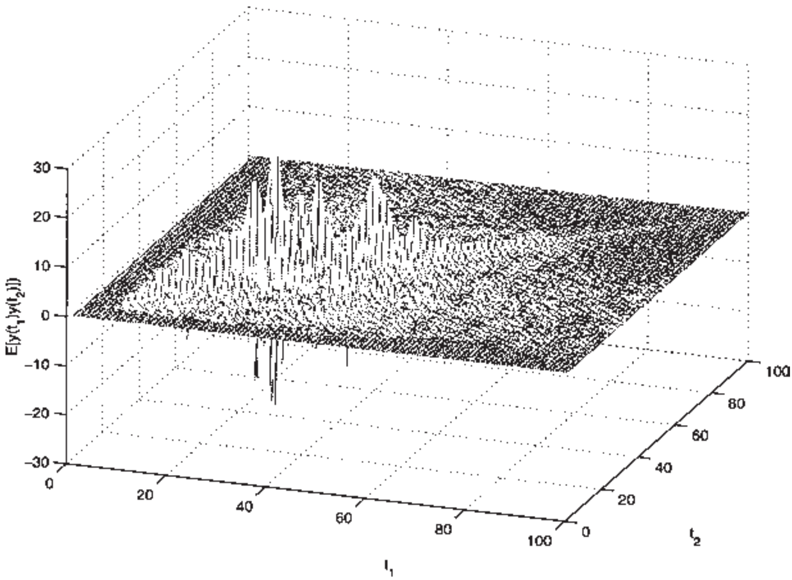

Figure 6 The estimated response covariance matrix for an SDOF system with natural frequency of 1 Hz and 5% critical damping.

the system. A comparison of the analytically estimated result from this procedure is shown in Fig. 7, versus the "exact" mean-square response computed by taking the statistics of the numerically integrated convolution integral for each input record. The "exact" result is therefore obtained effectively by Monte Carlo simulation, where each record is a sample realization of the input process. The accuracy of the method is clearly quite good, despite the acknowledged level of error introduced in the condensation procedure. This type of result can be used to obtain peak response statistics to quickly assess the impact of the event on certain categories of structures. For this same structural system, the peak mean-square response due to the 1994 Northridge earthquake ensemble was about 6.5 cm^2, versus about 37 cm^2 observed here.

5 CONCLUSIONS

A powerful analytical tool, utilizing orthogonal decomposition approaches for extracting the dominant features of a large ensemble of earthquake ground motion records, is applied to a subset of the records obtained from the 1999 Chi-Chi earthquake. The input covariance matrix eigenvalues and eigenvectors are

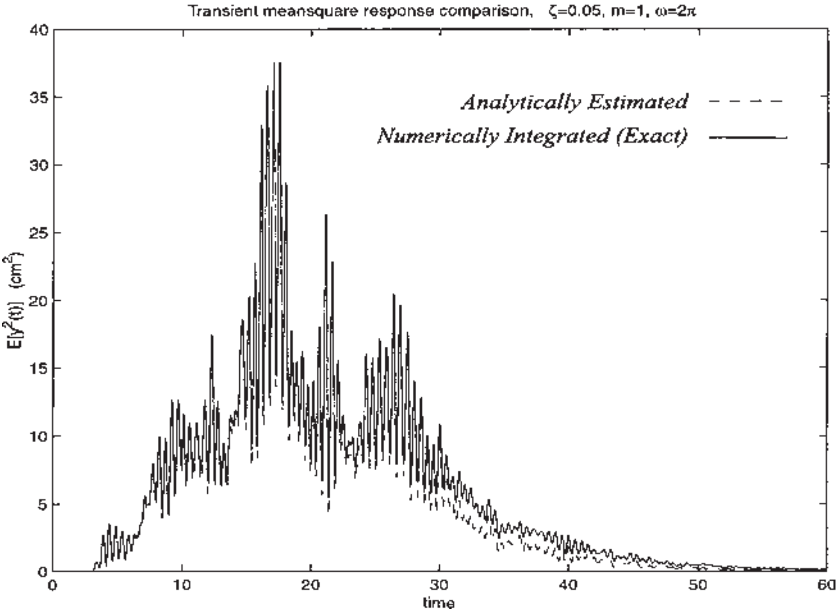

Figure 7 A comparison of the transient mean-square response of an SDOF system to the ensemble excitation process. The "exact" curve is computed by numerically integrating the response for each of the input records, and the dashed estimate curve is obtained through the analytical approximation technique.

determined and subsequently used to obtain the nonstationary mean-square response of linear systems. It is shown that this chapter's approach provides a useful tool for drastic data condensation in a probabilistic format that allows analytical determination of the transient response of structural systems, thus leading to the development of regional probabilistic response spectra. The authors are currently working on a more extensive study utilizing as many data-based ground motion recordings from the Chi-Chi event and its aftershocks as possible.

REFERENCES

SF Masri, RK Miller, M-I Traina. Probabilistic representation and transmission of earthquake ground motion records. *Earthquake Engineering and Structural Dynamics* 19: 1025–1040, 1990.

SF Masri, AW Smyth, M-I Traina. Probabilistic representation and transmission of nonstationary processes in linear MDOF systems. *ASME of Applied Mechanics* 65: 398–409, 1998.

AW Smyth. Experimental and analytical studies in nonlinear system identification and modeling for structural control. Ph.D. thesis, University of Southern California, 1998.

25

A Critical Review of Full-Scale Shaking Table Tests Conducted on Reinforced Soil Retaining Walls

Hoe I. Ling
Columbia University, New York, New York, U.S.A.

1 INTRODUCTION

Results from several small-scale shaking table tests have been reported in the literature. Most of them were conducted in Japan because of the availability of testing facilities and also because seismic consideration is a stringent design requirement in Japan. The most notable tests were that of the Japan Railway Technical Research Institute (Murata et al., 1994) and the Public Works Research Institutes (Matsuo et al., 1997). Both institutions conducted a series of model tests in establishing design specifications for the then Ministry of Transportation (railways) and Ministry of Construction (highways), respectively. The results were used to verify limit equilibrium design procedures. The above tests were limited to the Japanese version of reinforced soil structures. Koseki et al. (this volume) conducted an additional study on reinforced soil walls following the Kobe earthquake.

Matsuo et al. (1997) conducted reinforced soil models mostly of height 1 m having five cases of discrete panel wall facing and one case of continuous facing. The length of reinforcement was 40% of the height, with one case of a ratio of 0.7. The vertical spacing was 20 cm. The models were subjected to a sinusoidal wave ranging from 55 to 625 gal, having a frequency of 5 Hz. There was a case where a real earthquake record was used with an amplitude of 506 gal.

In North America, several shaking table tests have been conducted on modular block walls at the Royal Military College (RMC) Canada (e.g., Bathurst et al., 1997). The shaking table tests conducted at RMC were models of a modular block wall. The models were 240 cm long, 140 cm wide, and 102 cm high. Concrete blocks of dimensions 10 cm by 16 cm by 3.4 cm were used. The backfill soil was a silica sand that has a relative density of 67%. The reinforcement was an HDPE geogrid. The connection between the blocks was frictional or fixed, where as the block–geogrid interface was mostly frictional. The input acceleration was increased in several stages with a frequency of 5 Hz until it reached 0.35 g. The outward displacement of the facing was compared for four different models that had different combination of block–block and block–geogrid interfaces.

It has to be noted that because of the size of the shake table facilities, reduced modular blocks and reinforcements were used. However, these tests were possibly subject to scale and stress-level effects. Full-scale shaking table test for a wall above 5 m, for example, is almost impossible and not affordable because of the high cost in addition to lack of availability of test facilities. Japan has two shake tables that may accommodate a full-scale wall of 5 m and above. The two shake tables are available at the National Research Institute for Earth Science and Disaster Prevention (NIED) and the Building Research Institute (BRI), respectively. This chapter reviews the test results conducted on these two shake tables. A brief review for the Japan Railway shake table test is also included. Some general conclusions pertaining to the performance of these walls are made.

2 REINFORCED EARTH WALL

A full-scale reinforced soil wall, 6 m high, was conducted for the metallic reinforcement by the Building Research Institute using the shaking table facilities available at the National Research Institute for Earth Science and Disaster Prevention (Futaki et al. (1996)). The resonance frequency and response were determined at several different heights: 2.5 m, 3.5 m, 4.5 m, and 6.0 m. The wall was designed based on specifications to have a vertical spacing of 1.2 m, but the length of reinforcement was not reported. The wall was constructed inside a laminar box (or shear box) 3.0 m wide, 9.5 m long, and 6.0 m high. The box, which has a series of frictionless stacked rings of H-frames, eliminates the boundary effects at the end of the backfill. The grease was used to eliminate side friction between the wall and backfill.

Standard metallic reinforcements, concrete facing panels, and connections were used. The backfill soil is a silty sand that has 19% fines. The angle of friction was 34.4°. The dynamic properties of the sand (Young's modulus at small strain levels) were measured. The soil was compacted at a degree of compaction of 87% such that the unit weight was 13.4 kN/m^3.

The acceleration was applied through sweep sine wave and step wave at different wall heights (Tables 1 and 2). The sweep test was used to determine the resonance frequency of the wall. In the step tests, the acceleration was applied through several steps but the increment was not reported. The Taft earthquake record (EW component) was used as the input wave when the wall attained its final height.

The wall was well instrumented (Fig. 1). The earth pressure transducers were used at the bottom of the wall and the base of the backfill. The accelerometers were installed in the backfill and on the reinforcement strips. Tensile strains in the reinforcement layers and displacement in front of the wall were also measured.

The "static" earth pressure recorded in the reinforcement was larger than that predicted using the earth pressure theory, which could be attributed to compaction effect (see Fig. 2a). With the shaking, the earth pressure increased following an increase in the input acceleration (Fig. 2b).

The resonant frequencies of the wall at different heights are shown in Fig. 3a. It is seen that the resonant frequency reduced with the increase in height, and it was 3.5 Hz at the full height of 6 m. Significant phase difference between acceleration at resonance, as large as 7, was seen between the bottom and surface of the backfill as the base acceleration exceeded 150 gal.

An identical acceleration response was recorded in the backfill and in the reinforcement. Note, however, that the accelerations were inside the reinforced zone. During shaking, the vertical stress at the bottom of the backfill increased. The acceleration amplification of the wall during shaking is shown in Fig. 3b. The accelerations in the backfill, concrete facing, and the reinforcement were slightly different, but all amplified toward the surface of the backfill. The amplification ratio was greater than 3 when the input acceleration exceeded 150 gal (0.15 g).

Table 1 Input Acceleration During Testing for Reinforced Soil Wall

Wall Height (m)	Sweep test	Step test*	Input earthquake
2.5	0.5–8 Hz (49 gal)	2 Hz (35–145 gal)	–
3.5	0.5–10 Hz (38 gal)	2 Hz (42–145 gal)	–
4.5	1.0–10 Hz (46 gal)	2 Hz (67–203 gal)	–
6.0	1.0–10 Hz (46 gal)	2.3 Hz (35–178 gal)	Taft (EW), 112–220 gal

Source: Futaki et al., 1996.

*No information given about the increment of acceleration.

Table 2 Input Acceleration During Testing of Multianchored Retaining Wall

Wall height (m)	Sweep test	Step test*	Input earthquake
3	0.5–10 Hz (20 gal)	1.5, 2 Hz (50–150 gal)	–
4	0.5–10 Hz (20 gal)	1.5, 2 Hz (50–150 gal)	–
5	0.5–10 Hz (20 gal)	1.5, 2 Hz (50–150 gal)	Taft (EW) 180 gal

Source: Aoyama et al., 2000.
*No information given about the increment of acceleration.

The displacement at the top of facing was 25 mm for an input acceleration of 150 gal. It was symmetrical in the front and back of the facing. Residual deformation was rather small, in the order of a few mm (Fig. 4).

The tensile stress in the reinforcements under static and seismic loading conditions is shown in Fig. 5. The stress increased in response to the seismic loading. The exact magnitude was not reported in Futaki et al. (1996).

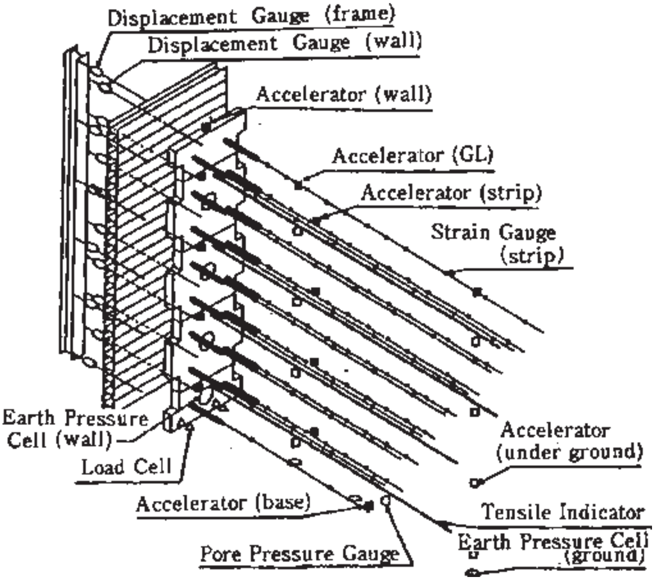

Figure 1 Instrumentation layout. (From Futaki et al., 1996.)

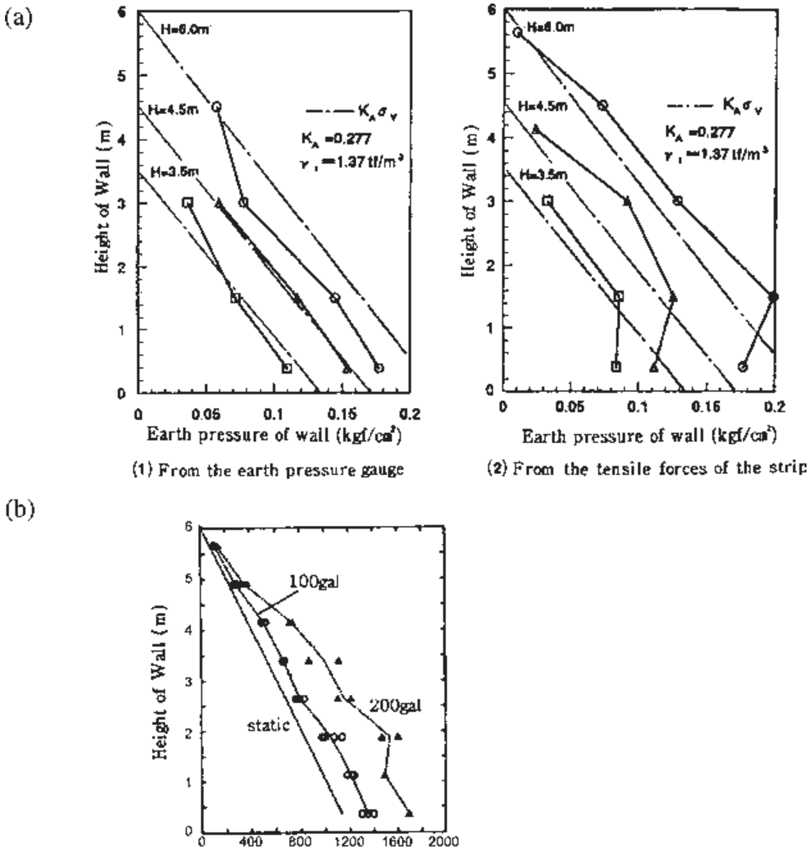

Figure 2 Earth pressure: (a) Static conditions; (b) seismic conditions. (From Futaki et al., 1996.)

3 MULTIANCHORED REINFORCED SOIL WALL

This information comes from Futaki et al. (2001), Aoki et al. (2000), and Futaki et al. (2000). Part of the information given below was extracted from the Japanese version of the papers.

Figure 6 shows the multianchored reinforced soil wall with its different components. This wall system was developed in Japan. The appearance of the multianchored reinforced soil wall is very similar to the conventional reinforced soil wall, but there is a fundamental difference in the reinforcement mechanism. Because an anchor plate is attached to the end of metallic strip, the mechanism of reinforcement is anchorage instead of frictional.

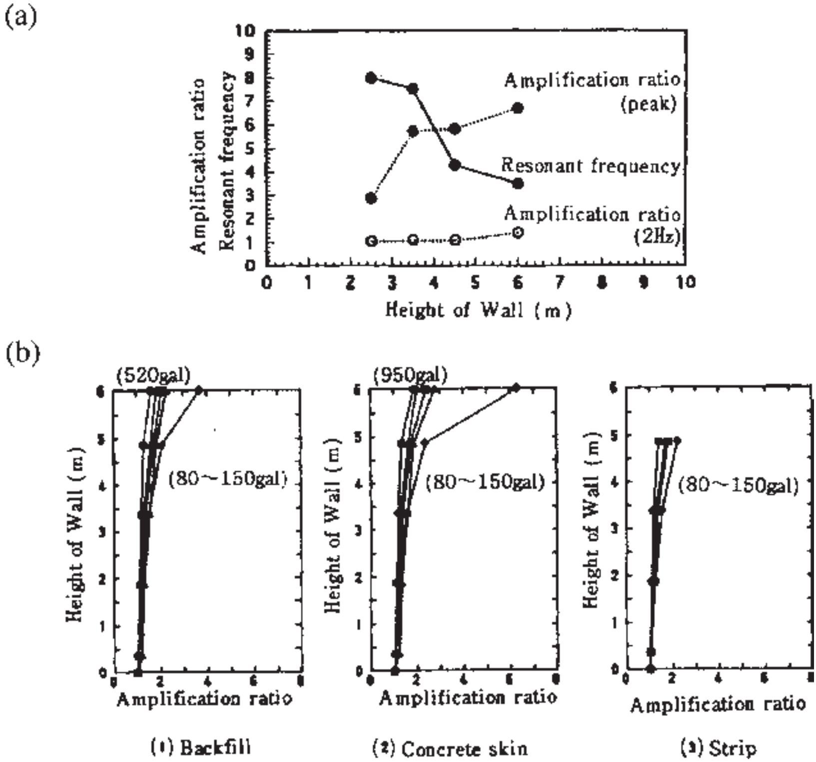

Figure 3 Acceleration amplification: (a) at resonant frequency; (b) during shaking. (From Futaki et al., 1996.)

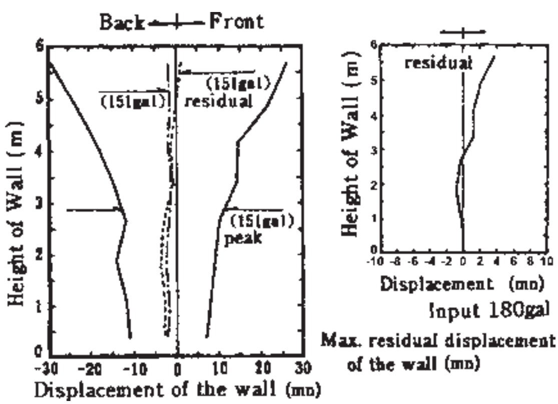

Figure 4 Horizontal displacement during shaking and residual displacement. (From Futaki et al., 1996.)

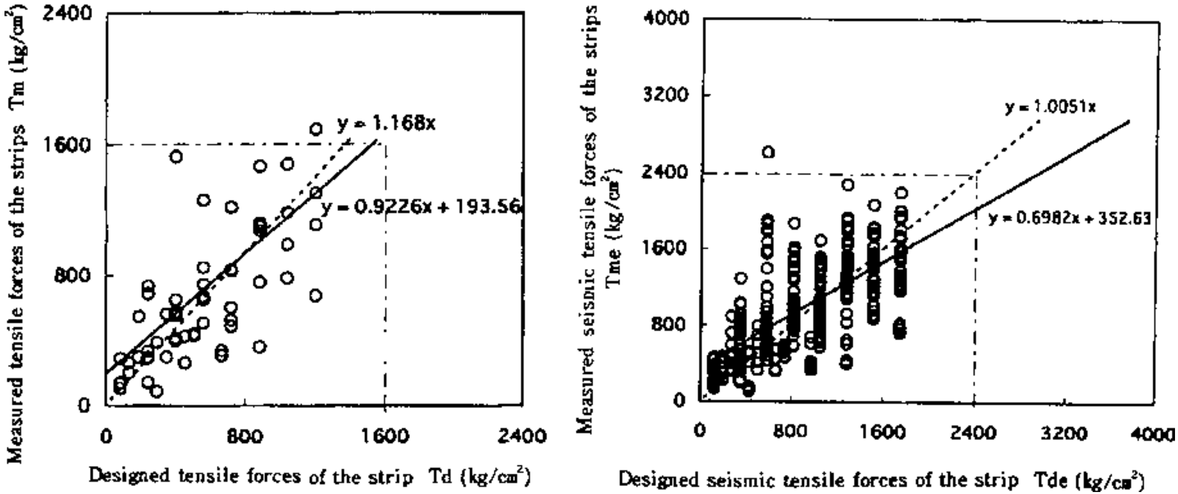

Figure 5 Comparison of tensile stress in the reinforcement under (left) static loading and (right) seismic loading. (From Futaki et al., 1996.)

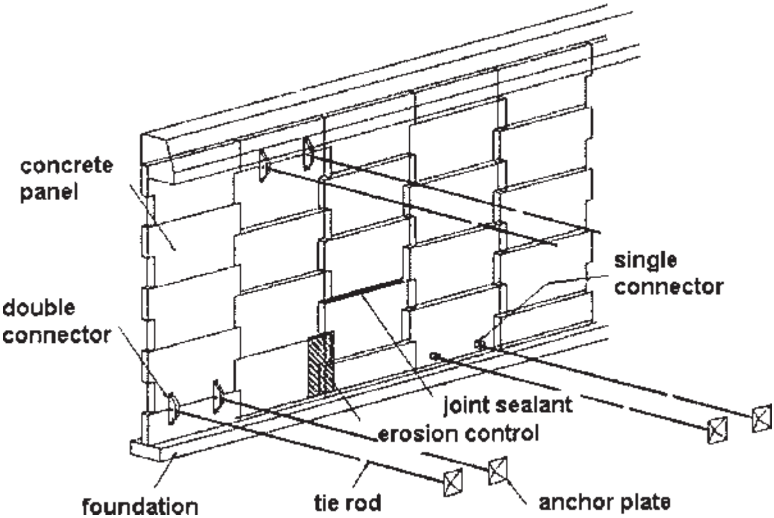

Figure 6 Multianchored reinforced soil wall.

The shaking table test was conducted using the facilities available at the Building Research Institute. The full-scale 5-m wall was constructed in a laminar box 3.6 m wide, 10 m long, and 5 m high. The tie bars were 3.5 m long. Fig. 7 shows the instrumentation of the wall where several different quantities were measured: horizontal and vertical forces at the bottom of the wall panels; vertical stress at the bottom of the backfill soil; tensile strain in the tie bars; acceleration in the panel; reinforced soil zone; displacements of the wall panel and backfill surface.

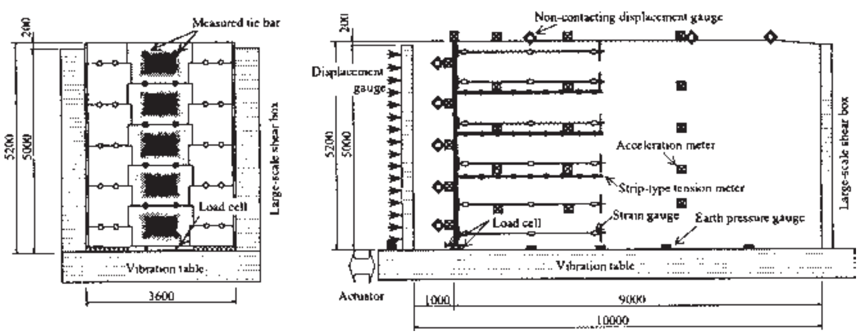

Figure 7 Testing setup and instrumentation of multianchored reinforced soil wall. (From Futaki et al., 2001.)

The sand used in this test was different from the previous wall. It was a sand with a fines fraction of 7%. The sand was compacted in 50 cm lifts. The average degree of compaction was 83%. The measured angle of friction was 32.8°. However, based on the Japanese version of the papers, the authors used an angle of 35° in design, yet in the comparison of test results as shown subsequently, they used a value of 30°. The seismic coefficient used in the design was 1.5, but the factors of safety were all larger than unity (pullout = 8.94, sliding = 1.75, rupture of tie bars = 1.87).

Similar to the previous wall, sweep vibration tests and step vibration tests were conducted at different heights of the wall: 3 m, 4 m and 5 m. The results of

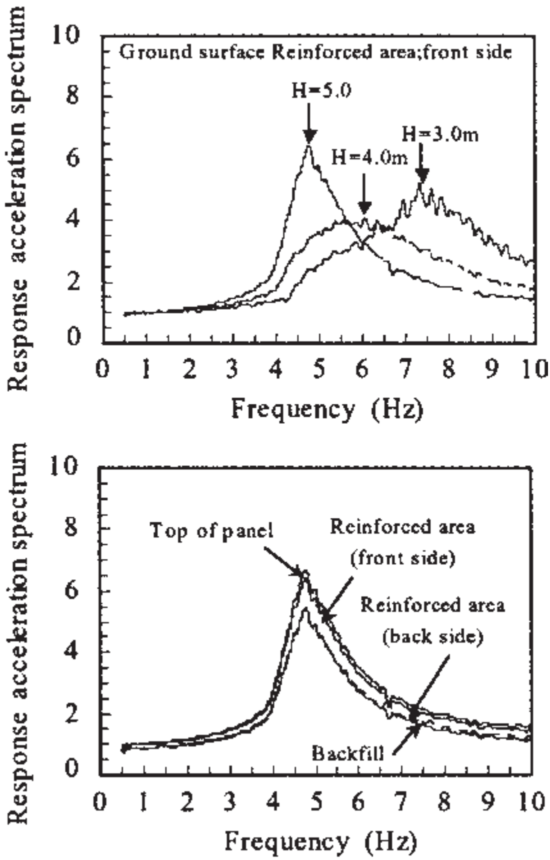

Figure 8 Results of sweep tests. (From Futaki et al., 2001.)

the sweep tests are shown in Fig. 8 for the wall at the heights of 3 m, 4 m, and 5 m. As the height increased, the resonant frequency reduced. The bottom figure shows that the wall panel and reinforced and backfill zones behaved as a coherent mass. There was, however, a phase difference between the three components of the wall, from 45° to 270°. The amplification of the wall was found to be dependent on the magnitude of input acceleration (Fig. 9).

The distribution of tensile force in the reinforcement is shown in Fig. 10. The increment due to shaking was less than the design value (note: the design value of soil friction angle was less than the measured value).

The pressure at the bottom of the backfill varied with the acceleration. The variation was the largest below the panel. The residual horizontal displacement and amplitude of displacement of the panel are shown in Fig. 11. At an acceleration of 420 gal, the amplitude was 50 mm.

Cracks were observed in the backfill surface behind the reinforcement zone (Fig. 12). The cracks were reported to be corresponding to the Coulomb wedge. Note, however, that an angle of internal friction of 30° was used in the calculation. The measured settlement of the backfill, also indicated in the figure, was between 10–15 cm.

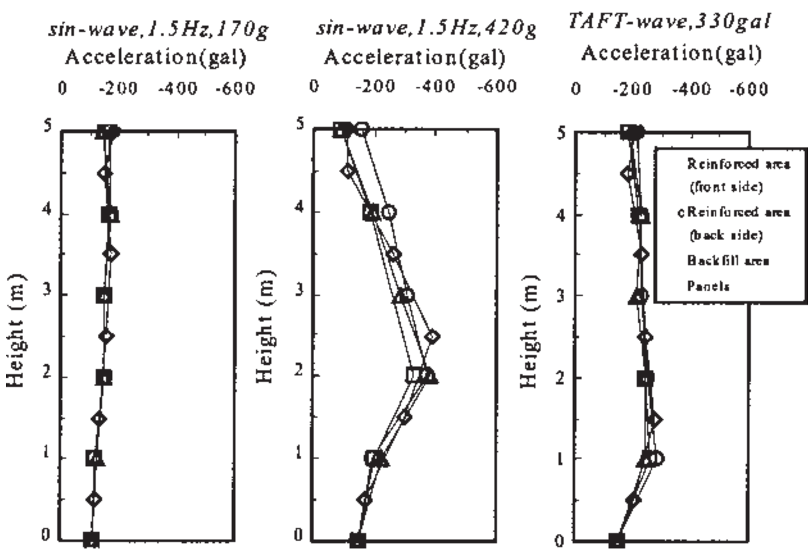

Figure 9 Amplification of acceleration. Note that accelerations are measured maximum average accelerations. (From Futaki et al., 2001.)

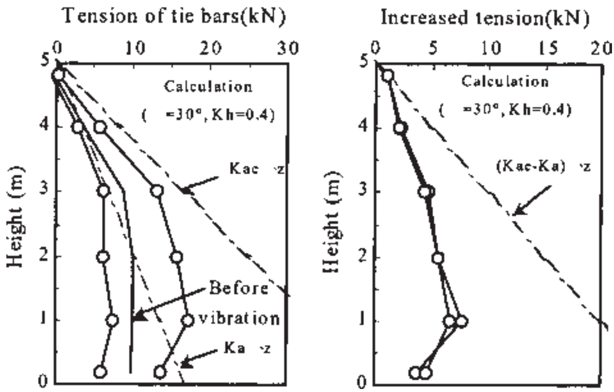

Figure 10 Distribution of tensile force in reinforcement. (From Futaki et al., 2001.)

4 JR WALL

The Japan Railway Technical Research Institute constructed a half-scale model shaking table test for the wall system that has a rigid facing and short reinforcement (Murata et al., 1994). Fig. 13 shows the test setup. The wall was 2.5 m high and 3.5 m wide. The backfill sand had a mean diameter of 0.2 mm, of dry unit weight 16 kN/m^3, and 16% fines. It was constructed on a medium loose foundation. A geogrid of strength 10 kN/m, which was one third of the prototype,

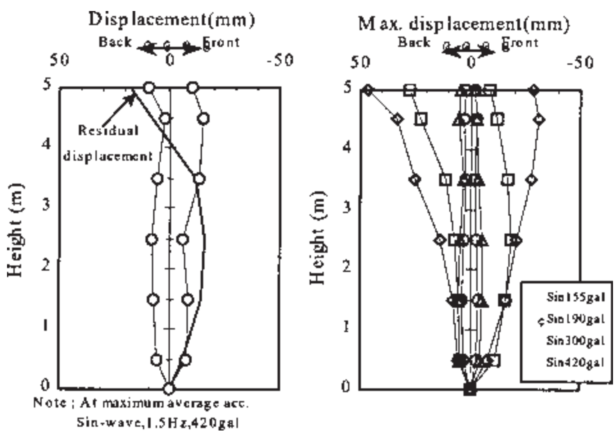

Figure 11 Horizontal displacement of wall panels. (From Futaki et al., 2001.)

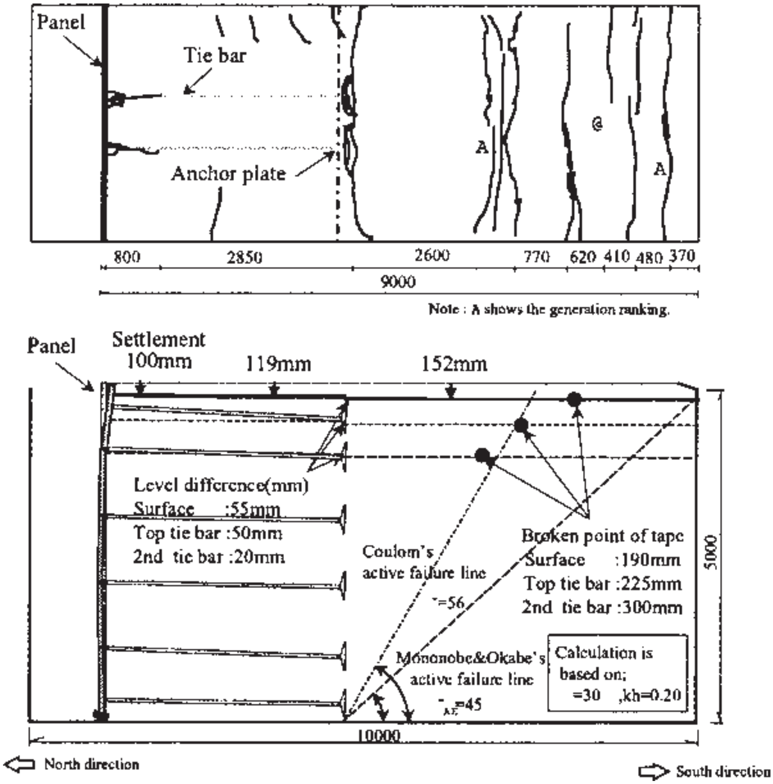

Figure 12 Cracking in backfill surface. (From Futaki et al., 2001.)

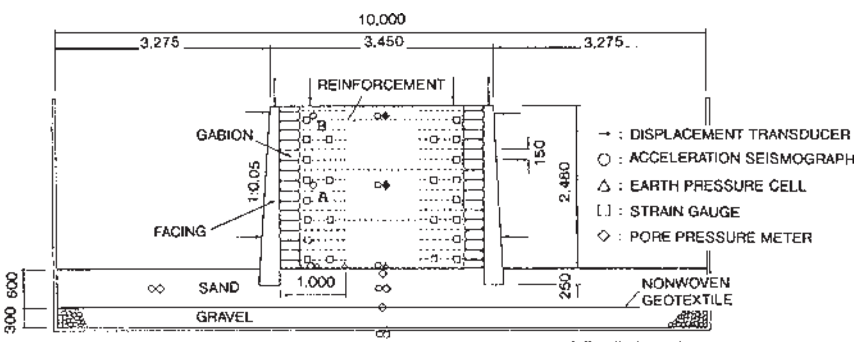

Figure 13 Test setup and instrumentation for JR wall. (From Murata et al., 1994.)

was used. The reinforcement layers were 40% of the wall height, but similar to field construction, a few layers were tied to the opposite side of the wall.

The wall was subject to three phases of shaking: A, B, and C. In A, the acceleration (3.4 Hz, 20 sec duration) was applied in nine stages, in nine stages, from 100 gal to 500 gal with an increment of 50 gal. In B, a real Japanese earthquake record was used, whereas in C, the accelerations of 200 gal and 400 gal were applied after saturating the foundation.

The test results indicated almost no amplification of acceleration up to mid-height of the wall (Fig. 14). The horizontal displacement of this wall was very small during shaking, less than k1 cm (Fig. 15), because it was developed to

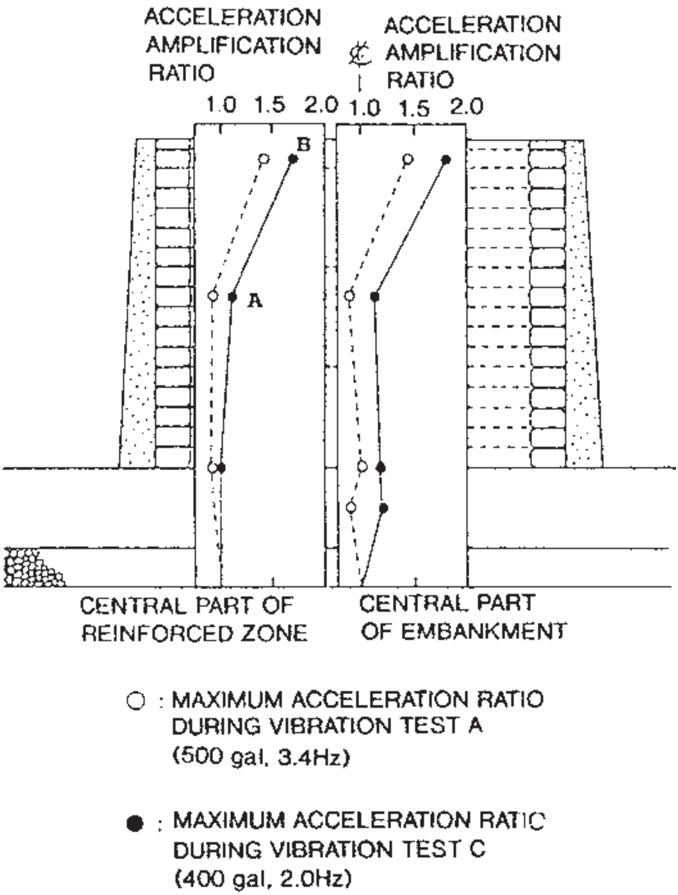

Figure 14 Amplification ratio in JR wall. (From Murata et al., 1994.)

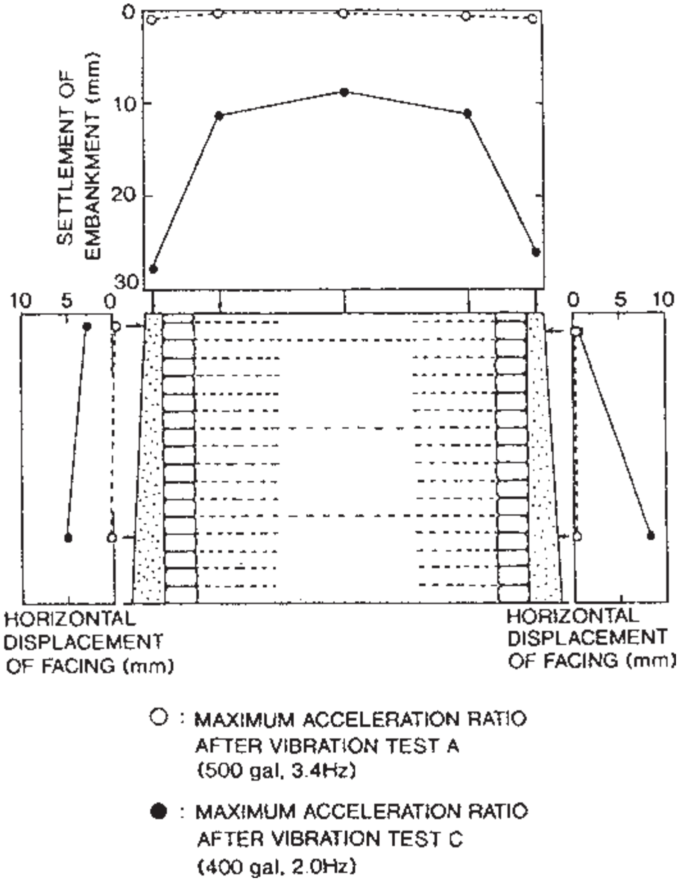

Figure 15 Deformation of JR wall. (From Murata et al., 1994.)

minimize deformation for use in the railway structure. At the surface of the backfill, the amplification ratio was about 1.5. The vertical stress under the reinforced zone showed a nonuniform distribution because of the overturning mode of deformation (Fig. 16).

5 PWRI WALL (NONSEISMIC, NONMODULAR BLOCK WALL)

This was one of the very few well-instrumented full-scale walls. It was constructed by the Public Works Research Institute in Japan. The wall was fully instrumented and subsequently failed by cutting the geosynthetic layers in stages

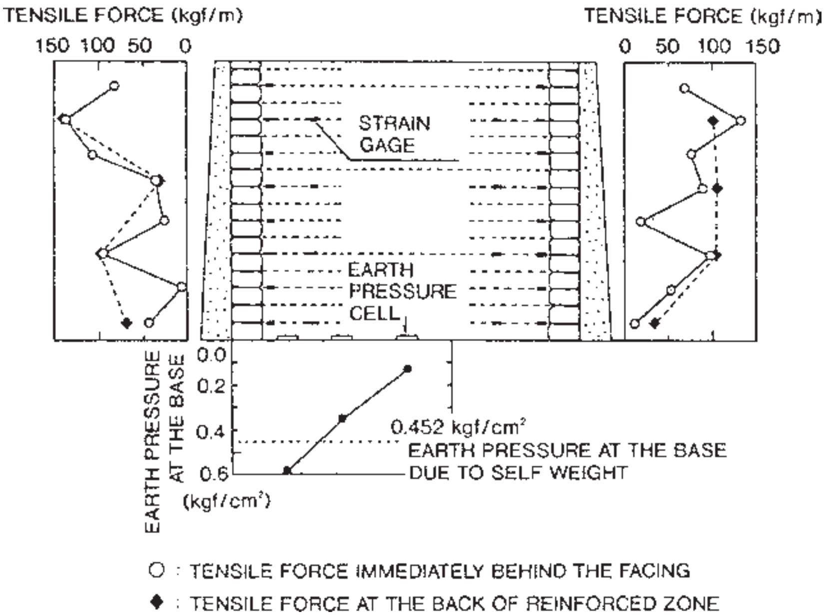

Figure 16 Maximum reinforcement force and vertical stress distribution. (From Murata et al., 1994.)

(Miyatake et al., 1995; Tajiri et al., 1996). The material properties of soils and geosynthetics were well defined. The geometry of the PWRI wall is shown in Fig. 17. It was 6 m high and 5 m wide, constructed in a concrete test pit on a concrete floor. The sides of the wall were lubricated using grease and polymer sheets. A silty sand ($D_{50} = 0.42$ mm, $\gamma = 16.0$ kN/m^3) was used as backfill. The stress–strain properties of the sand were also measured and reported by Ling et al. (2000).

A uniaxial geogrid (Tensar SR55), manufactured from high-density polyethylene (HDPE), was used as reinforcement. The spacings between the longitudinal and transverse ribs were 2.2 cm and 16.6 cm, respectively. The strength of the geogrid was 55 kN/m. The PWRI wall consisted of six primary and five secondary geosynthetic layers, each 3.5 m and 1.0 m long, respectively. The geosynthetic layers were bolted to the concrete blocks with the bolts and metal frame as shown in Fig. 17. (Note: Because of this bolting connection, it is considered different from the modular block wall.) A total of 12 concrete blocks was used along the wall height. Each block was 50 cm high and 35 cm wide, except the top and bottom blocks, which were 45 cm and 55 cm high, respectively.

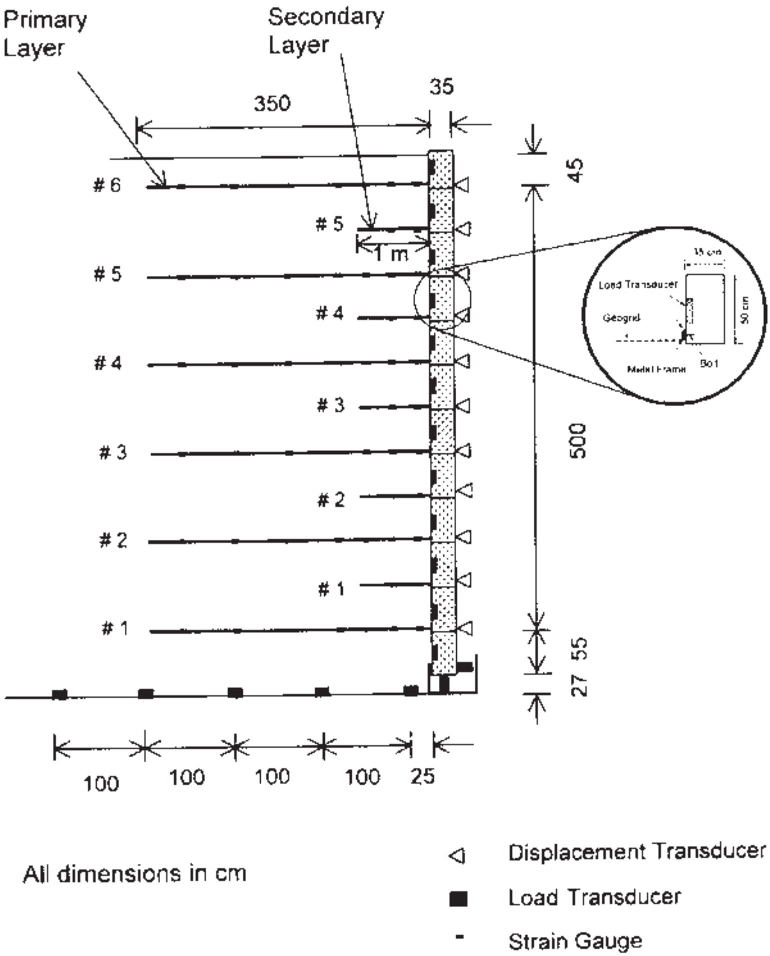

Figure 17 Experimental setup instrumentation of PWRI wall. (From Ling et al., 2000.)

A total of 52 strain gauges were used to measure the elongation of the geogrid, that is, 7 and 2 strain gauges on each layer of primary and secondary reinforcements, respectively. The horizontal displacement of the wall face was measured at 11 locations. The lateral load acting on the facing blocks was measured using 11 load transducers installed in the mid-height of each concrete block. The vertical and horizontal loads acting at the toe of the facing were also measured using load transducers. The vertical load due to the backfill soil was measured at six locations along the base of the soil mass.

Ling et al. (2000) conducted finite-element analysis to simulate the construction response of this wall. Nonlinear elastic behavior of soils and reinforcement, as well as the blocks–backfill soil and block–block interactions, was simulated. Ling et al. compared the wall deformation, vertical and lateral stresses along the wall face, and strains in the geogrid layers. The procedure was able to give satisfactory agreement between the measured and analyzed results. A series of parametric studies was also conducted (Ling and Leshchinsky, 2001).

There were several interesting findings from the measured and analyzed results of this wall.

1. The study confirmed high stress concentration at the connection between the geosynthetic layers and modular blocks (Fig. 18), including the secondary reinforcement layers. Note that in a separate parametric study, the frictional connection was used instead of the bolting connection.
2. The results also showed nonuniform vertical stress distribution at the bottom of the backfill, and it is the greatest at the bottom of the blocks. The nonuniform stress can be simulated in the analysis by considering the foundation soil instead of treating concrete floor as rigid.
3. The lateral stress measured in the concrete facing blocks was less than that in the soil, and the earth pressure coefficient was between that of the active and at-rest conditions.

6 GENERAL CONCLUSIONS FROM LARGE-SCALE SHAKING TABLE TESTS

An important conclusion that may be derived from the performance of reinforced soil is that the amplitude of lateral displacement exceeding 50 mm (corresponding to an earthquake with horizontal acceleration of 400 gal) is considered excessive depending on the types of application. If the bridge rests directly on the reinforced soil structure, dislocation of the bridge span is expected. In addition, an amplification ratio of 3 or greater will induce additional stresses to the superstructure.

The comparison between the seismic performance and design is somehow inconclusive because of the lack of details in evaluating the soil properties. For example, the measured and design values of the angle of internal friction and the value used for evaluation were slightly different.

The result related to full-scale modular block walls is lacking. The 6-m wall constructed in Japan was not a truly modular block wall because of the different connection mechanism between the wall and reinforcement. Besides, information

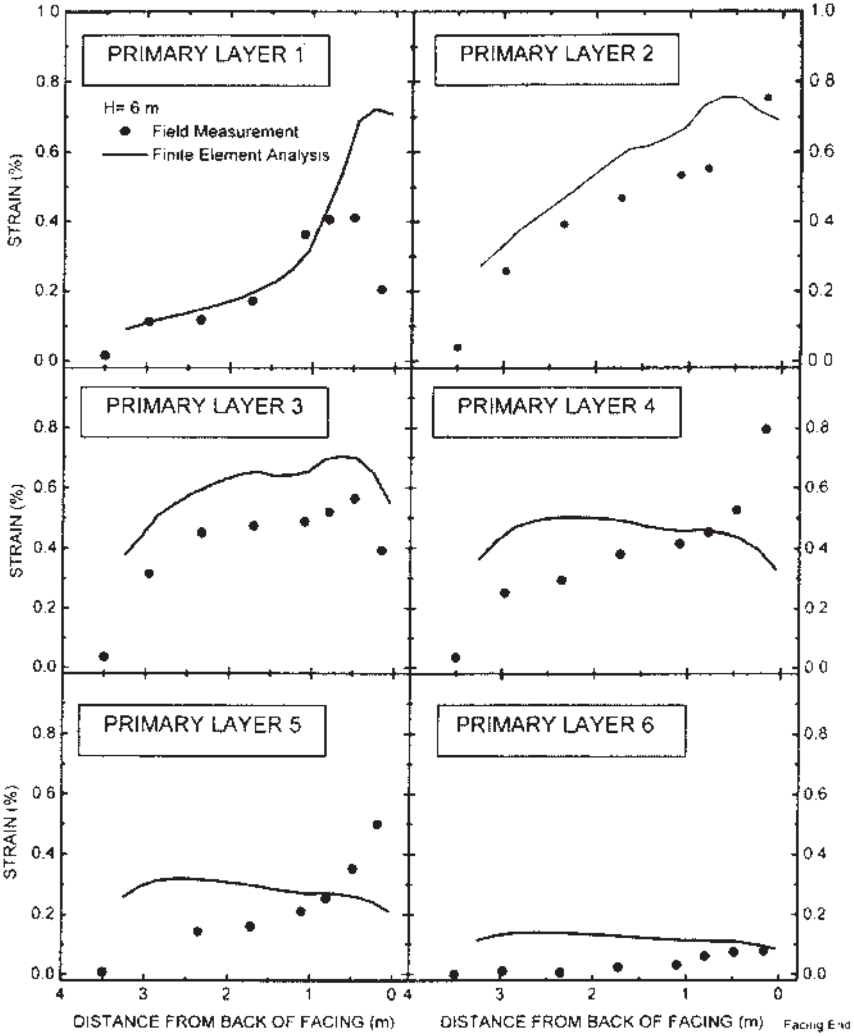

Figure 18 Tensile stress distribution in reinforcement at full height. (From Ling et al., 2000.)

that may be relevant for other analysis, such as creep and relaxation, is lacking. This kind of information would be highly required for predicting time-dependent behavior of geosynthetic on wall performance.

The wall facing contributed to a better performance, in terms of deformation and acceleration response. A rigid facing performed better than the discrete wall panel. This was consistent with the results of static tests as presented by Tatsuoka et al. (1989). The performance of modular block walls that now comprise a large portion of highway applications in the United States is not readily known.

For the purpose of validating numerical procedures and centrifuge models, additional test results should be made available in the public domain. No data are available on the shaking table tests conducted in Japan. For the PWRI wall, the author has managed the data and is making it available to the public through the web site.

Around the time of this book's publication, a study of three full-scale modular-block reinforced soil walls of height 3 m was conducted (Ling and Leshchinsky, 2003).

REFERENCES

N Aoyama, N Kikuchi, T Konami, K Mikami. Actual Size vibration test on the multianchored retaining walls with large scale shear box (Part 1). *Proc. 35* th *Geotechnical Eng. Conf*. Gifu, Japan, pp 2213-2214, 2000 (in Japanese).

RJ Bathurst, Z Cai, M Alfaro, M Pelletier. Seismic design issues for geosynthetic reinforced segmental retaining walls. In *Mechanically Stabilized Backfill*. Wu, ed. Rotterdam, Netherlands: Balkema, 1997, pp 79–97.

M Futaki, N Ogawa, M Sato, T Kumada, S Natsume. Experiments about seismic performance of reinforced earth retaining wall. *Proc. World Conf. on Earthquake Eng* Elsevier Science, Ltd, 1996.

M Futaki, K, Misawa, T Tatsui. Actual size vibration test on the multianchored retaining walls with large scale shear box (Part 2). Proc. 35th Geotechnical Eng. Conf. Gifu, Japan 2215-2216, 2000 (in Japanese).

M Futaki, N Aoyama, K Misawa, T Konami, M Sato, T Tatsui, K Mikami. Dynamic behavior of multianchored reinforced soil wall in large-scale shear box. In *Landmarks in Earth*. H Ochiai, J Otani, N Yasufuku, K Omine, eds. Balkema, 2001.

HI Ling, C Cardany, L-X Sun, H Hashimoto. Finite element analysis of a geosynthetic-reinforced soil retaining wall with concrete-block facing. *Geosynthetics International* 7(2): 137–162, 2000.

HI Ling, D Leshchinsky. Parametic studies of the behavior of segmented block reinforced soil retaining wall. *Geosinthetics International* 2003.

HI Ling, D Leshchinsky, Y Mohri. Full-scale shaking table tests of reinforced soil retaining walls with Allan blocks and Huesker geogrids. Department of Civil Engineering and Engineering Mechanics, Columbia University, New York, New York (unpublished report).

O Matsuo, T Tsutsumi, K Yokoyama, Y Saito. Shaking table tests and analyses of geosynthetic-reinforced soil retaining walls. *Geosynthetics International* 5(1-2): 97–126, 1998.

H Miyatake, Y Ochiai, S Maruo, A Nakane, M Yamamoto, T Terayama, T Maejima, Y Tsukada. Full-scale failure experiments on reinforced earth wall with geotextiles (Part 2)—Facing with concrete blocks. *Proc. 30th*: 2427–2430, 1995.

O Murata, M Tateyama, F Tatsuoka. Shaking table tests on a large geosynthetic-reinforced soil retaining wall model. In *Recent Case Histories of Permanent Geosynthetic–Reinforced Soil Retaining Walls*. *Recent Case Histories of Permanent Geosynthetic–Reinforced Soil Retaining Walls*, Tatsuoka and Leshchinsky, eds, Balkema, Tatsuoka, Leshchinsky, eds. Balkema, 1994, pp 259–264.

N Tajiri, H Sasaki, J Nishimura, Y Ochiai, K Dobashi. Full-scale failure experiments of geotextile-reinforced soil walls with different facings. In *Earth Reinforcement*. Ochiai, Yasufuku, Omine, eds. Rotterdam: Balkema, 1996, pp 525–530.

F Tastuoka, M Tateyama, O Murata. Earth retaining with a short geotextile and a rigid facing. *Proc. 12th*: 1311–1314, 1989.